Airborne Laser Hydrography II

(Blue Book II)

William Philpot, editor

TABLE OF CONTENTS

ACKNOWLEDGEMENTS ..... **v**
FOREWORD ..... **vi**
1 INTRODUCTION **1**
2 HISTORY **5**
2.1 AUSTRALIA 5
2.1.1 Early systems and developments 5
2.1.2 Current status 8
2.2 CANADA 9
2.2.1 Early systems and developments 9
2.2.1 Current status 10
2.3 UNITED STATES 11
2.3.1 Early Systems and developments 11
2.3.2 Current status 13
2.4 SWEDEN 15
2.4.1 Early systems and developments 15
2.4.2 Current status 16
2.5 AUSTRIA 17
2.5.1 Early systems and developments 17
2.5.2 Current status 18
2.6 REFERENCES 18
3 ENVIRONMENTAL OPTICAL PROPERTIES **25**
3.1 ATMOSPHERE 25
3.1.1 Atmospheric attenuation of the bottom and water return signals 25
3.1.2 Atmospheric backscatter signal 27
3.2 WATER SURFACE 29
3.2.1 Reflection and refraction 29
3.2.2 Effects of waves 31
3.2.3 Bubbles and foam 32
3.3 VOLUME 34
3.3.1 Apparent Optical Properties (AOPs) 34
3.3.2 Inherent optical properties 35
3.4 BOTTOM 41
3.4.1 Morphology 42
3.4.2 Color 43
3.4.3 Vegetation 44
3.5 REFERENCES 46
4 BASIC CONCEPTS AND SYSTEM DESIGN **53**
4.1 BASIC SYSTEM DESIGN – AN OVERVIEW 53
4.1.1 Transmitter unit 54
4.1.2 Scanner unit 54
4.1.3 Detector unit 56
4.1.4 Auxiliary systems for ALB performance and geo-referencing. 58

4.2 BASIC PHYSICAL CONCEPTS 58
4.2.1 Propagation geometry 58
4.2.2 Return waveform 62
4.3 BASIC SYSTEM DESIGN – AN OVERVIEW 67
4.3.1 Transmitter unit 67
4.3.2 Scanner unit 68
4.3.3 Detector unit 70
4.3.4 Auxiliary systems for ALB performance and geo-referencing. 71
4.4 MODEL OF THE LIDAR WAVEFORM 72
4.4.1 Receiver channel model 72
4.4.2 Improved small-angle-scattering models of lidar waveform components 76
4.4.3 Lidar waveform simulator 93
4.5 LIDAR SYSTEM CALIBRATION AND ALIGNMENT 109
4.5.1 Introduction: channel characteristics employed in waveform simulation and processing 109
4.5.2 Calibration measurements using the built-in system laser source 109
4.5.3 Calibration measurements with a continuous wave (CW) laser source 111
4.5.4 Practical realization of calibration measurements: Radiometric calibration of the SHOALS-1000 111
4.6 IMPLEMENTATION OF EYE SAFETY REQUIREMENT 116
4.6.1 Safe Operating Altitude 117
4.6.2 ALB Eye Safety Features 118
4.7 BATHYMETRIC SYSTEM DESIGN AND OPTIMIZATION OF PARAMETERS 119
4.7.1 Optimization criteria of bottom, scattering layers and objects detection 119
4.7.2 Concept and use of the *D*-index of discriminability 121
4.7.3 Implementation of D-index analysis to lidar optimization 124
4.7.4 Optimization of lidar system parameters 128
4.7.5 Laser source wavelength optimization 132
4.7.6 *D*-index for systems with high repetition rate and return signal summation 137
4.7.7 A universal parameter for the comparison of bathymetric lidars 138
4.8 REFERENCES 139
5 BASIC CONCEPTS IN DATA PROCESSING 147
5.1 DIRECT GEOREFERENCING OF THE LIDAR POINT 147
5.1.1 Sensor modeling 147
5.1.2 The position vector in the IBF 148
5.1.3 The position vector in the Local Geodetic Frame (LGF) 149
5.1.4 Refraction into the water 150
5.1.5 The position vector in the earth centered, earth fixed (ECEF) frame 151
5.2 INVERSE PROBLEMS OF LIDAR WAVEFORM PROCESSING 152
5.3 ESTIMATION OF THE DIFFUSE ATTENUATION COEFFICIENT FROM LIDAR WAVEFORM SLOPE 155
5.4 BOTTOM REFLECTANCE ESTIMATION 159
5.5 EFFECTS OF FORWARD SCATTERING 166
5.5.1 Effect of scattering and inherent optical properties 166
5.5.2 Lidar depth estimation algorithm 169
5.5.3 Effect of the effective surface Fresnel reflectance 171
5.5.4 Effect of the bottom reflectance 174
5.6 REFERENCES 175

6 PERFORMANCE EVALUATION 179
6.1 EXPECTATIONS FROM THE ALB SYSTEMS 179
6.2 KEY EVALUATION PARAMETERS 180
6.2.1 System health 180
6.2.2 Noise evaluation 181
6.2.3 Swath coverage 181
6.2.4 Geometric calibration 182
6.2.5 Relative accuracy evaluation 182
6.2.6 Radiometric evaluation 182
6.3 EVALUATION TESTS 182
6.3.1 BIST182
6.3.2 Boresight Calibration (Geometric Calibration) 183
6.3.3 Relative accuracy Test 188
6.3.4 Output formats 194
6.4 EXAMPLES OF PERFORMANCE EVALUATIONS 195
6.4.1 USACE/Navy performance evaluation tests 195
6.4.2 NOAA performance evaluation tests 200
6.5 REFERENCES 205
7 APPLICATIONS, ANCILLARY SYSTEMS, AND FUSION 207
7.1 NAUTICAL CHARTING 208
7.2 NAVIGATION PROJECT MONITORING 208
7.3 REGIONAL SEDIMENT MANAGEMENT 212
7.4 POST-STORM RESPONSE 214
7.5 GEOMORPHOLOGICAL FEATURE EXTRACTION 215
7.5.1 Shorelines and shoreline change 217
7.5.2 Dune and depositional coastal features 218
7.5.3 Bluff and cliff edge detection 220
7.6 ENVIRONMENTAL MAPPING 221
7.7 SUMMARY AND FUTURE WORK 223
7.8 REFERENCES 226
FULL REFERENCE LIST 231
APPENDIX A. STANDARD WORDS, PHRASES, ACRONYMS 257
APPENDIX B. LIST OF SYMBOLS 261

ACKNOWLEDGEMENTS

The Joint Airborne Lidar Bathymetry Technical Center of Expertise (JALBTCX) is acknowledged for its leadership role in airborne coastal mapping and charting and for creating a community of practice through its annual technical workshop that directly led to writing this book. JALBTCX is a partnership between the US Navy Meteorology and Oceanography Command's Naval Oceanographic Office, the National Oceanic and Atmospheric Administration, the US Geological Survey, and the US Army Corps of Engineers. Through 20 annual workshops (so far!) national and international government representatives, academics, lidar manufacturers, and lidar survey companies have a forum to meet one another, evolve topo/bathy lidar and ancillary technologies, and grow the global airborne coastal mapping and charting market. This compendium of worldwide knowledge is possible only through the JALBTCX collaboration and community.

Dr. William Philpot, the co-authors, and the reviewers Yves Pastol, Shachak Pe'eri, Michael Starek are acknowledged and thanked for their many hours and selfless contribution to share their knowledge and lessons learned, which makes this book so valuable. Without everyone's hard work and dedication, this book could not have been written.

FOREWORD

Gary Guenther

What is a Foreword? I guess it's typically a brief summary of the content to come. If that's true, then this should honestly be called a Backword, because you can read this new book for yourselves. I'd like to give you some background on how the original came to be. I believe in history and in people. Why are you reading this? I like to think it's because a fairly small number of dedicated people started something good a long time ago, and it is continuing today with fairly broad acceptance and support in the survey community. Given that this is a rather arcane topic, you, as a reader, are probably also a participant, contributing your interest, your labor, and hopefully your love.

This is the 32nd anniversary of the 1985 publication of the original Blue Book (a.k.a. "Airborne Laser Hydrography: System Design and Performance Factors"). It's actually a 385-page NOAA Professional Paper that I was able to get published under hard (navy blue) covers (as well as a second run of sky blue soft covers). Now you know why it's just called "The Blue Book"! Honestly, I wrote it as much for myself to refer to, as a memory device, as for anyone else. It's filled with ideas and equations and data and systems and experimental results and analyses, but if you look at the voluminous references, you can easily see that it's really about the people – the pioneers, at U.S. Navy, NASA, WRE Salisbury, NOAA, and Optech Inc., who dared to think out of the box and act. That was important to me, and it still is.

Let's begin with a little perspective here. Some of you reading this were probably not even born then! I began writing the Blue Book in 1981 – the same year the IBM PC was released to the public. I wrote it on a dedicated, table-sized word processor with an 8" floppy drive for storage. And don't you just love all those hand-drawn graphics? If I'm not mistaken, NOAA's on-board survey computer software at that time was still loaded from paper tapes! The first Nd:YAG laser was designed and demonstrated at Bell Labs in 1964, only 12 years before I started playing -- and I was a newbie, far from the first!

Those were exciting times. I would be remiss in not mentioning some of the original source material I learned the trade from. The U.S. Navy were "working with lasers" in the mid-1960s, virtually as soon as they were invented. That was very interesting reading – with particular kudos to the work done at NADC/Warminster. Dan Hickman did work at Syracuse University, specifically for bathymetry, in the late 60s. I spent many hours poring over Dan's subsequent SPARCOM reports from the early 70s of tank tests and thoughtful design criteria for ALB systems. I actually still have them in my files. In 1973, NASA Wallops sponsored a Symposium on the use of airborne, pulsed lasers for bathymetry and fluorosensing. I read every word of that many times. This was the basis for the 1975 design of the Airborne Oceanographic Lidar (AOL), subsequently built by Avco Everett. In Canada, in 1974, Optech, Inc. was created by Prof. Allan Carswell of York University and his grad student, Sebastian Sizgoric, and they started testing lasers and building systems with sponsorship from the Canada Centre for Remote Sensing. Down Under, things were also busy in the mid-70s at WRE Salisbury, forming the basis for WRELADS II and, subsequently, LADS. At NOAA, LCDR Lowell Goodman set up Workshops in 1975 and 1976 (labeled as First and Second, thereby relegating the 1973 NASA Workshop to 'Zeroth'). And that's where I entered the picture myself. It changed my life forever.

In 1976, I was working in a little techie enclave in NOAA's National Ocean Service created by Maurice (Mo) Ringenback. High tech for us was acoustics and radio positioning. But we wanted more. As noted above, one of my colleagues, Lowell Goodman, had spent some time at NASA Wallops where, purely as an aside, he met Frank Hoge and his AOL crew and came back with amazing tales of measuring water depth from aircraft. Who knew? I can still hear Mo's voice, as if it were yesterday, when he came back to my cube and asked: "Gary, what happens when light goes through water?" In all honesty, absurd bravado, and colossal ignorance, I said, "Give me a few hours." I picked up my pen and started drawing

pulses and writing equations on a piece of paper. (What, you wanted me to use my Post Versalog slide rule or my brand-new HP-35 hand calculator? Seriously?) The rest is history. Needless to say, instead of a couple hours, I was still working on it 30 years later, and it's still an area of active research today, as you know if you're reading this.

Recognizing how "under water" I was, I asked Bob Thomas, then of Wolf Research (soon to be bought out by EG&G) for some help, which was the start of one of those "beautiful friendships". Bob's Monte Carlo work is one of the main features in the Blue Book. Bob, I couldn't have done it without you. Thank you! You are the best!

The bulk of the content in the original Blue Book was based primarily on my relationships with two systems: NASA's AOL and the U.S. Navy's Hydrographic Airborne Laser Sounder ("HALS", then being built at Avco Everett after their success supplying the AOL). In 1977, NOAA and the U.S. Navy (via the newly-formed NORDA at Stennis) funded a survey of the brand-new AOL in Chesapeake Bay, for which I wrote the Field Test Plan. Heady times. That was great fun. In processing that data (day and night for many months, even analyzing the oversized outputs from the high-speed printers on my pool table at home), I was able to recognize two major, independent depth biases (tricky devils!) that are based purely on physics – surface uncertainty (flip flop), and propagation-induced pulse-stretching effects. The latter led to analytic approximations and then the Monte Carlo propagation simulations written by Bob Thomas. This was certainly part of the answer to Mo's original question! These results were originally reported at the 4th Symposium in 1980 in Salisbury, SA, and they got some attention! That was a real blowout ("a bursting of a container by pressure of the contents") conference with a huge number of papers, where the origins of much of what we take for granted today were first published. Get a copy of it – it will put a smile on your face, for all the obvious reasons.

Algorithm development was pressed by the needs of HALS, which, as described in the Blue Book, was originally designed to report accurate depths in the air in real time with a hardware processor. The biases changed that and forced us to find better, more accurate ways of processing with software on the ground. And what a ride that was! Basic software design concepts generated for HALS data processing were the basis for the subsequent SHOALS "Brown Book" ground-based waveform processor and the "Green Book" airborne processor. Colors are so much easier than formal names! The point is that it all began with the algorithm analyses -- precision and accuracy studies --reported in the Blue Book.

In terms of the hardware, we were constantly pushing hard, working a bit beyond the boundaries of available technology, and were concerned about things like the performance capabilities and limitations of detectors, digitizers, lasers, and scanners. Sound familiar? Some things never change. I am proud of the fact that most of the information in the original Blue Book is still valid, even though some of it has been outdated by the advance of technology, which has thankfully come a long way, baby!

Even after the successful AOL surveys, NOAA wouldn't build a system (up-front costs were too much for them, regardless of the ultimate operational payoffs), but they knew they should have access to one somehow, when the time came, so they supported my continuing work in this field. I owe the faith and resources invested in me in these critical years, by several understanding NOAA bosses, for my ability to complete the original volume.

Ultimately, after Bob and I worked on a shipboard positioning project for 18 months in the mid-80s, during a bit of a lull in ALB, serendipity won out. Shortly after the Blue Book came out, I was contacted by a brash young dude in the Army Corps of Engineers from Vicksburg, MS who claimed he not only *wanted* to build a new airborne lidar hydrography system but thought he could actually *do* it (with my help, of course). I believed in him, and the rest is SHOALS history. Thanks for the great ride, Jeff, and Paul and all.

I stopped working and contributing over ten years ago (yes, some days I really do miss it, but my head is now filled with wood art), so I am not up to speed on all the new hardware and politics (yes, the politics

was always there), but at the 2016 JALBTCX Workshop (my 40th anniversary in this field), I was both happy to see some faces I was familiar with, and encouraged to see so many young people participating and contributing. We got it off to a good start, and on it goes.

I was very encouraged at the 2016 Workshop to see so many impressive, fascinating things happening. But a word of caution: I was also concerned to see that some things may be being underserved for commercial purposes. Caveat Emptor. The hardware and software may change, but the physics doesn't.

I want to sincerely thank Bill and all the contributors to this new volume, from concept to fruition, who have put into it their force of will, time, energy, insights, perseverance, and passion. These are the spirits of the original. It's really nice to see how far we have come and what you have achieved. This book is full of exciting stories. I am honored, and I honor you, in turn.

I've had casual opportunities to reexamine my life and to recognize those forks in the road that forever changed who I was and who I have become. I would enjoy seeing some of those other outcomes, just for fun, but I've enjoyed this road thoroughly. Professionally, it's because of our ALB community at large -- the people I've worked with directly and indirectly, colleagues and competitors alike, and the successes we've shared and continue to have.
I wish I could personally thank and acknowledge, in these lines, each and every person (you know how I love references) that I worked with or taught (be it in a trailer, a university classroom, or a hotel lobby with a bottomless bourbon in my hand), but that is obviously not possible. You know who you are. I have a long memory; I know who you are.

Passages: Sebastian, Mike, Peter. Too soon.

It's undoubtedly not proper to dedicate a Foreword, even if it's a Backword, but with Bill's kind permission, I want to devote this brief look back at where we came from to my great friend, our friend, Sebastian Sizgoric -- for many reasons, but mainly because of his large love of life, his laugh, his questions, and how he made it all so much fun for those around him. It was real. We miss you. Cheers.

Turn the page, enjoy, and make your own history.

Gary C. Guenther
Silver Spring, MD
March 2017

eCommons (2019) https://doi.org10.7298/jxm9-g971

1 INTRODUCTION

Author: W. Jeff Lillycrop

U.S. Army Corps of Engineers, Engineer Research and Development Center, Technical Director, Civil Works Research and Development

To the Pioneers, and to those who keep the Faith

This book was written to document and share our updated knowledge of airborne lidar hydrography gained since Gary C. Guenther wrote the original seminal book *Airborne Laser Hydrography - System Design and Performance Factors* over 30 years ago. Like the first book, commonly referred to as *the Blue Book*, this *Blue Book II* updates the history, theory, and design challenges of bathymetric lidar. However, with over 30 years of advancements and most importantly with thousands of hours of operational experience from different international teams and system, *Blue Book II* provides knowledge gained through decades of operational experience over a wide range of applications and environmental conditions. Mr. Guenther's *Blue Book* laid the foundation that over 16 authors from a half dozen countries update in *Blue Book II*.

The Joint Airborne Lidar Bathymetry Technical Center of Expertise (JALBTCX) is a U.S. organization that focuses on lidar bathymetry and provides a U.S. focal point with international collaboration. Its mission is to perform operations, research, and development in airborne lidar bathymetry and complementary technologies to support the coastal mapping and charting requirements of the U.S. Army Corps of Engineers (USACE), the U.S. Naval Meteorology and Oceanography Command, the National Oceanic and Atmospheric Administration (NOAA), and the U.S. Geologic Survey (USGS). JALBTCX staff includes engineers, scientists, hydrographers, and technicians from the USACE Mobile District, the Naval Oceanographic Office, the USACE Engineer Research and Development Center, NOAA National Geodetic Survey, and the USGS Earth Resources Observation & Science Center.

JALBTCX executes survey operations worldwide and year-round using its third-generation systems named the Coastal Zone Mapping and Imaging Lidar (CZMIL) system as well as using other industry-based coastal mapping and charting systems. CZMIL is JALBTCX's in-house survey capability that includes a lidar instrument with simultaneous topographic and bathymetric capabilities integrated with a hyperspectral imager and a true-color high-resolution digital camera. JALBTCX research and development supports and leverages work in government, industry, and academics to advance airborne lidar and coastal mapping and charting technology and applications. The research is shared through various conferences, peer reviewed journals, and at the Annual Airborne Coastal Mapping and Charting Workshop sponsored by JALBTCX. The annual workshop participants typically include all the international teams and it is from this annual workshop that the collaboration for the *Blue Book II* originated.

In the 1980's and 1990's the majority of operational bathymetric lidar systems focused on hydrography for nautical charting and for surveying navigation channels to determine shoaling. These systems included the Laser Airborne Depth Sounder (LADS) in Australia, the Larsen 500 in Canada, the Scanning Hydrographic Operational Airborne Lidar Survey (SHOALS) system in the United States, and the

HawkEye system in Sweden, see Chapter 2 for a full history of these and other systems. As Chapter 2 points out there were various predecessors to these operational systems and other similar lidar systems developed for military applications. The focus of *Blue Book II* is on bathymetric lidar for nautical charting and coastal mapping.

Airborne lidar bathymetry began in the Unites States and elsewhere primarily focused on hydrography because accurate depths needed only two-dimensional positioning of the aircraft, which was possible in the 1970's and 1980's using microwave transponders. Depth measurements were calculated as a function of the laser light's time difference between the surface reflection and the bottom reflection, then corrected for light propagation and water surface fluctuations (waves and tides, river stage), to produce a measurement that met nautical charting accuracy standards. It was not until kinematic GPS in the 1990's that aircraft could be accurately positioned in three dimensions and airborne lidar could accurately produce above-water or topographic elevations. Once able to measure topography and bathymetry (topo/bathy) bathymetric lidar systems became a very valuable tool for mapping the ever-changing coastal region, both below and above water to support coastal zone management and regional sediment management requirements. Today, the combined topo/bathy applications are driving the requirements for mapping and future system designs.

Airborne lidar elevations are produced as a function of the travel time of a pulse of laser energy. A survey is produced by scanning a rapidly pulsing laser across the flight path of the aircraft, thus covering an area typically several hundred meters wide at aircraft speeds of 70 m/s to 100 m/s. The faster the laser pulses, the closer the measurements are spaced. For a constant laser pulse rate, the aircraft flying slower or faster and flying higher or lower may also adjust measurement spacing. There is a lot of physics involved when light passes through one medium into another. To accurately calculate depths requires understanding the physics and making design decisions that minimize adverse impacts. Chapter 3 *Environmental Optical Properties* describes the physics and optical properties associated with light propagation through the atmosphere, water surface, water column and the bottom. Chapter 4 *Basic Concepts and System Design* gives detail on system considerations, constraints and tradeoffs for signal processing of lidar waveforms to produce accurate results.

Producing an accurate elevation from a lidar pulse requires georeferencing the sensor using satellite a navigation system and an inertial measurement sensor. Knowing the exact location of an elevation begins with knowing the position and attitude of the laser pulse as it transmits through the sensor, out of the aircraft, through the atmosphere, air/water interface, water column reflecting off the bottom and returning along a similar path to the aircraft. In addition to the elevation and position, radiometrically calibrated bathymetric lidar systems may produce return signals that provide additional information about the water column, sea bottom and other environmental factors. Chapter 5 *Basic Concepts in Data Processing* provides more information on how this is done and what may be extracted through additional data processing.

The final two chapters address operational characteristics that were not covered in the first Blue Book; Chapter 6 *Performance Evaluation* and Chapter 7 *Applications, Ancillary Systems, Fusion* provide insight and best practices based on operating several generations of lidar bathymeters over thousands of hours. They cover topics on sensor calibration and what to test routinely to determine system health as well as non-standard radiometric calibration and calibrations based on survey mission type. Chapter 7 transforms

lidar bathymetry into coastal mapping and charting with the addition of other complementary sensors and the fusion of data across sensors. The examples show by adding additional sensors to the aircraft the combined or fused data may produce information none of the individual sensors alone are capable of. It is through this chapter that you see the transformation from a nautical charting focus to a coastal mapping and charting tool capable of supporting a wide range of applications.

Lidar bathymetry is an enabling tool that supports airborne coastal mapping and charting as well as other uses. What began in the 1970's with a focus on hydrography and nautical charting has charted thousands of square miles worldwide. Since the 1990's lidar bathymetry with complementary sensors has expanded to support coastal zone management and regional sediment management missions and already mapped thousands of miles. Actually, today it is likely that more missions are flown supporting these new applications than nautical charting, and the list of applications continues to grow.

It is interesting how the international bathymetric lidar teams challenged by the same physics, designed systems differently as the developers addressed the various tradeoffs to enhance system performance most important to their primary applications. This resulted in unique systems and design philosophies, each with slightly different operational strengths. An intrinsic value of *Blue Book II* is that the knowledge gained through these teams is included for the next generation to use to solve new challenges and create future systems. Also of note, what began in the 1980's with healthy competition has today become a global community that shares knowledge and lessons learned through various technical conferences, especially through the annual technical workshop sponsored by JALBTCX. Together these teams have pushed themselves, each other, and lidar bathymetry technology well beyond what was originally imagined. *Blue Book II* documents what we have learned and was produced to aid and encourage others who will continue to evolve lidar bathymetry and complementary sensors to measure and monitor the coastal and nearshore environment.

eCommons (2019) https://doi.org10.7298/jxm9-g971

2 HISTORY

Lead Author: Jennifer Wozencraft [a]

Contributing Authors: Paul LaRocque [b], Mark Penley [c], and Martin Pfennigbauer [d]

a) Director, Joint Airborne Lidar Bathymetry Technical Center of Expertise (JALBTCX)
USACE Engineer, Research and Development Center, Coastal and Hydraulics Laboratory,
b) Vice President, Special Projects, Teledyne Optech
c) Engineering Manager, Fugro
d) Director, Research & Intellectual Property, RIEGL

The early years of laser hydrography have been traced by Guenther (1985a). His review tracks the development of laser hydrography, now more commonly known as Airborne Laser Bathymetry (ALB), from the earliest theoretical and experimental efforts in the mid-1960's dealing with in-water lasers (Ott 1965; Sorenson, Honey, and Payne 1966; Prettyman and Cermak 1969; Duntley 1971) and the first demonstration systems capable of detecting bottom returns (Ott, Krumboltz, and Witt 1971a; Cunningham 1972a; Carswell and Sizgoric 1974) through the development of the first operational systems (Ryan and O'Neil 1980; Penny 1982; Anderson et al. 1983; Malone, Casey, and Monahan 1983; Gluch et al. 1983; Moniteq 1983b, 1983a; Calder 1980). The history was later extended to 1990 in a paper by Sizgoric, Banic and Guenther (1992). Guenther further detailed this history and provided descriptions of operational systems in the Airborne Lidar Bathymetry chapter of The DEM User's Manual (Guenther 2001), which he later updated in the 2nd Edition (Guenther 2007). This chapter summarizes and updates these reference documents.

2.1 Australia

In 1971, only about 15% of the Australian continental shelf, the critical area for safe navigation, was charted to modern standards (Setter and Willis 1994). The estimated backlog was 50 survey years using conventional ship-based acoustic equipment. Half of this area has depths less than 50 meters, and one quarter is less than 30 meters. The same year, an airborne land profiler, designed and constructed at the Weapons Research Establishment (WRE), now the Defence and Science Technology Organisation (DSTO), Adelaide, was put into service. In 1972, at the suggestion of the Royal Australian Navy (RAN) Hydrographer, Captain J.H.S. Osborne, this was further developed to profile the seabed and was first flight tested in June 1975. During flight tests in the vicinity of Adelaide, it was found that reflections from the seabed could be obtained from water depths in excess of 30 m. With such an airborne device it became possible to perform hydrographic surveying at a greatly improved rate.

2.1.1 Early systems and developments

WREMAPS I was the Airborne Terrain Profiler, mentioned above, which enabled land maps to be accurately contoured. WREMAPS I was in service for ten years with the Australian Army from 1970 – 1980. WREMAPS II was developed for the same purpose as WREMAPS I but incorporated improved technology using, for example, a pulsed Nd:YAG, frequency doubled laser. WRELADS II was in service

for 13 years from 1974 – 1986. The research and development activity at DSTO connected with the terrain profilers (WREMAPS I and II) was a natural springboard for a Navy sponsored task – that of developing a laser airborne depth sounder. A non-scanning experimental system, known as WRELADS I was built and tested in 1976 and 1977 (Abbot and Penny 1975). The results demonstrated that a scanning system as specified by the Navy was possible and this led to the production of WRELADS II. This more advanced system with full scanning, data recording and horizontal position fixing capabilities was developed and trialed from 1979 to 1984. The trials involved 550 hours of flying in a RAAF C47 Dakota which resulted in the gathering of large volumes of data. Analysis of this data showed that over the 2-30 m range, water depths could be measured with a standard deviation of 0.3m. The horizontal positions of soundings were known within an error circle of 11 m diameter and the aircraft was navigated consistently within 30 m of track (Penny et al. 1986).

Figure 2.1.2. The RAN LADS Aircraft with HMAS Moresby and a SMB off the coast of New South Wales on the occasion of the 75th anniversary of the Royal Australian Navy's Hydrographic Service.

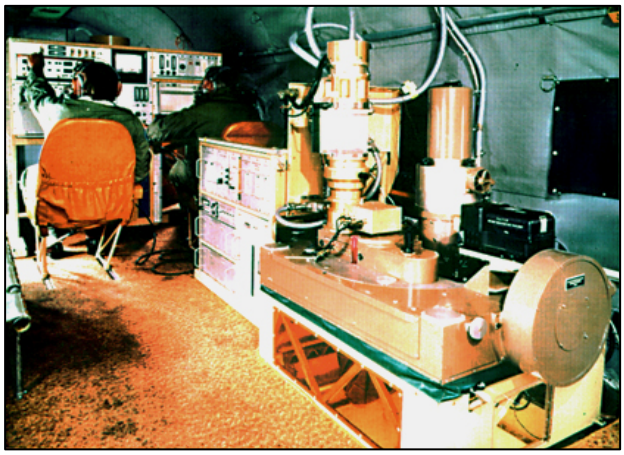

Figure 2.1.2. WRELADS II fitted to a RAAF C-47.

LADS is a product of the WRELADS programs (Setter and Willis 1994). It represents an engineered version of the experimental work, updated and integrated with all the additional features needed for a modern operational system which met the requirements of the RAN Hydrographer at that time. The contract to design, build and trial a LADS system for the RAN was awarded to Vision Systems Ltd, (VSL) in May 1989. This was to be known as RAN LADS 1. It operated a flash lamp pumped laser at 168Hz. RAN LADS 1 was accepted into Naval Service on 17 February 1993 and successfully carried out operations across Australasia internally mounted in a dedicated Fokker F27-500 series aircraft (Nairn, 1994). LADS was operated by the RAN LADS Flight unit, with logistical support from the system manufacturer, Tenix LADS Corporation Ltd. (formerly Visions Systems), a wholly owned subsidiary of Tenix Defence Systems Pty. Ltd. On one of its first RAN shakedown test flights in Spencer Gulf, LADS discovered a dangerous and previously uncharted granite pinnacle rising to an 11.9-m depth from an otherwise flat, 20-m bottom. The feature was first designated "Laser Shoal" and then, more aptly, renamed Penny Shoal, after Mike Penny, who directed development of WRELADS I and II.

In parallel with the development and support of systems for the RAN, Fugro LADS Corporation (formerly Tenix LADS) developed the next generations of LADS systems. After the release of RAN

LADS 1, the LADS Mk II system was developed, and was installed in de-Havilland Dash 8-200, VH-LCL (Spurling and Perry 1997; Sinclair 1998). This is the same aircraft that was later transferred to the RAN in 2009. This Dash 8 aircraft provided a modern aircraft with worldwide support, and qualities of speed, power, payload and endurance suitability for marine survey requirements (Sinclair 1997; Spurling and Perry 1997). The system had a a much higher pulse repetition rate and improved computer and navigation functions, operating at a sounding rate of 1 kHz and collected data to 70 m depth at IHO Order 1 charting accuracy (Sinclair, Stephenson, and Spurling 1999). The LADS MkII / Dash 8 conducted many successful surveys worldwide over the years of 1998 – 2009 operating in Europe, Middle East, North America and Australasia (Wellington 2001).

In 2008, the RAN LADS 2 System was introduced into service, providing functionality and performance improvements over the existing RAN LADS 1, whilst achieving the same standard of reliability and maintainability. The system was based upon core LADS functionality proven over the previous 15 years. It operated a diode pumped laser at 1 kHz. Initially the RAN LADS 2 system was installed in the Fokker F-27 Aircraft, but this was replaced in 2009 with the de-Havilland Dash 8-200 VH-LCL to relieve the pressure of operating with an ageing aircraft.

ALB SYSTEM	RAN LADS 1
AIRCRAFT	F-27 FOKKER
PERIOD OF SERVICE	1993 to 2008 (15 YEARS)
SORTIES FLOWN	2,232
KM^2 SURVEYED	116,215 KM^2

ALB SYSTEM	RAN LADS 2
AIRCRAFT	BOMBARDIER DASH 8-202
PERIOD OF SERVICE	Nov 2009 to Jun 2016 (6.5 YEARS)
SORTIES FLOWN	995
KM^2 SURVEYED	82,614 KM^2

Figure 2.1.3. Royal Australian Navy Laser Airborne Depth Sounder system statistics.

In 2009, LADS Mk3 was released into service with a new model of operation, where the equipment was mobilised to the location of aircraft of opportunity around the world, typically a Beechcraft A90, Cessna 441 or Cessna C208. The LADS Mk3 had enhanced performance over the LADS MkII and was much smaller and lighter – suitable for the smaller aircraft. The system operated at 1.5 kHz sounding rate and could now measure up to 80m depth. Incremental upgrades to the LADS Mk3 over the period of 2009 to 2015 were introduced. Significantly the sounding rate was increased to 2.5 kHz retaining the same 80m depth performance, and in 2012 a Riegl 820G sensor was integrated with LADS as a complimentary

eCommons (2019) https://doi.org10.7298/jxm9-g971

sensor, providing a second channel of high density 138 kHz soundings for enhanced shallow water and topography performance. In 2014 the Riegl sounding rate was increased to 250 kHz and then in 2015, the Riegl VQ-820-G was further upgraded to operate at 520 kHz. Successful surveys were conducted in Australia, France, New Zealand, Japan, Middle East, French Polynesia and Samoa with the LADS Mk3 System including the integrated Riegl sensor.

2.1.2 Current status

Early in 2016 the LADS HD system was released into service with a laser operating at 3 kHz plus new improved data processing capabilities including tightly integrated data processing of LADS and Riegl data combined, and Back 2 Base Data processing. The first survey conducted with this system was in Western Australia. Recently, in July 2016, the RAN LADS 2 system was replaced with a RAN LADS HD system operating with a sounding rate of 3 kHz. This is a customized LADS HD system installed in the Dash 8 aircraft, providing a comfortable operator console suitable for the 7hr survey endurance of the aircraft. This new capability allows the RAN to operate a more deployable model of operations where the survey team can deploy from site to site and transfer the data back to the Cairns Main Operating Base (MOB) for data processing.

Figure 2.1.4. LADS Mk II undergoing trials off the coast of South Australia, May 1998.

Figure 2.1.5. LADS HD system installed in Cessna 441 owned by Fugro.

Figure 2.1.6. RANHD installed in Dash 8 aircraft

Figure 2.1.7. LADS HD System; Change to 3 kHz

2.2 Canada

Airborne Lidar Bathymetry has a long history in Canada. The early years have been documented very well by Guenther (Guenther 2007) and hence we will only summarize briefly here. The very early work in Canada by Optech was in some profiling efforts with the Canada Centre for Remote Sensing (CCRS) (Ryan and O'Neil 1980). The next step was collaborating with the Swedish National Defense Institute (FOA) to augment the Mark-2 profiling system with a scanning mirror (Steinvall et al. 1981).

2.2.1 Early systems and developments

In the early eighties, the ALB systems were developed beyond the experimental learning stage and into the operational regime. Optech delivered the LARSEN-500 to the Canadian Hydrographic Service (CHS) and CCRS 1985 (Banic, Sizgoric, and O'Neil 1986). LARSEN-500 supported nautical charting missions in the Arctic during the few weeks a year the region is ice free (Casey, O'Neil, and Conrad 1985). As a result of its Arctic charting missions in 1985 and 1986, it fittingly deserves recognition as the world's first operational airborne lidar bathymeter. Lessons learned from LARSEN were incorporated into the Swedish and U.S. programs that followed. FOA of Sweden sponsored the development by Optech of a scanning ALB system called FLASH-I, which was delivered in 1988 (Steinvall, Koppari, and Karlsson 1993). Also, in 1988, Optech delivered to the US DARPA an airborne lidar for the detection of mines, the ALARMS system (Airborne Laser Radar Mine Sensor), which had a very advanced pulse repetition frequency (PRF) of 10 kHz.

Other significant developments in the late eighties included the first smooth sheet chart produced by an ALB for navigation in 1988, produced for CHS by the LARSEN-500. The same year, the U.S. Army Corps of Engineers (USACE) initiated an operational ALB system to be developed by Optech Incorporated under the program name SHOALS (Scanning Hydrographic Operational Airborne Lidar Survey). The goal of the SHOALS program was to develop a new hydrographic survey capability to support USACE dredging operations (Lillycrop and Banic 1992), and further, to transition the capability to industry so that it would be more widely available to USACE and others (Miles et al. 1994). The SHOALS system was field tested in March of 1994 at New Pass, near Sarasota, Florida (Lillycrop, Parson, and Irish 1996). The SHOALS laser pulsed 200 times per second, and was deployed in an external pod between the skids of a NOAA Bell-212 helicopter. In the late 1990's, the SHOALS laser was upgraded to 400 pulses-per-second (pps), allowing a transition from the helicopter to a fixed wing aircraft for even faster coverage rates (Wozencraft and Lillycrop 2003).

Optech delivered the CHARTS system to JALBTCX in 2003, comprising a SHOALS-1000T9, an integrated lidar system with a 1,000 pps bathymetric laser, a 9,000 pps topographic laser, and a DuncanTech (DT)-4000 digital RGB video camera with a Matrox screen grabber (LaRocque, Banic, and Cunningham 2004b). SHOALS-1000 is a further generational advancement of the original SHOALS technology, based on R&D and nine years of SHOALS operations (Wozencraft and Lillycrop 2003). In 2005, CHARTS was upgraded to include a 3,000 pps bathymetric laser, a 20,000 pps topographic laser, and an Itres Compact Airborne Spectrographic Imager (CASI)-1500 (Wozencraft and Millar 2005) Optech delivered a variant of the SHOALS-1000T9 to the Japan Coast Guard in 2003. Five of these 1 kHz models were made, one of which was delivered to Fugro Pelagos. The SHOALS-1000 system's

hazard detection capability was demonstrated to exceed IHO Order-1 in clear water, and IHO Special Order with appropriate survey planning (E. Yang and LaRocque 2010). Another SHOALS-3000 system was delivered to the UAE in 2010 and is still active in 2016.

The SHOALS family of systems was superseded by the development of the CZMIL system, built to have even greater depth penetration. The CZMIL system was designed at the US office of Teledyne Optech in Kiln MS (see section 1.3). Several subject matter experts from the Canadian office contributed to various subsystems of the CZMIL. The other major Canadian hardware contribution to CZMIL was the hyperspectral camera – the CASI-1500 built by ITRES of Calgary.

2.2.1 Current status

As work began on the next generation in the SHOALS family of systems at the Teledyne Optech office in the US, the Toronto office focused on smaller bathymeters that could also serve as terrain mappers. This was the beginning of the smaller, so-called “topo bathy” systems in the market. Optech had sold a large number of Airborne Laser Terrain Mappers (infrared topographic laser systems) and one of the popular ones was the Gemini. Along with the University of Houston and U.S. National Science Foundation National Center for Airborne Laser Mapping (NCALM), a green variant of the Gemini was conceived called Aquarius. This system was delivered to NCALM in 2010 (Fernandez-Diaz, Glennie, Carter, Shrestha, et al. 2014; LaRocque 2012). It was a “green-only” system which output its laser energy only at 532 nm, with a pulse repetition frequency (PRF) ranging from 33 kHz up to 70 kHz, which was a large leap forward in acquisition rate. The Aquarius system won the MAPPS Technology Innovation Award in 2011.

The current generation of shallow water mapper was made possible by the advances in fiber lasers. One limitation of the existing models was in the useful PRF. For example, the peak power of the laser in the Aquarius system would decrease with increasing PRF. Thus, its best depth performance was at its lowest PRF of 33 kHz. The newer fiber lasers did not have this restriction. In addition, while some people had combined lidar data of different wavelengths over the same area, there had never been a lidar that could collect three different wavelengths at the same time. Once again in collaboration with NCALM, Teledyne Optech completed the Optech Titan in 2014, a multi-purpose lidar useful for bathy as well as terrain mapping (LaRocque and Abdel-Rahman 2014; Fernandez-Diaz, Glennie, Carter, Shresha, et al. 2014). The depth performance of the Optech Titan is constant over its PRF of 50 to 300 kHz. It can serve as a 300 kHz shallow water mapper as well as a 900 kHz terrain mapper. The three wavelength intensity data has been very useful in enhancing bathymetry applications by helping the automatic classification of land from water (LaRocque et al. 2016). The simultaneous acquisition of three different wavelengths has also aided research on automatic land cover classification (Shaker et al. 2015). In 2015, the Optech Titan won the grand prize of the MAPPS Excellence Awards.

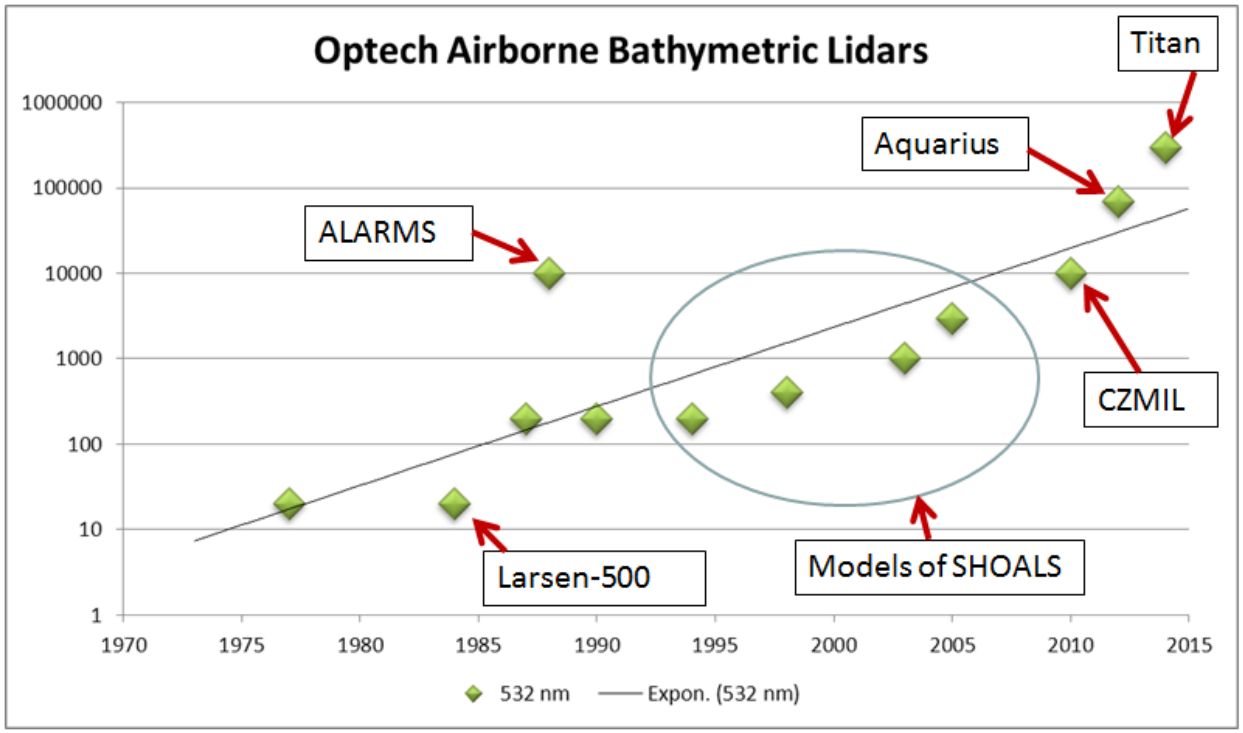

Figure 2.2.1. The evolution of ALBs in Canada. The laser PRF of the various ALBs made by Teledyne Optech is plotted on a log scale. The very early days used PRFs of 20 Hz while the latest value stands at 300 kHz for the Optech Titan.

The evolution of ALBs in Canada is illustrated in Figure 2.2.1, where the laser pulse repetition frequency (PRF) of the various ALBs made by Teledyne Optech is plotted on a log scale. The very early days used PRFs of 20 Hz while the latest value stands at 300 kHz for the Optech Titan.

2.3 United States

2.3.1 Early Systems and developments

U.S. work in the area of airborne lidar bathymetry began in the early 1960's with the concept that airborne, pulsed lasers could be used by the Navy to locate submarines. Early theoretical studies and system modeling for Naval Air Development Center (NADC) (Ott 1965; Sorenson, Honey, and Payne 1966; Prettyman and Cermak 1969) and field work (Duntley 1971) were followed by field tests of elementary bathymetric systems (Cunningham 1972b; Hickman and Hogg 1969; Ott, Krumboltz, and Witt 1971b). A system sponsored by the U.S. Air Force was successfully tested from a tower over the Gulf of Mexico (Levis et al. 1973). The Office of Naval Research (ONR), National Oceanic and Atmospheric Administration (NOAA), and U.S. Geological Survey (USGS) co-sponsored further studies of light transfer mechnisms, and development of design criteria for an airborne bathymetric system (Hickman et al. 1974; Hickman, Hogg, and Ghovanlou 1972; Hickman and Ghovanlou 1973).

AIRBORNE LASER HYDROGRAPHY II

National Aeronautics and Space Administration (NASA) sponsored a symposium on the use of lasers for hydrographic studies (H. H. Kim and Ryan 1973) with contributions from NOAA, ONR, the Naval Oceanographic Office (NAVOCEANO), NADC, US Environmental Protection Agency, and the CCRS. In the next few years, further design, construction, and field testing of airborne laser systems wasconducted by NASA (H. H. Kim, Cervenka, and Lankford 1975) and NADC (Ferguson 1975; Witt et al. 1976; Shannon 1975).

Avco Everett Research Laboratory, Inc. designed the Airborne Oceanographic Lidar (AOL) for NASA (Avco Everett Research Laboratory Inc. 1975) based on design goals and user requirements in the areas of hydrography and fluorosensing developed through symposia sponsored by NASA and NOAA. NOAA Laser Hydrography Development Project (Goodman 1975, 1976) and the Naval Ocean R&D Activity field tested AOL in 1977 to assess the potential of the basic technique of airborne laser bathymetry in terms of accuracy and maximum penetration depth and to determine the effects of the numerous system and environmental parameters (Guenther 1977). Final results of the NOAA test program of the AOL, and resulting analysis of: interrelationships among system design and performance factors, corrections for environmentally-induced biases in surface and bottom returns, and depth determination algorithms, were reported in Airborne Laser Hydrography: System Design and Performance Factors (Guenther 1985a).

In 1988, the U.S. Army Corps of Engineers (USACE) began the Scanning Hydrographic Operational Airborne Lidar Survey (SHOALS) program (J. Pope and Lillycrop 1988; Banic, Sizgoric, and Lillycrop 1990) to develop a new hydrographic capability for 40,000 km of USACE-maintained navigation channels (Guenther, Thomas, and LaRocque 1996; Lillycrop, Parson, and Irish 1996). Goals of the program were to develop an operational airborne lidar bathymetric technology, prove its application, and transition the mapping capability to the survey and mapping industry so that it would continue to be available to the USACE beyond the life of the SHOALS program (Miles et al. 1994). The SHOALS system was developed by Optech in Canada, and jointly funded by the US Army Corps of Engineers and the Canadian government. The SHOALS data processing software was developed in collaboration with Gary Guenther and based on Airborne Laser Hydrography: System Design and Performance Factors (Guenther 1985a).

From its field test in 1994 to 1997, SHOALS surveyed coastal engineering projects throughout the United States, demonstrating its capability to not only provide accurate, high-resolution data for navigation channels, but also the adjacent shoals and beaches (Wozencraft 2010a). SHOALS deployed in 1996 in support of a large nautical charting survey of the Yucatan Peninsula for NAVOCEANO (Irish, McClung, and Lillycrop 2000). The demonstration projects generated new user requirements that translated into a number of technological advancements including:

- extending depth measurement through the 0-2 m range, which had been prohibited by the long laser pulse and system response time, and up onto the subaerial beach (Brooks et al. 1998)
- using kinematic GPS data with on-the-fly ambiguity resolution for vertical reference, instead of the mean water surface (Guenther, Brooks, and LaRocque 1998)
- time- and geographic position-tagged analog video imagery collected concurrently with the lidar to assist in manual cleaning for the positioning of piers and other structures along the shoreline

- early work on the fusion of lidar and hyperspectral imagery for benthic classification was performed (Lillycrop and Estep 1995; Lillycrop, Irish, and Parson 1997)

USACE and NAVOCEANO formed the JALBTCX partnership in 1998 to further collaboration between the agencies in operations, research, and development in airborne lidar bathymetry (Wozencraft and Lillycrop 2006). Following its upgrade to a 400 pulse per second laser, and transition from a helicopter to a fixed wing platform, SHOALS was flown extensively for USACE projects in the US, including Alaska, Hawaii, and Puerto Rico. NAVOCEANO used SHOALS on tactical nautical charting missions in Guam, American Samoa, Hawaii, Bahamas, and Portugal. SHOALS-400 operated from 1999 to 2003. Signal processing work produced psuedoreflectance (a measure of the seafloor reflectivity) and water column parameters from the lidar waveforms (Lee 2003; Tuell and Park 2004), and produced the first hyperspectral image inversions constrained by these quantities (Tuell and Park 2004).

NASA fielded the Experimental Advanced Airborne Research Lidar (EAARL) in 2001 (Nayegandhi, Brock, and Wright 2009; Wright and Brock 2002) to map sandy beach topography, three-dimensional coastal vegetation structure, shallow bathymetry, coral communities, and near-shore benthic habitats simultaneously (Wright and Brock 2002; Brock et al. 2004; Nayegandhi et al. 2006; Nayegandhi, Brock, and Wright 2005). EAARL was the first of a new design philosophy for lidar bathymetry that uses narrow, low energy green laser pulses and narrow field of view. This design confers advantages in the areas of system size, accuracy, and resolution, but disadvantages in terms of overall depth detection capability (Feygels, Wright, et al. 2003a). EAARL was flown with a down-looking RGB digital camera and a high-resolution multi-spectral color infrared (CIR) camera, often in support of U.S. Geological Survey projects. EAARL operated from 2001 to 2013, surveying a number of coral reef areas in Florida and the Caribbean, rivers in the western U.S., and before and after hurricanes that made landfall in Florida in 2004 and 2005, and in New Jersey in 2012.

In 2000, NAVOCEANO undertook a sensor development effort called Compact Hydrographic Airborne Rapid Total Survey (CHARTS) based on the success of the SHOALS program (Wozencraft 2002). The goal of CHARTS was to increase the survey coverage rate, decrease the physical footprint and power requirements of SHOALS to take advantage of aircraft of opportunity, and to combine bathymetric lidar technology with topographic lidar and aerial photography. CHARTS development was jointly funded by the USACE, Canadian government and Optech. Technological advances supporting the CHARTS development in the U.S. centered on extraction of more information from lidar waveforms, and on fusion of lidar with hyperspectral imagery (Kopilevich et al. 2005a; Tuell, Feygels, et al. 2005; Tuell and Park 2004). The NAVOCEANO CHARTS systems were operated from 2003 to 2011 in support of NAVOCEANO Airborne Coastal Surveys in Nicaragua, Haiti, Philippines, Japan, Marshall Islands, Micronesia, Palau, Northern Marianas, Guam, Samoa, Bahrain, Oman, Portugal, Israel, Morocco, and Kenya. USACE used NAVOCEANO CHARTS systems to perform surveys along the sandy coasts of the United States for its newly initiated National Coastal Mapping Program (NCMP) from 2004 to 2011.

2.3.2 Current status

Coastal Zone Mapping and Imaging Lidar (CZMIL) was fielded in 2012 to meet the requirements of the USACE NCMP and NAVOCEANO Airborne Coastal Surveys: high-resolution, high-accuracy bathymetric lidar, topographic lidar, aerial photography, and hyperspectral imagery. CZMIL was a sensor

development effort in the USACE NCMP, and a partnership among the JALBTCX, Optech International in Kiln, MS (now Teledyne Optech), and The University of Southern Mississippi (USM). The design goal of CZMIL was to produce an integrated lidar, imagery sensor suite, and software package designed for highly automated generation of physical and environmental information products for the coastal zone. CZMIL was an opportunity to improve the design of current airborne lidar bathymeter hardware and software to meet the needs of the NCMP: accurate depth measurement; expanded environmental product generation by operationalizing the fusion of lidar with hyperspectral imagery (Park et al. 2010a); improved performance in turbid, shallow waters (Ramnath et al. 2010); and a very fast coverage rate.

CZMIL has a unique design that combines a broad beam, or large beam divergence angle, with a high peak power, but short laser pulse, and small field of view. The 10,000 pulse per second CZMIL laser emits 2-ns-wide laser pulses and scans them across the water surface in a circular pattern using a spinning Fresnel prism. Seven small, 2-milliradian each, field of view channels spatially sub-sample each 2.8 m diameter laser spot for high resolution measurements (70 cm spacing) in shallow water and on land. A large 40-milliradian field of view channel provides maximum depth performance in turbid water, and up to 60 m in clear water. Waveforms are digitized for each receiver and receiver segment, for a total of 9 waveforms per laser pulse. CZMIL Hydrofusion data processing software can extract up to 32 returns on each waveform, up to 256 per laser shot, with separation along the slant range as little as 10 cm on land. CZMIL Hydrofusion takes advantage of CZMIL radiometric calibration and produces advanced lidar products like lidar reflectance on land and in water, water column attenuation, and water-leaving reflectance. CZMIL is integrated with a medium format digital camera, a CASI-1500 hyperspectral imager, and Applanix POS AV for positioning. The advanced lidar products and hyperspectral imagery are input to CZMIL Hydrofusion spectral optimization technique that produces land and seafloor reflectance at multiple wavelengths by fusing lidar and hyperspectral imagery (Wozencraft and Park 2013).

The current suite of USACE NCMP and CZMIL Hydrofusion deliverable products includes (Wozencraft, 2010):

- Orthorectified aerial photography
- Classified LAS files
- 1-m and 5-m Bathymetric and Topographic Digital Elevation Models (“bare earth”) and Digital Surface Models (“first return”)
- Shoreline Contour
- Lidar-derived water column properties and seafloor reflectance
- Hyperspectral image mosaics (corrected for atmosphere)
- Hyperspectral-derived water column properties and seafloor reflectance (constrained with lidar-derived depth, water column, and seafloor parameters)
- Volume change and shoreline change (using successive surveys in a location)

Advances in processing bathymetric lidar signals and in the fusion of these signals with hyperspectral imagery provide the potential to expand the NCMP product line to include images of water column attenuation, chlorophyll concentration, and CDOM concentration, and automated bottom classification (M. Kim, Park, and Tuell 2010). CZMIL has collected the sandy coastlines of the US, the major

Hawaiian Islands, and the north shore of Puerto Rico for the USACE NCMP, and was used in response to Hurricanes Sandy (Wozencraft and Park 2013), Matthew (Virginia, North and South Carolina, Georgia, Florida), and Irma (Florida) for USACE and the Federal Emergency Management Agency (FEMA).

A significantly modified EAARL system was field tested in 2014 (Wright et al. 2016). EAARL-B is an extensive modification of the original NASA EAARL system. EAARL-B combines small and large FOVs like CZMIL, but emits much lower power (0.07 millijoules) and slightly shorter pulses (1.3 nanosecond). The outgoing pulses are split into 3 beamlets that result in 3-30 cm diameter laser footprints on the water surface, spaced 1.6 m in the along track direction. EAARL-B has 4 receivers for each laser pulse, one 60-cm FOV PMT receiver for each beamlet and another 5-m FOV PMT receiver that encompasses all three beamlets, and enables EAARL-B to see maximum depths in excess of 40 m in clear water. EAARL-B scans laser pulses across the land and water surface in a raster pattern tilted slightly forward to avoid Fresnel reflections at nadir that would saturate receivers in the aircraft. EAARL-B data are processed in the open-source Airborne Lidar Processing System (ALPS) developed at NASA and USGS (Nayegandhi, Brock, and Wright 2009). ALPS provides the capability to geometrically calibrate EAARL-B data, and apply appropriate depth-induced propagation biases to the shallow water beamlets and the deep channel. ALPS requires the user to interrogate representative waveforms in order to define a water column model for each dataset. After the model is subtracted from waveforms digitized by the system, potential bottom peaks, identified based on user-defined thresholds, are accepted or rejected based on expected bottom return characteristics like pulse width, rise time, and fall time (Wright et al. 2016). ALPS allows the user to run an Iterative Random Consensus Filter to remove noise points, and to manually delete any remaining noise points (Nayegandhi, Brock, and Wright 2009).

New sensors currently in the operational testing phase are the Arete PILLS and the Astralite, both designed to operate from UAS.

2.4 Sweden

Airborne laser hydrography in Sweden also leveraged system development capability of Canada's Optech. The driver was navigation safety. Nordstrom (2000) said it succinctly for the Swedish Maritime Administration: "the use of a helicopter-borne laser-beam system (in Sweden) is essential, especially in shallow and narrow waters in the archipelagos." In the middle 1980's, the Swedish Defense Research Establishment (FOA) worked with Optech Incorporated to develop the FLASH airborne lidar system to evaluate object detection and the performance of emerging ALB technology (Steinvall, Koppari, and Karlsson 1994).

2.4.1 Early systems and developments

The success of FLASH led to development of two identical Hawk Eye systems (Steinvall et al. 1997), largely derived from the SHOALS design, in the early 1990's by Saab Instruments AB (later Saab Dynamics AB), with Optech as the major subcontractor. The two pod-mounted systems were purchased by the Swedish Defence Material Administration (FMV) – one for the Royal Swedish Navy and one for the Swedish Maritime Administration. They were designed for helicopter operation in a Boeing Vertol and a Bell 212, and were deployed in 1994 and 1995 for the dual purposes of hydrography and submarine detection (Steinvall et al. 1997; Skogvik and Rune 2001). Two years after delivery, the Swedish

Maritime Administration sold their system to Blom A/S, a private Norwegian surveying contractor, for use in a large survey project in Indonesia and began sharing the remaining system with the Navy. The Swedish Navy Hawk Eye system conduced navy survey operations and nautical charting missions for the Maritime Administration off the South and West coasts of Sweden, as well as in the Baltic Sea (Skogvik and Rune 2001).

Airborne Hydrography AB (AHAB) was formed as an employee buy-out of the lidar work at Saab Dynamics AB to supply state-of-the-art laser bathymetry and terrestrial systems and hydrographic laser survey services. In 2004, AHAB and TopEye AB of Sweden and Admiralty Holdings Limited in the United Kingdom formed a collaboration called Admiralty Coastal Surveys AB (ACSAB) to create and produce an ALB and topography service based around their new Hawk Eye II lidar system. Hawk Eye II Laser Bathymetry and Topography System was tested in 2005 and delivered to ASCAB in early 2006. Surveys were performed in France, Germany, Denmark, Estonia, Sweden, and the U.S.

2.4.2 Current status

Chiroptera II and Hawk Eye III are the recent shallow and deep water bathymetric lidar systems fielded by Leica AHAB in 2013 and 2015, respectively. Airborne Hydrography AB built the Chiroptera system for the University of Texas, Bureau of Economic Geology. This shallow water system was designed in the tradition of deep water systems, with multiple wavelength transceivers and waveform processing. Chiroptera was delivered in 2012. Chiroptera II, which boasts greater depth penetration capability than its predecessor was launched in 2014 with HawkEye III by Leica Airborne Hydrography AB as a modular approach to coastal zone mapping. Chiroptera II surveys over land and shallow water, while the HawkEye III surveys deeper water.

Chiroptera II comprises a green laser for bathymetry that pulses 35,000 time per second, and an infrared laser that pulses 500,000 times per second. The lasers have separate transmit and receive paths. The green laser has pulse energy of 0.1 millijoules, which is an order of magnitude less powerful than the traditional bathymetric lidar sensors SHOALS, CZMIL, and LADS. With a beam divergence of 3 milliradians the on-water laser footprint size is 1.2 m at operational altitude of 400 m. The infrared laser beam divergence is 0.5 milliradians with an on-ground laser footprint size of 0.1 m. Maximum depth penetration expected for this system is 15 m in moderately clear water. The laser pulses are scanned over the ground and water surface using a Palmer scanner which results in an elliptical scan pattern that is 40 degrees across track and 26 degrees along track, and a swath width that is 70% of the operating altitude. Chiroptera II is optionally gyro-stabilized using a PAV-100 mount and maintains a near-constant scan pattern along the flightline.

Hawk Eye III is a Chiroptera II with the addition of a separate laser transceiver for deep water depths. It has characteristics similar to CZMIL in terms of laser power (3 millijoules) and pulse repetition rate (10,000 pulses per second), but has a slightly larger beam divergence so the size of the laser footprint is also larger (4m). Chiroptera II and HawkEye III both use Novatel SPAN with LCI-100 IMU for positioning and orientation, and are operated to meet both USACE “Class 1” and IHO “Order 1” hydrographic accuracy standards for most applications. Chiroptera II is integrated with a 5 MP camera for QA/QC and may be integrated with an 80-MP RCD30 for higher-resolution imagery. Leica MissionPro and FlightPro provide mission planning and flight operations support, while Leica Survey

Studio software and FramePro software provide lidar processing and image processing. Leica Survey Studio provides automated calibration for all three lasers (Chiroptera infrared and green, HawkEye III green), and uses all three in combination to apply the appropriate processing algorithm based on automated land/water and turbid water detection.

2.5 Austria

Having already gathered vast experience in airborne laser scanning, RIEGL entered the field of airborne laser bathymetry through a research project initiated by the University of Innsbruck in 2008. From the very beginning high resolution shallow water bathymetry was the declared target application. To this end, different technologies compared to the then established deep sounding systems were employed in many respects ranging from laser technology to scanning mechanism and receiver technology. Special focus was placed on compactness and minimizing the weight of the instrument hardware and the compatibility to RIEGL's established hardware and software solutions. Riegl teamed with the University of Innsbruck on a research project for the Bavarian Water Authority to develop and assess the capabilities of a new shallow water bathymetric lidar system (Pfennigbauer and Steinbacher 2012). This system was designed specifically to meet the inland water (riverine) mapping requirements set forth by the European Water Framework Directive and was made commercially available in 2011.

2.5.1 Early systems and developments

After a phase of research and development, RIEGL marketed the VQ-820-G in 2011. This instrument had a high pulse repetition rate (up to 485 kHz), a short laser pulse (just above 1 ns), and a comparatively small beam divergence (1 mrad). These parameters lead to high spatial resolution, but the low laser pulse energy (around 20 µJ) and the small receiver aperture (around 50 mm) limit the depth penetration to around 1 Secchi depth when operating the instrument from a flight altitude of 600 m. The laser pulses are scanned by a multifaceted mirror that describes an elliptical section across the land and water surface. The size of the laser footprint on the water surface at 400m altitude is 0.4 m and the footprint spacing is 0.2 m, up to 10 points per square meter. Furthermore, the instrument operates using only a green wavelength. The VQ 820-G utilizes echo digitization and online waveform processing (Pfennigbauer et al. 2014) techniques for real-time detection of returns on the lidar waveform, rather recording and storing waveforms for post-processing. As such, a refraction correction technique was developed using the lidar point cloud for location of the mean water surface to provide the angular and speed-of-light corrections for lidar point geolocation. The VQ-820-G was representative of a new class of ALB instruments, the so-called Topo-Bathy Laser Scanners.

The VQ-820-G was fielded in the USA for extensive coastal surveys for NOAA to update nautical charts after Hurricane Sandy, in France and Australia by Fugro, and also in central Europe by AHM and other surveying companies. AHM is a spinoff of the University of Innsbruck and another result of the research collaboration focusing on fresh water surveying. Fugro combined the VQ-820-G with its LADS deep sounding airborne laser bathymetry sensor in order to accomplish seamless surveying of the entire coastal zone using the VQ-820-G data for topography and shallow water and the LADS for the deeper regions. Extensive work was carried out with this combination. On special request of a customer the VQ-820-G has also been integrated in the Schiebel Camcopter S-100.

2.5.2 Current status

In 2014 RIEGL launched the VQ-880-G, a topo-bathy laser scanning system including an infrared channel, IMU, GNSS, and AVT 29-megapixel camera. The green channel of the VQ-880-G uses a rotating prism to perform a circular scan with an off-nadir angle of 20°. The IR channel uses a rotating polygonal mirror to perform a slightly arced scan in the center of the green's channel scan cone. This has the advantage of being able to pick up a signal from the water surface, even under unfavorable conditions. The laser has a slightly higher pulse repetition frequency, up to 550,000 pulses per second, but the pulse power and pulse width are similar to the VQ 820-G. The laser beam divergence is selectable from 0.7 to 2 mrad, as is the scan speed from 10 -200 scans/sec for the green channel. As a consequence of the scan mechanism design, the net measurement rate was nearly doubled. The VQ 880-G also utilizes onboard echo digitization, but has an add-on capability for recording all waveforms for post-processing, and is integrated with an APC 29-megapixel camera for concurrent aerial photography collection. Compared to the VQ-820-G the VQ-880-G has improved performance in every respect, most notably the depth penetration is significantly improved. Again, the first systems were deployed in the US and were later introduced in Europe.

Processing of the acquired data relies on the established RIEGL software suite for airborne laser scanning including tools for acquisition tasks like flight line planning and real-time feedback to the operator (RiAcquire), georeferencing (RiWorld), and strip adjustment, visualization, classification, and data export (RiProcessing). Water classification, water surface modeling and refraction correction are performed by the RiHydro addon.
In 2015 RIEGL announced a new concept of a laser rangefinder employing a green laser small enough to be operated from a small-scale UAV. This combination is capable of generating profiles of waterbodies.
In 2016 the RIEGL BDF-1 was presented to the market as a product. The BDF-1 surveying system including IMU, GNSS, and camera has successfully been operated from RIEGL's self-developed and manufactured octocopter, the RiCOPTER. Full waveform recording of the entire range gate allows for performance improvement through pre-detection averaging (Mandlburger et al. 2016).

2.6 References

Abbot, Ralph H., and Michael F. Penny. 1975. "Air Trials of an Experimental Laser Bathymeter." Vol. Tech Note. Salisbury, South Australia: Weapons Research Establishment, Department of Defence.

Anderson, N., P. Bellemare, M. J. Casey, K. Malone, R. MacDougal, D. Monahan, Robert A. O'Neil, and S. Till. 1983. "Beginning the Second Hundred Years - the Laser Sounder." In *Proceedings of Centennial Canadian Hydrographic Service Conference*. Ottawa, Ontario, CA: Fisheries and Aquatic Services, Special Publ. 67.

Avco Everett Research Laboratory Inc. 1975. "Airborne Oceanographic Lidar System, NASA Contractor Report CR-141407, Final Report." Everett MA.

Banic, John R., Sebastian Sizgoric, and W. Jeff Lillycrop. 1990. "Second-Generation Airborne Lidar System for Hydrographic Applications." In *Proc. Oceanology International*. Brighton, England.

Banic, John R., Sebastian Sizgoric, and Robert O'Neil. 1986. "Scanning Lidar Bathymeter For Water Depth Measurement." In *Laser Radar Technology and Applications.*, edited by James M. Cruickshank and Robert C. Harney, 663:187. Optech Inc, Downsview, Ont, Can, Optech Inc, Downsview, Ont, Can: SPIE. https://doi.org/10.1117/12.938673.

Brock, John C., C. Wayne Wright, Tonya D. Clayton, and Amar Nayegandhi. 2004. “LIDAR Optical Rugosity of Coral Reefs in Biscayne National Park, Florida.” *Coral Reefs* 23 (1): 48–59. https://doi.org/10.1007/s00338-003-0365-7.

Brooks, M. W., E. Culpepper, Gary C. Guenther, and Paul E. LaRocque. 1998. “Advancements and Applications of the SHOALS Laser Bathymetry System.” In *Proc. ION GPS 98*, 8. Institute of Navigation, Nashville, TN. https://www.ion.org/publications/abstract.cfm?articleID=3057.

Calder, M. 1980. “WRELADS - The Australian Laser Depth Sounding System.” *The International Hydrographic Review* 57 (1). https://journals.lib.unb.ca/index.php/ihr/article/view/23621.

Carswell, Allan I., and Sebastian Sizgoric. 1974. “Underwater Probing with Laser Radar.” In *Proceedings of the Uses of Lasers for Hydrographic Studies*, 89–104. Wallops Island, VA: NASA SP-375. https://ntrs.nasa.gov/archive/nasa/casi.ntrs.nasa.gov/19750022452.pdf.

Casey, M. J., Robert A. O’Neil, and P. Conrad. 1985. “The Advent of LARSEN.” In *Proc. Canadian Hydro. Conf.* Halifax, Nova Scotia, CA.

Cunningham, Linda L. 1972a. “Test Report on Pulsed Light Airborne Depth Sounder PLADS.” Vol. 6620-102–7. Washington, D.C.: Naval Oceanographic Office.

Cunningham, Linda L. 1972b. “Test Report on Pulsed Light Airborne Depth Sounder PLADS.” Vol. 6620-102–7. Washington, D.C.: Naval Oceanographic Office.

Duntley, Seibert Q. 1971. “Underwater Lighting by Submerged Lasers and Incandescent Sources.” Vol. SIO Ref. 7. La Jolla, CA: Scripps Institution of Oceanography Visibility Laboratory. http://oai.dtic.mil/oai/oai?verb=getRecord&metadataPrefix=html&identifier=AD0730721.

Ferguson, Gerald D. 1975. “Blue-Green Lasers for Underwater Applications.” In *SPIE Conference on Ocean Optics, Aug. 19-20*, 64:150–56. San Diego, CA: International Society for Optics and Photonics. https://doi.org/10.1117/12.954503.

Fernandez-Diaz, Juan Carlos, Craig L. Glennie, William E. Carter, R. L. Shresha, Michael P. Sartori, and Abhinav Singhania. 2014. “Multicolor Terrain Mapping Documents Critical Environments.” *Eos*. https://doi.org/10.1029/2016eo053489.

Fernandez-Diaz, Juan Carlos, Craig L. Glennie, William E. Carter, Ramesh L. Shrestha, Michael P. Sartori, Abhinav Singhania, Carl J. Legleiter, and Brandon T. Overstreet. 2014. “Early Results of Simultaneous Terrain and Shallow Water Bathymetry Mapping Using a Single-Wavelength Airborne LiDAR Sensor.” *IEEE Journal of Selected Topics in Applied Earth Observations and Remote Sensing* 7 (2): 623–35. https://doi.org/10.1109/JSTARS.2013.2265255.

Feygels, Viktor I., C. Wayne Wright, Yuri I. Kopilevich, and Alexey I. Surkov. 2003. “Narrow-Field-of-View Bathymetrical Lidar: Theory and Field Test.” In *Ocean Remote Sensing and Imaging II*, SPIE 5155:1–11. San Diego, CA: SPIE. https://doi.org/10.1117/12.506951.

Gluch, T., J. Piwowar, S. J. Till, and Robert A. O’Neil. 1983. “The Bathymetric Estimator Serach Technique for Processing Airborne Lidar Data.” In *Proceedings of the 8th Candian Symposium on Remote Sensing*. Montreal, Quebec, CA.

Goodman, L.R. 1975. “Laser Hydrography User Requirements Workshop, Minutes.” NASA Wallops Flight Center, Wallops Island, VA: National Oceanic and Atmospheric Administration, Rockville, MD.

———. 1976. “Laser Hydrography Technical Review Workshop, Minutes.” Rockville, MD.

Guenther, Gary C. 1977. “AOL Flight Test and Data Analysis Plan (Unpublished Manuscript).” Riverdale, MD.

———. 1985. *Airborne Laser Hydrography: System Design and Performance Factors*. Rockville, MD: NOAA Professional Paper Series, National Ocean Service 1. http://shoals.sam.usace.army.mil/downloads/Publications/AirborneLidarHydrography.pdf.

———. 2001. “Airborne Lidar Bathymetry.” In *Digital Elevation Model Technologies and Applications: The DEM User’s Manual*, edited by D. Maune, 1st ed., 253–320. Bethesda, Maryland: ASPRS. http://www.asprs.org/a/publications/2009PubsCatalog.pdf.

———. 2007. “Airborne Lidar Bathymetry.” In *Digital Elevation Model Technologies and Applications: The DEM Users Manual, 2nd Edition*, edited by D F Maune, 2nd ed., 253–320. Bethessda, Maryland: ASPRS. http://www.asprs.org/a/publications/2009PubsCatalog.pdf.

Guenther, Gary C., M. W. Brooks, and Paul E. LaRocque. 1998. “New Capabilities of the SHOALS Airborne Lidar Bathymeter.” In *5th Int’l Conf. on Remote Sensing for Marine and Coastal Environments*, 1:47–55. ERIM International.

Guenther, Gary C., Robert W. L. Thomas, and Paul E. LaRocque. 1996. “Design Considerations for Achieving High Accuracy with the SHOALS Bathymetric Lidar System.” In *SPIE 2964, CIS Selected Papers: Laser Remote Sensing of Natural Waters: From Theory to Practice, November 1, 1996*, edited by Victor I Feigels and Y Kopelivich, 2964:54–71. St. Petersburg, Russia: Society of Photo-optical Instrumentation Engineers (SPIE). https://doi.org/10.1117/12.258353.

Hickman, G. D., C. S. Gault, A. H. Ghovanlou, E. J. Friedman, and J. E. Hogg. 1974. “Airborne Laser Shallow Water Bathymetric System.” Technical Report ONR/NOAA/USGS Contract No. N000-14-71C-0202 Final Rep. Alexandria, VA: Sparcom, Inc.

Hickman, G. D., and A. H. Ghovanlou. 1973. *Preliminary Design Criteria*. Technical Report ONR/NOAA/USGS Contract No. N000-14-71C-0202. Alexandria, VA: Sparcom, Inc.

Hickman, G. D., J. E. Hogg, and A. H. Ghovanlou. 1972. *Pulsed Neon Laser Bathymetric Studies Using Simulated Delaware Bay Waters*. Technical Report ONR/NOAA/USGS Contract No. N000-14-71C-0202. Alexandria, VA: Sparcom, Inc.

Hickman, G D, and J E Hogg. 1969. “Application of an Airborne Pulsed Laser for near Shore Bathymetric Measurements.” *Remote Sensing of Environment* 1 (1): 47–58. https://doi.org/10.1016/S0034-4257(69)90088-1.

Irish, Jennifer L., J. K. McClung, and W. Jeff Lillycrop. 2000. “Airborne Lidar Bathymetry: The SHOALS System.” *The International Navigation Association, PIANC Bulletin* 103: 43–45.

Kim, Hongsuk H., P. Cervenka, and C. Lankford. 1975. “Development of an Airborne Laser Bathymeter.” Vol. NASA TN D-. Washington, D.C.: NASA. https://ntrs.nasa.gov/archive/nasa/casi.ntrs.nasa.gov/19750025550.pdf.

Kim, Hongsuk H., and Philip T. Ryan. 1973. “The Use of Lasers for Hydrographic Studies.” In *NASA SP-375*, edited by Hongsuk H. Kim and Philip T. Ryan, 202. Conference Proceedings. Wallops Island, VA, VA: National Aeronautics and Space Administration. http://ntrs.nasa.gov/search.jsp?R=19750022452.

Kim, Minsu, Joong Yong Park, and Grady H. Tuell. 2010. “A Constrained Optimization Technique for Estimating Environmental Parameters from CZMIL Hyperspectral and Lidar Data.” In *SPIE 7695: Algorithms and Technologies for Multispectral, Hyperspectral, and Ultraspectral Imagery XVI, April 5-8, 2010*. Vol. 7695. SPIE. https://doi.org/10.1117/12.851989.

Kopilevich, Yuri I., Viktor I. Feygels, Grady H. Tuell, and Alexey I. Surkov. 2005. “Measurement of Ocean Water Optical Properties and Seafloor Reflectance with Scanning Hydrographic Operational Airborne Lidar Survey (SHOALS): I. Theoretical Background.” In *SPIE 5885, Remote Sensing of the Coastal Oceanic Environment, July 31, 2005 - August 1*, 5885:1–9. Optech International, Inc.,

7225 Stennis Airport Drive, Kiln, MI 39556, United States: SPIE. https://doi.org/10.1117/12.618923.

LaRocque, Paul E. 2012. “Aquarius System: Compact Shoreline Mapper.” In *13th Annual JALBTCX Coastal Mapping & Charting Workshop*. Chicago, Illinois: JALBTCX.

LaRocque, Paul E., and Ahmed Shaker Abdel-Rahman. 2014. “New Multi-Wavelength Lidar System for 3D Land Classification & Coastal Bathymetry.” In *European Lidar Mapping Forum*. Amsterdam.

LaRocque, Paul E., Murtaza Safri, Wai Yeung Yan, and Ahmed Shaker. 2016. “New Hardware and Software for the Multispectral Optech Titan.” In *17th Annual JALBTCX Airborne Coastal Mapping and Charting Technical Workshop*. Silver Spring, MD.

LaRocque, Paul E, John R Banic, and A G Cunningham. 2004. “Design Description and Field Testing of the SHOALS-1000 Airborne Bathymeter.” In *Laser Radar Technology and Applications IX*, SPIE 5412:162–84. SPIE. https://doi.org/10.1117/12.564924.

Lee, Mark. 2003. “Benthic Mapping of Coastal Waters Using Data Fusion of Hyperspectral Imagery and Airborne Laser Bathymetry.” University of FLorida. http://etd.fcla.edu/UF/UFE0000730/lee_m.pdf.

Levis, C. A., W. G. Swarner, C. E. Prettyman, and G. W. Reinhardt. 1973. “An Optical Radar for Airborne Use over Natural Waters.” In *Proc. Oceans ’73*, 76–83. IEEE. https://doi.org/10.1109/OCEANS.1973.1161234.

Lillycrop, W. Jeff, and John R. Banic. 1992. “Advancements in the US Army Corps of Engineers Hydrographic Survey Capabilities: The SHOALS System.” *Marine Geodesy*, Mar. Geod. (USA), 15 (2–3): 177–85. https://doi.org/10.1080/01490419209388053.

Lillycrop, W. Jeff, and L. L. Estep. 1995. “Generational Advancements in Coastal Surveying and Mapping.” *Sea Technology* 36 (6): 10–16.

Lillycrop, W. Jeff, Jennifer L. Irish, and Larry E. Parson. 1997. “SHOALS System.” *Sea Technology* 38 (6): 17–25.

Lillycrop, W. Jeff, Larry E. Parson, and Jennifer L. Irish. 1996. “Development and Operation of the SHOALS Airborne Lidar Hydrographic Survey System.” In *CIS Selected Papers: Laser Remote Sensing of Natural Waters: From Theory to Practice, November 1, 1996 - November 1*, 2964:26–37. US Army Engineer Waterways Experiment Station, Coastal Engineering Research Center, 3909 Halls Ferry Road, Vicksburg, MS 39180-6199, United States: SPIE. https://doi.org/10.1117/12.258351.

Malone, A. K., M. J. Casey, and D. Monahan. 1983. “Scanning Lidar Bathymeter: (1) Deployment Strategies and (2) Data Processing.” *Lighthouse: Journal of the Candian Hydrographers Assn.* 27: 2–12. http://fohcan.org/lighthouse/ed27high.pdf.

Mandlburger, Gottfried, Martin Pfennigbauer, M. Wieser, U. Riegl, and N. Pfeifer. 2016. “Evaluation of a Novel UAV-Borne Topo-Bathymetric Laser Profiler.” In *ISPRS - International Archives of the Photogrammetry, Remote Sensing and Spatial Information Sciences*, XLI-B1:933–39. Copernicus GmbH. https://doi.org/https://doi.org/10.5194/isprs-archives-XLI-B1-933-2016.

Miles, M. K., W. Jeff Lillycrop, M. F. Kidby, and Larry E. Parson. 1994. “Transfer of the SHOALS System Technology to the U.S. Army Corps of Engineers.” In *U.S. Army Corps of Engineers 1994 Training Symposium, Survey and Mapping, Remote Sensing/GIS, SM:2D 1*.

Moniteq, Ltd. 1983a. “Determination of Parameters of Significance for Accuracy Optimization of a Scanning Lidar Bathymeter.” Concord, Ontario, Canada: Canadian Hydrographic Service.

———. 1983b. “Development of Correction Algorithms for Accurate Interpretation of Lidar Bathymetry Data.” Concord, Ontario, Canada: Canadian Hydrographic Service Contract No. 31SS.FP802-1-2168.

Nayegandhi, Amar, J. C. Brock, and C. Wayne Wright. 2005. “Classifying Vegetation Using NASA’s Experimental Advanced Airborne Research Lidar (EAARL) at Assateague Island National Seashore.” In *Proc. ASPRS Annual Conference, Baltimore, MD, [CD-ROM].*, Session 25, paper ID 500001, 15 pp. Baltimore, MD.

Nayegandhi, Amar, John C. Brock, and C. Wayne Wright. 2009. “Small-Footprint, Waveform-Resolving Lidar Estimation of Submerged and Sub-Canopy Topography in Coastal Environments.” *International Journal of Remote Sensing* 30 (4): 861–878. https://doi.org/10.1080/01431160802395227.

Nayegandhi, Amar, John C. Brock, C. Wayne Wright, and Michael J. O’Connell. 2006. “Evaluating A Small Footprint, Waveform-Resolving Lidar Over Coastal Vegetation Communities.” *Photogrammetric Engineering and Remote Sensing* 72 (12): 1407–17. https://doi.org/0099-1112.

Nordstrom, G. 2000. “The Swedish Hydrogaphic Service on the Eve of a New Millenium.” *Integrated Coastal Zone Management* Spring: 37–40.

Ott, L. M. 1965. “Underwater Ranging Measurements Using Blue-Green Laser.” Warminster, PA (Confidential): Naval Air Develpment Center, Report No. NADC-AE-6519.

Ott, L. M., H. Krumboltz, and A. K. Witt. 1971a. “Detection of Submerged Submarine by an Optical Ranging and Detection System and Detection of Pulses by a Submarine.” In *8th U.S. Navy Symposium of Military Oceanography, Vol. II*. Naval Postgraduate School, Monterey, CA (CONFIDENTIAL).

Ott, L M, H Krumboltz, and A K Witt. 1971b. “Detection of Submerged Submarine by an Optical Ranging and Detection System and Detection of Pulses by a Submarine.” In *8th U.S. Navy Symposium of Military Oceanography, Vol. II*. Naval Postgraduate School, Monterey, CA.

Park, Joong Yong, Vinod Ramnath, Viktor I. Feygels, Minsu Kim, Abhinav Mathur, Jennifer Aitken, and Grady H. Tuell. 2010. “Active-Passive Data Fusion Algorithms for Seafloor Imaging and Classification from CZMIL Data,” 769515. http://dx.doi.org/10.1117/12.851991.

Penny, Michael F. 1982. “Laser Hydrography in Australia.” In *Proceedings of the International Conference on Lasers ’81*.

Penny, Michael F., Ralph H. Abbot, D. M. Phillips, Brian Billard, D. Rees, D. W. Faulkner, D. G. Cartwright, et al. 1986. “Airborne Laser Hydrography in Australia.” *Applied Optics* 25 (13): 2046–58. https://doi.org/10.1364/AO.25.002046.

Pfennigbauer, Martin, and Frank Steinbacher. 2012. “Riverbed Surveying - High Resolution Shallow Water Mapping from an Airborne Platform.” *Hydro International* 16.

Pfennigbauer, Martin, Clifford Wolf, Josef Weindopf, and Andreas Ullrich. 2014. “Online Waveform Processing for Demanding Target Situatons.” In *Proc. SPIE 9080: Laser Radar Technology and Applications XIX and Atmospheric Propagation XI*. Baltimore, MD: SPIE. https://doi.org/10.1117/12.2052994.

Pope, J., and W. Jeff Lillycrop. 1988. “Development of a Helicopter Lidar Bathymeter System.” In *Proc. U.S. Army Corps of Engineers Surveying Conf.*, 213–16. Ft. Belvoir, VA.

Prettyman, C. E., and M. D. Cermak. 1969. “Time Variation of the Rough Ocean Surface and Its Effect on an Incident Laser Beam.” *Geoscience Electronics, IEEE Transactions on Geoscience Electronics* 7 (4): 235–43. https://doi.org/10.1109/TGE.1969.271357.

Ramnath, Vinod, Viktor I. Feygels, Yuri I. Kopilevich, Joong Yong Park, and Grady H. Tuell. 2010. “Predicted Bathymetric Lidar Performance of Coastal Zone Mapping and Imaging Lidar (CZMIL).” In *Algorithms and Technologies for Multispectral, Hyperspectral, and Ultraspectral Imagery XVI, April 5, 2010 - April 8*, 7695:The Society of Photo-Optical Instrumentation Engin. Optech

International Inc., 7225 Stennis Airport Drive, Kiln, MS 39556, United States: SPIE. https://doi.org/10.1117/12.851978.

Ryan, J. S., and Robert A. O'Neil. 1980. "Field Trials of an Airborne Lidar Bathymeter." In *Proceedings of the 19th Annual Canadian Hydrographic Conference*. Halifax, Nova Scotia, CA: Canadian Hydrographers Assn.

Setter, C., and R. J. Willis. 1994. "LADS—From Development to Hydrographic Operations." In *US Hydro. Conference*, 134–39.

Shaker, Ahmed, Wai-Yeung Yan, Paul E. LaRocque, Salem Morsy, and Nagwa El-Ashmawy. 2015. "Multi-Wavelength Lidar Data: Potentials of the New Technology in Land Cover Classification." In *ASPRS Annual Conference*. Tampa, FL: ASPRS.

Shannon, John G. 1975. "Correlation of Beam and Diffuse Attenuation Coefficients Measured in Selected Ocean Waters." In *Ocean Optic IV*, 64:3–11. San Diego, CA: International Society for Optics and Photonics. https://doi.org/10.1117/12.954489.

Sinclair, Mark J. 1997. "LADS Mk II Aircraft Launched." *Hydro International*, December 1997.

———. 1998. "Australians Get on Board with New Laser Airborne Depth Sounder." *Sea Technology*, 1998.

Sinclair, Mark J., D. J. Stephenson, and T. Spurling. 1999. "High Resolution Surveys in Shallow Water - LADS." In *Proc. Shallow Survey 99*, 9 pp. Sydney, Australia: Australian Defence Science and Technology Organization.

Sizgoric, Sebastian, John R. Banic, and Gary C. Guenther. 1992. "1970-1990: Airborne Lidar Hydrography Status." In *EARSeL Advances in Remote Sensing, Vol. 1, No.2 - II*. Firenza, Italy: EARSeL. http://www.earsel.org/Advances/1-2-1992/1-2_15_Sizgoric.pdf.

Skogvik, J., and Axelsson Rune. 2001. "Experience and Results from Swedish Laser Surveys and Post-Processing of Laser Bathymetry Data." In *Proc. Hydro 2001, Special Pub. 42*, Paper 20. Norwich, England.

Sorenson, G. P., Richard C. Honey, and J. R. Payne. 1966. "Analysis of the Use of Airborne Laser Radar for Submarine Detection and Ranging." Vol. Final. SRI Report No. 5583, Stanford Research Institute, Alexandria, VA: GKY & Associates, Inc.

Spurling, T., and G. Perry. 1997. "A New Generation Laser Airborne Depth Sounder." In *XVth International Hydrographic Conerence*, Session IV:1.1-1.16. Monaco: International Hydrographic Organization.

Steinvall, Ove K., Hakan Klevebrant, Jorgen Lexander, and Anders Widen. 1981. "Laser Depth Sounding in the Baltic Sea." *Applied Optics* 20 (19): 3284. https://doi.org/10.1364/AO.20.003284.

Steinvall, Ove K., K. Koppari, U. Lejdebrink, J. Winell, M. Nilsson, R. Ellsen, and E. Gjellan. 1997. "Theories and Experience of the Swedish Airborne Laser System." In *Proc. XVth International Hydrographic Conference*, IV.3.1. Monaco.

Steinvall, Ove K., Kurt R. Koppari, and Ulf C. M. Karlsson. 1993. "Experimental Evaluation of an Airborne Depth-Sounding Lidar." *Optical Engineering* 32 (6): 1307–21. https://doi.org/10.1117/12.135859.

———. 1994. "Airborne Laser Depth Sounding: System Aspects and Performance." In *Proc. SPIE 2258: Ocean Optics XII*, edited by Jules Jaffe, 392–412. Bergen, Norway: SPIE. https://doi.org/10.1117/12.190082.

Tuell, Grady H., Viktor I. Feygels, Yuri I. Kopilevich, Alan D. Weidemann, A. Grant Cunningham, Reza Mani, Vladimir Podoba, Vinod Ramnath, Joong Yong Park, and Jennifer Aitken. 2005. "Measurement of Ocean Water Optical Properties and Seafloor Reflectace with Scanning Hydrographic Operational Airborne Lidar Survey (SHOALS): II. Practical Results and Comparison with Independent Data." In *SPIE 5885: Remote Sensing of the Coastal Oceanic Environment, July 31- August 1, 2005*, edited by Robert J. Frouin, Marcel Babin, and Shubha Sathyendranath, 5885:58850E-58850E – 13. San Diego, CA: SPIE. https://doi.org/10.1117/12.619215.

Tuell, Grady H., and Joong Yong Park. 2004. "Use of SHOALS Bottom Reflectance Images to Constrain the Inversion of a Hyperspectral Radiative Transfer Model," 185–93. http://dx.doi.org/10.1117/12.564929.

Wellington, M. 2001. "The Laser Airborne Depth Sounder (LADS) - a Broad Range of Applications." In *Hydro 2001*, Special Pu:11 pp. Norwich, England: The Hydrographic Society.

Witt, A. K., John G. Shannon, M. B. Rankin, and L. A. Fuchs. 1976. "Air/Underwater Laser Radar Test Results, Analysis, and Performance Predictions." Warminster, PA (Confidential).

Wozencraft, Jennifer M. 2002. "Complete Coastal Mapping with Airborne Lidar." In *Ocean's 2002 Conference and Exhibition, October 29, 2002 - October 31*, 2:1194–98. Jt. Airborne Lidar Bathymetry T.C.E., US Army Corps of Eng., Mobile Dist., 109 St. Joseph Street, Mobile, AL 36602, United States: Institute of Electrical and Electronics Engineers Inc. https://doi.org/10.1109/OCEANS.2002.1192136.

———. 2010. "Requirements for the Coastal Zone Mapping and Imaging Lidar (CZMIL)." In *Algorithms and Technologies for Multispectral, Hyperspectral, and Ultraspectral Imagery XVI, April 5, 2010 - April 8*, SPIE 7695:The Society of Photo-Optical Instrumentation Engin. Orlando, FL: SPIE. https://doi.org/10.1117/12.851891.

Wozencraft, Jennifer M., and W. Jeff Lillycrop. 2003. "SHOALS Airborne Coastal Mapping: Past, Present, and Future." *Journal of Coastal Research* SI (81): 207–15. https://www-jstor-org.proxy.library.cornell.edu/stable/25736607.

———. 2006. "JALBTCX Coastal Mapping for the USACE." *The International Hydrographic Review* 7 (2): 28–37. https://journals.lib.unb.ca/index.php/ihr/article/view/20763.

Wozencraft, Jennifer M., and David Millar. 2005. "Airborne Lidar and Integrated Technologies for Coastal Mapping and Nautical Charting." *Marine Technology Society Journal* 39 (3): 27–35. https://doi.org/10.4031/002533205787442440.

Wozencraft, Jennifer M., and Joong Yong Park. 2013. "Integrated LiDAR and Hyperspectral." In *Coral Reef Remote Sensing*, 1st ed., 175–91. Dordrecht: Springer Netherlands. https://doi.org/10.1007/978-90-481-9292-2_7.

Wright, C. Wayne, and John C. Brock. 2002. "EAARL: A Lidar for Mapping Shallow Coral Reefs and Other Coastal Environments." In *Proceedings of the Seventh International Conference on Remote Sensing for Marine and Coastal Environments*, 8. Miami, Florida. https://www.tib.eu/en/search/id/TIBKAT%3A35324662X/Proceedings-Seventh-International-Conference-on/.

Wright, C. Wayne, Christine Kranenburg, Timothy A. Battista, and Christopher E. Parrish. 2016. "Depth Calibration and Validation of the Experimental Advanced Airborne Research Lidar, EAARL-B." *Journal of Coastal Research* SI (76): 4–17. https://doi.org/10.2112/SI76-002.

Yang, Eric, and Paul E. LaRocque. 2010. "SHOALS Object Detection." *The International Hydrographic Review*, no. 3 (March): 24–36. https://journals.lib.unb.ca/index.php/ihr/article/view/20849.

eCommons (2019) https://doi.org10.7298/jxm9-g971

3 ENVIRONMENTAL OPTICAL PROPERTIES

Lead Author: Shachak Pe'eri[a]

Contributing Authors: Viktor Feygels[b], Torbjörn Tingaker[c], Yuri Kopilevich[d], Minsu Kim[e], William Philpot[f], and Chi-Kuei Wang[g]

a) Center for Coastal and Ocean Mapping, University of New Hampshire, Durham, NH 03824 USA;
b) Teledyne Optech Inc., 7225 Stennis Airport Drive, Suite 400, Kiln, MS 39556 USA
c) Airborne Hydrography AB, 553 03 Jönköping Sweden.
d) St. Petersburg State Univ. (SPbITMO), St. Petersburg, Russia
e) USGS, 47914 252Nd Street, Sioux Falls, SD
f) School of Civil & Environmental Engineering, Cornell University, Ithaca, NY 14859 USA
g) Dept. of Geomatics, National Cheng Kung Univ., Tainan, Taiwan

Propagation of the lidar pulse, the change in its shape and distribution, and the light returned to the detector all depend critically on the inherent optical properties (IOPs) of the atmosphere, water surface, water column and bottom. The more descriptive apparent optical properties (AOPs) are also useful for characterizing the limits of penetration of the lidar in terms of perceived water quality. The key optical properties are defined and briefly described here, and the concepts will be used throughout the following chapters. More rigorous definitions and detailed descriptions can be found in references such as Dunt1ey (1971), Gordon et al. (Gordon, Smith, and Zaneveld 1979), Mobley (1994) and Mobley, Boss & Roesler (2013).

3.1 Atmosphere

Viktor Feygels

In this Section, two important questions are discussed: (a) attenuation of the bottom and backscattering return signals by the atmosphere, and (b) the strength of the atmospheric backscatter signal under various weather conditions.

3.1.1 Atmospheric attenuation of the bottom and water return signals

The lidar signal is attenuated by the atmosphere both when the sounding beam travels from the airborne lidar and the sea surface and during the return trip. The effect may be characterized by introducing a two-way transmission term, $T(H,\lambda)$, that depends on both the layer thickness, H, and the wavelength, λ:

$$T(H,\lambda) = \exp[-2\int_0^H \alpha(z,\lambda)dz] \quad , \tag{3.1.1}$$

where $\alpha(z,\lambda)$ is the atmospheric extinction coefficient at the distance z from the lidar. (For simplicity, here we consider the case of vertical propagation of the laser beam through the stratified medium. Eq. (3.1.1) expresses a specific form of the Lambert–Beer–Bouguer law for a lidar beam in which the factor 2 represents the two-way transmission over the same path.

For a homogeneous atmosphere,

$$T(H,\lambda) = \exp[-2H\alpha(\lambda)] \quad . \tag{3.1.2}$$

This approximation is applicable to an airborne bathymetrical lidar at the relatively low altitudes of 400-800 m.

The extinction coefficient $\alpha(\lambda)$ may be related to the atmospheric visibility range, or the visual range, V_r. According to Koschmieder's theory (Koschmieder 1924), the visual range is determined only by the contrast threshold an observer needs in order to distinguish an object from its background, and by the extinction coefficient, $\alpha(\lambda)$.

Koschmieder (1924) demonstrated that, for the wavelength 550 nm (the wavelength at which human visual sensitivity is a maximum),

$$V_r(550) = \frac{3.912}{\alpha(550)} \text{ and } \alpha(550) = \frac{3.912}{V_r(550)_r} \tag{3.1.3}$$

The value of $\alpha(\lambda)$ (in km^{-1}) at the wavelength, λ (in nm), of the lidar source may be estimated from a more sophisticated formula by Gorchakova et al. (1976) which accounts for wavelength dependence throughout the visible region (400-700nm):

$$\alpha(\lambda) = \frac{3.912}{V_r(550)}\left(\frac{550}{\lambda}\right)^{0.583\sqrt[3]{V_r(550)}} \tag{3.1.4}$$

In Figure 3.1.1, the atmospheric transmission is evaluated as a function of the visual range for the two values of lidar altitude, 400m and 800m, using equation (3.1.2) and (3.1.4) for λ=532nm:

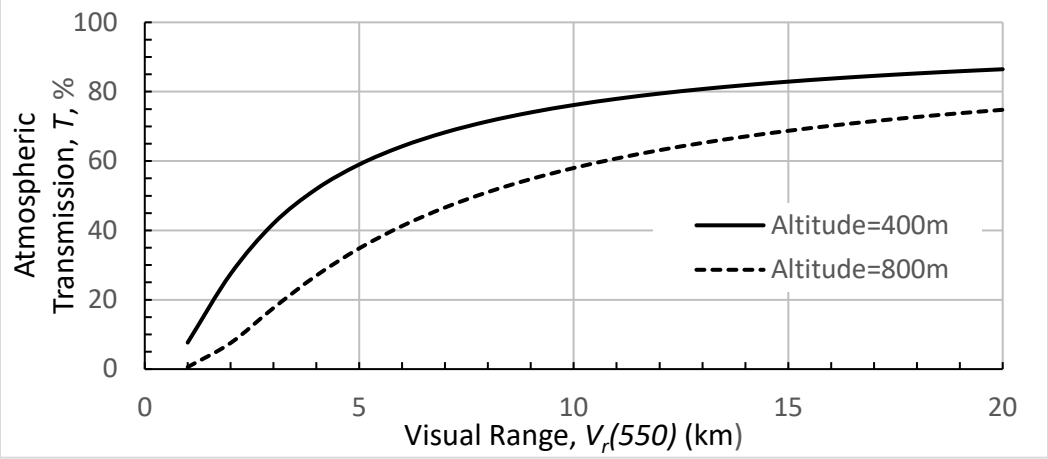

Figure 3.1.1. Atmospheric transmission (the two-way transmission path) a function of visual range for two lidar altitudes: 400 m and 800 m.

3.1.2 Atmospheric backscatter signal

Backscattering of the sounding laser beam in the atmosphere is a major nuisance factor for airborne lidar bathymetry performance. The backscattered signal arises immediately after the laser pulse emission, and therefore arrives at the detector before the sea surface reflected pulse, during the time $2H_s/c$, where H_s is the (slant) distance between aircraft and water surface and c is the speed of light. The atmospheric backscatter signal may significantly exceed in power the lidar return from the water column, sea surface, and bottom.

The lidar equation for the power of optical atmospheric backscattering signal, $P_{atm}(z,\lambda)$, can be written in a common approximate form (Wandinger 2005; Kovalev 2004)

$$P_{atm}(z,\lambda) = P_0 \frac{c\tau_p}{2} A_r \eta \frac{O(z)}{z^2} \beta_{atm}(z,\lambda) \exp[-2\int_0^z \alpha(r,\lambda)dr] \quad (3.1.5)$$

where:

P_{atm} (z, λ) is the power backscattered by the atmosphere and detected from range z at the laser wavelength λ;

$P_0(\lambda)$ is the transmitted laser pulse power;

τ_p is the (effective) laser pulse duration;

A_r is the area of the receiver aperture;

η is the total optical system loss factor;

$G_F(z)$ is the "lidar geometric factor", $0 \le G_F(z) \le 1.0$; $G_F(z) = 1$ for monostatic lidars

$\beta_{atm}(z,\lambda)$, is the backscattering coefficient of the atmosphere.

Calculations based on Eq. (3.1.5) may be simplified using the correlation relation proposed by Gorchakova et al. (1976) for the optical characteristics of the atmosphere in the visible light range:

$$\beta_{atm}(\lambda) = 0.0263\alpha(\lambda)^{0.69} \approx \frac{\alpha(\lambda)}{8\pi} \quad (3.1.6)$$

The above relation, together with Eqs. (3.1.3) and (3.1.4) for $\alpha(\lambda)$, makes it possible to express the atmospheric backscattered signal power via only one optical parameter of the atmospheric layer (assumed to be homogeneous) between the lidar carrier and the sea surface – the atmospheric visual range, V_r. Results of the calculations for are presented in Figure 3.1.2 for the atmospheric visual range (the meteorological visibility) of 10 km ($\lambda = 532\ nm$, $G_F(z) = 1$).

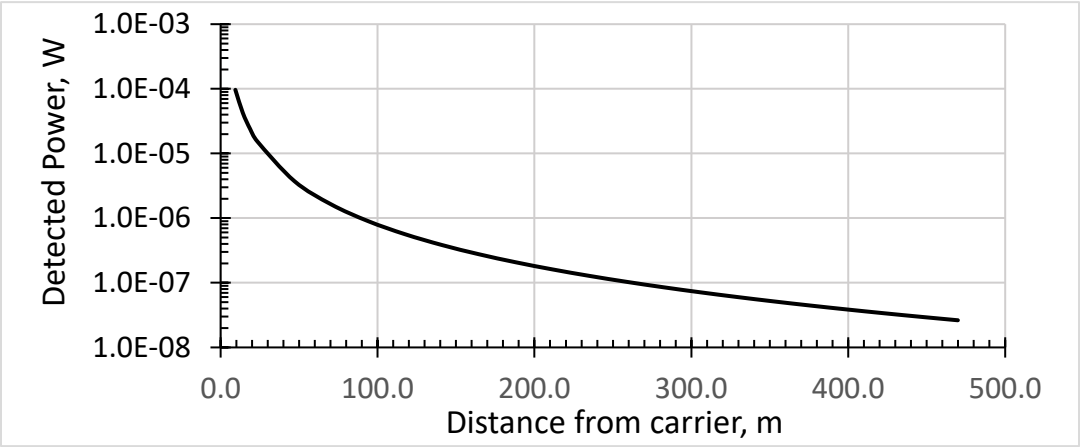

Figure 3.1.2. Detected atmospheric (visual range 10 km) backscattering signal for a bathymetric lidar as a function of distance from the carrier. Lidar parameters: pulse power = 0.5 MW; pulse duration = 2 ns; optical pupil diameter =10 cm; lidar optical efficiency = 60 %; the "geometrical factor" GF(z) = 1.0.

The powerful atmospheric signal may result in a variety of harmful effects on the lidar photodetector, such as temporary blindness, ringing, etc. In contrast to ambient sun light, the signal caused by elastic scattering of monochrome laser radiation in the atmosphere cannot be filtered out by a spectral selector. The known methods employed to protect lidar "green" detectors from the atmospheric backscattering are described by Measures (1984). These methods include: spatial separation of the lidar emitter and receiver axis (i.e., employment of a bi-static scheme); vignetting of the central part of the photodetector field of view; polarization selection; and "closing" the photodetector to radiation arriving immediately after sounding pulse generation.

Finally, we present in Figure 3.1.3., an illustrative, practical and convenient table of average values of visual range (meteorological visibility) and the coefficients $\alpha(\lambda)$ and $\beta(\lambda)$ for various weather conditions over the spectral range 350-1000 nm. Figure 3.1.3. is reproduced from Collis and Russell (1976).

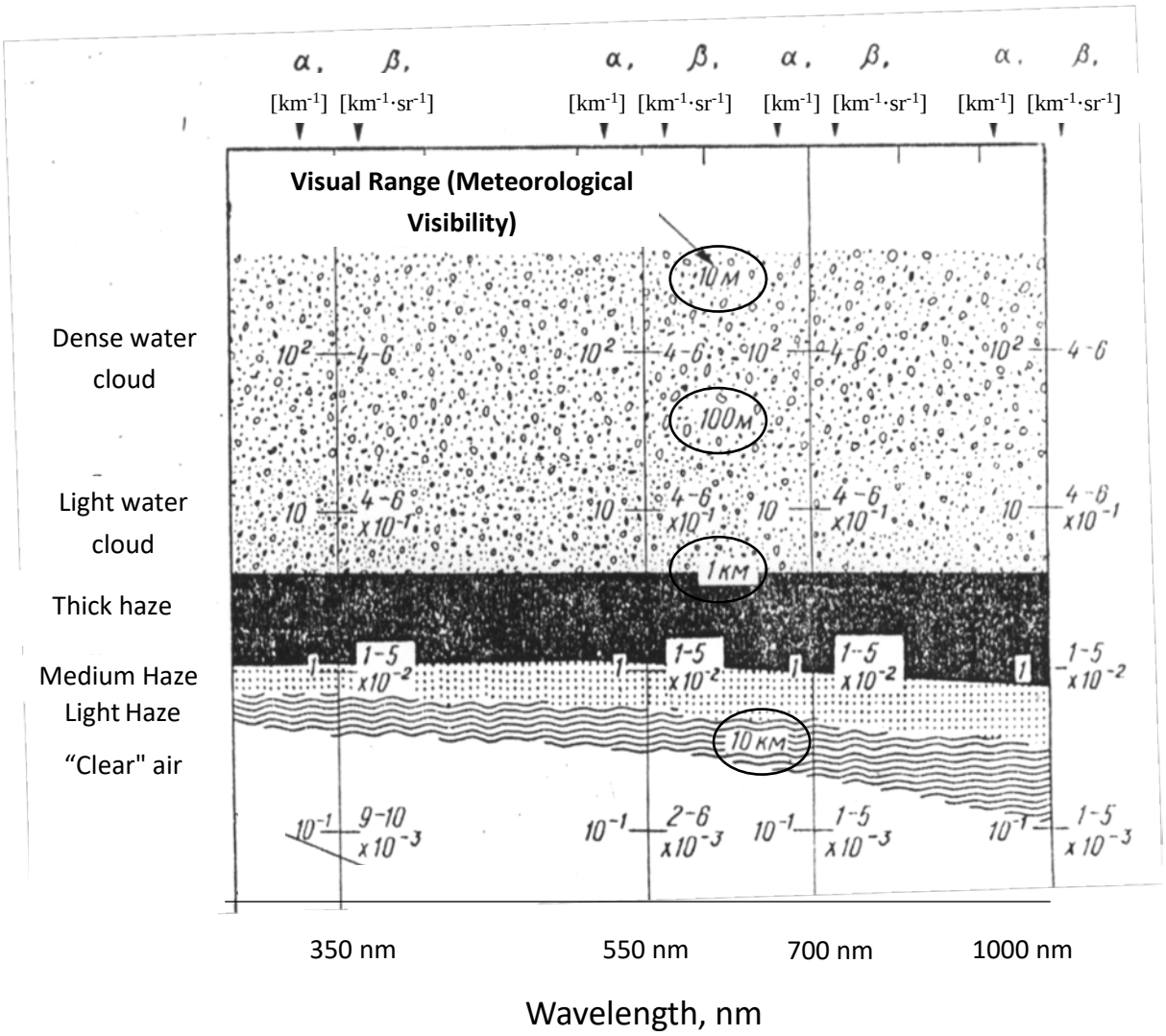

Figure 3.1.3. Attenuation (extinction), α, and backscattering coefficient, β, for various atmospheric conditions (left column) and wavelengths.

3.2 Water Surface

Shachak Pe'eri and Torbjörn Tingaker

3.2.1 Reflection and refraction

The surface return portion of the Airborne Lidar Bathymeter (ALB) waveform, a major reference point for water depth measurements, represents the interaction between the ALB laser beam and the air/water interface. The laser energy returned from the air/water interface and collected by the ALB detection unit can be described by two basic concepts in optics: reflection and refraction. In the case of ALB, reflection refers to the redirection of laser radiation from the air/water interface back into the air; refraction is the change in direction of radiation penetrating the air/water surface (Measures 1992; Mobley 1994). Both

mechanisms are dependent on the angle of incidence with respect to the local normal of the water surface. The water surface can be regarded as a transparent, specular (mirror-like) surface with some vertical variability (e.g., waves or swells). The law of reflection states the angle of incidence, θ_1, is equal to the angle of reflection. These angles are defined with respect to the local normal at the point of incidence (Figure 3.2.1). The direction, θ_2, of the laser energy after transmission across the air/water interface is calculated using Snell's law:

$$\frac{\sin(\theta_1)}{\sin(\theta_2)} = \frac{n_2}{n_1} \tag{3.2.1}$$

For light incident on the water surface from above and transmitted into the water we have $n_1 = n_a$, the index of refraction of air and $n_2 = n_w$, the index of refraction of water. The value of index of refraction for air is typically assumed to be 1.000 while the value of the index of refraction for water can range from 1.350 at 400 nm to 1.320 at 1100 nm (Segelstein 1981) with only a subtle sensitivity to temperature and salinity over the range typically encountered in the field (Aly and Esmail 1993; Austin and Halikas 1976; Quan and Fry 1995). In most cases, Snell's law can be approximated as $1.333\ sin(\theta_w) = sin(\theta_a)$ (Saleh and Teich 1991a).

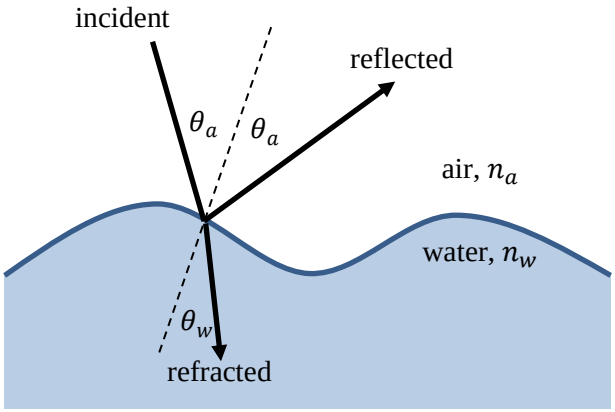

Figure 3.2.1. Reflection and refraction at the air-water interface.

The Fresnel equations are used to estimate the amount of light reflected and refracted at the interface between two dielectric media (Saleh and Teich 2007). The reflection coefficient, *R*, for unpolarized light is:

$$R = \frac{1}{2}(R_{\parallel} + R_{\perp}) = \frac{1}{2}\left(\frac{sin^2(\theta_a - \theta_w)}{sin^2(\theta_a + \theta_w)} + \frac{tan^2(\theta_a - \theta_w)}{tan^2(\theta_a + \theta_w)}\right) \tag{3.2.2}$$

where $R_{\parallel}$ and $R_{\perp}$ are the reflection coefficients for parallel and perpendicularly polarized radiation, respectively. Equation (3.2.2) provides a useful approximation for the overall loss at the surface due to reflection. However, evaluation of the amount of the laser pulse returned to the receiver will generally require more precise examination of the reflectance at the water surface.

3.2.2 Effects of waves

The length of sea-surface waves ranges from a few millimeters up to several hundreds of meters and may be divided into two general categories: capillary and gravity waves (Holthuijsen 2007). Capillary waves are short wavelength waves that are generated locally and restored by surface tension; the longer wavelength gravity waves may be generated either locally or from outside the survey area, and are restored by gravity (Open_University 2005). For waves that are generated locally, the structure of sea surface is often described using the Beaufort scale which relates a visual description of a sea state to wind speed (Table 2.1). Although the Beaufort scale is a qualitative characterization of the sea state, it is useful for relating wind speed observations to approximate environmental conditions for ALB surveying. It is important to note that when breaking waves start to appear on the sea surface (Beaufort Sea State 3) and bubbles are generated as a result, the chances are reduced for ALB systems to successfully detect the bottom. Accordingly, Guenther (2007) suggested limiting ALB surveying to wind speed of less than 5.5 m/s (10 knots).

Under ideal ALB survey conditions, the water surface would be horizontal on a macroscale (i.e., at a scale larger than the size of the lidar footprint on the water surface) with a uniform roughness on a micro-scale (i.e., vertical variability that ranges from a few millimeters to a few centimeters). In that case, a moderate amount of energy would be returned from the surface, the angle of refraction would be directly predictable given the horizontal surface, and only position and attitude data would be needed to calculate the position of the laser measurement underwater. However, the morphology of the sea surface is complex and highly variable in time and space. Capillary waves, with wavelengths smaller than the laser footprint on the water surface, might be expected to disperse the beam in the water. Water waves with lengths on the order of the laser footprint could act as a lens to focus or disperse the beam, and water waves much larger than the laser footprint could redirect the lidar beam since the local water surface will no longer be horizontal. These conditions can introduce several errors:

1) Range errors - Identification of the surface return in the ALB waveform.
2) Positioning error - Angle of refraction, θ_w, of the ALB beam.
3) Illumination area contributing to the measurements - Estimation of the ALB beam pattern below the water surface is used to as the initial conditions to calculate the scattering and absorption interaction of the laser beam as it passes through the water column.

Table 3.1. Beaufort wind force scale from 0 to 3

Beaufort Number	Wind speed	Appearance on the Water
0	**Less than 0.3 m/s**	**Flat, smooth sea surface, mirror-like**
1	**0.3–1.5 m/s**	**Scaly ripples without crests**
2	**1.6–3.4 m/s**	**Small wavelets, glassy crests, not breaking**
3	**3.5–5.4 m/s**	**Large wavelets, crests begin to break, scattered whitecaps**

The physical dimension of a wave with respect to the size of the ALB footprint is an important consideration. Tulldahl and Steinvall (2004) considered the change in direction of the transmitted laser

pulse after passing through a sloped air/water interface with capillary waves, by applying Monte Carlo ray-tracing simulations to realistic ocean surface models (Mobley and Preisendorfer 1988; Preisendorfer and Mobley 1985) corresponding to wind speeds according to the wave-slope wind-speed law (Cox and Munk 1954b, 1954a; Duntley 1954). Tulldahl and Steinvall (2004) investigated the variance of ALB beams based on HawkEye specifications for wind speeds that range from 0 to 20 m/s. His conclusion was that very little change (a few percent change) was calculated for the refracted angles of the ALB beam over a flat water surface with capillary waves.

Monte Carlo ray-tracing simulations have also been used to calculate the variance of ALB beams after passing through the water surface. These studies investigated micro-scale and macro-scale slopes over a sea surfaces generated from an Elfouhaily, Chapron, Katsaros, and Vandemark (ECKV) wave spectrum model (Elfouhaily et al. 1997) with wind conditions of up to 5.4 m/s. The simulation results showed that wind speed and footprint size were the two main parameters contributing to changes in the laser beam pattern underwater (Figure 3.2.2). The model results were confirmed with empirical measurements in a laboratory setting. Statistically, the mean direction of the laser beam over a large number of realizations (> 1000 realizations) does not deviate much from the refracted beam direction under a horizontal water surface. The standard deviation of along-wind, σ_u, and cross-wind, σ_c, directions of the ALB beam increased as the wind speeds over the water surface increased from 3 m/s to 5.4 m/s with a fixed beam diameter (4.5 m) and fetch length (10,000 km) (Figure 3.2.2a). The area of the ALB footprint over the water surface also affected the standard deviation. The standard deviation increased as the footprint size was reduced from 4.5 m in diameter to an area of a single ray (>5 mm in diameter) with a fixed wind speed (5.4 m/s) and fetch length (10,000 km) (Figure 3.2.2b). The standard deviation of the rays for a 4.5-m in diameter beam with a wind speed of 3.5 m/s remains constant as the fetch length increases from 100 km to 10,000 km.

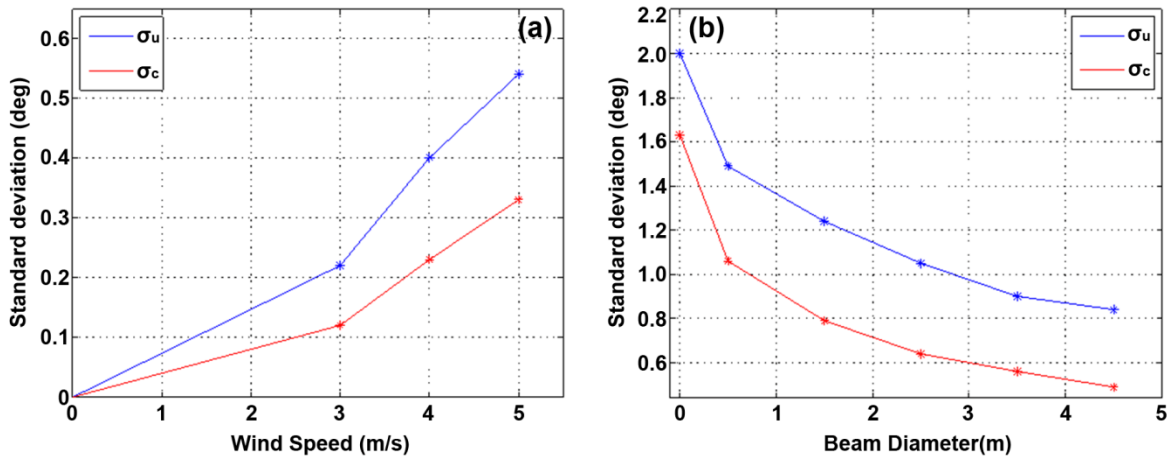

Figure 3.2.2. Standard deviation along-wind, $\boldsymbol{\sigma_u}$, and cross-wind, $\boldsymbol{\sigma_c}$, directions as a function of: (a) wind speed and (b) ALB beam diameter (Karlsson 2011).

3.2.3 Bubbles and foam

Typically, ALB surveys are conducted under relatively benign sea state conditions with small wavelets, glassy crests and no breaking waves (up to Beaufort Sea State 2) (Guenther 2007). At higher sea states

when larger wavelets occur at the water surface and crests begin to break, optical scattering from whitecaps (foam) and associated sub-surface gas bubbles increasingly distort the ALB waveforms. If unaccounted for, these sea surface and volume scattering effects may reduce the accuracy with which the water depth can be measured and, at high enough sea states, may mask the seafloor entirely. Although bubbles and foam are a source of noise during operations focused on seafloor characterization, there is great potential scientific value in using ALB to remotely characterize the air bubbles themselves. Gas bubbles, generated through the breaking of wind-driven sea waves, influence the air-sea gas exchange, aerosol formation, sea surface chemistry, fractionation of organic and inorganic materials and cavitation (Bortkovskii et al. 2007; Loisel et al. 2007; Sorooshian et al. 2009; Stigebrandt 1991; Woolf 1993). Bubbles can also be an indicator of environmental events occurring on the seafloor, such as a methane seep (Solomon et al. 2009; Westbrook et al. 2009).

Monahan and Lu (1990) characterize the main stages in the evolution of a plume of air bubbles. Spilling wave crests and active whitecaps are generated when winds that are well above 4 m/s blow over the water surface. The bubble plume at this stage is visible from a ship or a plane with an optical albedo of about 0.5 (Monahan and Mac Niocaill 1986). The active whitecaps and the concentrated sub-surface bubble plumes have surface expressions with very short characteristic lifetimes (less than 1 s) (Donelan, Longuet-Higgens, and Turner 1972). The sub-surface bubble plumes associated with the spilling/breaking wave crests have void or air volume fractions estimated to range from 3% up to 30%, depending on the water depth and exposed features (e.g., jetty or dam) that may influence the breaking wave (Monahan and Lu 1990). These plumes will quickly decay into a mature whitecap or hazy foam patches whose size decreases exponentially with time. Mature plumes are relatively large sea-surface features with an average albedo of about 0.2 (Monahan and Mac Niocaill 1986) and a void fraction ranging from 1% in a fully developed sea condition to 0.1% for a bubble plume that is a few seconds old (Monahan and Muircheartaigh 1980). Even after the bubble plume is not visible anymore, a large subsurface bubble plume exists. Compared with the visible bubble plumes, the size spectrum of the bubbles is narrower but the lifetime of the subsurface plume is typically hundreds of seconds (Monahan and Mac Niocaill 1986). In this final stage of the plume's lifetime, the larger bubbles have risen to the surface while near-surface turbulence has mixed the micro-bubbles (10s to 100s of μm in radius) throughout a near-surface layer. The size distribution and evolution of the micro-bubble plume depends on the aqueous concentrations of nitrogen and oxygen in the surface waters (Thorpe 1982) and the gas transfer rate across the air-water interface of the bubbles (the bubble wall) into the surrounding water (Medwin 1970), with all bubbles eventually either returning to the surface to burst or going into solution. It is important to note that ship wakes or water surface circulation (e.g., Langmuir circulation) may dramatically change the lifetime and distribution of the bubble population. These changes occur partly as a result of changes in the flow dynamics, but also because organic materials, such as oils and surfactants, and particulates collected on the surface of a bubble can modify the rate of dissolution and substantially increase the lifetimes of bubbles (Johnson and Cooke 1981; Thorpe 1985; T. C. Weber, Lyons, and Bradley 2005). The void fraction of these late-stage micro-bubble plumes is estimated to be in the range of $1 \times 10^{-4}\%$ to $1 \times 10^{-5}\%$ (Thorpe 1982). Even after the plume has disappeared, the surfactants that have been scavenged by bubbles and deposited at the surface can change the sea-surface roughness for long periods of time. This is particularly noticeable in synthetic aperture radar images of ship wakes (T. C. Weber, Lyons, and Bradley 2005).

Research on the use of ALB surveys to map bubble plumes is still in its infant stages. Most of the work has focused on the use of ALB surveys to correct for ocean color estimates of chlorophyll concentration that are modified by bubbles (Terrill, Melville, and Stramski 2001; X. Zhang, Lewis, and Johnson 1998) and to identify ship tracks and fish schools (Krekova, Krekov, and Shamanaev 2004; Li et al. 2009). These studies are based on theoretical work and laboratory experiments, in which the key assumption is that ALB amplitude is proportionally related to void fraction and the presence of organic materials. In the calculations, seawater is considered to be a multi-component medium, for which the backscatter radiation is a function of water molecules, hydrosol particles, and air bubbles (Churnside 2010; Krekova, Krekov, and Shamanaev 2004). The optical models for the ALB are based on the work of (X. Zhang, Lewis, and Johnson 1998) which defines the bulk optical properties of the bubble population.

In addition to the elastic scattering approaches to mapping bubble plumes in the ocean, there are also efforts to use inelastic scattering, such as Raman scattering. Bunkin et al. (2011) demonstrated experimentally that Raman scattering can be used to detect a micro-bubble plume 4.5 minutes from the time a boat passed by, whereas with elastic scattering it is only possible to detect larger bubbles that are present, and only within the first 0.5 to 0.75 minutes from the time a boat passes by.

3.3 Volume

An understanding of the optical properties of the water is essential for understanding of the propagation and spread of the laser pulse as it passes through the water. The treatment here is necessarily brief and is focused on the characteristics that are most important for lidar bathymetric mapping. The material presented here will be widely used in the later sections. More thorough and detailed treatments can be found in references such as Duntley (1971), Gordon et al. (1975), and Mobley (1994) or on line (Mobley, Boss, and Roesler 2013).

We will be concerned with both inherent and apparent optical properties. The inherent optical properties (IOPs), absorption and scattering, are the properties that are not dependent on the ambient light or viewing conditions. Apparent optical properties (AOPs) "*are those properties that (1) depend both on the medium (the IOPs) and on the geometric (directional) structure of the radiance distribution, and that (2) display enough regular features and stability to be useful descriptors of a water body.*" (Mobley, Boss, and Roesler 2013).

3.3.1 Apparent Optical Properties (AOPs)

William Philpot

Although it is the IOPs that will be most important for the description of the transmission of the lidar pulse through water and the overall operation and performance of the lidar system, AOPs are useful for describing the general optical characteristics of the water. The description that they provide is relatively coarse, but intuitive. Indeed, AOPs have provided a useful, if crude, characterization of the penetration depth of bathymetric lidar.

3.3.1.1 Secchi Depth

As observed from above the water surface, objects lowered into the water become less distinct as the depth increases, eventually merging with the background. This is the principle behind the Secchi disk, the

first device designed to document the transparency of natural waters (Tyler 1968). Originally, a simple white disk, the Secchi disk is now most commonly divided into black and white quadrants in order to maximize contrast, and the depth at which the black and white disk disappears from view is called the "Secchi depth". Clear waters will have a 1arger Secchi depth than more turbid waters, and the size of the Secchi disk may need to be adjusted for different water clarity conditions (Holmes 1970). The disk disappears because the light traversing the water column is subject to absorption and scattering processes which reduce the magnitude of the reflected radiation and increase the volume backscatter noise background. The measurement, while common and useful, is only semi-quantitative since the results depend on a number of factors such as the angle and distribution of ambient illumination, surface wave structure, the type of particulates in the water, and the visual acuity of the observer, to name only a few (Pilgrim 1984). The Secchi depth is consequently an AOP.

Although it is only approximate, the Secchi depth remains a useful, intuitive measure of water clarity and is commonly used to characterize the penetration depth of ALB systems. It is worth remembering, however, that the Secchi depth does not properly describe the attenuation of a collimated light beam. In addition, it is an observation that spans the visible wavelengths and is not specifically tuned to the narrow waveband of a laser.

3.3.1.2 Diffuse Attenuation Coefficient

A more quantitative measurement of water clarity involves measuring the rate of change of irradiance with increasing depth. For this purpose we consider cosine irradiance, $E(\lambda)$, the cosine-weighted integral of the radiance distribution over a hemisphere. We are particularly interested in the downwelling cosine irradiance on a horizontal plane, $E_d(z,\lambda)$, at depth z. The rate of change of E_d with depth is a measure of water clarity that is similar in concept to the Secchi depth in that the rate of change will be faster in turbid waters than in clear waters. The rate of change of E_d, or logarithmic derivative of E_d is the diffuse attenuation coefficient, K_d, which is given by (Mobley, Boss, and Roesler 2013):

$$K_d = -\frac{d \ln E_d(z,\lambda)}{dz} = -\frac{1}{E_d(z,\lambda)}\frac{dE_d(z,\lambda)}{dz} \quad (m^{-1}) \quad . \tag{3.3.1}$$

This attenuation coefficient is an AOP because of its sensitivity to the distribution of downwelling light (thus, the term *diffuse* in the name). Values for K_d will be different if the measurement is made under cloudy conditions or under clear skies, although such differences are often relatively small. On the other hand, K_d is not dependent on the individual viewer, it can be tuned to the wavelength of the laser, and the measurement can be made over discrete depth ranges, allowing for characterization of stratified water bodies. For these reasons, K_d is sometimes referred to as a "quasi-inherent" optical property. K_d is useful for laser hydrography in that it can provide effective general description of the attenuation of the broadened laser pulse (Feygels et al. 2013; Kopilevich 2002; Wozencraft and Millar 2005).

3.3.2 Inherent optical properties

Minsu Kim

As a laser pulse propagates through natural waters, it interacts with the optical constituents of the water with the radiant power decreasing due to the absorption of the medium, and its radiance distribution is

dispersing due to the scattering. A small fraction of radiant power is backscattered and available for detection by the distant lidar receiver. The properties of the water responsible for this light interaction are: IOPs (defined above), properties of the medium itself, and independent of the light field (Mobley 1994; Mobley, Boss, and Roesler 2013; Preisendorfer 1976). The bulk IOPs of natural waters are a sum of properties of the optically dominant constituents. In describing a real-world light field, the macro-level radiance propagation is properly explained using absorption and scattering, which is why these two quantities (absorption coefficient and volume scattering function precisely) are called IOPs. We will describe the definition of these IOPs here. There are, however, more fundamental physical parameters than the macroscopic absorption and scattering coefficients. These are the refractive indices of the dielectric medium that controls the propagation of the electromagnetic wave, microscopic properties that underlie the macroscopic properties. Thus, we begin with a description of the refractive index of water, which is the dominant component.

3.3.2.1 Refractive index of natural water

Radiative transfer describes the rate of change of the macroscopic radiant power as a result of all the microscopic interactions between electromagnetic waves and matter: absorption of a photon, re-emission, diffraction, etc. For our purposes, absorption and the volume scattering function (VSF) are the two fundamental parameters. Along with these typical IOPs, the *complex refractive index* is another important, and more fundamental IOP. It is also a very important parameter in lidar ranging and depth penetration. The complex refractive index of a dielectric medium determines the interaction with the incoming electromagnetic wave in terms of refraction and absorption. It is expressed as

$$m = n - in_i \quad . \tag{3.3.2}$$

The real part, n, is the index of refraction that determines the phase speed of the electromagnetic wave in the medium, and the imaginary part, n_i, is related to absorption by the medium. Both n and n_i are dependent on the wavelength, λ. The absorption coefficient, a, is related to the imaginary part of the index of refraction, n_i by the following relationship (Kerker 1969)

$$a = \frac{4\pi n_i}{\lambda} \quad . \tag{3.3.3}$$

The absorption coefficient of water plays a major role in shaping the reflected water-leaving radiance. A relatively rapid rise in the absorption coefficient near 600 nm characterizes typical coastal water (Figure 3.3.1), resulting in a sharp drop in reflectance at that point. Beyond 600 nm the reflectance disappears in all but very shallow or turbid water.

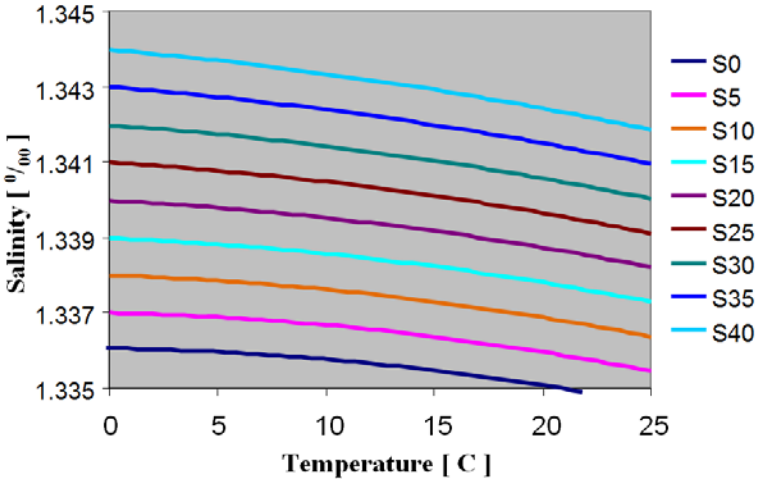

Figure 3.3.1. Refractive index of water with varying temperature and salinity.

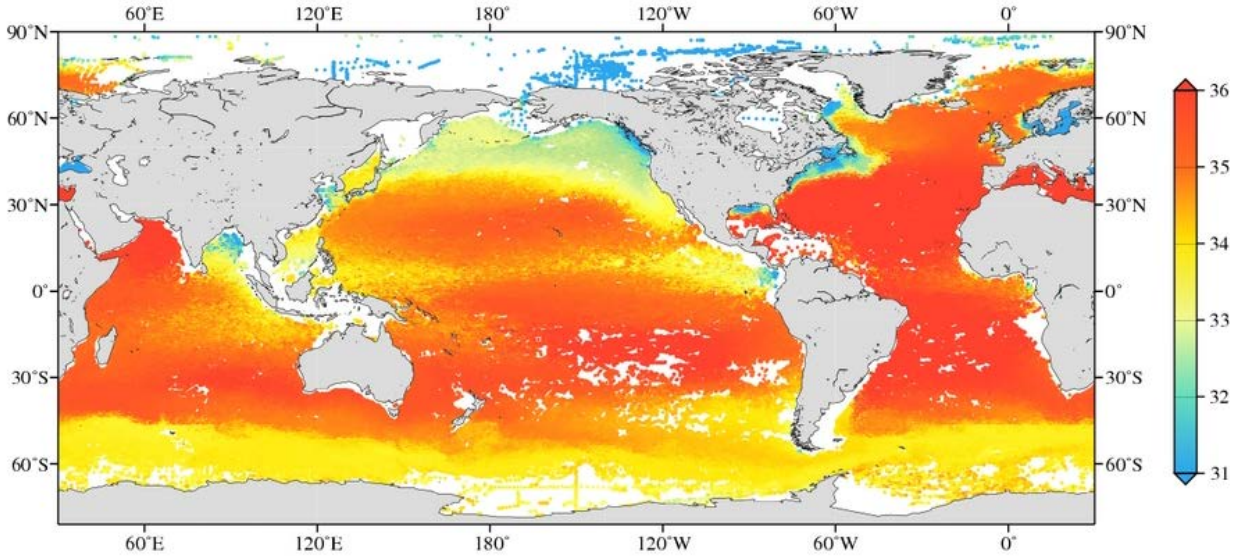

Figure 3.3.2. Annual mean surface salinity, 2005-2013 (NODC 2013).
http://www.nodc.noaa.gov/OC5/woa13f/index.html

3.3.2.2 Bulk water optical properties

There are only two fundamental IOPs for the bulk medium of natural water: the absorption coefficient and the volume scattering function (Mobley 1994; Preisendorfer 1976). Other IOPs are simply parameters derived from these two fundamental IOPs.

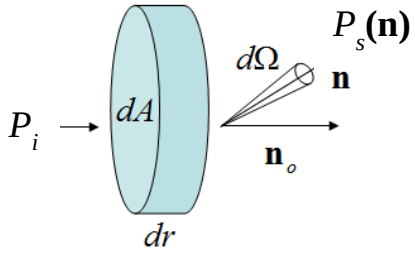

Figure 3.3.3. Interaction of radiant power with a small volume of water.

Consider a narrow, collimated beam with a radiant power, P_i, that is incident onto a small volume of an absorbing and scattering medium (Figure 3.3.4). Some of the radiant power, P_a, is absorbed by the medium. Light absorption is assumed to follow simple Beer's law and most of the natural water satisfies this condition. According to Beer's law, the *absorption coefficient*, a, is defined as absorptance, P_a/P_i, per unit propagation distance in the medium,

$$a = \frac{P_a}{P_i}\frac{1}{dr} \quad . \tag{3.3.4}$$

A fraction of the radiant power is scattered in all directions, with a portion of the scattered power, $P_S(\boldsymbol{n})$, being directed into a solid angle, $d\Omega$, centered on the direction, $\boldsymbol{n}$. The distribution of scattered radiation is described by the *volume scattering function* (VSF), β, defined as the directional scatterance per unit distance of the medium,

$$\beta(\boldsymbol{n}) = \frac{P_S(\boldsymbol{n})/d\Omega}{P_0}\frac{1}{dr} \quad . \tag{3.3.5}$$

It is customary to express the VSF as a function of the scattering angle, θ, where θ is measured from the forward direction, so that $\theta = cos^{-1}(\boldsymbol{n} \cdot \boldsymbol{n_0})$.

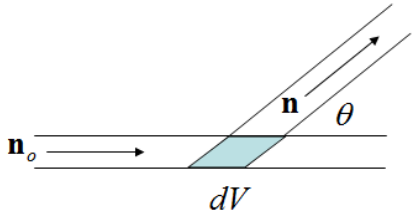

Figure 3.3.4. Conceptual diagram for VSF measurement.

The measurement geometry of the VSF is illustrated in Figure 3.3.5, where an incident, collimated irradiance, E_0 , illuminates the water volume, dV, and the scattered power in the direction $\boldsymbol{n}$, $P_S(\boldsymbol{n})$, is viewed by a detector. This allows us to express the VSF as

$$\beta(\boldsymbol{n}) = \frac{P_S(\boldsymbol{n})/d\Omega}{E_0}\frac{1}{dV} \quad . \tag{3.3.6}$$

The major practical difficulty with evaluating $\beta(\boldsymbol{n})$ is in the accurate determination of the scattering volume, dV, the volumetric intersection between the incident beam and the viewing field. This is not simply a matter of determining the 3-D geometry of two intersecting volumes; it is complicated by the need to characterize the divergence of the incident beam and the exact response function of the viewing field. The characterization is particularly problematic at very small angles (forward near 0º) and very large angles (backward near 180º).

Having defined the two fundamental IOPs of hydro-optics, the remaining IOPs can all be derived from these two. The total *scattering coefficient, b*, is simply the integral of the VSF of the full sphere,

$$b = \int_{4\pi} \beta(\boldsymbol{n}) d\Omega(\boldsymbol{n}) \quad . \tag{3.3.7}$$

Using spherical coordinates and assuming azimuthal symmetry, the integration is expressed

$$b = 2\pi \int_0^{\pi} \beta(\theta) \sin\theta \, d\theta \quad . \tag{3.3.8}$$

The *volume scattering phase function* (VSPF) is simply a normalized VSF, defined as

$$\chi(\theta) = \beta(\theta)/b \quad . \tag{3.3.9}$$

Therefore, $\chi(\theta)$ satisfies the normalization condition

$$1 = 2\pi \int_0^{\pi} \chi(\theta) \sin\theta \, d\theta \quad . \tag{3.3.10}$$

The *forward scattering coefficient, b_f*, and the *backward scattering coefficient, b_b*, which describe the proportion of light scattered in the forward and backward hemispheres, respectively, are defined as

$$b_f = 2\pi \int_0^{\pi/2} \beta(\theta) \sin\theta \, d\theta \quad , \qquad \text{and} \qquad b_b = 2\pi \int_{\pi/2}^{\pi} \beta(\theta) \sin\theta \, d\theta \quad . \tag{3.3.11a,b}$$

By the above definitions, the following equality holds:

$$b = b_f + b_b \quad . \tag{3.3.12}$$

Another noteworthy IOP is the *lidar backscattering coefficient*, which is simply the VSF in the opposition direction, β_π. This is particularly useful for describing the lidar waveform.

The total *beam attenuation coefficient*, c, is the sum of the absorption and scattering coefficients,

$$c = a + b \quad . \tag{3.3.13}$$

Although it is possible to calculate the scattering coefficient from the integration of the VSF, it is common practice to use the relationship, $b = c - a$, because of the practical difficulty of making the VSF measurement. Thus, it is important to understand the principles of measurements of a and c. The absorption coefficient is measured using a cylindrical sample chamber whose inner wall is highly reflective. The conceptual diagram of the absorption meter is shown in Figure 3.3.6. A fraction of light will be absorbed and lost over the distance, r. At the same time a fraction of the light will be multiply-scattered and directed forward by the reflective wall. Any light not absorbed will eventually reach the end of the tube, adding to the uninterrupted (transmitted without being absorbed or scattered) light to make up a total measured power, $P(r)$. The lost power is ascribed entirely to absorption, and the absorption coefficient is calculated using the formula

$$P(r) = P_i \exp(-a \cdot r) \quad . \tag{3.3.14}$$

where the exponential term represents the probability that a photon will survive being absorbed.

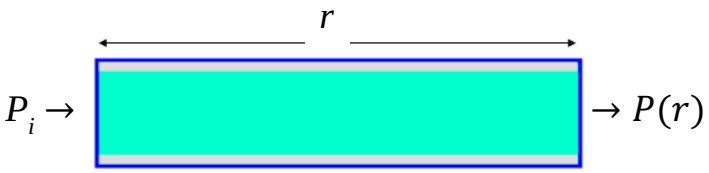

Figure 3.3.5. Conceptual diagram for absorption measurement using reflective wall sample cell.

In order to calculate the total beam attenuation, c, both absorbed and scattered power must be accounted for. An estimate of the power loss due to scattering can be obtained conceptually using a cylindrical sample cell with walls designed to absorb all the scattered power. Only the power that has not been either absorbed or scattered will reach the detector. The probability of a photon surviving any interaction with water is expressed using the beam attenuation coefficient, and the transmitted power can be expressed as

$$P(r) = P_i \exp(-c \cdot r) \quad . \tag{3.3.15}$$

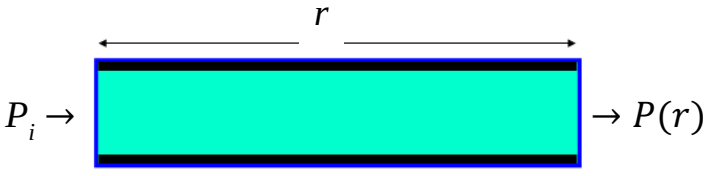

Figure 3.3.6. Conceptual diagram for beam attenuation using a sample cell with a black-painted wall.

The *single-scattering albedo*, ω_0, is the ratio of the total amount of power scattered to the total power removed from a beam and is defined as

$$\omega_0 = b/c\,. \tag{3.3.16}$$

Water containing mostly absorbing material will have a low ω_0, while water in which scattering dominates the attenuation will have a high ω_0. Thus, the single scattering albedo indicates the probability of photon being scattered when a photon interacts with water.

3.4 BOTTOM

Shachak Pe'eri and Chi-Kuei Wang

The primary function of the bottom return is to mark the time of arrival of the laser pulse at the bottom. The time of arrival is essential to the determination of the distance traveled by the ALB pulse from the air/water interface. The shape of the bottom return is also of value in that it carries information about the character of the bottom; however, it is also a function of hardware and environmental parameters. In addition to the detector and digitizer that log the returning laser energy as a waveform, other parameters that need to be considered are: laser output power, P_0 the total optical system loss factor η, the ALB receiver's aperture area A_r, the optical thickness, τ_a, of the air layer between the lidar and the laser impact point on the surface, the length of the laser-beam path above the sea surface H_s, the index of refraction of the water n_w, Fresnel's reflection coefficient of the air-water boundary ρ_w, the length of the laser beam path underwater, h_s, the water attenuation coefficient, k, based on the ALB receiver's field of view, and the bottom reflectance ρ_b. Feigels et al. (Victor I. Feigels et al. 2002) and Guenther (1985a) expressed the power returning from seafloor, P_{bot}, as follows:

$$P_{bot} = P_0 A_r \eta \left(1-\rho_w\right)^2 \cdot \frac{exp(-2\,\tau_a)}{(H_s n_w + h_s)^2}\, exp(-2h_s k)\frac{\rho_b}{\pi} \quad . \tag{3.4.1}$$

Wang and Philpot (2007) simplified equation (3.4.1) by considering the optical loss of the ALB hardware, $A_r\eta(1-\rho_w)^2$ and the atmospheric attenuation, $exp(-2\,\tau_a)/(H_s n_w + h_s)^2$ as constants in relatively shallow waters (< 13 m), and combining them into a single term, W:

$$P_{bot} = P_0 W\, exp(-2h_s k)\frac{\rho_b}{\pi} \quad . \tag{3.4.2}$$

A natural log of equation (3.4.2) yields a linear relationship between the power returned from the seafloor and the bottom reflectance:

$$ln(P_{bot}) = ln(P_0 W) + ln\left(\frac{\rho_b}{\pi}\right) - 2h_s k \quad . \tag{3.4.3}$$

Equation (3.4.3) effectively separates the bottom reflectance from the attenuation and system effects suggesting that it will be meaningful to consider the effects of bottom type and morphology on the shape and strength of the bottom return pulse.

The following section is a review of the seafloor characteristics and their radiometric contributions to the ALB returned beam. The review includes different approaches for calculating ρ_b. Key seafloor characteristics include: morphology of the seafloor, color of the seafloor including sediments, rocky outcrops and submersed aquatic vegetation (SAV). Separate discussions of the contributions of the ALB system design, water surface and the water column to the ALB waveform are provided in other sections of this book.

3.4.1 Morphology

In conventional laser hydrography, the morphology of the seafloor is a concern primarily because of the effect on the accuracy of depth measurements and the ability to resolve objects (e.g., large rocks or ship wrecks) that are hazards to navigation (Guenther, Thomas, and LaRocque 1996). An ideal surveying case has a flat and smooth bottom. Thus, any bottom detection by the laser measurement above the background bottom/seafloor depth is either a large object emerging from the seafloor or a feature in the water column (e.g., fish and nets). However, many natural coastal areas have slopes (i.e., a height difference between adjacent laser measurements) and a roughness (i.e., small-scale height variability within the footprint of the laser measurement) that can vary from one local area to another. Steinvall and Koppari (1996) conducted a set of simulations to investigate the accuracy of depth measurements for different bottom slopes and laser angles of incidence. Although their results show a 3% change in the depth estimation over angle of 0° to 15°, the intensity value of the bottom return also changed significantly. Similar results were observed for bottom slopes that range from -40° to 40° with respect to the normally incident unscattered beam on the bottom (Figure 3.4.1 left). Wang and Philpot (2002) also observed such a phenomenon using a SHOALS-400 dataset north of Egmont Key, FL (Figure 2.4.1, right). The ALB dataset was collected over a sloped sandy bottom at a water depth of 4.4 m. The survey contains flightlines in two opposite directions (north- and south-bound). Peak values of the bottom returns were consistent within each individual flightline and among flightlines in the same direction. However, a significant difference in the peak values of the bottom returns is observed between flightlines in opposite directions. Steinvall and Kompari (1996) defined this phenomenon as a pulse stretching effect and considered it as a means of estimating the slope. (The “geometrical stretch” will be discussed in Section 4.2.) Wang and Philpot (2007) restated the bottom slope issue and also discussed the bottom roughness as it relates to the Bi-directional Reflectance Distribution Function (BRDF). The BRDF describes the reflectivity behavior of a surface as a function of illumination geometry and viewing geometry (Haner et al. 1998).

The influence of the slope and roughness was also identified by Pe’eri et al. (2011) at a study site offshore of Gerrish Island, ME. The relationship between ALB bottom detection and the bottom slope and roughness characteristics was quantified using high-resolution multibeam bathymetry and underwater video imagery as independent measures of the water depth and the seafloor characteristics (Figure 3.4.2). The results indicate that a lack of bottom detection by ALB does not necessarily indicate water depths deeper than the surrounding areas that have strong bottom detection by the lidar. Consequently, lack of bottom detection could be misinterpreted to indicate deeper depths and could be a hazard to navigation.

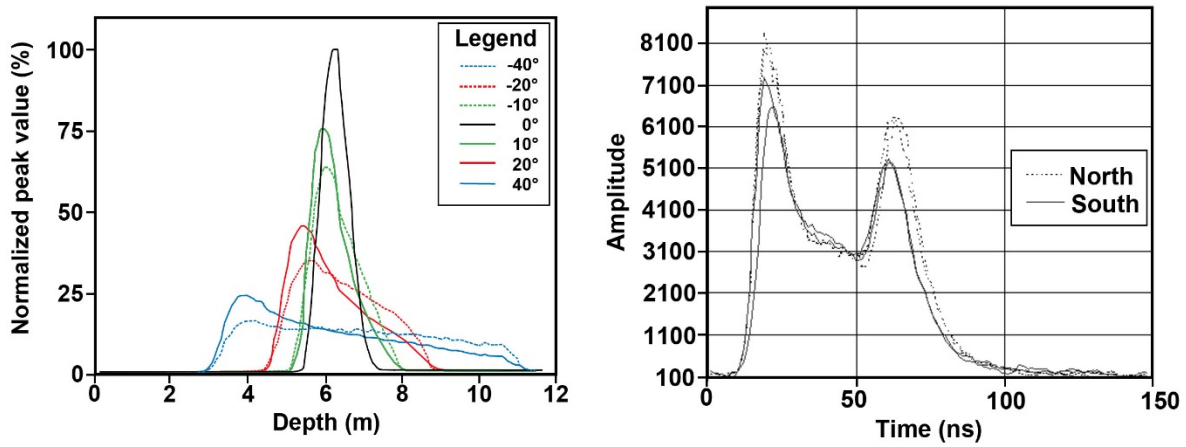

Figure 3.4.1. (Left) Normalized peak values from simulated bottom returns at varying slope angles as a function of depth ($\boldsymbol{K_d = 0.17\ m^{-1}}$) (Steinvall and Koppari 1996). (Right) Four SHOALS-400 waveforms over a sloped sandy bottom at the depth of 4.4 m near Egmont Key, FL. The dashed and continuous lines represent ALB waveforms extracted from the north-bound and the south-bound flight lines, respectively (C.-K. Wang and Philpot 2002).

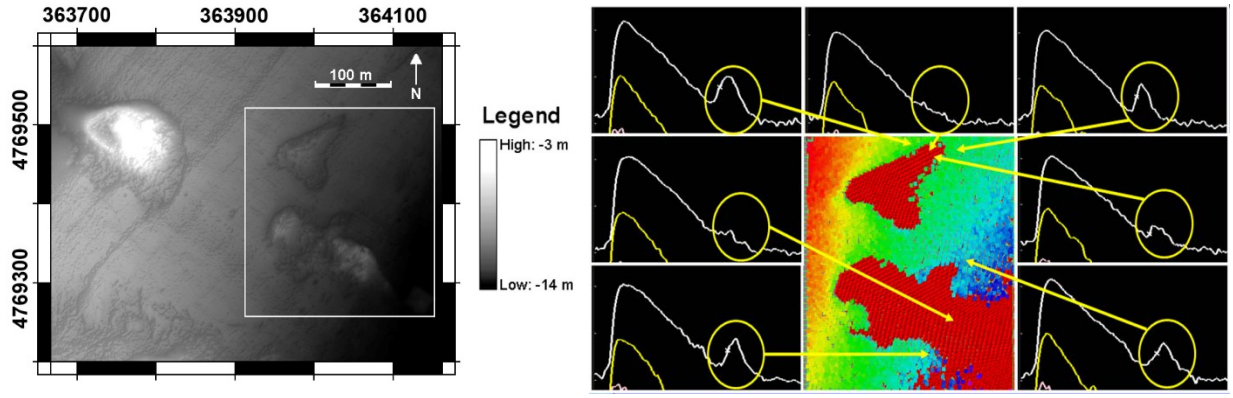

Figure 3.4.2. (Left) Grey-scale shaded relief multibeam-bathymetry map of the Pe'eri et al. (2011) study area. The depth values are relative to the Mean Lower Low Water (MLLW). (Right) ALB waveforms over a subset of the study area (denoted by the rectangle area in the left image), where the bottom returns are circled in yellow). A color ramp indicates successful bottom detection by the ALB system. Laser measurements that were not detected are colored dark red.

3.4.2 Color

The color of many bottom types – sediments, various vegetation types and manmade materials – provides a unique spectral signature that can be used as an identifier (Goetz et al. 1985). The spectral signature of the bottom type can be defined in ocean optics as bottom reflectance, $\rho_b(\lambda)$, where the radiance reflected back from the seafloor, $I_{bot}(\lambda)$, is normalized with solar irradiance at the water surface, $E_{sun}(\lambda)$, and the solar zenith angle, θ_{sun} (Gordon and Wang 1994; Mobley 1994):

$$\rho_b(\lambda) = \frac{\pi}{\cos\theta_{sun}} \cdot \frac{I_{bot}(\lambda)}{E_{sun}(\lambda)} \quad . \tag{3.4.4}$$

A common approach for classifying sediment and vegetation over terrestrial environments is to use hyperspectral imagery collected using a scanning radiometer, that records imagery in narrow spectral bands (~10 nm) from ultraviolet (350 nm) to short-wave infrared (2500 nm). However, such passive, hyperspectral sensors are dependent on the Sun's illumination as the light source, leaving the sensor susceptible to changes in atmospheric and water conditions.

ALB provides only a single wavelength (i.e., 532 nm), but its intensity can be used to calculate the bottom reflectance at that wavelength. ALB is an active sensor, where the solar radiation (passing through the green band filter) is considered environmental background noise source (Guenther 1985a, 2007). Recent studies have used the ALB intensity to constrain the radiative transfer equations in order to estimate the passive spectral reflectance (Kopilevich et al. 2005a; Park et al. 2010a; Tuell, Park, et al. 2005; Tuell and Park 2004). Kopilevich et al. (Kopilevich et al. 2005a) and Tuell et al. (Tuell, Park, et al. 2005) demonstrated their work using a SHOALS-1000 system over an area off of Hollywood, FL. Concurrent hyperspectral imagery, collected by a CASI-2 system over an area where the water depth ranged from 8 m to 30 m, was constrained to match the ALB reflectance at 532 nm using the 534 nm band in the hyperspectral imagery. A thematic map of the seafloor bottom type was then produced using an unsupervised classification (Park et al. 2010b).

3.4.3 Vegetation

The research on seagrass and macroalgae using ALB is very limited. Healthy vegetation typically contains chlorophyll-*a*, a pigment that generates a spectral response characterized by a steep slope at around 680 - 690 nm (i.e., the red edge) between a strong red wavelength absorption and a strong near-infrared reflection (Kirk 1994). However, this red-edge spectral response can only be clearly observed from vegetation above water; it is rapidly attenuated at water depths of more than 1 or 2 m (Nils Gunnar Jerlov 1976). In addition, spectral scattering and absorption by phytoplankton, suspended matter and dissolved organic matter (DOM) further restrict the passage of light underwater (A. G. Dekker et al. 2002). Bottom reflectance from SAV is typically low, often lower than the reflectance from a deep water column. In addition, self-shading takes place within the canopy and further reduces the amount of returning energy (Zimmerman 2003). Another mapping challenge is that there are many species of seagrass and macroalgae that can grow at varying densities over the seafloor and these are often mixed with other biological materials (e.g., other species of submerged vegetation, detritus and corals).

Because of the mapping challenges of seagrasses and macroalgae mentioned above, it is important to first understand the interaction between light and the plant canopy. Macroalgae require a relatively low level of light ranging from 0.1% to 1% of the surface irradiance. However, seagrasses require much greater light levels ranging from 10% to 37% of the surface irradiance (Duarte 1991; Olesen and Sand-Jensen 1993; Zimmerman 2006). This light sensitivity makes seagrass beds a very useful environmental indicator for deteriorated water quality (Short and Wyllie-Echeverria 1996) that can be mapped by optical remote sensing in more favorable conditions.

The common calculation for remote sensing reflectance, R_{RS}, calculated over a seagrass bed requires the *a priori* knowledge of the remote sensing reflectance over optically deep waters, R_∞ (Philpot 1989; Bierwirth, Lee, and Burne 1993; Dierssen et al. 2003; A. Dekker et al. 2006):

$$R_{RS} = R_\infty + (R_b - R_\infty)\, exp(-2h_s k) \quad , \tag{3.4.5}$$

where R_b, is the remote sensing bottom reflectance. The calculation assumes a homogenous water body and no contribution from the atmosphere. Also, the diffuse attenuation coefficients for the upwelling and downwelling light are assumed to be the same. Zimmerman (2006, 2003) further developed the bottom reflectance by including the changing morphology of the seagrass bed with currents (Figure 3.4.3):

$$R_b = \rho_{sg} \frac{h_c \Phi_{sg} B_{sg}}{cos(\theta_c)}\, sin(\theta_{sg}) \quad , \tag{3.4.6}$$

where ρ_{sg} is the reflectance of pure seagrass leaves, θ_c is the zenith angle of a collimated beam incident to the seagrass bed plane, and θ_{sg} is the average bending angle of the seagrass leaf orientation with respect to the zenith. The leaf biomass is described as a function of: 1) the height distribution of the eelgrass bed over a given area, B_{sg}, with the seagrass canopy height distribution that range from 0.1 m to over 1.0 m, and 2) the peak canopy height h_c, and 3) seagrass-shoot density Φ_{sg}.

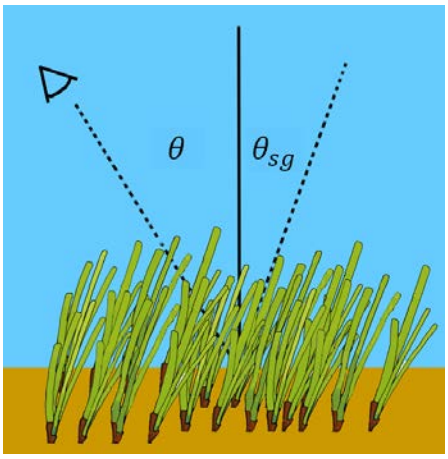

Figure 3.4.3. Simplified angular relationship based between the laser beam incident angle ($\boldsymbol{\theta}$) and leaf orientation of the seagrass field ($\boldsymbol{\theta_{sg}}$). The figure is based on Zimmerman (2006).

Zimmerman (2006) suggests that light loss through the biomass should be included in the light attenuation because the seagrass can be regarded as an additive attenuation media that absorbs and scatters the light. Thus, the seagrass-leaf absorption coefficient, a_{sg}, and the seagrass leaf thickness Δd_{sg}, should be integrated over the path through the seagrass, replacing the term $(-2h_s k)$ in equation (3.4.5) with:

$$-2 \cdot \left(a_{sg} \Delta d_{sg} \frac{h_c \rho_{sg} B_{sg}}{cos(\theta)} \right) - k h_s \quad (3.4.7)$$

The seagrass biomass measurements reported by Zimmerman (2003) provide the basis for Monte Carlo simulation of seagrass beds in a model designed to explore possible biases in lidar bathymetry estimates due to the presence of seagrass (C.-K. Wang et al. 2011).

Wang and Philpot (2007) use natural log scatter plots of the power returning from seafloor and the water depth to discriminate between sand and vegetation. In their study, ALB data were collected using a SHOALS-400 system over a study site east of Egmont Key, FL. In addition to sand/vegetation discrimination, Wang and Philpot (2007) were able to separate the seagrass beds into sparse and dense seagrass patches. Two sources of error mentioned in their study are bottom morphology and the presence of surface waves.

A different approach for mapping seagrasses and macroalgae is an investigation of the bottom return characteristics (e.g., shape and amplitude) of an ALB to map habitat composition (Collin, Archambault, and Long 2008; Collin, Long, and Archambault 2011a). Four benthic habitats were classified using twelve statistical properties that describe the shape of the bottom return. ALB data were collected using a SHOALS-3000 system over Bonaventure, Gulf of Saint Lawrence, Quebec, Canada. Collin et al. (2011a), were able to demonstrate an improvement in accuracy of the results using the statistical properties of the ALB bottom return and a supervised classification (Support Vector Machine) approach. This approach achieved an overall accuracy of 93.3%, which is a 5.3% accuracy increase compared to results using unsupervised (K-means) classification.

3.5 References

Aly, K. M., & Esmail, E. (1993). Refractive index of salt water: effect of temperature. *Optical Materials*, *2*(3), 195–199. http://doi.org/10.1016/0925-3467(93)90013-Q

Austin, R. W., & Halikas, G. (1976). *The index of refraction of seawater*. *Final Report* (Vol. SIO Ref. 7). La Jolla, California: Scripps Institute of Oceanography. Retrieved from http://misclab.umeoce.maine.edu/education/VisibilityLab/reports/SIO_76-1.pdf

Bierwirth, P. N., Lee, T. J., & Burne, R. V. (1993). Shallow sea-floor reflectance and water depth derived by unmixing multispectral imagery. *Photogrammetric Engineering and Remote Sensing*, *59*(3), 331–338. Retrieved from http://eserv.asprs.org/PERS/1993journal/mar/1993_mar_331-338.pdf

Bortkovskii, R. S., Egorov, B. N., Kattsov, V. M., & Pavlova, T. V. (2007). Model estimates for the mean gas exchange between the ocean and the atmosphere under the conditions of the present-day climate and its changes expected in the 21st century. *Izvestiya, Atmospheric and Oceanic Physics*, *43*(3), 378–383. http://doi.org/10.1134/S0001433807030127

Bunkin, A. F. A. F., Klinkov, V. K., Lukyanchenko, V. A., & Pershin, S. M. (2011). Ship wake detection by Raman lidar. *Applied Optics*, *50*(4), A86–A89. http://doi.org/10.1364/AO.50.000A86

Churnside, J. H. (2010). Lidar signature from bubbles in the sea. *Optics Express*, *18*(8), 8294–8299. http://doi.org/10.1364/OE.18.008294

Collin, A., Archambault, P., & Long, B. (2008). Mapping the shallow water seabed habitat with the SHOALS. *IEEE Transactions on Geoscience and Remote Sensing*, *46*(10), 2947–2955. http://doi.org/10.1109/TGRS.2008.920020

Collin, A., Long, B., & Archambault, P. (2011). Benthic Classifications Using Bathymetric LIDAR Waveforms and Integration of Local Spatial Statistics and Textural Features. *Journal of Coastal Research*, *27*, 86–98. http://doi.org/10.2112/SI_62_9

Collis, R. T. H., & Russell, P. B. (1976). Lidar measurement of particles and gases by elastic backscattering and differential absorption. In E. Hinkley (Ed.), *Laser Monitoring of the Atmosphere* (pp. 71–151). Springer Berlin Heidelberg. http://doi.org/10.1007/3-540-07743-X_18

Cox, C., & Munk, W. (1954a). Measurement of the roughness of the sea surface from photographs of the Sun's glitter. *Journal of the Optical Society of America*, *44*(11), 838–850. http://doi.org/10.1364/JOSA.44.000838

Cox, C., & Munk, W. (1954b). Statistics of the sea surface derived from sun glitter. *Journal of Marine Research*, *13*, 198–227.

Dekker, A., Brando, V., Anstee, J. M., Fyfe, S., Malthus, T., & Karpouzli, E. (2006). Remote Sensing of Seagrass Ecosystems: Use of Spaceborne and Airborne Sensors. In *Seagrasses: Biology, Ecology and Conservation* (pp. 347–359). Springer Netherlands. http://doi.org/10.1007/978-1-4020-2983-7_15

Dekker, A. G., Brando, V. E., Anstee, J. M., Pinnel, N., Kutser, T., Hoogenboom, J., … Malthus, T. J. (2002). Imaging Spectroscopy of water. In F. D. van der Meer (Ed.), *Imaging spectroscopy: basic principle and prospective applications* (pp. 307–360). Netherlands: Springer. http://doi.org/10.1007/978-0-306-47578-8

Dierssen, H. M., Zimmerman, R. C., Leathers, R. A., Downes, T. V., & Davis, C. O. (2003). Ocean Color Remote Sensing of Seagrass and Bathymetry in the Bahamas Banks by High-Resolution Airborne Imagery. *Limnology and Oceanography*, *48*(1, Part 2; Light in Shallow Waters), 444–455. Retrieved from http://www.jstor.org/stable/3597765

Donelan, M., Longuet-Higgens, M. S., & Turner, J. S. (1972). Periodicity in Whitecaps. *Nature*, *239*(5373), 449–451. http://doi.org/10.1038/239449a0

Duarte, C. M. (1991). Seagrass depth limits. *Aquatic Botany*, *40*(4), 363–377. http://doi.org/10.1016/0304-3770(91)90081-F

Duntley, S. Q. (1954). Measurements of the Distribution of Water Wave Slopes. *Journal of the Optical Society of America*, *44*(7), 574_1. http://doi.org/10.1364/JOSA.44.0574_1

Duntley, S. Q. (1971). *Underwater Lighting by Submerged Lasers and Incandescent Sources* (Vol. SIO Ref. 7). La Jolla, CA: Scripps Institution of Oceanography Visibility Laboratory. Retrieved from http://oai.dtic.mil/oai/oai?verb=getRecord&metadataPrefix=html&identifier=AD0730721

Elfouhaily, T., Chapron, B., Katsaros, K., & Vandemark, D. (1997). A Unified Directional Spectrum for Long and Short Wind-Driven Waves. *Journal of Geophysical Research*, *102*(97), 15781–15796. http://doi.org/10.1029/97JC00467

Feigels, V. I., Evans, B., Feygels, L., Guenther, G. C., & Kopilevich, Y. I. (2002). Prediction of bathymetric lidar performance with Ocean Scientific 2001 simulation code. In R. J. Frouin & G. D. Gilbert (Eds.), *SPIE 4488, Ocean Optics: Remote Sensing and Underwater Imaging* (Vol. SPIE 4488, pp. 61–70). San Diego, CA, United States: SPIE. http://doi.org/10.1117/12.452826

Feygels, V. I., Park, J. Y., Wozencraft, J. M., Aitken, J., Macon, C., Mathur, A., … Ramnath, V. (2013). CZMIL (Coastal Zone Mapping and Imaging Lidar): from First Flights to First Mission through System Validation. In W. W. A. Hou RA (Ed.), *Proceedings of SPIE* (Vol. 8724, p. 87240A–1–87240A–15). Baltimore, MD: SPIE. http://doi.org/10.1117/12.2017935

Goetz, A. F. H., Vane, G., Solomon, J. E., & Rock, B. N. (1985). Imaging Spectrometry for Earth Remote Sensing. *Science*, *228*(4704), 1147–1153. http://doi.org/10.1126/science.228.4704.1147

Gorchakova, G. I., & Isakov, A. A. (1976). Some results on light scattering in the location angles domain (in Russian). In *1st All-union conference on atmospheric optics* (pp. 218–221). Tomsk, IOA SO AN SSSR.

Gordon, H. R., Brown, O. B., & Jacobs, M. M. (1975). Computed relationships between the inherent and apparent optical oroperties of a flat homogeneous ocean. *Applied Optics*, *14*(2), 417–427. http://doi.org/10.1364/AO.14.000417

Gordon, H. R., Smith, R. C., & Zaneveld, J. R. V. (1979). Introduction to Ocean Optics. In *Proceedings of SPIE Ocean Optics VI, Vol. 208*. La Jolla, California.

Gordon, H. R., & Wang, M. (1994). Retrieval of water-leaving radiance and aerosol optical-thickness over the oceans with SeaWIFS - A Preliminary Algorithm. *Applied Optics*, *33*, 443–452.

Guenther, G. C. (1985). *Airborne Laser Hydrography: System design and performance factors*. Rockville, MD: NOAA Professional Paper Series, National Ocean Service 1. Retrieved from http://shoals.sam.usace.army.mil/downloads/Publications/AirborneLidarHydrography.pdf

Guenther, G. C. (2007). Airborne Lidar Bathymetry. In D. F. Maune (Ed.), *Digital Elevation Model Technologies and Applications: The DEM Users Manual, 2nd Edition* (2nd ed., pp. 253–320). Bethessda, Maryland: ASPRS. Retrieved from http://www.asprs.org/a/publications/2009PubsCatalog.pdf

Guenther, G. C., Thomas, R. W. L., & LaRocque, P. E. (1996). Design considerations for achieving high accuracy with the SHOALS bathymetric lidar system. In V. I. Feigels & Y. Kopelivich (Eds.), *SPIE 2964, CIS Selected Papers: Laser Remote Sensing of Natural Waters: From Theory to Practice, November 1, 1996* (Vol. 2964, pp. 54–71). St. Petersburg, Russia: Society of Photo-optical Instrumentation Engineers (SPIE). http://doi.org/10.1117/12.258353

Hale, G. M., & Querry, M. R. (1973). Optical Constants of Water in the 200-nm to 200-microm Wavelength Region. *Applied Optics*, *12*(3), 555–563. http://doi.org/10.1364/AO.12.000555

Haner, D. A., McGuckin, B. T., Menzies, R. T., Bruegge, C. J., & Duval, V. (1998). Directional-hemispherical reflectance for Spectralon by integration of its bidirectional reflectance. *Applied Optics*, *37*, 3996–3999. http://doi.org/10.1364/AO.37.003996

Holmes, R. W. (1970). The Secchi disk in turbid coastal waters. *Limnology and Oceanography*, *15*(5), 688–694. http://doi.org/10.4319/lo.1970.15.5.0688

Holthuijsen, L. H. (2007). *Waves in Oceanic and Coastal Waters*. Cambridge University Press.

Jerlov, N. G. (1976). *Marine Optics*. Amsterdam: Elsevier. Retrieved from http://www.sciencedirect.com/science/bookseries/04229894/14

Johnson, B. D., & Cooke, R. C. (1981). Generation of Stabilized Microbubbles in Seawater. *Science*, *213*(4504), 209–211. Retrieved from http://www.jstor.org/stable/1687157

Karlsson, T. (2011). *Uncertainties Introduced by the Ocean Surface when Conducting Airborne Lidar Bathymetry Surveys*. Lund Institute of Technology, Lund, Sweden.

Kerker, M. (1969). *The Scattering of Light and Other Electromagnetic Radiation* (Vol. 16). New York: Elsevier. http://doi.org/10.1016/B978-0-12-404550-7.50001-4

Kirk, J. T. O. (1994). Light and photosynthesis in aquatic ecosystems. 2nd edition, xvi, 509p. Cambridge University Press, 1994. Price £50.00. *Journal of the Marine Biological Association of the United Kingdom*. Cambridge Journals Online. http://doi.org/10.1017/S0025315400044180

Kopilevich, Y. I. (2002). Prediction of bathymetric lidar performance with Ocean Scientific 2001 (052001) simulation code, *4488*(052001), 61–70.

Kopilevich, Y. I., Feygels, V. I., Tuell, G. H., & Surkov, A. (2005). Measurement of ocean water optical properties and seafloor reflectance with Scanning Hydrographic Operational Airborne Lidar Survey (SHOALS): I. Theoretical background. In *SPIE 5885, Remote Sensing of the Coastal Oceanic Environment, July 31, 2005 - August 1* (Vol. 5885, pp. 1–9). Optech International, Inc., 7225 Stennis Airport Drive, Kiln, MI 39556, United States: SPIE. http://doi.org/10.1117/12.618923

Koschmieder, H. (1924). Theorie der horizontalen sichtweite. *Beiträge Zur Physik Der Freien Atmosphäre*, *12*, 171–181.

Kovalev, V. A. (2004). Elastic lidar : theory, practice, and analysis methods. Hoboken, N.J.: John Wiley. Retrieved from http://proxy.library.cornell.edu/login?url=http://onlinelibrary.wiley.com/book/10.1002/0471643173

Krekova, M. M., Krekov, G. M., & Shamanaev, V. S. (2004). Influence of Air Bubbles in Seawater on the Formation of Lidar Returns. *Journal of Atmospheric and Oceanic Technology*, *21*(5), 819–824. http://doi.org/10.1175/1520-0426(2004)021<0819:IOABIS>2.0.CO;2

Li, W., Yang, K., Xia, M., Rao, J., & Zhang, W. (2009). Influence of characteristics of micro-bubble clouds on backscatter lidar signal. *Opt.Express*, *17*(20), 17772–17783. http://doi.org/10.1364/OE.17.017772

Loisel, H., Meriaux, X., Berthon, J.-F. J.-F., & Poteau, A. (2007). Investigation of the optical backscattering to scattering ratio of marine particles in relation to their biogeochemical composition in the eastern English Channel and southern North Sea. *Limnology and Oceanography*, *52*(2), 739–752.

Measures, R. M. (1984). *Laser remote sensing: fundamentals and applications* (1st ed.). New York: John Wiley & Sons.

Measures, R. M. (1992). *Laser remote sensing: fundamentals and applications* (2nd ed., Vol. 2nd). New York: John Wiley & Sons. http://doi.org/0471081930, 9780471081937

Medwin, H. (1970). In situ acoustic measurements of bubble populations in coastal ocean waters. *Journal of Geophysical Research*, *75*(3), 599–611. http://doi.org/10.1029/JC075i003p00599

Mobley, C. D. (1994). *Light and water: radiative transfer in natural waters*. San Diego: Academic Press. Retrieved from http://www.curtismobley.com/LightandWater.zip

Mobley, C. D., Boss, E., & Roesler, C. (2013). Ocean Optics Web Book.

Mobley, C. D., & Preisendorfer, R. W. (1988). *A numerical model for the computation of radiance distributions in natural waters with wind-roughened surface* (Vol. NOAA Tech.). Seattle, WA: NOAA. Retrieved from http://www.pmel.noaa.gov/publications/search_abstract.php?fmContributionNum=813

Monahan, E. C., & Lu, M. (1990). Acoustically relevant bubble assemblages and their dependence on meteorological parameters. *IEEE Journal of Oceanic Engineering*, *15*(4), 340–349. http://doi.org/10.1109/48.103530

Monahan, E. C., & Mac Niocaill, G. (1986). Oceanic Whitecaps and Their Role in the Air-Aea Exchange Process. In E. C. Monahan & G. Mac Niocaill (Eds.), (Vol. 2). Dordrecht: Springer Netherlands. http://doi.org/10.1007/978-94-009-4668-2

Monahan, E. C., & Muircheartaigh, I. (1980). Optimal power-law description of oceanic whitecap coverage dependence on wind speed. *Journal of Physical Oceanography*, *10*(12), 2094–2099. http://doi.org/10.1175/1520-0485(1980)010<2094:OPLDOO>2.0.CO;2

NODC. (2013). World Ocean Atlas 2013. Retrieved August 21, 2015, from http://www.nodc.noaa.gov/OC5/woa13f/index.html

Olesen, B., & Sand-Jensen, K. (1993). Seasonal acclimatization of eelgrass Zostera Marina growth to light. *Marine Ecology Program Series*, *94*(1), 91–99. http://doi.org/10.3354/meps094091

Open_University. (2005). *Waves, Tides, and shallow-water processes*. (G. Bearman, Ed.)*Open University Oceanography Series* (Vol. 4). Boston, MA: Butterworth-Heinmann.

Park, J. Y., Ramnath, V., Feygels, V. I., Kim, M., Mathur, A., Aitken, J., & Tuell, G. H. (2010). Active-passive data fusion algorithms for seafloor imaging and classification from CZMIL data, 769515. Retrieved from http://dx.doi.org/10.1117/12.851991

Pe'eri, S., Gardner, J. V, Ward, L. G., & Morrison, J. R. (2011). The Seafloor: A Key Factor in Lidar Bottom Detection. *IEEE Transactions on Geoscience and Remote Sensing*, *49*(3), 1150–1157. http://doi.org/10.1109/TGRS.2010.2070875

Philpot, W. D. (1989). Bathymetric mapping with passive multispectral imagery. *Applied Optics*, *28*(8), 1569–1578. http://doi.org/10.1364/AO.28.001569

Pilgrim, D. A. (1984). The Secchi disk in principle and in use. *The Hydrographic Journal*, *33*(July), 25–30.

Pope, R. M., & Fry, E. S. (1997). Absorption spectrum (380-700 nm) of pure water. II. Integrating cavity measurements. *Applied Optics*, *36*(33), 8710–8723. http://doi.org/10.1364/AO.36.008710

Preisendorfer, R. W. (1976). *Hydrologic Optics* (Vol. 1: Basic P). Honolulu, Hawaii: National Oceanic and Atmospheric Administration Environmental Research Laboratories. Retrieved from http://archive.org/details/hydrologicopt00prei

Preisendorfer, R. W., & Mobley, C. D. (1985). *Unpolarized irradiance reflectances and glitter patterns of random capillary waves on lakes and seas, by Monte Carlo simulation*. *NOAA Tech. Memo* (Vol. ERL PMEL-6). Retrieved from http://www.pmel.noaa.gov/publications/search_abstract.php?fmContributionNum=784

Quan, X., & Fry, E. S. (1995). Empirical equation for the index of refraction of seawater. *Applied Optics*, *34*(18), 3477–3480. http://doi.org/10.1364/AO.34.003477

Saleh, B. E. A., & Teich, M. C. (1991). *Fundamentals of Photonics* (1st ed.). New York: Wiley-Interscience. Retrieved from http://web.ebscohost.com/ehost/ebookviewer/ebook/nlebk_26193_AN?sid=305fb078-c2e9-47a7-a406-694f63a9402c@sessionmgr198&vid=1&format=EB

Saleh, B. E. A., & Teich, M. C. (2007). *Fundamentals of Photonics* (2nd ed.). New York: Wiley-Interscience. Retrieved from http://web.ebscohost.com/ehost/ebookviewer/ebook/nlebk_26193_AN?sid=305fb078-c2e9-47a7-a406-694f63a9402c@sessionmgr198&vid=1&format=EB

Segelstein, D. J. (1981). *The complex refreactive index of water*. *Ph.D. Dissertation, Department of Physics, University of Missouri-Kansas City*. Department of Physics, University of Missouri-Kansas City, MO.

Short, F. T., & Wyllie-Echeverria, S. (1996). Natural and human-induced disturbance of seagrasses. *Environmental Conservation*, *23*(01), 17. http://doi.org/10.1017/S0376892900038212

Solomon, E. A., Kastner, M., MacDonald, I. R., & Leifer, I. (2009). Considerable methane fluxes to the atmosphere from hydrocarbon seeps in the Gulf of Mexico. *Nature Geosci*, *2*(8), 561–565. http://doi.org/10.1038/ngeo574

Sorooshian, A., Padro, L. T., Nenes, A., Feingold, G., McComiskey, A., Hersey, S. P., … Stephens, G. L. (2009). On the Link Between Ocean Biota Emissions, Aerosol, and Maritime Clouds: Airborne, Ground, and Satellite Measurements Off the Coast of California. *Global Biogeochemical Cycles*, *23*(4), n/a-n/a. http://doi.org/10.1029/2009GB003464

Steinvall, O. K., & Koppari, K. R. (1996). Depth sounding lidar: An overview of Swedish activities and future prospects. In V. I. Feigels & Y. I. Kopilevich (Eds.), *CIS Selected Papers: Laser Remote Sensing of Natural Waters: From Theory to Practice* (Vol. SPIE 2964, pp. 2–25). St. Petersburg, Russia: SPIE. http://doi.org/10.1117/12.258342

Stigebrandt, A. (1991). Computations of oxygen fluxes through the sea surface and the net production of organic matter with application to the Baltic and adjacent seas. *Limnol.Oceanogr*, *36*(3), 444–454. http://doi.org/10.4319/lo.1991.36.3.0444

Terrill, E. J., Melville, W. K., & Stramski, D. (2001). Bubble entrainment by breaking waves and their influence on optical scattering in the upper ocean. *Journal of Geophysical Research: Oceans*, *106*(C8), 16815. http://doi.org/10.1029/2000JC000496

Thorpe, S. A. (1982). On the clouds of bubbles formed by breaking wind-waves in deep water, and their role in air -- sea gas transfer. *Philosophical Transactions of the Royal Society of London.Series A,*

Mathematical and Physical Sciences, *304*(1483), 155–210. Retrieved from http://www.jstor.org/stable/36969

Thorpe, S. A. (1985). Small-scale processes in the upper ocean boundary layer. *Nature*, *318*(6046), 519–522. http://doi.org/10.1038/318519a0

Tuell, G. H., & Park, J. Y. (2004). Use of SHOALS bottom reflectance images to constrain the inversion of a hyperspectral radiative transfer model, 185–193. Retrieved from http://dx.doi.org/10.1117/12.564929

Tuell, G. H., Park, J. Y., Aitken, J., Ramnath, V., Feygels, V. I., Kopilevich, Y. I., & Kopelivich, Y. (2005). Fusion of SHOALS bathymetric lidar and passive spectral data for shallow water rapid environmental assessment. In *Oceans 2005 - Europe, June 20, 2005 - June 23* (Vol. 2, pp. 1046–1051). Optech International, 7225 Stennis Airport Drive, Kiln, MS 39520, United States: Institute of Electrical and Electronics Engineers Computer Society. http://doi.org/10.1109/OCEANSE.2005.1513202

Tulldahl, H. M., & Steinvall, O. K. (2004). Simulation of sea surface wave influence on small target detection with airborne laser depth sounding. *Applied Optics*, *43*(12), 2462–2483. http://doi.org/10.1364/AO.43.002462

Tyler, J. E. (1968). The Secchi disc. *Limnology and Oceanography*, *13*(1), 1–6. http://doi.org/10.4319/lo.1968.13.1.0001

Wandinger, U. (2005). Introduction to Lidar. In *Lidar : range-resolved optical remote sensing of the atmosphere* (pp. 1–18). New York: Springer Science+Business Media. http://doi.org/10.1007/0-387-25101-4_1

Wang, C.-K., & Philpot, W. D. (2002). Using SHOALS LIDAR system to detect bottom material change. In *IGARSS '02* (Vol. 5, pp. 2690–2692). http://doi.org/10.1109/IGARSS.2002.1026743

Wang, C.-K., & Philpot, W. D. (2007). Using airborne bathymetric lidar to detect bottom type variation in shallow waters. *Remote Sensing of Environment*, *106*(1), 123–135. http://doi.org/10.1016/j.rse.2006.08.003

Wang, C.-K., Philpot, W., Kim, M., & Lei, H.-M. (2011). A Monte Carlo study of the seagrass-induced depth bias in bathymetric lidar. *Optics Express*, *19*(8), 7230. http://doi.org/10.1364/OE.19.007230

Weber, T. C., Lyons, A. P., & Bradley, D. L. (2005). An estimate of the gas transfer rate from oceanic bubbles derived from multibeam sonar observations of a ship wake. *Journal of Geophysical Research: Oceans*, *110*(C4), C04005. http://doi.org/10.1029/2004JC002666

Westbrook, G. K., Thatcher, K. E., Rohling, E. J., Piotrowski, A. M., Pälike, H., Osborne, A. H., … Aquilina, A. (2009). Escape of methane gas from the seabed along the West Spitsbergen continental margin. *Geophysical Research Letters*, *36*(15), n/a. http://doi.org/10.1029/2009GL039191

Woolf, D. K. (1993). Bubbles and the air-sea transfer velocity of gases. *Atmosphere-Ocean*, *31*(4), 517–540. http://doi.org/10.1080/07055900.1993.9649484

Wozencraft, J. M., & Millar, D. (2005). Airborne Lidar and Integrated Technologies for Coastal Mapping and Nautical Charting. *Marine Technology Society Journal*, *39*(3), 27–35. http://doi.org/10.4031/002533205787442440

Zhang, X., Lewis, M. R., & Johnson, B. (1998). Influence of bubbles on scattering of light in the ocean. *Applied Optics*, *37*(27), 6525. http://doi.org/10.1364/AO.37.006525

Zimmerman, R. C. (2003). A Biooptical Model of Irradiance Distribution and Photosynthesis in Seagrass Canopies. *Limnology and Oceanography*, *48*(1, Part 2; Light in Shallow Waters), 568–585. http://doi.org/10.4319/lo.2003.48.1_part_2.0568

Zimmerman, R. C. (2006). Light and Photosynthesis in Seagrass Meadows. In *SEAGRASSES: BIOLOGY, ECOLOGYAND CONSERVATION* (pp. 303–321). Springer Netherlands. http://doi.org/10.1007/978-1-4020-2983-7_13

eCommons (2019) https://doi.org10.7298/jxm9-g971

4 BASIC CONCEPTS AND SYSTEM DESIGN

Lead Authors: Viktor Feygels[a] and Yuri Kopilevich[b]

Contributing Authors: Minsu Kim[c], Paul LaRocque[d], Shachak Pe'eri[e], and William Philpot[f]

a) Teledyne Optech Inc., 7225 Stennis Airport Drive, Suite 400, Kiln, MS 39556
b) St. Petersburg State University of Information Technologies, Mechanics and Optics
c) USGS, 47914 252Nd Street, Sioux Falls, SD
d) Optech, Inc., 300 Interchange Way, Vaughan, Ontario, Canada L4K 5Z8
e) Center for Coastal and Ocean Mapping, University of New Hampshire, Durham, NH 03824 USA;
f) School of Civil & Environmental Engineering, Cornell University, Ithaca, NY 14853

All airborne lidar bathymeter (ALB) systems locate the bottom of a water body by tracking the progression of a short light pulse from its initial contact with the water surface through its interaction with the bottom. The detected signal is the light backscattered by the water column, or reflected by the water surface or the bottom as represented by the waveform – a time-series of the return intensity. All systems share a common set of design elements, face a similar set of design constraints, and ultimately rely on an analysis of a series of detected waveforms to produce a map of the bathymetry. The characteristics of the waveform depend both on the environmental optical properties – especially the water inherent optical properties (IOPs, see Chap. 2) – and on system design. A major purpose of this chapter is to present a mathematical description of the process, incorporating realistic representations of the system elements and pulse propagation geometry. Using a special implementation of the small-angle approximation, a closed form expression for the waveform is presented. This solution is then used to explore contributions to the observed waveform following adjustments in ALB system design and to examine implications of the model for calibration. The chapter closes with consideration of eye-safety requirements and a discussion of the optimization and technical constraints and tradeoffs on system design.

4.1 Basic System Design – an overview

Shachak Pe'eri

The design of all scanning lidar systems (terrestrial, atmospheric, topographic or bathymetric) is similar in general (Bunkin and Voliak 2001; Measures 1992; Renslow 2012; Wehr 2009). All require the same basic set of system components: a laser transmitter, a scanning mechanism, a receiving telescope, a narrow band filter matched to the laser wavelength, a detector – usually a photomultiplier tube (PMT) or an avalanche photodiode (APD) – and signal processing hardware to digitize, filter and store the returning backscatter. For airborne lidar bathymetry (ALB) systems it is convenient to divide the components into four main system units: a laser transmitter unit, a scanning unit (moving mirror), a detector unit (telescope, filter, detector and digitizer) and auxiliary systems (e.g., stabilization, time, attitude and position). Each of the main system units contributes to the overall uncertainty of an ALB survey, and the specific characteristics of each must be considered in evaluating the overall design (S. A. White et al.

2011b). In this section a general description will be provided for each of the system units. For an introduction to the more basic calculations based on the parameters of each system unit, the authors recommend Balstavias (1999) as a starting point reference. A detailed development of the design characteristics specific to ALB is presented subsequent sections of this chapter.

4.1.1 Transmitter unit

The laser transmitter unit includes the laser together with the optical elements that define the energy of the laser pulse, the pulse repetition frequency (PRF) and the beam divergence. ALB systems use a pulsed, frequency-doubled Nd:YAG (neodymium-doped yttrium aluminum garnet) laser that transmits at 532 nm, in the green part of the spectrum, near the optimal wavelength for maximum transmission in water over a wide range of conditions (Austin and Petzold 1984).

The power of the laser transmitter is a fundamental issue in lidar design. Simplistically, the greater the power, the greater the penetrations depth will be. However, power is limited by a number of considerations, probably the most significant being eye safety. The American National Standards Institute (ANSI) publishes a recommendation for the maximum permissible exposure (MPE) for direct ocular exposure in an outdoor environment (ANSI 2005). The MPE is determined by averaging the incident power of the beam over an area defined by a 7-mm diameter aperture that is equal to a fully dilated pupil of the human eye. In the case of a green laser pulse (532 nm) the MPE is 5×10^{-7} J cm^{-2} for an exposure time that is less than 10^4 ns. In the case of a fixed ALB system, the laser power per unit area, A, must conform to the following relationship at ground level:

$$MPE \geq \frac{\langle Q \rangle PRF}{A} = \frac{\langle Q \rangle PRF}{\pi \cdot (0.5 \cdot H \cdot \Theta_E)^2} \tag{4.1.1}$$

where $\langle Q \rangle$ is the pulse energy in Joules, PRF is the pulse repetition rate in Hertz, H is the height of the ALB above the water surface and Θ_E is the beam divergence in milliradians. It is important to emphasize that the MPE value used here is based on a total exposure time of less than 10^4 ns. It is clear from equation (4.1.1) that higher pulse energy can be balanced by a lower repetition rate, a higher altitude, or a larger beam divergence. Beam divergence and repetition rate combine to define the range of possibilities for the scanning pattern. Typically, the two are adjusted together to meet the requirements of a particular application. For example, a survey in deeper waters for which depth penetration is a major concern will be better served with higher overall power and a relatively large beam divergence in order to meet eye-safety requirements. Such an adjustment is effective as long as the resulting lower repetition rate and wider sample spacing are acceptable (Penny et al. 1986). For surveys in shallow waters, a higher ground sampling is often advantageous for better definition of channels and underwater obstructions. This requires a smaller beam divergence and higher repetition rate (Guenther et al. 1996; E. Yang et al. 2009).

4.1.2 Scanner unit

The scanner unit defines the laser measurement pattern as well as the spot size and spacing on the water surface. In order to cover a large area with laser measurements, the scanner must distribute the laser pulses along a swath below the aircraft. The specific pattern of samples on the water surface is not particularly important for bathymetric mapping as long as the spatial density of the laser measurements is

moderately uniform and meets the survey specifications (Guenther 1985b). This need for uniformity means that the scan rate and sampling rate must be matched to the aircraft speed and altitude.

There are three predominant styles of mechanical scanning typical of ALB systems (Petrie and Toth 2009; Wehr 2009): oscillating mirrors, polygonal scanners and nutating mirrors. Oscillating mirrors can have one or two axes (Baltsavias 1999). A one-axis oscillating mirror scanner combines with the aircraft motion to produce a zig-zag sampling pattern on the ground. Using gimbals or galvanometers, the motion of the oscillating mirror can adjust for the forward motion of aircraft, resulting in a parallel line pattern, i.e. parallel scan lines/arcs (Axelsson and Alfredsson 1999). Most commercial ALB systems use the oscillating scanner mechanism. The zig-zag line pattern is used in both the LADS and the EAARL ALB systems, whereas a two-axis parallel arc pattern is used in HawkEye and SHOALS systems (LaRocque, Banic, and Cunningham 2004a; Lillycrop and Banic 1992).

A polygon scanner, also known as a rotating multi-facet mirror, is a continuously spinning optical polygon parallel elliptical arc-like line pattern. The polygon scanner is typical for Riegl laser scanners, including the VQ-820-G system (Steinbacher et al. 2012).

In a nutating mirror mechanism, the laser beam is deflected by a rotating mirror, where the rotational axis of the mirror is not normal to the mirror surface. Typically, the rotating axis of the mirror is mounted so that the scanner shaft and the laser beam form an angle of 45°. The resulting pattern on ground is an approximately elliptical scanning pattern. Due to the elliptical scan, most of the measurement points on ground are scanned twice, once in the forward view and a second time in the backward view (Fuchs and Mathur 2010). The redundant information for the same ground spot can be favorably used to calibrate the scanner and the position files as far as the pitch angle is concerned (Gonsalves 2010a). A Palmer scanner (nutating wedged mirror) was used in the Airborne Oceanographic Lidar (AOL) system in late 70's and early 80's (Guenther 1985b). Only recently, in 2012, was a nutating scanner mechanism re-introduced in CZMIL with a Fresnel prism (Fuchs and Mathur 2010). More details on other available scanner mechanisms that are currently only used in topographic lidar systems and not in ALB systems, such as rotating polygon and fiber scanner, can be found in Wehr (2009) and Baltsavias (1999).

Regardless of the method, the scanner distributes the pulses in a swath to either side of the aircraft. The swath width, SW, is dependent on the maximum off nadir angle across track, θ_{max}, and the height above the water surface, H. Under ideal survey conditions (no pitch or roll), the swath width on the water surface will be:

$$SW = 2H \cdot tan\left(\frac{\theta_{max}}{2}\right) \tag{4.1.2}$$

Similarly, the footprint diameter, d^{sf}, just above the water surface will vary with viewing angle. With the aircraft at a height, H, above the water surface, using a laser with a beam divergence, Θ_E, at an off-nadir angle in air, θ_a, the beam diameter just above the water surface, d^{sf}, is:

$$d^{sf} \approx H_s \cdot \Theta_E \quad . \tag{4.1.3}$$

where H_s is the slant range distance between the lidar and the sea surface along the lidar axis. Sample spacing is different along track, Δx, and across track, Δy. Although the exact sample spacing depends on the scanner type and the off-nadir angle, a first-order approximation of the sample spacing is given by:

$$\Delta x = v_{plat}/f \quad , \tag{4.1.4}$$

and

$$\Delta y = (SW \cdot f)/PRF \tag{4.1.5}$$

where v_{plat} is the platform (e.g., aircraft) velocity, f is the scan rate from side to side and PRF is the pulse repetition frequency. In order to achieve a uniform density, the cross-track point spacing should be roughly equivalent to the along-track point spacing which constrains the aircraft velocity, that is, if

$$\Delta x \approx \Delta y \tag{4.1.6}$$

then,

$$v_{plat} \approx SW \times f^2/PRF \quad . \tag{4.1.7}$$

4.1.3 Detector unit

The detector unit collects, digitizes and stores the returning laser energy as a sequence of events from the interaction of the laser pulse with the water surface to the interaction with the bottom. The sequence is referred to as a waveform (Guenther 1985b; Pe'eri, Morgan, et al. 2011; Billard, Abbot, and Penny 1986b). Waveform observations can be analyzed off-line using digital signal processing methods in order to extract the surface and bottom returns and calculate the laser measurement range underwater. In addition to bathymetry, the water surface, water column and seafloor can be characterized based on the shape of the returns and additional features in the volume scattering (Pe'eri and Philpot 2007; Tuell, Feygels, et al. 2005).

The returning laser energy is collected by a telescope having an adjustable field of view (FOV). The size of the receiver FOV is always larger than the transmitted beam divergence since the beam is broadened by scattering in the water (Guenther 1985b; Feygels, Wright, et al. 2003b). Two general types of ALB systems have evolved based on the differing requirements in shallow and deeper water environments. The first type, optimized for deeper water applications, is a broad-beam ALB system (e.g., SHOA Guenther, 1985, LS, LADS MK3, CZMIL, HawkEye II, and Hawkeye III) that transmits a beam having a large divergence (3-11 mrad) with a typical footprint size of 2 to 4 m on the water surface. The detector FOV in SHOALS and LADS is around 100 mrad, whereas HawkEye has a narrower FOV of about 1-3 mrad. CZMIL uses a wide FOV (40 mrad) for deep water, but a narrow FOV (1.9 mrad) can be selected for shallow water operation. The second type is the narrow-beam ALB systems, specifically designed for shallow water applications (e.g., EAARL-B; Chiroptera, RIEGL VQ820G, Aquarius), that transmit using a small beam divergence (1-3 mrad) with a typical footprint size of less than 1 m on the water surface and a correspondingly smaller telescope FOV. Broad-beam ALB systems are designed for mapping bathymetry in areas that are not cost-efficient for a multi-beam echo sounder (MBES) at the International Hydrographic Office (IHO) order 1b standards. i.e., in water depths of 2 m to 15 m (Guenther 1985b; Imahori et al. 2013). Narrow-beam ALB systems can typically acquire depth measurement in extremely shallow water areas from the shoreline to 4 m, depending on the environmental conditions. The narrow-

beam ALB systems are ideal for rivers and estuaries, when water conditions allow bottom detection (McKean et al. 2009).

The returning energy is converted from an optical signal into an electrical signal using an optical detector. Two types of detectors are commonly used for logging the backscattered signal: avalanche photodiodes (APD) and photomultiplier tubes (PMT). The typical APD is a multi-photon detection sensor, in which an electric signal is generated that is directly proportional to the optical power of the incident light (Wilson and Hawkes 1998). Multi-photon detection APD sensors are able to detect power changes of up to 3 orders of magnitude. PMT and Geiger-mode APD (GAPD) detectors are single detection sensors, in which a single photon can set off a significant avalanche of electrons using a reverse bias voltage (Wilson and Hawkes 1998; Hamamatsu 2007). These single-photon detection sensors typically detect power changes up to 6 orders of magnitude. In order to log the returning optical energy as a waveform, the electrical signal of the photo-detectors is sampled using a digitizer. It is important to note that the sampling rate of the digitizer defines the resolution of the waveforms, but the bandwidth of the photo-detectors and the digitizer limit the accuracy with which the waveform is digitized.

Range is determined by the time-of-flight of the laser pulse, i.e., the time difference between the emitted pulse and the returning backscatter (Measures 1992). The laser pulse traverses the range twice (from the laser to the target and from the target to the detector). The laser transmits a short pulse which is reflected (scattered) by an object at a distance, or range to the target, *r*, the total distance traveled by the pulse is $2r$. The time, t, required for the round trip is then found from the relation: $2r = v * t$ where v is the velocity of light in the medium. Thus, the range of the target is given by:

$$\mathrm{r} = v * \mathrm{t}/2 \quad . \tag{4.1.8}$$

The range resolution of the lidar, Δr, designates the smallest distance between two targets that can be discriminated, and is limited by the sampling rate of the detector, f_d. The time of travel to targets at ranges r and $r + \Delta r$ are then $t_1 = 2r/v$ and $t_2 = 2(r + \Delta r)/v$, respectively. To be resolvable, the difference in return time, $\Delta t = t_2 - t_1 = 2\,\Delta r/v$, must be greater than or equal to the interval between successive observations: $\Delta t > 1/f_d$, thus, the range resolution will be:

$$\Delta r > \frac{1}{2} c\Delta t \;\; or\; \Delta r > \frac{v}{2f_d} \tag{4.1.9}$$

We are concerned primarily with the optical path in water. The speed of light in water is $\mathrm{v}_w = \mathrm{c}/n_w$, where $c = 3.00 \times 10^8\ m\ s^{-1}$ is the speed of light in a vacuum and the index of refraction of water can be approximated as $n_w \approx 1.333$ (Saleh and Teich 1991b). Thus, in water, a 1 GHz sampling rate ($f_d = 1\ GHz$), which is typical of ALB systems, corresponds to a range resolution limit of about 11.2 cm. In fact, the range resolution can be refined further for narrow-beam systems (e.g. EAARL-B and VQ-820-G) by measuring the local sea surface wave height and slope angle for each laser measurement (Tulldahl, Andersson, and Steinvall 2000) or by using online waveform processing for measuring relative pulse broadening (Pfennigbauer et al. 2014).

4.1.4 Auxiliary systems for ALB performance and geo-referencing.

The range measured in the waveforms is the line-of-site vector from the aircraft to the water surface in air and from the water surface to the seafloor underwater. In order to reference the range measurement and dataset in a known coordinate system, e.g. WGS-84 or NAD-83, the ALB system must be supported by information logged by the auxiliary systems for ALB performance (attenuator, gimbals, cooling, etc.) and geo-referencing (GPS, IMU). This dataset of referenced measurement is also known as a point cloud. The position and direction of the laser beam recorded by these devices must be synchronized with the scanner information and the digitized waveforms (range measurements) with nanosecond precision. Measurement errors of the range, position, and beam direction or any temporal misregistration errors will also influence the accuracy of the final product (Baltsavias 1999; S. A. White et al. 2011b) The two main external sensors that are used in concert with the ALB system are an inertial measurement unit (IMU) and a global positioning system (GPS) receiver that measure the attitude and location of the aircraft (and the ALB sensor) during the survey (Wehr 2009; Habib et al. 2010). The GPS data is typically collected at a sample rate of 1 to 2 Hz, and then processed in a differential post-processing mode (DGPS), whereby the data from the aerial receiver is processed at GPS ground stations. In order to achieve positioning measurements with accuracy better than ±10 cm, the GPS ground station are positioned on known benchmarks at a maximum distance of 25 km from the survey line. The orientation of the aircraft is determined using the IMU at a sample rate of 100 Hz with a typical accuracy better than 0.01 of a degree. After the flight, in a post-processing mode, an integrated position and orientation solution is applied to the laser range in order to calculate bathymetry. It is important to note that, in addition to the internal accuracy of the ALB system, the GPS receiver and the IMU, the mounting parameters that relate each of these units also affect the accuracy of the laser measurements. The offset and orientation between the units, known as the lever-arm components and bore-site angles, should be determined through a calibration procedure (Habib et al. 2010). Another issue that affects the accuracy of the range measurements is random angular movement caused by wind and engine vibration of the aircraft (Abdullah 2004). In order to ensure vibration-free conditions, manual and automatic mounts are used stabilize the ALB system.

4.2 Basic Physical Concepts

Viktor Feygels, Yuri Kopilevich

4.2.1 Propagation geometry

An understanding of the ray-path geometry of the lidar pulse as it is transmitted from an aircraft into the water, reflected from the bottom, and returned to the receiver, is critical to the analysis of the lidar waveform. The propagation geometry associated with ALB has been considered in detail by Guenther (1985b) and need not be repeated here. The following is a description of the critical geometrical parameters and an introduction to the notation that will be used throughout Sections 4.2-4.4.

The basic geometry of an ALB measurement is illustrated in Figure 4.2.1. The length of atmospheric path traversed by the sounding pulse to the water surface, or slant path, H_s, is equal to $H/\cos\theta_a$, where H is the altitude of the lidar platform directly above the water surface and θ_a is the angle formed by the nadir direction and the optical axis of the sounding laser beam (coincident with the axis of the receiving

telescope). Maximum values for θ_a range from 20° to 30°. Due to refraction of the beam at the water surface, the in-water sounding angle is θ_w, and it is related to θ_a according to Snell's law,

$$sin\,\theta_a = n_w\, sin\theta_w \quad sin\,\theta_a = n_w\, sin\theta_w \quad . \tag{4.2.1}$$

with n_w being the refractive index of the seawater. (The index of refraction of air is assumed to be ~1.00.)

The angular width of the conical sounding beam in the atmosphere – the beam divergence – is described by the plane angle, Θ_E. Similarly, the angular width of the lidar receiver field-of-view may be described by corresponding plane angle, Θ_R. Typically, both angles are relatively small (less than 100 mr) with $\Theta_E \leq \Theta_R$. For example, for the CZMIL, $\Theta_E = 7\ mr$, and $\Theta_E = 40\ mr$ for shallow-water and "deep" receivers, respectively. Similarly, for each of the seven channels of the special "shallow-water" segmented receiver in the CZMIL, $\Theta_R = 1.9\ mr$ (Feygels et al. 2012).

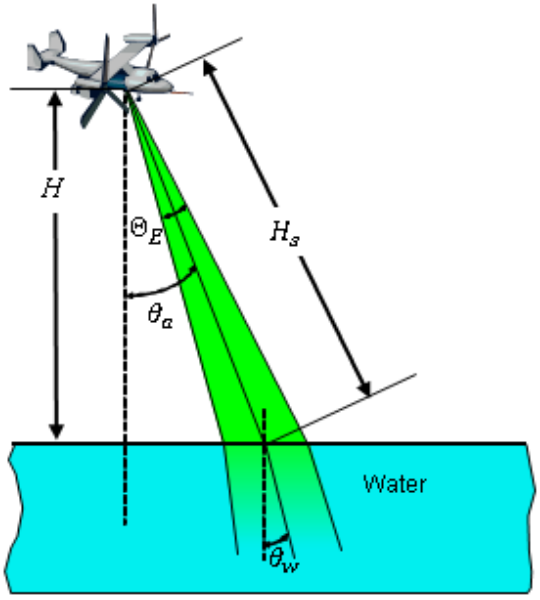

Figure 4.2.1. General diagram of ray-path geometry of the ALB beam entering the water.

Far from the emitter (near the water surface), the sounding beam front forms a spherical cap (Figure 4.2.2). Over the small divergence angle, Θ_E, the front is well approximated by a plane perpendicular to the beam axis. Since the departure, ΔH_s, of the spherical cap from the plane (over the cap) does not exceed the limit of:

$$\max \Delta H_s = H_s\left[1 - \cos\left(\frac{\Theta_E}{2}\right)\right] \approx H_s \frac{\Theta_E^2}{8} \quad , \tag{4.2.2}$$

the difference may be neglected for beam divergences, Θ_E, typical of an operational lidar. Thus, the diameter, d^{sf}, of the sounding beam cross-section near the water surface (Figure 3.2.3) for $\Theta_E \ll \pi$ can be approximated as:

$$d^{sf} \approx H_s \cdot \Theta_E \quad . \tag{4.2.3}$$

eCommons (2019) https://doi.org10.7298/jxm9-g971

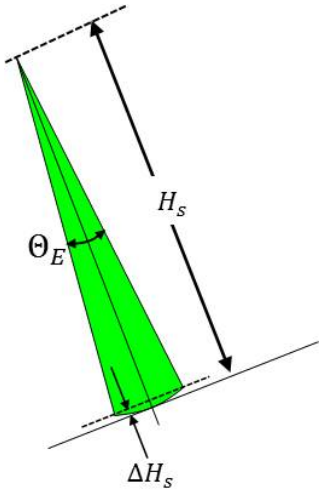

Figure 4.2.2. Illustration of the ALB sounding wavefront near the water surface; the spherical cap is approximated as a plane.

Different portions of the wave front arrive at the water surface at different times, resulting in a "geometrical stretch" of the laser pulse at the water surface, illustrated in Figure 4.2.3. Even for an infinitesimally short (delta function) sounding pulse, the surface-reflected signal at the receiver extends over the finite time interval from $t = t^{sf} - \Delta t^{sf}/2$ to $t = t^{sf} + \Delta t^{sf}/2$, where t^{sf} represents the arrival time at the receiver of surface-reflected light from the center of the beam, and the reflected pulse duration, Δt^{sf}, is related to the beam cross-section near the water surface d^{sf} by:

$$\Delta t^{sf} = \frac{2 \cdot d^{sf} \tan\theta_a}{c} \approx \frac{2 \cdot H_s \cdot \Theta_E \tan\theta_a}{c} \quad , \tag{4.2.4}$$

where c is the speed of light, and Eq. (3.2.3) has been applied. This result brings out the relationship between the sounding beam divergence, Θ_E, and geometrical stretch of surface-reflected pulse, Δt^{sf}.

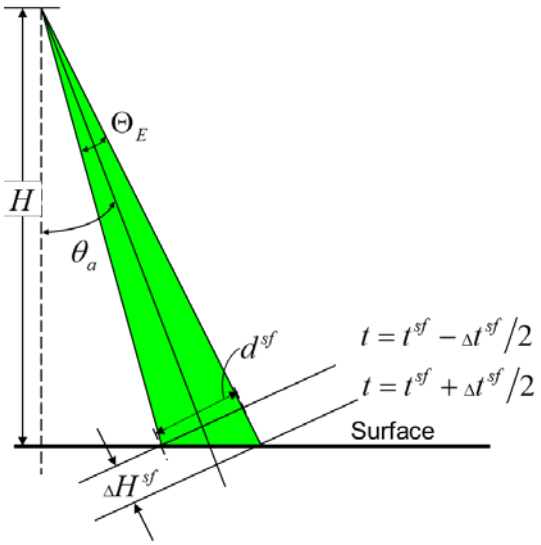

Figure 4.2.3. "Geometric stretch" of a surface-reflected sounding pulse.

In what follows, it is convenient to consider the equivalent geometry illustrated in Figure 4.2.4 instead of the actual geometry depicted in Figure 4.2.1. The equivalent geometry uses the same refractive index, n, both above and below the air/water interface (Kopilevich and Surkov 2008). In the "equivalent" geometry, the sounding beam does not undergo refraction at the interface, and the inclination of the lidar axis is θ_w on both sides of the interface. The "equivalent" lidar parameters (position, incidence angle, pulse energy, emitted beam divergence, receiver field-of-view) are specified in a way that retains the actual sounding beam light field under the interface. Evaluation of the "equivalent" parameters is described in detail in Section 4.3.2.7 (Emitted beam modeling). In this section, we restrict ourselves to the simplest (and typically sufficient) case of a modest viewing angle when $\cos\theta_w/\cos\theta_a \approx 1$. In the equivalent geometry for the simple case, the lidar is located at point O', at the altitude $H' = nH$, so that the length, H'_s, of the sounding beam path from the emitter to the air/-water interface is $H'_s = H'/\cos\theta_w = nH_s = nH/\cos\theta_a$. The actual beam divergence, Θ_E, and receiver field-of-view angle, Θ_R, are replaced by $\Theta'_E = \Theta_E/n$ and $\Theta'_E = \Theta_R/n$, respectively.

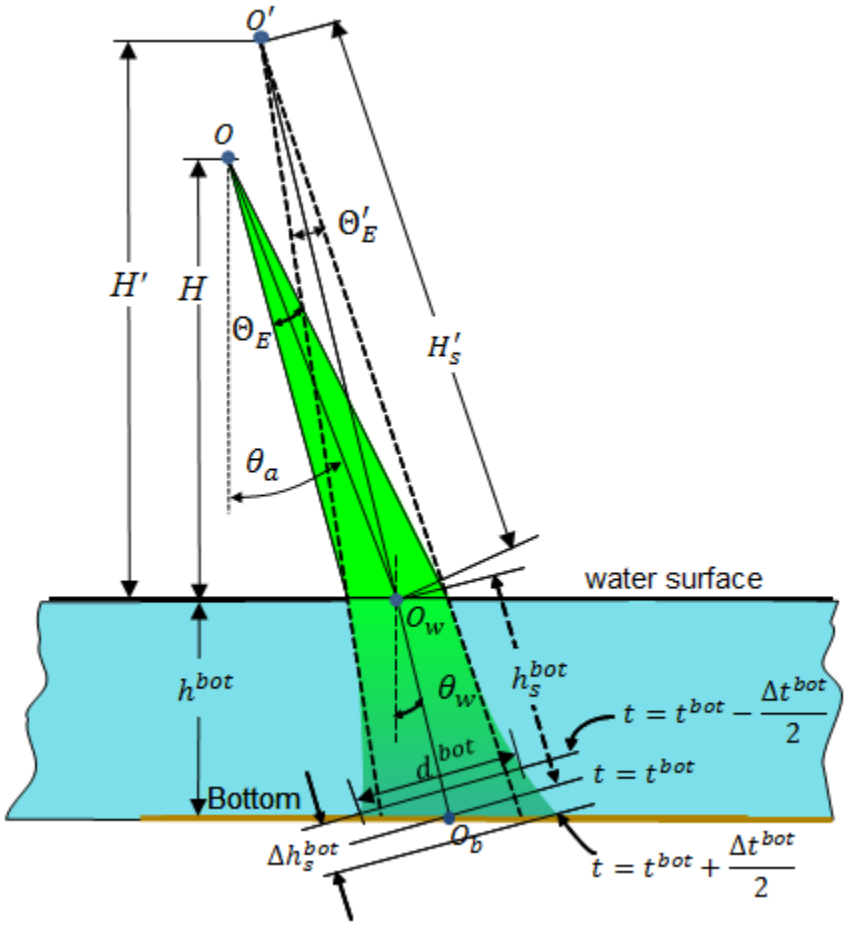

Figure 4.2.4. "Geometric stretch" of bottom-reflected lidar signal and the "equivalent" geometry.

The equivalent geometry illustrated in Figure 4.2.4 makes it possible to describe the physical nature of the "geometric stretch" of the light pulse in analogy with Figure 4.2.3. For an infinitesimally short (delta function) sounding pulse, the bottom-reflected signal at the receiver extends over the finite time interval $[t = t^{bot} - \Delta t^{bot}/2\ ,\ t = t^{bot} + \Delta t^{bot}/2]$, where t^{bot} is the moment when light from the central part of

the pulse front arrives at the receiver after reflection by the bottom. The reflected pulse duration, Δt^{bot}, is related to the sounding beam cross-section near the bottom, d^{bot}, by:

$$\Delta t^{bot} = \frac{2n \cdot d^{bot} \tan\theta_w}{c} \geq \frac{2n \cdot \left(H_s' + h_s^{bot}\right) \cdot \Theta_E \tan\theta_w}{c} \quad . \tag{4.2.5}$$

The inequality in equation (4.2.5) accounts for widening of the sounding beam with depth due to light scattering in the water in that d^{bot} exceeds the "geometrical" value, $\left(H_s' + h_s^{bot}\right) \cdot \Theta_E$ (Guenther 1985b). A quantitative description of scattering effects on the lidar waveform will require the use of an adequate theory of light beam propagation, and is presented in Section 3.3, where the role of the receiver field-of-view angle, Θ_R, will also be discussed. In deep, strongly scattering waters, the effect of the finite field-of-view may be significant even when $\Theta_E \ll \Theta_R$.

4.2.2 Return waveform

Guenther (1985b) introduced two functions that are useful for describing the temporal patterns in a lidar return signal resulting from a single emitted laser pulse:

- The "Impulse Response Function" (ImpRF), $S_\delta(t)$, defined as the temporal distribution of optical signal power at the lidar photo-detector for the case of infinitesimally short sounding pulse (delta-function),
- The "Environmental Response Function" (EnvRF), $S_p(t)$, defined as the distribution of optical signal power at the photo-detector, generated by an actual (finite-duration) sounding laser pulse shape, $p(t)$, $0 \leq t < \infty$. In this chapter, $p(t)$ will be defined as a Gaussian function.

The environmental response function, $S_p(t)$, may be represented as a convolution of the ImpRF, $S_\delta(t)$, with the sounding pulse shape,

$$S_p(t) = \int_0^\infty S_\delta(t - t') \cdot p(t')\, dt' = S_\delta(t) * p(t) \quad , \tag{4.2.6}$$

where the symbol "$*$" denotes a convolution operation. Any realistic waveform one can derive from the output electrical signal of the lidar receiver channel will be inevitably distorted as it traverses the channel electronic track: detector-amplifier-digitizer (Section 4.3.1). The resulting waveform is a discrete version of the temporal distribution, $S_p(t) * \omega(t)$, where $\omega(t)$, $0 \leq t < \infty$ is the instrument response function, also known as the "optical response", and represents the distortions introduced by the channel electronic track. In view of equation (4.2.6), it seems reasonable to define the function as:

$$S_p(t) * \omega(t) = S_\delta(t) * p(t) * \omega(t) \equiv S_\delta * R(t) \quad , \tag{4.2.7}$$

with $R(t) \equiv p(t) * \omega(t)$. Comparison with equation (3.2.6) shows that the function $R(t)$ may reasonably be called "the effective pulse shape". Thus, in addition to the ImpRF and EnvRF described above, it seems appropriate to introduce a third function:

- The "real waveform", $S_R(t)$, retrievable from the output lidar signal.

This real waveform may be calculated by convolving the ImpRF with the effective sounding pulse shape, $R(t)$:

$$S_R(t) = \int_{-\infty}^{\infty} S_\delta(t - t') \cdot R(t')dt' \equiv S_\delta(t) * R(t) \quad . \tag{4.2.8}$$

The simulated "real waveform" (equation 5.2.8) is in the optical domain. In what follows, the effective sounding pulse shape duration, the full width half maximum (FWHM), is designated as τ_R.

There are four major components of the lidar waveform (Guenther 1985b):

1. the surface return (surface-reflected pulse);
2. the volume backscattered return (backscattered signal);
3. the bottom return (bottom-reflected pulse);
4. the background noise.

The return waveform components, illustrated in Figure 4.2.5–Figure 4.2.8, represent the idealized components of the ImpRF and the real waveform using arbitrary units in order to avoid the need to specify specific environmental characteristics (effective surface reflectance, the backscattering coefficient, the bottom reflectance). The presented curves were obtained using the lidar waveform model described in Sec. 4.3.2; the values of the lidar parameters used in the simulation are listed in Table 4.1.

Table 4.1. Values of lidar parameters used in the waveform simulation

Parameter & symbol	Units	Value
Lidar carrier height above the sea surface, H	m	400
Nadir angle in the atmosphere, θ_a	deg	20
Sounding beam divergence angle (full plane angle), Θ_E	mr	5
Receiver field-of-view (full plane angle), Θ_R	mr	40
Bottom depth, h^{bot}	m	20
Effective sounding pulse duration (FWHM), τ_R	ns	3.5

In Figure 4.2.5, the blue, solid curve illustrates the shape of the idealized surface-reflected component of the ImpRF. The stretch of the idealized pulse is derives only from the ray-path geometry (neglecting any contribution from waves), and may be estimated directly from equation (4.2.4). Typically, the sounding beam divergence is small compared to the receiver field-of-view, and the reflected peak duration, Δt^{sf}, is determined using equation (4.2.4).

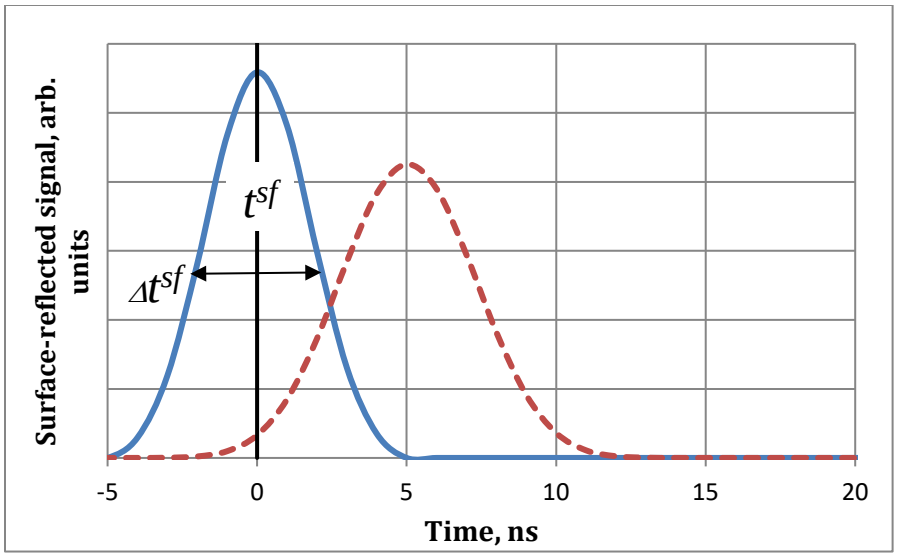

Figure 4.2.5. The shape of the idealized, surface-reflected component of the ImpRF (blue, solid line), and of a realistic waveform (red, dashed line) with an effective sounding pulse duration of 3.5 ns.

Note that the maximum of the ImpRF occurs at $t^{sf} = 0$, while the maximum for the real waveform (red, dashed curve) is shifted. Both the shift and the real pulse shape are a result of both geometric and instrumental stretching, the latter being related to the effective sounding pulse duration of 3.5 ns. The surface return signal is proportional to the effective reflectance of the water surface, ρ_{sf}, which depends strongly on the instantaneous wave configuration and can vary over an extreme dynamic range within tens or hundreds of nanoseconds (Guenther 1985b).

The shape of volume backscatter component is shown in Figure 3.2.6 where it is assumed that the bottom is deep enough that the bottom-reflected signal does not affect the volume backscatter from near-surface water. In the case of the ImpRF (blue, solid curve), the leading edge of the backscattered component starts at $t = t^{sf} - \Delta t^{sf}/2$ (Figure 3.2.3); it reaches a maximum at the time $t \leq t^{sf} + \Delta t^{sf}/2$, with equality corresponding to negligible attenuation of the sounding beam in the water. The peak magnitude is proportional to the volume backscattering coefficient, β_π. For a receiver FOV that is sufficiently large, the decay of the ImpRF in the near-surface water layer is approximately exponential in time for $t > t^{sf} + \Delta t^{sf}/2$, and the exponential decay rate equals to $c \cdot a_1/n$, where the effective attenuation coefficient, a_1, accounts for both absorption and scattering of light for large angles, $a < a_1 < a + b$. For the real waveform (red, dashed curve in Figure 4.2.6), the exponential decay in deep water with the same exponential decay rate, begins at time $t \approx t^{sf} + \Delta t^{sf}/2 + \tau_R$, (see equation (3.2.4)). The decay of the backscattered signal from surface water (in deep water) diverges from the pure exponential dependence due to effect of small-angle forward scattering, an effect described quantitatively by Dolin and Levin (1991). The divergence from exponential decay depends strongly on the receiver field-of-view angle, Θ_R. If Θ_R is allowed to increase indefinitely, the exponential decay of backscattered signal will hold for the entire waveform.

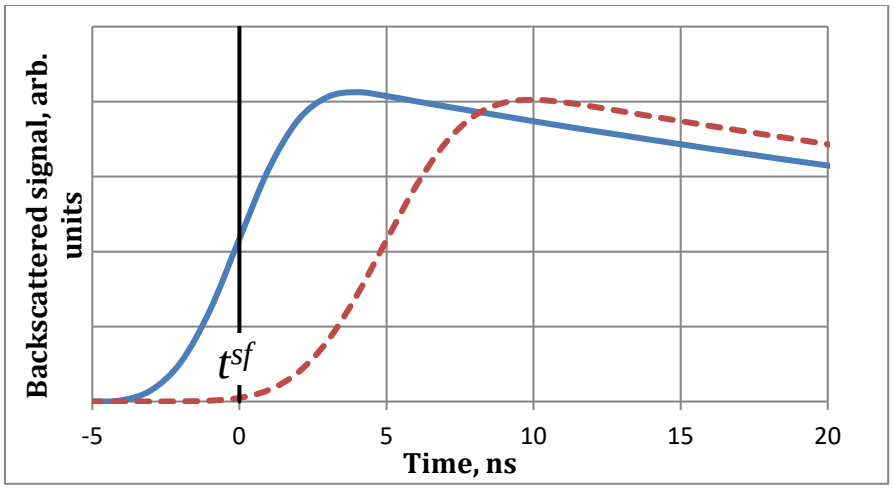

Figure 4.2.6. The shape of the idealized, backscattered component of the bathymetric waveform of the ImpRF (blue, solid), and of a real waveform with an effective sounding pulse duration of 3.5 ns (red, dashed).

The above discussion of the amplitudes and positions of the surface-reflected and backscattered peaks in the ImpRF shows that, when the surface and backscatter returns are combined, the actual maximum of the ImpRF will be delayed with respect to the "surface only" ImpRF maximum at t = 0 (Figure 4.2.5) by an amount of time that depends on the relationship between the instantaneous effective surface reflectance, ρ_{sf}, and the backscattering coefficient, β_π. For a large surface reflectance and clear water, the ImpRF maximum will occur close to $t = 0$. If backscattering from the near-surface water layer is substantial, the maximum will be shifted by $t < t^{sf} + \Delta t^{sf}/2$, toward the backscattered signal maximum (Figure 4.2.6). The ImpRF and real waveform shown in Figure 4.2.7 were obtained for a surface reflectance, $\rho_{sf} = 0.02$ and backscattering, $\beta_\pi = 0.001\ m^{-1} \cdot sr^{-1}$.

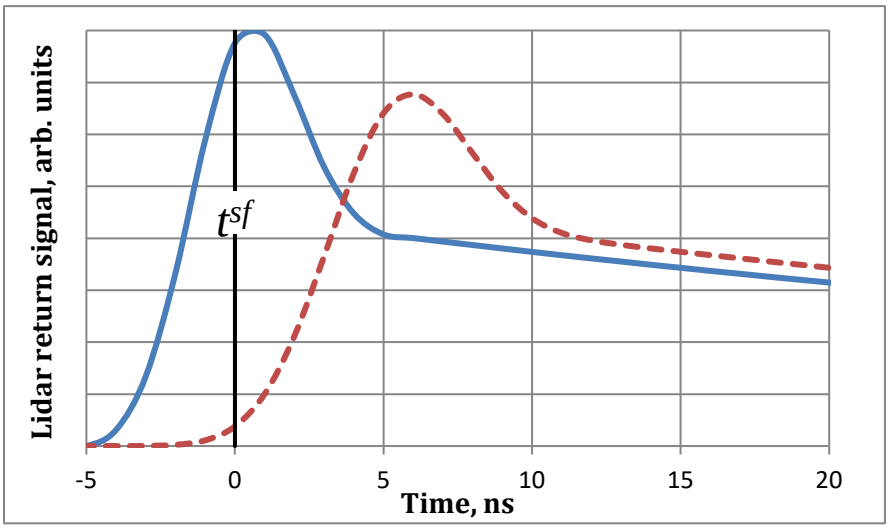

Figure 4.2.7. Idealized shape of the combined surface-reflected and backscattered components of the ImpRF (infinitesimally short sounding pulse) (blue, solid), and of a realistic waveform with an effective sounding pulse duration of 3.5 ns (red, dashed) with no bottom effect.

Guenther (1985) points to the uncertainty in position of the waveform "surface" peak as a source of biased depth results. Another possible source of depth measurement error relates to the position of the bottom-reflected peak (see Figure 4.2.8). The maximum of the bottom return component of the ImpRF (blue, solid curve) occurs at

$$t^{bot} = \frac{h^{bot}}{\cos\theta_w} \cdot \frac{2n_w}{c} \quad . \tag{4.2.9}$$

The arrival time dispersion due to scattering (R. E. Walker and McLean 1999), has been neglected in equation (4.2.9). Note that the bottom pulse duration, Δt^{bot}, includes the effect of widening of the sounding beam due to light scattering in the water. As a result, the position of bottom-reflected peak in the real waveform is dependent on the water optical properties in equation (4.1.9).

In the time interval $[t^{bot} - \Delta t^{bot}/2\ , t^{bot} + \Delta t^{bot}/2]$, the "tail" of backscattered component is also present in the lidar waveform, along with the bottom-reflected signal. The "tail" causes an additional uncontrolled shift of the bottom-related maximum in the composite waveform (i.e., the sum of surface-reflected, backscattered, and bottom-reflected signals) as illustrated in Figure 4.2.9. It should also be noted that, for deep enough water, the backscattered signal will drop below the noise level and will therefore be invisible at time when a bottom-reflected peak of sufficient amplitude is observed. (The sources and levels of the background noise component are considered in detail in Section 4.6.3.)

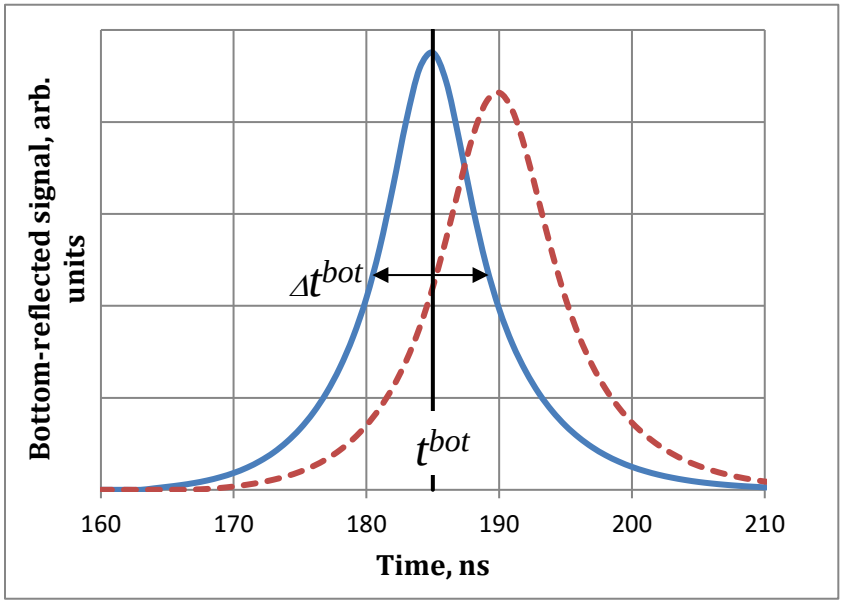

Figure 4.2.8. Idealized shape of bottom-reflected component of the ImpRF (infinitesimally short sounding pulse) (blue, solid), and of the realistic waveform with an effective sounding pulse duration of 3.5 ns (red, dashed).

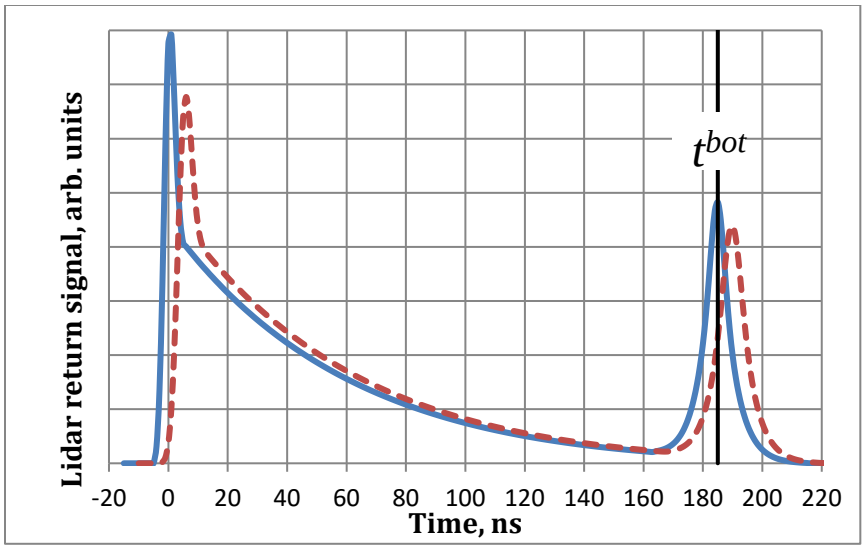

Figure 4.2.9. Idealized shape of bathymetric waveform (surface-reflected plus backscattered plus bottom-reflected components) of the EnvRF (infinitesimally short sounding pulse) (blue, solid), and of real waveform (effective sounding pulse duration of 3.5 ns) (red, dashed).

4.3 Basic System Design – an overview

Shachak Pe'eri

The design of all scanning lidar systems (terrestrial, atmospheric, topographic or bathymetric) is similar in general (Bunkin and Voliak 2001; Measures 1992; Renslow 2012; Wehr 2009). All require the same basic set of system components: a laser transmitter, a scanning mechanism, a receiving telescope, a narrow band filter matched to the laser wavelength, a detector – usually a photomultiplier tube (PMT) or an avalanche photodiode (APD) – and signal processing hardware to digitize, filter and store the returning backscatter. For airborne lidar bathymetry (ALB) systems it is convenient to divide the components into four main system units: a laser transmitter unit, a scanning unit (moving mirror), a detector unit (telescope, filter, detector and digitizer) and auxiliary systems (e.g., stabilization, time, attitude and position). Each of the main system units contributes to the overall uncertainty of an ALB survey, and the specific characteristics of each must be considered in evaluating the overall design (S. A. White et al. 2011a). In this section a general description will be provided for each of the system units. For an introduction to the more basic calculations based on the parameters of each system unit, the authors recommend Balstavias (1999) as a starting point reference. A detailed development of the design characteristics specific to ALB is presented subsequent sections of this chapter.

4.3.1 Transmitter unit

The laser transmitter unit includes the laser together with the optical elements that define the energy of the laser pulse, the pulse repetition frequency (PRF) and the beam divergence. ALB systems use a pulsed, frequency-doubled Nd:YAG (neodymium-doped yttrium aluminum garnet) laser that transmits at 532 nm, in the green part of the spectrum, near the optimal wavelength for maximum transmission in water over a wide range of conditions (Austin and Petzold 1984).

The power of the laser transmitter is a fundamental issue in lidar design. Simplistically, the greater the power, the greater the penetrations depth will be. However, power is limited by a number of considerations, probably the most significant being eye safety. The American National Standards Institute (ANSI) publishes a recommendation for the maximum permissible exposure (MPE) for direct ocular exposure in an outdoor environment (ANSI 2005). The MPE is determined by averaging the incident power of the beam over an area defined by a 7-mm diameter aperture that is equal to a fully dilated pupil of the human eye. In the case of a green laser pulse (532 nm) the MPE is 5×10^{-7} J cm^{-2} for an exposure time that is less than 10^4 ns. In the case of a fixed ALB system, the laser power per unit area, A, must conform to the following relationship at ground level:

$$MPE \geq \frac{\langle Q \rangle PRF}{A} = \frac{\langle Q \rangle PRF}{\pi \cdot (0.5 \cdot H \cdot \Theta_E)^2} \tag{4.1.1}$$

where $\langle Q \rangle$ is the pulse energy in Joules, PRF is the pulse repetition rate in Hertz, H is the height of the ALB above the water surface and Θ_E is the beam divergence in milliradians. It is important to emphasize that the MPE value used here is based on a total exposure time of less than 10^4 ns. It is clear from equation (4.1.1) that higher pulse energy can be balanced by a lower repetition rate, a higher altitude, or a larger beam divergence. Beam divergence and repetition rate combine to define the range of possibilities for the scanning pattern. Typically, the two are adjusted together to meet the requirements of a particular application. For example, a survey in deeper waters for which depth penetration is a major concern will be better served with higher overall power and a relatively large beam divergence in order to meet eye-safety requirements. Such an adjustment is effective as long as the resulting lower repetition rate and wider sample spacing are acceptable (Penny et al. 1986). For surveys in shallow waters, a higher ground sampling is often advantageous for better definition of channels and underwater obstructions. This requires a smaller beam divergence and higher repetition rate (Guenther et al. 1996; E. Yang et al. 2009).

4.3.2 Scanner unit

The scanner unit defines the laser measurement pattern as well as the spot size and spacing on the water surface. In order to cover a large area with laser measurements, the scanner must distribute the laser pulses along a swath below the aircraft. The specific pattern of samples on the water surface is not particularly important for bathymetric mapping as long as the spatial density of the laser measurements is moderately uniform and meets the survey specifications (Guenther 1985b). This need for uniformity means that the scan rate and sampling rate must be matched to the aircraft speed and altitude.

There are three predominant styles of mechanical scanning typical of ALB systems (Petrie and Toth 2009; Wehr 2009): oscillating mirrors, polygonal scanners and nutating mirrors. Oscillating mirrors can have one or two axes (Baltsavias 1999). A one-axis oscillating mirror scanner combines with the aircraft motion to produce a zig-zag sampling pattern on the ground. Using gimbals or galvanometers, the motion of the oscillating mirror can adjust for the forward motion of aircraft, resulting in a parallel line pattern, i.e. parallel scan lines/arcs (Axelsson and Alfredsson 1999). Most commercial ALB systems use the oscillating scanner mechanism. The zig-zag line pattern is used in both the LADS and the EAARL ALB systems, whereas a two-axis parallel arc pattern is used in HawkEye and SHOALS systems (LaRocque, Banic, and Cunningham 2004a; Lillycrop and Banic 1992).

A polygon scanner, also known as a rotating multi-facet mirror, is a continuously spinning optical polygon parallel elliptical arc-like line pattern. The polygon scanner is typical for Riegl laser scanners, including the VQ-820-G system (Steinbacher et al. 2012).

In a nutating mirror mechanism, the laser beam is deflected by a rotating mirror, where the rotational axis of the mirror is not normal to the mirror surface. Typically, the rotating axis of the mirror is mounted so that the scanner shaft and the laser beam form an angle of 45°. The resulting pattern on ground is an approximately elliptical scanning pattern. Due to the elliptical scan, most of the measurement points on ground are scanned twice, once in the forward view and a second time in the backward view (Fuchs and Mathur 2010). The redundant information for the same ground spot can be favorably used to calibrate the scanner and the position files as far as the pitch angle is concerned (Gonsalves 2010a). A Palmer scanner (nutating wedged mirror) was used in the Airborne Oceanographic Lidar (AOL) system in late 70's and early 80's (Guenther 1985b). Only recently, in 2012, was a nutating scanner mechanism re-introduced in CZMIL with a Fresnel prism (Fuchs and Mathur 2010). More details on other available scanner mechanisms that are currently only used in topographic lidar systems and not in ALB systems, such as rotating polygon and fiber scanner, can be found in Wehr (2009) and Baltsavias (1999).

Regardless of the method, the scanner distributes the pulses in a swath to either side of the aircraft. The swath width, SW, is dependent on the maximum off nadir angle across track, θ_{max}, and the height above the water surface, H. Under ideal survey conditions (no pitch or roll), the swath width on the water surface will be:

$$SW = 2H \cdot tan\left(\frac{\theta_{max}}{2}\right) \tag{4.1.2}$$

Similarly, the footprint diameter, d^{sf}, just above the water surface will vary with viewing angle. With the aircraft at a height, H, above the water surface, using a laser with a beam divergence, Θ_E, at an off-nadir angle in air, θ_a, the beam diameter just above the water surface, d^{sf}, is:

$$d^{sf} \approx H_s \cdot \Theta_E \quad . \tag{4.1.3}$$

where H_s is the slant range distance between the lidar and the sea surface along the lidar axis. Sample spacing is different along track, Δx, and across track, Δy. Although the exact sample spacing depends on the scanner type and the off-nadir angle, a first-order approximation of the sample spacing is given by:

$$\Delta x = v_{plat}/f \quad , \tag{4.1.4}$$

and

$$\Delta y = (SW \cdot f)/PRF \tag{4.1.5}$$

where v_{plat} is the platform (e.g., aircraft) velocity, f is the scan rate from side to side and PRF is the pulse repetition frequency. In order to achieve a uniform density, the cross-track point spacing should be roughly equivalent to the along-track point spacing which constrains the aircraft velocity, that is, if

$$\Delta x \approx \Delta y \tag{4.1.6}$$

then,

$$v_{plat} \approx SW \times f^2/PRF \quad . \tag{4.1.7}$$

4.3.3 Detector unit

The detector unit collects, digitizes and stores the returning laser energy as a sequence of events from the interaction of the laser pulse with the water surface to the interaction with the bottom. The sequence is referred to as a waveform (Guenther 1985b; Pe'eri, Morgan, et al. 2011; Billard, Abbot, and Penny 1986b). Waveform observations can be analyzed off-line using digital signal processing methods in order to extract the surface and bottom returns and calculate the laser measurement range underwater. In addition to bathymetry, the water surface, water column and seafloor can be characterized based on the shape of the returns and additional features in the volume scattering (Pe'eri and Philpot 2007; Tuell, Feygels, et al. 2005).

The returning laser energy is collected by a telescope having an adjustable field of view (FOV). The size of the receiver FOV is always larger than the transmitted beam divergence since the beam is broadened by scattering in the water (Guenther 1985b; Feygels, Wright, et al. 2003b). Two general types of ALB systems have evolved based on the differing requirements in shallow and deeper water environments. The first type, optimized for deeper water applications, is a broad-beam ALB system (e.g., SHOA Guenther, 1985, LS, LADS MK3, CZMIL, HawkEye II, and Hawkeye III) that transmits a beam having a large divergence (3-11 mrad) with a typical footprint size of 2 to 4 m on the water surface. The detector FOV in SHOALS and LADS is around 100 mrad, whereas HawkEye has a narrower FOV of about 1-3 mrad. CZMIL uses a wide FOV (40 mrad) for deep water, but a narrow FOV (1.9 mrad) can be selected for shallow water operation. The second type is the narrow-beam ALB systems, specifically designed for shallow water applications (e.g., EAARL-B; Chiroptera, RIEGL VQ820G, Aquarius), that transmit using a small beam divergence (1-3 mrad) with a typical footprint size of less than 1 m on the water surface and a correspondingly smaller telescope FOV. Broad-beam ALB systems are designed for mapping bathymetry in areas that are not cost-efficient for a multi-beam echo sounder (MBES) at the International Hydrographic Office (IHO) order 1b standards. i.e., in water depths of 2 m to 15 m (Guenther 1985b; Imahori et al. 2013). Narrow-beam ALB systems can typically acquire depth measurement in extremely shallow water areas from the shoreline to 4 m, depending on the environmental conditions. The narrow-beam ALB systems are ideal for rivers and estuaries, when water conditions allow bottom detection (McKean et al. 2009).

The returning energy is converted from an optical signal into an electrical signal using an optical detector. Two types of detectors are commonly used for logging the backscattered signal: avalanche photodiodes (APD) and photomultiplier tubes (PMT). The typical APD is a multi-photon detection sensor, in which an electric signal is generated that is directly proportional to the optical power of the incident light (Wilson and Hawkes 1998). Multi-photon detection APD sensors are able to detect power changes of up to 3 orders of magnitude. PMT and Geiger-mode APD (GAPD) detectors are single detection sensors, in which a single photon can set off a significant avalanche of electrons using a reverse bias voltage (Wilson and Hawkes 1998; Hamamatsu 2007). These single-photon detection sensors typically detect power changes up to 6 orders of magnitude. In order to log the returning optical energy as a waveform, the electrical signal of the photo-detectors is sampled using a digitizer. It is important to note that the

sampling rate of the digitizer defines the resolution of the waveforms, but the bandwidth of the photo-detectors and the digitizer limit the accuracy with which the waveform is digitized.

Range is determined by the time-of-flight of the laser pulse, i.e., the time difference between the emitted pulse and the returning backscatter (Measures 1992). The laser pulse traverses the range twice (from the laser to the target and from the target to the detector). The laser transmits a short pulse which is reflected (scattered) by an object at a distance, or range to the target, *r*, the total distance traveled by the pulse is $2r$. The time, t, required for the round trip is then found from the relation: $2r = v * t$ where v is the velocity of light in the medium. Thus, the range of the target is given by:

$$\mathrm{r} = v * \mathrm{t}/2 \quad . \tag{4.1.8}$$

The range resolution of the lidar, Δr, designates the smallest distance between two targets that can be discriminated, and is limited by the sampling rate of the detector, f_d. The time of travel to targets at ranges r and $r + \Delta r$ are then $t_1 = 2r/v$ and $t_2 = 2(r + \Delta r)/v$, respectively. To be resolvable, the difference in return time, $\Delta t = t_2 - t_1 = 2\,\Delta r/v$, must be greater than or equal to the interval between successive observations: $\Delta t > 1/f_d$, thus, the range resolution will be:

$$\Delta r > \frac{1}{2} c \Delta t \;\; or \; \Delta r > \frac{v}{2 f_d} \tag{4.1.9}$$

We are concerned primarily with the optical path in water. The speed of light in water is $\mathrm{v}_w = \mathrm{c}/n_w$, where $c = 3.00 \times 10^8\ m\ s^{-1}$ is the speed of light in a vacuum and the index of refraction of water can be approximated as $n_w \approx 1.333$ (Saleh and Teich 1991b). Thus, in water, a 1 GHz sampling rate ($f_d = 1\ GHz$), which is typical of ALB systems, corresponds to a range resolution limit of about 11.2 cm. In fact, the range resolution can be refined further for narrow-beam systems (e.g. EAARL-B and VQ-820-G) by measuring the local sea surface wave height and slope angle for each laser measurement (Tulldahl, Andersson, and Steinvall 2000) or by using online waveform processing for measuring relative pulse broadening (Pfennigbauer et al. 2014).

4.3.4 Auxiliary systems for ALB performance and geo-referencing.

The range measured in the waveforms is the line-of-site vector from the aircraft to the water surface in air and from the water surface to the seafloor underwater. In order to reference the range measurement and dataset in a known coordinate system, e.g. WGS-84 or NAD-83, the ALB system must be supported by information logged by the auxiliary systems for ALB performance (attenuator, gimbals, cooling, etc.) and geo-referencing (GPS, IMU). This dataset of referenced measurement is also known as a point cloud. The position and direction of the laser beam recorded by these devices must be synchronized with the scanner information and the digitized waveforms (range measurements) with nanosecond precision. Measurement errors of the range, position, and beam direction or any temporal misregistration errors will also influence the accuracy of the final product (Baltsavias 1999; S. A. White et al. 2011b) The two main external sensors that are used in concert with the ALB system are an inertial measurement unit (IMU) and a global positioning system (GPS) receiver that measure the attitude and location of the aircraft (and the ALB sensor) during the survey (Wehr 2009; Habib et al. 2010). The GPS data is typically collected at a sample rate of 1 to 2 Hz, and then processed in a differential post-processing mode (DGPS), whereby the data

from the aerial receiver is processed at GPS ground stations. In order to achieve positioning measurements with accuracy better than ±10 cm, the GPS ground station are positioned on known benchmarks at a maximum distance of 25 km from the survey line. The orientation of the aircraft is determined using the IMU at a sample rate of 100 Hz with a typical accuracy better than 0.01 of a degree. After the flight, in a post-processing mode, an integrated position and orientation solution is applied to the laser range in order to calculate bathymetry. It is important to note that, in addition to the internal accuracy of the ALB system, the GPS receiver and the IMU, the mounting parameters that relate each of these units also affect the accuracy of the laser measurements. The offset and orientation between the units, known as the lever-arm components and bore-site angles, should be determined through a calibration procedure (Habib et al. 2010). Another issue that affects the accuracy of the range measurements is random angular movement caused by wind and engine vibration of the aircraft (Abdullah 2004). In order to ensure vibration-free conditions, manual and automatic mounts are used stabilize the ALB system.

4.4 Model of the Lidar Waveform

V. Feygels, Yu. Kopilevich, M. Kim

4.4.1 Receiver channel model

An ALB receiver is designed to collect radiation that results from reflection of the emitted pulse at the sea surface, backscattering in the water column, and reflection at the sea floor. The radiation is spectrally filtered to observe only at the emitted wavelength (532 nm, a “green receiver”) in order to minimize "noise" from natural sources, especially sunlight. In order to collect as much of the reflected laser radiation as possible, the returning radiance is spatially integrated over the receiver telescope pupil area, Σ, and over the receiver channel field-of-view solid angle, Ω. The resulting power, $S_p(t)$, is collected for the duration of the pulse return, defined as the time span that begins with the initial return of the pulse from the water surface, and ends with the final return from the sea bottom. The initial return includes a short rise time that, for oblique sounding, exceeds that of the transmitted laser pulse duration due to the geometric stretch effect (see Section 4.2.1). Another consideration is the dynamic range of the pulse power, $S_p(t)$, which may span as much as 50 – 60 dB, depending on the water optical properties, bottom depth and reflectance.

The output from the receiver channel, $D(t)$ is a digitized, amplified signal resulting from the initial signal, $S_p(t)$. The dynamic range of the received signal can span 5 to 6 orders of magnitude. In order to collect successfully both the bottom return and the surface return, the digitizer requires either that the photodetector operate in a logarithmic mode, or that it operate in a linear mode, followed by a log-amplifier. Given the rapid changes in the signal, $S_p(t)$, each of the elements in the electronic segment (photodetector, log amplifier, & digitizer) must have either a wide frequency band pass, or a short response time.

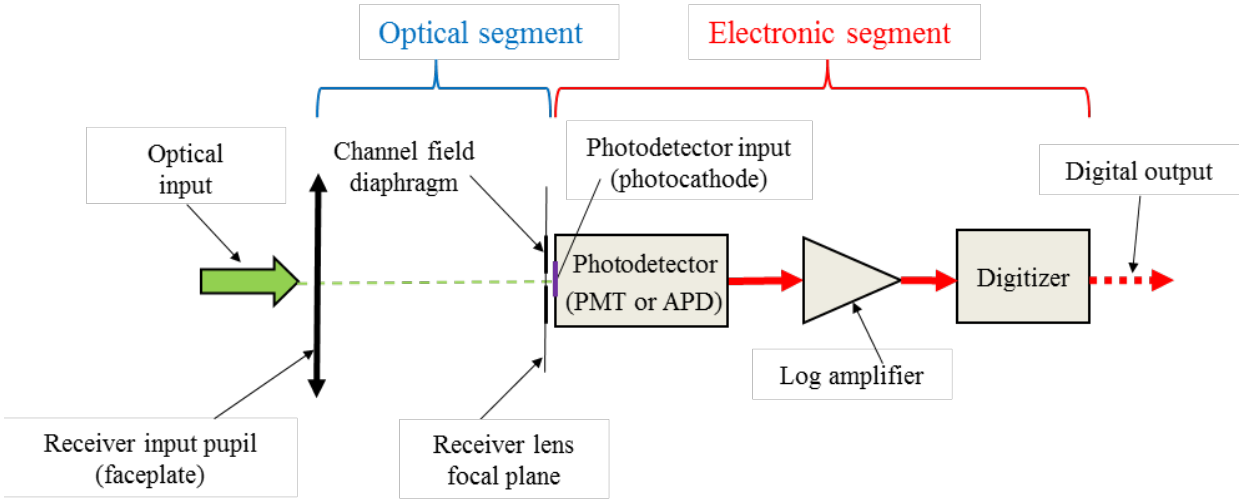

Figure 4.3.1. General schematic diagram of a lidar receiver. The sequence includes an optical segment (from the receiver lens faceplate to the photodetector input, e.g. the PMT photocathode) and an electronic segment (from the photodetector input to the digitizer output).

A general schematic of a receiver is presented in Figure 4.3.1 the sequence includes an optical segment (from the receiver lens faceplate to the photodetector input, e.g. the PMT photocathode) and an electronic segment (from the photodetector input to the digitizer output). Figure 4.3.1 represents a conventional, single-FOV design. The sequence includes: an optical segment which is designed as a mirror telescope instead of refracting one (Fuchs and Tuell 2010); the spectral selector (a narrow band filter) has been omitted from the scheme; the log amplifier is only used when photodetector operates in linear mode.

A “multi-FOV” bathymetric lidar (Sugimoto et al. 2001; Feygels, Kopilevich, et al. 2003) may be designed with a single telescope furnishing several receiving channels, each having a different FOV. The incoming light field can be divided into several channels in a number of ways and in a given ratio. For example, beam or beam sampler elements can reflect part of the light and allow the rest to pass through with the use of wavelength splitters – optical elements with special coatings designed to reflect a selected range of wavelengths while passing others (Victor I. Feigels et al. 2002).

An implementation of the schematic is illustrated in Figure 4.3.2 with a variant of the CZMIL receiver system optical design (Fuchs and Tuell 2010). In this design a Field Separator (FS) element is used to divide incoming light into a “deep” channel with a plane FOV angle, Θ_R, of 40 mr, and seven “shallow” channels with equal FOV angles $\Theta_R = 1.9\ mr$. The division of light among the narrow-FOV channels is performed using a fiber optic bundle (FOB) to split the incoming signal into separate beams. The beam splitter (BS), together with infrared (FIR) and “green” (FG1 and FG2) interference filters, is used to separate the optical signals into the seven 532 nm channels and the single 1064 nm channel. (The beam splitter and the IR channel are not used in all ALB systems. These variants of the optical segment design do not lead to any loss in generality of the consideration of the electronic segment of the receiver channel.)

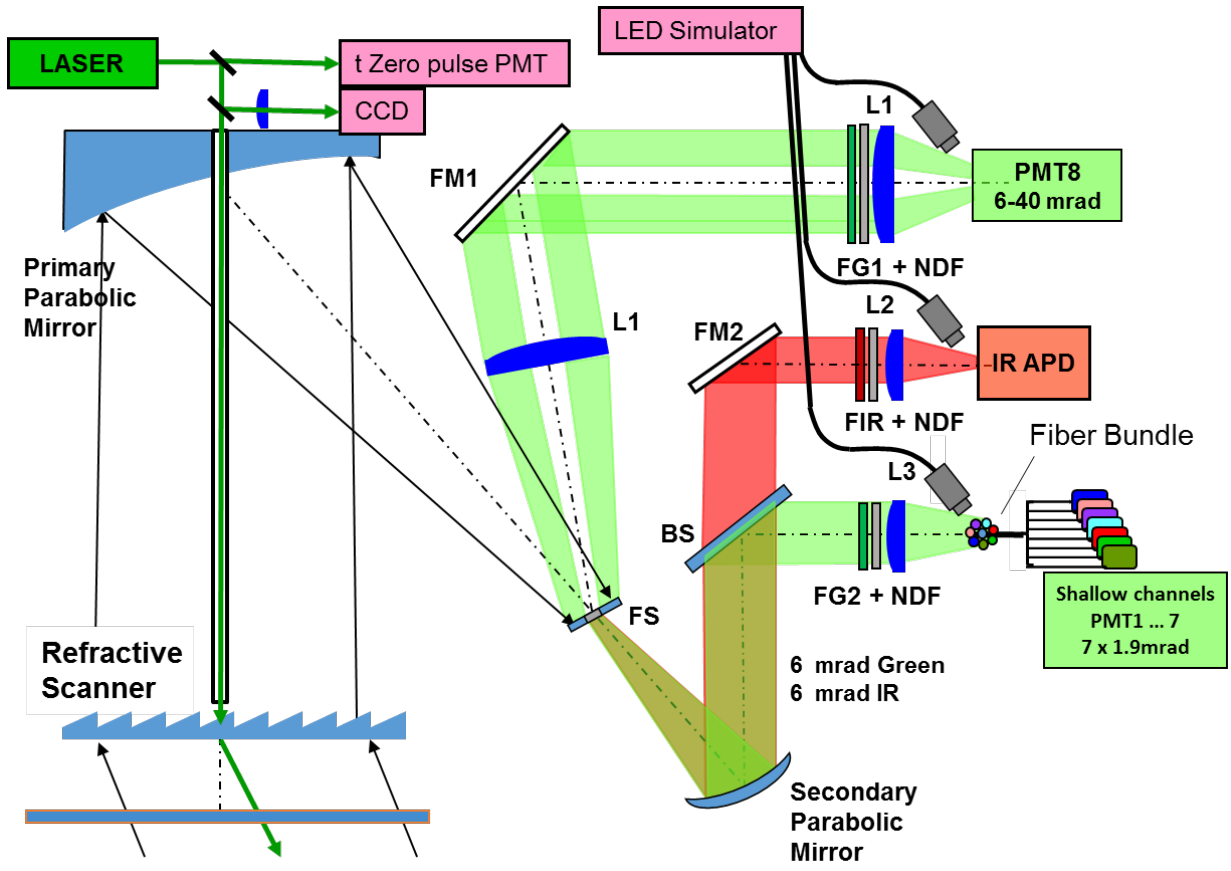

Figure 4.3.2. General schematic (one of the variants) of CZMIL receiver optical system. L1-L4 – lenses; FS – Field Separator: FG1-FG2 –green (532nm) interference filters; FM1-FM2 – Folding Mirror; FIR – infrared (1064nm) interference filter; NDF – neutral density filters; BS – beam separator.

The relationship between the input optical signal, $S_p(t)$, and the discretized waveform output signal, $D(t)$, is fundamental to the quantitative interpretation of lidar sounding data. The relationship is described by a mathematical model of the receiving channel (Kopilevich et al. 2005b). In accordance with that model, the conversion of the input optical signal, $S_p(t)$, into the output electrical signal, $D(t)$, is achieved by characterizing the key hardware in the receiving channel (i.e., PMT or APD, multiplier, and digitizer) as:

$$S_R(t) = \int_0^\infty S_P(t-t') \cdot \omega(t')dt' \equiv S_P(t) * \omega(t) \quad , \tag{4.3.1}$$

and

$$D(t) = \chi[S_R(t)] \ . \tag{4.3.2}$$

The symbol " $*$ " in equation (4.3.1) denotes the operation of convolution, and $\omega(t)$, is the normalized function describing the effect of a finite response time (or the restricted bandpass) of the channel,

$$\int_0^\infty \omega(t')dt' = 1 \quad . \tag{4.3.3}$$

Equation (4.3.2) introduces the function, $\chi[\cdot]$, to denote a count-valued, monotonically increasing function of an argument in Watts. This function will hereafter be referred to as "the channel Watt-count characteristic". The physical meaning of the channel Watt-count characteristic is readily seen when a constant optical signal is considered. Letting $S_p(t) = S_{const} = const(t)$, and recalling that $\int_0^\infty \omega\,(t')dt' = 1$, equation (4.3.2) yields:

$$D(t) = D_{\text{const}} = \chi(S_{\text{const}}) \quad . \tag{4.3.4}$$

The function, $\omega(t)$, describes the "optical response" of the channel to a delta-function impulse, i.e., for $S_p = \delta(t)$, equation (4.3.1) gives $S_R(t) = \omega(t)$. The function may be expressed as the convolution of the responses of each of the elements in the electronic segment (see Figure 4.3.1):

$$\omega(t) = \omega_{PMT}(t) * \omega_{amp}(t) * \omega_{dig}(t) \quad , \tag{4.3.5}$$

where, $\omega_{PMT}(t)$ is the response function of the PMT, $\omega_{amp}(t)$ is the response of the amplifier, and $\omega_{dig}(t)$ is the response of the digitizer. It should be noted that equation (4.3.1) describes a mathematical model of the receiving channel. The validity of the model for a given receiver channel must be tested experimentally. For example, the channel response function, $\omega(t)$, in (4.3.1) may depend on the input signal level and therefore the model in question will be applicable only for a limited input power range. In spite of such limitations, the model has proven to be quite efficient in simulating lidar signals and in processing waveforms collected during surveys [see, e.g., Tuell et al. (Tuell, Feygels, et al. 2005)].

To summarize, the following steps are required to use the lidar receiving channel model for simulating a lidar waveform:

1. Calculate the input optical signal, $S_\delta(t)$, corresponding to a delta-function sounding pulse, $Q\eta_R \cdot \delta(t - t_0)$, where Q is the actual transmitted laser pulse energy (after accounting for atmospheric attenuation and lidar transmitter system losses) and η_R is the transmittance of the receiver optical system (the optical segment in Figure 4.3.1) that is determined through channel radiometric calibration (see Section 4.4.1). The calculation of $S_\delta(t)$ is based on an accepted theory of airborne oceanographic lidar return (see Section 4.3.2).
2. Convolve the input optical signal, $S_\delta(t)$, with the laser pulse shape, $p(t)$, to obtain the actual input signal in the optical domain:

$$S_p(t) = S_\delta(t) * p(t) \quad , \quad \int_0^\infty p(t)\,dt = 1 \quad . \tag{4.3.6}$$

Recalling equations (4.2.6)-(4.2.8) and (4.3.1), the simulated waveform in the optical segment, $S_R(t)$, may be expressed as:

$$S_R(t) = S_\delta(t) * R(t) \quad , \tag{4.3.7}$$

with

$$R(t) \equiv p(t) * \omega(t) \tag{4.3.8}$$

According to (4.3.7), function $R(t)$ may be called "the receiving channel response to lidar pulse", or just "the channel response function". On the other hand, comparison of (4.3.7) with (4.3.6) clarifies the physical meaning of the function $R(t)$ as the effective shape of the sounding pulse.

Combining (4.3.8) and (4.3.5), the effective pulse shape, $R(t)$, may be expressed as the convolution of the actual pulse shape with the response functions of the individual elements in the electronic segment:

$$R(t) = p(t) * \omega_{PMT}(t) * \omega_{amp}(t) * \omega_{dig}(t) \quad . \tag{4.3.9}$$

If the transmitted pulse shape, $p(t)$, and the response functions, $\omega_{PMT}(t)$, $\omega_{amp}(t)$, and $\omega_{dig}(t)$ are all described by Gaussian distributions, then the duration of the effective pulse, τ_R, (e.g., at FWHM) will be given by the formula

$$\tau_R^2 = \tau_p^2 + \tau_{PMT}^2 + \tau_{amp}^2 + \tau_{dig}^2 \quad , \tag{4.3.10}$$

where τ_p is the transmitted pulse duration, and τ_{PMT}, τ_{amp}, and τ_{dig} are the widths of the corresponding hardware response functions (at the same level), respectively. For non-Gaussian functions, equation (4.3.10) may be used as a helpful estimate of τ_R provided that the response characteristics of the electronic track are known.

If, in addition to the optical waveform, $S_R(t)$, it is also necessary to simulate the output signal waveform in the electrical domain, $\chi[\cdot]$ may be used to derive $D(t)$:

$$D(t) = \chi[S_\delta(t) * R(t)] \ . \tag{4.3.11}$$

Processing an experimentally obtained waveform, $D^{exp}(t)$ in order to estimate environmental properties (e.g., bottom depth and reflectance, IOPs) relies on a comparison of the experimental waveform with simulated waveforms. It is convenient to perform the comparison in the optical domain. For this purpose, the electrical signal, $D^{exp}(t)$, (in digital counts) must be transformed into the optical signal, S_R^{exp} (in Watts):

$$S_R^{exp}(t) = \chi^{-1}[D^{exp}(t)] \quad , \tag{4.3.12}$$

with $\chi^{-1}[\cdot]$ being the inverse of the channel Watt-count characteristic, $\chi[\cdot]$, from equation (4.3.2).

4.4.2 Improved small-angle-scattering models of lidar waveform components

4.4.2.1 Introduction.

The need for improved mathematical modeling of oceanographic lidar signals along with the initial development of lidar systems in the 1960s [see, e.g., Hickman & Hogg (1969); Guenther (1985b)]. In accordance with the main purpose – using oceanographic lidar for bathymetric mapping – the existing mathematical models were designed to estimate the maximum measurable depth for specific lidar systems

for given optical characteristics of the seawater, and to optimize the parameters of the lidar systems (Victor I. Feigels et al. 2002; Victor I. Feigels 1992; Kopilevich and Feigels 2002). New applications using ALB systems, such as reconstruction of the optical characteristics of the water from the lidar waveform (Billard, Abbot, and Penny 1986a; Feygels, Kopilevich, et al. 2003; Allocca et al. 2002), have substantially increased the requirements on the accuracy of the mathematical models.

The first (and simplest) mathematical model describing the power, $S^{back}(t)$, of the elastic backscattering signal received from the water column used a single backward-scattering approximation at a nadir incidence angle and had the form (Gordon 1982; Maffione and Dana 1996):

$$S^{back}(\mathrm{t}) = Q \cdot {\tau_F}^2 \frac{\Sigma}{(Hn_w + h_{bot})^2} \beta_\pi \frac{c}{2n_w} \exp\left(-K_{sys} \frac{ct}{n_w}\right) \quad . \tag{4.3.13}$$

Here t is time, with $t = 0$ corresponding to the instant that the signal reflected from the surface is recorded; Q is the energy of the laser probe pulse, taking into account the attenuation along the atmospheric track and the transmission of the receiver system; τ_F is the Fresnel transmission of the water–air interface; Σ is the pupil area of the lidar receiver; β_π is the backscattering coefficient of sea water; c is the speed of light in vacuum; n_w is the refractive index of sea water; H is the altitude of the lidar platform above sea level; h_{bot} is the current depth, $h_{bot}(t) = ct/2n_w$; and K_{sys} is the so-called system attenuation coefficient.

The model described by equation (4.3.13), with $K_{sys} = a + b_b$, where a is the absorption and b_b the backward scattering coefficient of the water (see Section 3.3.2), is valid only when the receiver is able to collect virtually all of the backscattered radiation, i.e., either the FOV of the lidar receiver is wide enough (tending to 2π sr) and/or the backscattering is vanishingly weak (the backscattering coefficient $b_b \to 0$). Attempts to generalize the model (equation (4.3.13)) in order to describe a real system by treating the system attenuation coefficient, K_{sys}, as an apparent optical property of the seawater, were not very effective because K_{sys} was determined to be depth-dependent even in homogeneous sea water (Gordon 1982).

Fundamental progress in the development of a mathematical model of a lidar signal was made by Bravo-Zhivotovsky, Dolin, Luchinin, & Savel'ev (1969), Dolin & Savel'ev (1971b), and Dolin & Savel'ev (1979). This model was then brought to the level of handbook equations for engineering calculations in Dolin & Levin (1991).

In the following sections, a consistent derivation of a mathematical model of the ALB signal is presented. The model is a generalization of the results of Dolin & Levin (1991) in that it removes the substantial limitation on the FOV of the lidar receiver system, and therefore makes it possible to describe narrow-field ALB systems (Feygels, Kopilevich, et al. 2003; Feygels, Wright, et al. 2003b). In addition, allowance is made for the deviation of the lidar optical axis from the vertical (off-nadir probing), measurements typical in operational airborne systems (see Section 4.3.2.6).

4.4.2.2 Governing equations.

Instead of the actual lidar sounding geometry depicted in Figure 4.2.3, it is convenient to turn to the monostatic "equivalent lidar sounding problem" described earlier in Section 4.2.1 and illustrated in Figure

4.2.4. In the "equivalent" ALB problem, the media both below and above the air/water interface is assumed to have the same refractive index, n_w. Thus, the sounding beam does not undergo refraction at the interface, and the “equivalent” lidar parameters (position, sounding angle, sounding pulse energy, emitted beam divergence, receiver field-of-view) are specified in such a way as to retain the optical and geometrical properties of the actual sounding beam light field under the interface. A simplified version of Figure 4.2.4, revised to show the variables relevant to the improved model, is shown in Figure 4.3.3. (Evaluation of the “equivalent” lidar characteristics will be considered in detail later in Section 4.3.2.7 Emitted beam modeling). In the equivalent geometry (Figure 4.3.3), the lidar receiver, located at point O', is at an equivalent height, H', above the water surface. The equivalent slant path in air is H'_s, the distance along the slant path is denoted as z, and the equivalent receiver FOV is Θ'_R.

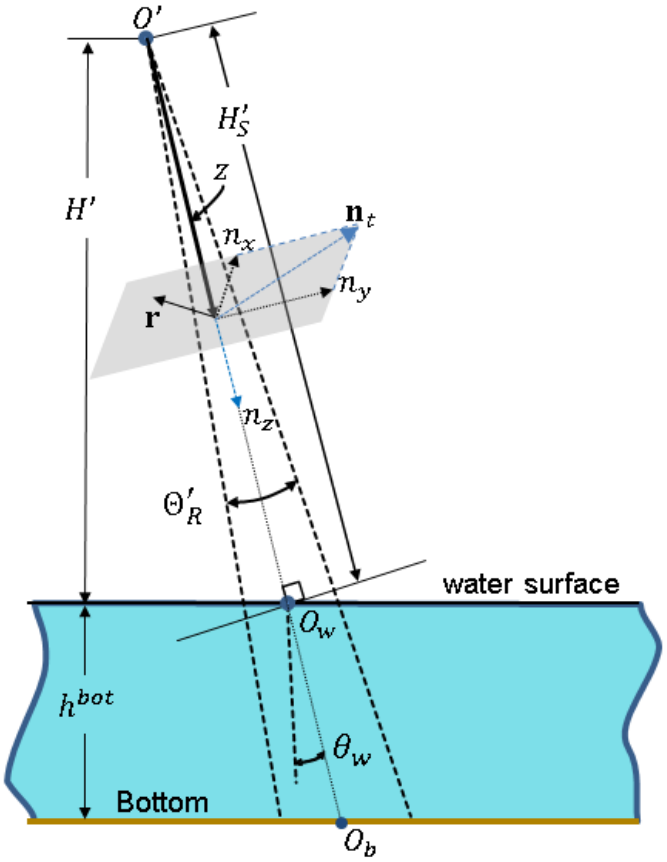

Figure 4.3.3. Geometry and variables used for the "equivalent geometry".

In the equivalent problem, let $(t, z = 0, \mathbf{r}, \mathbf{n})$, be the backscattered radiance arriving at the equivalent lidar receiver pupil, point (at $z = 0$), and distributed on a plane perpendicular to the optical axis of the receiver. Here, the local coordinate system is described by the 3D unit vector, $\mathbf{n} = \{n_z, \mathbf{n}_t\} = \{n_z, n_x, n_y\}$ with n_z oriented along the receiver axis and $\mathbf{n}_t = \{n_x, n_y\}$ belonging to the perpendicular plane. A 2D vector, $\boldsymbol{r} = \{r_x, r_y\}$, describes a location on that plane. The symbol I^{up} is specifically used to describe the distribution of upwelling radiance above the plane at $z = 0$. At each point, $\boldsymbol{r} = \{r_x, r_y\}$ on the plane, the radiance depends on a direction determined by the 3-D unit vector $\mathbf{n}$. Since only the upwelling light is considered for I^{up}, the z-component of the directional vector from the lidar receiver is negative, $n_z < 0$.

Let the received radiance, $I_R^{norm}(0, \mathbf{r}, \mathbf{n})$, $n_z < 0$, be the normalized characteristic function of the lidar receiver (Kopilevich and Surkov 2008), so that integration over the backscattering hemisphere yields:

$$\int_{z=0} d^2\mathbf{r} \int_{n_z \le 0} d\Omega(\mathbf{n}) I_R^{norm}(0, \mathbf{r}, \mathbf{n}) = 1 \quad . \tag{4.3.14}$$

The power, $S(t)$, of the lidar signal at the receiver may then be written as:

$$S(t) = \Sigma\ \Omega \int d^2\mathbf{r} \int_{n_z \le 0} d\Omega(\mathbf{n}) I_R^{norm}(0, \mathbf{r}, \mathbf{n}) I^{up}(t, 0, \mathbf{r}, \mathbf{n}) \quad , \tag{4.3.15}$$

with Σ and Ω being the pupil area and the solid angle (FOV) of the receiver, respectively. Now consider an infinitesimally short (delta-function) initial laser pulse; symbols for beam radiances, irradiances, and lidar signal components corresponding to the delta-function pulse will be specified by the subscript δ. The so-called "multiple forward-single backscattering" approximation [see, e.g., Dolin & Levin, (1991); Monin, (1983) is used for this case. In view of the small divergence angle and the strong anisotropy of light scattering by sea water, the scattered radiation is concentrated in a narrow cone around the direction of the incident beam. This allows us to approximate the leading edge of the sounding pulse in the water at time t by a distribution on a plane located at $z = ct/2n_w$, and perpendicular to the beam axis. (Compare with the analogous approximation used in Sec. 4.2.1, Figure 4.2.2. This approximation makes it possible to regard the backscattered light radiance at the receiver, $I_\delta^{up}(t, 0, \mathbf{r}, \mathbf{n})$, as the solution to a stationary radiation transfer equation (RTE) in the layer $0 \le z \le ct/2n_w$ (for backward propagation) with the following boundary conditions at the plane $z = ct/2n_w$:

$$I_\delta^{up}\left(t, z = \frac{ct}{2n_w}, \mathbf{r}, \mathbf{n}\right) = \frac{c}{2n_w}\ Q' \int_{n'_z \ge 0} d\Omega(\boldsymbol{n}')\, \beta(z, \mathbf{r}, \mathbf{n} \wedge \boldsymbol{n}')\, I'_E(z, \mathbf{r}, \boldsymbol{n}') \quad ; \quad n'_z < 0 \quad . \tag{4.3.16}$$

Here:

$Q' = Q \cdot \tau_F^2$ is the emitted laser pulse energy in the equivalent problem (Q is the actual laser pulse energy after accounting for atmospheric attenuation and lidar transmitter system losses, and τ_F is the transmittance of the air-water interface);

$\beta(z, \boldsymbol{r}, \boldsymbol{n}_1 \wedge \boldsymbol{n}_2)$ is the volume scattering function for the angle $\boldsymbol{n_1} \wedge \boldsymbol{n_2}$, where $\boldsymbol{n}_1$ is the direction of beam propagation, and $\boldsymbol{n}_2$ is the direction of the scattered light; the function is taken to be zero if the point $\{z(t), \mathbf{r}\}$ is not within the water body;

$I'_E(z, \boldsymbol{r}, \boldsymbol{n})$ is the solution of stationary RTE for downwelling emitted radiation in the half-space, $z > 0$, with the normalized boundary value $I'_E(0, \mathbf{r}, \mathbf{n})$ related to the given radiance distribution $I_E(t, z' = 0, \mathbf{r}, \mathbf{n})$, $n_z \ge 0$, at the lidar emitter output (plane $z = 0$) by:

$$I_E(t, z=0, \mathbf{r}, \mathbf{n}) = Q' \cdot \delta(t)\ \mathrm{I}'_E(0, \mathbf{r}, \mathbf{n})\ , \quad n_z \geq 0;$$
$$\iint \mathrm{I}'_E(0, \mathbf{r}, \mathbf{n}) d^2\mathbf{r}\, d\Omega(\mathbf{n}) \ = 1 \quad . \tag{4.3.17}$$

The prime symbol defines the direction of the scattered light.

In what follows, water optical properties are assumed to be independent of coordinates (i.e., the water is assumed to be vertically and horizontally homogeneous), so that

$$\beta(z, \boldsymbol{r}, \boldsymbol{n}_1 \wedge \boldsymbol{n}_2) \equiv \beta(\boldsymbol{n}_1 \wedge \boldsymbol{n}_2) \quad , \tag{4.3.18}$$

for any point $\{z'(t), \mathbf{r}\}$ inside the water body.

4.4.2.3 Application of the optical reciprocity theorem.

The radiance, $I_\delta^{up}(t, 0, \mathbf{r}, \mathbf{n})$, may be expressed using the boundary condition in (4.3.16) together with Green's function, $G(z_1, \boldsymbol{r}_1,\ \boldsymbol{n}_1;\ z_2, \boldsymbol{r}_2, \boldsymbol{n}_2)$, defined in Dolin & Levin (1991) as the radiance at the point $\{z_1, \boldsymbol{r}_1\}$ in the direction $\boldsymbol{n}_1$, caused by a mono-directed point source $\delta(z - z_2)\delta(\boldsymbol{r} - \boldsymbol{r}_2)\ \delta(\boldsymbol{n} - \boldsymbol{n}_2$(4.3.16):

$$I_\delta^{up}(t, 0, \mathbf{r}, \mathbf{n}) = \int d^2\boldsymbol{r}' \int\limits_{n_z \leq 0} d\Omega(\boldsymbol{n}')\, G(0, \mathbf{r}, \mathbf{n}; z(t), \boldsymbol{r}', \boldsymbol{n}') \cdot I_\delta^{up}\left(t, z = \frac{ct}{2n_w}, \boldsymbol{r}', \boldsymbol{n}'\right) =$$
$$= \frac{c}{2n} Q \int d^2\boldsymbol{r}' \int\limits_{\mathbf{n}'_z \leq 0} d\Omega(\boldsymbol{n}')\, G(0, \mathbf{r}, \mathbf{n}; z(t), \boldsymbol{r}', \boldsymbol{n}') \int\limits_{\mathbf{n}''_z \geq 0} d\Omega(\boldsymbol{n}'')\, \beta(\boldsymbol{n}' \wedge \mathbf{n}'')\, \mathrm{I}'_E(z, \boldsymbol{r}', \mathbf{n}'')\ ; \tag{4.3.19}$$
$$z(t) \equiv \frac{ct}{2n_w}$$

Substitution of the latter formula into (4.3.15) gives the following expression for the backscattered signal power:

$$S_\delta^{back}(t) = \Sigma\ \Omega \int d^2\,\mathbf{r} \int\limits_{n_z \geq 0} d\Omega(-\mathbf{n}) \mathrm{I}'_R(0, \mathbf{r}, -\mathbf{n}) I_\delta^{up}(t, 0, \mathbf{r}, -\mathbf{n})$$
$$= Q'\Sigma\, \Omega \frac{c}{2n_w} \int d^2\boldsymbol{r} \int\limits_{n_z \geq 0} d\Omega(-\mathbf{n}) \mathrm{I}'_R(0, \mathbf{r}, -\mathbf{n}) \int d^2\,\mathbf{r}' \int\limits_{n'_z \geq 0} d\Omega(-\mathbf{n}') G(0, \mathbf{r}, \mathbf{n}; z(t), \boldsymbol{r}', -\boldsymbol{n}') \tag{4.3.20}$$
$$\times \int\limits_{\mathbf{n}''_z \geq 0} d\Omega(\boldsymbol{n}'')\, \beta(\boldsymbol{n}' \wedge \mathbf{n}'')\, \mathrm{I}'_E(z, \boldsymbol{r}', \mathbf{n}'') \quad .$$

Here $I'_R(0, \mathbf{r}, -\mathbf{n})$ is the radiance distribution at the receiver input plane normalized, by analogy with $\mathrm{I}'_E(0, \mathbf{r}, -\mathbf{n})$ in equation (4.3.17), such that:

$$\iint \mathrm{I}'_R(0, \mathbf{r}, \mathbf{n}) d^2\mathbf{r}\, d\Omega(\mathbf{n}) \ = 1 \quad . \tag{4.3.21}$$

For convenience, the sign of the variables has been switched in equation (4.3.19) so that all the directional vectors are “looking down”.

Now we apply the optical reciprocity theorem for the RTE formulated in Dolin & Levin (1991) as the equality

$$G(0,\mathbf{r}'',-\mathbf{n}'';z,\mathbf{r},-\mathbf{n}') = G(z,\mathbf{r},\mathbf{n}';0,\mathbf{r}'',\mathbf{n}'') \quad . \tag{4.3.22}$$

With the use of (4.3.22), one can write [see Kopilevich & Surkov (2008)]:

$$\begin{aligned} &\int d^2\,\mathbf{r} \int\limits_{n_z\geq 0} d\Omega(-\mathbf{n})\mathrm{I}'_R(0,\mathbf{r},-\mathbf{n})G(0,\mathbf{r},-\mathbf{n};z(t),\mathbf{r}',-\mathbf{n}') = \\ &= \int d^2\,\mathbf{r} \int\limits_{n_z\geq 0} d\Omega(\mathbf{n})\mathrm{I}'_{R+}(0,\mathbf{r},\mathbf{n})G(z(t),\mathbf{r}',\mathbf{n}';0,\mathbf{r},\mathbf{n}) = \mathrm{I}'_{R+}(z(t),\mathbf{r}',\mathbf{n}') \end{aligned} \tag{4.3.23}$$

The radiance, I'_{R+}, in equation (4.3.23) is virtual in that it does not describe actual radiant power; rather, it describes the distribution of the sensitivity of the receiver to radiant power on a plane perpendicular to the pulse axis. Analogous to the real laser pulse source, the sensitivity distribution function of the receiver optical system can be treated as a source, $\mathrm{I}'_{R+}(0,\mathbf{r},\mathbf{n}) \equiv \mathrm{I}'_R(0,\mathbf{r},-\mathbf{n})$, $n_z \geq 0$, which was introduced in equation (4.3.21). In the same way that a propagating laser pulse interacts with the medium to create a diffuse radiance field at the plane, $z(t)$, the receiver sensitivity distribution can be treated as propagating through the medium, undergoing diffusion, and creating a virtual diffuse radiance field $\mathrm{I}'_{R+}(z(t),\mathbf{r}',\mathbf{n}')$ at the plane $z(t) \equiv ct/2n_w$. Thus, the virtual light beam” parameters (initial beam radius, divergence) correspond to the parameters of the virtual receiver pupil radius and the field-of-view angle, respectively.

4.4.2.4 The general lidar equation.

With the use of (4.3.23), the lidar equation (3.3.20) takes the form (Dolin and Levin 1991):

$$\begin{aligned} S_\delta^{back}(t) = \ \mathrm{Q}'\,\Sigma\,\Omega\frac{c}{2n_w}\int d^2\,\mathbf{r} \int\limits_{n''_z\geq 0} d\Omega(\mathbf{n}'') \int\limits_{n'_z\geq 0} d\Omega(\mathbf{n}') \ \times \\ \beta(-\mathbf{n}'\wedge\mathbf{n}'')\ I'_E(z(t),\mathbf{r},\mathbf{n}'')\,I'_{R+}(z(t),\mathbf{r},\mathbf{n}') \end{aligned} \tag{4.3.24}$$

The final step to obtain the Classical Lidar Equation [see, e.g., Feigels & Kopilevich (1993)] entails the use of the "small-angle approximation" (Monin 1983; L. S. Dolin and Levin 1991). The approximation assumes that each of the radiances $\mathrm{I}'_{E,R+}(z,\mathbf{r},\mathbf{n})$ involved in (4.3.24), is distinct from zero only when the direction vector $\mathbf{n} = \{n_z,\mathbf{n}_t\}$, $\mathbf{n}_t \equiv \{n_x,n_y\}$, satisfies the condition

$$n_z \approx 1\,, \quad |\mathbf{n}_t| << 1\,. \tag{4.3.25}$$

Thus, for the radiances $I'_{E,R+}(z,\mathbf{r},\mathbf{n})$, the alternative notation $I'_{E,R+}(z,\mathbf{r},\mathbf{n}_t)$ may be used. The condition (4.3.25) also justifies the following approximated equalities for the irradiances, $E_{E,R}(z(t),\mathbf{r})$, caused by the actual and virtual light beams, respectively, on the plane $z(t) \equiv ct/2n_w$:

$$\int_{n_z'' \geq 0} d\Omega(\mathbf{n}'')\ I_E'(z(t), \mathbf{r}, \mathbf{n}'') \approx E_E(z(t), \mathbf{r})\ ;$$
$$\int_{n_z' \geq 0} d\Omega(\mathbf{n}')\ I_{R+}'(z(t), \mathbf{r}, \mathbf{n}') \approx E_R(z(t), \mathbf{r}) \quad . \tag{4.3.26}$$

Note that the relationships in Equations (4.3.26) are approximations because there is no cosine term. This is reasonable because, in the receiver geometry, the cosine is near unity. Thus, the lidar equation (4.3.24) for the backscattered signal returning from the water body may be rewritten:

$$S_\delta^{back}(t) = \ Q' \Sigma\, \Omega\, \beta_\pi \frac{c}{2n_w} \int d^2\,\mathbf{r}\ E_E(z(t), \mathbf{r}) E_R(z(t), \mathbf{r}) \ ; \quad z(t) \equiv \frac{ct}{2n_w} \quad , \tag{4.3.27}$$

where $\beta(-\mathbf{n}' \wedge \mathbf{n}'') \approx \beta_\pi$, the backscattering coefficient.

A generalization of the equation to account for both backscattering by the water and reflection from boundary surfaces (air-water interface, bottom, solid body in the water) may be written in the form:

$$S_\delta(t) = Q' \Sigma\, \Omega \frac{c}{2n_w} \int d^2\,\mathbf{r}\, \gamma(z(t), \mathbf{r}) E_E(z(t), \mathbf{r}) E_R(z(t), \mathbf{r}) \quad ;$$
$$z(t) \equiv \frac{ct}{2n_w} \quad . \tag{4.3.28}$$

Here $\gamma(z(t), \mathbf{r})$ is a generalized interaction function that describes both backscattering by the water and reflection from boundary surfaces (air-water interface, bottom, solid body in the water). It has the value of zero if the point $\{z(t), \mathbf{r}\}$ lies outside of the water, and $\gamma(z(t), \mathbf{r}) = \beta_\pi$ inside the water body. If the point $\{z(t), \mathbf{r}\}$ belongs to a boundary surface, then $z = z_{sf}(\mathbf{r})$, and

$$\gamma(z(t), \mathbf{r}) = \frac{\rho}{\pi} \delta\big(z(t) - z_{sf}(\mathbf{r})\big) \cdot \cos\alpha\left(z_{sf}(\mathbf{r}), \mathbf{r}\right) \quad , \tag{4.3.29}$$

where $\alpha\left(z_{sf}(\mathbf{r}), \mathbf{r}\right)$ is the angle between the local normal to the surface at the boundary and the lidar beam axis; ρ is equal to the (Lambertian) reflectance, ρ_{bot} or ρ_{sb} for the bottom and a submerged solid body, respectively. For the sea surface in the equivalent problem, $\rho = {\tau_F}^{-2}\rho_{sf}$ with ρ_{sf} being the effective Lambertian reflection of the surface.

4.4.2.5 Solution to the small-angle RTE

In order to solve the general lidar equation, (4.3.28), we need to solve for the two irradiances $E_{E,R}(z, \mathbf{r})$ and, in order to solve for the irradiances, we must integrate over the radiance field shown in equation (4.3.26). The radiance field is calculated by solving the full RTE. In general, the RTE for the laser pulse propagation is a full 3D problem with no analytical solution. In order to find an approximate analytical solution, we rely on the fact that water is a highly forward scattering medium. In that case, we can apply a small angle approximation that is appropriate to lidar applications [see, e.g., Feigels & Kopilevich (1993), Monin (1983), Dolin and Levin (1991)]. The approximation assumes that each of the radiances

$I'_{E,R+}(z,\mathbf{r},\mathbf{n})$ involved in (4.3.26), is non zero only when the direction vector $\mathbf{n}=\{n_z,\mathbf{n}_t\}$, $\mathbf{n}_t \equiv \{n_x,n_y\}$, is subject to the condition

$$n_z \approx 1\,,\quad |\mathbf{n}_t| << 1 \quad . \tag{4.3.30}$$

Thus, for the radiances, $I'_{E,R+}(z,\mathbf{r},\mathbf{n})$, the alternative notation $I'_{E,R+}(z,\mathbf{r},\mathbf{n}_t)$ may be used. This small angle approximation also justifies performing the integral over the projected plane rather than a solid angle. The results are the following approximated equalities for the irradiances, $E_{E,R}(z(t),\mathbf{r})$, caused by the actual and virtual light beams, respectively, on the plane $z(t)\equiv ct/2n$:

$$E_{E,R}(z,\mathbf{r}) = \int d^2\mathbf{n}_t\, I'_{E,R+}(z,\mathbf{r},\mathbf{n}_t) \quad . \tag{4.3.31}$$

When the small-angle RTE (Monin 1983; L. S. Dolin and Levin 1991) is applied, it is natural to accept the approximate representation of the volume scattering phase function, $\chi(\vartheta)\equiv\frac{1}{b}\beta(\vartheta)$, of the medium as the sum of the small-angle and isotropic components (Dolina et al. 2007)

$$\chi(\vartheta) = \left(1-2\,\frac{b_b}{b}\right)\cdot\chi_s(\vartheta) + (2\pi)^{-1}\,\frac{b_b}{b} \tag{4.3.32}$$

,

where b is the scattering coefficient, b_b is the backscattering coefficient (as defined in Eq. (3.3.11a,b)). The optical characteristics of the medium are assumed to be independent of the coordinates). The forward-scattering phase function $\chi_s(\vartheta)$ is nonzero only for small angles ϑ and follows the normalization condition

$$2\pi\int_0^{\pi}\chi_s(\vartheta)\sin\vartheta\,d\vartheta = 2\pi\int_0^{\infty}\chi_s(\vartheta)\vartheta\,d\vartheta = 1 \quad . \tag{4.3.33}$$

In order to examine the effect of these assumptions and the solutions, we begin with the case of nadir sounding. When $\theta_w = 0$ each of the radiances in question is the solution to the boundary value problem in the layer $z_0 < z < z_0 + h_{bot}$, where $z_0 = H'$ is the lidar altitude above the interface in the equivalent problem. Beginning with equation 5.3.32:

$$\begin{aligned}&\frac{\partial}{\partial z}I(z,\mathbf{r},\mathbf{n}_t) + \mathbf{n}_t\cdot\nabla_t I(z,\mathbf{r},\mathbf{n}_t) = \\ &= -(a_s+b_s)I(z,\mathbf{r},\mathbf{n}_t) + b_s\int I(z,\mathbf{r},\boldsymbol{n}'_t)\,\chi_s(|\mathbf{n}_t-\boldsymbol{n}'_t|)d^2\boldsymbol{n}'_t \quad ; \\ &I(z=z_0,\mathbf{r},\mathbf{n}_t) = I_0(\mathbf{r},\mathbf{n}_t)\ ,\end{aligned} \tag{4.3.34}$$

where, $a_s = a + 2b_b$ is the effective absorption coefficient, and $b_s = b - 2b_b$ is the small-angle forward-scattering coefficient. Note that

$$a_s + b_s = a + b_b + (b_b + b_s) = a + b_b + b_f = a + b \equiv c \quad , \tag{4.3.35}$$

where a is the absorption coefficient, and b_f is the forward-scattering coefficient.

A rigorous solution to the problem (4.3.34) has been presented by Bremmer (1964) and Dolin (1964). The following derivation of the solution follows basically the approach described in Ishimaru (1978); see also Apresian & Kravatsov (1983).

The first step in solving the problem (4.3.32) consists of using the Fourier transformation of $I(z, \boldsymbol{r}, \boldsymbol{n_t})$ with respect to 2D vector, $\boldsymbol{r}$:

$$\hat{I}(z, \mathbf{k}, \mathbf{n}_t) = \frac{1}{2\pi} \int \exp(i\mathbf{kr})\, I(z, \mathbf{r}, \mathbf{n}_t) d^2\mathbf{r} \quad , \tag{4.3.36}$$

where $\mathbf{k}$ is the spatial frequency vector resulting from the Fourier transform of the two-2D spatial vector, $\boldsymbol{r}$, and $\hat{I}(z, \mathbf{k}, \mathbf{n}_t)$ is the frequency domain expression for radiance. Taking the Fourier transform of the initial RTE (4.3.34) leads to

$$\begin{gathered} \left(\frac{\partial}{\partial z} - i\mathbf{n}_t\mathbf{k} + c\right) \hat{I}(z, \mathbf{k}, \mathbf{n}_t) = b_1 \int \hat{I}(z, \mathbf{k}, \boldsymbol{n_t'}) \cdot x_s(\mathbf{n}_t - \mathbf{n}_t')\, d^2\mathbf{n}_t' \\ \hat{I}(z = z_0, \mathbf{k}, \mathbf{n}_t) = \hat{I}_0(\mathbf{k}, \mathbf{n}_t) \equiv \frac{1}{2\pi} \int \exp(i\mathbf{kr})\, I_0(\mathbf{r}, \mathbf{n}_t) d^2\mathbf{r} \quad , \end{gathered} \tag{4.3.37}$$

Let us define a new function

$$\hat{I}'(\mathrm{z}, \mathbf{k}, \mathbf{n}_t) = \hat{I}(\mathrm{z}, \mathbf{k}, \mathbf{n}_t) \exp\left\{ - \int_{z_0}^{z} [i\boldsymbol{n}_t\boldsymbol{k} - c] dz' \right\} \quad , \tag{4.3.38}$$

which, after rearranging $\hat{I}$ and $\hat{I}'$, becomes

$$\hat{I}(\mathrm{z}, \mathbf{k}, \mathbf{n}_t) = \hat{I}'(\mathrm{z}, \mathbf{k}, \mathbf{n}_t) \exp\left\{ + \int_{z_0}^{z} [i\boldsymbol{n}_t\boldsymbol{k} - c] dz' \right\} \quad . \tag{4.3.39}$$

This expression for $\hat{I}(\mathrm{z}, \mathbf{k}, \mathbf{n}_t)$ can then be introduced into equation (4.3.37), yielding

$$\begin{aligned} &\frac{\partial}{\partial z}\ \hat{I}'(\mathrm{z}, \mathbf{k}, \mathbf{n}_t) \exp\left\{ + \int_{z_0}^{z} [i\mathbf{n}_t\boldsymbol{k} - c] dz' \right\} \\ &= b_1 \int \hat{I}'(\mathrm{z}, \mathbf{k}, \mathbf{n}_t') \exp\left\{ + \int_{z_0}^{z} [i\mathbf{n}_t'\boldsymbol{k} - c] dz' \right\} \chi_s(\boldsymbol{n}_t - \mathbf{n}_t')\, d^2\mathbf{n}_t' \quad . \end{aligned} \tag{4.3.40}$$

Then, after dividing the both parts by $\exp\left\{ + \int_{z_0}^{z} [i\mathbf{n}_t\mathbf{k} - c] dz' \right\}$, we arrive at the expression

$$\frac{\partial}{\partial z}\ \hat{I}'(\mathrm{z}, \mathbf{k}, \mathbf{n}_t) = b_s \int \hat{I}'(\mathrm{z}, \mathbf{k}, \mathbf{n}_t')\ \exp\left\{ - \int_{z_0}^{z} [i(\mathbf{n}_t - \mathbf{n}_t')\mathbf{k} + c] dz' \right\} \chi_s(\mathbf{n}_t - \mathbf{n}_t') d^2\mathbf{n}_t' \,, \tag{4.3.41}$$

$$\hat{I}'(\mathrm{z} = z_0, \mathbf{k}, \mathbf{n}_t) = \hat{I}_0(\mathbf{k}, \mathbf{n}_t) \quad .$$

Equation (4.3.41) may be solved more readily by applying the Fourier transformation with respect to $\mathbf{n}_t'$, defined as

$$\widetilde{I}'(z, \mathbf{k}, \mathbf{p}) = \frac{1}{2\pi} \int \exp(i\mathbf{n}_t\mathbf{p})\, \hat{I}'(\mathrm{z}, \mathbf{k}, \mathbf{n}_t) d^2\mathbf{n}_t \quad , \tag{4.3.42}$$

where $\mathbf{p}$ the frequency domain version of $\mathbf{n}_t$. After applying the Fourier Transform to equation (4.3.41), the result is

$$\begin{aligned} \frac{\partial}{\partial z}\, \widetilde{I}'(z, \mathbf{k}, \mathbf{p}) &= 2\pi \cdot \widetilde{I}'(z, \mathbf{k}, \mathbf{p}) b_1 \cdot \tilde{\chi}_s[\mathbf{p} - \mathbf{k}(z - z_0)] \ ; \\ \widetilde{I}'(z = z_0, \mathbf{k}, \mathbf{p}) &= \widetilde{I}_0(\mathbf{k}, \mathbf{p}) \equiv \frac{1}{2\pi} \int \exp(i\mathbf{n}_t\mathbf{p})\, \hat{I}_0(\mathbf{k}, \mathbf{n}_t) d^2\mathbf{n}_t \quad , \end{aligned} \tag{4.3.43}$$

where $\tilde{\chi}_f(\mathbf{p})$ is the Fourier transformation of the scattering phase function, $\chi_s(\mathbf{n}_t)$,

$$\tilde{\chi}_s(\mathbf{p}) = \frac{1}{2\pi} \int \exp(i\mathbf{n}_t\mathbf{p})\, \chi_s(\mathbf{n}_t)\, d^2\mathbf{n}_t \tag{4.3.44}$$

so that

$$\frac{1}{2\pi} \int \exp(i\mathbf{n}_t\mathbf{p}) \cdot \exp\left\{ - \int_{z_0}^{z} [i\mathbf{n}_t\mathbf{k}] dz' \right\} \chi_s(\mathbf{n}_t)\, d^2\mathbf{n}_t = \tilde{\chi}_s[\mathbf{p} - \mathbf{k}(z - z_0)] \tag{4.3.45}$$

The solution to the problem (4.3.43),

$$\widetilde{I}'(z, \mathbf{k}, \mathbf{p}) = \widetilde{I}'(z_0, \mathbf{k}, \mathbf{p}) \exp\{2\pi\} \int_{z_0}^{z} b_s \cdot \tilde{\chi}_s\, [\mathbf{p} - \mathbf{k}(z - z_0)] dz' \quad , \tag{4.3.46}$$

leads to the so-called “auto-model” solution to the RTE which describes the Fourier-transform of the radiance $I(z, \mathbf{r}, \mathbf{n}_t)$ with respect to both $\boldsymbol{r}$ and $\mathbf{n}_t$,

$$\begin{aligned} \tilde{I}(z, \mathbf{k}, \mathbf{p}) &= \frac{1}{2\pi} \int \exp(i\mathbf{n}_t\mathbf{p})\, \hat{I}(z, \mathbf{k}, \mathbf{n}_t)\, d^2\mathbf{n}_t \\ &= \frac{1}{(2\pi)^2} \int \int \exp(i\mathbf{r}\mathbf{k} + i\mathbf{n}_t\mathbf{p})\, I(z, \mathbf{r}, \mathbf{n}_t)\ d^2\mathbf{r}\, d^2\mathbf{n}_t \end{aligned} \tag{4.3.47}$$

It then follows from (4.3.38), (4.3.42), and (4.3.47) that,

$$\begin{aligned} \widetilde{I}'(z, \mathbf{k}, \mathbf{p}) &= \frac{1}{2\pi} \int \hat{\mathrm{I}}(z, \mathbf{k}, \mathbf{n_t}) \exp\left\{ i\mathbf{n}_t\mathbf{p} - \int_{z_0}^{z} [i\mathbf{n}_t\mathbf{k} - \mathrm{c}] dz' \right\} d^2\mathbf{n}_t \\ &= \exp\left\{ \int_{z_0}^{z} c\ dz' \right\} \tilde{I}\big(z, \mathbf{k}, \mathbf{p} - \mathbf{k}(z - z_0)\big) \quad . \end{aligned} \tag{4.3.48}$$

The solution is then given by the formula following from (4.3.46) and (4.3.47):

$$\exp\left\{\int_{z_0}^{z} c\,dz'\right\}\tilde{I}(z,\mathbf{k},\mathbf{p}-\mathbf{k}(z-z_0)) = \tilde{I}_0(\mathbf{k},\mathbf{p})\exp\left\{2\pi\int_{z_0}^{z} b_s\cdot\tilde{\chi}_s[\mathbf{p}-\mathbf{k}(z'-z_0)]dz'\right\}, \tag{4.3.49}$$

or, finally,

$$\tilde{I}(z,\mathbf{k},\mathbf{p}) = \tilde{I}_0\big(\mathbf{k},\mathbf{p}+\mathbf{k}(z-z_0)\big)\exp\left\{-\int_{z_0}^{z}\big[c-2\pi b_s\cdot\tilde{\chi}_s\big(\mathbf{p}+\mathbf{k}(z-z')\big)\big]dz'\right\}\quad , \tag{4.3.50}$$

In order to proceed from this point to the lidar equation (4.3.27), it is necessary to convert radiance to the corresponding irradiance,

$$E(z,\mathbf{r}) = \int I(z,\mathbf{r},\mathbf{n}_t)d^2\mathbf{n}_t\ ,\ \text{where}\ z\geq z_0\quad , \tag{4.3.51}$$

using the radiance distribution along the boundary plane $I(z_0,\mathbf{r},\mathbf{n}_\perp)$. In view of (4.3.48),

$$E(z,\mathbf{r}) = \int \tilde{I}(z,\mathbf{k},0)\exp(-i\mathbf{r}\mathbf{k})\,d^2\mathbf{k}\quad , \tag{4.3.52}$$

and substitution of (4.3.49) gives

$$E(z,\mathbf{r}) = \int \tilde{I}_0\big(\mathbf{k},\mathbf{k}(z-z_0)\big)\exp\left\{-\int_{z_0}^{z}\big[c-2\pi b_s\cdot\tilde{\chi}_s\big(\mathbf{k}(z-z')\big)\big]dz'\right\}\exp(-i\mathbf{r}\mathbf{k})\,d^2\mathbf{k}\ . \tag{4.3.53}$$

The above results are applicable to stratified media with optical characteristics that depend on depth. In this case, the parameters $a_s,\ c,\ x_s$ appearing in the integrands in formulas (4.3.49) and (4.3.52), must also be treated as functions of the integration variable, z'.

For a (statistically) homogeneous medium, of course, the formulas may be simplified. Specifically, the expression for the irradiance distribution, (4.3.52) may, with the use of the relation, $c = a_s + b_s$, be rewritten as:

$$E(z,\mathbf{r}) = \int \tilde{I}_0\big(\mathbf{k},\mathbf{k}(z-z_0)\big)\exp\big\{-(z-z_0)\cdot a_s - a_{bs}\big(k(z-z_0)\big)\big\}\exp(-i\mathbf{r}\mathbf{k})\,d^2\mathbf{k}\ , \tag{4.3.54}$$

where

$$a_{bs}(k(z-z_0)) = \frac{b_s}{z-z_0}b_s\int_0^{z-z_0}[1-2\pi\tilde{\chi}_s(\mathrm{k}z'))]\,dz'\quad . \tag{4.3.55}$$

The function $a_{bs}(kz)$, introduced in Kopilevich, Kononenko, and Zadorozhnaya (2010, 2011), characterizes the contribution from small-angle scattering to the attenuation of spatial harmonics of the spatial frequency k in the initial distribution of radiance within a light beam when propagated over the distance z in a turbid medium.

The general expression (4.3.54) may be applied to the incident irradiances, $E_E(z,\mathbf{r})$, $E_R(z,\mathbf{r})$, in the lidar equation (4.3.27)

$$E_{E,R}(z,\mathbf{r}) = \\ = \int \widetilde{I}'_{E,R+}\big(z_0,\mathbf{k},\mathbf{k}(z-z_0)\big)\, exp\{-(z-z_0)\big[a_s + a_{bs}\big(k(z-z_0)\big)\big]\}exp(-i\mathbf{rk})\, d^2\mathbf{k} \quad . \tag{4.3.56}$$

Here,

$$\widetilde{I}'_{E,R+}\big(z_0,\mathbf{k},\mathbf{k}(z-z_0)\big) = \frac{1}{(2\pi)^2}\iint I'_{E,R+}(z_0,\mathbf{r},\mathbf{n})\ exp\{i\mathbf{rk} + i\mathbf{n}_t\mathbf{k}(z-z_0)\}\, d^2\mathbf{r}\, d^2\mathbf{n}_t \tag{4.3.57}$$

with $I'_E(z_0,\mathbf{r},\mathbf{n}_t)$ being the stationary radiance distribution corresponding to the actual emitted beam [see (3.3.17)], and $I'_{R+}(z_0,\mathbf{r},\mathbf{n}_t)$ being the radiance at a virtual "receiver" of the light beam at the boundary $z = z_0$.

4.4.2.6 Extension to formulas for oblique soundings

For the straightforward case of nadir sounding, equations (4.3.27), (4.3.28), (4.3.56), and (4.3.57) provide a full set of formulas describing the lidar return signal for an infinitesimally short (delta-function shaped) initial pulse [the "impulse response function", see Section 4.1.2 and Guenther (1985)]. This result is based on a rigorous solution of the RTE using the small-angle scattering approximation. A similar, exact solution for a more general, oblique sounding geometry does not exist. However, a reasonable approximation can be achieved based on the equations developed for nadir sounding, by substituting the actual length of the in-water propagation, $z_w(t,r)$, for $z(t) - z_0$ in the "effective absorption" factor, $exp\{-(z-z_0)\cdot a_s\}$ in (4.3.55).

Consider the leading edge of a sounding pulse in the water for the case of a laser beam obliquely incident on the sea surface. If the small-angle approximation is valid, the leading edge of the pulse (at a fixed moment of time, *t*, can be treated as a plane perpendicular to the beam axis in the water, a plane which is inclined by θ_w with respect to the water surface (the "leading edge plane" in Figure 4.3.4). A "ray" traveling from the water surface to the leading-edge plane along a path that is parallel to the lidar axis covers a distance, z_w in the water. Although the length of the in-water path of a ray will vary over the plane, it will be constant along any line parallel to the water surface. For example, for a ray arriving at the leading-edge plane anywhere along the line parallel to the water surface and passing through the lidar axis (the principal line in Figure 4.3.4), the in-water path will be constant and equal to the in-water path along the lidar axis, $z_w = z_t$. The in-water path length will also be constant for rays arriving at the leading-edge plane along a line parallel to the principal line. In that case, only the separation distance from the principal line, $r_=$, is required for scaling, i.e, $z_w(t,r_=)$. Equation (4.3.58) describes the calculation of the length z_w. Given the total distance from the source to the leading-edge, $z(t) \equiv ct/2n_w$, one must subtract the

atmospheric path, z_0, and add the product $-r_{=}\tan\theta_w$ (may be positive or negative depending on direction of coordinate, $r_{=}$, in the leading-edge plane,

$$z_w(t, r_{=}) = z(t) - z_0 - r_{=}\tan\theta_w \quad . \tag{4.3.58}$$

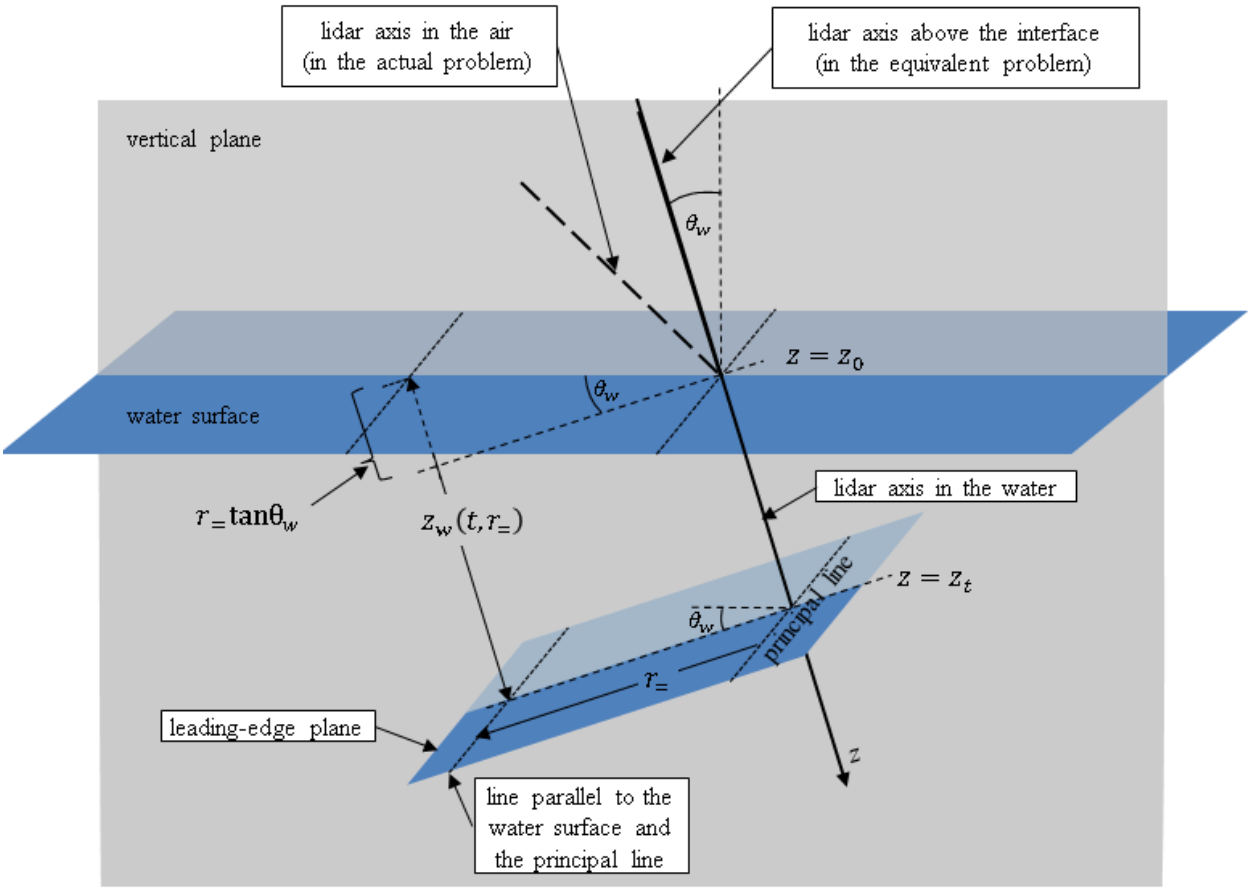

Figure 4.3.4. In-water propagation path, $z_w(t, r_{=})$, for the case of an oblique laser measurement.

The advantage of equation (4.3.58), is that the full, 3-dimensional expression for the optical path is represented by a one dimensional variable, greatly simplifying the expression for the attenuation of irradiance. The lidar equation, (4.3.38), and the corresponding expressions for irradiances, $E_E(z, \mathbf{r})$ and radiance, $E_R(z, \mathbf{r})$, and $\widetilde{I}'_E\big(z_0, \mathbf{k}, \mathbf{k}(z - z_0)\big)$ and $\widetilde{I}'_{R+}\big(z_0, \mathbf{k}, \mathbf{k}(z - z_0)\big)$, may now be written:

$$S_\delta(t) = Q'\,\Sigma\Omega\frac{c}{2n_w}\int d^2\,\mathbf{r}\,\gamma(z(t), \mathbf{r})E_E(z(t), \mathbf{r})E_R(z(t), \mathbf{r}) \quad , \quad z(t) \equiv \frac{ct}{2n_w} \quad ;$$

$$E_{E,R}(z, \mathbf{r}) = \int \widetilde{I}'_{E,R+}\big(z_0, \mathbf{k}, \mathbf{k}(z - z_0)\big) \times \\ \times\, exp\big\{-z(t, r_{=}) \cdot a_s - (z - z_0) \cdot a_{bs}\big(k(z - z_0)\big)\big\} exp(-i\mathbf{rk})\, d^2\mathbf{k}\,; \tag{4.3.59}$$

$$\widetilde{I}'_{E,R+}\big(z_0, \mathbf{k}, \mathbf{k}(z - z_0)\big) \\ = \frac{1}{(2\pi)^2}\iint I'_{E,R+}(z_0, \mathbf{r}, \mathbf{n}_t)\; exp\{i\mathbf{rk} + i\mathbf{n}_t\mathbf{k}(z - z_0)\}\, d^2\mathbf{r}\, d^2\mathbf{n}_t$$

with $\gamma(z(t), \mathbf{r})$ defined by (4.3.29) and $z_w(t, r_{=})$ given by (4.3.58).

4.4.2.7 Emitted beam modeling

Finally, it is necessary to take into account the boundary conditions in equation (4.3.34), $I(z = z_0, \mathbf{r}, \mathbf{n}_t) = I_0(\mathbf{r}, \mathbf{n}_t)$. To begin, we return to the actual problem for emitted beam radiance (Figure 4.2.3) and use the notation $\{z_a, \mathbf{r}_a\}$ for Cartesian coordinates, where z_a is the distance along the beam axis from the pupil plane, $\mathbf{r}_a$ is the 2D coordinate vector perpendicular to the axis, and $\mathbf{n}_{at}$, $|\mathbf{n}_{at}| \ll 1$, for the component of the directional vector, $\mathbf{n}_a$, $|\mathbf{n}_a| = 1$, normal to the axis; see (4.3.25). [The subscript a is introduced to distinguish between coordinate and directional vectors, as well as distinguishing the emitted radiance, $I_{a\,E}$, in the **actual problem** from analogous vectors, $\{z, \mathbf{r}\}$, $\mathbf{n} = \{n_z, \mathbf{n}_t\}$, and functions, I_E, and I'_E, in the **"equivalent" problem**. Compare with (3.3.17)].

The following model for radiance $I_{a\,E}\,(t, z_a = 0, \mathbf{r}_a, \mathbf{n}_{at})$ at the emitter pupil seems to be adequate:

$$I_{a\,E}\,(t, z_a = 0, \mathbf{r}_a, \mathbf{n}_{at}) = Q \cdot \delta(t) I'_{a\,E}\,(0, \mathbf{r}_a, \mathbf{n}_{at})\,, \qquad n_{az} \geq 0;$$

$$\begin{aligned} &\iint I'_{a\,E}(0, \mathbf{r}_a, \mathbf{n}_{at}) d^2\mathbf{r}_a\, d\Omega(\mathbf{n}_{at}) = 1\,; \\ &I'_{E\,act}(0, \mathbf{r}_a, \mathbf{n}_{at}) = A\left(\frac{\mathbf{r}_a}{r_E}\right) \cdot D\left(\frac{\mathbf{n}_{at}}{\Theta_E}\right)\,; \\ &\int A\left(\frac{\mathbf{r}_a}{r_E}\right) d^2\mathbf{r}_a = \int D\left(\frac{\mathbf{n}_{at}}{\Theta_E}\right) d\Omega(\mathbf{n}_{at}) = 1 \end{aligned} \tag{4.3.60}$$

Here Q is the emitted pulse energy, and r_E and Θ_E are the initial beam radius and divergence, respectively. The laser beam may be further adjusted by spatial, *A*, and angular, *D*, functions. It is supposed that, for each of the functions, $A(\mathbf{x})$ and $D(\mathbf{x})$, the diameter of 2-dimensional support of the functions (i.e. the range of **x** over which the functions are positive) is on the order of unity, so that the initial radiance distribution $\mathrm{I}'_{aE}(0, \mathbf{r}_a, \mathbf{n}_{a\perp})$ is concentrated in the spatial domain $|\mathbf{r}_a| \leq r_E$ and the angular domain (cone) $|\mathbf{n}_{at}| \leq \Theta_E$. In other words, $I'_{a\,E}(0, \mathbf{r}_a, \mathbf{n}_{a\perp})$ represents the normalized radiance at the emitter output that contains only radial and angular distributions.

While absorption and scattering in the atmosphere are neglected, the distribution of the beam radiance $\mathrm{I}'_{aE}(z_a = H_s, \mathbf{r}_a, \mathbf{n}_{at})$ at the water surface, i.e., at a distance H_s from the pupil is

$$\mathrm{I}'_{aE}(H_s, \mathbf{r}_a, \mathbf{n}_{at}) = I'_{aE}(0, \mathbf{r}_a - H_s\mathbf{n}_{at}, \mathbf{n}_{at}) = A\left(\frac{\mathbf{r}_a - H_s\mathbf{n}_{at}}{r_E}\right) \cdot D\left(\frac{\mathbf{n}_{at}}{\Theta_E}\right)\,. \tag{4.3.61}$$

Let us consider $N(\mathbf{n}_{at}) \equiv A(\mathbf{r}_a - H_s\mathbf{n}_{at}/r_E)$ as a function of $\mathbf{n}_{at}$ when the distance H_s increases infinitely. The diameter of the function support is $\sim 2r_E/H_s$ and tends to zero as $H_s \to \infty$. Furthermore, (4.3.60) implies that the normalization condition ${H_s}^2 \int N(\mathbf{n}_{at})\, d^2\mathbf{n}_{at} = \int A(\mathbf{r}_a - H_s\mathbf{n}_{at}/r_E)\, d^2\mathbf{r}_a = 1$ will hold at all possible distances of H_s, suggesting that the following limit representation may be written:

$$\lim_{H_s/r_E \to \infty} {H_s}^2 \cdot N(\mathbf{n}_{at}) = \delta_2\left(\mathbf{n}_{at} - {\mathbf{r}_a}/{H_s}\right)\,, \tag{4.3.62}$$

where $\delta_2\left(\mathbf{n}_{at} - {}^{\mathbf{r}_a}/_{H_s}\right)$ is the two-dimensional Dirac delta function. Finally, we arrive at the "far field" approximation of the radiance distribution $\mathrm{I}'_{aE}(H_s, \mathbf{r}_a, \mathbf{n}_{at})$ from (4.3.61) that will be valid for $H_s/r_E \gg 1$:

$$\begin{aligned}\mathrm{I}'_{aE}(H_s, \mathbf{r}_a, \mathbf{n}_{at}) &\approx \delta_2\left(\mathbf{n}_{at} - {}^{\mathbf{r}_a}/_{H_s}\right)\delta_2 \cdot H_s^{-2} D\left(\frac{\mathbf{n}_{at}}{\Theta_E}\right) \\ &= {H_s}^{-2} D\left({}^{\mathbf{r}_a}/_{H_s\Theta_E}\right) \cdot \delta_2\left(\mathbf{n}_{at} - {}^{\mathbf{r}_a}/_{H_s}\right) \quad .\end{aligned} \tag{4.3.63}$$

The approximation replaces the actual radiance with the radiance emitted by a point source with a cone-shaped directivity diagram having a vertex angle of $\sim\Theta_E$. It is worth noting that this approximation would not be appropriate for a shipboard or submerged system for which the assumption $H_s/r_E \gg 1$ would not be valid.

The next step is purely geometric, and consists of projecting the modeled radiance distribution, $\mathrm{I}'_{aE}(z_a = H_s, \mathbf{r}_a, \mathbf{n}_{at})$ computed along the normal (to the propagation direction) plane, $z_a = H_s$, using (4.3.63), onto the radiance distribution along the water surface. Since difficulties will arise with off-nadir sounding where the distribution to be found depends on direction in the plane of the water surface, $\mathbf{s} = \{s_=, s_\perp\}$, the two components of the vector are to be treated separately.

Using (4.3.62), it is possible to calculate the radiance distribution $\mathrm{I}'_{aE}(\mathbf{s}, \mathbf{n}_{at}) \equiv \mathrm{I}'_{aE}(s_=, s_\perp; n_{a=}, n_{a\perp})$ along the air-water interface (see Figure 4.3.5.). Here, $\mathbf{s} = \{s_=, s_\perp\}$ is the 2D Cartesian coordinate vector in the plane parallel to the water surface, with $s_=$ being parallel to the plane of incidence; $n_{a=}$ and $n_{a\perp}$ are corresponding projections of the transverse component, $\mathbf{n}_{at}$, of the 3D directional vector $\mathbf{n}_a$. Note that

$$\begin{aligned}&\mathrm{I}'_{aE}(s_=, s_\perp; n_{a=}, n_{a\perp}) = \cos\theta_a \cdot \mathrm{I}'_{aE}(H(\mathbf{s}), r(\mathbf{s}), \mathbf{n}_{at}) \ ; \\ &H_s(\mathbf{s}) = H_s + s_=\sin\theta_a \approx H_s \ ; \\ &r_= = s_=\cos\theta_a \ ; \quad r_\perp = s_\perp \quad .\end{aligned} \tag{4.3.64}$$

Then

$$\begin{aligned}\mathrm{I}'_{aE}(s_=, s_\perp; n_{a=}, n_{a\perp}) = \cos\theta_a \cdot H_s^{-2} \times \\ D\left(\frac{s_{a=}\cos\theta_a}{H_s\Theta_E}, \frac{s_{a\perp}}{H_s\Theta_E}\right) \cdot \delta\left(n_{a=} - \frac{s_{a=}\cos\theta_a}{H_s}\right) \cdot \delta\left(n_{a\perp} - \frac{s_{a\perp}}{H_s}\right) \quad ,\end{aligned} \tag{4.3.65}$$

where $D(s_=, s_\perp) \equiv D(\mathbf{s})$, $\mathbf{s} = \{s_=, s_\perp\}$. The latter formula describes the radiance distribution, I'_{aE}, along the UPPER side of the interface (just ABOVE the water); what we need is the radiance distribution, I'_E, (without "a" in the subscript), along the LOWER side of the interface (just below the water surface).

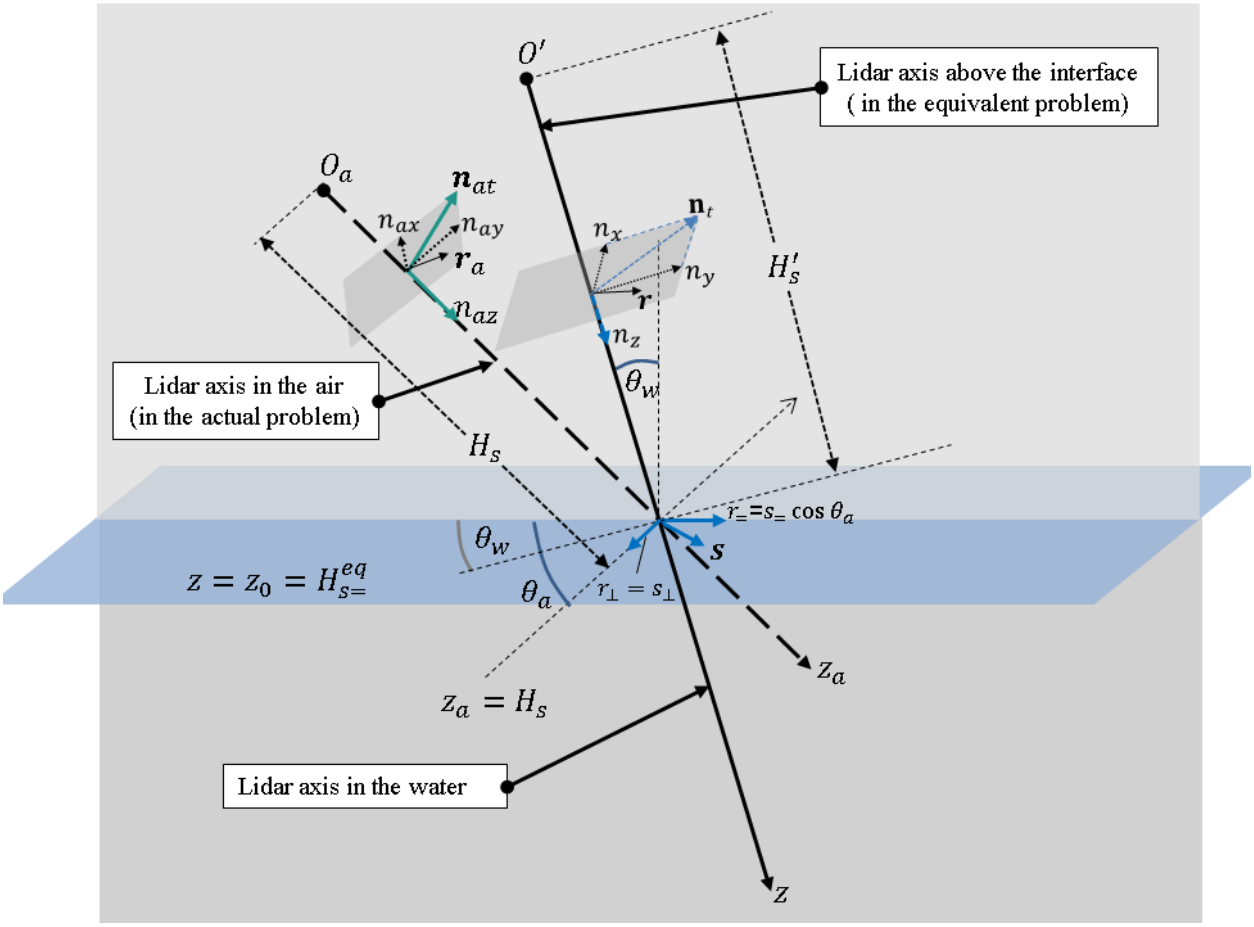

Figure 4.3.5. Actual sounding geometry with Cartesian coordinates $\{z_a, \mathbf{r}_a\}$ and radiance directional vector, $\mathbf{n}_a = \{n_{az}, \mathbf{n}_{at}\}$, and "equivalent" problem configuration with corresponding vectors $\{z, \mathbf{r}\}$ and $\mathbf{n} = \{n_z, \mathbf{n}_t\}$, as well as the projections on the water surface, $\{r_{=}, r_\perp\}$.

As a result of beam refraction at the water surface, the stationary radiance of the sounding beam just below the interface takes the form $I'_E(s_{=}, s_\perp; n_{=}, n_\perp)$ (note that subscript a in the symbol I'_E is omitted and, in view of (3.3.17), the power losses due to Fresnel reflection are taken into account):

$$I'_E(s_{=}, s_\perp; n_{=}, n_\perp) = \cos\theta_a \cdot H_s^{-2} \times D\left(\frac{s_{a=}\cos\theta_a}{H_s\Theta_E}, \frac{s_{a\perp}}{H_s\Theta_E}\right) \cdot \delta\left(n_{=} - \frac{s_{a=}\cos^2\theta_a}{nH_s\cos\theta_w}\right) \cdot \delta\left(n_\perp - \frac{s_{a\perp}}{n_w H_s}\right) \tag{4.3.66}$$

Here symbol n_w denotes the refractive index of the seawater; $n_{=}$ and $n_\perp$ are the transverse components underwater along the lidar beam axis derived from the corresponding projections of the transverse component, $\mathbf{n}_{at}$, of the 3D directional vector $\mathbf{n}_a$, i.e. $n_{a=}$, $n_{a\perp}$:

$$n_{=} = n_{a=}\frac{\cos\theta_a}{n_w \cdot \cos\theta_w} \;\; ; \quad n_\perp = n_{a\perp}\frac{1}{n_w} \quad ; \tag{4.3.67}$$

The equations are valid within the context of the small-angle approximation [see equation (4.3.30)]. This can be demonstrated by applying a Taylor decomposition (Taylor series) to both sides of the equality $\sin(\theta_a + n_{a=}) = N\sin(\theta_w + n_=)$. For small enough $n_{a=},\ n_=$, the zeroth order term is $\sin\theta_a = N\sin\theta_w$ (the ordinary form of Snell's Law), and the first order term is $\sin\theta_a = N\sin\theta_w$.

Let us rewrite (4.3.66) as

$$I'_E(s_=, s_\perp; n_=, n_\perp) = \frac{n^2\cos^2\theta_w}{H^{eq}_{s=}\cdot H^{eq}_{s\perp}} \times D\left(\frac{s_{a=}\cos\theta_w}{H^{eq}_{s=}\Theta^{eq}_{E=}}, \frac{s_{a\perp}}{H^{eq}_{s\perp}\Theta^{eq}_{E\perp}}\right)\cdot\delta\left(n_= - \frac{s_{a=}\cos\theta_w}{H^{eq}_{s=}}\right)\cdot\delta\left(n_\perp - \frac{s_{a\perp}}{H^{eq}_{s\perp}}\right) \tag{4.3.68}$$

with the new parameters

$$H^{eq}_{s=} = \frac{n_w H_s\cos^2\theta_w}{\cos^2\theta_a}\ ;\quad H^{eq}_{s\perp} = n_w H_s\ ;\quad \Theta^{eq}_{E=} = \frac{\Theta_E}{n_w}\frac{\cos\theta_a}{\cos\theta_w}\ ;\quad \Theta^{eq}_{E\perp} = \frac{\Theta_E}{n_w} \tag{4.3.69}$$

The final task is to determine the radiance, $I'_E(z, \mathbf{r}, \mathbf{n}_t)$ in the equivalent geometry. The radiance distribution along the interface plane ("just above" or "just below" has the same meaning in the equivalent problem) must coincide with our model described in equations (4.3.68) and (4.3.69). In the equivalent problem, the formula coincides with the far-field approximation (4.3.63) of radiance projected on the interface plane by the stationary, astigmatic light beam.

It is important to note that the spatial and angular dependences of the laser beam cannot be separated, i.e., function A is dependent on both **r** and **n**. Such a beam does not have a "waist" plane, rather, there are two different planes for z=const corresponding to a minimal spot size in one (that is, "=" or "⊥") of the two orthogonal directions:

$$I'_E(z, \mathbf{r}, \mathbf{n}_t) = A\left(\frac{r_= - z\cdot n_=}{r_E}, \frac{r_\perp - (z - \Delta H^{eq})\cdot n_=}{r_E}\right)\cdot D\left(\frac{n_=}{\Theta^{eq}_{E=}}, \frac{n_\perp}{\Theta^{eq}_{E\perp}}\right)\ , \quad \Delta H^{eq} \equiv H^{eq}_= - H^{eq}_\perp \tag{4.3.70}$$

In the "far field zone", that is at the distance $z = z_0 = H^{eq}_= >> r_E$ [compare with (4.3.63)], and:

$$I'_E\left(H^{eq}_=, \mathbf{r}, \mathbf{n}_t\right) = A\left(\frac{r_= - H^{eq}_{s=}\cdot n_=}{r_E}, \frac{r_\perp - H^{eq}_{s\perp}\cdot n_=}{r_E}\right)\cdot D\left(\frac{n_=}{\Theta^{eq}_{E=}}, \frac{n_\perp}{\Theta^{eq}_{E\perp}}\right) \approx D\left(\frac{r_=}{H^{eq}_{s=}\Theta^{eq}_{E=}}, \frac{r_\perp}{H^{eq}_{s\perp}\Theta^{eq}_{E\perp}}\right)\cdot\delta\left(n_= - \frac{r_=}{H^{eq}_{s=}}\right)\cdot\delta\left(n_\perp - \frac{r_\perp}{H^{eq}_{s\perp}}\right) \tag{4.3.71}$$

Equation (4.3.71) describes a simple (elliptical cross-section) sounding light beam. It is just the expression to be used as the boundary condition, $I(z = z_0 = H^{eq}_=, \mathbf{r}, \mathbf{n}_t) = I_0(\mathbf{r}, \mathbf{n}_t)$, in the equivalent problem (4.3.34) for emitted laser beam radiance of the laser beam, I'_E. For the radiance at a virtual "receiver", I'_R, the condition is quite analogous, with the substitution of a receiver field-of-view solid angle Θ_R for the laser's beam divergence solid angle Θ_E:

$$I'_R(H^{eq}_{s=},\mathbf{r},\mathbf{n}_t) = A\left(\frac{r_= - H^{eq}_{s=}\cdot n_=}{r_E},\frac{r_\perp - H^{eq}_{s\perp}\cdot n_=}{r_E}\right)\cdot D\left(\frac{n_=}{\Theta^{eq}_{R=}},\frac{n_\perp}{\Theta^{eq}_{R\perp}}\right)\approx$$
$$D\left(\frac{r_=}{H^{eq}_{s=}\Theta^{eq}_{R=}},\frac{r_\perp}{H^{eq}_{s\perp}\Theta^{eq}_{R\perp}}\right)\cdot\delta\left(n_= - \frac{r_=}{H^{eq}_{s=}}\right)\cdot\delta\left(n_\perp - \frac{r_\perp}{H^{eq}_{s\perp}}\right) \quad ; \tag{4.3.72}$$
$$\Theta^{eq}_{R=} = \frac{\Theta_R}{n_w}\frac{\cos\theta_a}{\cos\theta_w} \quad ; \quad \Theta^{eq}_{R\perp} = \frac{\Theta_R}{n_w} \quad .$$

For a modest viewing angle, θ_a, when the approximate equality, $\cos\theta_a/\cos\theta_{aw} \approx 1$, holds, the "equivalent" lidar may be regarded as a "point" emitter/receiver at the slant altitude $H^{eq}_s = n_w H_s$, the "equivalent" beam divergence and receiver field-of-view angle are $\Theta^{eq}_E = \frac{\Theta_E}{n_w}$, $\Theta^{eq}_R = \frac{\Theta_R}{n_w}$, and (4.3.70) and (4.3.71) may be simplified to:

$$I'_E(H^{eq}_s,\mathbf{r},\mathbf{n}_t) = D\left(\frac{\mathbf{r}}{H^{eq}_s\Theta^{eq}_E}\right)\cdot\delta_2\left(\mathbf{n}_t - \frac{\mathbf{r}}{H^{eq}_s}\right) \quad ;$$
$$I'_R(H^{eq}_s,\mathbf{r},\mathbf{n}_t) = D\left(\frac{\mathbf{r}}{H^{eq}_s\Theta^{eq}_R}\right)\cdot\delta_2\left(\mathbf{n}_t - \frac{\mathbf{r}}{H^{eq}_s}\right) \quad . \tag{4.3.73}$$

In (4.3.73), "elliptical" beams are approximated by "circular" beams.

4.4.3 Lidar waveform simulator

Minsu Kim

In order to design an optimal lidar system, it is very useful to have an accurate simulation tool. An ALB waveform is a complicated response that is related to the system parameters (laser power, receiver aperture size, optical system transmittance, efficiency of photo detector, and digitizer) and the environmental parameters (surface condition, vertical profile of scattering particles and absorbing medium, suspended object and sea floor). This section describes a simulator based on the RTE solution described in previous sections. It is a powerful tool designed to simulate the changes in waveforms as the environmental and system parameters vary (M. Kim et al. 2016).

4.4.3.1 Computational aspects of waveform calculation

4.4.3.1.1 Introducing the model for sounding radiance and receiver sensitivity distribution

The discussion in Sec. 4.3.2.7 presents a description of the radiance distribution of both sounding beam (I'_E) and the fictitious receiving beam (I'_R) in the water at the sea surface using the functions,

$$I'_{E,R}(n_w H_s,\mathbf{r},\mathbf{n}_t) = D_{E,R}\left(\frac{\mathbf{r}}{n_w H_s \Theta_{E,R}}\right)\cdot\delta_2\left(\mathbf{n}_t - \mathbf{r}/n_w H_s\right) \quad , \tag{4.3.74}$$

Recall that $D_E(\mathbf{n}_{at})$ is the emitted beam angular distribution (the function in transversal component of the directional vector $\mathbf{n}_a = \{n_{az},\mathbf{n}_{at}\}$), parameter, Θ_E, characterizes the beam angular width (divergence), $D_R(\mathbf{n}_{at})$ is the analogous distribution for the virtual receiving beam, and Θ_R is the receiver field of view angle. Substitution of the expression into (4.3.59) gives

$$E_{E,R}(z,\mathbf{r}) = \frac{1}{2\pi}\exp\{-z(t,r_{=})\cdot a_s\}\times$$
$$\times\int \widetilde{D}_{E,R}\left[\frac{\mathbf{k}}{z_0\Theta_{E,R}}\left(1+\frac{z-z_0}{n_w H_s}\right)\right]\cdot exp\{-(z-z_0)\cdot a_{bs}\big(k(z-z_0)\big)\}\cdot exp(-i\mathbf{rk})\,d^2\mathbf{k} \tag{4.3.75}$$

where $\widetilde{D}_{E,R}$ is the Fourier transform of the corresponding distribution:

$$\widetilde{D}_{E,R}(\mathbf{k}) = \tfrac{1}{2\pi}\int D_{E,R}(\mathbf{r}_1)exp(i\mathbf{r}_1\mathbf{k})\,d^2\mathbf{r}_1 \quad . \tag{4.3.76}$$

In the simulator, the distributions are assumed to be axially symmetrical, so that $D_{E,R}(\mathbf{n}_{at}) \equiv D_{E,R}(n_{at})$, $\widetilde{D}_{E,R}(\mathbf{k}) \equiv \widetilde{D}_{E,R}(k)$.

4.4.3.1.2 Application of a practical model for the water Volume Scattering Function (VSF)

The lack of measurements of the VSF, especially for small forward scattering angles, necessitates employment of an effective model for the small-angle component of the phase function, $\chi_s(\vartheta)$, introduced in (4.3.32), in the waveform simulator. We use Dolin's well-known model proposed in Bravo-Zhivotovsky et al. (1969), see also Dolin and Levin (1991) (in Russian):

$$\chi_s(\vartheta) = \frac{1}{2\pi}\cdot\frac{m}{\vartheta}\cdot exp(-m\vartheta) \quad . \tag{4.3.77}$$

The single VSF shape parameter, *m*, required by the model, is related to the average cosine of the scattering angle via the formula presented in Dolin et al. (1988). Note that the model is applicable only for small angles, $\vartheta \approx n_t \ll 1$. For larger angles, $\chi_s(\vartheta)$ in (4.3.32) is set equal to zero (here n_t is the module of tangential component $\mathbf{n}_t$ of directional vector $\mathbf{n}, |\mathbf{n}| = 1$, for scattered radiance). The Fourier transform (4.3.44) of the model scattering phase function is then:

$$\widetilde{\chi_s}(n_t) = \frac{1}{2\pi}\,\frac{1}{\sqrt{1+\left(\frac{n_t}{m}\right)^2}} \quad , \tag{4.3.78}$$

and substitution of the latter formula into (4.3.55) yields:

$$S_\delta(t) = Q'\Sigma\Omega\frac{c}{2n_w}\int d^2\,\mathbf{r}\,\gamma(z(t),\mathbf{r})E_E(z(t),\mathbf{r})E_R(z(t),\mathbf{r}) \quad , \quad z(t)\equiv\frac{ct}{2n_w} \quad ; E_{E,R}(z,\mathbf{r})$$
$$= \int \widetilde{I'}_{E,R+}\big(z_0,\mathbf{k},\mathbf{k}(z-z_0)\big)\times$$
$$\times\, exp\{-z(t,r_{=})\cdot a_s - (z-z_0)\cdot a_{bs}\big(k(z-z_0)\big)\}exp(-i\mathbf{rk})\,d^2\mathbf{k} \quad ; \tag{4.3.79}$$

$$\widetilde{I'}_{E,R+}\big(z_0,\mathbf{k},\mathbf{k}(z-z_0)\big)$$
$$= \frac{1}{(2\pi)^2}\iint I'_{E,R+}(z_0,\mathbf{r},\mathbf{n}_t)\;exp\{i\mathbf{rk}+\;i\mathbf{n}_t\mathbf{k}(z-z_0)\}\,d^2\mathbf{r}\,d^2\mathbf{n}_t$$

$$a_{bs}(zk) = b_s\left\{1-\frac{m}{hk}\cdot\ln\left[\frac{zk}{m}+\sqrt{1+\left(\frac{zk}{m}\right)^2}\right]\right\} \quad . \tag{4.3.80}$$

Now (4.3.79) takes the form

$$S_\delta(t) = Q'\Sigma\Omega\frac{c}{2n_w}\int d^2\,\mathbf{r}\,\gamma(z(t),\mathbf{r})E_E(z(t),\mathbf{r})E_R(z(t),\mathbf{r}) \quad , \quad z(t) \equiv \frac{ct}{2n_w} \quad ;$$
$$E_{E,R}(z,\mathbf{r}) = \exp\{-z(t,r_=)\cdot a_s - (\mathrm{z}-\mathrm{z}_0)\cdot b_s\}\times$$
$$\times\int \tilde{\mathrm{I}}'_{\mathrm{E,R+}}(\mathrm{z}_0,\mathrm{k},\mathrm{k}(\mathrm{z}-\mathrm{z}_0))\left[\frac{(\mathrm{z}-\mathrm{z}_0)\mathrm{k}}{\mathrm{m}}+\sqrt{1+\left(\frac{(\mathrm{z}-\mathrm{z}_0)\mathrm{k}}{\mathrm{m}}\right)^2}\right]^{\frac{\mathrm{m}\cdot\mathrm{b_s}}{\mathrm{k}}}\exp(-\mathrm{irk})\,\mathrm{d}^2\mathrm{k} \qquad (4.3.81)$$

4.4.3.1.3 Specifics of backscattered signal calculation

In order to describe the in-water propagation of the laser pulse more efficiently, it is convenient to make a change in the notation used in equation (4.3.56).

$$E(h_s,\mathbf{r}) = \int \tilde{I}(0,\mathbf{k},h_s\mathbf{k})\exp[-h'(\mathbf{r})a_s - a_{bs}(h_s k)h_s]\exp(-i\mathbf{k}\cdot\mathbf{r})\;d^2\mathbf{k} \quad , \qquad (4.3.82)$$

where, h_s is the in-water propagation distance of the beam center, **k** is the spatial frequency range, and $h'(\boldsymbol{r})$ is the in-water path length to a position $\boldsymbol{r}$ on the leading-edge plane (Figure 4.3.4). Recalling that the $r_=$-axis is defined (Sec. 4.3.2.6) as the intersection between the leading-edge plane and a plane that includes both the nadir and the propagation direction, then, for the case of an incident angle, θ_a, and the corresponding refractive angle, θ_w, we can let $h'(\boldsymbol{r}) = h_s - r_= \cdot tan\theta_w$ (Eq. (4.3.58)). This means that $h'(\boldsymbol{r})$ is a function of $r_=$ only. The $r_\perp$-axis is determined from $r_=$-axis following the right-hand rule. The source function, $\tilde{I}(0,\mathbf{k},h\mathbf{k})$, in (4.3.82) must be defined. Consider a lidar located at altitude, H, with a source radiance distribution characterized by the angle, Θ (the divergence for the beam, and the FOV for receiver). A Gaussian source model at the surface may then be expressed as

$$I_\Theta(0,\mathbf{r},\mathbf{n}_t) = \frac{1}{\pi r_0^2}\exp\left[-\frac{\mathbf{r}^2}{r_0^2}\right]\delta_2\left(\mathbf{n}_t - \frac{\mathbf{r}}{n_w H_s}\right) \quad , \qquad (4.3.83)$$

where the effective radius is expressed as $r_0 = H_s\left(\frac{\Theta}{2}\right)$, and δ_2 is the 2D delta function defined in equation (4.3.62). A Fourier transform of this Gaussian light source will result in $\tilde{I}(0,\mathbf{k},\mathbf{p})$, calculated as:

$$\frac{1}{(2\pi)^2}\iint\frac{1}{\pi\,{r_0}^2}\exp\left(-\frac{\mathbf{r}^2}{{r_0}^2}\right)\;\delta_2\left(\mathbf{n}_t - \frac{\mathbf{r}}{n_w H_s}\right)\;\exp[i(\mathbf{kr}+\mathbf{pn}_t)]d^2\mathbf{r}d^2\mathbf{n}_t \quad . \qquad (4.3.84)$$

Grouping the 2D-delta function term with the frequency conjugate, **p,** yields:

$$\frac{1}{2\pi}\int\frac{1}{\pi\,{r_0}^2}\exp\left(-\frac{\mathbf{r}^2}{{r_0}^2}\right)\;\left\{\frac{1}{2\pi}\int\delta_2\left(\mathbf{n}_t - \frac{\mathbf{r}}{n_w H_s}\right)\;\exp[i\mathbf{pn}_t]d^2\mathbf{n}_t\right\}\exp[i\mathbf{kr}]d^2\mathbf{r} \quad . \qquad (4.3.85)$$

The expression in curly brackets is the Fourier transform of the 2D-delta function, for which the solution is $\frac{1}{2\pi}\exp\left[i\mathbf{p}\frac{\mathbf{r}}{n\,H_s}\right]$. This allows (4.3.85) to be rewritten as:

$$\frac{1}{(2\pi)^2}\int \frac{1}{\pi\, {r_0}^2}\exp\left(-\frac{\mathbf{r}^2}{{r_0}^2}\right)\ \exp\left[i\mathbf{k}\mathbf{r}+i\mathbf{p}\frac{\mathbf{r}}{n_w H_s}\right]d^2\mathbf{r}\quad . \tag{4.3.86}$$

The frequency variable, $\boldsymbol{p}$, may be replaced by $h_s\boldsymbol{k}$ according to the equation (4.3.82). With this replacement, the two exponential terms can be combined and modified to yield:

$$-\frac{\mathbf{r}^2}{{r_0}^2}+i\mathbf{k}\mathbf{r}\left[1+\frac{h_s}{n_w H_s}\right]=-\frac{1}{{r_0}^2}\left[\mathbf{r}-i\mathbf{k}\left(1+\frac{h_s}{n_w H_s}\right)\ \frac{{r_0}^2}{2}\right]^2-\mathbf{k}^2\left(1+\frac{h_s}{n_w H_s}\right)^2\left(\frac{r_0}{2}\right)^2 \tag{4.3.87}$$

If equation (4.3.87) is plugged into equation (4.3.86), the first squared term in (4.3.87) reduces to πr_0^2 after integration, and is canceled by the $1/\pi r_0^2$ factor outside of the integral. Thus, finally, the Fourier transform of the Gaussian source that is used in the equation (4.3.82) may be expressed as:

$$\tilde{I}(0,\mathbf{k},h\mathbf{k})=\frac{1}{(2\pi)^2}\exp\left[-\mathbf{k}^2\left(1+\frac{h_s}{n_w H_s}\right)^2\left(\frac{r_0}{2}\right)^2\right]\quad . \tag{4.3.88}$$

If the characteristics of the source radiance distribution can be described by a Heaviside step function, $G_{st}(x)$, the source model will be given by:

$$I_\Theta(0,\mathbf{r},\mathbf{n}_t)=\frac{4}{\pi\, {H_s}^2\Theta^2}\mathrm{G}_{st}\left(\left|\frac{2\mathbf{r}}{H_s\cdot\Theta}\right|\right)\ \delta_2\left(\mathbf{n}_t-\frac{\mathbf{r}}{n_w H_s}\right)\quad . \tag{4.3.89}$$

The Fourier Transform, $\tilde{I}(0,\mathbf{k},\mathbf{p})$, is again defined as in (4.3.84) and, using the Fourier Transform of the 2D-delta function, as in (4.3.85), equation (4.3.89) becomes:

$$\frac{1}{2\pi}\int \frac{4}{\pi\, {H_s}^2\Theta^2}G_{st}\left(\left|\frac{2\mathbf{r}}{H_s\cdot\Theta}\right|\right)\quad\left\{\frac{1}{2\pi}\exp\left[i\mathbf{p}\frac{\mathbf{r}}{n_w H_s}\right]\right\}\exp[i\mathbf{k}\mathbf{r}]d^2\mathbf{r}\quad . \tag{4.3.90}$$

Replacing the frequency variable, $\mathbf{p}$, with $h\mathbf{k}$ then yields:

$$\frac{1}{(2\pi)^2}\int \frac{4}{\pi\, {H_s}^2\Theta^2}G_{st}\left(\left|\frac{2\mathbf{r}}{H_s\cdot\Theta}\right|\right)\ \exp\left(i\mathbf{k}\mathbf{r}\left[1+\frac{z}{n_w H_s}\right]\right)d^2\mathbf{r}\quad . \tag{4.3.91}$$

Assuming radial symmetry, the exponential term may be expressed via a 0^{th} order Bessel function of the first kind, $J_0()$:

$$\frac{4}{\pi\, {H_s}^2\Theta^2}\frac{1}{2\pi}\int_0^\infty G_{st}\left(\frac{2r}{H_s\cdot\Theta}\right)\mathrm{J}_0\left(rk\left[1+\frac{z}{n_w H_s}\right]\right)\cdot r\ dr\quad . \tag{4.3.92}$$

Next, using the relationships: $x=\frac{2}{H_s\Theta}r$, and $xdx=\frac{4}{{H_s}^2\Theta^2}rdr, \mathrm{G}_{st}(x)=1$, expression (4.3.92) becomes

$$\frac{1}{(2\pi)^2}\int \frac{4}{\pi\, {H_s}^2\Theta^2}\mathrm{G}_{st}\left(\left|\frac{2\mathbf{r}}{H_s\cdot\Theta}\right|\right)\ \exp\left(i\mathbf{k}\mathbf{r}\left[1+\frac{z}{n_w H_s}\right]\right)d^2\mathbf{r}\quad . \tag{4.3.93}$$

Finally, invoking the equality, $\int_0^1 x^{\nu+1} \mathrm{J}_n(ax)\,dx = a^{-1}\mathrm{J}_{\nu+1}(a)$, the Fourier Transform of the Step-source function becomes:

$$\tilde{I}_\Theta(0,\mathbf{k},h\mathbf{k}) = \frac{2}{(2\pi)^2}\frac{1}{k\frac{H_s\Theta}{2}\left[1+\frac{z}{n_w H_s}\right]}\mathrm{J}_1\left(k\frac{H_s\Theta}{2}\left[1+\frac{z}{n_w H_s}\right]\right) \tag{4.3.94}$$

When the Gaussian source radiance model based on equation (4.3.88) is then plugged into equation (4.3.82), the normalized irradiance function can be written as

$$\begin{aligned} E_\Theta(h_s,\boldsymbol{r}) &= \frac{\exp\left(-a_s h'(r_=)\right)}{2\pi} g(h_s,\boldsymbol{r}) \ , \\ g(h_s,\boldsymbol{r}) &= \int J_0(\boldsymbol{kr})\exp\left[-a_{bs}(\boldsymbol{k}\cdot h_s)h_s - \boldsymbol{k}^2\left(\frac{\mathrm{r}_e}{2}\right)^2\right]\boldsymbol{k}d\boldsymbol{k} \ , \\ \mathrm{r}_e &= \left(\frac{\Theta}{2}\right)\left(H_s+\frac{h_s}{n_w}\right) \ , \end{aligned} \tag{4.3.95}$$

where r_e is the effective radius. Note that, although both $g(h_s,\boldsymbol{r})$ and $E_\Theta(h_s,\boldsymbol{r})$ represent irradiance, they are normalized and dimensionless. The physical unit, (W/m^2), is realized when $g(h_s,\boldsymbol{r})$ or $E_\Theta(h_s,\boldsymbol{r})$ are multiplied by laser pulse power.

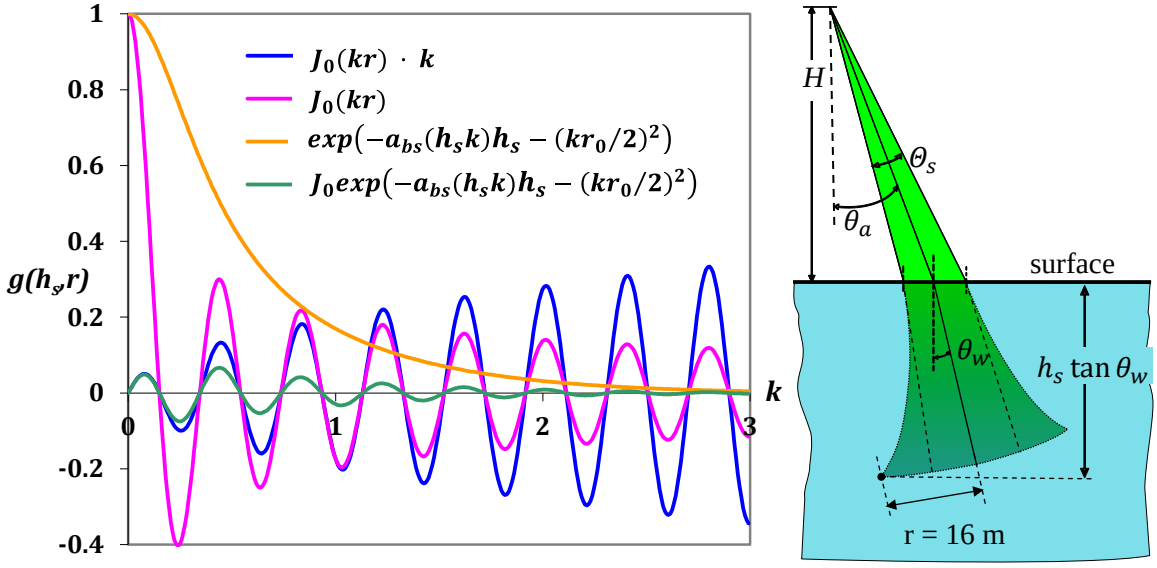

Figure 4.3.6. a) Decomposition of the integrand function for a scattered pulse front at a point significantly away from the center; b) location of the point ($h_s = 20\ m, r = 16\ m$) used in this example.

The decomposition of the integrand of the function, g, in equation (4.3.95) is illustrated in Figure 4.3.6a for a point on the pulse front at a depth of 20 m and 16 m away from the axis of the pulse front (Figure 4.3.6b). In this example, the pulse front has undergone significant dispersion due to scattering. Because of the relatively large distance, r, along the pulse axis, many cycles of the power function, J_0, occur within the limited spatial frequency range, $\boldsymbol{k}$. The exponential term effectively determines the damping of the integrand function. The first term in the exponent is proportional to the scattering coefficient and the slant path, h_s, and is negligibly small compared to the second term in most cases. However, when h_s is

very large, the rapid increase of the $a_{bs}(h_s\boldsymbol{k})$ function (see Eq. (4.3.55)) along with the multiplication by large h_s results in a large amplitude for small value of $\boldsymbol{k}$. In contrast, the second term is a quadratic function of $\boldsymbol{k}$ and the quadratic coefficient is related to the square of the effective radius at the surface. Thus, the upper limit of the integral $\boldsymbol{k}$ can be determined using the formula

$$\boldsymbol{k}_{\max}{}^2(\mathrm{r}_e/2)^2 \approx MAX \tag{4.3.96}$$

where a reasonable value for MAX would be about 10, in which case the exponential term is effectively zero.

Once the upper limit of the integral boundary of the spatial frequency range, $\boldsymbol{k}$, is determined, the following equation may be used to calculate the integral,

$$g(h,r) = \sum_{i=1}^{\infty} \int_{\boldsymbol{k}_{i-1}}^{\boldsymbol{k}_i} d\boldsymbol{k}\cdot\boldsymbol{k}\cdot J_0(\boldsymbol{k}r)\exp[-a_{bs}(\boldsymbol{k}\cdot h_s)h_s - \boldsymbol{k}^2(\mathrm{r}_e/2)^2] \quad . \tag{4.3.97}$$

The node value of the spatial frequency range, $\boldsymbol{k}_i$, is determined from the root of the power function, S_0, by dividing by the distance of the position from the center, $\boldsymbol{k}_i = J_0^{root\_i}/\boldsymbol{r}$.

A contrasting example of the decomposition of the integrand of equation (4.3.97) is shown in Figure 4.3.7, for near-surface water where the optical depth is very small and scattering is minimal. The major difference relative to Figure 4.3.6 is that there are only a small number of cycles of J_0 within the spatial frequency range since the position on the wavefront is not far from the pulse axis. As a result, convergence happens rather quickly, requiring an integral over only a few cycles of J_0.

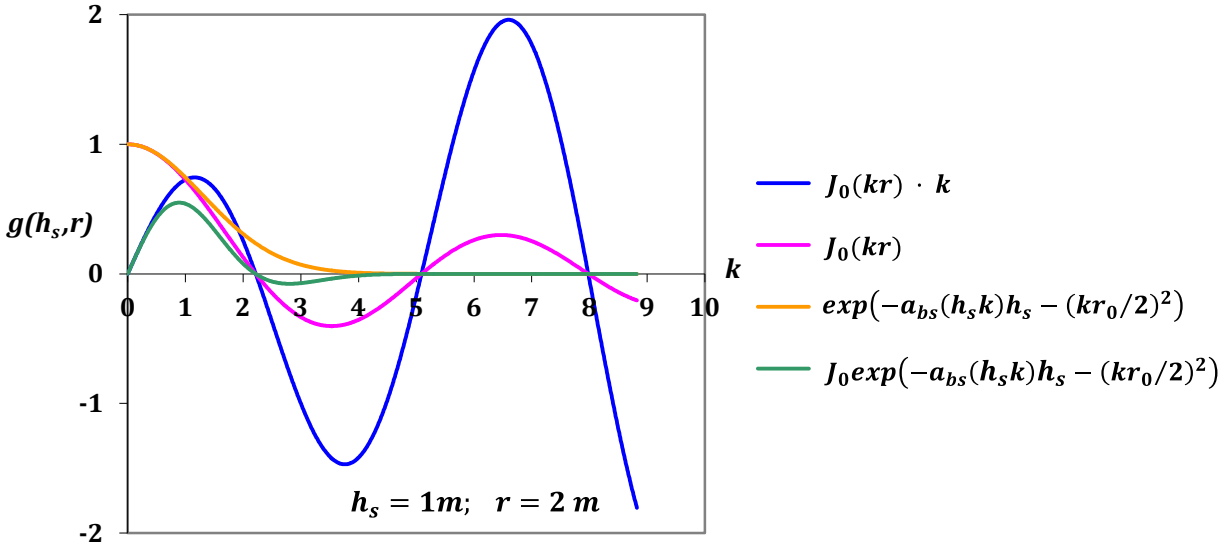

Figure 4.3.7. Decomposition of the integrand function for a minimally scattered beam front at a point close to the center of the beam ($h_s = 1\,m$ at $\boldsymbol{r} = 2\,m$).

We may now consider a collection of integrand functions at varying distances from the pulse axis. For example, Figure 4.3.8 illustrates the dependence of the integrand function on spatial frequency, $\boldsymbol{k}$, at a

shallow depth, $h_s = 1\ m$, as the location on the pulse edge is gradually shifted from the pulse axis (0.0 m) to the pulse boundary (0.45 m) as illustrated in 0.05 m increments.

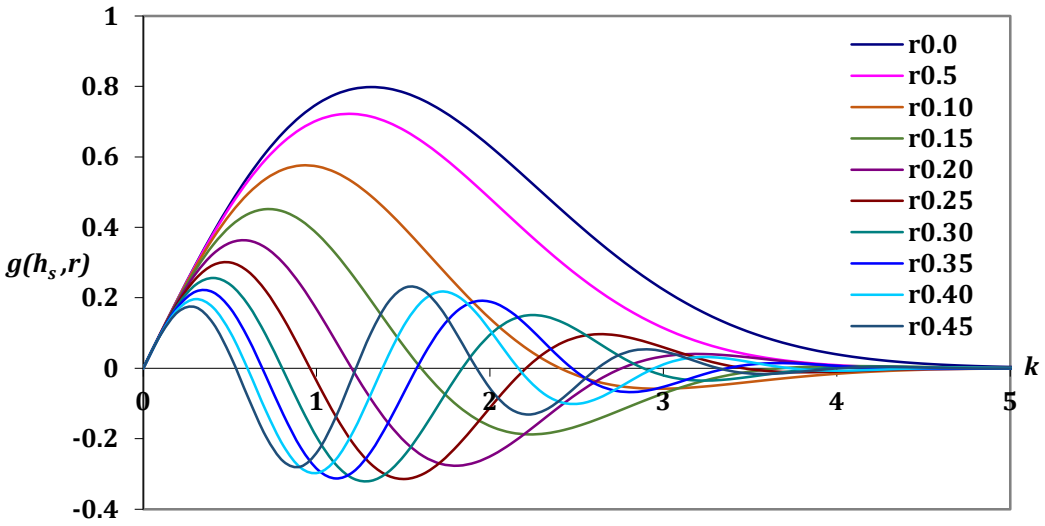

Figure 4.3.8. Normalized integrand functions, $g(h_s, \boldsymbol{r})$ at varying distances from the pulse axis for optically very shallow water, $(h_s = 1\ m)$.

The distance variable, $\boldsymbol{r}$, from the pulse center controls the shape of the overall magnitude, J_0 ,by acting as a scaling factor, with the function contracting as r increases. Thus, the integrand function, $g(h_s, \boldsymbol{r})$, nearest the pulse axis has only one large lobe while integrand functions farther from the axis have multiple lobes. The integrated value for the function near the pulse center is dominated by the area under the first lobe. As points move farther from the center, the area under the first lobe of the integrand function decreases as a second, negative lobe forms. The shrinking positive lobe combined with the growing negative lobe result in much faster decrease of the integral value. This trend results in an overall Gaussian distribution of the $g(h_s, r)$function .

As the optical depth increases, scattering becomes an increasingly important factor in pulse propagation, substantially altering the distribution of the integrand function. For the optically deep case $(h_s = 20\ m)$ shown in Figure 4.3.9, two differences are immediately apparent relative to Figure 4.3.8. First, the integrand function, $g(h_s, \boldsymbol{r})$, is rapidly compressed into a smaller range of spatial frequencies as the distance, $\boldsymbol{r}$, from the beam axis increases. Second, the magnitude of the integrand function is much smaller. This is a result of the increase in effective attenuation due to the overall increase in scattering at the greater depth. The scattering attenuation term is much larger than the second term in the exponent in equation (4.3.97) resulting in a decrease of the integrand function. As the exponential attenuation term saturates with increasing **k**, the second term dominates due to the $\boldsymbol{k}^2$ factor. Thus, the exponential term in (4.3.97) decreases much faster, reducing the magnitude of the integrand function, giving the integrand function, $g(h_s, \boldsymbol{r})$ a stretched, Gaussian-like shape. The profiles of the calculated $g(h_s, \boldsymbol{r})$ functions are shown in Figure 4.3.10a for a laser beam with a small divergence angle (5 mrad), while Figure 4.3.11 illustrates the virtual viewing field determined by a large FOV (40 mrad). The displayed functions describe profiles of irradiance functions for several different propagation distances: the tall Gaussian

curve represents a near surface beam distribution and the wide Gaussian represents the beam after long distance propagation.

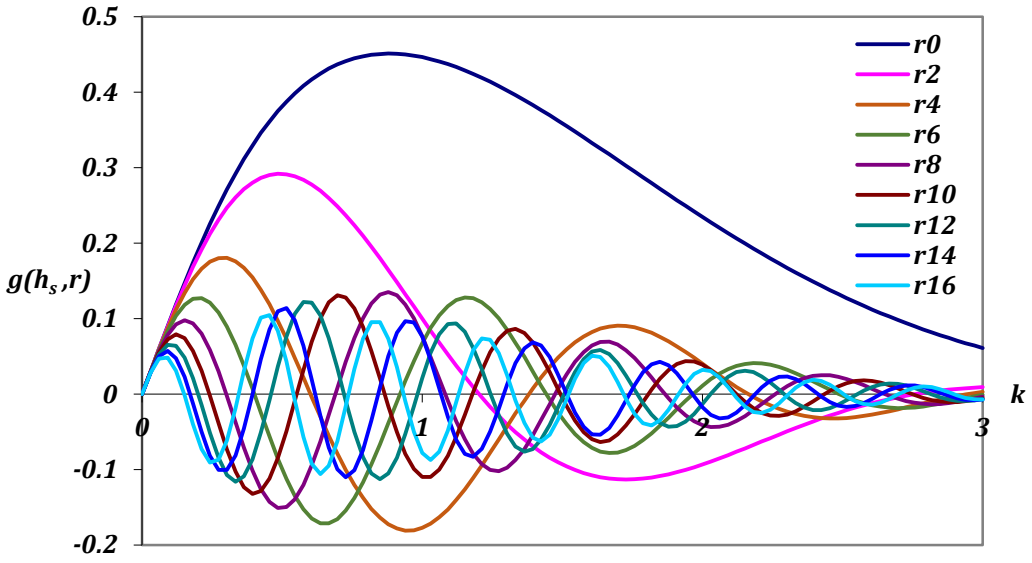

Figure 4.3.9. Normalized integrand functions, $g(h_s, r)$ at varying distances (r) from the pulse axis for optically deep water ($h_s = 20\ m$).

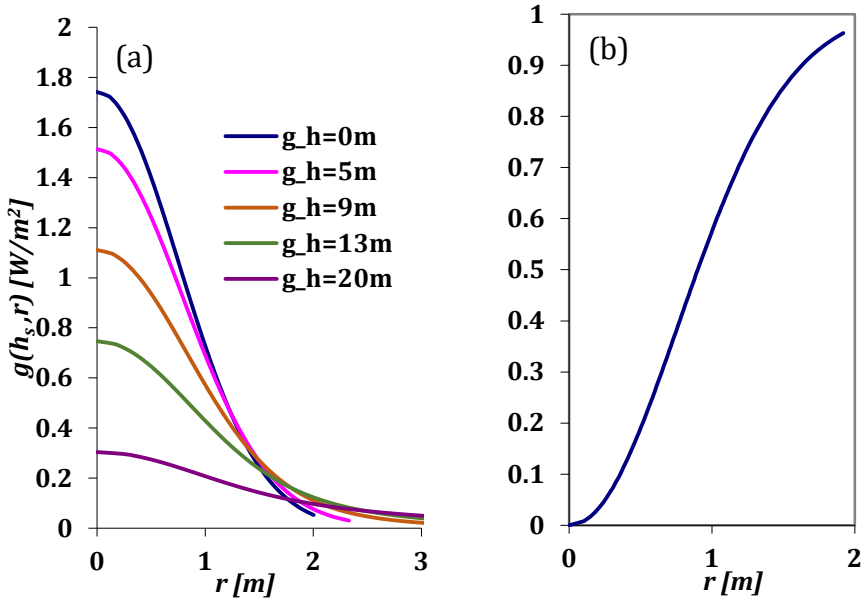

Figure 4.3.10. Calculated irradiance for the laser pulse with a 5 mrad at FWHM. (a) The profile of $g(h_s, \boldsymbol{r})$ function over distance r from the center; (b) the cumulative irradiance for the normalized function.

Note that the beam with a small divergence (Figure 4.3.9a) disperses faster as it propagates. In contrast, the wide FOV angle of the virtual viewing beam does not show rapid dispersion. The normalization condition $\int_0^\infty g(h_s, \boldsymbol{r})\, r\, d\boldsymbol{r} = 1$ is met precisely in both cases (Figure 4.3.10b and Figure 4.3.11b), assuring that the numerical calculation has been done correctly.

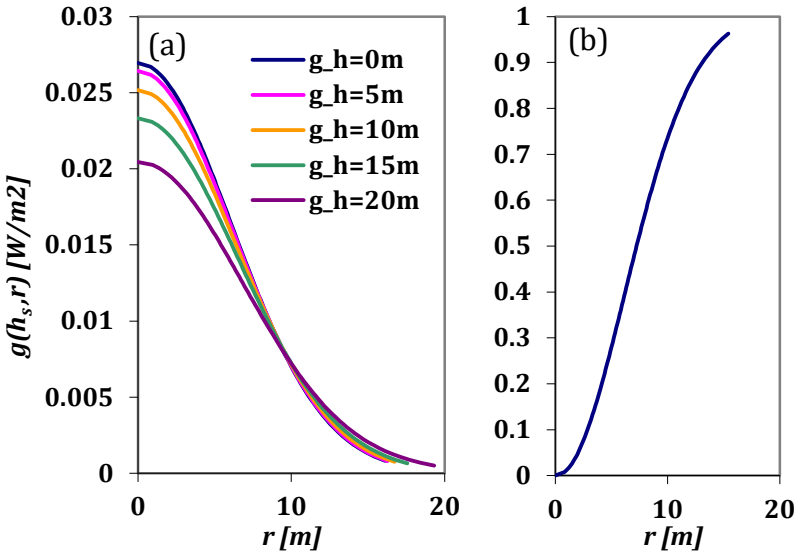

Figure 4.3.11. Calculated irradiance for a view field of 40 mrad at FWHM: (a) The profile of $g(h, \boldsymbol{r})$ function over distance r from the center (b) The cumulative irradiance for the normalized function.

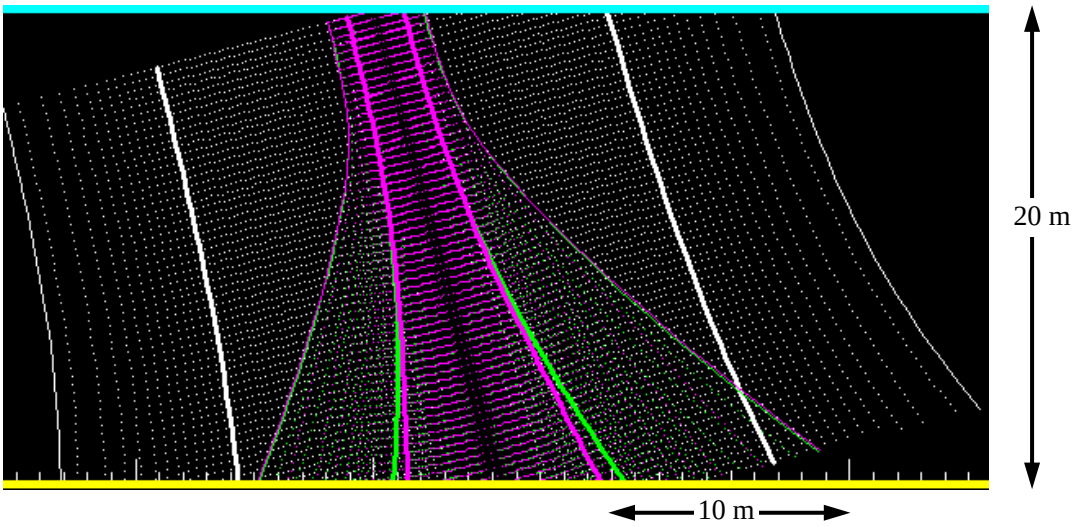

Figure 4.3.12. Dispersion of slant-incident mono-static system. The thick and thin white lines represent the FOV at 70% and 98% of the total accumulated irradiance, respectively. The green lines represent the lidar pulse distribution, and the magenta lines represent the product of the two irradiances in the general lidar equation (4.3.27).

Figure 4.3.12 shows a side view (2D projection) of the irradiance distribution. The figure is scaled with the depth set to 20 m. The cyan-colored top line represents water surface, the yellow-colored bottom line represents sea floor, and the vertical distance is 20m. The wide 40 mrad FOV for the viewing irradiance is illustrated with white dotted lines representing incremental changes in the viewed irradiance. The thickest white line represents 70% of the total accumulated irradiance and the thin, solid white line on both edges represents the 98% boundary encompassing the cumulative irradiance. The equivalent

distribution for the narrow beam dispersion is illustrated using green dotted and solid lines. The magenta color represents the product of the two irradiances found in the general lidar equation (4.3.28). Since the beam divergence is much smaller than the FOV divergence, it is the narrow beam that determines the overall system resolution, which is well illustrated in Figure 4.3.12. At greater depths, the irradiance distributions become increasingly similar even though there is a huge discrepancy near the surface. The implication is that the use of a narrow beam does not guarantee good spatial resolution in the deep water when scattering is strong.

There are circumstances for which the Gaussian function is not appropriate and in which, for example, the cross-sectional profile of the lidar pulse might be better modeled via a Step function rather than the Gaussian. Indeed, the receiver sensitivity distribution of most of the optical system is close to the Step function. The $g(h, \boldsymbol{r})$ function calculated using the Step source function is

$$g(h,r) = \frac{2}{r_e}\int_0^{\infty} exp\{-a_{bs}(h_s k)h_s\}J_0(kr)\,J_1(kr_e)dk \quad , \tag{4.3.98}$$

where J_1 is a first order Bessel function of the first kind. The Step function also exhibits dispersion due to scattering. Similar to the Gaussian function, the smaller divergence experiences much faster dispersion as shown Figure 4.3.13a. Except for near the surface, the Step function is quickly smoothed to resemble a Gaussian function. The spatial extent, $\boldsymbol{r}$, is shown only up to 2 m in Figure 4.3.13a, since the rapid dispersion is evident. In Figure 4.3.13b, however, because the rate of scattering dispersion of the large FOV is small, the overall shape of Step function irradiance profile is displayed out to a significant depth. The comparison of the magnitude between the small beam divergence and large FOV shows a strong disparity with almost 50 times the difference in the peak magnitude.

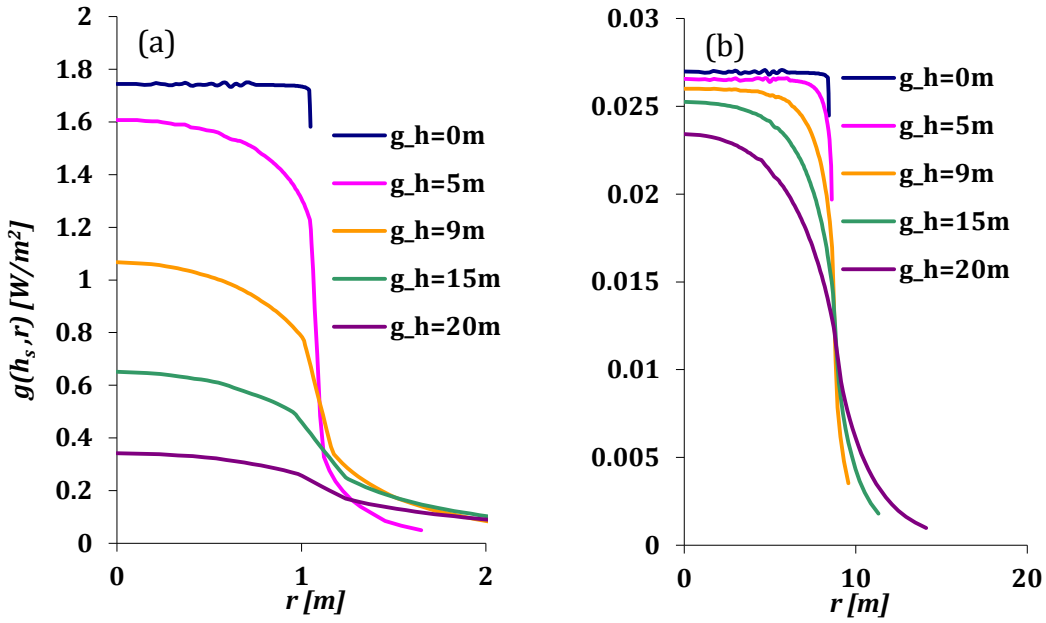

Figure 4.3.13. Irradiance profile using the Step function.

4.4.3.2 Simulation of lidar waveforms for the varying system parameters

The next task is to demonstrate the effect of various system parameters on the waveform. The system parameters include the laser pulse energy, the optical system, and the electronic system properties. However, we exclude system parameters that have a linear effect on the waveform such as laser pulse energy, receiver pupil size (diameter of the receiving optics), optical system attenuation coefficient and more. The reason for the exclusion is that the behavior of these system parameters is completely predictable in a linear fashion. For instance, if the laser power is doubled, then the magnitude of the recorded waveform is also doubled if all other parameters remain the same. Our focus is on parameters with more practical importance: the effect of sensor altitude, the FOV angle, beam divergence angle, beam incidence angle, and the system response function.

4.4.3.2.1 Effect of the sensor altitude

Without changing the laser pulse or the optical system, the collected energy in the waveform decreases as the altitude increases as illustrated in Figure 4.3.14a simply because the projected solid angle from the target to the aperture is smaller. The rate of change in the energy that the waveform carries for varying sensor altitude is shown in Figure 4.3.14b, with the Fresnel peak, volume backscattering, and the bottom plotted over the increasing sensor altitude. The number in parenthesis in Figure 4.3.14b is the coefficient of the power function with which the energy plot is modeled and fitted. The energy is calculated by integration of the waveform within the proper temporal range. The Fresnel peak which is the near-surface return has the value that is closest to the simple analytical model prediction, -2, which arises from the term $(nH_s + h_s)^{-2}$ in the approximate lidar waveform equation (4.3.13). The term describes the trend of solid angle change for the lidar return in the ideal case for which the FOV is large enough to collect all of the return from a Lambertian surface. The volume backscattered energy shows a very similar rate of decrease; however, the rate of decrease of the bottom peak energy deviates significantly from others.

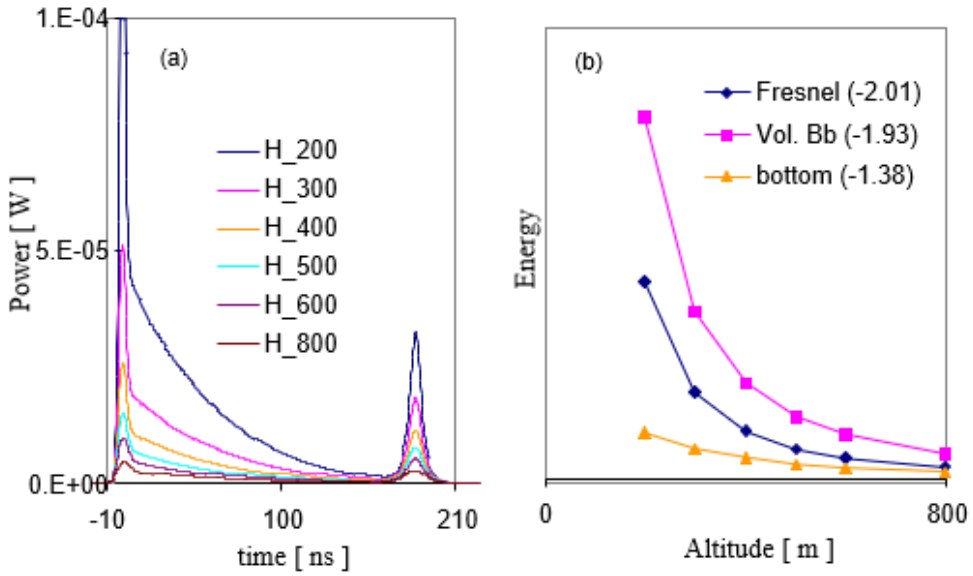

Figure 4.3.14. Effect of the sensor altitudes varying from 200m to 800m. Water depth is fixed at 20 m. a) changes in the waveform for varying altitude; b) rate of decrease in energy of the Fresnel peak, volume backscatter, and bottom return

The reason for the different power coefficient for the bottom return can be explained as follows. The surface peak is entirely within the 40 mrad FOV for a transmitted 5 mrad pulse divergence angle. As the sensor altitude increases, the surface beam illumination area and the viewing area linearly increases together resulting in the same rate of change. The bottom peak, however, arises from deep water where dispersion due to scattering is relatively high. This dispersion occurs on both the downward and return paths, resulting in a large surface area over which the scattered bottom return emerges. As the sensor altitude increases, the viewing area of the fixed FOV increases as the square of the altitude. Thus, the effect of decreasing solid angle is somewhat compensated by the increased surface area from which the bottom return emerges. The final result is that the bottom energy decay rate is significantly less than that of the surface energy. In fact, a similar situation occurs for the volume backscattered energy. The power coefficient of the overall volume backscattering is -1.93. However, as with the bottom peak, if we limit only the near surface volume return the coefficient is near -2 and if we limit the part of the volume backscattering energy near the bottom the coefficient will be closer to that of the bottom energy.

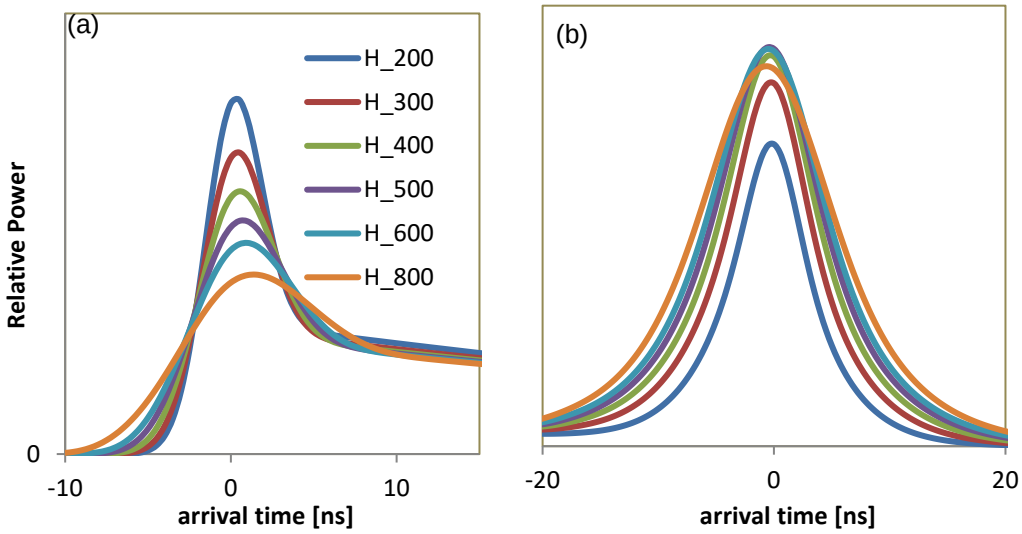

Figure 4.3.15. (a) Surface peaks and (b) bottom peaks aligned at the arrival time of the center of the beam for different sensor altitudes

The peak width differences can be more easily appreciated when the surface peaks are aligned at the surface-arrival time (when the beam center enters the water) and the bottom peaks are aligned at the arrival time of the beam center at the bottom. As the altitude increases, both the FOV and the surface illuminated by the laser beam increase. Thus, a narrower slant beam (oblique measurement) at the lower altitude will create a smaller geometric stretch, and the wider slant beam at the higher altitude will create a larger geometric stretch. The length of geometric stretch is reflected directly in the temporal width of the waveform peaks. At both the surface peak and the bottom peak the same trend is found as shown in Figure 4.3.15

4.4.3.2.2 Effect of the receiver FOV

The effect of the FOV on the received signal has a close theoretical connection to the effect of altitude. At a fixed FOV, increasing the sensor altitude results in an increase in the surface area viewed, concurrently increasing the signal originating from deep water or the bottom. When all other parameters

are fixed, an increase in the FOV will result in an increase in the returned energy. An example is shown in Figure 4.3.16 using a beam divergence fixed at 5 mrad. The increase in energy for the surface peak and volume return is dramatic from 1 mrad until about 10 mrad. Beyond a 10 mrad FOV, any additional increase in FOV angle will result in only small increases in the surface return. The reason for the small increase is that a 10 mrad FOV is enough to include most of the surface reflection from a transmitted laser measurement with a 5 mrad beam divergence.

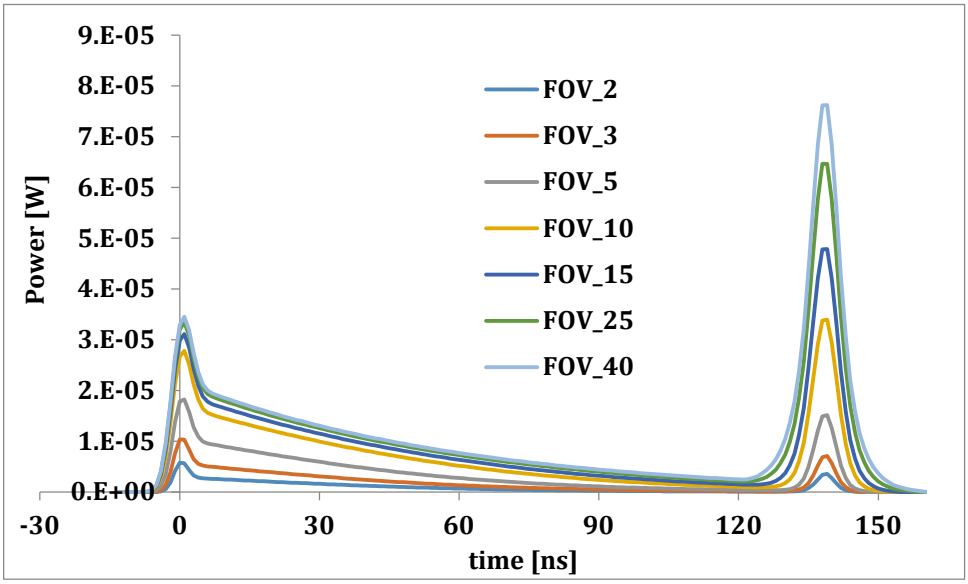

Figure 4.3.16. Effect of the FOV with beam divergence fixed at 5 mrad.

In contrast, the bottom peak continues to increasesharply as the FOV increases. This is because scattering broadens the beam, with even more broadening occurring during the return trip back to the surface. This greatly increases the surface area that can contribute to the received signal. The received signal is complicated by the effect of the daylight background contribution. Although the background energy level is not very high, it is constant throughout waveform recording and can damage the PMT. The increase in detected daylight background is proportional to the square of the FOV increase, and is in sharp contrast to the relatively small increase in bottom energy. The increased background signal is usually accompanied by an increase in the noise level which, in turn, decreases the chance of small peak detection. Thus, the optimal size of the FOV must be determined by considering both factors.

It is also worth investigating how a variable FOV is related to the system attenuation coefficient. The apparent attenuation coefficient calculated from a waveform can be quite different from the inherent water attenuation. A laser pulse propagating downward loses power due to absorption, backward scattering, and some wide angle forward scattering. This combined effect is the total water attenuation which, for this simulation, is taken to be $0.08\ m^{-1}$.

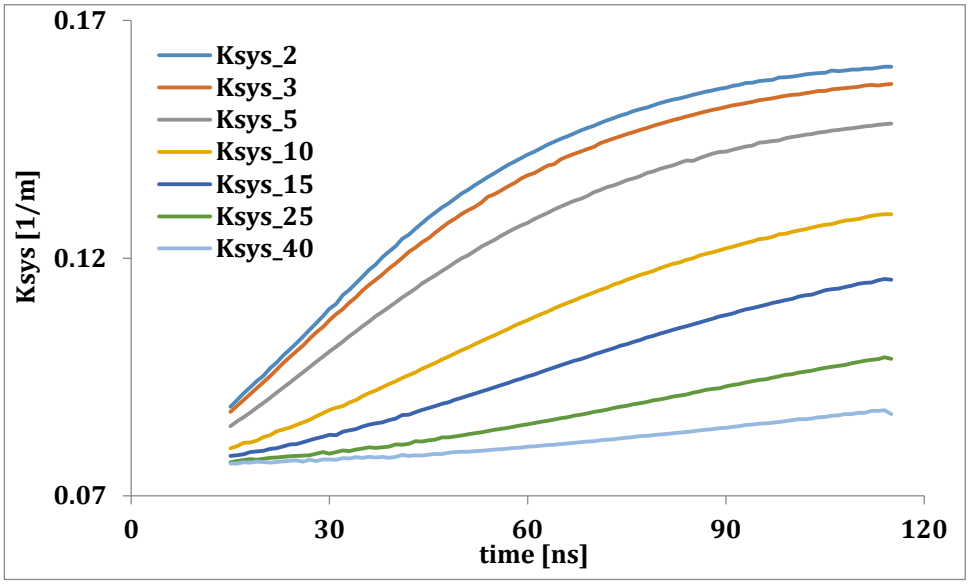

Figure 4.3.17 System attenuation coefficients for varying FOV. The water attenuation coefficient used in the simulation is 0.08 m^{-1}.

If all of the upward return power is collected by the receiver, then the apparent attenuation would be the same as the water attenuation. However, this is never actually possible, in large part because the FOV is never large enough to collect all the upwelling light. The calculated change in the apparent system attenuation is shown in Figure 4.3.17. Due to dispersion by scattering, the region from which the backward scattered signal originates expands quickly as the distance from the source increases, but energy beyond the viewing area is not collected. That means loss due to energy emerging at the water surface, but outside the viewing area results in additional attenuation. The calculated system attenuation is always higher than the inherent water attenuation and much higher for the smaller FOV. In most cases, scattering is the fundamental reason for the additional loss. For example, if there were no scattering dispersion, even a FOV much less than beam divergence would result in a system attenuation coefficient identical to water attenuation. Thus, system attenuation is a function of the FOV and its inter-relationship with scattering.

4.4.3.2.3 Effect of the beam divergence

The effect of divergence on the waveform (shown in Figure 4.3.17) is examined using a FOV fixed at 40 mrad, a fixed laser pulse energy, and with all optical system parameters fixed as well. The results of the simulation are shown in Figure 4.3.18. It appears that the major effect of the divergence angle is on the peak sharpness with both surface and bottom peak amplitudes increasing as the divergence decreases. For a given off-nadir incidence angle, a smaller beam diameter results in a smaller geometrical stretch of the peak at both the air-water interface and water-bottom interface. The FWHM of the surface return is limited by the 3 ns system response time. Nevertheless, the improved peak sharpness is noticeable for smaller divergence angles. A similar, but weaker narrowing of the peak width is apparent for the bottom peak. Changes in scattering will also play an important role since increased scattering will result in more dispersion, and the smaller initial beam divergence will disperse much faster than a larger initial beam divergence. As a result, both a small divergence angle and a large divergence will have similar dispersion

in the deeper part of the water. Ultimately, the optimal beam divergence angle must be determined considering laser eye safety regulations (see Sec. 4.5).

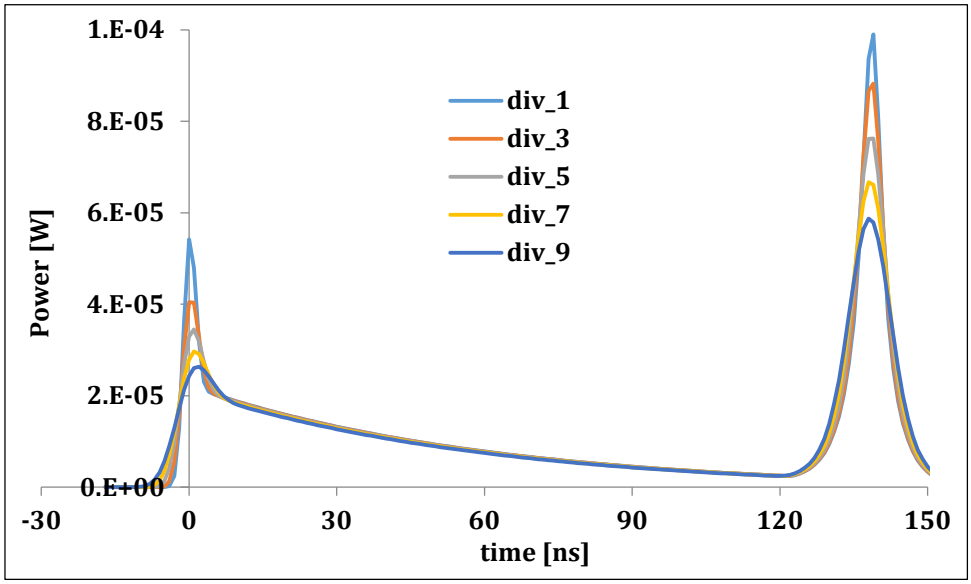

Figure 4.3.18. Waveforms with varying beam divergence angle.

4.4.3.2.4 Effect of the beam incident angle

Waveforms were also simulated using different beam-incident angles in air (Figure 4.3.19). Similar to the simulated results related to the beam divergence angle, an increase in the slant angle (oblique measurement) will result in a larger geometric stretch of the return pulse at both the water surface and the sea bottom. The stretch of the width in the surface return indicates a diminished dominance of the peak-value. Thus, not only does the peak-value magnitude drop as the incident angle increases, but also the apparent peak shifts toward a later time.

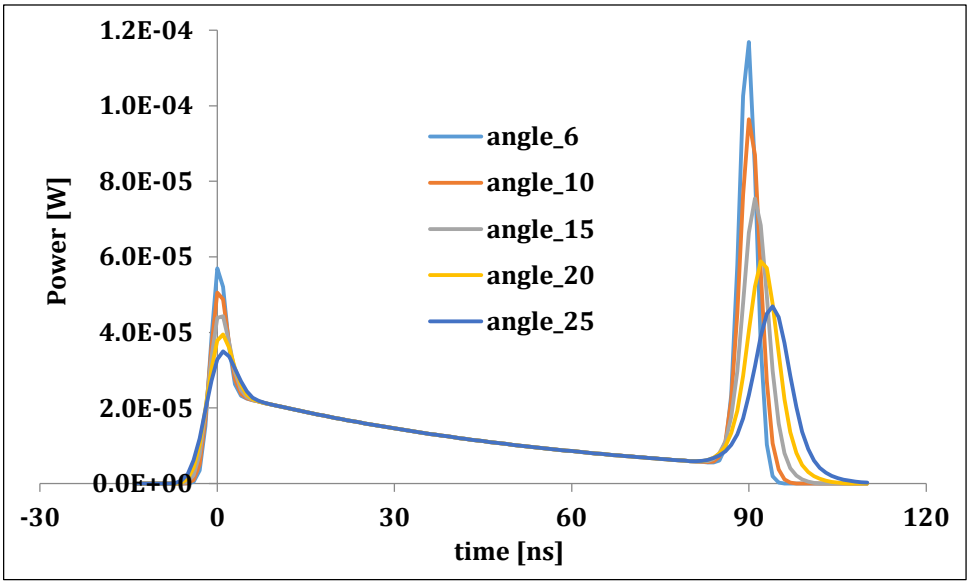

Figure 4.3.19. Waveforms with varying beam incident angle

The same pattern of broadening of the peak and decrease of the peak-value is observed in the bottom returns. The return times of the simulated bottom returns are also characterized by larger delays in return times as the slant angle increases. In this example, the peak-value and width increase is due not only to the increasing slant angle but also to the scattering stretch from the longer in-water slant path. The conspicuous shift of the bottom peak (i.e., delayed return time) is also caused by the increase of the in-water slant path.

4.4.3.2.5 Effect of the system response function

The overall system response function, which includes the effect of pulse duration, PMT rise time, and digitizer response, is one of the most important parameters affecting ALB performance. The effect of changing the system response function is illustrated in Figure 4.3.20, which shows waveforms computed for a 15 m depth in relatively clean water (0.075 m^{-1} of absorption and 0.2 m^{-1} of scattering) for a system with 5 mrad transmitted beam divergence and 40 mrad FOV. An increase in the FWHM of the system response function results in an increase in the peak width and a decrease in the peak magnitude for both surface and bottom peaks. In addition, the surface peak shows a significant shift of the peak position toward a later time. This is because the decrease in the peak magnitude due to the increase of the system response FWHM make the surface peak less prominent compared to the rising surface volume backscattering. Thus, a system response FWHM that is as small as possible will be beneficial for all aspect of the system performance.

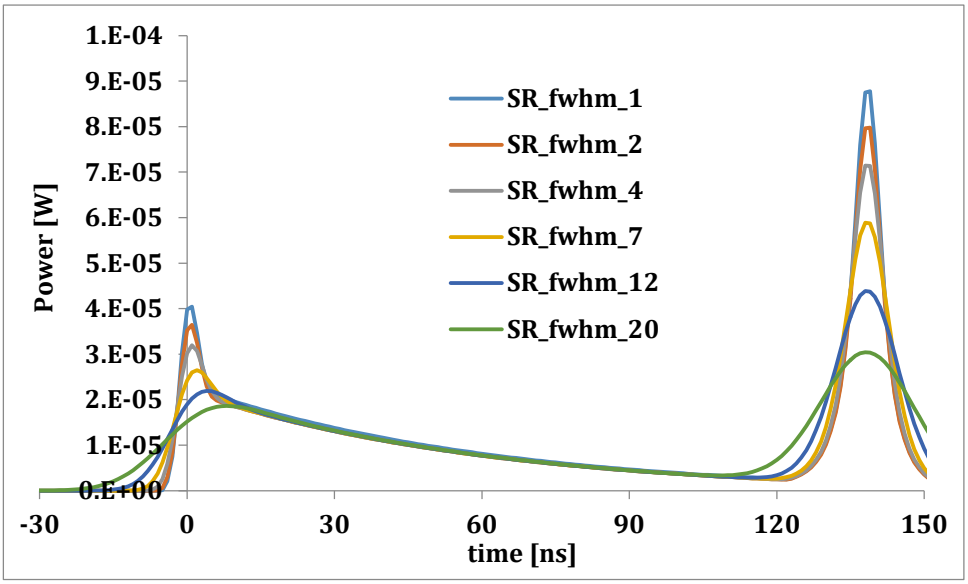

Figure 4.3.20. Waveforms with varying system response function widths (at FWHM)

eCommons (2019) https://doi.org10.7298/jxm9-g971

4.5 Lidar system calibration and alignment

V. Feygels, Yu. Kopilevich

4.5.1 Introduction: channel characteristics employed in waveform simulation and processing

Lidar waveform simulation, based on an accepted theory of ALB return (see Sec. 4.3.2), was addressed in Sec. 4.3.1. According to Equation (4.3.7), a simulated waveform in the optical domain, $S_R(t)$, is given by the formula:

$$S_R(t) = S_\delta(t) * R(t) \tag{4.4.1}$$

Here $S_\delta(t)$ is the input optical signal corresponding to a delta-function sounding pulse with the initial shape, $Q\eta_R \cdot \delta(t - t_0)$, where Q is the actual transmitted laser pulse energy after accounting for atmospheric attenuation and lidar transmitter system losses. The parameter, η_R, describes the transmittance of the receiver optical system (the optical segment in Figure 4.3.1. Function, $R(t)$, in (4.4.1) is the receiving channel response to the lidar pulse, or the effective sounding pulse shape.

The above calculation calls for two characteristics of the receiving channel – the function, $R(t)$ and the optical system transmittance, η_R. If it is necessary to simulate the output signal (waveform) in the electric domain, $D(t)$, the Watt-count characteristic of the channel, $\chi[\cdot]$, is also needed (see Equations (4.3.2) and Equation (4.3.11):

$$D(t) = \chi[S_\delta(t) * R(t)] \tag{4.4.2}$$

The goal of lidar waveform processing is the estimation of environmental properties (bottom reflectance, IOPs), as well as precise bottom depth retrieval. This requires a comparison of an experimentally obtained waveform, $D(t)$, with simulated waveforms (see Sec. 4.3.1). In order to perform the comparison in the optical domain, the electrical signal, $D^{exp}(t)$, (in digital counts) is transformed into the corresponding optical signal, $S_R^{exp}(t)$, (in Watts):

$$S_R^{exp}(t) = \chi^{-1}[D^{exp}(t)] \tag{4.4.3}$$

where $\chi^{-1}[\cdot]$ is the inverse of the channel Watt-count characteristic, $\chi[\cdot]$ in Equation (4.3.2).

Measurement of the specific characteristics of a given receiver channel is the concern of radiometric calibration of that channel. The procedure is carried out to obtain:

- the channel response to the laser pulse, or the effective pulse shape, $R(t)$;
- the channel transmittance, η_R;
- the channel Watt- count characteristic, $\chi[\cdot]$.

4.5.2 Calibration measurements using the built-in system laser source

In order to calibrate the lidar receiving channel using the system laser source, the sounding light beam is directed at a planar remote target positioned perpendicular to the beam axis. The reflected pulse arriving at the receiving telescope then retains the initial pulse shape, $p(t)$, so that the input optical signal at the

channel photodetector may be expressed as $W \cdot p(t)$. The pulse energy, Q, is then varied over a wide range (with the use of attenuating optical filters introduced into the channel optical segment). In what follows, the "calibration" input optical signal for a range of energies is designated as, $S_Q^{calib}(t)$:

$$S_Q^{calibr}(t) = Q \cdot p(t) \tag{4.4.4}$$

The energy, Q, of the calibration pulse is measured with a power meter installed in the optical segment behind the field diaphragm (see Figure 4.3.1). The power meter reading is divided by the laser pulse repetition rate to obtain the energy of an individual pulse.

For a given input optical signal $S_Q^{calib}(t)$, the output electrical signal, $D_Q^{calibr}(t)$, may be written as [see (4.3.2), (4.3.7).

$$D_Q^{calibr}(t) = \chi[Q \cdot R(t)] \tag{4.4.5}$$

The channel Watt-count characteristic, $\chi[\cdot]$, is a monotonically increasing function. Thus, for the maximum recorded signal, (4.4.5) yields:

$$\max D_Q^{calibr}(t) = \chi[Q \cdot \max R(t)] \quad , \tag{4.4.6}$$

Using a set of waveforms, $\max D_Q^{calibr}(t)$, recorded at various levels of input pulse energy, Q, the right-hand side of (4.4.6) defines a scaling function with the argument, Q, in Watts, and the value in counts:

$$C(Q) \equiv \chi[Q \cdot \max R(t)] \quad . \tag{4.4.7}$$

Now (4.4.5) may be re-written as:

$$\begin{aligned} D_Q^{calibr}(t) = \chi[Q \cdot R(t)] = \chi\left[Q \cdot \max R(t) \cdot \frac{R(t)}{\max R(t)}\right] = \left[Q \cdot \max R(t) \cdot \frac{R_t}{\max R(t)}\right] \\ = \mathrm{C}\left(Q \cdot \frac{R(t)}{\max R(t)}\right) \quad . \end{aligned} \tag{4.4.8}$$

Application of the reverse transformation, C^{-1}, to a separate waveform, $D_Q^{calibr}(t)$, with a known fixed energy, Q, gives

$$R(t) = \frac{\max R\,(t)}{Q} \cdot \mathrm{C}^{-1}\left(D_Q^{calibr}(t)\right) \quad . \tag{4.4.9}$$

The formula determines the function, $R(t)$, within an unknown factor, $\max R\,(t)$, which is easily derived from the normalization condition:

$$\int_0^\infty R(t)dt = 1 \tag{4.4.10}$$

[see (4.3.2), (4.3.4), and (4.3.6)]. The effective pulse shape[1,2], $R(t)$, or channel response to the laser pulse, is now determined, and $\chi[W]$, the Watt-count characteristic of the receiving channel, may be obtained as

$$\chi[W] = C\left(\frac{W}{\max R(t)}\right) \tag{4.4.11}$$

where W is a current value of output electrical signal (in Watts).

4.5.3 Calibration measurements with a continuous wave (CW) laser source

Application of a continuous wave (CW) laser source provides an alternative (and more straightforward) way to derive the Watt-count characteristic, $\chi[\cdot]$, of a receiving channel. Substitution of a constant input signal, $S_P^{calibr} = P = const(t)$, in Eq. (5.3.1), where P is the (adjustable) power of the incident signal at the receiver photodetector, gives rise to the constant output electric signal

$$D_P^{calibr} = \chi[P]\,. \tag{4.4.12}$$

Since P is continuous, the determination of the Watt-count characteristic, $\chi[\cdot]$, based on (4.4.1), does not require that the effective pulse shape, $R(t)$, be evaluated. Thus, the characteristic is not subject to inevitable inaccuracies in the reconstruction of $R(t)$ from a recorded, pulsed signal (see *Note 2* in Sec. 4.4.2 above).

4.5.4 Practical realization of calibration measurements: Radiometric calibration of the SHOALS-1000

Radiometric calibration of the SHOALS-1000 receiving channels was performed with the use of the method described in Sec. 3.4.2 above. The laser pulse power, which was inherently variable, was applied as input signals (Tuell, Feygels, et al. 2005). The target (a wall covered by painted concrete tiles) was located 80 m away from the system. The calibration setup is shown in Figure 4.4.1.

---

[1] While formal evaluation of the effective pulse shape, $R(t)$, based on (4.4.9) may be carried out with the use of a unique waveform, $D_Q^{calibr}(t)$, obtained for a known energy, Q, of a given input optical signal, it seems reasonable to repeat the procedure for a set of energy values from a wide range of energies in order to estimate the signal level interval in which the accepted model of the receiving channel (Sec. 4.3) is valid. In other words, the function, $R(t)$, estimated from (4.4.9), remains independent of the pulse energy, Q).

[2] With a short effective pulse shape (~ 2-5 ns), discrete values of a recorded waveform, $D_Q^{calibr}(t)$, in (4.4.5), obtained with a digitizer having a 1ns time bin, are insufficient for exact determination of the waveform maximum in (4.4.6)-(4.4.9). The error in evaluation of, $\max R(t)$ may lead to inaccurate derivation of the channel Watt-count characteristic, $\chi[\cdot]$, see (4.4.11). The errors may be avoided with calibration measurements carried out with the use of a continuously operated laser source.

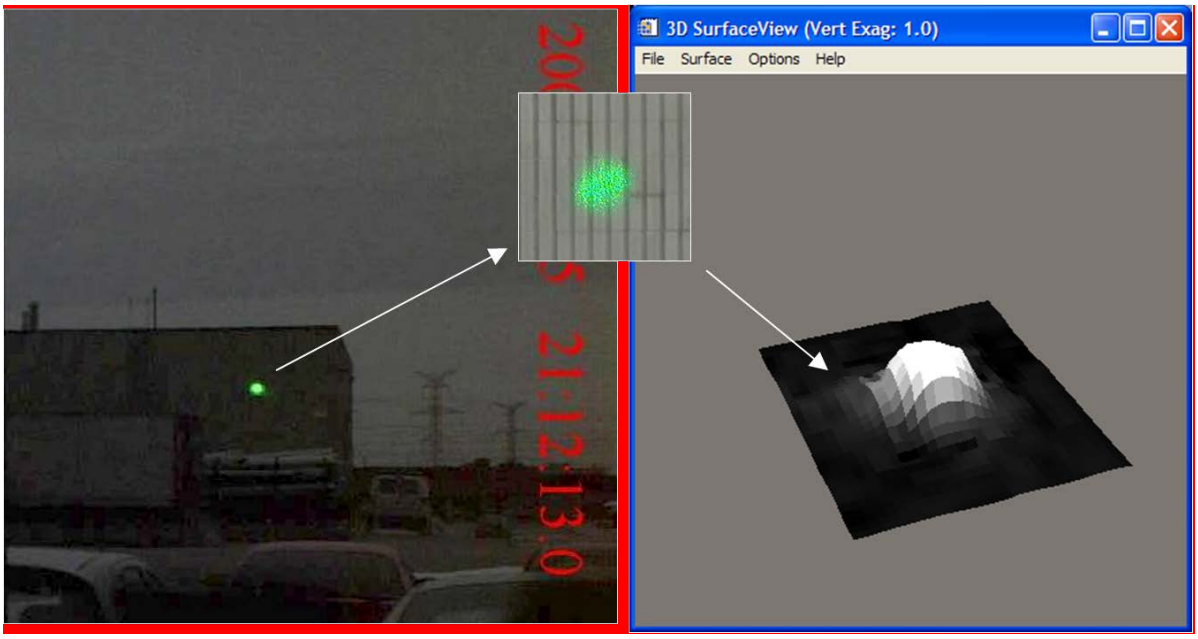

a. b.

Figure 4.4.1. a) View of the laser spot produced by the SHOALS-1000 on the concrete wall at a distance of 80 m, and b) the radiation distribution inside the laser spot.

A simple jig was used for the absolute measurements of the average return optical power. It included a plano-convex lens of 500 mm focal length focusing the return beam on an OPHIR power meter with an interference filter in front of it as shown in Figure 4.4.2. A portion of the light scattered by the target is collected by the lens and focused onto the power meter through a narrow-band filter identical to that in SHOALS-1000 receiver.

The return pulse energy, Q, was varied by introducing calibrated neutral density filters in the SHOALS-1000 receiver. During the calibration measurements, output signal pulses $D_Q^{calibr}(t)$ were recorded for a set of input peak power values in the range $1 \cdot 10^{-7} W$ to $1 \cdot 10^{-3} W$.

eCommons (2019) https://doi.org10.7298/jxm9-g971

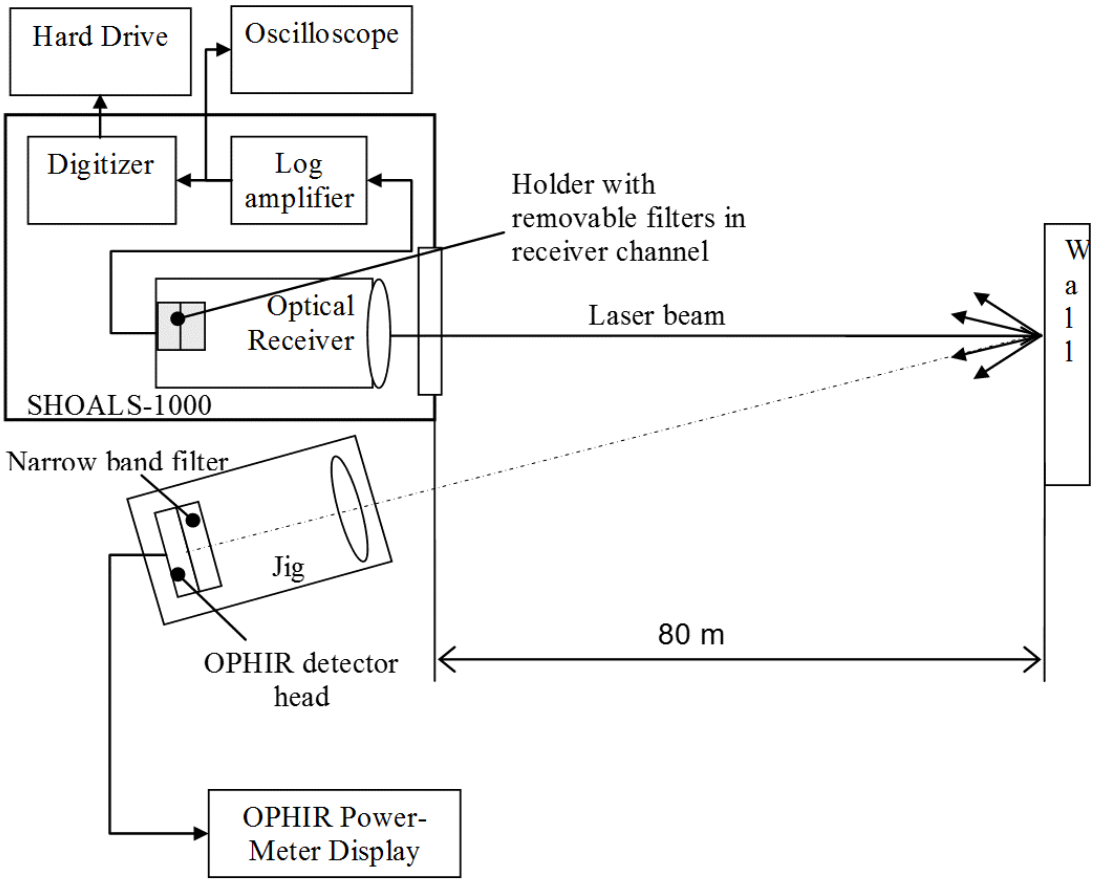

Figure 4.4.2. General schematic of the SHOALS-1000 radiometric calibration measurement..

Results of the derived channel response to the laser pulse, or the effective pulse shape, $R(t)$, carried out as described in Sec. 4.4.2, are presented in Figure 4.4.3 and Figure 4.4.4. Each curve corresponds to a given value of the initial optical pulse amplitude from $W = 1 \cdot 10^{-7} W$ to $1 \cdot 10^{-3} W$ for the PMT and from $W = 1 \cdot 10^{-6} W$ to $1 \cdot 10^{-3} W$ for the APD.

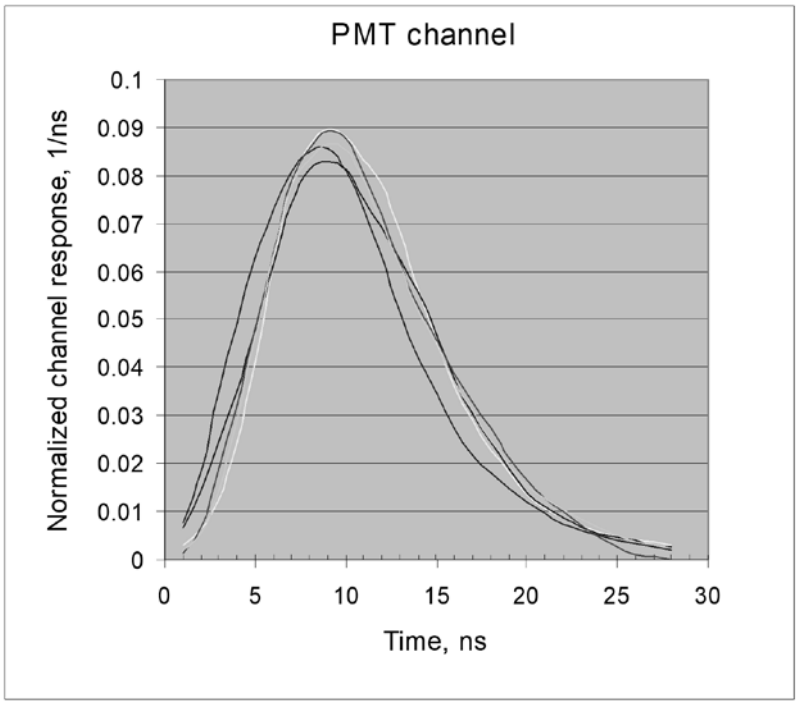

Figure 4.4.3. Normalized SHOALS-1000 PMT-channel response, *R(t)* to initial laser pulse for the pulse amplitudes in the range $1 \cdot 10^{-7} - 1 \cdot 10^{-3} W$.

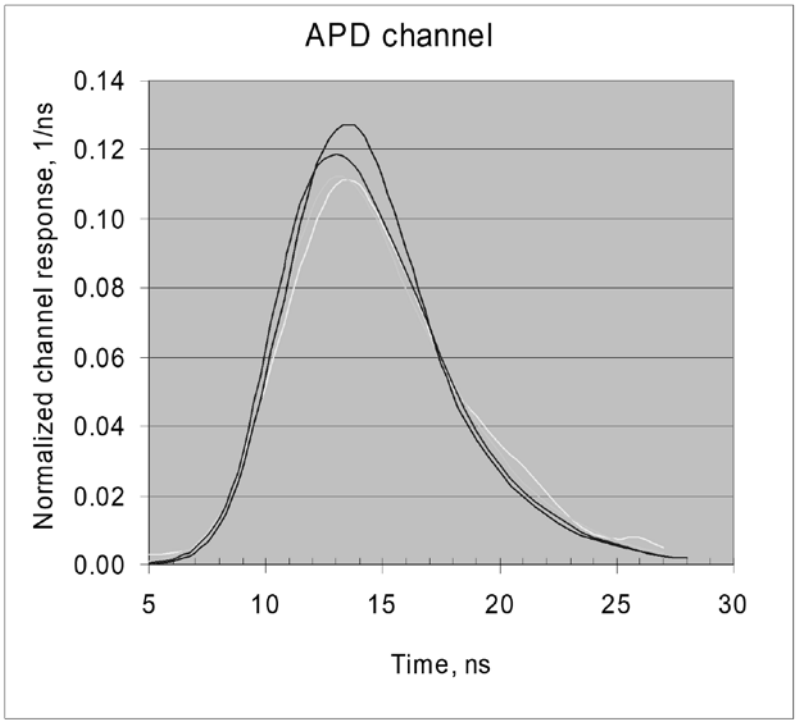

Figure 4.4.4. SHOALS-1000 Normalized APD-channel response, *R(t)* to initial laser pulse for the pulse amplitudes in the range $1 \cdot 10^{-6} - 1 \cdot 10^{-3} W$.

These results seem to verify the assumption that the channel response to the initial laser pulse is not strongly dependent on the pulse power.

The channel Watt-count characteristic $\chi[W]$ derived from the measurements for the two channels are plotted in Figure 4.4.5 and Figure 4.4.6. The number of counts is limited in these plots due to use of an 8 bit digitizer in SHOALS-1000.

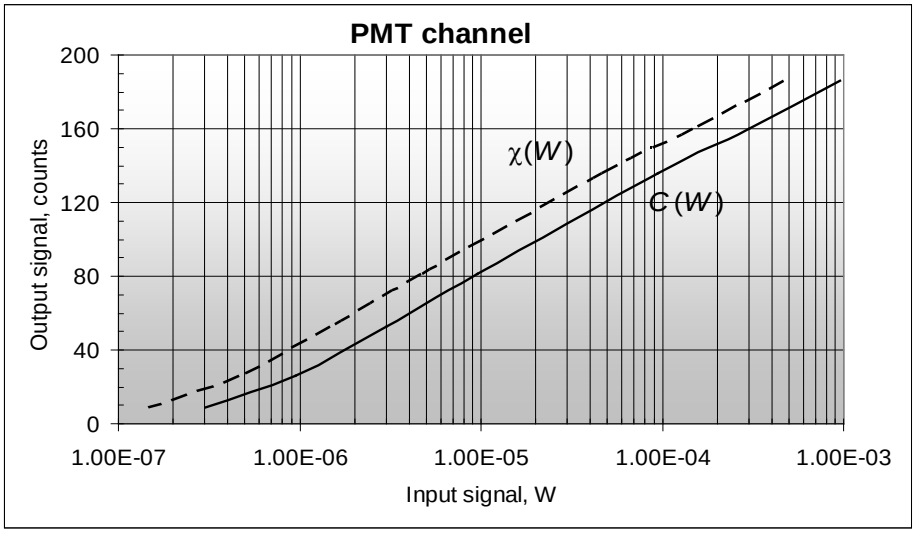

Figure 4.4.5. The PMT-channel Watt-count characteristic $\chi[W]$ and the calibration characteristic of the channel *C(W)*.

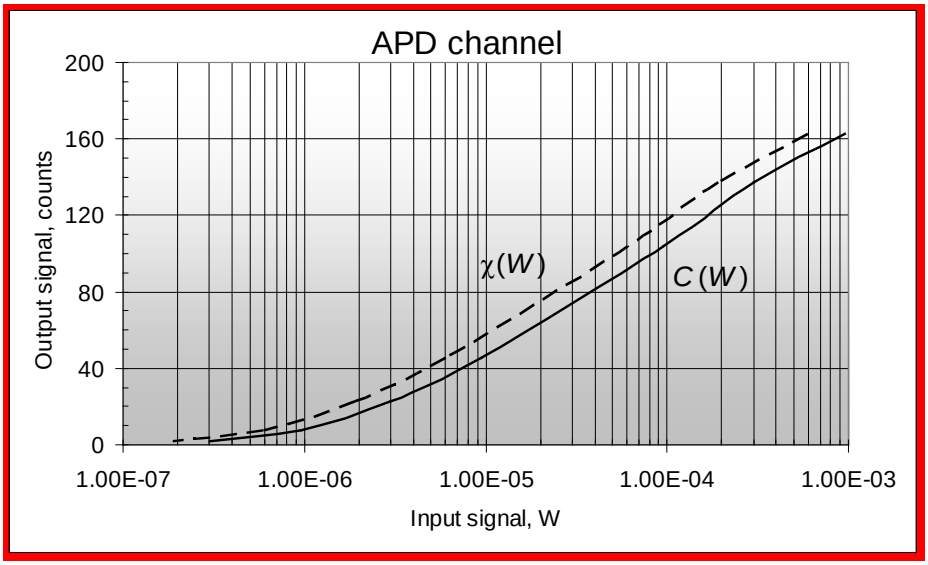

Figure 4.4.6. The APD-channel Watt-count characteristic $\chi[W]$ and the calibration characteristic of the channel *C(W)*.

It is quite obvious from the above Section, that radiometric calibration of a lidar is a rather complicated and laborious procedure, and needs to be performed by a well-qualified staff. When built-in laser is used for the calibration, it is necessary to keep strictly to the established eye safety requirements for the corresponding laser class (mostly, class 4), see the next Sec. 4.5.

It should be also emphasized that calibration of the system must be carried out periodically (at least, once a year) and renewed after each replacement of lidar transmitter or receiver elements (laser, PMT, APD, digitizer, interference filters, etc.).

4.6 Implementation of Eye Safety Requirement

John Banic

Laser eye safety is an essential consideration for the safe operation of airborne lidar bathymetry (ALB) systems. ALB systems must be eye safe to an observer on the ground, and must conform to guidelines and requirements as set by the International Electrotechnical Commission (IEC), the U.S. Food and Drug Administration (FDA) and the American National Standards Institute (ANSI). The respective documents pertaining to published standards (ANSI 2014; IEC 2014; FDA 2013).

Lasers used in ALB systems are typically frequency-doubled Nd:YAG Class 4 devices operating at a wavelength of 532 nm. Laser classification relates to the potential hazard of the accessible laser radiation in respect to eye or skin damage. Class 4 lasers are those for which intrabeam viewing and skin exposure is hazardous and for which viewing of diffuse reflections may be hazardous. In the Visible (400-700 nm) and Infrared-A (700-1400 nm) range, severe damage can occur to the retina due to the focusing effect of the cornea and lens, which can increase the irradiance by as much as 100,000 times.

To be Class 4, an ALB laser must exceed at least one of the Accessible Emission Limits (AEL) for Class 3B at 532 nm, which are 1) 30 mJ for a single pulse of a duration from 1 ns to 0.06 s, and 2) 0.5 W for exposures >0.25 s. Most ALB lasers have pulse energies well below the single-pulse limit of 30 mJ. However, the average power output is typically >1 W, thus putting them in the Class 4 category. For example, the average power of the laser in the CZMIL system is 25 W (2.5 mJ @ 10 kHz PRF).

When working with lasers in the laboratory, eye protection is required, to prevent accidental exposure. Laser eyewear is normally categorized by its optical density (D_λ). The required value of D_λ for a typical ALB laser is determined from the radiant exposure (H) averaged over a limiting aperture, which is 7 mm for visible wavelengths.

For a laser pulse energy of 2.5 mJ, and a beam diameter that is less than the limiting aperture, the radiant exposure averaged over 7 mm is, therefore,

$$H = \frac{2.5\ mJ}{0.385\ cm^2} = 6.5\ mJ/cm^2 \tag{4.5.1}$$

To determine the ocular hazard, the above radiant exposure must be compared to the Maximum Permissible Exposure (MPE) limit, which is generally expressed in J/cm^2, and is a function of the Exposure Time (T_E). The maximum permissible exposure to laser radiation at a wavelength of 532 nm is 0.2 μJ/cm^2 for a single pulse of duration between 10 ps and 5 μs. The minimum required optical density is then

$$D_\lambda = log\left(\frac{H}{MPE}\right) = log\left(\frac{6.5x10^{-3}}{2x10^{-7}}\right) = 4.5 \quad (4.5.2)$$

To account for multiple-pulse viewing, which is typically the case for repetitively-pulsed lasers, the required optical density would be higher than the above value.

The MPE for a train of pulses is calculated as follows:

$$MPE_T = MPE_P \times N^{-0.25} \quad (4.5.3)$$

where MPE_P is the maximum permissible exposure for a single pulse, and MPE_T is the maximum permissible exposure to a train of pulses (N). N can, in turn, be expressed as

$$N = f \times T_E \quad (4.5.4)$$

where f is the laser pulse repetition frequency and T_E is the exposure time. The exposure time used for visible wavelengths (400-700 nm) is typically 0.25 s, due the natural aversion reflex of the eye.

4.6.1 Safe Operating Altitude

Due to the high laser pulse energy (Q) required for adequate penetration through the water column, the laser beam divergence (Θ_E) must be set to provide a sufficiently-large spot on the ground, such that the radiant exposure to an observer does not exceed the MPE limit at the laser wavelength. This requirement is particularly challenging since the eye is most sensitive to green wavelengths, where the single-pulse MPE is 0.2 µJ/cm^2.

This compares with an MPE of 2 µJ/cm^2 at 1064 nm, 3 mJ/cm^2 in the ultraviolet, and 1 J/cm^2 at 1.54 µm. The latter two MPE values are much larger, as exposure in the ultraviolet and far infrared regions of the spectrum falls outside of the retinal hazard zone (400 – 1400 nm).

The lowest eye safe altitude, at which an ALB system can operate, is given by the Nominal Ocular Hazard Distance (NOHD), according to the following expression:

$$NOHD = \frac{1}{\Theta_s}\sqrt{\frac{4Q}{\pi \cdot MPE} - a^2} \quad (4.5.5)$$

where a is the output beam diameter of the laser. Using typical values for an ALB system: Θ_E = 5 mrad (1/e), Q = 2.5 mJ and a = 0.5 cm, gives an NOHD of 250 m. The flying height of an ALB aircraft is usually 300-400 m, well above the NOHD limit.

The above analysis assumes exposure to a single laser pulse, which is normally the case for airborne operation where the laser beam is scanning and the aircraft is moving. However, if the aircraft was hovering (e.g. helicopter installation) or if the system was put into profile mode (scanning disabled), a ground observer could be subjected to multiple laser pulses. In that case, the MPE would be reduced from the single-pulse value, MPE_P, to the multiple-pulse value, MPE_T, and the corresponding NOHD would increase. This situation is also typical for the new topo-bathy airborne lidar systems that use high-PRF/low-pulse-energy lasers. For these systems, where the laser PRF can be in the 100s of kHz, a ground

observer could be exposed to multiple pulses, even when the aircraft is moving and the system is scanning.

The NOHD limit is for the unaided eye. However, if the laser radiation is viewed through magnifying optical instruments, the NOHD will increase to a distance called the Extended Ocular Hazard Distance (eNOHD or EOHD), which can be calculated using the following equation:

$$eNOHD = NOHD \times \sqrt{G} \tag{4.5.6}$$

where G is the gain, or magnifying power, of the instrument. When viewing with typical 7x50 mm binoculars, with a gain of 49 and optical transmission of 90%, the eNOHD is 7x greater than the NOHD. For the above example, the eNOHD ≈ 1670 m. For most ALB systems, the eNOHD is >1000 m. It is impractical for ALB systems to operate at such high altitudes, as performance would be severely limited. Thus, when surveying over populated areas or regions with many boats operating in the waters, the recommended practice is to temporarily turn off the laser, to minimize potential viewing hazards to ground-based observers.

Nevertheless, for the above laser parameters and a flying height of 300 m, studies have shown that if a person sees a laser pulse directly with binoculars, the probability of eye damage in daytime is $< 3 \times 10^{-3}$. For the sake of comparison, the probability of eye damage at the eNOHD of 1670 m is $< 7 \times 10^{-9}$. One can see that the damage probability at a distance of 300 m is greater than that at the eNOHD, but is still small.

Furthermore, a study was conducted for SHOALS system operation to estimate the probability of eye injury in one year of operation. The analysis used a statistical model that took into consideration the following probabilities:

- Probability of a person in a boat being illuminated by the laser per unit area
- Probability of a person in a boat looking at the aircraft with binoculars
- Probability of eye damage when that person sees the laser light through binoculars
- Total area covered in one year

The above probabilities were determined individually, and then multiplied together to determine the probability of eye injury in one year of operation. The results of the analysis showed that the probability was 10^{-3} for binocular viewing. Similar analysis showed a probability of 10^{-10} for unaided viewing.

4.6.2 ALB Eye Safety Features

ALB systems incorporate many safety features to prevent accidental exposure to a person. These include the following:

- Eye safe range (NOHD) monitor
- Eye safe power-on default
- Unsafe operation warning
- Laser emission delay
- Laser status displays
- Hardware safety interlock
- Shutter control

One of the key operational features of an ALB system is the ability to automatically stop laser emission if the aircraft altitude falls below NOHD. ALB systems monitor the range to the ground/water on a shot-by-

eCommons (2019) https://doi.org10.7298/jxm9-g971

shot basis. As an example, if a pre-determined number of consecutive laser pulses are detected that have a range < NOHD, the laser emission is stopped immediately. Several consecutive pulses are allowed, so that the laser is not shut off due to false alarms such as haze in the beam path, insects, birds, etc. Laser emission does not resume automatically when the aircraft rises above the minimum eye safe range again. It must be re-initiated by the operator. The system also inhibits laser firing in the event of an attempt to activate the laser before the aircraft has reached the minimum eye safe range.

Additionally, a laser emission pause switch is provided to the pilot/co-pilot to permit shutting off laser emission whenever necessary. Likewise, the system operator has the capability to shut down the laser at any time, if needed.

4.7 Bathymetric System Design and Optimization of Parameters

V. Feygels, Yu. Kopilevich

4.7.1 Optimization criteria of bottom, scattering layers and objects detection

The problem of comparing different lidar systems (by which we mean the entire transmitting-receiving optical block, down to the detector) inevitably calls for the application of statistical decision theory (Raiffa 1968). From the point of view of this theory, the diagnostic effectiveness of a lidar system, whether it is a sounding or imaging system, should be evaluated via the possible (or theoretically achievable with the use of the system in question) performance of an ideal detector (Helstrom 1968; B. Levin 1960). Optimization of the lidar system, i.e., choosing the most appropriate optical parameters for the transmitting and receiving devices, and selecting the most appropriate elements, from the laser to the spectral selector and detector, is reduced to a maximization of the overall effectiveness (Victor I. Feigels and Kopilevich 1994b, 1996; Victor I. Feigels 1992).

In lidar bathymetry the system performance is characterized by the highest probability of bottom detection achievable at a given false alarm probability – the so-called Neyman–Pearson criterion (Helstrom 1968; Egan 1975). Analogous characterization of system effectiveness may be employed when other applications of sounding lidar are considered, like submerged object location, or detection of water layers with contrasting optical properties (Victor I. Feigels and Kopilevich 1993b; Kopilevich and Feigels 1993; Victor I. Feigels and Kopilevich 1994a). In all cases, optimal signal processing (employed by the “ideal observer” theory) means making the best threshold choice to discriminate between “wanted, or useful signal plus noise”, and “noise only”.

Synthesis of an optimal working algorithm for imaging lidar (Ulich et al. 1997; Keeler and Ulich 1994), which includes image processing down to decision making regarding the presence of an object and estimation of its coordinates, appears to be a very complicated problem. Experience with sounding lidar system design suggests that one can assume that the performance evaluation of the receiving and transmitting segments of the system may be performed independently of the image processing method. Such an approach (hereafter referred to as “quasi-optimal approach”) seems to be quite acceptable as a first step. Under this assumption, the output part of an imaging lidar – the image processing unit – may be analyzed independently. This allows the optical transmitting and receiving (pre-detector) block, together with the photo detector to be treated separately. The photo detector may include PMT matrices and linear arrays, Microchannel Plate Photomultiplier Tubes (MCP-PMTs), APD linear arrays, CCDs, CMOSs, or

streak tube; (see e.g. the Hamamatsu Photonics web site http://www.hamamatsu.com/us/en/index.html). A detailed description of a streak tube used in a lidar imaging application may be found in Degnan et al. (2011).

Within the framework of the quasi-optimal approach, the problem of performance evaluation of the optical block of an imaging lidar may be reduced to a one-dimensional system by examining input signals at an individual pixel of a matrix detector. It is obvious that such an "elementary lidar" may be treated in the same manner as sounding lidar (bearing in mind the essential differences between a single-pixel of any of the detectors named above and individual PMT or APD).

In general, evaluation of lidar system performance (as defined above), requires rather tedious computations with given probability distributions for "useful signal plus noise" and for "noise only", and thus the problem of system optimization (i.e., finding the parameter values which maximize the system effectiveness) seems to be too complicated to be usable. In practice, the problem is replaced by the problem of maximization of a single parameter – a discriminability index (Egan 1975), which characterizes the degree of overlap between the two distributions, and is determined by only the lowest moments of the distributions. Implementation of this practical approach presupposes (often implicitly) that the system effectiveness (acquisition probability for a given probability of false alarm) is uniquely determined by the chosen discriminability index via a monotonically increasing function.

The signal-to noise ratio (SNR) is the best known example of a discriminability index. It is used to great advantage for signal detection problems in the radio and microwave regions. SNR use in these fields is justified by the fact that, to sufficient accuracy, random variables representing useful signal and noise follow normal distributions of equal variance (Helstrom 1968; Egan 1975). The latter property is afforded by a prevailing contribution from thermal (kT) noise to fluctuations of both signals, and the noise does not depend on the presence of a useful signal.

Despite the wide parallels between radio and optical detection/ranging methods, the lidar signal detection problem is fundamentally different from that for radar. As described aphoristically by E. R. Pike (1974), *"Between the microwave and optical regions of the spectrum we cross the value of $h\nu$ equal to kT. In the optical region the detector is effectively cold and operates by annihilation only of photons"*. Nonetheless, the general unsuitability of the SNR for the evaluation of lidar effectiveness is often ignored. It is quite obvious, however, that the basic assumption of equal variance for both useful signal and noise distributions is inappropriate for shot noise or photon noise of a quantum nature, both of which play leading roles, particularly with low-noise PMT, APD (see e.g., the Hamamatsu Photonics web site http://www.hamamatsu.com/us/en/index.html) or streak-tube detectors with their relative greater noise level (Wu et al. 2012; H. Yang et al. 2012).

In addition, replacement of a discrete Poisson distribution of photo-electrons by a continuous normal distribution may produce a significant error, especially when registered photo-electrons may only number in the tens or even single digits, as is the case for the short-gated, single-pixel detectors of imaging lidar.

An effective replacement for the SNR as a measure of detectability in lidar problems – a "D-index of discriminability" (Egan 1975; Sakitt 1973) – is considered in the next Section.

eCommons (2019) https://doi.org10.7298/jxm9-g971

4.7.2 Concept and use of the D-index of discriminability

Let $p_{sn}(m)$ be a known probability distribution for "signal with noise" measured by the number, m, of photo-electrons released at detector load during a given time interval, Δt, of registration, i.e. for the lidar response from bottom, layer, object, etc., together with additional noise.

Let $p_n(m)$ be the analogous probability distribution for the "noise only" case when useful signal to be detected (from bottom, layer, object, etc.) is absent. When analysis of the sounding lidar effectiveness is performed (specifically, when the marginal operation ability of a system is estimated), it is possible to describe the distribution functions for lidar response at the photo-detector output by Poisson distributions in accordance with the formulas:

$$p_{sn}(m) = \frac{(\bar{m}_s + \bar{m}_n)^m}{m!} e^{-(\bar{m}_s+\bar{m}_n)} \quad , \qquad p_n(m) = \frac{(\bar{m}_n)^m}{m!} e^{-(\bar{m}_n)} \tag{4.6.1}$$

where: $\bar{m}_s$ is the mean number of "signal" photoelectrons registered during the time interval Δt;

$\bar{m}_n$ is the same for "noise" photoelectrons.

Then, for the false alarm probability, P_f, and the acquisition probability, P_{ac}, one has

$$P_f(m) = 1 - \sum_{m=0}^{m_0-1} \frac{(\bar{m}_n)^m}{m!} e^{-(\bar{m}_n)} \quad , \quad P_{ac}(m) = 1 - \sum_{m=0}^{m_0-1} \frac{(\bar{m}_s + \bar{m}_n)^m}{m!} e^{-(\bar{m}_s+\bar{m}_n)} \tag{4.6.2}$$

with m_0 being the threshold of the discriminator.

From (3.6.2), P_{ac} may be evaluated, for a given value of P_f, as a function of two variables, $\bar{m}_s$ and $\bar{m}_n$ (the threshold, m_0, does not enter the final dependence). It is quite obvious that such an approach is difficult to apply to the problem of system optimization. It turns out, however, that a single parameter, D, may be introduced in such a way that P_{ac} for a given P_f is determined, to sufficient accuracy, by D only.

The D-index parameter was first introduced by Sakitt (1973) as a measure of distinguishability between two probability distributions, A and B, for random quantities at the detector output in the absence (A) and in the presence (B) of the signal to be detected. According to Egan (1975), the parameter is

$$D = \frac{|i_B - i_A|}{(S_A \cdot S_B)^{1/2}} \tag{4.6.3}$$

where i_A and i_B are the mean values for distributions A and B, respectively;

S_A and S_B are the corresponding standard deviations.

Specifically, for Poisson processes p_n and p_{sn} from Equation (4.6.1), the D-parameter is expressed by the ratio:

$$D = \frac{\bar{m}_s}{[(\bar{m}_s + \bar{m}_n) \cdot \bar{m}_n]^{1/4}} \tag{4.6.4}$$

The applicability of the D-index is demonstrated in Figure 4.6.1 (curves 1–4), where results of P_{ac} evaluated from Equation (4.6.3) are presented as functions of D for various values of $\bar{m}_n$. The discrepancy among the curves appears to be insignificant.

It is evident from (4.6.4) that D coincides with the "signal to noise ratio" (*SNR*) when $S_A = S_B$, and thus, the D-index may be regarded as a generalization of the *SNR* for optics. Application of the *SNR* in the form

$$SNR = \frac{\bar{m}_s}{\sqrt{\bar{m}_n}} \tag{4.6.5}$$

to P_{ac} evaluation, however, is open to significant errors, as can be seen in Figure 3.6.2; the P_{ac} *(SNR)* curve essentially depends on $\bar{m}_n$, and underestimates P_{ac} at low numbers of photo-electrons. Moreover, the SNR criterion justifies an improvement which adds SNR, even if it is accompanied by a sufficient loss in $\bar{m}_s$, and thus, as is apparent in Figure 3.6.2, leads to degradation of lidar performance. A typical situation would be the case of using a polarization filter on the incoming signal (Vasilkov, Goldin, and Gureev 1993); the improvement in contrast is not worth the inevitable decrease in the total number of registered photons.

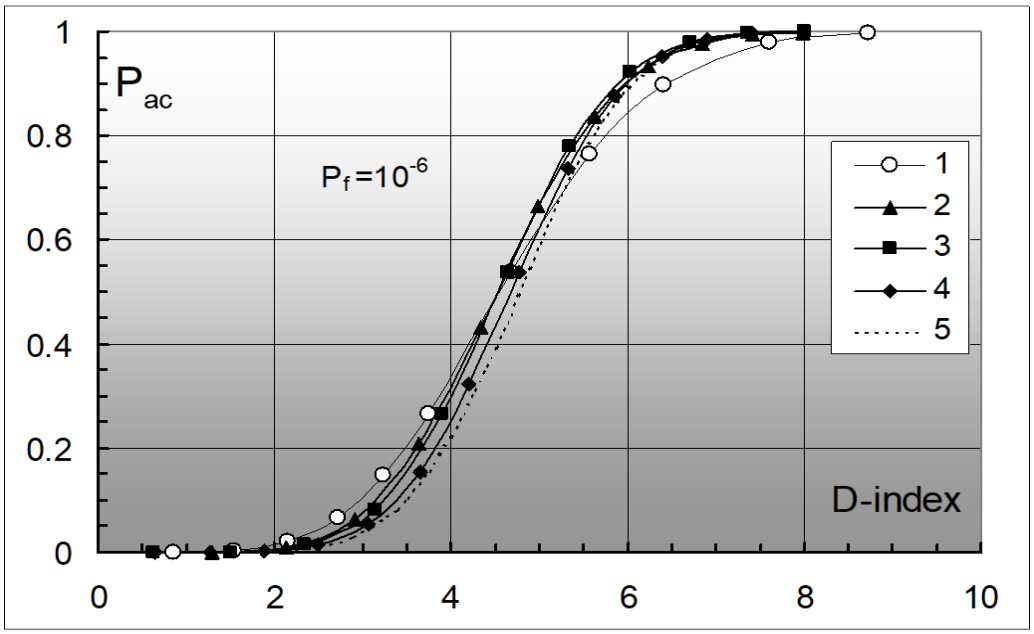

Figure 4.6.1. Plot of the acquisition probability, P_{ac}, versus the D-index for fixed false-alarm probability, $P_f = 10^{-6}$. Curves 1–4 corresponds to Poisson distributions in equation (4.6.1) with $\bar{m}_n = 1$; 8; 40; and 151, respectively. Curve 5 corresponds to the approximation given by equation (4.6.8).

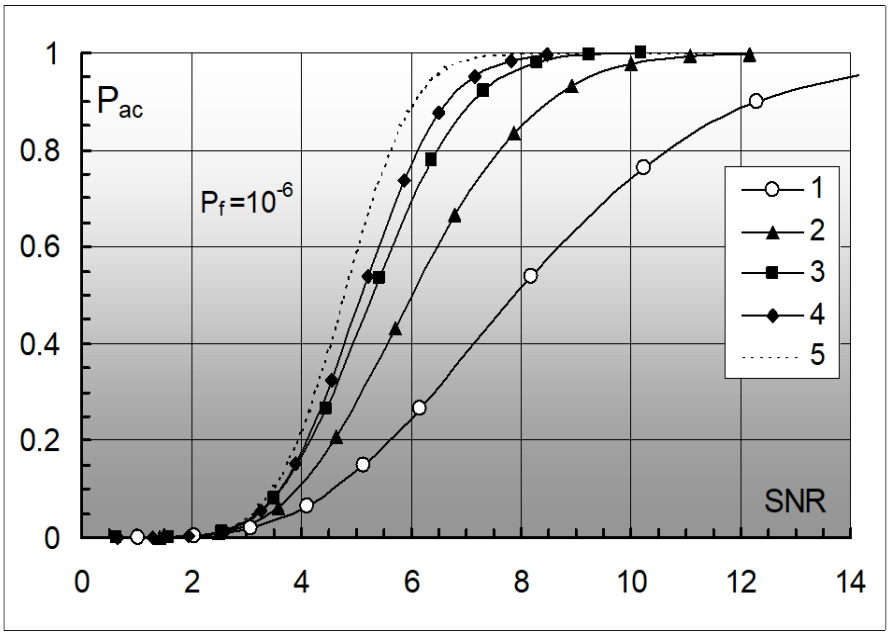

Figure 4.6.2. Plot of the acquisition probability, P_{ac}, versus the SNR for fixed false-alarm probability, $P_{ac} = 10^{-6}$. Curves 1–4 corresponds to Poisson distributions (Figure (4.6.1)) with $\bar{m}_n$ =1; 8; 40; and 151, respectively. Curve 5 corresponds to the approximation (4.6.8).

In reality, the conditions under which lidar systems are employed are almost always characterized by a large number and variety of noise factors and processes simultaneously. It is convenient, then, to replace Poisson distributions by appropriate normal distribution functions for continuous random variables instead of discrete ones. This leads to a comparatively simple expression for P_{ac} in terms of P_f (Lebed'ko, Porfir'ev, and Hajtun 1984):

$$P_{ac} = \frac{1}{2} Erfc\left[Erfc^{-1}(2P_f) \frac{\sqrt{\bar{m}_n}}{\sqrt{\bar{m}_n + \bar{m}_s}} - \frac{\bar{m}_s}{\sqrt{\bar{m}_n + \bar{m}_s}} \right] \tag{4.6.6}$$

where $Erfc(x) = \frac{2}{\sqrt{\pi}} \int_x^\infty exp(-y^2) dy$ is the error function (Abramowitz and Stegun 1972), and $Erfc^{-1}(x)$ is the corresponding inverse function, $Erfc[Erfc^{-1}(x)] = x$

When

$$\bar{m}_n \gg \bar{m}_s \tag{4.6.7}$$

equation (4.6.6) may be rewritten as

$$P_{ac} = \frac{1}{2} Erfc\left[Erfc^{-1}(2P_f) - D \right] , \quad \text{or} \quad P_{ac} = \frac{1}{2} Erfc\left[Erfc^{-1}(2P_f) - SNR \right] \tag{4.6.8}$$

because under the condition (3.6.7), *D* and *SNR* coincide [cf. Equations (4.6.4) and (4.6.5)].

The use of a continuous normal distributions requires that the number of registered photoelectrons be large enough; in particular, the replacement is not valid when the threshold, m_0, is less than 15 and/or when P_f does not exceed 10^{-4} (Kuriksha 1973). The requirement, together with inequality (4.6.7),

eCommons (2019) https://doi.org10.7298/jxm9-g971

appears to form the condition of *SNR* applicability to the problem in question as an exhaustive characteristic of system effectiveness (see (4.6.2)). On the other hand, the dependence of $P_{ac}(D)$, shown in Equation (4.6.8) is presented as curve 5 in Figure 4.6.1, does not differ noticeably from those obtained with the use of initial Poisson distributions (4.6.1) because under the condition (4.6.7), D and *SNR* coincide [cf. Equations (4.6.4) and (4.6.5)].

The above consideration demonstrates that the efficiency of a lidar system may be uniquely determined, to sufficient accuracy, by the *D*-index. System optimization may thus be reduced to maximization of the *D*-index, in accordance with plots of P_{ac} versus *D* at various P_f in (4.6.3). It should be particularly emphasized that the *D*-parameter is easy-to-use because it may be obtained with the known moments of the corresponding distributions only, and normalization of *a posteriori* probabilities is not necessary (as a rule, it is a rather complicated problem).

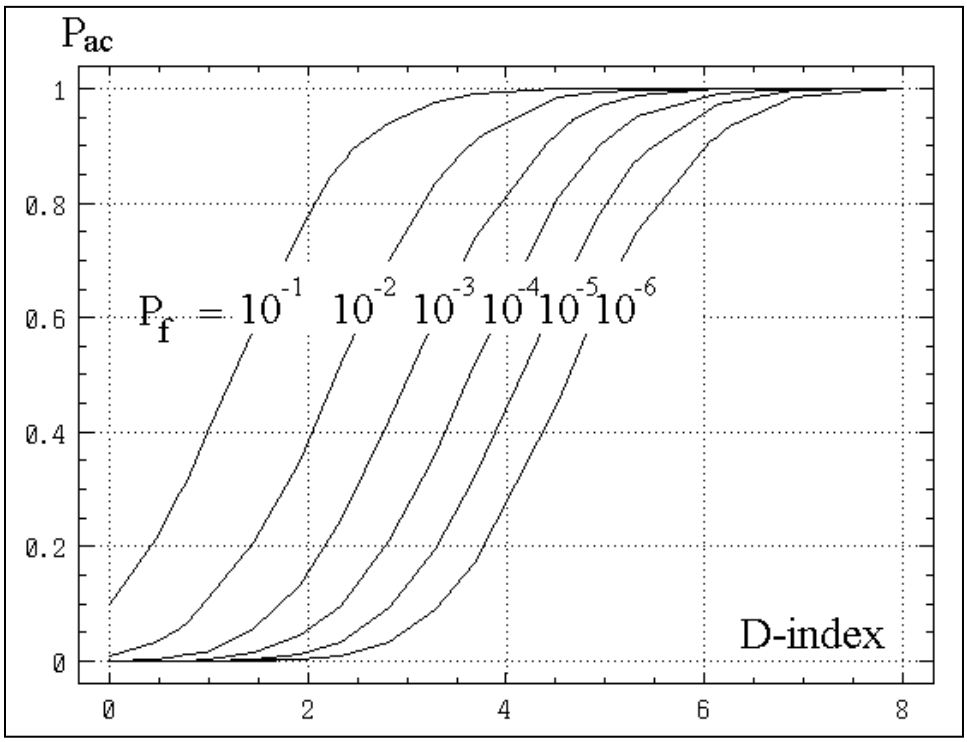

Figure 4.6.3. The connection between D-index and the acquisition probability, P_{ac} , for different levels of false-alarm probability, P_f , in the case of Poisson distribution.

4.7.3 Implementation of D-index analysis to lidar optimization

It is obvious that concept of an “optimal” system cannot be universal, i.e. independent of the application of the lidar system (bathymetry, water column sounding, submerged objects detection, etc.) and the external conditions (day or night time, optical properties of the water, bottom/object reflectivity, and so on). That is, optimal system parameters for one situation may be far from optimal in another.

The power, P, of the light coming to lidar's detector, together with the intrinsic noise sources at the detector, may be written as the sum:

$$P = P_{sun} + P'_{sun} + P_{bw} + P'_{bw} + P''_{bw} + P_{ba} + P'_{ba} + P''_{ba} + \{P_{bot} + P'_{bot} + P''_{bot}\} + \{P_{obj} + P'_{obj} + P''_{obj}\} + P_{kT} + P_d \quad (4.6.9)$$

The subscript *"sun"* indicates the terms related to sunlight exposure, *"bw"* to light pulse power backscattered by the water-body, *"ba"* to backscattering in the atmosphere (more exactly, these terms result from laser pulse reflection at the sea surface, consequent backscattering in the air, and surface reflection back to the receiver aperture); terms with the subscripts *"bot"* and *"obj"* are related to laser light reflected by the bottom and an object to be detected, respectively.

Symbols with one prime stand for fluctuation components of corresponding quantities caused by sea surface roughness, variations of atmospheric transitivity, water characteristics and bottom (object) reflectivity, as well as uncontrolled variations in platform altitude and orientation, receiver field of view (FOV), and so on. Symbols with double primes correspond to random deviations induced by laser pulse power variations.

P_{kT} and P_d are the terms corresponding to thermal noise (limited to the detector input) and the dark current of the detector, respectively. All of the single-prime components and the sum of double primed components may be treated as statistically independent random variables with zero mean values. They are also independent of shot-noise fluctuations (contained in P_{sun}, P_{bw}, P_{ba}, P_{bot}, P_{obj}, and P_d) as well as of thermal noise, P_{kt}.

If the lidar application under consideration is the analysis of inherent water optical parameters, the two terms in braces in Equation (4.6.9) have to be omitted.

In the application is bathymetry or the detection of submerged object, either $\{P_{bot} + P'_{bot} + P''_{bot}\}$ or $\{P_{obj} + P'_{obj} + P''_{obj}\}$ must be added to the expression for the total power at the receiver. In that case, the first term of the sum in braces, P_{bot} *or* P_{obj}, represents the useful signal, while $P_{sun} + P_{bw} + P_{ba} + P_{kT} + P_d$ comprise the background and thus represent noise components (in addition to the noise caused by the signal itself and the other two fluctuation terms in the braces).

To evaluate the D-index in the case of bathymetry, one has to apply the definition in equation (4.6.3) to the following two alternative events:

(A) Useful signal is absent.

In the absence of a useful signal, the power, P_A, at the detector, in view of (4.6.9), is given by

$$P = P_{sun} + P'_{sun} + P_{bw} + P'_{bw} + P''_{bw} + P_{ba} + P'_{ba} + P''_{ba} + P_{kT} + P_d \quad . \quad (4.6.10)$$

In accordance with the above, the mean value, i_A, of the corresponding distribution is

$$\bar{P}_A = i_A = \bar{P}_{sun} + \bar{P}_{bw} + \bar{P}_{ba} + \bar{P}_{kT} + \bar{P}_d \quad . \quad (4.6.11)$$

In order to derive an expression for variance, S_A^2, the following reasoning has to be taken into account. The power, P, of light at the input of a receiving/amplifying device (PMT, or photo-diode with electric

eCommons (2019) https://doi.org10.7298/jxm9-g971

signal amplifier), is related to the (random) number, m, of photoelectrons generated at the device photocathode during the time Δt (accumulation time interval), by the formula

$$m = P \cdot \left(\frac{s_\lambda \Delta t}{e}\right) = P/C \tag{4.6.12}$$

where s_λ is the spectral sensitivity of the detector;

e is the electron charge;

Δt is the digitizing time interval;

$C = e/(s_\lambda \Delta t)$

It is commonly assumed that the random variable m follows the Poisson distribution law, and thus, $m = S^2(m) = \overline{(m - \bar{m})^2}$. If reduced to the detector input, the latter yields:

$$S^2(P) = \overline{(P - \bar{P})^2} = (m - \bar{m})^2 \cdot C^2 = \bar{P} \cdot C \tag{4.6.13}$$

Following equation (4.6.13), the variance, $S^2(P_A) = S_A^2$, of the power, P_A , from equation (4.6.10)) is given by

$$\begin{aligned} S^2(P_A) = (\bar{P}_{sum} + \bar{P}_{bw} + \bar{P}_{ba} + \bar{P}_d) \cdot C + S^2(P_{kT}) \\ + \varepsilon_{sun}^2 \bar{P}_{sun}^2 + \varepsilon_{bw}^2 \bar{P}_{bw}^2 + \varepsilon_{ba}^2 \bar{P}_{ba}^2 + \varepsilon_{sys}^2 \left(\bar{P}_{bw}^2 + \bar{P}_{ba}^2\right) \end{aligned} \tag{4.6.14}$$

where the variance of the sum of the independent variables is represented by the sum of their variances, and equation (4.6.13) is applied to the variance of the sum $(\bar{P}_{sum} + \bar{P}_{bw} + \bar{P}_{ba} + \bar{P}_d)$. Here, ε_{sun} , ε_{bw} , and ε_{ba} are the normalized variances of P'_{sun} , P'_{bw}, and P'_{ba}, that is:

$$\varepsilon_\alpha = S\,(P'_\alpha)/\bar{P}_\alpha \tag{4.6.15}$$

where the subscript α stands for *"sun", "bw", or "ba"* correspondingly. Analogously, ε_{sys} is the normalized variance of $(P''_{bw} + P''_{ba})$.

(B) Useful signal is present.

In this case,

$$\begin{aligned} P_{\boldsymbol{B}} = P_{sun} + P'_{sun} + P_{bw} + P'_{bw} + P''_{bw} + P_{ba} + P'_{ba} + P''_{ba} \; + \; P_{bot} + P'_{bot} + P''_{bot} + P_{kT} \\ + P_d \end{aligned} \tag{4.6.16}$$

$$\bar{P}_B = i_B = \bar{P}_{sun} + \bar{P}_{bw} + \bar{P}_{ba} + \bar{P}_{kT} + \bar{P}_d + + \bar{P}_{bot} \quad ; \tag{4.6.17}$$

$$\begin{aligned} S^2(P_B) = (\bar{P}_{sum} + \bar{P}_{bw} + \bar{P}_{ba} + \bar{P}_d + \bar{P}_{bot}) \cdot C + S^2(P_{kT}) \\ + \varepsilon_{sun}^2 \bar{P}_{sun}^2 + \varepsilon_{bw}^2 \bar{P}_{bw}^2 + \varepsilon_{ba}^2 \bar{P}_{ba}^2 + \varepsilon_{bot}^2 \bar{P}_{bot}^2 + \varepsilon_{sys}^2 \left(\bar{P}_{bw}^2 + \bar{P}_{ba}^2 + \bar{P}_{bot}^2\right) \end{aligned} \tag{4.6.18}$$

where ε_{bot} is the normalized variance of P'_{bot}.

Substitution of equations (4.6.10)-(4.6.18) into (4.6.3) yields:

$$D_{bot} = P_{bot}/\left[\left(C\,\overline{P}_B + B_{bot}^2\right)\cdot\left(C(\overline{P}_B + \overline{P}_{bot}) + B_{bot}^2 - \varepsilon_{bot}^2(\bar{P}_{bot})^2 - \varepsilon_{sys}^2(\bar{P}_{bot})^2\right)\right]^{1/4} \quad (4.6.19)$$

where

$$B_{bot}^2 = S^2(P_{kT}) + \varepsilon_{sun}^2\bar{P}_{sun}^2 + \varepsilon_{bw}^2\bar{P}_{bw}^2 + \varepsilon_{ba}^2\bar{P}_{ba}^2 + \varepsilon_{bot}^2\bar{P}_{bot}^2 + \varepsilon_{sys}^2\left(\bar{P}_{bw}^2 + \bar{P}_{ba}^2 + \bar{P}_{bot}^2\right) \quad . \quad (4.6.20)$$

Now we employ the well-known expression for variance of thermal fluctuations of output current through the detector load resistor, R_L , $2kT/(R_L\Delta t)$, where k is the Boltzmann constant, and T is absolute temperature. The corresponding variance of the equivalent light power at the detector input is

$$S^2(P_{kT}) = \frac{2kT}{R_L\cdot\Delta t}\cdot\frac{1}{M^2 s_\lambda^2} \quad , \quad (4.6.21)$$

with M being the receiver amplification factor.

In the case of a PMT detector, the contribution of thermal noise [i.e., the term $S^2(P_{kT})$ in (4.6.21)] is usually neglected as compared with the shot noise (Lebed'ko, Porfir'ev, and Hajtun 1984); the factor C in this case should be modified in order to take into account the noise amplification by the dynode system: $C \Rightarrow C(1 + b_d)$, where the parameter b_d, which accounts for the additional contribution by the PMT dynodes to the shot noise, is in the range $1.5 \le b_d \le 3$ (Lebed'ko, Porfir'ev, and Hajtun 1984).

On the other hand, for photodiodes and other solid state detectors (including CCDs) the shot noise caused by useful signals is much smaller than the dark current contribution (Lebed'ko, Porfir'ev, and Hajtun 1984). Streak tube detectors (McLean and Murray 1998) and ICCDs (Moran et al. 1997) seem to fall into an intermediate category, for which all the sources of noises should be considered.

The application of a lidar system to the detection of an opaque object in water is similar to bathymetry. For the case in question equation (4.6.23), (4.6.19), and (4.6.20) have to be modified:

$$D_{bot} = \overline{P}_{obj}/\left[\left(C\,\overline{P}_B + B_{obj}^2\right)\cdot\left(C\left(\overline{P}_B - \overline{P}_{obj}\right) + B_{obj}^2 - \varepsilon_{obj}^2\left(\bar{P}_{obj}\right)^2 - \varepsilon_{sys}^2\left(\bar{P}_{obj}\right)^2\right)\right]^{1/4} \quad (4.6.22)$$

Where

$$\bar{P}_B = i_B = \bar{P}_{sun} + \bar{P}_{bw} + \bar{P}_{ba} + \bar{P}_{kT} + \bar{P}_d + \bar{P}_{obj} \quad ; \quad (4.6.23)$$

$$B_{bot}^2 = S^2(P_{kT}) + \varepsilon_{sun}^2\bar{P}_{sun}^2 + \varepsilon_{bw}^2\bar{P}_{bw}^2 + \varepsilon_{ba}^2\bar{P}_{ba}^2 + \varepsilon_{obj}^2\bar{P}_{obj}^2 + \varepsilon_{sys}^2\left(\bar{P}_{bw}^2 + \bar{P}_{ba}^2 + \bar{P}_{obj}^2\right) \quad . \quad (4.6.24)$$

with ε_{obj} being the normalized variance of P'_{obj}.

An effective approach for estimating P'_{obj} was proposed in Dolin & Levin (1991), accounting for observation conditions and object features, as well as water optical characteristics.

When the purpose of a lidar survey is the detection of subsurface water layers with contrasting optical parameters (e.g., for polluted stream location, biological productivity analysis, etc.), the following expression is valid:

$$D_{lay} = \frac{\Delta\bar{P}_{bw}}{\left[\left(C\bar{P}_B + B_{lay}^2\right)\cdot\left(C(\bar{P}_B + \Delta\,\bar{P}_{bw}) + B_{lay}^2 - \left(\varepsilon_{bw}^2 + \varepsilon_{sys}^2\right)(2\bar{P}_{bw}^{-}\cdot\Delta\bar{P}_{bw} + (\Delta\bar{P}_{bw})^2)\right)\right]^{1/4}} \quad (4.6.25)$$

where

$$\bar{P}_B = i_B = \bar{P}_{sun} + \bar{P}_{bw}^{-} + \bar{P}_{ba} + \bar{P}_{kT} + \bar{P}_d \quad ; \quad (4.6.26)$$

$$B_{lay}^2 = S^2(P_{kT}) + \varepsilon_{sun}^2\bar{P}_{sun}^2 + \varepsilon_{bw}^2\bar{P}_{bw}^{-\,2} + \varepsilon_{ba}^2\bar{P}_{ba}^2 + \varepsilon_{sys}^2\left(\bar{P}_{bw}^{-\,2} + \bar{P}_{ba}^2\right) \quad . \quad (4.6.27)$$

Here $\Delta\bar{P}_{bw}$ is the increase in backscattered signal from within the layer, $\Delta\bar{P}_{bw} = |\bar{P}_{bw}^{+} - \bar{P}_{bw}^{-}|$, that is, the difference between the value of backscattered signal power from the above-lying water, $\bar{P}_{bw}^{+}$, and that from the layer to be detected, $\bar{P}_{bw}^{-}$.

4.7.4 Optimization of lidar system parameters

The formulae for *D*-index of discriminability obtained in Section 4.6.3 may be applied to evaluate optimal values of a separate lidar system parameter. Of course, the formulae have to be complemented with expressions for light fluxes caused by bottom reflection of the sounding laser beam, P_{bot}, water backscattering, P_{bw}, and so on, as well as for P_{obj}. The necessary expressions are to be derived from an adequate physical model of laser sounding of ocean waters (see, e.g., Dolin and Levin (1991), Dolin et al. (1988)).

Results presented here are obtained with the use of a PC program, "OCEAN-SCIENTIFIC" (Victor I. Feigels and Kopilevich 1993a); the models used for the sounding laser beam propagation and for the optical properties of ocean water have been detailed in Viktor I Feigels & Kopilevich (L. S. Dolin and Levin 1991). Sounding conditions and values of system parameters (with the exception of those varied or otherwise specified) are summarized in Table1:

Table 4.2 : Sounding conditions and systems parameters

Lidar platform altitude	200 m
Wind velocity above the sea surface	5 m/s;
Meteorological visibility	5 km;
ε_{sys} (laser pulse power fluctuations, random variations in the PMP gain, etc.)	15 %;
Beam attenuation coefficient, c,	0.2 and 0.5 m^{-1}
Zenith sun angle	20^0
Receiver FOV	50 mr
Sounding laser power	1 MW
Receiving system diameter	0.2 m
Receiver spectral bandpass half-width	1 nm
Detector photo-cathode	S-20
Type of the bottom	sand

Figure 4.6.4 depicts the D-index as a function of the receiver input pupil diameter (application to bathymetry; bright day sounding conditions). It is seen that systems with receiver aperture diameters above 15-20 cm, have no advantages under day-time conditions. The curve in Figure 4.6.5 demonstrates only a formal influence of optical filter half-width. In actual practice, one has to account for the fact that reduction in bandpass beyond 0.1-1.0 nm is followed by a significant decrease in its transmittance, restricts the system FOV, and requires additional temperature control (better than ± 0.02°C) cell (Rees et al. 1996). These negative effects are particularly unsuitable at night, when there are no advantages to narrow optical filtering.

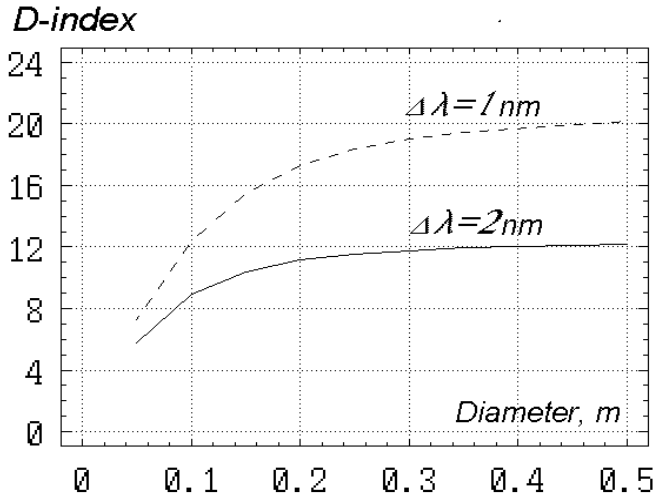

Figure 4.6.4. D-index for a mud bottom sounding (depth 25-m; "bright-day" conditions) as a function of receiver aperture diameter for different spectral selector bandpass half-width.

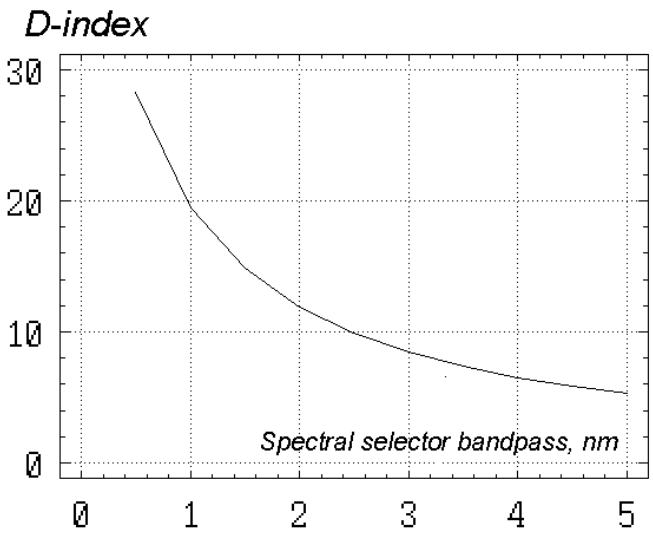

Figure 4.6.5. D-index versus spectral selector bandpass for mud bottom sounding at 25-m depth ("bright-day" conditions; receiving system diameter - 0.2 m)

A more recent version of the software, OS-2001 is described in Feigels et al. (Victor I. Feigels et al. 2002) and with a more sophisticated theoretical background in Kopilevich et al. (Kopilevich, Feygels, and Surkov 2003).

To clarify the combined effect of the receiver pupil area, spectral bandpass and transmittance of the optical receiver trunk, as well as of the laser pulse power, it is convenient to consider two limiting cases (Victor I. Feigels and Kopilevich 1994b)

A. "ideal night" conditions: zero sun light exposure, unperturbed sea surface, and negligible system instability. Then

$$D \sim \sqrt{P_T A_R \tau_R} \tag{4.6.28}$$

B. "bright-day" conditions: rough sea, and considerable system instability. In this case a simple expression for the D-index is valid:

$$D \sim P_T \sqrt{A_R / \Delta\lambda} \tag{4.6.29}$$

Where P_T is the laser transmitter power, A_R is the receiver aperture area, τ_R is the optical receiver trunk transmittance (filter included), and $\Delta\lambda$ is the receiver spectral bandpass half-width.

Equation (4.6.29) leads to an unexpected conclusion: the effectiveness of the lidar system does not depend on the receiver aperture area when the background light power significantly exceeds the echo-signal from the bottom (for bathymetry), or from the scattering layer to be detected.

Proceeding to the problem of field-of-view (FOV) optimization, it is important to remember that we are considering a sounding lidar system; for imaging system the following may be applied to an “elementary” lidar with separate pixel taken as detector.

When the effect of surface waves, system instability and detector thermal noise may be neglected, the expression for the *D*-index for case **A** ("ideal night") is

$$D = c_1 F_{obj}\left[m\theta, m\theta_{obj}, bh\right] \cdot \sqrt{F[m\theta, bh]} \tag{4.6.30}$$

and for case **B** ("bright-day") it is

$$D = c_2 \frac{F_{obj}\left[m\theta, m\theta_{obj}, bh\right] \cdot F[m\theta, bh]}{FOV} \tag{4.6.31}$$

where the constants c_1 and c_2 do not depend on the receiving system FOV, and where

$F[*,*]$ is a function, introduced by Dolin and Levin (1991) to describe the effect of FOV and the shape of scattering phase function on the rate of decrease in P_{bot} and P_{bw};

$F[*,*,*]$ is a special function (L. S. Dolin and Levin 1991) accounting for the object angular dimension, θ_{obj}, reduced to the sea surface;

H and h are the lidar platform altitude and sounding depth, correspondingly;

n is the refractive index and *b* is the scattering coefficient of the water;

$\theta = \tan^{-1}\left[0.5 \cdot FOV\left(\frac{H}{h} + \frac{1}{n}\right)\right]$;

m is a parameter in the scattering phase function approximation of the form $p(\gamma) \sim exp(-m\gamma)/\gamma$.

When angular dimension of the object to be detected is big enough, $\theta_{obj} \gg \theta$ (as it is, e.g., in bathymetry), $F_{obj}\left[m\theta, m\theta_{obj}, bh\right] \equiv 1$, and (4.6.30) and (4.6.31) may be rewritten as:

$$D = c_1\sqrt{F[m\theta, bh]} \qquad \text{case } \mathbf{A} \quad , \tag{4.6.32}$$

$$D = c_2\, F[m\theta, bh]/\tan\theta \qquad \text{case } \mathbf{B} \quad . \tag{4.6.33}$$

Setting the derivative, $dD/d\theta$, equal to zero, we obtain an equation for θ_{opt}, *maximizing D* for a given value of bh and m. The dependence of θ_{opt} (case **B**) on optical scattering depth, bh, is depicted in Figure 4.6.6 for $m = 8$. It is seen that θ_{opt} tends to ≈30° for maximal scattering depth values.

From (4.6.33), the FOV in the case of strong sunlight is given by

$$FOV_{opt} \approx \frac{2\tan\left(\theta_{opt}\right)}{H/h} \tag{4.6.34}$$

Comparison of the result with Guenther and Thomas (1984) data shows that the FOV_{opt} for different systems lies in the angle interval related to the 50-70% level of bottom reflected energy.

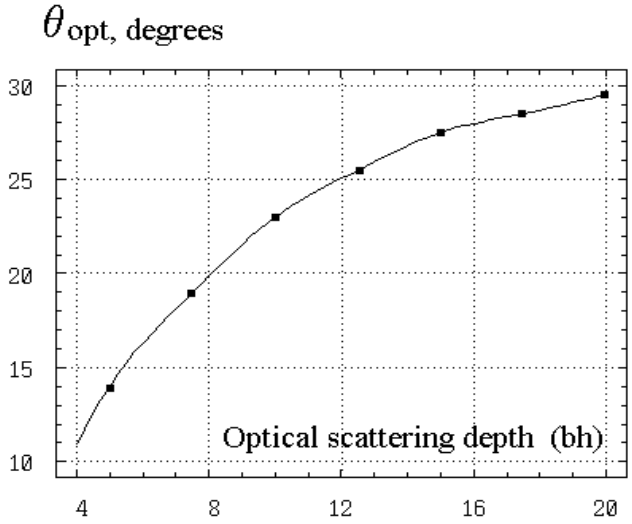

Figure 4.6.6. The optimal FOV value, θ opt,, as a function of dimensionless optical scattering thickness, *bh*, of the water for large object detection and "bright-day" conditions (case B).

4.7.5 Laser source wavelength optimization

The problem of laser source wavelength optimization may appear to be simple since a correspondence to the spectral range of maximal transparency, or minimal absorption, of the water column, is typically considered to be a requirement.

For the wavelength of a laser source to be appropriate for use in sea water remote sensing instruments, it should match the transmission maximum of the water. The transmission maxima for various types of natural waters are known to lie in the interval from 470 nm to 580 nm (Nils Gunnar Jerlov 1976; Measures 1984). Fine structure of spectral dependence of the attenuation coefficient measured with the help of a dye laser for different water samples (Cariou and Lotrian 1982) with spectral resolution better than 1 nm (see Figure 4.6.7) seem to show a potential advantage of the wavelength tuning that can provided by dye lasers introduced in the novel models of airborne lidars (Parson and Harvan 1990; Lutomirski et al. 1994).

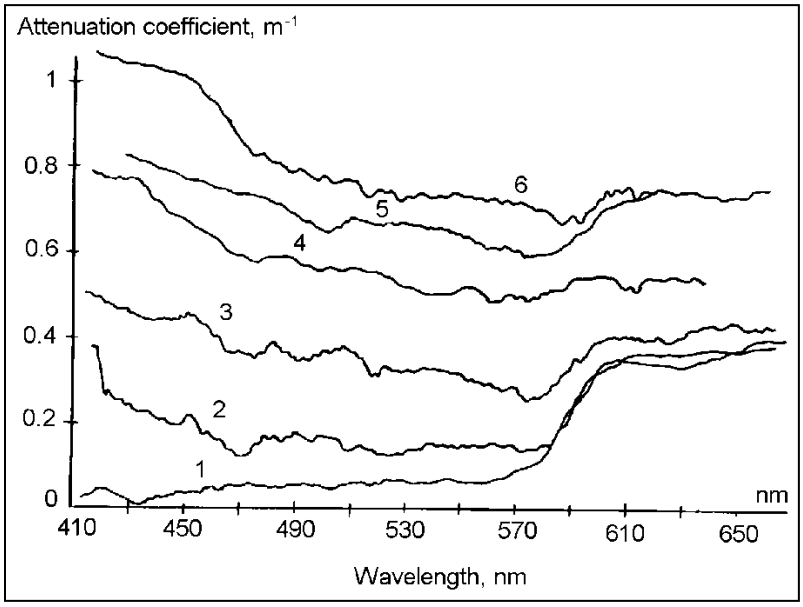

Figure 4.6.7. Variations of the attenuation coefficient for pure water (curve 1) and sea water samples (2-6) (reproduced from Cariou and Lotrian 1982).

It is quite obvious, though, that an approach based on the spectral dependency of only the absorption coefficient, is not quite correct. To begin with, one should considered that the effective attenuation coefficient, K, as in the most simplified lidar equation (L. S. Dolin and Savel'ev 1971a) for the power, $P_{bw}(h)$, returned to airborne receiver from the depth h,

$$P_{bw}(h) = B(h)\exp\left(-2\int_0^h K(z)\,dz\right) \tag{3.6.35}$$

lies within the bounds $a \le K \le c = a + b$, where a, b, and c are the absorption coefficient, scattering coefficient, and the beam attenuation coefficient, correspondingly (Kopilevich and Feigels 1993; Gordon 1982). The contribution from scattering to the value of $K(z)$ depends both on optical the properties of the water column between the surface and the horizon, z, and on parameters of the lidar system such as the platform altitude and the receiver FOV. For example, at limiting depth values, due to strong scattering of the sounding laser beam and a wide FOV angle, $K(z)$ approaches the absorption coefficient, $K(z) = a(z) + b_b(z) \approx a(z)$ (L. S. Dolin and Levin 1991), while the backward scattering coefficient b_b ($b_b \ll b$) is usually small compared with absorption. In contrast – especially with imaging lidar systems – when the depth is small, the essential part of echo-signal is caused by the coherent, or "non-scattered" component of laser beam in the water, so one has $K(z) \cong c(z)$ (L. S. Dolin and Levin 1991). In the latter case, it is just the scattering coefficient, not attenuation spectral dependence which determines the optimal wavelength for the lidar source.

The parameter $B(h)$ in (3.6.35), is proportional to an "effective backscatter coefficient", β, at the same depth, $B = C\beta$, with the quantity, C, depending only on lidar transmitter and receiver parameters and the platform altitude. β is shown to be equal to the volume backscattering coefficient, $\beta(180°)$, when dealing with signal from near-surface layer (Kopilevich and Feigels 1993); for deep-water soundings, β is a

eCommons (2019) https://doi.org10.7298/jxm9-g971

certain mean value of the volume scattering function (VSF), $\beta(\theta)$, over a solid angle around $\theta = 180°$ direction, in accordance with the angular spread of the light beam due to scattering in sea water (Maffione and Dana 1996). The effective backscattering by sea water determines the background signal in lidar sounding; specifically, in bathymetry (as well as in small object imaging) the possibility of bottom (object) detection obviously depends on the relationship between bottom (object) reflectivity, R, and the effective backscattering coefficient of the near-bottom (near-object) water layer. The wavelength dependence of $\beta(\theta)$ is found to be rather sharp in the spectral region of interest (Maffione and Dana 1996); in particular, the measurements in the Gulf of Mexico, depicted in Figure 4.6.8, give $\beta(180°) \sim \lambda^{-4.1}$.

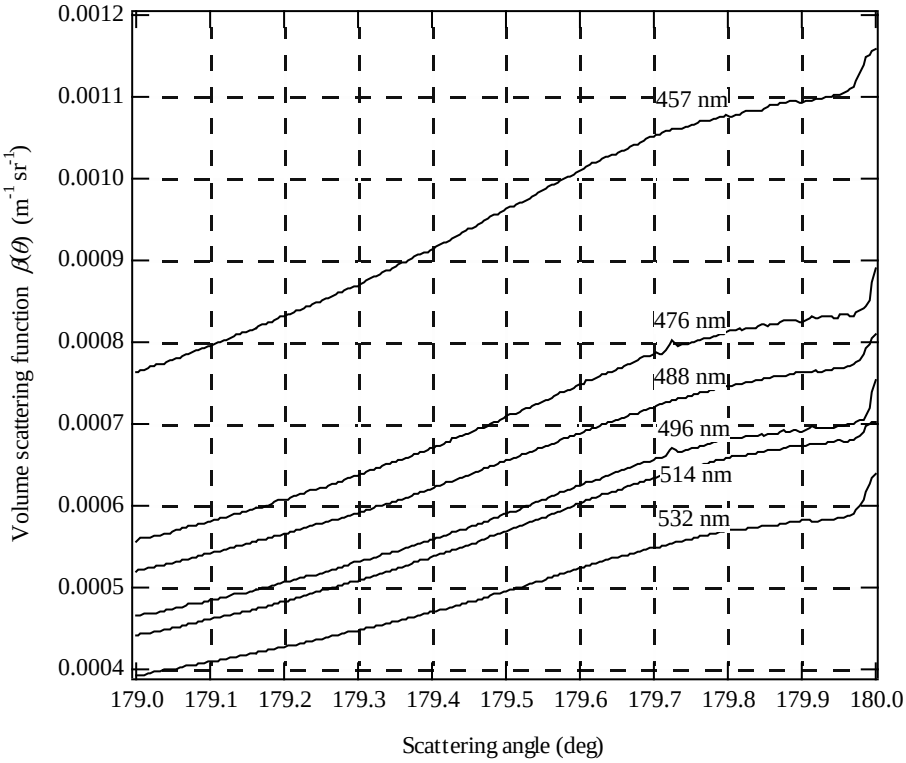

Figure 4.6.8. The spectral volume scattering function β(θ) over the angular range 179 to 180 degrees for water in the Gulf of Mexico (Maffione and Dana 1996).

According to these data, when passing from “green” to “blue” wavelengths, backscattering from the water increases by a factor of approximately 1.5; at the same time, reflection by various types of bottom decreases significantly (see Figure 4.6.9). The joint effect of the two factors outweigh the beneficial effect of higher water transparency on lidar performance, both for bathymetry and for small object detection (the curve in Figure 4.6.9 related to mud bottom can serve as a model for black painted artificial surfaces).

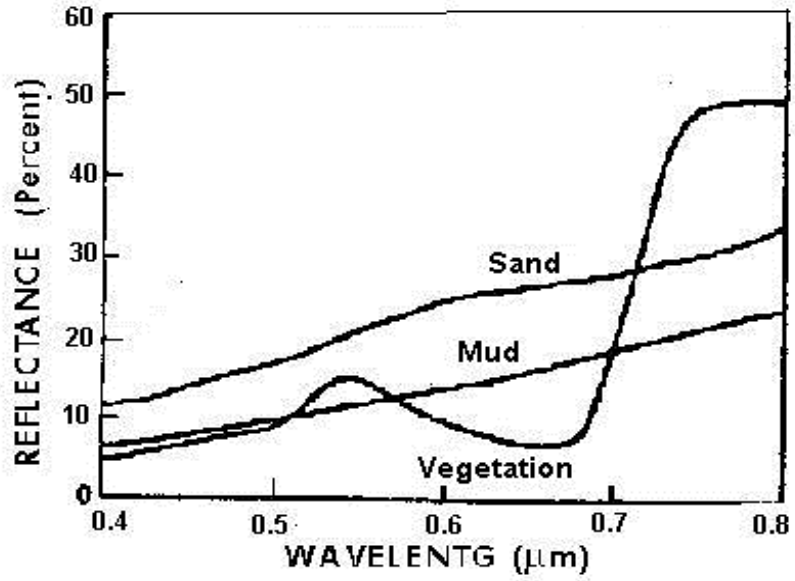

Figure 4.6.9. Spectral reflectance of different bottom materials (sand, mud and green vegetation) (Lyzenga 1978).

From the above discussion it appears that, in order to solve the problem of laser wavelength optimization, one must take into account:

- the spectral characteristics of the water body and the bottom reflectivity (or reflectivity of the object to be detected);
- background radiation at the lidar detector input, which depends on the sun zenith angle and other external conditions like the surface wave intensity, etc.;
- the spectral sensitivity, $S_{ph}(\lambda)$, of the PMT photocathode or ICCD for radiometric and imaging lidar systems, correspondingly; and
- variations in laser pulse power, $S_t(\lambda)$ (accompanying, e.g., dye laser wavelength tuning).

Quantitative estimates of the dependence of lidar system performance on the laser source wavelength, presented below, are based on spectral reflectance data from Figure 4.6.9 for mud bottom. The spectral sensitivity of the PMT photocathode S-20 (Ross 1966) was used for this example. For background radiation at the lidar detector, the sum of diffuse sunlight reflected by surface, and that backscattered by water body is used (Austin 1974). (It is worth noting that the spectral maximum of the background radiation lies within the region of seawater maximum transparency!) It is presupposed that mirror-reflection of sunlight by the surface is not observable, and that the role of sunlight backscattering by the atmospheric layer between lidar platform and the surface is negligible (true for altitudes up to 300 -500 m).

Figure 4.6.10a and b, demonstrate the calculated dependence of the *D*-parameter on the sounding bottom depth (bathymetry) for daylight conditions (case **B** described above). Note that for, relatively clear water (Figure 4.6.10a), a typical level of $D \approx 6$ corresponds to a maximal depth value of 68 m for the optimal wavelength, $\lambda = 490\ nm$, while $\lambda = 532\ nm$ (YAG:Nd) gives only 48 m, and $\lambda = 511\ nm$ (copper vapor laser) achieves 55 m. The effect seems to be considerable; one should note, however, that wavelength optimization (with the use of tunable dye laser) may be ineffective if accompanied with

substantial loss in transmitted power. Figure 4.6.10b corresponds to the case of rather turbid water for which the optimal wavelength is 500 nm, and the effect of wavelength is negligible.

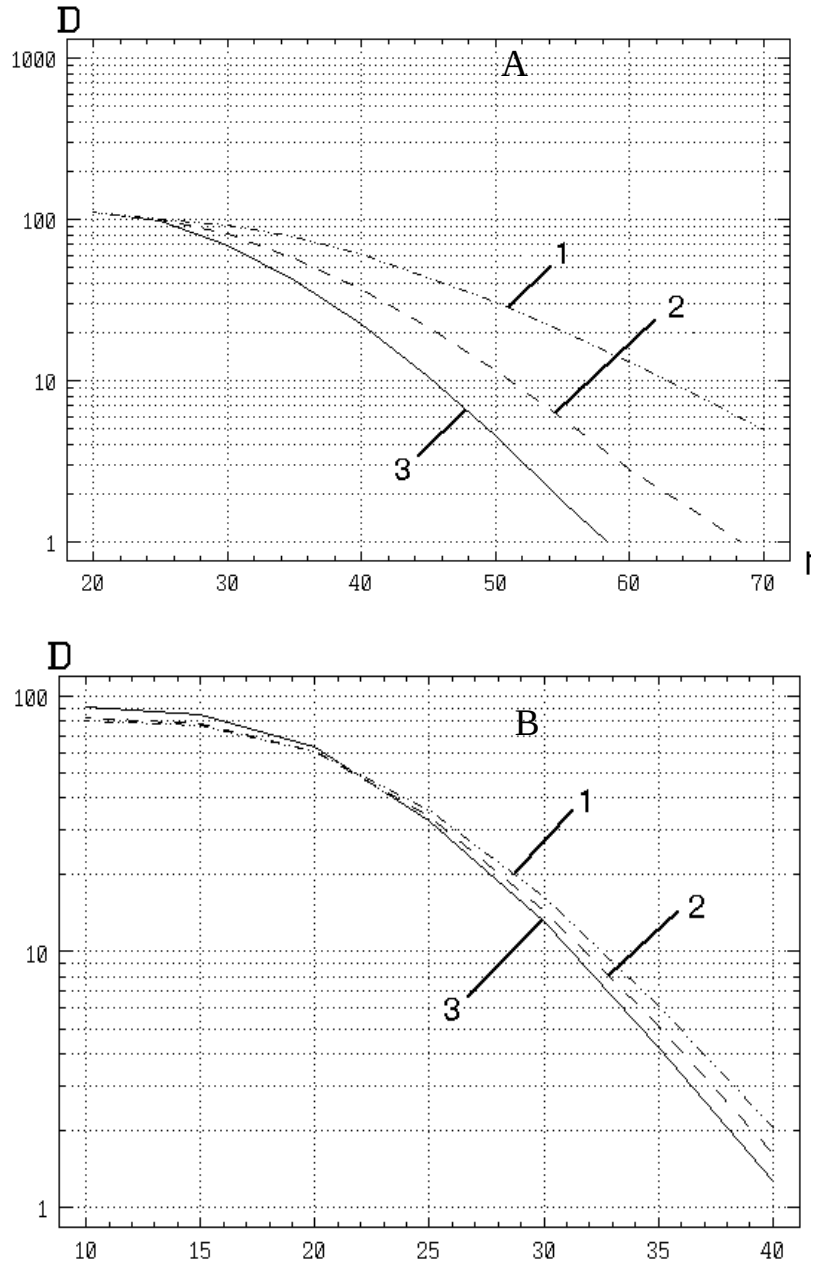

Figure 4.6.10. D-index of discriminability as a function of bottom depth for the different laser wavelengths: 1) 490 nm, 2) 511 nm, 3) 532 nm; **A**) $c = 0.2\ m^{-1}$, **B**) $c = 0.5\ m^{-1}$

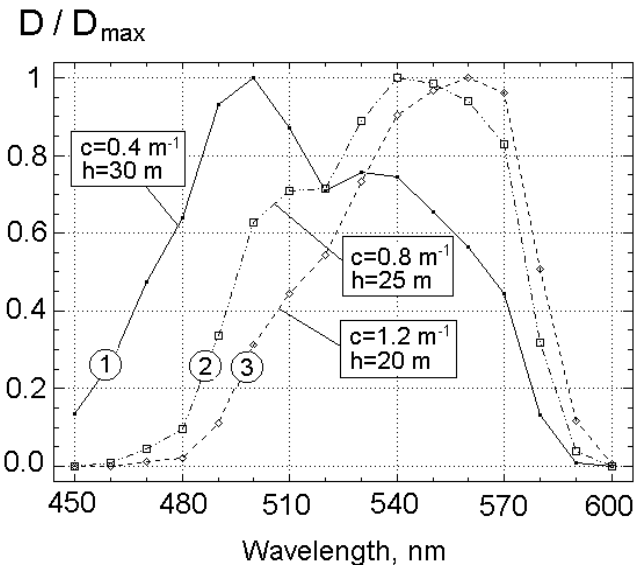

Figure 4.6.11. Calculated spectral dependencies of the D-index (normalized to the maximum value) for "day-time" conditions; curve 1 corresponds to water type III according to Jerlov's classification (Nils Gunnar Jerlov 1976), curves 2 and 3 – to water types 5 and 7, correspondingly.

The results presented above make it evident that the question of an optimal laser source for laser remote sensing does not have a simple and universal answer. Practical optimization requires one to take into account not only spectral variations in the optical characteristics of the water body and bottom reflectivity, but also the spectral dependence of the sensitivity of the specific detector used. The joint action of the listed factors typically provides a "red' shift of the optimal wavelength by 10–20 nm from the spectral range of maximal transparency of ocean water. The effectiveness of dye wavelength-tunable lasers in bathymetric airborne systems depends on generated light pulse power variations attendant on wavelength tuning. Of course, the problems connected with increased danger of excimer-pumped lasers for operators must also be taken into account.

4.7.6 *D*-index for systems with high repetition rate and return signal summation

In order to compare the system effectiveness of high repetition range lasers (hundreds of kHz), with that of other systems (particularly, systems with relatively high pulse peak energy and low, to moderate repetition rate (30-30,000Hz) we may again use the comparison criterion based on Sakitt's *D*-index of discriminability. The *D*-index of discriminability for summing over accumulated pulses in bathymetry, D^N, is determined by the following expression (Svetlykh and Feigels 1993)

$$D^N = N^{1/2} \cdot D \tag{4.6.36}$$

where *D* is the value of the *D*-index, calculated for a single laser pulse in accordance with the formulae presented in above paragraphs, and *N* is the number of pulses accumulated.

eCommons (2019) https://doi.org10.7298/jxm9-g971

4.7.7 A universal parameter for the comparison of bathymetric lidars

Under certain conditions and assumptions typically found in lidar bathymetry practice, we may compare the operational depths achieved by different systems through the analysis of a single parameter for Bathymetric Lidars, C_{BL}, determined according to the equation (4.6.29) (Feygels, Kim, et al. 2014; Feygels, Kopilevich, et al. 2014)

$$C_{BL} = P_T \cdot d_0 \cdot \sqrt{\frac{\eta}{\Delta\lambda}} \qquad \left[\text{kW} \cdot \text{m} \cdot (nm)^{-1/2}\right] \tag{4.6.37}$$

where: P_T is the transmitter (laser) pulse power in kW;

d_0 is the receiver aperture diameter in m;

η is the transmittance (efficiency) of the transmitter-receiver optical tract;

$\Delta\lambda$ is the optical bandwidth of the spectral selector (optical filter) in nm.

The value of this universal parameter for CZMIL C_{BL}^{CZMIL}, is (Tuell, Barbor, and Wozencraft 2010; Feygels et al. 2013):

$$C_{BL}^{CZMIL} = 1500 \cdot 0.2 \cdot \sqrt{\frac{0.62}{1}} = 232.4 \qquad \text{kW} \cdot \text{m} \cdot (nm)^{-1/2} \tag{4.6.38}$$

(The CZMIL system was optimized in the design stage of the OCEAN-SCIETIFIC-2001 software (Fuchs and Tuell 2010)).

To predict the maximal optical depth for a given lidar system, (X), as compared to CZMIL, it is necessary to assume that:

- Environmental (atmosphere, water, bottom) conditions are the same;
- Altitude and depth are the same;
- Fields-of-view of the lidar receivers are nearly the same, and close to optimal;
- Photoreceiver sensitivities are the same.

Then:

$$(K_d D_{max})_X = (K_d D_{max})_{CZMIL} + \ln\left(C_{BL}^X / C_{BL}^{CZMIL}\right)/2 \tag{4.6.39}$$

where $(K_d \cdot D_{max})_{CZMIL} = 4.15$.

Figure 4.6.12 illustrates the sensitivity of the parameter $(K_d \cdot D_{max})_X$ to the ratio of the universal parameter for the "unknown" system, C_{BL}^X, to that for CZMIL, C_{BL}^{CZMIL}.

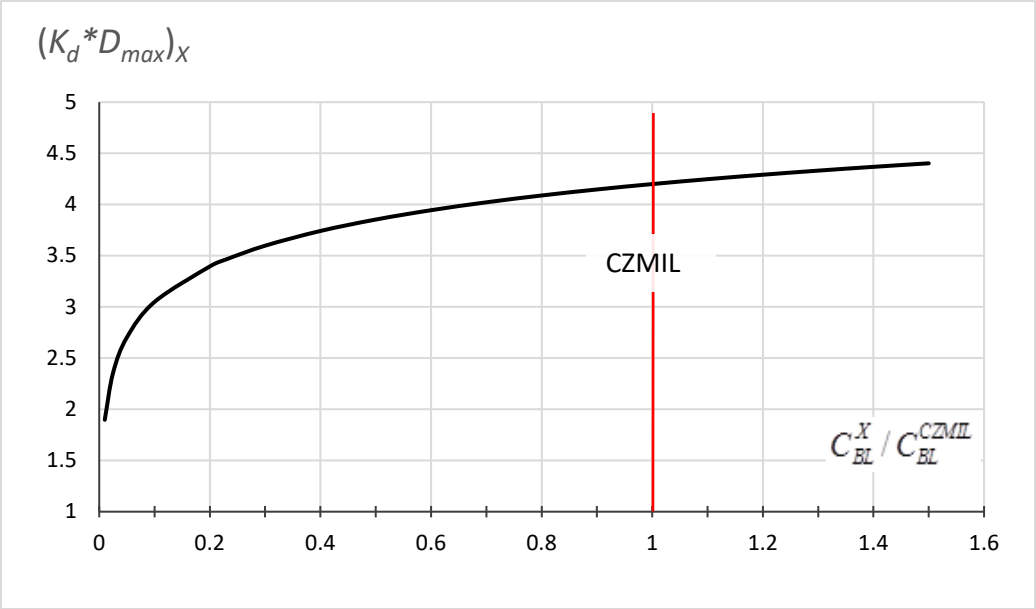

Figure 4.6.12. Prediction of $(K_d \cdot D_{max})_X$ for system (X) based on a ratio of universal parameters.

The universal parameter can be used under certain assumptions to compare lidar systems and predict their maximum penetration depth. For a more accurate systems comparison (and optimization), a special simulated computer program (Victor I. Feigels et al. 2002) should be employed.

4.8 References

Abdullah, Q A. 2004. “Photogrammetric Platforms.” In *Manual of Photogrammetry. Fifth Edition*, edited by J Chris McGlone, Edward M Mikhail, and James S Bethel, 705–17. Bethesda, MD: ASPRS. https://doi.org/978-1570830716.

Abramowitz, M., and I. A. Stegun. 1972. *Handbook of Mathematical Functions with Formulas, Graphs, and Mathematical Tables (Partially Mathcad-Enabled)*. U.S. Department of Commerce, NIST. http://app.knovel.com/hotlink/toc/id:kpHMFFGMT1/handbook-mathematical/handbook-mathematical.

Allocca, David M, Mark A London, Thomas P Curran, Brian M Concannon, V Michael Contarino, Jennifer Prentice, Linda J Mullen, and Timothy J Kane. 2002. “Ocean Water Clarity Measurement Using Shipboard Lidar Systems.” In *Ocean Optics: Remote Sensing and Underwater Imaging*, 4488:106–14. San Diego, CA: SPIE 4488. https://doi.org/10.1117/12.452807 [doi].

ANSI. 2005. “Safe Use of Lasers Outdoors.” Vol. ANSI Z136. Laser institute of America. https://doi.org/978-0-912035-66-6.

———. 2014. “American National Standard for Safe Use of Lasers.” *ANSI Z136.1-2014*. http://webstore.ansi.org/RecordDetail.aspx?sku=ANSI+Z136.1-2014.

Apresian, L A, and Yu A Kravstov. 1983. *The Theory of Radiative Transfer*. Nauka (in Russian).

Austin, Roswell W. 1974. “The Remote Sensing of Spectral Radiance from below the Ocean Surface.” In *Optical Aspects of Oceanography*, edited by N G Jerlov and E Steemann Nielsen, 317–44. New York: Academic Press.

Austin, Roswell W., and T. J. Petzold. 1984. “Spectral Dependence Of The Diffuse Attenuation Coefficient Of Light In Ocean Waters.” https://doi.org/10.1117/12.943302.

Axelsson, Rune, and Mats Alfredsson. 1999. “Capacity and Capability for Hydrographic Missions.” In *Proc. 1999 U.S. Hydrographic Conference*. Mobile, AL. http://www.jalbtcx.org/downloads/Publications/30Axelsson_Alfredsson_99.pdf.

Baltsavias, E P. 1999. “Airborne Laser Scanning: Basic Relations and Formulas.” *ISPRS Journal of Photogrammetry and Remote Sensing* 54 (2–3): 199–214. https://doi.org/10.1016/S0924-2716(99)00015-5.

Billard, Brian, Ralph H Abbot, and Michael F Penny. 1986a. “Airborne Estimation of Sea Turbidity Parameters from the Wrelads Laser Airborne Depth Sounder.” *Applied Optics* 25 (13): 2080–88. https://doi.org/10.1364/AO.25.002080.

———. 1986b. “Modeling Depth Bias in an Airborne Laser Hydrographic System.” *Applied Optics* 25 (13): 2089–98.

Bravo-Zhivotovski, Dmitri, D M Dolin, Alexander G Luchinin, and V A Savel’ev. 1969. “On the Structure of a Narrow Light Beam in Sea Water.” *Izv. Akad. Nauk SSSR, Fiz. Atmos. Okeana* 5 (2): 160.

Bremmer, H. 1964. “Random Volume Scattering.” *Radio Science* 68D (9): 967–81. https://doi.org/http://dx.doi.org/10.6028/jres.068D.096.

Bunkin, Alexei F., and Konstantin I. Voliak. 2001. *Laser Remote Sensing of the Ocean: Methods and Applications*. Vol. 56. John Wily & Sons.

Cariou, J., and J. Lotrian. 1982. “Transmission Characteristics of a Pulsed Laser Beam in Natural Sea-Water: Determination of the Attenuation Coefficients in the 415-660 Nm Spectral Range.” *Journal of Physics D: Applied Physics* 15 (10): 1873–80. https://doi.org/10.1088/0022-3727/15/10/007.

Degnan, John J., Roman Machan, Edward Leventhal, Gabriel Jodor, Christopher B. Field, and J. Marcos Sirota. 2011. “Cryosphere and Biomass Measurements Using a Photon-Counting 3D Imaging Lidar.” In *CLEO 2011: Laser Applications to Photonic Applications*, ATuA3. Washington, D.C.: OSA. https://doi.org/10.1364/CLEO_AT.2011.ATuA3.

Dolin, Lev S., and Iosif M. Levin. 1991. *Reference Book on the Underwater Vision Theory*. Leningrad: Gidrometeoizdat Press (in Russian).

Dolin, Lev S., Iosif M. Levin, O. V. Kopelevich, and Victor I. Feigels. 1988. “Few-Parameter Models of Light Field at Sea, and Integral Parameters of the Phase Function of Water.” *Izvvestiya, Atmospheric and Oceanic Physics* 24 (11): 1217–22.

Dolin, Lev S., and V. A. Savel’ev. 1971a. “Characteristics of the Backscattering Signal and Pulse Radiation of Turbid Media by a Narrow Directional Light Beam.” *Atmospheric and Oceanic Physics* 7 (5): 505–10.

Dolin, Lev S. 1964. “Light Beam Scattering in a Turbid Medium Layer.” *IIzv. Vyssh. Uchebn. Zaved. Radiofiz.* 7: 471–78.

Dolin, Lev S, and V A Savel’ev. 1971b. “Determining the Parameters of a Back-Scattered Signal of Pulsed Radiation in a Turbid Medium with a Narrow Directed Laser Beam.” *Izv. Akad. Nauk SSSR, Fiz. Atmos. Okeana* 7: 505.

Dolin, LevS, and V A Savel’ev. 1979. “On the Theory of Narrow Light Beam Propagation in a Stratified Scattering Medium.” *IIzv. Vyssh. Uchebn. Zaved. Radiofiz.* 12: 1310–17.

Dolina, I S, Lev S Dolin, Iosif M Levin, A A Rodionov, and V A Savel’ev. 2007. “Inverse Problems of Lidar Sensing of the Ocean.” In *Proceedings of the III International Conference Current Problems of Natural Waters*, 6615:66150C-1-66150C – 10. St. Petersburg, Russia: SPIE 6615. https://doi.org/10.1117/12.740451.

Egan, James P. 1975. *Signal Detection Theory and ROC Analysis*. Academic Press.

FDA. 2013. “Performance Standards for Light-Emitting Products.” Code of Federal Regulations, Title 21, Volume 8. http://www.accessdata.fda.gov/scripts/cdrh/cfdocs/cfcfr/cfrsearch.cfm?fr=1040.10.

Feigels, Victor I. 1992. “Lidars for Oceanographical Research: Criteria for Comparison, Main Limitations, Perspectives.” In *Ocean Optics XI*, 1750:473–85. San Diego, CA: SPIE 1750. https://doi.org/10.1117/12.140676.

Feigels, Victor I., Blair Evans, Lev Feygels, Gary C. Guenther, and Yuri I. Kopilevich. 2002. “Prediction of Bathymetric Lidar Performance with Ocean Scientific 2001 Simulation Code.” In *SPIE 4488, Ocean Optics: Remote Sensing and Underwater Imaging*, edited by Robert J. Frouin and Gary D. Gilbert, SPIE 4488:61–70. San Diego, CA, United States: SPIE. https://doi.org/10.1117/12.452826.

Feigels, Victor I., and Yuri I. Kopilevich. 1993a. “Ocean-Scientific for Windows: User’s Guide.” EG&G Washington Analytical Service, Inc.

———. 1993b. “Remote Sensing of Subsurface Layers of Turbid Sea Water with the Help of Optical Lidar System.” In *SPIE 2048: Underwater Light Measurements*, 34–42. https://doi.org/10.1117/12.165508.

———. 1994a. “Applicability of Lidar Remote Sensing Methods for Vertical Structure Investigation of Ocean Optical Properties Distribution.” In *SPIE 2258: Ocean Optics XII*, edited by Jules S Jaffe, 2258:449–57. https://doi.org/10.1117/12.190087.

———. 1994b. “Lasers for Lidar Bathymetry and Oceanographic Research: Choice Criteria.” In *Proceedings of IGARSS ’94 - 1994 IEEE International Geoscience and Remote Sensing Symposium*, 1:475–77. Proceedings of the 1994 International Geoscience and Remote Sensing Symposium. St. Petersburg Inst of Fine, Mechanics Optics, St. Petersburg, Russia: IEEE. https://doi.org/10.1109/IGARSS.1994.399157.

———. 1996. “Optimization of Laser Wavelength in Oceanographic Lidars.” In *CIS Selected Papers: Laser Remote Sensing of Natural Waters: From Theory to Practice, November 1, 1996 - November 1*, 2964:128–37. St. Petersburg Institute of Fine Mechanics and Optics (PIFMO), Department of Laser Technology and Ecological Engineering, 14 Sablinskaya st., St. Petersburg, 197101, Russia: SPIE. https://doi.org/10.1117/12.258343.

Feigels, Viktor I, and Yuri I Kopilevich. 1993. “Ocean-Scientific for Windows, Basic Concepts, Description of the Theory.” EG&G Washington Analytical Service, Inc.

Feygels, Viktor I., Minsu Kim, Joong Yong Park, and Yuri I. Kopilevich. 2014. “A Universal Parameter for the Comparison of Lidar Bathymeters.” In *15th Annual JALBTCX Airborne Coastal Mapping and Charting Worshop*. Mobile, AL. http://shoals.sam.usace.army.mil/Workshop_Files/2014/Day3_pdf/1100_Feygels.pdf.

Feygels, Viktor I., Yuri I. Kopilevich, Joong Yong Park, Minsu Kim, and Jennifer Aitken. 2014. “Particularities of Hydro Lidar Missions in the Asia-Pacific Region.” In *SPIE 9262: Lidar Remote Sensing for Environmental Monitoring XIV*, edited by Upendra N. Singh and Kazuhiro Asai, 92620X. https://doi.org/10.1117/12.2069871.

Feygels, Viktor I., Joong Yong Park, Jennifer M. Wozencraft, Jennifer Aitken, Christopher Macon, Abhinav Mathur, Andy Payment, et al. 2013. “CZMIL (Coastal Zone Mapping and Imaging Lidar): From First Flights to First Mission through System Validation.” In *Proceedings of SPIE*, edited by W W Arnone Hou RA, 8724:87240A-1-87240A – 15. Baltimore, MD: SPIE. https://doi.org/10.1117/12.2017935.

Feygels, Viktor I, Yuri I Kopilevich, Alexey Surkov, James K Yungel, and Michael J Behrenfeld. 2003. “Airborne Lidar System with Variable Field-of-View Receiver for Water Optical Properties Measurement.” In *Ocean Remote Sensing and Imaging II, August 5, 2003 - August 6*, 5155:12–21. EG and G Technical Service Inc., Wallops Flight Facility, Wallops Island, VA 23337: SPIE. https://doi.org/10.1117/12.506976.

Feygels, Viktor I, Joong Yong Park, Jennifer Aitken, Minsu Kim, Andy Payment, and Vinod Ramnath. 2012. “Coastal Zone Mapping and Imaging Lidar (CZMIL): First Flights and System Validation.” In *Remote Sensing of the Ocean, Sea Ice, Coastal Waters, and Large Water Regions 2012*, SPIE 8532. Edinburgh, U.K. https://doi.org/10.1117/12.2014617.

Feygels, Viktor I, Charles Wayne Wright, Yuri I Kopilevich, and Alexey I Surkov. 2003. “Narrow-Field-of-View Bathymetrical Lidar: Theory and Field Test.” In *Ocean Remote Sensing and Imaging II*. Vol. SPIE 5155. San Diego, CA: SPIE. https://doi.org/10.1117/12.506951.

Fuchs, Eran, and Abhinav Mathur. 2010. “Utilizing Circular Scanning in the CZMIL System.” In *5-18 Apr 2010*, SPIE 7695. Optech International, 7225 Stennis Airport Rd, Kiln, MS 39556: SPIE. https://doi.org/10.1117/12.851936.

Fuchs, Eran, and Grady H. Tuell. 2010. “Conceptual Design of the CZMIL Data Acquisition System (DAS): Integrating a New Bathymetric Lidar with a Commercial Spectrometer and Metric Camera for Coastal Mapping Applications.” In *SPIE 7695, Algorithms and Technologies for Multispectral, Hyperspectral, and Ultraspectral Imagery XVI, April 5-8, 2010*, edited by Sylvia S. Shen and Paul E. Lewis, SPIE 7695:769501. Orlando, FL: SPIE. https://doi.org/10.1117/12.851919.

Gonsalves, Michael Oliver. 2010. “A Comprehensive Uncertainty Analysis and Method of Geometric Calibration for a Circular Scanning Airborne Lidar.” Edited by Stephan Howden. *ProQuest Dissertations and Theses*. Hattiesburg, MS: The University of Southern Mississippi. http://search.proquest.com/docview/835075165/fulltextPDF/BB0E363A81F246C3PQ/1?accountid=10267.

Gordon, Howard R. 1982. “Interpretation of Airborne Oceanic Lidar: Effects of Multiple Scattering.” *Applied Optics* 21 (16): 2996–3001. https://doi.org/10.1364/AO.21.002996.

Guenther, Gary C., and Robert W. Thomas. 1984. “Effects Of Propagation-Induced Pulse Stretching In Airborne Laser Hydrography.” In *SPIE 0489: Ocean Optics VII*, edited by Marvin A. Blizard, 287–96. Monterey, CA: International Society for Optics and Photonics. https://doi.org/10.1117/12.943315.

Guenther, Gary C. 1985. *Airborne Laser Hydrography: System Design and Performance Factors*. Rockville, MD: NOAA Professional Paper Series, National Ocean Service 1. http://shoals.sam.usace.army.mil/downloads/Publications/AirborneLidarHydrography.pdf.

Guenther, Gary C, Thomas J Eisler, Jack L Riley, and Steven W Perez. 1996. “Obstruction Detection and Data Decimation for Airborne Laser Hydrography.” In *1996 Canadian Hydrographic Conference*. Halifax, Nova Scotia, Canada. http://handle.dtic.mil/100.2/ADA487820.

Habib, Ayman, A P Kersting, Ki In Bang, and Dong-Cheon Lee. 2010. “Alternative Methodologies for the Internal Quality Control of Parallel LiDAR Strips.” *Geoscience and Remote Sensing, IEEE Transactions On* 48 (1): 221–36. https://doi.org/10.1109/TGRS.2009.2026424.

Hamamatsu. 2007. *Photomultiplier Tubes: Basics and Applications*. Vol. 3rd. Hamamatsu Photonics, K.K. http://www.hamamatsu.com/resources/pdf/etd/PMT_handbook_v3aE-Chapter1.pdf.

Helstrom, C. W. 1968. *Statistical Theory of Signal Detection*. Pergamon Press, Oxford.

Hickman, G D, and J E Hogg. 1969. “Application of an Airborne Pulsed Laser for near Shore Bathymetric Measurements.” *Remote Sensing of Environment* 1 (1): 47–58. https://doi.org/10.1016/S0034-4257(69)90088-1.

IEC. 2014. *Safety of Laser Products*. *IEC 60825-1:2014*. International Electrotechnical Commission (IEC). https://webstore.iec.ch/publication/3587.

Imahori, Gretchen, Jeff Ferguson, Toshi Wozumi, David Dave Scharff, Shachak Pe’eri, Christopher E Parrish, Stephen A White, et al. 2013. “A Procedure for Developing an Acceptance Test for Airborne Bathymetric Lidar Data Application to NOAA Charts in Shallow Waters.” *NOAA Technical Memorandum CS 32*. Vol. NOS CS-32. Silver Spring, MD: National Oceanographic and Atmospheric Administration. http://www.nauticalcharts.noaa.gov/csdl/publications/TM_NOS-CS32_FY13_Lidar.pdf.

Ishimaru, Akira. 1978. *Wave Propagation and Scattering in Random Media: Multiple Scattering, Turbulence, Rough Surfaces, and Remote Sensing*. *IEEE/OUP Series on Electromagnetic Wave Theory*. Vol. 2. Academic Press.

Jerlov, Nils Gunnar. 1976. *Marine Optics*. Amsterdam: Elsevier. http://www.sciencedirect.com/science/bookseries/04229894/14.

Keeler, R. N., and Bobby Lee Ulich. 1994. “Some Aspects of Wide-Beam Imaging Lidar Performance.” In *SPIE 2258, Ocean Optics XII*, edited by Jules S Jaffe, 2258:480–500. SPIE. https://doi.org/10.1117/12.190091.

Kim, Minsu, Yuri I. Kopilevich, Viktor I. Feygels, Joong Yong Park, and Jennifer M. Wozencraft. 2016. “Modeling of Airborne Bathymetric Lidar Waveforms.” *Journal of Coastal Research* Spec.Issue (76): 18–30. https://doi.org/10.2112/SI76-003.

Kopilevich, Yuri I., and Victor I. Feigels. 1993. “Characteristics of Light Backscattering by Sea Water and Lidar Sounding of Water Column.” In *SPIE 2048: Underwater Light Measurements*, 85–95. https://doi.org/10.1117/12.165494.

———. 2002. “On Multispectral Lidar Sounding of Ocean Waters.” In *SPIE 4488, Ocean Optics: Remote Sensing and Underwater Imaging*, edited by Robert J. Frouin and Gary D. Gilbert, 4488:51–60. San Diego, CA: International Society for Optics and Photonics. https://doi.org/Unsp 4488-12\r10.1117/12.452804.

Kopilevich, Yuri I., Viktor I. Feygels, and Alexey I. Surkov. 2003. “Mathematical Modeling of Input Signals for Oceanographic Lidar Systems.” In *SPIE 5155: Ocean Remote Sensing and Imaging II*, 5155:30–39. St. Petersburg Inst. Fine Mech./Opt., 14 Sablinskaya St., St. Petersburg, 197101, Russia: SPIE. https://doi.org/10.1117/12.506980.

Kopilevich, Yuri I, Viktor I Feygels, Grady H Tuell, and Alexey Surkov. 2005. “Measurement of Ocean Water Optical Properties and Seafloor Reflectance with Scanning Hydrographic Operational Airborne Lidar Survey (SHOALS): I. Theoretical Background.” In *SPIE 5885, Remote Sensing of the Coastal Oceanic Environment, July 31, 2005 - August 1*, 5885:1–9. Optech International, Inc., 7225 Stennis Airport Drive, Kiln, MI 39556, United States: SPIE. https://doi.org/10.1117/12.618923.

Kopilevich, Yuri I, M E Kononenko, and E I Zadorozhnaya. 2010. “The Effect of the Forward-Scattering Index on the Characteristics of a Light Beam in Sea Water.” *Journal of Optical Technology* 77 (10): 598–601. https://doi.org/10.1364/JOT.77.000598.

———. 2011. “Prediction of Bathymetric Lidar Performance with the Account for the VSF Shape.” In *ONW 2011: Current Problems in Optics of Natural Waters*, 183–86. St. Petersburg, Russia.

Kopilevich, Yuri I, and A G Surkov. 2008. “Mathematical Modeling of the Input Signals of Oceanological Lidars.” *Journal of Optical Technology* 75 (5): 321–26. https://doi.org/10.1364/JOT.75.000321.

Kuriksha, A. A. 1973. “Quantum Optics and Quantum Location (Statistical Theory).” *Soviet Radio*.

LaRocque, Paul E., John R. Banic, and A. Grant Cunningham. 2004. “Design Description and Field Testing of the SHOALS-10001 Airborne Bathymeter.” In *Laser Radar Technology and Applications IX, April 13, 2004 - April 15*, 5412:162–84. Optech Incorporated, 100 Wildcat Road, Toronto, Ont. M3J 2Z9, Canada: SPIE. https://doi.org/10.1117/12.564924.

Lebed’ko, E. G., L. F. Porfir’ev, and F. I. Hajtun. 1984. *Theory and Design of Optical-Electronic Systems*. Leningrad: Mashinostoenie (in Russian).

Levin, BR. 1960. *Theory of Random Processes and the Applications in Radiotechnique (In Russion)*. Soviet Radio, Moscow.

Lillycrop, W. Jeff, and John R. Banic. 1992. “Advancements in the US Army Corps of Engineers Hydrographic Survey Capabilities: The SHOALS System.” *Marine Geodesy*, Mar. Geod. (USA), 15 (2–3): 177–85. https://doi.org/10.1080/01490419209388053.

Lutomirski, R., S. Halmbach, Thomas P. Curran, and J. Gibbons. 1994. “Performance Modelling and Analysis of the Ocean Water Lidar (OWL) Hydrographic System.” In *U.S. Hydrographic Conference*, 200–205.

Lyzenga, David R. 1978. “Passive Remote Sensing Techniques for Mapping Water Depth and Bottom Features.” *Applied Optics* 17 (3): 379–83. http://ao.osa.org/abstract.cfm?URI=ao-17-3-379.

Maffione, Robert A., and David R. Dana. 1996. “In-Situ Characterization of Optical Backscattering and Attenuation for Lidar Applications.” In *Laser Remote Sensing of Natural Waters: From Theory to Practice*, 2964:152–61. St. Petersburg, Russia: SPIE 2964. https://doi.org/10.1117/12.258345.

McKean, Jim, Dave Nagel, Daniele Tonina, Philip Bailey, Charles Wayne Wright, Carolyn Bohn, and Amar Nayegandhi. 2009. “Remote Sensing of Channels and Riparian Zones with a Narrow-Beam Aquatic-Terrestrial LIDAR.” *Remote Sensing* 1 (4): 1065–96. https://doi.org/10.3390/rs1041065.

McLean, John W., and J. T. Murray. 1998. “Streak Tube Lidar Allows 3-D Surveillance.” *Laser Focus World*, 171–76.

Measures, Raymond M. 1984. *Laser Remote Sensing: Fundamentals and Applications*. 1st ed. New York: John Wiley & Sons.

———. 1992. *Laser Remote Sensing: Fundamentals and Applications*. 2nd ed. Vol. 2nd. New York: John Wiley & Sons. https://doi.org/0471081930, 9780471081937.

Monin, A S. 1983. “Physical Optics of the Ocean.” In *Ocean Optics*, edited by A S Monin. Vol. 1. Nauka, Moscow (in Russian).

Moran, Steven E., Bobby Lee Ulich, William P. Elkins, Richard J. Strittmatter, and Michael J. DeWeert. 1997. “Intensified CCD (ICCD) Dynamic Range and Noise Performance.” In *SPIE 3173: Ultrhigh- and High-Speed Photography and Image-Based Motion Measurement*, 28 pages. SPIE. https://doi.org/10.1117/12.294535.

Parson, Kevin J., and Michael P. Harvan. 1990. “Power Oscillator as a LIDAR Transmitter.” In *SPIE 1302: Ocean Optics X*, edited by Richard W. Spinrad, 583–90. Orlando, FL: International Society for Optics and Photonics. https://doi.org/10.1117/12.21472.

Pe’eri, Shachak, Lynnette V Morgan, William D Philpot, and Andrew A Armstrong. 2011. “Land-Water Interface Resolved from Airborne LIDAR Bathymetry (ALB) Waveforms.” *Journal of Coastal Research* SI 62: 75–85. https://doi.org/10.2112/SI_62_8.

Pe’eri, Shachak, and William D. Philpot. 2007. “Increasing the Existence of Very Shallow-Water LIDAR Measurements Using the Red-Channel Waveforms.” *IEEE Transactions on Geoscience and Remote Sensing* 45 (5): 1217–23. https://doi.org/10.1109/TGRS.2007.894584.

Penny, Michael F., Ralph H. Abbot, D. M. Phillips, Brian Billard, D. Rees, D. W. Faulkner, D. G. Cartwright, et al. 1986. “Airborne Laser Hydrography in Australia.” *Applied Optics* 25 (13): 2046–58. https://doi.org/10.1364/AO.25.002046.

Petrie, Gordon, and Charles K Toth. 2009. “Terrestrial Laser Systems.” In *Topographic Laser Ranging and Scanning: Principles and Processing*, edited by Jie Shan and Charles K Toth, 87–128. Boca Raton, FL: CRC Press,Taylor and Francis Group.

Pfennigbauer, Martin, Clifford Wolf, Josef Weindopf, and Andreas Ullrich. 2014. “Online Waveform Processing for Demanding Target Situatons.” In *Proc. SPIE 9080: Laser Radar Technology and Applications XIX and Atmospheric Propagation XI*. Baltimore, MD: SPIE. https://doi.org/10.1117/12.2052994.

Pike, E. R. 1974. *Photon Correlation and Light Beating Spectroscopy: Introductory Lecture*. Edited by H. Z. Cummins and E. R. Pike. Boston, MA: Springer US. https://doi.org/10.1007/978-1-4615-8906-8.

Raiffa, Howard. 1968. *Applied Statistical Decision Theory*. Cambridge, Mass.: M.I.T. Press. http://newcatalog.library.cornell.edu/catalog/31356.

Rees, Simon M., Jacqueline Staromlynska, Michael P. Gillyon, and Julianne R. Davy. 1996. “High-Performance Optical Filter for the Australian Laser Airborne Depth Sounder.” In *SPIE 2964: Laser Remote Sensing of Natural Waters: From Theory to Practice*, edited by Victor I. Feigels and Yurij I. Kopilevich, 138–44. St. Petersburg, Russia: International Society for Optics and Photonics. https://doi.org/10.1117/12.258344.

Renslow, Michael. 2012. *Manual of Airborne Topographic Lidar*. Vol. First. Bethesda, Maryland: American Society of Photogrammetry and Remote Sensing.

Ross, Monte. 1966. *Laser Receivers: Devices, Techniques, Systems*. New York, NY: Wiley.

Sakitt, B. 1973. "Indices of Discriminability." *Nature* 241 (5385): 133–34. https://doi.org/10.1038/241133a0.

Saleh, Bahaa E A, and Malvin C Teich. 1991. *Fundamentals of Photonics*. New York: Wiley-Interscience. http://web.ebscohost.com/ehost/ebookviewer/ebook/nlebk_26193_AN?sid=305fb078-c2e9-47a7-a406-694f63a9402c@sessionmgr198&vid=1&format=EB.

Steinbacher, Frank, Martin Pfennigbauer, Markus Aufleger, and A Ullrich. 2012. "High Resolution Airborne Shallow Water Mapping." In *ISPRS 2012*. Melbourme, Australia.

Sugimoto, N, Z Liu, P Voelger, A Shimizu, Y Sasano, K Asai, M Ishizu, T Itabe, and T Imai. 2001. "Science Applications of the Multi-FOV Lidar for ATMOS-B1/ERM." *SPIE* 4153. https://doi.org/10.1117/12.417074.

Svetlykh, Alexander A., and Victor I. Feigels. 1993. "Gain in Lidar Performance Provided by Increase of Pulse-Repetition Rate and Narrowing of Optical Filter Band." In *SPIE 2111: Symposium on Russian Airborne Geophysics and Remote Sensing*, edited by Norman Harthill, 75–94. Golden, CO: International Society for Optics and Photonics. https://doi.org/10.1117/12.162884.

Tuell, Grady H., Ken Barbor, and Jennifer M. Wozencraft. 2010. "Overview of the Coastal Zone Mapping and Imaging Lidar (CZMIL): A New Multi-Sensor Airborne Mapping System for the U.S. Army Corps of Engineers." In *SPIE 7695: Algorithms and Technologies for Multispectral, Hyperspectral, and Ultraspectral Imagery XVI, April 5-8, 2010*, SPIE 7695:The Society of Photo-Optical Instrumentation Engin. Optech International, 7225 Stennis Airport Dr., Kiln, MS 39556, United States: SPIE. https://doi.org/10.1117/12.851905.

Tuell, Grady H., Viktor I. Feygels, Yuri I. Kopilevich, Alan D. Weidemann, A. Grant Cunningham, Reza Mani, Vladimir Podoba, Vinod Ramnath, Joong Yong Park, and Jennifer Aitken. 2005. "Measurement of Ocean Water Optical Properties and Seafloor Reflectace with Scanning Hydrographic Operational Airborne Lidar Survey (SHOALS): II. Practical Results and Comparison with Independent Data." In *SPIE 5885: Remote Sensing of the Coastal Oceanic Environment, July 31- August 1, 2005*, edited by Robert J. Frouin, Marcel Babin, and Shubha Sathyendranath, 5885:58850E-58850E – 13. San Diego, CA: SPIE. https://doi.org/10.1117/12.619215.

Tulldahl, H Michael, Marie Andersson, and Ove Steinvall. 2000. "Airborne Laser Depth Sounding: Improvements in Position Adn Depth Estimates by Local Corrections for Sea Surface Slope." In *Oceans 2000 MTS/IEEE*, 2:1421–29. Providence, RI: IEEE. https://doi.org/10.1109/OCEANS.2000.881803.

Ulich, Bobby Lee, Philip Lacovara, Steven E. Moran, and Michael J. DeWeert. 1997. "Recent Results in Imaging Lidar." In *SPIE 3059, Advances in Laser Remote Sensing for Terrestrial and Oceanographic Applications*, 3059:95–108. https://doi.org/10.1117/12.277603.

Vasilkov, Alexander P., Yuri A. Goldin, and Boris A. Gureev. 1993. "Airborne Lidar Remote Sensing of Vertical Distribution of Sea Water Scattering Coefficient." In , 1936:233–44. SPIE. https://doi.org/10.1117/12.157108.

Walker, Ronald E, and John W McLean. 1999. "Lidar Equations for Turbid Media with Pulse Stretching." *Applied Optics* 38 (12): 2384–97.

Wehr, Aloysius. 2009. "LiDAR Systems and Calibration." In *Topographic Laser Ranging and Scanning: Principles and Processing*, edited by Jie Shan and Charles K Toth, 129–72. Boca Raton, Florida: CRC Press, Taylor and Francis Group. ftp://ftp.ecn.purdue.edu/jshan/Zproject/proofs/04/51423_C004_corr.pdf.

White, Stephen A, Christopher E Parrish, Brian R Calder, Shachak Pe'eri, and Yuri Rzhanov. 2011. "LIDAR-Derived National Shoreline: Empirical and Stochastic Uncertainty Analyses." *Journal of Coastal Research*, 62–74. https://doi.org/10.2112/SI_62_7.

Wilson, John, and John Hawkes. 1998. *Optoelectronics: An Introduction (3rd Edition)*. Prentice-Hall. https://doi.org/978-0131039612.

Wu, Lei, Xiaopeng Wang, Hongru Yang, Bing Yu, Chao Chen, Bin Yang, Liang Yuan, et al. 2012. "Signal-to-Noise Performance Analysis of Streak Tube Imaging Lidar Systems. II. Theoretical Analysis and Discussion." *Applied Optics* 51 (36): 8836–47. https://doi.org/10.1364/AO.51.008836.

Yang, Eric, Michael Sitar, Paul E LaRocque, Wenbo Pan, Karen Francis, and David Reid. 2009. "Small Object Detection Using SHOALS Bathymetric Lidar." In *U.S. HYDRO 2009*. Norfolk, VA. http://www.thsoa.org/hy09/0514A_03.pdf.

Yang, Hongru, Lei Wu, Xiaopeng Wang, Chao Chen, Bing Yu, Bin Yang, Liang Yuan, et al. 2012. "Signal-to-Noise Performance Analysis of Streak Tube Imaging Lidar Systems. I. Cascaded Model." *Applied Optics* 51 (36): 8825–35. https://doi.org/10.1364/AO.51.008825.

eCommons (2019) https://doi.org10.7298/jxm9-g971

5 BASIC CONCEPTS IN DATA PROCESSING

Lead Authors: Viktor Feygels[a] and Yuri Kopilevich[b]

Contributing Authors: Minsu Kim[c], Chi-Kuei-Wang[d]

a) Teledyne Optech Inc., 7225 Stennis Airport Drive, Suite 400, Kiln, MS 39556
b) St. Petersburg State University of Information Technologies, Mechanics and Optics
c) USGS, 47914 252Nd Street, Sioux Falls, SD
d) Department of Geomatics, National Cheng Kung Univ., Tainan, Taiwan

5.1 Direct georeferencing of the lidar point

Minsu Kim

Lidar data processing is usually considered to be synonymous with the production of a digital elevation model (DEM). While this is obviously critical – and the topic of this section – some advanced ALB systems are radiometrically calibrated so that the data can also be used to estimate the optical properties of a water body and the reflectance of the ocean bottom, topics which will be treated in Sections 5.2, 5.3 and 5.4. Still, the heart of the lidar system is to produce a georeferenced point cloud of laser bathymetry measurements. This introductory section is devoted to describing the georeferencing of the lidar point cloud. All modern airborne lidar imaging systems use direct georeferencing, using an IMU (inertial measurement unit) together with the GNSS (global navigation satellite system) in order to obtain position and orientation. The georeferencing of each lidar point then requires a sequence of coordinate transformations and translations between a series of reference frames.

5.1.1 Sensor modeling

Airborne lidar systems use scanning devices to distribute observations on a surface, making the lidar an imaging system. There are several different types of scanning mechanisms, each of which distributes laser measurements in a different pattern. Examples (with the associated scanning patterns) are: oscillating mirror (zigzag), rotating polygon mirror (parallel lines), nutating mirror (overlapping ellipse), and rotating prism (overlapping circle).

The first step in defining a mathematical model of a scanning system (scanner model) is to define a proper 3D Cartesian coordinate system to describe the direction vector of the laser pulse propagation. This Cartesian reference coordinate system is defined based on the sensor body, and thus is called a sensor body frame (SBF). The simplest example of an SBF would be the case of a bidirectional oscillating scanning mirror. Figure 5.1.1 illustrates the scan pattern and the definition of the sensor model. Usually the sensor is installed on the aircraft so that x-axis and y-axis are aligned to the nose (forward) and the right wing (starboard) of the aircraft, respectively. Then, according to the right-hand rule, the z-axis points downward.

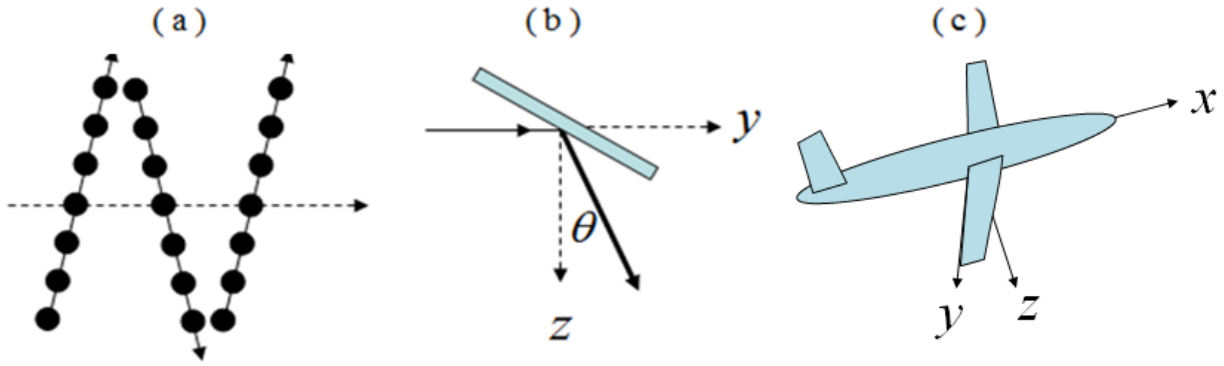

Figure 5.1.1 (a) scan pattern of the oscillating mirror scanner (b) laser pulse direction with scan angle θ_a in SBF (b) typical installation of the sensor with SBF extended on the aircraft

The sensor model in this case is simply a function of the scan angle, θ. The normalized direction vector directed toward the surface point O_w in the SBF is defined as:

$$\mathbf{d}_{O_w}^{SBF} = [0, \sin\theta, \cos\theta]^T \quad . \tag{5.1.1}$$

This direction vector is valid only for a simple oscillating mirror. The exact direction vector depends on the sensor model for the specific scanning device. Describing the details for different types of scanning systems is beyond the scope of this document, but it is important to note that the determination of the precise scan angle, θ, for each laser pulse is not a simple matter. Each scanner is equipped with an encoder that records the GNSS-synchronized time for the moment of encoding. For instance, if a system has a 30 Hz scanner rate, it records 30 GNSS times. However, the precise direction of the laser pulse propagation at the time of encoding is not known. As a result, the precise angular offset at the time of encoding is very difficult to measure. In addition, while the IMU system is installed so that its coordinates align as closely as possible to those of the optical sensor, there is always a small misalignment that must be accounted for (boresight procedure). It is also very difficult to make direct measurements of these three angles. Thus, in all lidar scanning system the boresight procedure (i.e., calculation of the angular offsets between the ALB system and the aircraft) includes this scanner offset angle as well as the usual three angular misalignment angles that are determined via optimization during calibration.

5.1.2 The position vector in the IBF

The range, r_a, that the lidar system measures is from the SBF origin (O_SBF) to the surface that reflects the laser pulse. The position vector in the SBF is determined by:

$$\boldsymbol{X}_{O_w}^{SBF} = r_a \cdot \mathbf{d}_{O_w}^{SBF} \quad . \tag{5.1.2}$$

The 3-element position vector, $\boldsymbol{X}_{O_w}^{SBF}$, represents the SBF Cartesian coordinates of the lidar point, O_w, from which the earth surface reflects the laser pulse back to the receiver. Coordinates expressed in SBF, however, are not useful by themselves (i.e., in the ALB reference system) because the reference system is not geo-referenced to a known datum. The position vector in SBF must be converted to the position vector in a global geodetic frame in a sequence of coordinate transformations.

In order to convert a position vector in an arbitrary SBF into the position vector in a global geodetic frame, the information contained in the GNSS antenna position and the IMU orientation is used to establish an IMU body frame (IBF). The IBF is a 3D Cartesian frame whose origin (O_IBF) is at the IMU center, and the definition of the coordinate system is usually printed on the top surface of the IMU housing. The physical location of the lidar point is invariant, but the coordinate representation can change depending on which reference coordinate system is used. Thus, the position vector in SBF, $\boldsymbol{X}_{O_w}^{SBF}$, is transformed to the position vector in IBF using the following relationship:

$$\boldsymbol{X}_{O_w}^{IBF} = \boldsymbol{R}_{SBF}^{IBF} \cdot \boldsymbol{X}_{O_w}^{SBF} + \boldsymbol{X}_{O_{SBF}}^{IBF} \quad , \tag{5.1.3}$$

where, $\boldsymbol{X}_{O\_SBF}^{IBF}$ is the lever-arm vector to the SBF origin in the IBF, and $\boldsymbol{R}_{SBF}^{IBF}$ is a rotation matrix that transforms $\boldsymbol{X}_{O_w}^{SBF}$ to $\boldsymbol{X}_{O_w}^{IBF}$ is defined using three boresighting angles that represent roll (ω), pitch (φ), and yaw ((κ)):

$$\boldsymbol{R}_{SBF}^{IBF} = \begin{bmatrix} \cos\kappa & -\sin\kappa & 0 \\ \sin\kappa & \cos\kappa & 0 \\ 0 & 0 & 1 \end{bmatrix} \begin{bmatrix} \cos\varphi & 0 & \sin\varphi \\ 0 & 1 & 0 \\ -\sin\varphi & 0 & \cos\varphi \end{bmatrix} \begin{bmatrix} 1 & 0 & 0 \\ 0 & \cos\omega & -\sin\omega \\ 0 & \sin\omega & \cos\omega \end{bmatrix} \tag{5.1.4}$$

$$= \begin{bmatrix} \cos\varphi\cos\kappa & \sin\omega\sin\varphi\cos\kappa - \cos\omega\sin\kappa & \cos\omega\sin\varphi\cos\kappa + \sin\omega\sin\kappa \\ \cos\varphi\sin\kappa & \sin\omega\sin\varphi\sin\kappa + \cos\omega\cos\kappa & \cos\omega\sin\varphi\sin\kappa - \sin\omega\cos\kappa \\ -\sin\varphi & \sin\omega\cos\varphi & \cos\omega\cos\varphi \end{bmatrix}$$

5.1.3 The position vector in the Local Geodetic Frame (LGF)

The success of direct georeferencing depends on the accuracy with which the position and the orientation parameters are measured using the IMU-GNSS subsystem. Once the position vector in the IBF reference system, $\boldsymbol{X}_{O_w}^{IBF}$, is known, it is transformed into a new position vector in a local geodetic frame (LGF), $\boldsymbol{X}_P^{LGF}$. An LGF is defined in reference to a global geodetic frame, such as WGS84. An arbitrary position on a local tangent plane is defined with a positive x-axis pointing to the local north (N), a positive y-axis pointing to the local east (E), and a positive z-axis pointing downward (D) to the center of the ellipsoid. Thus, the arbitrary position follows a coordinate axes convention of a North-East-Down (NED) reference frame. The orientation of the IBF with respect to the LGF is described by three angles: roll (R), pitch (P), and heading (H):

$$\boldsymbol{R}_{IBF}^{LGF} = \begin{bmatrix} \cos H & -\sin H & 0 \\ \sin H & \cos H & 0 \\ 0 & 0 & 1 \end{bmatrix} \begin{bmatrix} \cos P & 0 & \sin P \\ 0 & 1 & 0 \\ -\sin P & 0 & \cos P \end{bmatrix} \begin{bmatrix} 1 & 0 & 0 \\ 0 & \cos R & -\sin R \\ 0 & \sin R & \cos R \end{bmatrix} \tag{5.1.5}$$

$$= \begin{bmatrix} \cos P\cos H & \sin R\sin P\cos H - \cos R\sin H & \cos R\sin P\cos H + \sin R\sin H \\ \cos P\sin H & \sin R\sin P\sin H + \cos R\cos H & \cos R\sin P\sin H - \sin R\cos H \\ -\sin P & \sin R\ \cos P & \cos R\cos P \end{bmatrix}$$

Thus, the position vector $\boldsymbol{X}_{O_w}^{IBF}$ is transformed to the position vector in the LGF as follows

$$\boldsymbol{X}_{O_w}^{LGF} = \boldsymbol{R}_{IBF}^{LGF} \cdot \boldsymbol{X}_{O_w}^{IBF} \quad . \tag{5.1.6}$$

Note that there is no lever-arm vector correction because the origin of LGF is identical to O_IBF.

5.1.4 Refraction into the water

In case of ALB system only a small fraction of the laser pulse energy is reflected at the air-water interface to produce a surface return in the lidar waveform (Chapter 0). The majority of the energy is refracted into the water and propagates until it reaches the bottom where it is reflected back up to the system, producing a bottom return in the waveform. The two returns, one from the surface and one from the bottom, define the slant range in the water. By taking the refracted direction and the in-water range into account it is possible to calculate the 3D digital elevation model (DEM) of the ocean floor.

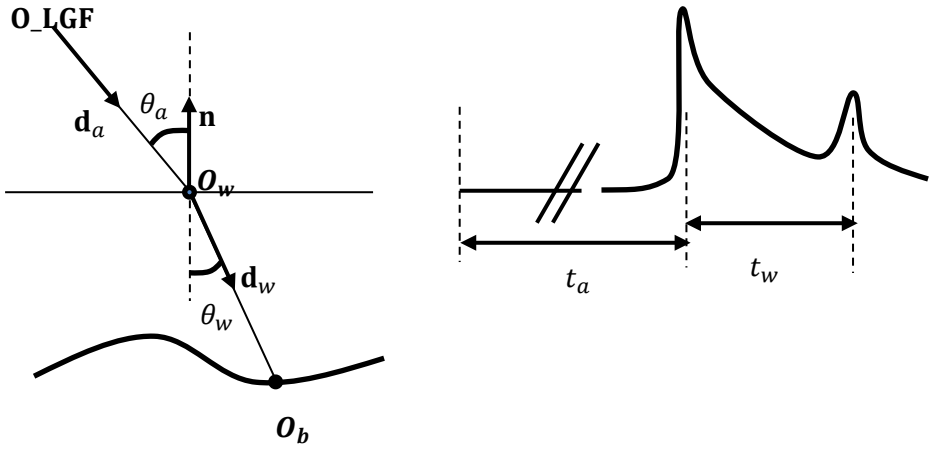

Figure 5.1.2 Refraction at the air-water interface and the waveform

It is important to note that it is only possible to calculate the refraction after the position vector is represented in LGF. This is because the x,y-plane of the SBF and IBF are not parallel to the water surface. There is also a slight mismatch between the local ellipsoid surface and the water surface; this inaccuracy is minimal for the purpose of in-water ranging.

The position vector, $X_{O_w}^{LGF}$, is the vector from O_LGF to the surface point O_w in Figure 5.1.2. The time of travel, t_a, from origin to the first peak of the waveform is related to the in-air range H_s by the relationship, $H_s = c \cdot t_a/2$. Using the vector version of Snell's law, the air-incident angle is calculated as:

$$\cos\theta_a = -\mathbf{n} \cdot \mathbf{d}_{O_w}^{LGF} \quad , \qquad \mathbf{d}_a = \boldsymbol{X}_{O_w}^{LGF}/H_s \quad . \tag{5.1.7}$$

Here, $\mathbf{d}_a$ is a unit in-air direction vector and $\mathbf{n}$ is an upward normal vector at the water surface. If we write $\boldsymbol{X}_{O_w}^{LGF} = [x, y, z]$ with $\mathbf{n} = [0, 0, -1]$, then equation (4.6.7) reduces to: $\cos\theta_a = z/H_s$.
Subsequently, the in-water refracted angle is calculated using the refractive index of water, n_w, such that

$$\cos\theta_w = \sqrt{1 - \sin^2\theta_a / n_w^2} \quad , \qquad \sin^2\theta_a = -(z/H_s)^2 \quad . \tag{5.1.8}$$

The unit direction vector of the in-water refracted beam is calculated as:

$$\mathbf{d}_{P_b}^{LGF} = (1/n_w) \cdot \mathbf{d}_a + [(1/n_w)\cos\theta_a - \cos\theta_w] \cdot \mathbf{n}. \tag{5.1.9}$$

Finally, the position vector at the ocean bottom point, O_b, is described by:

$$\mathbf{X}_{P_b}^{LGF} = \mathbf{X}_{O_w}^{LGF} + r_w \cdot \mathbf{d}_w \ , \quad h_s = c \cdot t_w/(2n_w) \quad , \tag{5.1.10}$$

where t_w is the travel time in water. If the lidar point is at the ocean bottom, $\mathbf{X}_{P_b}^{LGF}$ can be used in the place of $\mathbf{X}_{O_w}^{LGF}$ in the subsequent georeferencing calculations.

5.1.5 The position vector in the earth centered, earth fixed (ECEF) frame

The position of the phase center of the GNSS antenna can be provided by either in an ECEF (earth centered earth fixed) frame (using Cartesian coordinates or geographic coordinates) or in global ellipsoid datum (using geographic coordinates). Once the position of the GNSS antenna phase center is known, then the lever-arm distances between the IMU origin and the antenna can be used to calculate the position of the O_IBF (which is same as O_LGF). Using the latitude ϕ, longitude λ, and ellipsoid height, h, from O_LGF, it is possible to form a rotation matrix that transforms an arbitrary position vector in LGF to the position vector in ECEF:

$$\begin{aligned} \boldsymbol{R}_{LGF}^{ECEF} &= \begin{bmatrix} \cos\lambda & -\sin\lambda & 0 \\ \sin\lambda & \cos\lambda & 0 \\ 0 & 0 & 1 \end{bmatrix} \begin{bmatrix} \cos\left(-\varphi - \frac{\pi}{2}\right) & 0 & \sin\left(-\varphi - \frac{\pi}{2}\right) \\ 0 & 1 & 0 \\ -\sin\left(-\varphi - \frac{\pi}{2}\right) & 0 & \cos\left(-\varphi - \frac{\pi}{2}\right) \end{bmatrix} \begin{bmatrix} 1 & 0 & 0 \\ 0 & \cos 0 & -\sin 0 \\ 0 & \sin 0 & \cos 0 \end{bmatrix} \\ &= \begin{bmatrix} -\sin\varphi\cos\lambda & -\sin\lambda & -\cos\varphi\cos\lambda \\ -\sin\varphi\sin\lambda & \cos\lambda & -\cos\varphi\sin\lambda \\ \cos\varphi & 0 & -\sin\varphi \end{bmatrix} \end{aligned} \tag{5.1.11}$$

In addition to the rotation matrix, the geodetic position (φ, λ, h) of O_LGF itself can be transformed into the position in the ECEF coordinate using the following relationship:

$$\boldsymbol{R}_{O\_LGF}^{ECEF} = \begin{bmatrix} (r_N + h)\cos\varphi\cos\lambda \\ (r_N + h)\cos\varphi\sin\lambda \\ [(1 - e^2)r_N + h]\sin\varphi \end{bmatrix} \quad , \quad r_N = \frac{a}{\sqrt{1 - e^2\sin^2\varphi}} \quad , \tag{5.1.12}$$

where, a is the semi-major axis, e is the eccentricity, and r_N is the position in ECEF coordinates. We may now solve for the position vector in ECEF coordinates:

$$\boldsymbol{X}_{O_w}^{ECEF} = \boldsymbol{R}_{LGF}^{ECEF} \cdot \boldsymbol{X}_{O_w}^{LGF} + \boldsymbol{X}_{O\_LGF}^{ECEF} \tag{5.1.13}$$

The goal of georeferencing is achieved by calculating the position of the lidar point in ECEF. In practice, however, the ECEF reference system is not a convenient form for geospatial data. Most mapping products are in ellipsoidal reference systems (latitude/longitude/ellipsoid height). Thus, there is a need to convert the laser measurements from an ECEF reference system to an ellipsoidal reference system. The final

eCommons (2019) https://doi.org10.7298/jxm9-g971

product may also need to be projected to a map coordinate system (e.g., Universal Transverse Mercator or local state plane), depending on the application.

5.2 Inverse problems of lidar waveform processing

V. Feygels, Yu. Kopilevich

Retrieval of inherent optical properties (IOPs) of seawater from ALB data represents a supplemental application of bathymetrical lidar systems, along with bottom reflectance measurement. Bottom reflectance is considered later in Section 4.4. In this Section, a general approach to the inverse problem of lidar waveform processing (initially proposed in Kopilevich et al. (2005)), is discussed; the special problem of estimation of the diffuse attenuation coefficient is considered further in Section 5.3.

As was discussed above in Section 4.3.1, processing of an experimentally obtained waveform, $D^{exp}(t)$ (the output electrical signal from the receiver channel) in order to estimate environmental properties (bottom depth, reflectance, and IOPs) relies on a comparison of the experimental waveform with simulated waveforms. To perform the comparison in the optical domain using radiometric units, the electrical signal (in digital counts) must be transformed into the optical signal, S_R^{exp} in Watts ("real waveform", see Equation (4.3.12)

$$S_R^{exp}(t) = \chi^{-1}\left[D^{exp}(t)\right] \quad , \tag{5.2.1}$$

where, $\chi^{-1}[\cdot]$ is the inverse of the channel Watt-count characteristic, $\chi[\cdot]$, which is determined from radiometric calibration of the receiving channel (Section 3.3.1).

A (simulated) waveform, $S_R^{sim}(t)$, may be calculated from a theoretically derived Impulse Response Function, $S_\delta(t)$, i.e. the lidar signal corresponding to an infinitesimally short (delta-function shaped) initial laser pulse (see Section 3.2.2). Following the same procedure presented in Section 3.3.2, $S_R^{sim}(t)$ may be calculated by convolving $S_\delta(t)$ with the effective sounding pulse shape (or the channel response function), $R(t)$:

$$S_R^{sim}(t) = \int_{-\infty}^{\infty} S_\delta(t-t')\cdot R(t')dt' \equiv S_\delta(t) * R(t) \quad , \tag{5.2.2}$$

where $R(t)$, is determined from radiometric calibration measurements (see Section 3.3.1).

Water IOPs are estimated by fitting the simulated signal, $S_R^{sim}(t)$, to the actual experimental waveform, $S_R^{exp}(t)$, on a time interval, $t_- \le t \le t_+$, where t_- corresponds to a near-surface horizon deep enough to obviate the need to account for surface effects, and t_+ corresponds to a near-bottom horizon for which bottom reflection is still undetected. The problem formally reduces to minimizing the difference between the two functions using appropriate metrics. Using the least squares method, the functional of the pulse energy, Q, may be written as:

$$Q = \int_{t_-}^{t_+} \left|S_R^{\exp}(t) - S_R^{sim}(t)\right|^2 dt \quad . \tag{5.2.3}$$

In reality, one uses the discrete analogue of the functional, i.e., the sum of the squared differences between the experimental waveform samples, $\{S_R^{\exp}(t_i)\},\ t_- \le t_i \le t_+,\ i = 1,\ 2,\ \ldots$, and the corresponding discrete values $\{S_R^{sim}(t_i)\}$.

It should be recognized that the estimates obtained with the above algorithms, using simulated waveforms calculated for a homogeneous water column, ignore vertical stratification of water optical properties and thus correspond to effective (or "averaged") values of the IOPs. The estimates are also subject to any inaccuracies of the accepted models: small-angle scattering approximation for the RTE, models used for emitted laser pulse and receiver channel, modeled VSF (Kopilevich, Kononenko, and Zadorozhnaya 2011). Corresponding errors in the IOP estimates are difficult to assess.

Unfortunately, a straightforward approach to the problem of minimization of the pulse energy functional (Equation (5.2.3)) as a variational problem using the absorption coefficient, a, backscattering coefficient, b_b, forward-scattering coefficient, b_f, and VSF shape parameter m (see Sec. 4.3.3, Equation (4.3.77) is mathematically ill-posed. However, it is possible to regularize the fitting problem using statistical relationships among the IOPs in order to restrict *a priori* the range of acceptable solutions (Dolin et al. 1988). A practical realization of the approach consists of the following steps:

Step 1. The beam attenuation coefficient, *c*, is taken as an independent variable in order to obtain an estimate, c^*, which minimizes the functional (4.2.3),

$$Q(c^*) = \min_c Q(c) \quad . \tag{5.2.4}$$

All the other IOPs are calculated for a given value of c via a set of regression relations. The single-scattering albedo ω_0 (dimensionless) is evaluated as (I. M. Levin and Kopelevich 2003) via the beam attenuation coefficient, *c*, in 1/m:

$$\omega_0 = 0.944 - 0.048/c \quad , \tag{5.2.5}$$

For the scattering coefficient, b we use the relationship:

$$b = c\omega_0 \quad . \tag{5.2.6}$$

The hydrosol (suspended particulate) volume concentration for large particles, V_{lg}, in cm^3/m^3 is then evaluated using (Dorogin et al. 1988):

$$V_{lg} = 1.44 \cdot 10^{-2} + 1.68 \cdot b \quad , \tag{5.2.7}$$

where *b* is measured in m^{-1}, and

$$b = V_{sm} \cdot b_{sm} + V_{lg} \cdot b_{lg} + b_w \quad . \tag{5.2.8}$$

Here, the specific scattering coefficients for small, b_{sm}, and large, b_{lg}, hydrosol particles, and the scattering coefficient for "pure" (hydrosol-free) seawater at 500 nm, b_w, are specified in Monin (1983) as:

$$b_{sm} = 1.34\ m^{-1};\ b_{lg} = 0.312\ m^{-1};\ b_w = 1.7 \cdot 10^{-3}\ m^{-1}. \tag{5.2.9}$$

To be precise, equations (5.2.8) and (5.2.9) are established based on 500 nm and not 532 nm (Monin, 1983), but the corresponding error is negligible for the ALB case here. Knowing V_l and V_s, it is possible to approximate the VSF, $\beta(\theta)$, as proposed by Kopelevich & Mezhericher (1983):

$$\beta(\theta) = \left(\frac{550}{\lambda}\right)^{1.7} \cdot \beta_{sm}(\theta, 550) \cdot V_{sm} + \left(\frac{550}{\lambda}\right)^{0.3} \cdot \beta_{lg}(\theta, 550) \cdot V_{lg} + \left(\frac{550}{\lambda}\right)^{4.3} \cdot \beta_w(\theta, 550)\,, \tag{5.2.10}$$

where the wavelength, $\lambda = 532\ nm$. The functions, $\beta_{sm}(\theta, 550)$ and $\beta_l(\theta, 550)$ are the VSF for water suspensions of small and large particles respectively, for unit concentrations of the suspensions; $\beta_w(\theta, 550)$ is the VSF for pure seawater. The values of these functions are tabulated in Monin (1983) for a range of scattering angles, θ.

Integration of (5.2.10) over the appropriate solid angles gives the forward and backward scattering coefficients, b_f and b_b:

$$b_f = 2\pi \int_0^{\pi/2} \beta(\theta) \cdot \sin(\theta)\, d\theta \quad , \quad b_b = 2\pi \int_{\pi/2}^{\pi} \beta(\theta) \cdot \sin(\theta)\, d\theta \quad . \tag{5.2.11}$$

Finally, the values are used to obtain the VSF asymmetry coefficient, b_f/b_b, and the average cosine of the scattering angle, $\overline{\cos\theta}$; the latter is required for the parameter, m, in Dolin's model VSF [see Dolin & Levin (1991) and Sec. 4.3.3, Equation (4.3.77]:

$$m = [0.142 - 0.132 \cdot \overline{\cos\theta}]^{-1/2} \quad . \tag{5.2.12}$$

Equation (5.2.10) also yields an estimate for the backscattering coefficient, $\beta_\pi = \beta(180°)$. Since (5.2.12) is based on *in-situ* measurements that do not cover angles greater than ~170°, the equation does not account for the angular dependence of the VSF for angles near 180°, where a pronounced "enhanced backscattering effect" can occur (Maffione and Dana 1996). For a more realistic estimate allowing for the backscattering effect, we may use

$$\beta_\pi = C \cdot \beta(180^o) \quad , \tag{5.2.13}$$

with $\beta_\pi = \beta(180°)$ calculated from (5.2.10) and C ={1.3-1.9}

Step 2: consists of finding a better estimate of ω_0^* than that given by equation (5.2.5) by varying the value of the single scattering albedo, ω_0, at the fixed $c = c^*$:

$$Q(c^*, \omega_0^*) = \min_{\omega_0} Q(c^*, \omega_0) \quad . \tag{5.2.14}$$

During this estimation, all the other IOPs (a, b_b, b_f, and m) are assumed to be unambiguously defined by ω_0 using equations (5.2.6)-(5.2.8) and (5.2.10)-(5.2.12), with $c = c^*$. This step of the fitting algorithm makes it possible to account for local peculiarities of the sea water optical properties, rather than simply using equation (5.2.5), which is a statistical average over various regions of the ocean.

It is important to emphasize that the algorithm described above is limited to waters deep enough to provide an extended time interval (t_-, t_+) for which the waveform is not subject to surface or bottom effects. In accordance with the waveform components considered in Sec. 4.2.2 [see Figure 4.2.6 – Figure 4.2.8],

$$t_- \geq t^{sf} + \frac{\Delta t^{sf}}{2} + \tau_R \quad ; \quad t_+ \leq t^{bot} - \frac{\Delta t^{bot}}{2} \quad , \tag{5.2.15}$$

where the "geometrical stretch" of the surface-reflected pulse, Δt^{sf}, given by (4.2.4), depends on the lidar sounding geometry (i.e., it increases with the sounding angle, the emitter divergence, and the receiver field-of-view angle). Similarly, the reflected bottom pulse duration, Δt^{bot}, given by equation (4.2.5), is augmented by the small-angle scattering effect, and τ_R is the effective pulse duration. An additional constraint is the requirement that the received power, $S_R^{\exp}(t_+)$, exceed the output signal noise level, acknowledging the strong attenuation of the laser beam by seawater.

5.3 Estimation of the diffuse attenuation coefficient from lidar waveform slope

V. Feygels, Yu. Kopilevich

The diffuse attenuation coefficient, K_d, is a key physical characteristic in the field of ocean optics, and is a prominent example of an apparent optical properties (AOPs) (see Section 3.3.1 and (Mobley 1994)). To calculate K_d in terms of the inherent optical properties (IOPs), the following relation proposed by Morel & Loisel (Morel and Loisel 1998) may be applied:

$$K_d = (\cos\theta_w^{sun})^{-1} \cdot 1.0395 \cdot a_s \quad , \tag{5.3.1}$$

where 1.0395 is a theoretical constant; θ_w^{sun}, is solar zenith angle in the water; and a_s is the effective absorption coefficient. The coefficient a_s defined in Section 4.3.2 as $a_s = a + 2b_b$ (a is the absorption coefficient and b_b is the backscattering coefficient) is to be identified with the property $a + b_b$ used by Morel & Loisel (1998) and others. The ratio K_d/a_s calculated for various solar zenith angles using equation (5.3.1), are presented in Table 5.1:

Table 5.1. K_d/a_s calculated for various solar zenith angles using equation (4.3.1)

solar zenith angle			$\cos\theta_w^{sun}$	$1/\theta_w^{sun}$	K_d/a_s
in the air, θ_a^{sun} degree	in the water, θ_w^{sun}				
	Radian	Degree			
0	0	0	1	1	1.0395
5	0.0651	3.7292	0.9979	1.0021	1.041706
10	0.13	7.4458	0.9916	1.0085	1.04834
15	0.1944	11.137	0.9812	1.0192	1.05945
20	0.2581	14.788	0.9669	1.0343	1.07511
25	0.3209	18.384	0.949	1.0538	1.095406
30	0.3824	21.909	0.9278	1.0778	1.12042
35	0.4423	25.343	0.9038	1.1065	1.150196
40	0.5003	28.665	0.8774	1.1397	1.1847
45	0.5559	31.85	0.8494	1.1773	1.223753
50	0.6085	34.867	0.8205	1.2188	1.266941
55	0.6577	37.684	0.7914	1.2636	1.313506
60	0.7027	40.262	0.7631	1.3105	1.362217

In practical calculations, accounting for "reasonable" sun zenith angles for a given site latitude, the ratio K_d/a_s may be approximated by a constant. For example, an approximate relationship derived from equation (5.3.1) and Table 5.1 [see Tuell et al. (Tuell, Feygels, et al. 2005)]:

$$K_d = 1.17 \cdot a_s \quad , \tag{5.3.2}$$

Estimation of the diffuse attenuation coefficient from lidar sounding data consists in retrieval of the effective absorption coefficient, a_s, from the lidar waveform, and the application of equation (4.3.1) [or its approximate form analogous to equation (5.3.2)]. Formally, the value of a_s may be estimated from the inverse problem described in Section 4.2 by fitting an experimental waveform with a simulated waveform that is calculated using a variable set of IOP values. For the specific task of estimating the diffuse attenuation coefficient, however, the general ill-posed problem may be regularized without invoking statistical relationships among the IOPs. The practical approach is based on the backscattered lidar signal model (see Sections 4.3.2 and 4.3.3) for an infinitesimally short pulse, which may be written in two equivalent forms [compare with (4.3.13)]:

$$\begin{aligned} S_\delta^{back}(t) &= Q \cdot \tau_F^2 \frac{\Sigma}{(H_s n_w + h_s)^2} \beta_\pi \frac{c}{2\mathrm{n}_w} \exp\left[-2h_s \cdot K_{sys}(h_s)\right] \\ &= Q \cdot \tau_F^2 \frac{\Sigma}{(H_s n_w + h_s)^2} \beta_\pi \frac{c}{2\mathrm{n}_w} \exp(-2h_s \cdot a_s) \cdot F_D(h_s) \end{aligned} \tag{5.3.3}$$

Here the slant depth, h_s is related to the time, t, as $h_s = h_s(t) = ct/2n_w$ (where c/n_w is the speed of light in the water); Q is the energy of the incident laser pulse (taking into account the attenuation over the

atmospheric path and the transmission of the receiver system); τ_F is the Fresnel transmission of the water–air interface; Σ is the pupil area of the lidar receiver; β_π is the backscattering coefficient of sea water; and H_s is length of beam pass in the air (slant path of the lidar beam above sea level). The so-called "system attenuation coefficient", K_{sys} may then be expressed as

$$K_{sys}(h_s) = a_s + K'_{sys}(h_s) = a_s - \ln F_D(h_s) \qquad (5.3.4)$$

The function $F_D(h_s)$ was introduced by Dolin & Savel'ev (1971a) [see also Dolin & Levin (1991) to account for the effect of forward scattering on the decay of the lidar signal with water depth; $F_D(h_s) = 1$ at $h_s = 0$ and decreases with the water depth. The decay rate of the function increases with the small-angle forward-scattering coefficient $b_s = b - b_b$, and strongly depends on the lidar receiver field-of-view angle Θ_R. Figure 5.3.1 illustrates the function $F_D(h_s)$, calculated for two CZMIL receiver channels: the wide-field channel ($\Theta_R = 40\ mrad$) and the narrow-field channel ($\Theta_R = 1.9\ mrad$). The IOP values used in the calculations were: $a_s = 0.075\ m^{-1}$; $b_s = 0.2\ m^{-1}$; VSF shape parameter in Dolin's model, $m = 7$. In the case of the wide-field channel, the approximation $F_D(h_s) \approx 1$ may be used for small enough depth values, $h_s \le h_s^{max}(b_s, \Theta_R)$, with the additional condition (from (4.3.4) that $K_{sys}(h_s) \approx a_s$. According to equation (3.3.1, the backscattered signal $S_\delta^{back}(t)$ for the wide-field receiver channel over the time interval, $t \le t^{sc}(b_s, \Theta_R) \equiv 2h_s^{max}(b_s, \Theta_R)/n_w c$, (where t^{sc} is the upper limit of the backscattered signal argument that corresponds to a negligible impact of forward scattering) may be approximated with the exponential relationship:

$$S_\delta^{back}(t) \approx const \cdot exp[-2h_s \cdot a_s], \qquad t \le t^{sc}(b_s, \Theta_R) \qquad (5.3.5)$$

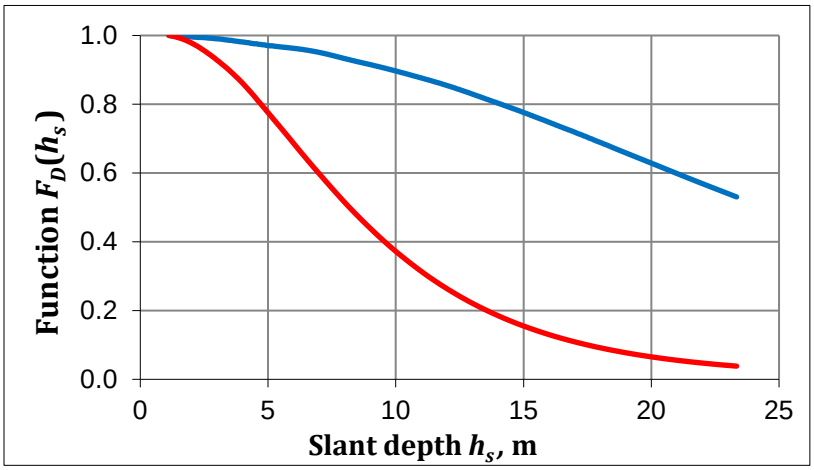

Figure 5.3.1. The function $F_D(h_s)$ calculated for the wide-field CZMIL channel with the field-of-view angle $\Theta_R = 40\ mrad$ (blue) and for the narrow-field channel with $\Theta_R = 1.9\ mrad$ (red); $a_s = 0.075\ m^{-1}$; $b_s = 0.2\ m^{-1}$; VSF shape parameter in Dolin's model $m = 7$.

Figure 4.3.2 illustrates the backscattered signal decay with slant depth. The simulated backscattered components of the waveforms $S_\delta^{back}(t)$ in each of the channels are shown as functions of the slant depth, $h_s = ct/2n_w$. It is seen that, for the narrow-field channel, the signal tends to zero at the upper limit of the time interval, $t^{sc}(b_s, \Theta_R)$, where the approximation (5.3.5) is accurate enough for realistic forward scattering.

For water that is sufficiently deep, there exists a time interval $t^{sf} + \Delta t^{sf} < t < t^{bot} - \Delta t$ (see Section 5.3.2 for the notation) for which the effects of surface and bottom reflection may be neglected. In that case, the backscattered signal $S_\delta^{back}(t)$ coincides with the ImpRF, $S_\delta(t)$ (the waveform corresponding to an infinitesimally short sounding pulse, see Section 3.3.2). In virtue of equation (4.3.5),

$$S_\delta(t) \approx const \cdot exp\left[-\frac{ct}{n} \cdot a_s\right] \quad , \quad t^{sf} + \Delta t^{sf} < t < \min\{t^{sc}(b_s, \Theta_R), t^{bot} - \Delta t^{bot}\} \quad . \qquad (5.3.6)$$

The time interval specified in equation (5.3.6) exists (is not empty) only for clear water with weak enough scattering and absorption for $S_\delta(t)$ to be well above the noise level, if the receiver field of view is wide enough to ensure existence of the time interval specified in (5.3.6).

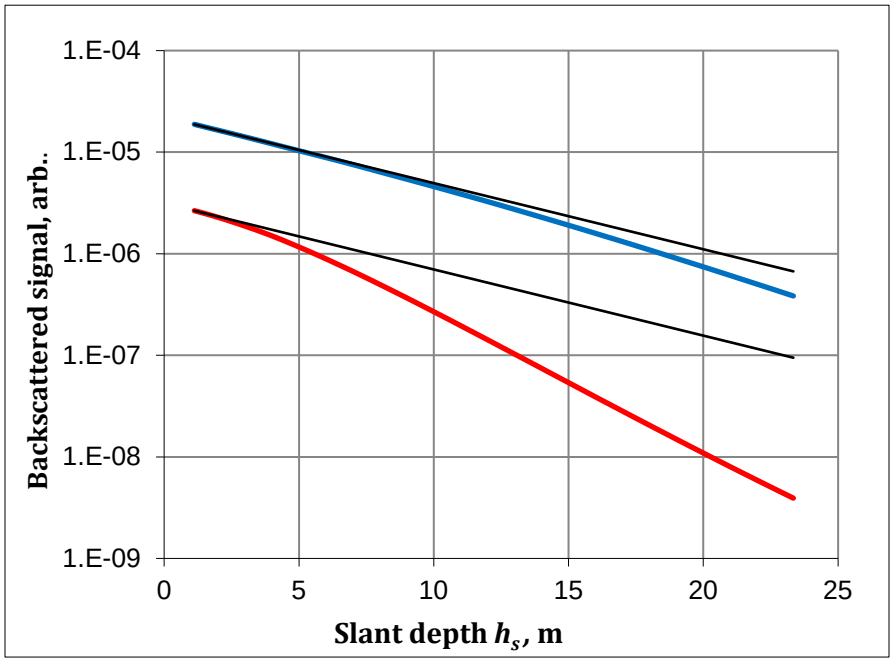

Figure 5.3.2. Backscattered components, S_δ^{back}, of delta-function sounding pulse waveforms in the wide-field CZMIL channel with the field-of-view angle, $\Theta_R = 40\ mrad$ (blue) and for the narrow-field channel with $\Theta_R = 1.9\ mrad$ (red); $a_s = 0.075\ m^{-1}$; $b_s = 0.2\ m^{-1}$; VSF shape parameter in Dolin's model $m = 7$. Black lines correspond to exponential approximation, $S_\delta^{back} \sim exp(-2a_s h_s)$.

In order to estimate the effective absorption coefficient, a_s , from the lidar waveform, it is essential that equation (4.3.6) yield a formula for the "real waveform", $S_R(t)$ [equation (4.2.8)], similar to that retrievable from the output lidar signal:

$$S_R(t) = \int_{-\infty}^{\infty} S_\delta(t - t') \cdot R(t') dt' \equiv S_\delta(t) * R(t) \quad , \qquad (5.3.7)$$

where $R(t)$ is the effective sounding pulse shape (see Section 4.3.1). In effect, equation (5.3.6) requires that:

$$\int_{-\infty}^{\infty} exp\left[-\frac{c(t-t')}{n} \cdot a_s\right] \cdot R(t')\, dt' = exp\left[-\frac{ct}{n} \cdot a_s\right] \cdot \int_{-\infty}^{\infty} exp\left[-\frac{ct'}{n} \cdot a_s\right] \cdot R(t') \qquad (5.3.8)$$

in which case (5.3.6) and (5.3.7) yield

$$S_R(t) \approx const \cdot exp\left[-\frac{ct}{n} \cdot a_s\right] \quad , \qquad t^{sf} + \Delta t^{sf} + \tau_R < t < \min\{t^{sc}(b_s, \Theta_R), t^{bot} - \Delta t^{bot}\} \quad . \tag{5.3.9}$$

Compared to equation (5.3.6), the time interval in equation (5.3.9) is reduced by the effective sounding pulse duration, τ_R.

Based on equation (5.3.9), the problem of estimating the effective absorption coefficient from the lidar waveform is reduced to the derivation of the $\{S_R(t)\}$ values from output signal samples at discrete times in the interval specified in equation (5.3.8) and a linear regression of the values in logarithmic scale ((5.3.2)). The estimate for a_s is then easily obtained from the line slope regression.

Note that the approach to estimating the diffuse attenuation coefficient from the lidar waveform calls for application of the receiver channel Watt-count characteristic (Section 4.3.1) obtained in the course of radiometric calibration of the receiver channel described in Section 4.4. Knowledge of the channel response to the laser pulse or effective pulse shape, $R(t)$, is not necessary. Applicability of the procedure described above is restricted by the limitations imposed by both environmental properties (water clarity and the sea depth) and lidar receiver characteristics (the receiver field of view, the effective sounding pulse duration). The procedure also assumes homogeneity of the water column. Thus, the estimates for the effective absorption and the diffuse attenuation coefficient obtained using this method relate to "effective averaged" values of the optical properties. It should be noted that other approaches to estimation of diffuse attenuation profiles from lidar waveforms are presented in Steinvall, Koppari, & Karlson (1993) and Smart & Kwon (1996).

5.4 Bottom reflectance estimation

Yuri Kopilevich and Chi-Kuei Wang

The ability to estimate seafloor reflectance from ALB waveforms, first demonstrated by Lee and Tuell (Lee and Tuell 2003), may have direct value in the analysis of bottom habitat type (Tuell, Feygels, et al. 2005). The lidar-derived bottom reflectance is also used (together with depth) as a constraint in inversion of airborne hyperspectral imagery data for benthic mapping applications (Park et al. 2010b; Tuell and Park 2004; Tuell, Feygels, et al. 2005).

As indicated above in 5.1 (see also 4.3.1), processing experimentally obtained waveforms in order to estimate bottom reflectance requires a preliminary transformation from the output electrical signal from the receiver channel, $D^{exp}(t)$ (in digital counts), into the optical signal, S_R^{exp} in Watts (i.e., the "real waveform", see Section 4.3.1). The channel Watt-count characteristic, $\chi[\cdot]$, used in the procedure, should be known from radiometric calibration of the receiving channel (Section 4.3.1).

In shallow water, the bottom-reflected component of the lidar return is superimposed on the backscattering from the water column (Pe'eri and Philpot 2007) as shown in Figure 5.4.1). In deep, clear water, the backscattered signal from near-bottom water layer can be below the noise level in which case it does not interfere with the bottom-reflected pulse (Figure 5.4.2).

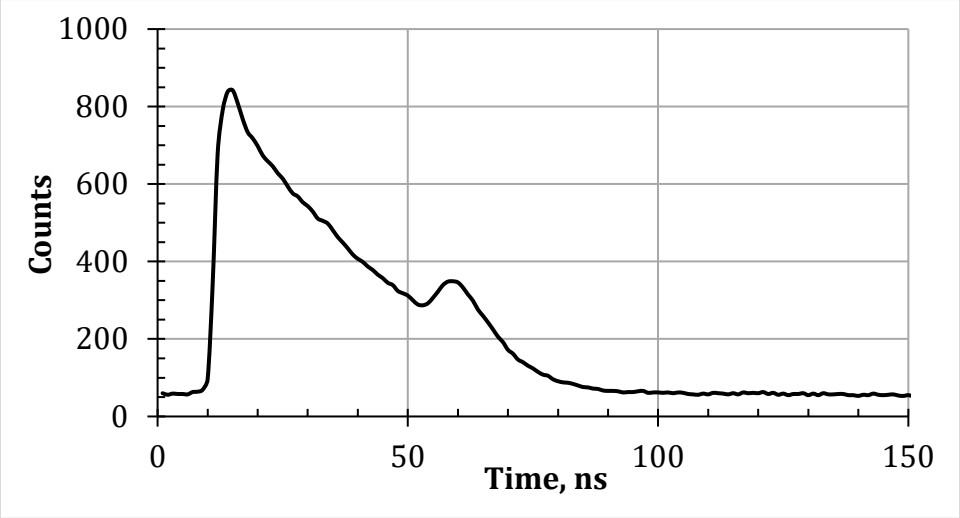

Figure 5.4.1. CZMIL waveform from the Cat Island region, Mississippi Coast; depth 6.5 m. The bottom-reflected peak rides on the background caused by backscattering from the water.

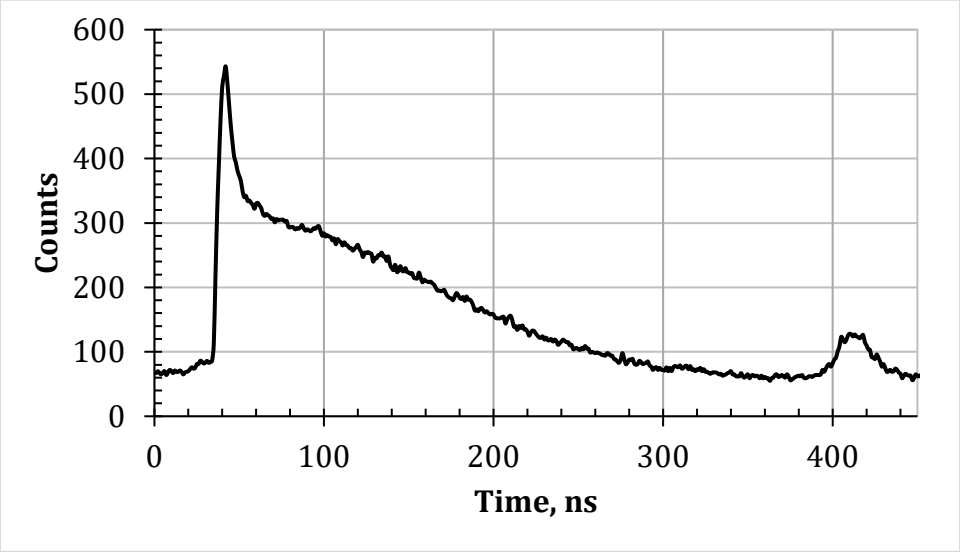

Figure 5.4.2. CZMIL waveform from the Fort Lauderdale coastal zone, Florida; depth 39 m. The backscattered signal from the near-bottom layer falls below the noise level.

In the shallow-water case, bottom reflectance can be extracted from the ALB “real waveform” (optical signal), provided that the bottom return can be decoupled from the volume scattering. Two common methods for bottom return extraction are described below and their schematic plots are shown in Figure 5.4.3:

1) Extrapolation approach: The exponentially-decaying signal of the volume scattering return is extrapolated toward the trailing end of the waveform, extending over the time bins of the bottom return. The residual signal, which is the difference between the bottom return (in the original waveform) and the extrapolated curve is then used to estimate bottom return signal(C.-K. Wang and Philpot 2007).

2) Gaussian deconvolution: The bottom return signal is decomposed into several parametric curves. Symmetrical Gaussian functions are often employed for representing the surface (air/water interface) and bottom returns; exponentially modified Gaussian function have also been employed in situations where the asymmetry of the returns are not negligible (Cottin, Forbes, and Long 2009; Wong and Antoniou 1991, 1994)

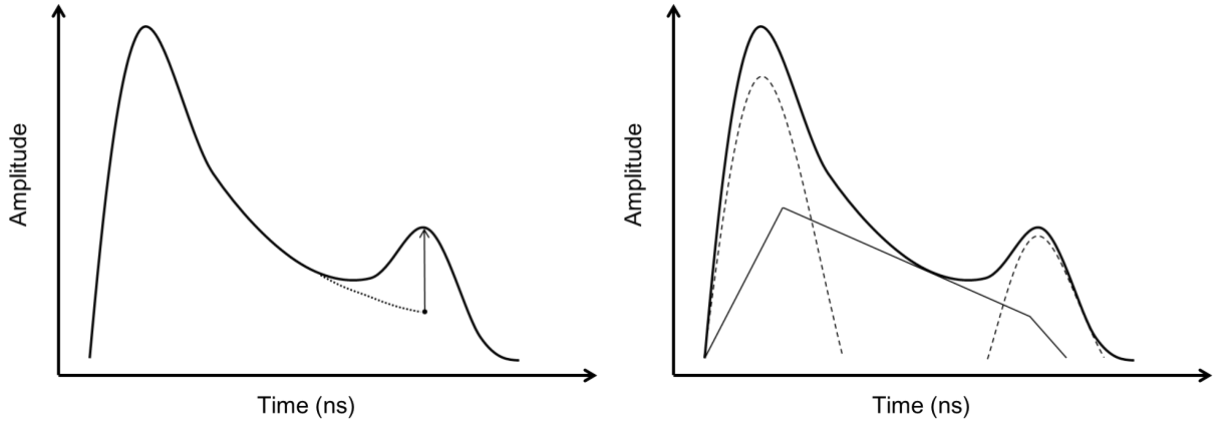

Figure 5.4.3. The schematic plots of extrapolation approach (left) and Gaussian deconvolution (right), where the water volume is modeled as a quadrilateral function, for bottom return extraction.

Modeling the water volume return is not trivial. As will be shown below, the modeling procedure can be well-described for a homogeneous water column; however, the assumption that the water column is vertically homogeneous is not always correct. Thus, linear, exponential, triangular, quadrilateral or successive Gaussian functions are all possible candidates for the modeling task (Abady et al. 2014; Collin et al. 2007; Wong and Antoniou 1991). The selection of an appropriate function to model the volume scattering depends on the specific task of interest. The bottom return obtained by the Gaussian deconvolution approach provides a complete set of information, e. g., amplitude and shape, which can be useful for bottom classification. Nonetheless, the numerical instability and the computation cost are the major obstacles for conducting a Gaussian decomposition on ALB waveforms that contain a large number of laser measurements.

The bottom return power decreases in concert with the backscattered signal (see Figure 5.4.4). In order to obtain the bottom reflectance, the bottom return signals must be normalized to remove the water attenuation, which is described by the exponential factor [Section 5.3, Equation (4.3.1]:

$$\exp\left[2h_s^{bot} \cdot K_{sys}\left(h_s^{bot}\right)\right] \quad , \tag{4.4.1}$$

where h_s^{bot} is the slant bottom depth, and K_{sys} is the system attenuation coefficient described in details in Section 5.3. According to equation (5.3.4), the system attenuation coefficient may be expressed as:

$$K_{sys}\left(h_s^{bot}\right) = a_s - K'_{sys}\left(h_s^{bot}\right) = a_s - \ln F_D\left(h_s^{bot}\right) \quad , \tag{4.4.2}$$

where a_s is the effective absorption coefficient of the water, and the function F_D accounts for the effect of forward scattering of laser beam in the water on lidar signal decay with depth (Dolin and Levin 1991). The function is described in Sections 4.3.3 and 5.3). In the case of clear water and moderate depth, it is

important to note that the contribution from forward scattering to the system attenuation coefficient may be neglected for a lidar receiver with wide enough field-of-view. As a result, K_{sys} in equation (4.4.2) may be approximated (for homogeneous water column) by the effective absorption coefficient, a_s. Figure 5.4.4 provides an example for such a case (i.e., a nearly exponential signal decay $\sim\exp[-2h_s^{bot} \cdot a_s]$). In the extremely clear water ($a_s \approx 0.05\ m^{-1}$), the forward scattering effect does not manifest itself in the decay rate of the waveforms from the CZMIL "deep channel" up to the depth of ~ 40 m.

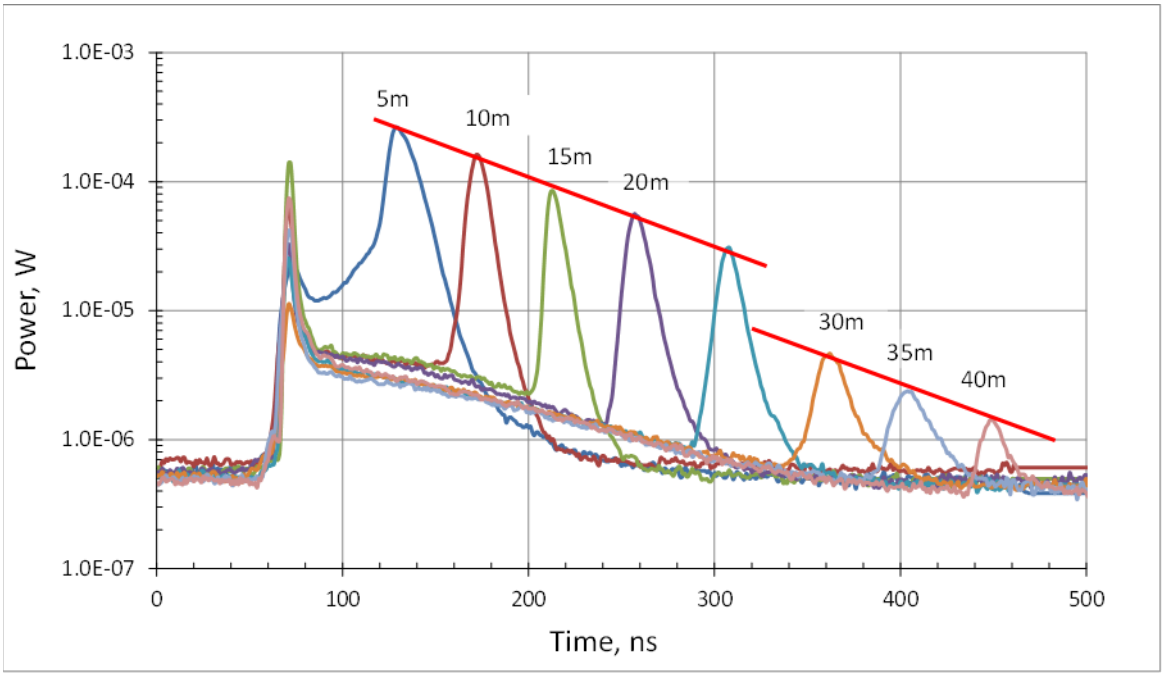

Figure 5.4.4. Attenuation of backscattered signal and bottom-reflected peaks at various depths. Superposition of waveforms from Fort Lauderdale coastal zone, Florida, obtained with CZMIL "deep channel" (PMT in "logarithmic" mode). The abrupt change in the magnitude of the bottom return between 25-30 m is indicative of a change in the water properties.

In the case under consideration (that is, in the situation when the forward scattering effect may be neglected), the exponential attenuation factor, $\exp[-2h_s^{bot} \cdot a_s]$, may be derived using an estimate of an effective absorption coefficient – assumed to be approximately constant throughout the water column – obtained from the lidar waveform as described in Section 4.3 above. The water attenuation factor can also be obtained by regression of the bottom return signals from a range of depths of the same bottom type. The latter method requires depth information and assumes that bottom composition and morphology are uniform over the survey area (Philpot 1989). In the example shown in Figure 5.4.4 calculating the attenuation coefficient assuming a constant bottom reflectivity is valid for depths up to 25 m, but at greater depths the bottom reflectivity falls noticeably.

Earlier estimates of the bottom reflectance from SHOALS data were produced using a constant value of K_{sys} for the entire data set; specifically, an *a priori* value selected by the operator at the time of data acquisition was applied to the entire data set. Such estimates were called "pseudo-reflectance" (Lee and Tuell 2003). In the more recent rapid environmental assessment (REA) processor of Optech, algorithms which estimate SHOALS K_{sys} for each waveform were implemented, and these values were used to

improve the pseudoreflectance of the dataset (Tuell, Feygels, et al. 2005). The improvement in the resulting bottom images proved to be significant for seafloor areas with varying morphology, such as a series of reefs separated by regions of sand, seagrass, and mixed vegetation (Tuell and Park 2004).

Table 5.2. Values of lidar parameters and environmental characteristics used in the waveform simulation

Parameter & symbol	Units	Value
The lidar carrier height above the sea surface, *H*	m	400
The nadir angle in the atmosphere, $\boldsymbol{\theta_a}$	deg	20
The sounding beam divergence (full plane angle), $\boldsymbol{\Theta_E}$	mr	5
The receiver field-of-view (full plane angle)	mr	40
The pulse energy, *Q*	mJ	3
The effective sounding pulse duration (for 0.5 level), $\boldsymbol{\tau_R}$	ns	3.5
The bottom depth, $\boldsymbol{h^{bot}}$	m	20; 40
The effective absorption coefficient, $\boldsymbol{a_s}$	m-1	0.075
The forward scattering coefficient, $\boldsymbol{b_s}$	m-1	0; 0.2
The VSF shape parameter in Dolin's model, $\boldsymbol{m}$	-	7
The water surface reflectance, $\boldsymbol{\rho_{sf}}$	-	0.002
The bottom reflectance, $\boldsymbol{\rho_{bot}}$	-	0.15

In the general case (e.g., for more turbid waters), forward scattering of the sounding light beam may seriously affect the applicability of the above approach for bottom reflectance estimation. The impacts of forward scattering include: (1) departure of the waveform decay rate from a purely exponential dependence, $\sim exp[-2h_s \cdot a_s]$, and (2) a stretch of the bottom-reflected pulse caused by the spread of the sounding laser beam (Tuell, Feygels, et al. 2005). The effects are illustrated in Figure 5.4.5 through Figure 5.4.8 using simulated waveforms obtained with the CZMIL simulator (Section 4.3.3) and the lidar waveform model described in Section 4.3.2. The values of the lidar parameters and environmental characteristics used in the simulation are listed in Table 5.2.

The effect of forward scattering in the water on the waveform decay rate was discussed in Section 5.3 (Figure 5.3.2). Neglecting the waveform decay rate effect (in the case of deep / turbid enough water) will lead to underestimate of the bottom return decrease with depth, and a corresponding error in normalization of the bottom return signal for attenuation by the water column [Section 5.3, Eq. (4.3.1)]. As a result, bottom reflectance may be overestimated. In Figure 5.4.5 (forward scattering coefficient, b_s= 0.2 m^{-1}), the error does not exceed ~20%, at 20 m depth. However, for the deeper water example in Figure 5.4.6; (depth 40 m, $b_s = 0.2\ m^{-1}$), the error reaches up to 200%.

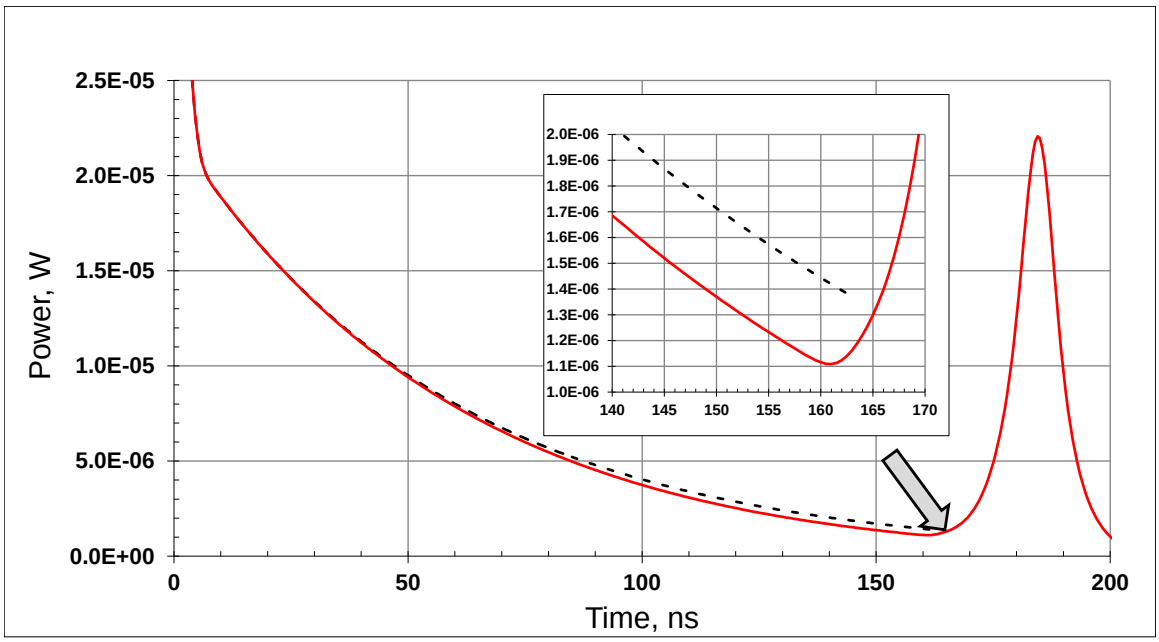

Figure 5.4.5. Simulated CZMIL deep channel waveform for a bottom depth of 20 m. The red, solid line is the waveform calculated for the forward scattering coefficient, $b_{sf} = 0.2\ m^{-1}$; the black line corresponds to zero forward scattering ($b_s = 0\ m^{-1}$) and demonstrate the "pure exponential" decay of backscattered signal, $\sim exp[-2h_s \cdot a_s]$.

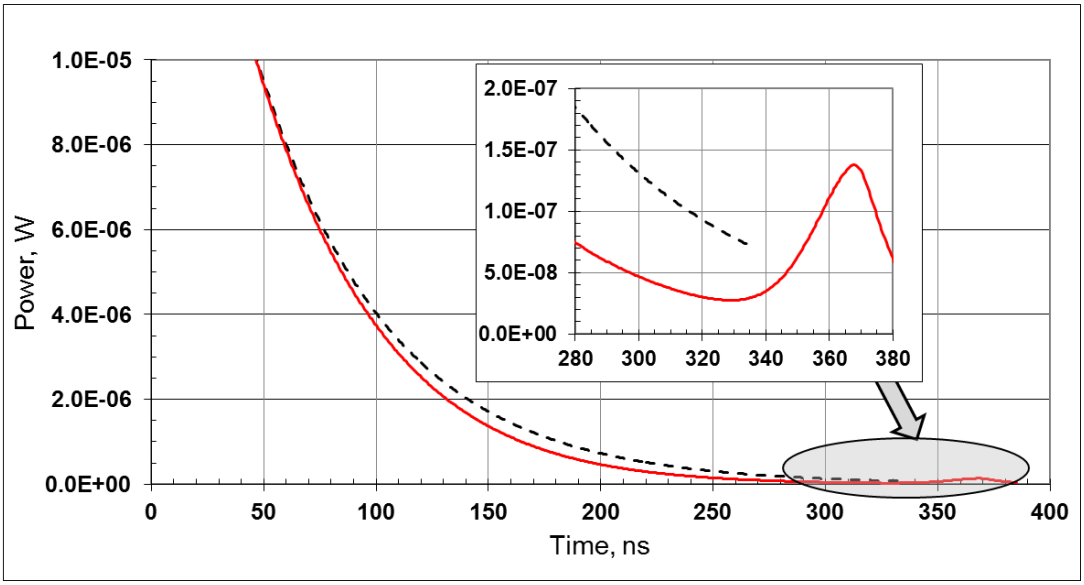

Figure 5.4.6. Simulated CZMIL deep channel waveform for a bottom depth of 40 m. Red, solid line is the waveform calculated for the forward scattering coefficient $b_s = 0.2\ m^{-1}$; black, dashed line corresponds to zero forward scattering, $b_s = 0\ m^{-1}$, and demonstrate "pure exponential" decay of the backscattered signal, $\sim exp[-2h_s \cdot a_s]$.

Figure 5.4.8 and Figure 5.4.9 demonstrate the bottom-reflected pulse stretch due to small-angle forward scattering of the laser beam in water (the "environmental stretch"). The stretch reduces the amplitude of bottom return. If the pulse stretch is not taken into account, the result may lead to significant underestimation of bottom reflectance. The pulse stretch effect increases with depth and water turbidity

(with the forward scattering coefficient, b_f). The "environmental stretch" is observed against the background stretch of the reflected peak due to the ray-path geometry ("geometrical stretch", Section 4.2.1) and the effective pulse duration ("hardware-based stretch", Section 4.2.2). Therefore, the effect of "environmental stretch" is the less prominent with wider effective pulses or at greater off-nadir (incidence) angles.

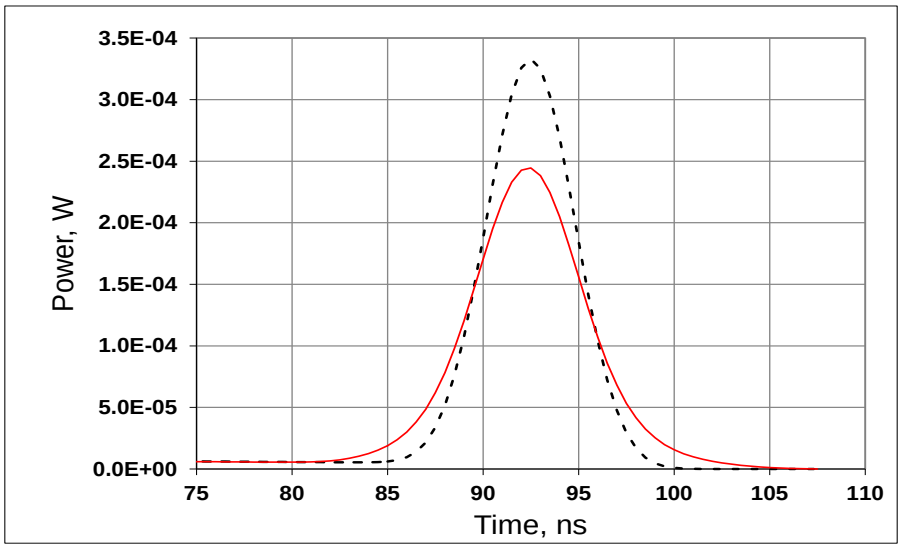

Figure 5.4.7. A simulated CZMIL deep channel waveform over the time interval of the bottom-reflected signal for a bottom depth of 10 m. The black, dashed line corresponds to zero forward scattering (b_s= 0 m-1), when the shape of bottom peak is determined only by the "geometric" and the "hardware-based" stretch. The red, solid line depicts the waveform calculated for the forward scattering coefficient b_s= 0.2 m-1 and demonstrates the additional "environmental stretch" of the peak.

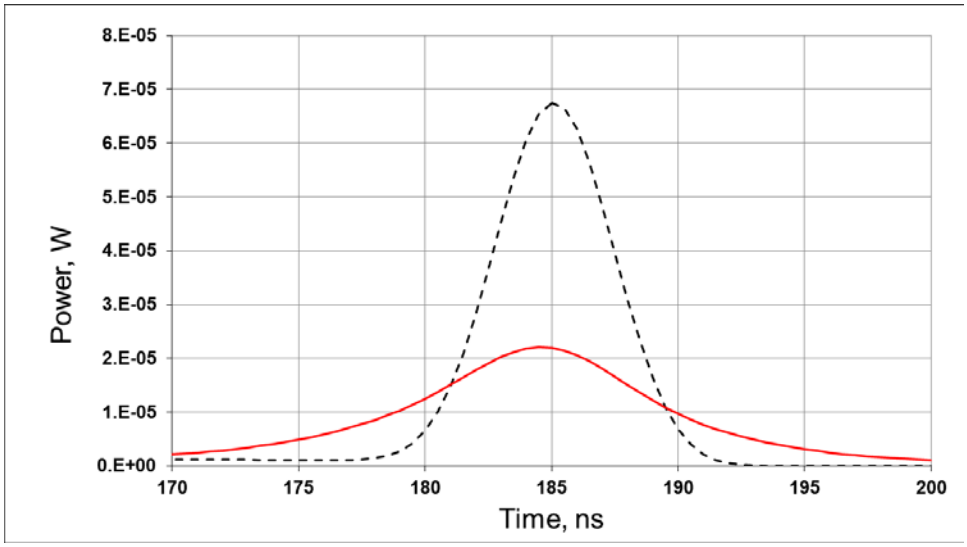

Figure 5.4.8. Simulated CZMIL deep channel waveform in the time interval of bottom-reflected signal for the bottom depth of 20 m. The black, dashed line corresponds to zero forward scattering ($b_s = 0\ m^{-1}$), when the shape of bottom peak is determined only by "geometric" and "hardware-based" stretch. The red, solid line depicts the waveform calculated for the forward scattering coefficient, $b_s = 0.2\ m^{-1}$, and illustrates the additional "environmental stretch" of the peak.

To summarize, bottom return signals need to be inverted using an estimate of the water attenuation (Equation (4.4.1) in order to obtain bottom reflectance. The water attenuation coefficient can be obtained either by the regression of the bottom return signals over range of depths of the same bottom type or from the water volume return as a result from the waveform decomposition method. Previous studies for extracting bottom reflectance required depth information and assumes that bottom composition and morphology are uniform over the survey area.

Caution must be exercised when compiling bottom reflectance maps using several flight lines. Environmental factors, such as water surface and bottom slopes may affect the reflectance estimation (Section 3.4). The light field is continuously varying over the transmission and return path (Section 5.3). Also, the laser beam undergoes focusing as the laser pulse enters the water, and defocusing as the return pulse exits the water. As a consequence, the magnitude and variability of the bottom return signal initially increases as the water depth decreases and may reach maximum values at a depth that is related to the water surface geometry. This is the phenomenon of double focusing (Abrosimov and Luchinin 1999; Luchinin 1987; McLean and Freeman 1996)). Wang and Philpot (2007) showed using data from a study site near Egmont Key, FL, that the effect of double focusing can be reduced in turbid water. Nonetheless, the asymmetric shape of the water surface, typically in coastal areas, alters the light field differently for adjacent survey flight lines. As a result, the estimated bottom reflectance over the same area may have different values for adjacent survey flight lines.

It is also important to note that bottom slope affects the shape of the bottom return, where the pulse is more stretched with increasing angle of incidence (Steinvall and Koppari 1996). The benefit of employing the waveform decomposition method is that the complete information of the bottom return in that the shape of the bottom return is appropriately depicted by the Gaussian. On the other hand, using the peak value of the bottom return signal requires that the signal correction must rely on other simulation results or experiments (Tulldahl and Wikström 2012; C.-K. Wang and Philpot 2007).

5.5 Effects of forward scattering

Minsu Kim

When a laser pulse propagates through an attenuating (absorbing and scattering) medium, environmental parameters control the varying rate of the decreasing return, and may deform the position and shape of the surface reflection and bottom reflection peaks of the ALB waveform. Since these are used for estimating depth, the deformations introduce uncertainties in the depth estimate. The environmental parameters include atmosphere, air-water interface, water body, and the bottom surface characteristics. As will be demonstrated in this section, the most prominent factor among the environmental parameters is the scattering coefficient. Other environmental factors add only minor variations to that of the main scattering effect. Accordingly, we describe the scattering effect first and, since the scattering coefficient cannot vary independently from other inherent optical properties (IOPs), we introduce a single formula that constrains several inherent optical properties.

5.5.1 Effect of scattering and inherent optical properties

As described in Section 3.3.2, it is possible to derive several environmental parameters using two fundamental IOPs, the absorption coefficient, a, and the volume scattering function (VSF). The scattering coefficient, b, is obtained by integrating the VSF over the all possible directions (equation (3.3.7)). The

lidar backscattering coefficient, β_π (a.k.a. beta pi), is the value of the VSF in the exact backward direction. The degree of forward scattering – which is critical for understanding the beam spread – is also determined from the VSF. While it is possible that one parameter can vary independently of the other parameters, it is generally most reasonable to simulate IOPs assuming that they are mutually constrained. . There is no unique relationship among IOPs, however, for convenience, we simulate IOPs with the following simple formula: we assume that the single scattering albedo (equation (3.3.16)), $\omega_0 = b/(a+b)$, is constant and that the lidar backscattering coefficient is determined by the scattering coefficient via $\beta_\pi = 0.005 \cdot b$.

Figure 5.5.1 illustrates waveforms computed using sets of IOPs for which the constant single-scattering albedo is 0.7, the scattering coefficient varies from 0.2 to 0.5 m^{-1}, and the rest of IOPs are derived using the formulas above. Based on simulation results, we are able to observe several fundamental characteristics of the waveforms:

- As the scattering coefficient increases the bottom return is reduced dramatically due to the exponential increase in attenuation.
- In relatively clear water ($K_d(532nm) < 0.1m^{-1}$), the loss of laser pulse energy during propagation is due primarily to absorption.
- Scattering becomes increasingly dominant as the water becomes more turbid, and can become comparable to absorption in its contribution to attenuation.
- Backscattering has a relatively minor effect on the returns compared to absorption and forward scattering; the increased attenuation of the ALB returns is due primarily to forward scattering, spreading the beam as it propagates through the scattering medium, and redistributing the beam energy over the beam cross-sectional area.
- The increase in attenuation with increasing scattering is particularly noticeable in the last 2/3 of the waveform. The bottom reflectance return decreases correspondingly.

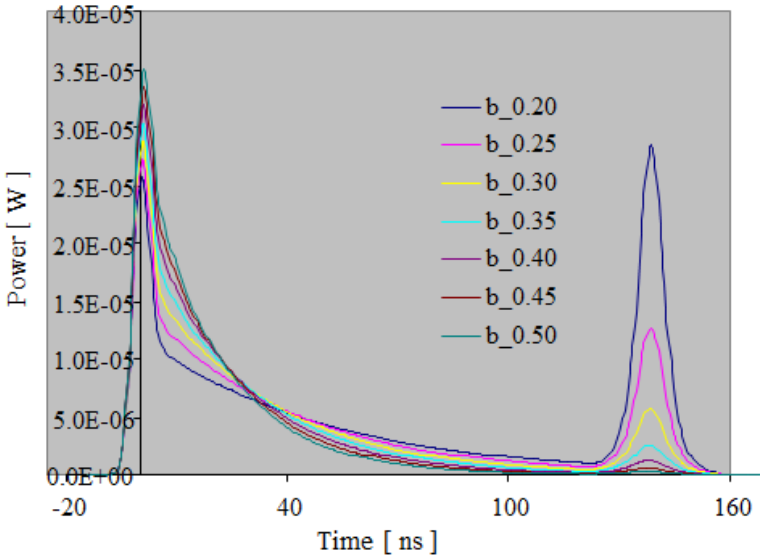

Figure 5.5.1. Changes in waveforms from 15 m deep water due to changes in the scattering coefficient (ranging from 0.2 to 0.5 m^{-1}) and related IOPs.

In order to investigate the effect of variation in the IOPs on the lidar depth accuracy, we also simulated the optical properties affecting the surface and bottom return. The Fresnel peak (fixed value) and the different backscatter curves are shown in Figure 5.5.2a. The combined Fresnel + backscatter curves are shown in Figure 5.5.2b. In both figures, the true geometrical position of the water surface is marked as a solid line at time 0 ns.

It is important to note that the magnitude and position of the peak of the surface return is determined by two factors: the effective Fresnel reflectance and the lidar backscattering coefficient. In the simulation results shown in Figure 5.5.1, the effective Fresnel reflectance is constant, and the backscattering coefficient increases linearly with the scattering coefficient values. The superposition of a fixed, pure Fresnel peak and increasing volume backscattering has two consequences: greater peak magnitude and the shift of the maximum position to a later time (Figure 5.5.2b)

Note also, that the surface return signal increases as the scattering coefficient increases because of the increased backscattering near the surface. However, as the laser pulse propagates through the medium, however, it loses intensity much more quickly because so much energy has been lost due to the high scattering and absorption. This is the reason for the apparent convergence of the curves near 30 ns in (Figure 5.5.2a).

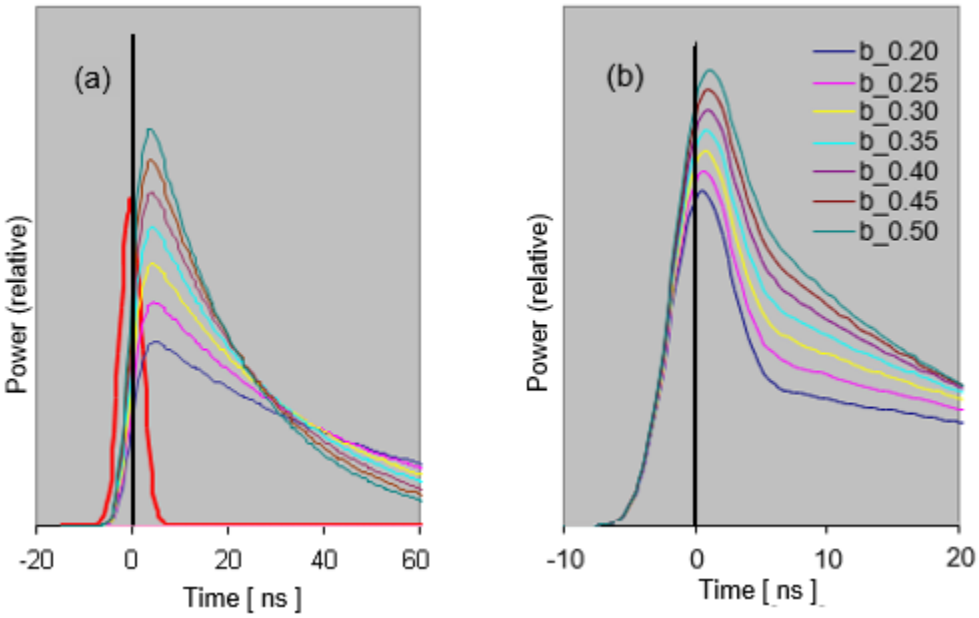

Figure 5.5.2. Details of surface return data from Figure 5.5.1: (a) Fresnel peak (thick red line) and the variable volume backscattering; (b) superposition of the two components.

The bottom return peak also experiences a shift due to scattering dispersion. In Figure 5.5.3 the bottom peaks were normalized by the bottom peak energy (integrated power over the duration of bottom peak) in order to facilitate comparison. Clearly, the increase in the scattering coefficient, and the corresponding IOPs, not only lowers the magnitude of the bottom peak, but also shifts the peak position to an earlier time. The shift can be explained as follows. A laser pulse approaching the bottom at a substantial optical depth will have broadened significantly due to forward scattering. The increase in the rate of dispersion with optical depth is significant, so that, when a beam front intersects the bottom boundary, the later part

of the beam front (farther from the laser source) experiences more dispersion than the earlier part of the beam front (see Figure 4.2.4). The later signal is also further attenuated by absorption. As a result, the bottom peak always occurs earlier than the true geometric bottom (at 140 ns), defined as point at which the beam center meets the bottom.

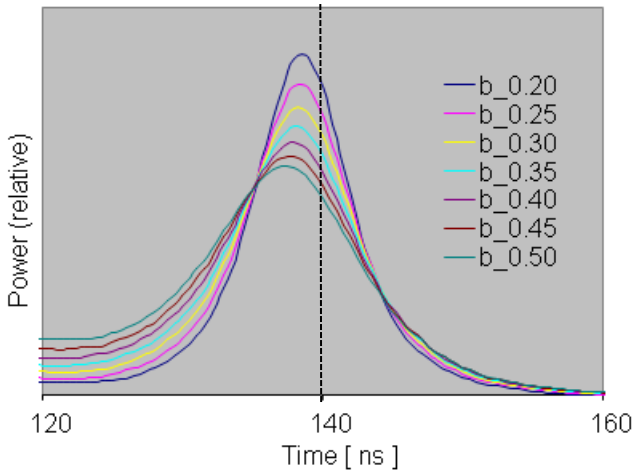

Figure 5.5.3. Normalized bottom peaks using the bottom peak energy Lidar depth estimation algorithm

5.5.2 Lidar depth estimation algorithm

When a lidar waveform is generated by a laser pulse at a slant incidence angle, the slant distance between the two peaks is used as a close approximation to the true slant distance. An intuitive method to calculate the slant distance is based on the time separation of the two apparent peaks which we will call the "peak algorithm". Another common practice is to calculate the distance based on the time separation of the two half-peaks where the waveform value is the half of the maximum, or the "half-peak algorithm". With the peak algorithm it is assumed that the peaks occur close in time to the real surface and the bottom peaks. If the overall system response is short enough – having a short laser pulse duration, fast photo-detector and electronic response, and small incident angle for minimal geometrical stretch – the peak algorithm is an ideal approach. As these conditions are violated more and more, the peak algorithm will be subject to be subject to greater depth estimation errors.

The key assumption in the half-peak algorithm is that the two peaks have the same width; however, different factors contribute to the widths of the two peaks. The geometric stretch of the surface peak is a combination of many system factors, such as beam divergence angle, receiver FOV, sensor altitude, and system response function. At shallow depths, the effective beam divergence angle and the FOV both decrease according to Snell's law, after refraction at the water surface. The width of the resulting bottom and surface return may be quite similar, despite the dispersion due to scattering. However, the ALB beam spreads rapidly as the optical depth increases, leading to significant stretching of the bottom return. Thus, depth estimation error for the half-peak algorithm will be closely related to the beam dispersion due to forward scattering.

As an example of the two approaches, consider a model in which the two peaks of a waveform are represented using a Gaussian curve, with the FWHM being the measure of the peak width. In this

example, both the peak algorithm and the half-peak algorithm exhibit an increasing bias from the true surface arrival time, as illustrated in Figure 5.5.4.

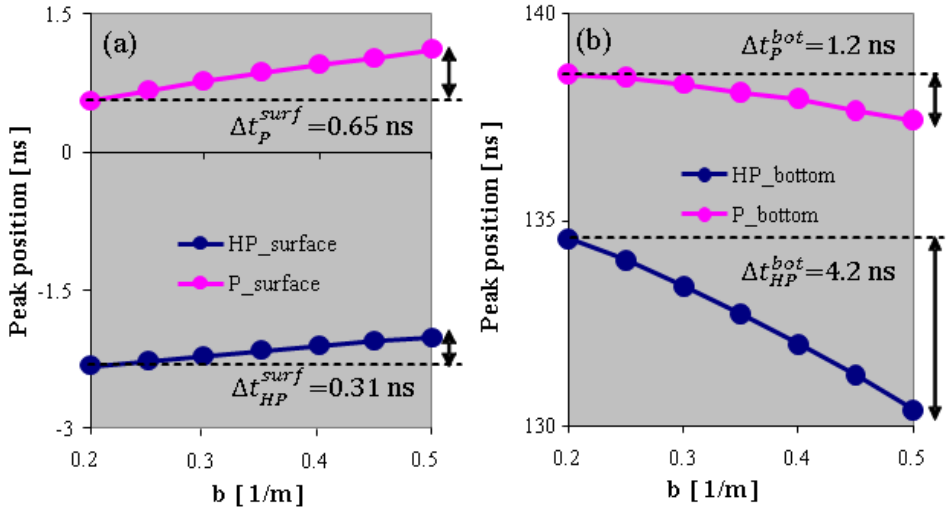

Figure 5.5.4. Bias of estimates relative to the true locations of (a) the surface (Δt_P^{surf} and Δt_{HP}^{surf}), and (b) the bottom (Δt_P^{bot} and Δt_{HP}^{bot}), using the peak algorithm (P) and the half-peak algorithm (HP) as the scattering coefficient increases. The dashed lines represent the arrival times at the surface and bottom along the slant path.

As the scattering coefficient increases (along with corresponding changes in the other IOPs), both the peak and half-peak estimates of the surface arrival time shift toward a later time. For $b = 0.5\ m^{-1}$, the position shift for the peak algorithm is slightly more than that of the half-peak algorithm. In contrast, the estimate of the bottom peak location shifts to an earlier time for both algorithms. For the same conditions, the bottom peak shift is about twice the surface peak shift; however, the half-peak shift of the bottom location is more than 10 times the surface half-peak shift. The combined error when $b = 0.5\ m^{-1}$ is a 1.8 ns bias for the peak algorithm, while for the half-peak algorithm the combined error is a 4.5 ns bias. The increased total error demonstrates the greater vulnerability of the half-peak algorithm to beam dispersion by forward scattering. Depth estimation errors using the 2 algorithms for varying IOPs are calculated for several depths in Figure 4.5.5.

The time difference (Δt) between two peak positions or half-peak positions is converted to the depth error, Δd, using the simple formula

$$\Delta d = \left(\frac{c}{2n_w}\right) \Delta t \cos\theta_w \quad , \tag{4.5.1}$$

where θ_w is the incidence (sounding) angle in water. The resulting depth estimation error using the peak algorithm is much smaller than the error produced using the half-peak algorithm.

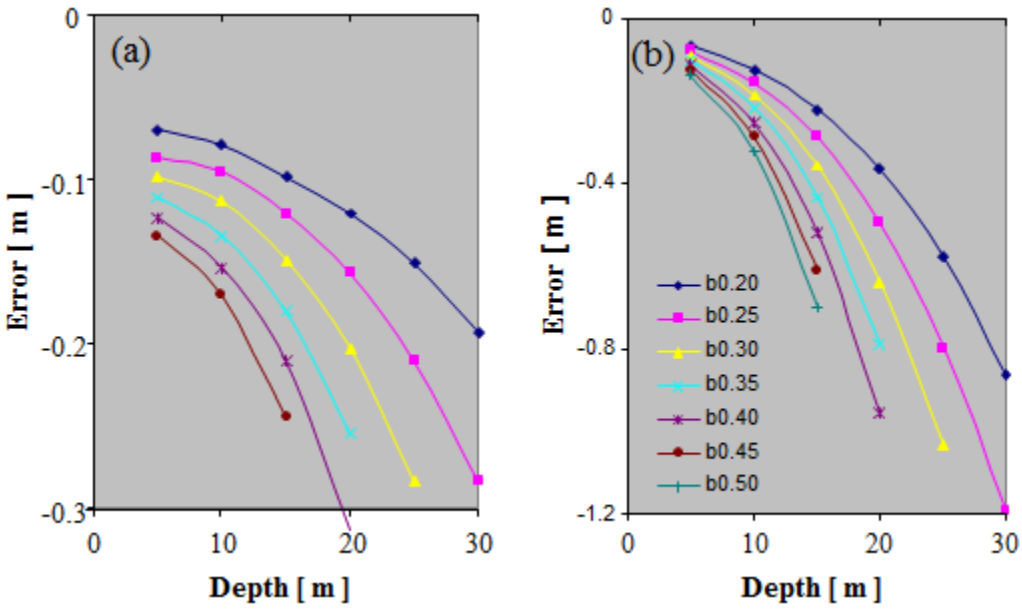

Figure 5.5.5. Depth error for varying IOPs using (a) Peak and (b) Half-Peak algorithm.

5.5.3 Effect of the effective surface Fresnel reflectance

Under most conditions (other than flat calm) there are many small facets of the complicated surface wave structure aligned such that a small portion of the laser pulse will be specularly reflected back to the receiver (Section 3.2). The effective Fresnel reflectance is then related to the probability of specular reflection. If the entire water surface were perpendicular to the beam axis, the effective Fresnel reflectance would be near 0.02 which is the Fresnel reflectance due to the normal incidence to the water with refractive index $n_w = 1.33$. Thus, 0.02 is the theoretical maximum. Of course, if the water surface is covered with white caps due to breaking waves, the effective Fresnel reflectance can be much higher, but such a case is not considered.

Figure 5.5.6a illustrates a set of waveforms produced using a range of effective Fresnel reflectance values; Figure 5.5.6b is a close-up of the surface peak region. The surface peak is the sum of the effective Fresnel reflectance and the volume backscattering. When the effective Fresnel reflectance is low, the contribution to the apparent surface peak by the surface reflection is small and the apparent surface peak occurs significantly later than the time when the true center of the beam passes the water surface. With high effective Fresnel reflectance, however, the surface peak is dominated by the Fresnel reflectance, and the apparent peak position occurs very close to the time when the true center of the beam passes the surface.

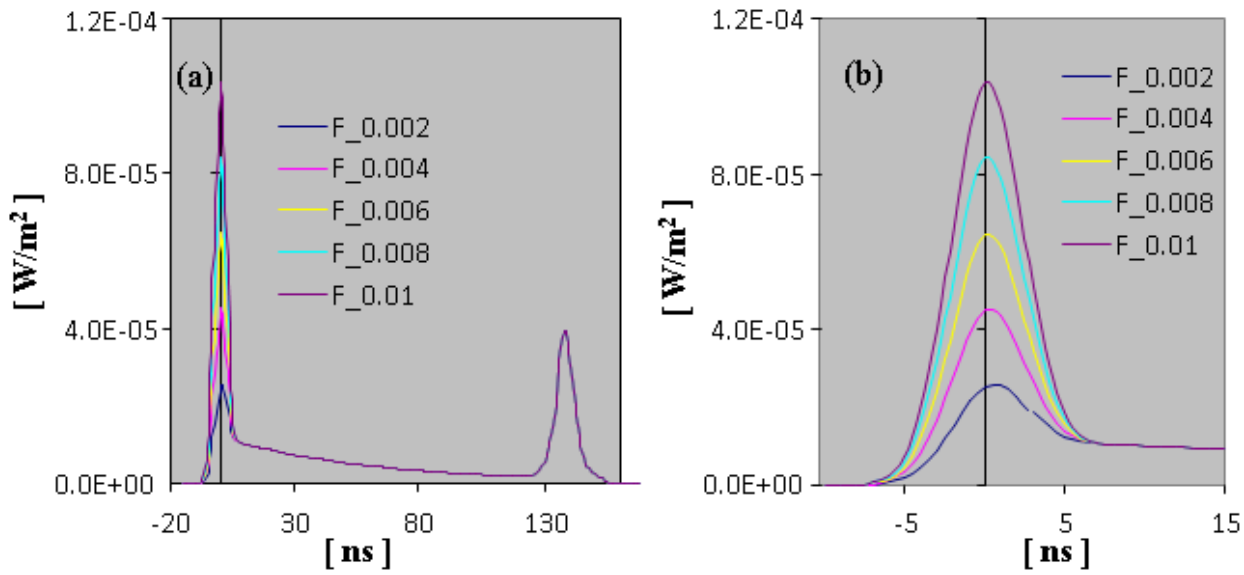

Figure 5.5.6. Waveforms for varying effective Fresnel reflectance.

An increase in the effective Fresnel reflectance has the effect of increasing the error in the depth calculation (Figure 5.5.7). As with the effect of IOPs on the surface peak, the error introduced by the peak algorithm is less than half of that introduced by the half-peak algorithm. On the other hand, the variation in the depth estimate produced by the half-peak position is less than that of the peak position. Thus, the depth error plot using the peak algorithm (Figure 5.5.7a) shows a wider range of error for varying effective Fresnel reflectance than the half-peak algorithm (Figure 5.5.7b) at any one depth. Interestingly, the range of uncertainties is nearly constant for any one depth when using the half-peak algorithm. This is because the effective Fresnel reflectance affects only the near surface part of the waveform. Thus, the bottom peak is not affected by the Fresnel reflectance regardless of the depth.

The greatest apparent trend with increasing depths is due to the effect of beam dispersion due to scattering. As a result, the bottom peak stretching affects the depth error. To demonstrate this idea, we can generate a new error plot using a larger scattering coefficient. The first group of data was simulated using $b = 0.2\ m^{-1}$.. The new data set was simulated using $b = 0.4\ m^{-1}$. Figure 5.5.8 shows two groups of error plots. It is evident that the Fresnel variation explains the width of the band and that the overall trend is due to the scattering. The upper group is for $b = 0.1\ m^{-1}$ and the lower group is for $b = 0.2\ m^{-1}$.

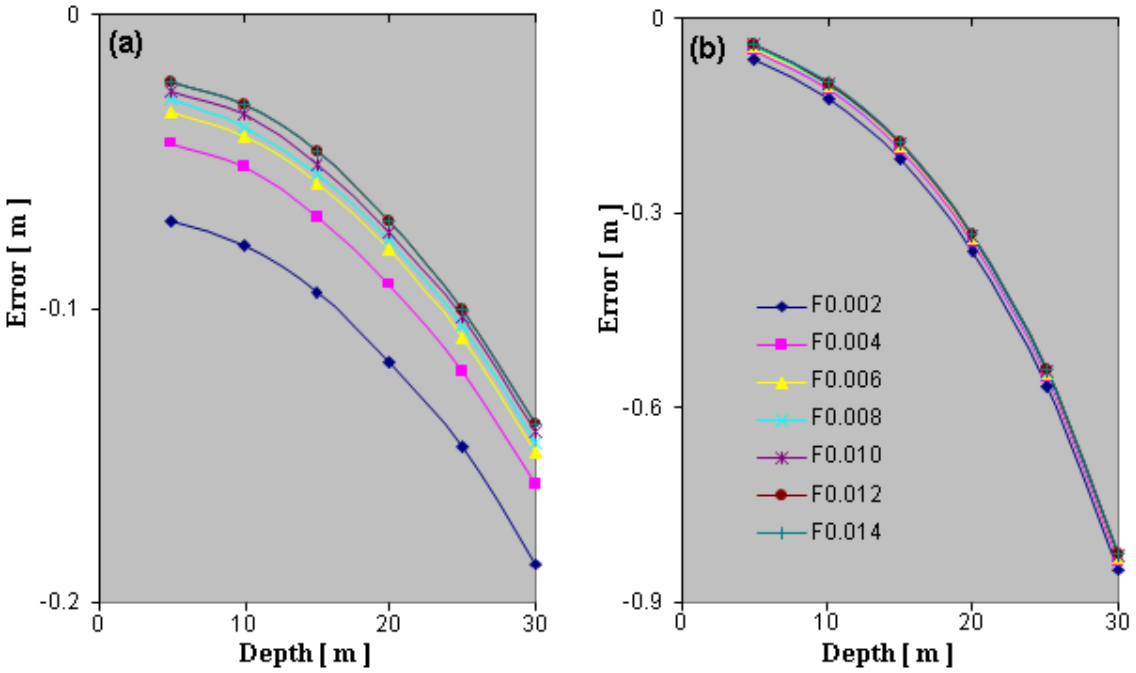

Figure 5.5.7. Depth estimation error for varying effective Fresnel reflectance using (a) Peak and (b) Half-Peak algorithm. Note that the overall error of the peak algorithm is much less than the half-peak algorithm, and that the spacing of the peak curves (a) is nearly independent of depth while the half-peak curves (b) converge with increasing depth.

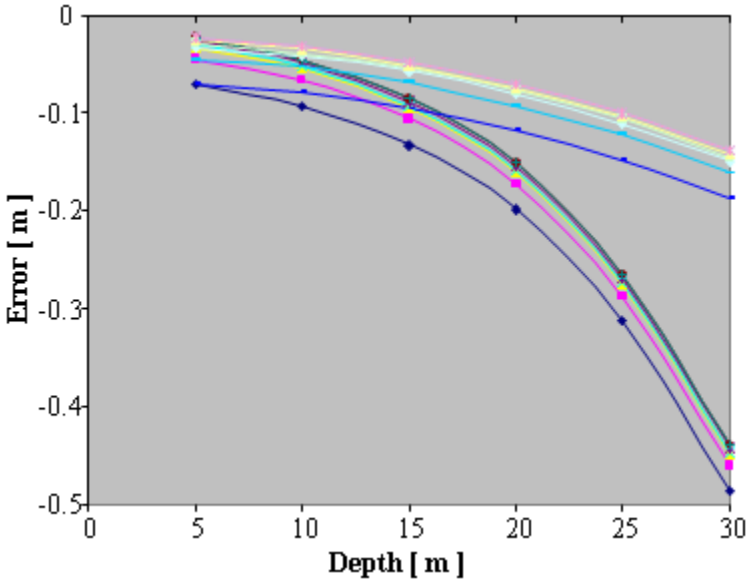

Figure 5.5.8. Effect of the Fresnel reflectance for 2 different scattering coefficient. The upper group of curves is for b = 0.1; the lower group is for b = 0.2.

5.5.4 Effect of the bottom reflectance

A change in bottom reflectance affects nothing but the bottom peak; the surface return and the volume backscattering return are invariant while the bottom peak rises as the bottom reflectance increases. The effect is illustrated in Figure 5.5.9 in which the bottom peak represents the sum of the pure bottom peak and the volume backscattering. Since the volume backscattering is constant, the increase in bottom reflectance results in a bottom peak that is more representative of the bottom, resulting in a shift of the apparent peak or half-peak closer to the true values. The peak and half-peak positions are marked as dots in Figure 5.5.9b. Both peak and half-peak positions are delayed as the bottom reflectance increases and as the pure bottom peak becomes stronger than volume backscattering base. Convergence occurs rather quickly. It is worth keeping in mind, however, that even the strongest bottom peak position is still affected by the scattering attenuation, so that the converged peak is optically shifted from the true geometrical bottom (see Figure 5.5.3). As mentioned in the IOPs section, an overall quick increase of depth estimation error over the increasing depth is caused by the beam stretch of the forward scattering. Thus, the error caused by the bottom reflectance variation is represented by the small differences between the curves in Figure 5.5.10.

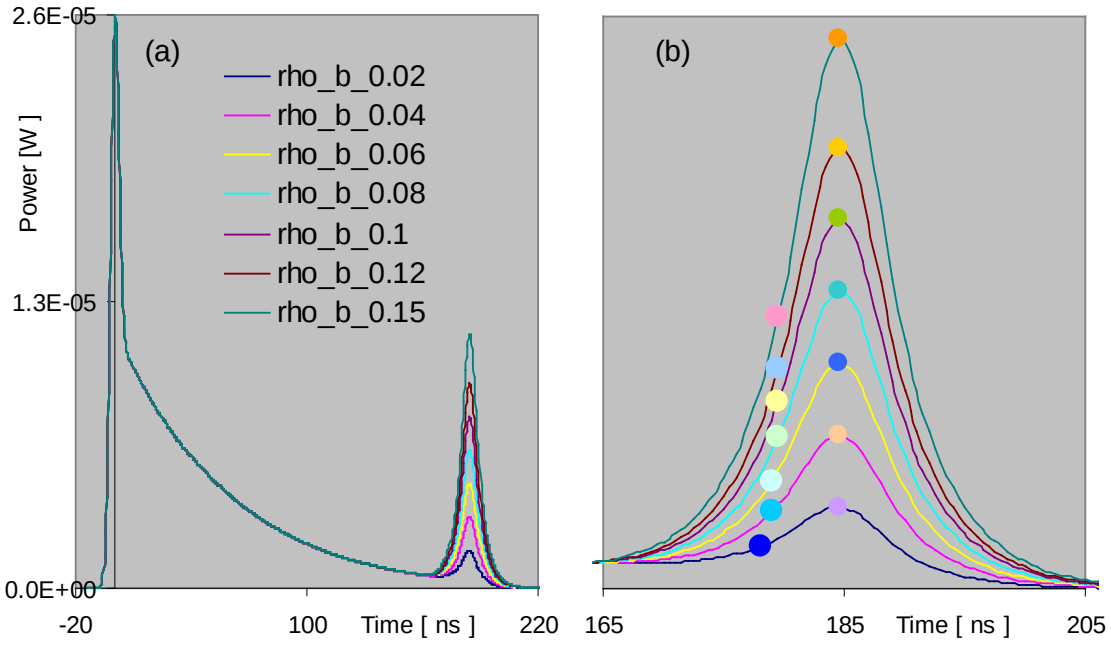

Figure 5.5.9. The effect of increasing bottom reflectance: a) full waveform, b) detail of the bottom peak with the peak and half-peak positions marked as dots.

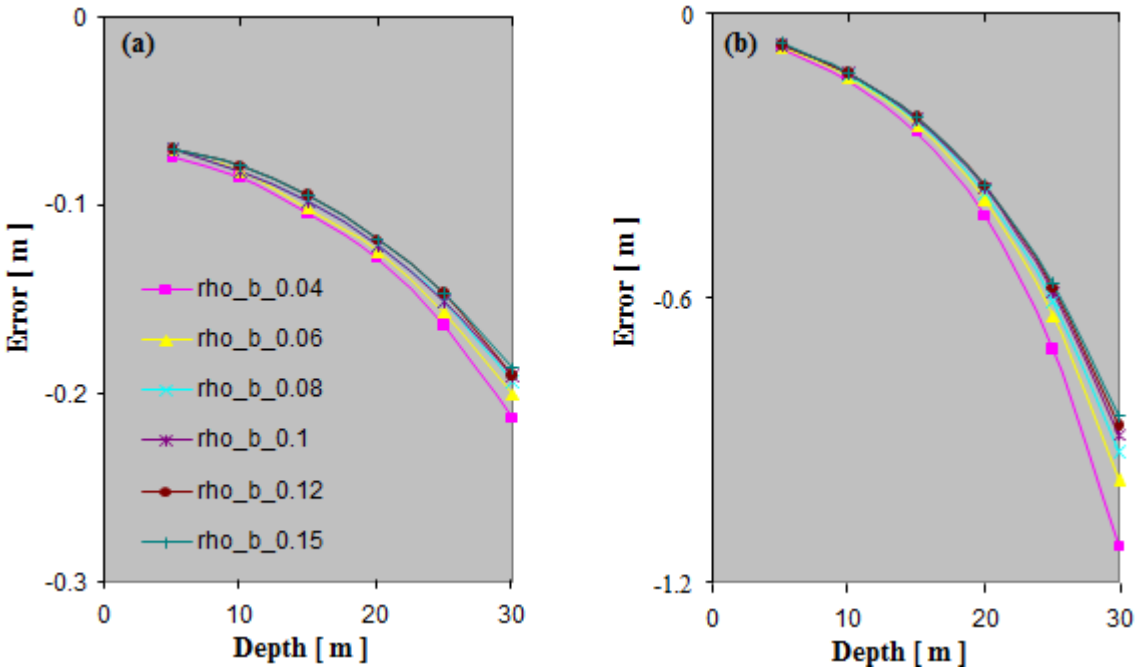

Figure 5.5.10. Depth error for varying bottom reflectance using (a) Peak and (b) Half-Peak algorithm.

5.6 References

Abady, L., Bailly, J.-S., Baghdadi, N., Pastol, Y., & Abdallah, H. (2014). Assessment of Quadrilateral Fitting of the Water Column Contribution in Lidar Waveforms on Bathymetry Estimates. *Geoscience and Remote Sensing Letters, IEEE*, *11*(4), 813–817. https://doi.org/10.1109/LGRS.2013.2279271

Abrosimov, D. L., & Luchinin, A. G. (1999). Signal statistics of lidar sounding of the upper ocean through its rough surface. *Izvestiya, Atmospheric and Oceanic Physics (in Russian)*, *35*, 266–272.

Collin, A., Cottin, A. G., Long, B. F., Kuus, P., Clarke, J. H., Archambault, P., … Miller, J. (2007). Statistical classification methodology of SHOALS 3000 backscatter to mapping coastal benthic habitats. In *2007 IEEE International Geoscience and Remote Sensing Symposium, IGARSS 2007, June 23, 2007 - June 28* (pp. 3178–3181). Department of Geology, INRS-ETE, University of Quebec, QC, Canada: Institute of Electrical and Electronics Engineers Inc. https://doi.org/10.1109/IGARSS.2007.4423520

Cottin, A. G., Forbes, D. L., & Long, B. F. (2009). Shallow seabed mapping and classification using waveform analysis and bathymetry from SHOALS lidar data. *Canadian Journal of Remote Sensing*, *35*(5), 422–434.

Dolin, L. S., & Levin, I. M. (1991). *Reference book on the underwater vision theory*. Leningrad: Gidrometeoizdat Press (in Russian).

Dolin, L. S., & Savel'ev, V. A. (1971). Characteristics of the backscattering signal and pulse radiation of turbid media by a narrow directional light beam. *Atmospheric and Oceanic Physics*, *7*(5), 505–510.

Dorogin, A. N., Kopelevich, O. V., Levin, I. M., & Feigels, V. I. (1988). Correlation among some hydrooptical properties. In *Optics of the sea and the atmosphere (in Russian)* (pp. 136–137). Academy of Science of the USSR.

Lee, M., & Tuell, G. H. (2003). A technique for generating bottom reflectance images from SHOALS data. In *U.S. HYDRO 2003*. New Orleans, LA.

Levin, I. M., & Kopelevich, O. V. (2003). Relationships between seawater optical properties at 550 nm. In I. M. Levin & G. D. Gilbert (Eds.), *Current Probles in Optics of Natural Waters (ONW 2003)*. St. Petersburg, Russia.

Luchinin, A. G. (1987). Some properties of a backscattered signal in laser sounding of the upper ocean through a rough surface. *Izvestiya, Atmospheric and Ocean Physics (in Russian)*, *23*, 725–729.

McLean, J. W., & Freeman, J. D. (1996). Effects of ocean waves on airborne lidar imaging. *Applied Optics*, *35*(18), 3261–3269. https://doi.org/10.1364/AO.35.003261

Mobley, C. D. (1994). *Light and water: radiative transfer in natural waters*. San Diego: Academic Press. Retrieved from http://www.curtismobley.com/LightandWater.zip

Monin, A. S. (1983). Physical optics of the ocean. In A. S. Monin (Ed.), *Ocean Optics* (Vol. 1). Nauka, Moscow (in Russian).

Morel, A., & Loisel, H. (1998). Apparent Optical Properties of Oceanic Water: Dependence on the Molecular Scattering Contribution. *Applied Optics*, *37*(21), 4765–4776. https://doi.org/10.1364/AO.37.004765

Park, J. Y., Ramnath, V., Feygels, V. I., Kim, M., Mathur, A., Aitken, J., & Tuell, G. H. (2010). Active-passive data fusion algorithms for seafloor imaging and classification from CZMIL data, 769515. Retrieved from http://dx.doi.org/10.1117/12.851991

Pe'eri, S., & Philpot, W. D. (2007). Increasing the existence of very shallow-water LIDAR measurements using the red-channel waveforms. *IEEE Transactions on Geoscience and Remote Sensing*, *45*(5), 1217–1223. https://doi.org/10.1109/TGRS.2007.894584

Philpot, W. D. (1989). Bathymetric mapping with passive multispectral imagery. *Applied Optics*, *28*(8), 1569–1578. https://doi.org/10.1364/AO.28.001569

Smart, J. H., & Kwon, K. H. K. (1996). Comparisons between in-situ and remote sensing estimates of diffuse attenuation profiles. In V. I. Feigels & Y. I. Kopilevich (Eds.), *SPIE 2964: Laser Remote Sensing of Natural Waters: From Theory to Practice* (Vol. 2964, pp. 100–109). International Society for Optics and Photonics. https://doi.org/10.1117/12.258356

Steinvall, O. K., & Koppari, K. R. (1996). Depth sounding lidar: An overview of Swedish activities and future prospects. In V. I. Feigels & Y. I. Kopilevich (Eds.), *CIS Selected Papers: Laser Remote Sensing of Natural Waters: From Theory to Practice* (Vol. SPIE 2964, pp. 2–25). St. Petersburg, Russia: SPIE. https://doi.org/10.1117/12.258342

Steinvall, O. K., Koppari, K. R., & Karlsson, U. C. M. (1993). Experimental evaluation of an airborne depth-sounding lidar. *Optical Engineering*, *32*(6), 1307–1321. https://doi.org/10.1117/12.135859

Tuell, G. H., Feygels, V. I., Kopilevich, Y. I., Weidemann, A. D., Cunningham, A. G., Mani, R., … Aitken, J. (2005). Measurement of ocean water optical properties and seafloor reflectace with scanning hydrographic operational airborne lidar survey (SHOALS): II. Practical results and comparison with independent data. In R. J. Frouin, M. Babin, & S. Sathyendranath (Eds.), *SPIE 5885: Remote Sensing of the Coastal Oceanic Environment, July 31- August 1, 2005* (Vol. 5885, pp. 58850E-58850E – 13). San Diego, CA: SPIE. https://doi.org/10.1117/12.619215

Tuell, G. H., & Park, J. Y. (2004). Use of SHOALS bottom reflectance images to constrain the inversion of a hyperspectral radiative transfer model, 185–193. Retrieved from http://dx.doi.org/10.1117/12.564929

Tulldahl, H. M., & Wikström, S. A. (2012). Classification of aquatic macrovegetation and substrates with airborne lidar. *Remote Sensing of Environment*, *121*, 347–357. https://doi.org/10.1016/j.rse.2012.02.004

Wang, C.-K., & Philpot, W. D. (2007). Using airborne bathymetric lidar to detect bottom type variation in shallow waters. *Remote Sensing of Environment*, *106*(1), 123–135. https://doi.org/10.1016/j.rse.2006.08.003

Wong, H., & Antoniou, A. (1991). Characterization and decomposition of waveforms for Larsen 500 airborne system. *Geoscience and Remote Sensing, IEEE Transactions On*, *29*(6), 912–921. https://doi.org/10.1109/36.101370

Wong, H., & Antoniou, A. (1994). One-Dimensional Signal-Processing Techniques for Airborne Laser Bathymetry. *IEEE Transactions on Geoscience and Remote Sensing*, *32*(1), 35–46. https://doi.org/10.1109/36.285187

6 PERFORMANCE EVALUATION

Lead Author: Shachak Pe'eri[a]

Contributing Authors: Christopher Parrish[b], Nicholas Johnson[c], Christopher Macon[c], and Stephen White[b]

a) Center for Coastal and Ocean Mapping, University of New Hampshire, Durham, NH 03824 USA;
b) Remote Sensing Division, National Geodetic Survey, NOAA, Silver Spring, MD 20901, USA
c) Joint Airborne Lidar Bathymetry Technical Center of Expertise, USACE, Kiln, MS 39556, USA

As with any survey system, it is strongly recommended that the service provider evaluate the performance of the ALB system prior to conducting the survey. The specifics of the evaluation can vary substantially based on user requirements and available resources. In this chapter, a general overview is provided regarding the approaches used for an ALB system performance evaluation. It is important to note that "performance evaluation" here refers to the tests that accompany the delivery of the ALB system from the manufacturer to the service provider, and that the approaches presented are based on the experience of U.S. government agencies and service providers. Some of the approaches reviewed below have been used with topographic lidar systems and for acoustic ship-borne transducers (namely, multibeam echosounders), but have not yet been tested with ALB systems. Although the manufacturer may have already conducted some calibration tests, it is important to repeat the procedures again using the service provider's aircraft. The six parameters that are used to evaluate the systems are: system health, noise evaluation, coverage evaluation, geometric calibration, accuracy evaluation and image/intensity quality evaluation (Beaudoin, Johnson, and Flinder 2013). In addition to acceptance, these parameters can be used as a baseline for future evaluation on the system, namely degradation or changes in the ALB system over time.

6.1 Expectations from the ALB systems

Every service provider, whether government agency or private sector company, is addressing a specific client or constituent group, and the performance expectations of a given ALB system are defined by the product specifications of the client. Although the primary product for most ALB surveys is bathymetry, the environmental conditions may vary and survey configurations may differ among service providers (LaRocque, Banic, and Cunningham 2004b; Imahori et al. 2013). Technical and economic considerations limit the capacity of the ALB system to perform all the expected tasks at the same level of performance. Thus, prioritizing the specifications of the ALB system according to the specific mission is important.

As an example, two U.S. government agencies that use broad-beam ALB systems for coastal mapping have different requirements. The mission of the USACE National Coastal Mapping Program (NCMP) is to provide repetitive, regional, high-resolution, high-accuracy, seamless bathymetric-topographic data to support regional sediment management among coastal navigation, flood damage risk reduction, and ecosystem restoration projects. The program focuses on data collection where sediment is moving the most – along sandy coasts, and from the onshore dune system to the depth of closure (an offshore depth

beyond which the depths do not change with time). USACE has broader data requirements on other types of coasts with a more extensive cross-shore expression than are addressed by other programs. These data, and a series of information products derived from them, are used to characterize engineering, environmental, and economic conditions along the shoreline, and their changes over time (Wozencraft 2014). USACE's mission also includes a requirement to monitor changes that occur naturally or due to manmade construction, which is typically over sandy areas. The USACE survey standards are that the ALB system should be able to acquire data at a spot spacing of $4m \times 4m$ with 100% coverage (i.e., no gaps in the survey flight plan) and achieve the same accuracy over the same area in the next survey cycle, which is every 5 to 7 years (Wozencraft 2010b; USACE 2012). On the other hand, the goals of the NOAA ALB survey missions are to provide accurate, consistent, and up-to-date bathymetry and shoreline around the coasts of the U.S. and its territories (Imahori et al. 2013). The survey products need to meet international hydrographic survey standards, such as the IHO S-44 survey standards (IHO 2008). Accordingly, ALB survey data for hydrographic charting in NOAA are expected to: 1) fill in the data gap shoreward of the navigable area limit line (NALL) (0 to 4 m), and 2) overlap with surveys collected using sonar systems (e.g. multibeam, side scan or single beam) from 4 m to 10 m with a 0.5 m tolerance (Imahori et al. 2013). Many of coastal areas surveyed by NOAA include muddy, sandy and rocky coastal regions. The NOAA survey standards are that the ALB system should be able to acquire data up to a depth of 10 m at a spot spacing of $3\text{m} \times 3\text{m}$ with 200% coverage (i.e., two survey lines cover the same area). Also, each ALB survey needs to meet IHO order 1b standards (IHO 2008).

Theoretically, ALB systems can perform all the tasks mentioned above successfully. However, variations in environmental conditions (Chapter 3) and hardware degradation (Chapter 4) limit the ALB performance. A narrow-beam ALB will not provide successful bottom detection at depths greater than 10 m and broad-beam ALB systems do not provide spot spacing smaller than $2\text{m} \times 2\text{m}$. Thus, the service provider needs to identify and prioritize the tasks that the ALB system is expected to perform. In addition to the survey products, these tasks should include repeatability and degradation in performance over time.

6.2 Key Evaluation Parameters

6.2.1 System health

When delivering the ALB system, the manufacturer provides a list of specifications for the system. The list should include specifications for the laser, scanner, detection unit, and the auxiliary systems (e.g., positioning and attitude). Also, the manufacturer should provide recommended operational parameters on: operational altitude range, nominal aircraft speed, minimum eye-safe altitudes, temperature requirements and power requirements. Based on the system specifications and recommended operational parameters, it is possible to predict the swath width, the spot spacing and the ALB footprint diameter on the water surface.

It is also recommended that a full Built In Self Test (BIST) diagnostic routine be conducted at a calibration site (bench test), and then again after the system has been mounted in the aircraft on the runway prior to flying. The BIST provides the opportunity to perform measurements on the ALB system (i.e., laser, scanner, detector unit and auxiliary sensors) and to establish benchmarks for the health of the

system components as they degrade with time. It is important to note that the BIST cannot provide a full characterization of the components as conducted at the manufacturer's laboratory facilities; however, this evaluation test provides a good indication of the overall ALB system's health. The BIST is particularly useful for monitoring the system health when conducted on a routine basis.

6.2.2 Noise evaluation

Mechanical and electrical noises may affect the ability of the ALB system to detect and track the seafloor using laser measurements. As with the tests described in the previous section (system health), a comprehensive noise analysis can only be conducted in an appropriate laboratory facility. However, a BIST diagnostic routine can be designed to assess if the aircraft platform is "quiet" (i.e., aircraft noise does not affect the recorded sensor measurements) and to determine if noise levels could be responsible for significant changes in the observations. The noise tests should be performed both statically on an optical bench, and again in flight (after the system has been mounted in the aircraft) at different speeds. Here, the signal-to-noise ratio (SNR) can be defined as the power ratio between the signal in the lidar return from a target, P_{signal} , to the background noise in the lidar return, P_{noise} , or as the square ratio of the amplitudes of signal, A_{signal} , and the background noise, A_{noise}:

$$SNR = \frac{P_{signal}}{P_{noise}} = \left(\frac{A_{signal}}{A_{noise}}\right)^2 \tag{6.2.1}$$

6.2.3 Swath coverage

The system health and noise tests evaluate only some of the factors that control the scanning performance of the ALB system. Swath coverage should be tested over different water depths in order to evaluate the achievable coverage and to compare it to a baseline performance level. As mentioned in Section 4.1.2, the swath width is dependent on the maximum off nadir angle across track and the height above the water surface. It is important to note that environmental conditions can also affect the achievable coverage (Section 3.3), and caution must be exercised when interpreting or comparing results from areas with different oceanographic regimes and/or seafloor composition (Beaudoin, Johnson, and Flinder 2013). A swath coverage test should include a land survey of a flat area (e.g., airport or football field) and a marine survey where the flight lines are running perpendicular to the depth contours. If the aircraft is able to maintain a constant height and fixed attitude angles, then the swath width should also be fixed throughout the survey line. Then, if any changes are observed in the swath width during the evaluation, further investigation of the cause is needed. Possible causes for the changes in the swath width over land are: synchronization issues between the ALB system and the auxiliary systems (Global Position System, GPS, and Inertial Navigation System, INS) (Wehr 2009), or calibration issues that include boresight-angle bias or offset, and biases of the laser beam range and angle calculations (Gonsalves 2010a; Habib 2009). It is important to note that the term Boresight Calibration mentioned later in this chapter refers to both spatial and orientations between sensors or between a sensor to the reference frame of the survey vessel, whereas boresight angles refer only to the orientation. Possible causes for the changes in the swath width underwater maybe related to an evaluation issue of the optical conditions underwater, variability of water conditions in a given swath (e.g. current causing differences in turbidity), or miscalculation of the optical geometry (Chapter 4).

6.2.4 Geometric calibration

Bathymetric data may contain geometric artifacts that can result from a number of sources. Two possible sources related to the system and/or ancillary sensors include: 1) faulty configuration of the systems in the aircraft, or 2) degradation in performance of the systems over time. Geometric calibration is the first of two procedures needed to confirm the quality of the acquired bathymetric data. The calibration procedure can be conducted over land (Gonsalves 2010a, 2010b). In that case, the system can be tested over a well-controlled environment without the need to correct for the sea surface morphology or distortions caused by the water column (Chapter 3). Geometric calibration serves to verify the relative contributions from the GPS, INS and the ALB system (Vaughn et al. 1996; Schenk 2001; El-Sheimy, Valeo, and Habib 2005; Habib et al. 2010). Misalignments would be expressed as translational or rotational offsets. This procedure is also common in acceptance tests for acoustic survey systems where it is known as a "Boresight Calibration" and will be discussed in more detail in Section 6.3.2

6.2.5 Relative accuracy evaluation

After the geometric calibration has been accomplished, and the biases between the ALB system and the auxiliary systems are within survey specifications, a follow-up relative accuracy test is conducted. In essence, the relative accuracy test is a comparison of the ALB survey (conducted according the survey configuration defined by the service provider) to a reference acoustic survey (typically, a multibeam survey meeting IHO order 1a survey standards). In addition to an overall accuracy evaluation of the system as a function of depth, it is also possible to assess the accuracy of the laser measurements as a function of the scan angle (azimuth). The overall accuracy provides information on bottom detection and dependence on the environmental conditions. More details on the relative accuracy evaluation are provided in Section 6.3.3.

6.2.6 Radiometric evaluation

The amplitude of the return waveform, whether from the seabed or the water column, is another data product commonly available from ALB systems. The amplitude is commonly used to produce an image of bottom reflectance or column backscattering. Similar to bathymetry, any degradation of the health of the system, increase in noise or drift in calibration can degrade the quality of imagery. Image quality can be especially sensitive to transient noise events. Other potential sources of image artifacts include improper correction for range and water column attenuation. In contrast to bathymetric accuracy standards, there has not yet been a concerted effort to standardize the quality of ALB intensity imagery.

6.3 Evaluation tests

6.3.1 BIST

A typical BIST for multibeam systems is conducted on a ship at a dock with the engines off (Beaudoin, Johnson, and Flinder 2013). In contrast to multibeam systems, it is impossible to conduct such a test with an ALB system. Instead, it is recommended that, before the system is mounted to the plane, the ALB system should be tested by the manufacturer under laboratory conditions on an optical bench. The ALB system should be configured to measure a set of white and black targets at horizontal distances ranging

from 300 to 500 m, a typical operational altitude range for ALB surveying. The manufacturer should supply the service provider with the waveforms (if available) and ranges in Laser file format (LAS). All of these observations should be compared to the distances and the reflectance values of the targets. The range measurements results should be within the tolerance values declared by the manufacturer. If possible, a transformation should be established between the reflectance measurements from the ALB (in arbitrary units) to the physical radiometric reflectance values of the targets measured by a spectrometer.

Next, the ALB system should survey at altitudes similar to the target ranges used in the bench measurement. A flat concrete or asphalt platform that is uniform in color (e.g., road or parking lot) can be used as a reference area. A set of survey lines in a cross-strip configuration should be collected at different speeds. From this evaluation survey, it is possible to conduct an analysis of the system performance for a set of ALB hardware parameters that include:

1. ***Swath width*** – The strip widths from different strips are compared in order to discern any changes in the swath width. It is also important to determine if the swath width is uniform along the strip.
2. ***Waveforms*** – The noise in the waveform should be evaluated with respect to the speed of the aircraft. Waveforms collected during the bench test measurement are used as a reference waveform that was collected in a "quiet" environment.
3. ***Ranges*** – The range distances of laser measurements of the same location on adjoining strips are evaluated. Systematic changes in range distance should be also compared to the incident angle.
4. ***Peak value (intensity)*** – The consistency of the bottom return shape characteristics and/or the intensity peak values of the laser measurements are evaluated. The average peak value and the variability in intensity within each strip are calculated and compared to the other strips. In addition to the peak value, the shape characteristics of the bottom return are evaluated as a function of the angle of incidence.

All the BIST results should be compared to the ALB system specification. It is recommended that the BIST results be shared with the manufacturer, highlighting any inconsistencies between the BIST results and either the ALB system specification or the BIST results from previous years. The manufacturer should discuss options for addressing any issues identified. All the BIST output results should be documented for comparison with the next BIST results.

6.3.2 Boresight Calibration (Geometric Calibration)

Organizations, such as IHO or ASPRS, have yet to standardize a Boresight Calibration procedure for ALB systems. Instead, the various geometric calibration procedures used for ALB systems are hybrids combining multibeam calibration procedures (OCS 2014; Beaudoin, Johnson, and Flinder 2013) and topographic lidar quality control procedures (Filin 2003; Habib et al. 2010; Toth 2009). Geometric calibrations for ALB systems are typically self-consistent, i.e. they do not require an external reference dataset. In contrast to standard calibration in photogrammetry, it is practically impossible to establish a direct correspondence between two point cloud datasets in overlapping multibeam or lidar calibration strips. Therefore, the data should be resampled for processing. Each laser measurement in the point cloud can be described by the general lidar geo-location equation (6.3.1) using the vector from the origin of the ground coordinate system to the INS body frame, $\vec{X}_0$, the offset between the laser unit and the INS body frame with respect to the laser unit coordinate system, $\vec{P}_G$, and the vector between the laser beam firing

point and the target point, ρ. The ground position, $\vec{X}_G$, is derived by applying three rotation matrixes: the rotation matrix between the Inertial Navigation System (INS) body and the mapping frame, $R_{yaw,pitch,roll}$, the boresight matrix between the laser frame and the INS body frame, $R_{\Delta\omega,\Delta\phi,\Delta\kappa}$, and the scan angle rotation in the laser sensor frame, $R_{\alpha,\beta}$ (El-Sheimy, Valeo, and Habib 2005; Habib 2009):

$$\vec{X}_G = \vec{X}_0 + R_{yaw,pitch,roll} \cdot R_{\Delta\omega,\Delta\phi,\Delta\kappa} \cdot \vec{P}_G + R_{yaw,pitch,roll} \cdot R_{\Delta\omega,\Delta\phi,\Delta\kappa} \cdot R_{\alpha,\beta} \begin{bmatrix} 0 \\ 0 \\ -\rho \end{bmatrix} \quad (6.3.1)$$

A comparison between two calibration strips provides the 3D offset parameters that describe an affine transformation, The seven parameters that are required to define the geometric relationship between the point cloud in one strip to the point cloud in another strip include three parameters for the translation vector between the strips$(X_T, Y_T, Z_T)^T$, three for the rotation matrix for the co-alignment between the strips, $R_{\Omega,\Phi,K}$, and a scale factor, S:

$$\begin{bmatrix} x_{q_i'} \\ y_{q_i'} \\ z_{q_i'} \end{bmatrix} = \begin{bmatrix} X_T \\ Y_T \\ Z_T \end{bmatrix} + S \times R_{(\Omega,\Phi,K)} \begin{bmatrix} x_{q_i} \\ y_{q_i} \\ z_{q_i} \end{bmatrix} \quad (6.3.2)$$

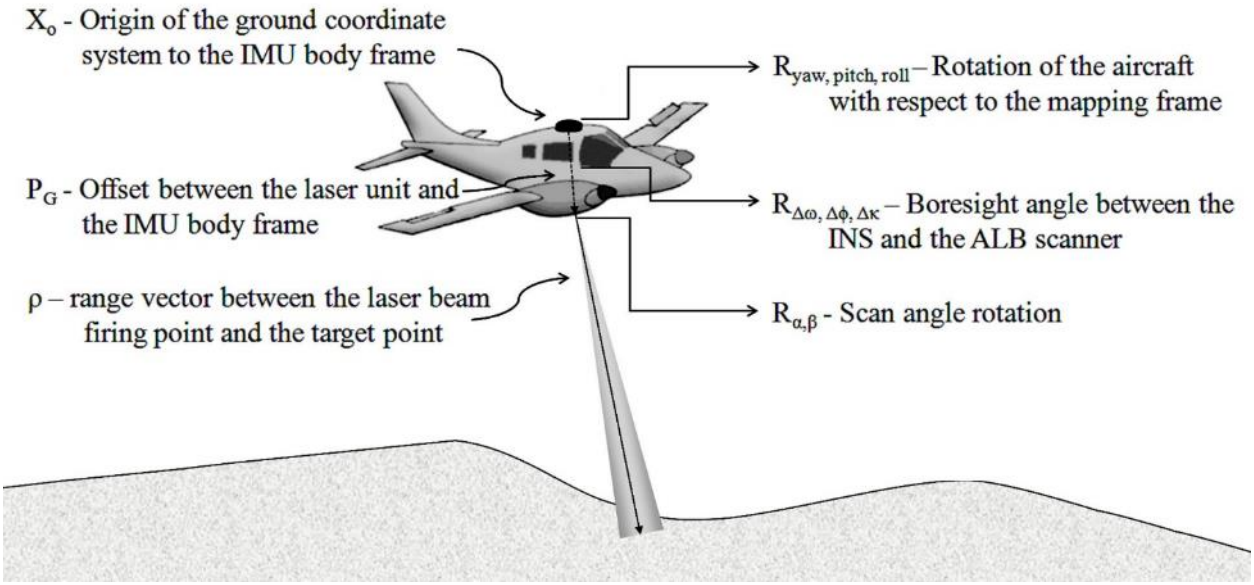

Figure 6.3.1. Geometric components for the general lidar geo-location equation.

It is recommended that the two calibration strips be collected over a flat terrain in order to provide the vertical offset, and over a prominent feature to provide the horizontal offset between the two datasets. The horizontal offset can also be evaluated by comparing the intensity images from the calibration strips. The calibration strips should be overlapping (ideally, 100% overlap). Also, it is assumed that the ALB strip does not contain synchronization issues in order to avoid any internal deformation within the strip. The internal deformation is defined for cases for which the rigid body model is not adequate to describe the

relationship between the ground surface and the lidar system. Since geometric calibration will serve as a validation test for the measured offsets, it is required for both marine and aerial surveying in order to measure the lever-arm (position) offsets between a survey system to the GPS and INS systems. The lever-arm offsets measurement steps include the following recommendations (OCS 2014):

1) that the aircraft's approximate center of motion be coincident with the origin of the INS' local reference frame. This will reduce the number of physical offset measurements and, as a result, minimize the sources of error in position and attitude data.
2) that the horizontal and vertical distances to each of the sensors with respect to the origin of the INS' local reference frame will be determined by a professional surveyor using theodolites, laser range finders, total station, or optical levels. The service provider should consult with the manufacturer to define the specific accuracy requirements for the offset measurements between system components during installation.

For multibeam survey systems, the surveyed area that is used as a Boresight Calibration must either contain a prominent feature on the seafloor (e.g., rock or pipe) or be featureless, depending on the survey parameter that is investigated (Beaudoin, Johnson, and Flinder 2013). In a ship-borne survey, two survey lines in opposing directions are used to evaluate the attitude of the vessel, where roll and yaw are evaluated over any bottom profile, and pitch is evaluated over a sloping bottom. It is important to note that yaw evaluation requires the survey lines to completely overlap. Once the survey lines are acquired, carefully chosen subsets of the soundings are examined to systematically determine each calibration value. This procedure is commonly done manually, but there are, some software packages that offer semi-automated procedure (Gonsalves 2010a). The challenge in underwater geometric calibration is that line features, such as pipes, are difficult to find. As a result, many underwater Boresight Calibrations contain rocks as a prominent feature. Thus, the feature is observed with only one or two measurements, and those may not be representative of "the peak (least-depth) of the feature" (Gonsalves 2010b).

Quality assurance of topographic lidar is conducted from an airborne platform over land. Similar to the multibeam calibration procedure, topographic lidar calibration lines are acquired in pairs under the same survey conditions with a bias in one survey parameter between the lines (Vaughn et al. 1996; Schenk 2001; Filin 2003; El-Sheimy, Valeo, and Habib 2005; Habib 2009; Habib et al. 2010). The main difference between an underwater calibration procedure and a calibration over land is that potential errors related to the water surface and the water column (e.g., glint, refraction, and attenuation) are absent and prominent linear features (e.g., buildings with slope roofs) are more abundant (Gonsalves 2010b; Habib 2009).

Before conducting strip adjustment, well-defined reference areas, patches, are selected. In addition to the requirement that both strips should cover these reference areas completely, the patches should be evenly distributed across the swath of the strip in order to provide a strong geometric solution for the adjustment. The size of the patches depends on the point density, but is typically larger than 10 m for narrow-beam ALB systems with 2 to 5 pt/m^2, and 50 m for broad-beam ALB systems with 1/9 to 1/16 pt/m^2. Roads and parking lots are recommended features for patch areas. Also, moderately-sloped terrains or building structures can be used as patch areas. It is important to avoid vegetation that can cause multiple scattering within the biomass (such as shrubs or trees). Golf courses that contain lawn with very short grass can be used as patches if no other candidate patch areas are available. The water surface in a pond and a lake can

also be used as a patch; however, it is important that the water surface does not contain gravity waves (see Section 3.2).

There are a variety of strip adjustment approaches that can be grouped into five main categories (Habib 2009; Chen and Medioni 1992):

1. ***Gridded surface*** **-** The point clouds in both strips are converted into a surface. A comparison (matching of conjugate points) between the two grids allows one to calculate the deviation between the two strips. Gridding is typically used for surface generation for the whole strip, intensity point clouds, or for a patch area that contains multiple facets. Common grids use inverse distance weighted, natural neighbor interpolation, spline, or kriging interpolation methods.

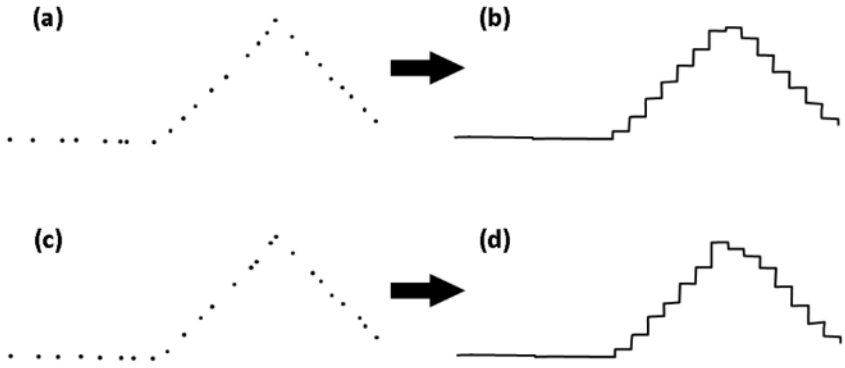

Figure 6.3.2. A schematic illustration of a gridded surface approach (side view in 2D). Point cloud from one strip (a) is compared to point cloud from an overlapping strip (c) by gridding the two point clouds (b and d, respectively) and comparing the surfaces.

2. ***Linear features*** **-** Linear features are extracted from the point clouds. These lines can be derived manually or automatically using an image processing algorithm, such as the Hough transform. Deviations from the optimum values (zero shifts, zero rotations, and unit scale factors) can be used as indications of systematic biases in the lidar system. It is important to note that only the orientation of the linear features must match; there is no requirement for the length of the features to match as well (i.e., the end point do not need to match).

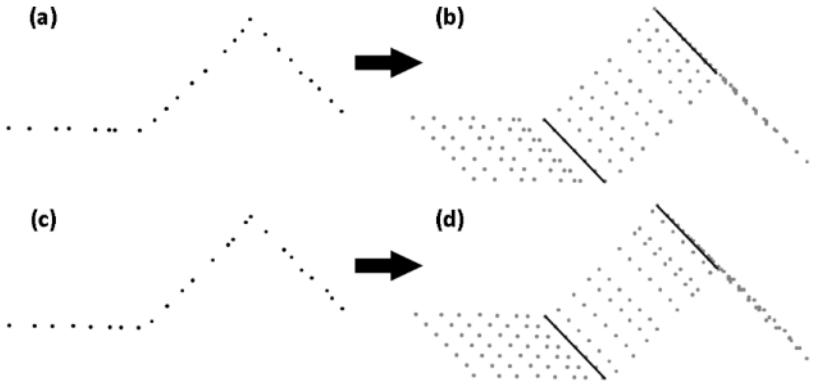

Figure 6.3.3. Schematic illustration of the linear features approach. A point cloud from one strip (a) is compared to a point cloud from an overlapping strip (c) by selection of linear features from overlapping surfaces between the two point clouds (b and d, respectively). Note: (a) and (c) are presented as a side views in 2D, whereas (b) and (d) are presented as an oblique views in 3D.

3. ***Iterative Closest Point (ICP)*** – Similar to linear features approach, it is possible to extract key points from point clouds of overlapping strips. By keeping a set key points from one strip fixed, an interactive calculation is used to estimate the rotation and translation of the second set using a mean squared error cost (i.e., minimum difference between two set of key points). After each rotation and translation estimation, the second set is transformed and then undergoes another iteration to re-associate the points until they two sets of key points converge to a threshold distance.

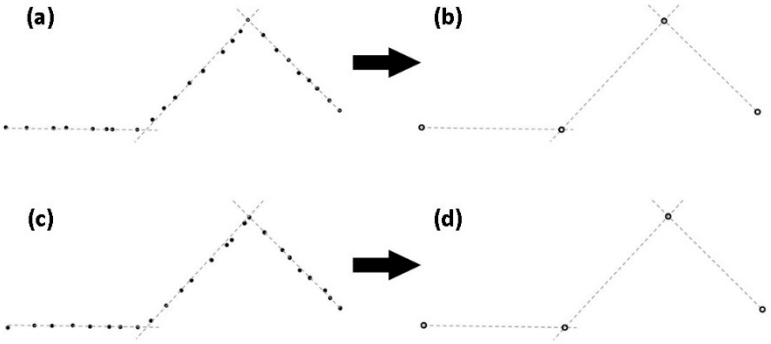

Figure 6.3.4. Schematic illustration of the ICP approach. A point cloud from one strip (a) is compared to a point cloud from an overlapping strip (c) by selection of key points from vertex point between the overlapping surfaces of the two point clouds (b and d, respectively).

4. ***Planar patches*** - Similar to the linear feature approach, planar patches can be used for matching. A least square adjustment is used to fit a planar surface from the point cloud. It is important that the reference area of the point cloud be identified as a flat surface. Also, the geometric calibration should include multiple patches at different slopes in order to have a strong solution to recover the transformation parameters.

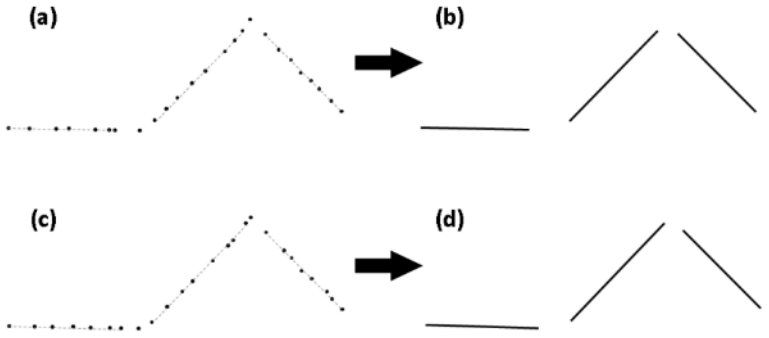

Figure 6.3.5. A schematic illustration of the planar patches approach (side view in 2D). A point cloud from one strip (a) is compared to a point cloud from an overlapping strip (c) by generating overlapping planar patches (flat surfaces) from the two point clouds (b and d, respectively).

5. ***Interpolated point cloud*** - An alternative approach to the gridded surface matching is resampling the point cloud in one ALB strip to match the location of the point cloud in the other strip. A surface is generated by a triangle irregular network (TIN).

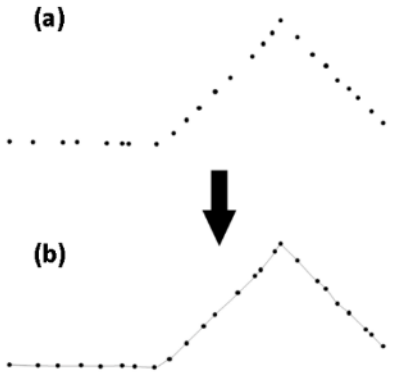

Figure 6.3.6. A schematic illustration of the Interpolated point cloud approach (side view in 2D). Point cloud from one strip (a) is used as a surface reference. Point cloud from an overlapping strip (b) is resampled horizontally based on the reference surface.

6.3.3 Relative accuracy Test

The relative accuracy test is an empirical comparison of the test data set against a reference data set that is assumed to be over a stable bottom (i.e., the reference data should be collected over a sandy bottom at the entrance to an inlet). The comparison results consist of a number of summary statistics that may include properties, such as mean, root mean square error (RMSE), and standard deviation, as well as histograms of differences. One of the goals of this test is to evaluate the performance of the ALB system in the field over a given seafloor type with a well-defined bathymetry. A multibeam echosounder or a dense single-beam echounder survey meeting the IHO order 1a survey standards is recommended as a reference bathymetry for evaluating a broad-beam ALB system in waters deeper than 3 m. For shallower depths

(< 2 m), bathymetry derived from a beach profiling survey is recommended for evaluating a narrow-beam ALB system. The relative accuracy test provides an evaluation for ALB surveying under typical water and weather conditions, such as a survey on a rising tide (flood stage) with winds less than 3.4 m/s (Beaufort sea stage 2 or less). The comparison between the two datasets is conducted after the ALB dataset has been edited and outliers have been removed. The evaluation consists of several steps that are conducted using tools available in commercial-off-the-shelf (COTS) software, such as ArcGIS, ENVI, CARIS, Fledermaus and MapInfo):

Preprocessing - In order to compare the ALB survey to the reference bathymetry, the ALB survey should be in a format that can be loaded into COTS software and have the same coordinate system as the reference bathymetry. The ALB data are typically acquired in a proprietary binary format. Two common, publicly available format types are ASCII format (e.g., XYZ or grid) and LAS format (ASPRS 2008a, 2008b). The manufacturer typically provides a converter to parse the proprietary binary ALB data into one of these two, allowing them to be loaded into COTS software.

The comparison between the ALB and reference data should be in the same vertical and horizontal system. It is important to note that ALB surveys are referenced to an ellipsoidal or orthometric vertical datum, whereas the reference bathymetry might be referenced to a tidal datum. If sufficient tidal data is not available for chart datum transformation, the comparison should be done in the ellipsoidal or orthometric vertical system. A similar situation may also occur with the horizontal system, where one dataset uses geographic units (i.e., longitude and latitude) and the other dataset is projected using northing and easting coordinates. Figure 6.3.8 provides an example of a transformation flow diagram from the JALBTCX ALB survey data coordinate system (geographic horizontal system and an ellipsoidal North American Datum 1983 (NAD83) vertical system) to the reference system of the NOAA multibeam echosounder survey (Universal Transverse Mercator (UTM) projected horizontal system and a tidal Mean Lower Low Waters (MLLW) vertical system) using NOAA's VDatum transformation tool (S. White 2007).

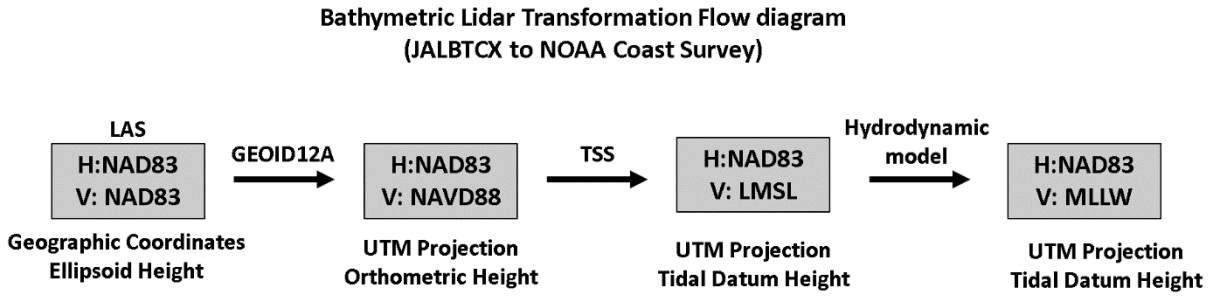

Figure 6.3.7. Transformation flow diagram of NCMP lidar data from JALBTCX archives (USACE – JALBTCX), to NOAA's Office of Coast Survey (OCS). NAD83 – North American Datum 1983; NAVD88 – North American Vertical Datum 1988; LMSL – Local Mean Sea Level; MLLW - Mean Lower Low Waters; TSS – Topography of the Sea Surface; UTM - Universal Transverse Mercator.

Density map - Coverage maps with density values (number of laser measurements per square meter) provide spatial information on the ALB performance that includes areas with low or no

bottom detection. These density maps allow the operator to intersect these maps with the reference bathymetry and infer the effective operation depth of the ALB system and its performance over different strata (Figure 6.3.8). The average spot spacing, which is a function of the density can be also calculated as a function of depth. For example, an ALB survey with a $4\text{ m} \times 4\text{ m}$ spot spacing is equal to a density of $(1/16) = 0.06\text{ pts/m}^2$. Figure 6.3.8 presents two examples of density maps (Imahori et al. 2013). On the left is a density map of a USACE SHOALS survey over an area near Port Everglades, FL (2009). The density map shows a uniform distribution that ranges between 0.06 to 0.17 pts/m^2, which is typical for a survey using this type of ALB over a sandy coral bottom with clear water conditions. On the right is a density map of a 2007 USACE SHOALS survey over an area near Kittery, ME. The density map is patchy with a density that ranges 0.04 to 0.13 pts/m^2. Such density map characteristics may be attributed to the seafloor type (sandy with rocky outcrops) and the water clarity (~0.2 m) (Pe'eri, Morgan, et al. 2011).

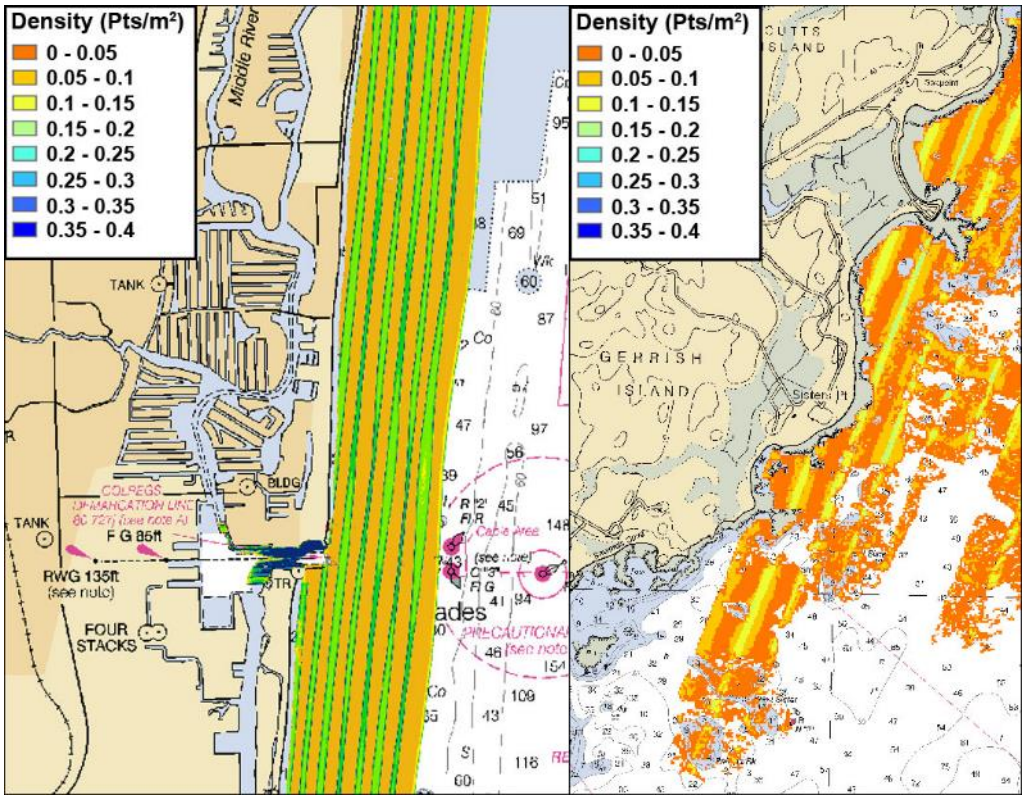

Figure 6.3.8. Density maps of USACE CHARTS system (Imahori et al. 2013): (left) Port Everglades, FL (2009) and (right) Kittery, ME (2007).

Difference map - It is important to note that, before generating a difference map, both datasets should be in the same horizontal and vertical systems. Also, both datasets should be gridded to a scale smaller than the spot spacing. Otherwise, the interpolation method will affect the results and aliasing may occur. A difference map of derived elevations can be generated by the subtraction of the ALB bathymetry grid from the reference bathymetry grid. In addition to the accuracy of the systems, spatial changes in the difference between the two datasets may indicate an actual change

in bathymetry (e.g., over tidal inlets) or spatial variability of water clarity or the seafloor type (Figure 5.3.6.3.10). It is also important to note that some hydrographic offices consider a systematic bias of up to 0.2 m to be a reasonable difference between ALB surveys and the reference bathymetry. Figure 5.3.9 presents two examples of difference maps (Imahori et al. 2013). On the left is a density map showing the difference between a 2009 USACE SHOALS survey and a 2008 NOAA MBES (Multibeam Echo Sounder) survey (Ocean Surveys 2009) over an area near Port Everglades, FL that contains a stable seafloor (bathymetry changes are mainly due to major weather events). The depth difference between the two datasets is uniform (standard deviation of 0.24 m) with a small average (0.54 m). On the right is a difference map between a 2004 USACE SHOALS survey and a 2008 NOAA MBES over a tidal inlet near Pensacola, FL. The depth difference map in this case is not uniform (standard deviation of 1.72 m with an average difference of 0.57 m) and indicates that the bottom morphology has changed during the 5 years between the two surveys.

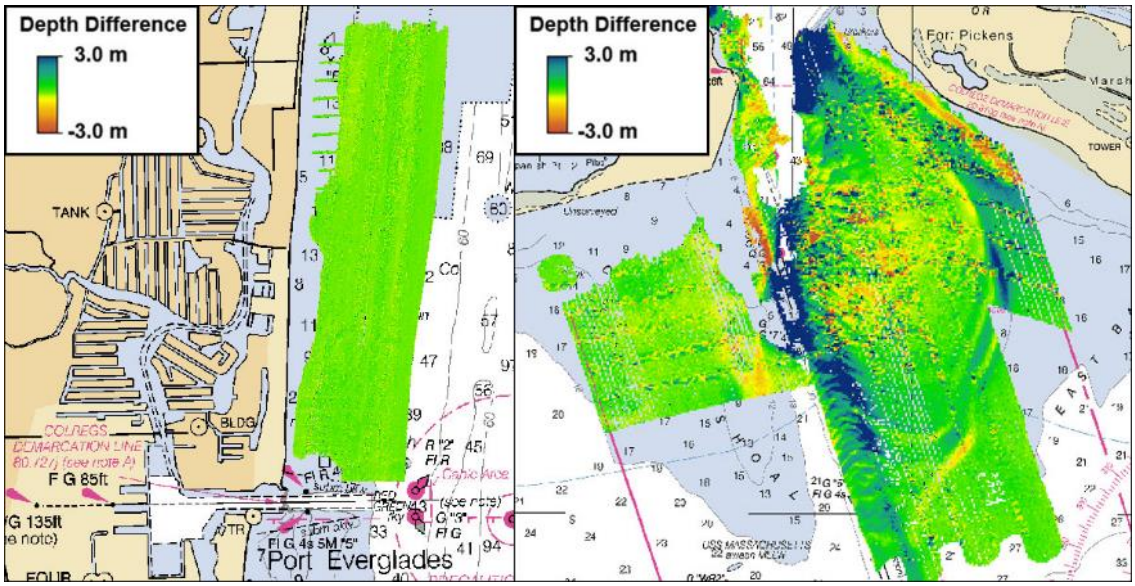

Figure 6.3.9. Difference maps between USACE CHARTS surveys to NOAA multibeam surveys: (left) Port Everglades, FL and (right) a tidal inlet near Pensacola, FL.

Histogram - For a general evaluation of the whole survey area, or for only a subset section, the histogram provides a visual aid showing the difference frequency between the two datasets (Figure 6.3.10). The mean and standard deviation indicate if there is a systematic offset (especially, if the two dataset have not been referenced correctly) and the value of the measurement error. Figure 5.3.10 illustrates the difference distribution for the two USACE SHOALS surveys presented in Figure 5.3.9.

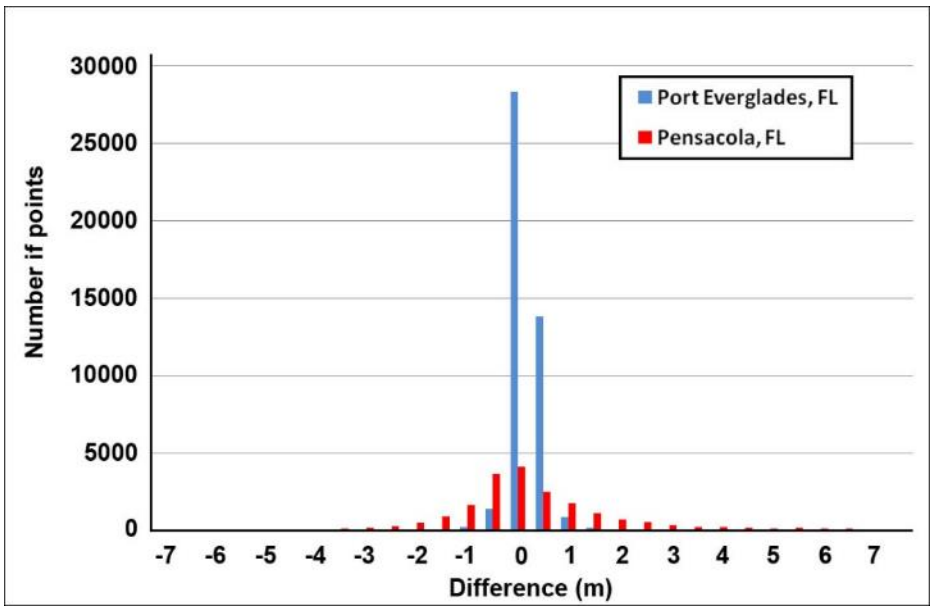

Figure 6.3.10. Histograms for the data presented in Figure 5.3.9 of the depth differences between the USACE CHARTS surveys of Port Everglades, FL acquired in 2009 (blue bars) and Pensacola, FL acquired in 2004 (red bars) compared to NOAA multibeam survey data from 2008, respectively.

Scatter plot - When the difference values between the two datasets are intersected with the depth values, it is possible to evaluate the ALB performance as a function of depth (Figure 6.3.11). The scatter plot also provides a mean and standard deviation that can be segmented as a function of depth. It is common to notice an increase in standard deviation over very shallow coastal areas (less than 1 meter) because of wave action and suspended particulates. Figure 6.3.11 shows a scatter plot comparison between a CHARTS ALB survey from 2012 conducted by the USACE, and a LADS MKII ALB survey from 2009 conducted by NOAA. The scatter plot shows an overall good agreement in depth. The overall mean and standard deviation (1σ) are 0.17 m and 0.32 m, respectively. An investigation of depth difference measurements as a function of depth in the scatter plot shows the standard deviation is less than 0.5 m at depths ranging from 3 m up to 20 m. At depths shallower than 3 m, the standard deviation increases to more than 1.0 m. This may be attributed to coastal processes (e.g., breaking waves). Accordingly, it is better to conduct the relative accuracy over bottom depths deeper than 2 m.

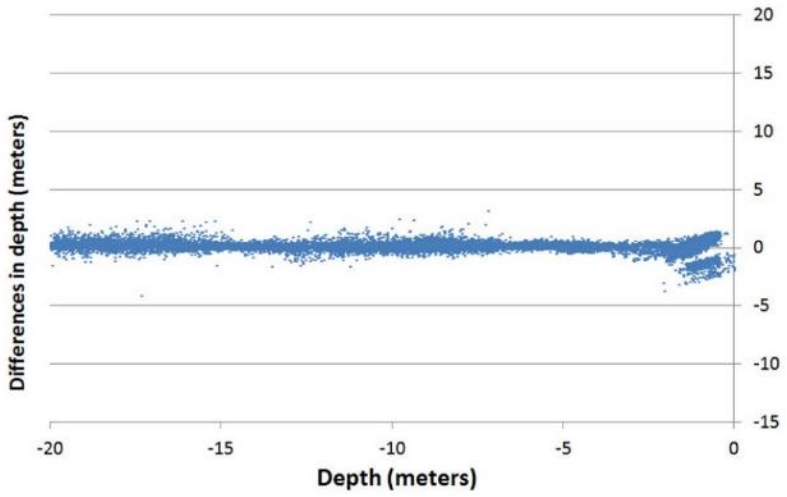

Figure 6.3.11. Histogram of the depth difference between a CHARTS ALB survey from 2012 conducted by the USACE and LADS MKII ALB survey from 2009 contracted by NOAA.

Results from the accuracy test are checked against hydrographic survey standards (e.g., IHO or USACE) and system performance defined in the service provider's requirements:

Depth penetration **-** The depth penetration capability (maximum depth) is a performance requirement based on the diffuse attenuation coefficient, K_d, combined with a depth requirement, d and is dependent on the survey capabilities of the service provider. Some require an absolute depth requirement (e.g., 10 m) because the ALB survey will overlap with an acoustic survey with a criterion of $K_d * d > 1$. Others may plan to use the ALB system measurements alone, which would require a $K_d * d > 3$ criterion.

Vertical accuracy **-** The total vertical accuracy (TVU) underwater is typically evaluated based on the IHO S-44 standards (IHO 2008). The IHO TVU describes the 95% confidence level of the measurements and is dependent on the IHO order coefficients (Table 5.1), *a* and *b*, and the water depth, *d*:

$$\sqrt{a^2 + (b * d)^2} \tag{6.3.3)}$$

Table 6.1. TVU Coefficient values for the different IHO orders (IHO 2008)

IHO order	a	b
Special	0.25	0.0075
1	0.5	0.013
2	1.0	0.023

Horizontal accuracy **-** The total horizontal accuracy (THU) underwater for an ALB survey describes the 95% confidence level of the measurements and is also typically evaluated based on the IHO S-44 standards (Table 6.2):

Table 6.2. THU values for the different IHO orders (IHO 2008)

IHO order	THU
Special	2 m
1	5 m + 5%*d
2	20 m + 10%*d

6.3.4 Output formats

Typically, the manufacturer provides processing software that can post-process the lidar raw observations (waveforms) with the auxiliary systems. However, additional software is required for surface analysis or for further processing of the referenced point cloud data with additional data (e.g., seafloor character maps, information of marine protected areas, location of navigational channels and anchorage areas). Common software include: ArcMap, Global Mapper, Caris, Fledermaus, PFMabe and AutoCad Map. In order to load the data into these software packages, the laser measurements need to be converted from a proprietary format (i.e., a file structure intended for internal processing and is not open to the public) into a conventional exchangeable binary format or a common ASCII format.

The simplest form for an output file is ASCII format, such as XYZ or ESRI GRID format. The challenge of using ASCII format is that these are very large files that can fill the data archive or storage device with less survey coverage than would be achieved with a survey file in a binary format. Instead, LAS format files are commonly used as a deliverable format. These files are binary and contain a specific structure that is defined by the American Society for Photogrammetry and Remote Sensing (ASPRS 2010). Documentation for the LAS format is publically available allowing vendors and customers to export and import the data between different software. To date, ASPRS has published a fourth revision of the LAS format specification (LAS 1.4) since its initial version 1.0 release (ASPRS 2008b). In addition to XYZ, the LAS 1.4 format provides a header block, variable length records (VLR), extended variable length records (EVLR), and a full point data record (Table 6.3). The header block provides information on the survey, calibration parameters of the ALB system, and how to read the information in VLR and EVLR. Any additional information that the manufacturer or the service provider are interested in providing (e.g., full waveforms) can be recorded in the VLR and the EVLR. The VLR block is used by vendors that wish to maintain legacy compatibility. If the vendors are not concerned with legacy LAS reader software, then the EVLR can be used to store auxiliary information, especially to update information (normally contained within a VLR) without the need of rewriting the point data block. The most used block in LAS is the full point data record that, in addition to XYZ information, contains information on the intensity, return number, number of returns (given pulse), scan direction flag, edge of flight line, classification, scan angle rank, and user defined data for each point.

Table 6.3. LAS 1.4 Format Definition (ASPRS 2008b)

PUBLIC HEADER BLOCK
VARIABLE LENGTH RECORDS (VLR)
POINT DATA RECORDS
EXTENDED VARIABLE LENGTH RECORDS (EVLR)

It is recommended that the service provider verify the LAS versions that are currently available in the lidar processing software used for import and export operations. There is the possibility that import and export LAS files are in different LAS versions. It is also recommended that the lidar files be exported into LAS during the acceptance test procedures and to verify that all key parameters are exported. This verification can be done with one of the COTS software packages (e.g., LAStools or LP360).

6.4 Examples of Performance Evaluations

It is hard to find documentation of ALB field acceptance tests in the open literature. This is because BIST and geometric calibration tests are typically reported as result tables or as internal company reports and only a few of the relative accuracy tests are published as conferences proceedings. This section provides examples on several of the ALB systems based on published reports and personal communication with manufacturers. It is important to note that while the previous section provided theoretical background for an ideal situation (no budget or time constraints), the goal of this section is to provide a realistic perspective using examples of acceptance tests conducted by service providers and manufacturers.

6.4.1 USACE/Navy performance evaluation tests

Over the past 20 years, the USACE and the Navy have conducted performance evaluation tests on different ALB systems in the process of either acquiring the system or using service providers that operate such ALB systems. Two of the most recent ALB systems purchased by the USACE were the SHOALS-1000T/3000 and the CZMIL systems. A SHOALS-1000T/3000 evaluation test was conducted by the USACE and the U.S. Navy (Optech 2005). The goals of the test were to evaluate depth penetration capability (maximum depth), vertical accuracy underwater and horizontal accuracy underwater. Specifically, the USACE and U.S. Navy evaluated the ability of SHOALS-1000T to meet IHO Order 1 standards (IHO 2008), to detect the bottom based on a $K_d * d > 3$ (K_d is the diffuse attenuation coefficient and d is depth) criteria, and to perform topographic coastal mapping.

The BIST procedure for the SHOALS included two tests conducted at the Optech facilities in York, ON, Canada. The first BIST test was a dry run (i.e., the laser unit was not active) using an optical simulator. Laser pulses were generated using a board containing diodes that acted as a signal generator (Figure 6.4.1). The input parameters for Optech's Optical Simulator were: survey altitude of the aircraft, water depth, amplitudes of the bottom and surface returns, and false return range (Optech 2005). The laser pulses were used to test both the scanner unit and the detector unit. After validating all the electro-optical components in the dry run, the ALB system was tested using the transmitter unit over a target at a known distance (~80.0 m) and through a fiber optic cable. The next step, a test from an optical bench (not from an air craft) at operational ranges (300 to 500 m), was complicated by the need to maintain eye safety.

The solution was to conduct the second BIST by transmitting the laser pulses through a spool of fiber optic cable. Optech calls this configuration a "laser power timing test", where structure and timing of the pulse were tested in a well-controlled environment. An additional benefit of the laser power timing test is the ability to radiometrically characterize the system's detectors and calibrate new replacement detectors to the specifications of the previous ones. After the BIST, the SHOALS system was mounted in a Beechcraft King Air 90 and was flown over Oshawa or Peterborough airports, which are located near Toronto, CA. The airport runway and local structures (namely, buildings) were used for calculation of the boresight angles.

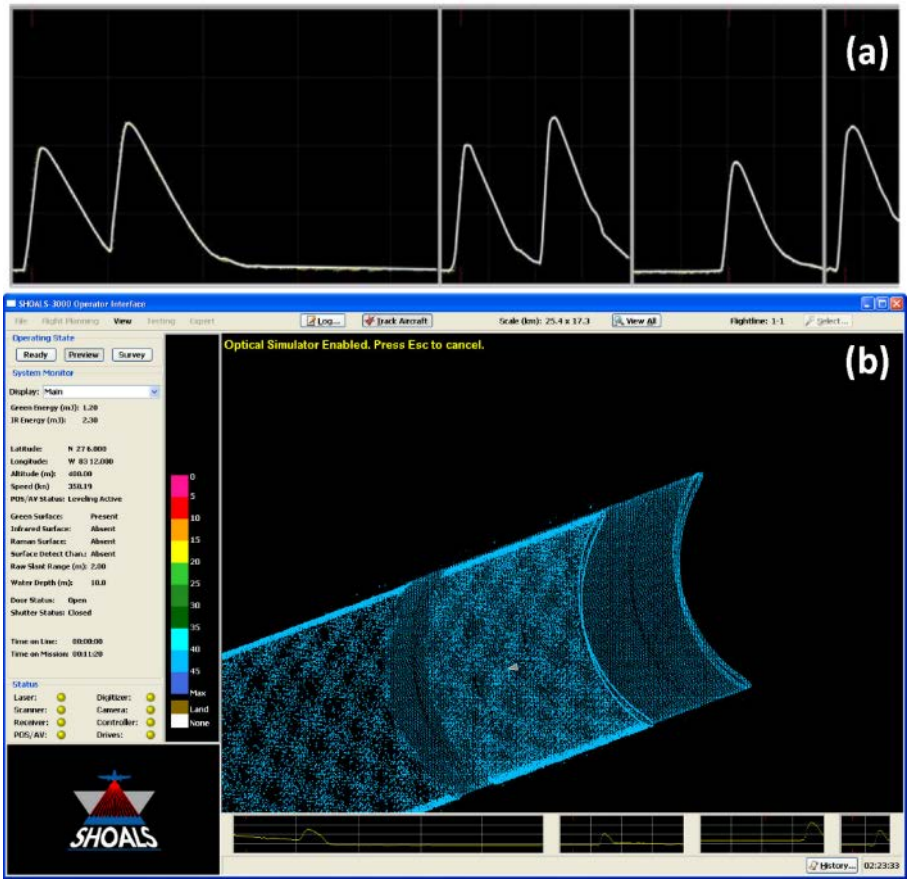

Figure 6.4.1. Optech's Optical Simulator: (a) Typical waveforms, and (b) screen shot of a BIST using the optical simulator.

USACE's and U.S. Navy's relative accuracy tests of the SHOALS-1000T (also known as Compact Hydrographic Airborne Rapid Total Survey, CHARTS) were conducted over the Naval South Florida Testing Facility (SFTF), Fort Lauderdale, FL, USA. The system was tested in several aircraft including: Beechcraft King Air 90, Beechcraft King Air 200, Beechcraft King Air 350, and deHavilland Twin Otter. The acceptance tests were conducted during July 2003, and were compared to a reference bathymetry that was collected using Kongsberg EM-1002 and EM-3000 multibeam system. In addition, ground truth data were collected using sidescan sonar and *in situ* spectral measurements of the water column. The ALB survey data was tide coordinated and was converted from WGS-84 to MLLW using a NOAA tide gauge that was located 20 miles south of the study site (Virginia Key, FL).

The results were an evaluation of the depth penetration capability of SHOALS 1000T in three locations. In addition, the depth penetration of the lidar system was predicted using an ocean optical model (Ocean Scientific 2003). A maximum depth was calculated to be around 45 m based on the density of the laser measurement criteria from lidar survey. The depth penetration results (Table 5.4) showed that the ALB system met the $K_d * D > 3$ requirement. The horizontal and vertical accuracies were evaluated using ten sites, all with depths less than the maximum penetration depth. The empirical error at each site was calculated as the sum of the mean (μ) with two standard deviations (2σ) of the depth differences between the ALB and the MBES surveys (i.e., $\mu + 2\sigma$). The resulting errors were compared to the IHO order 1 95% specification. Both the vertical and horizontal accuracy results showed that the ALB system meets the IHO order 1 requirement in most cases.

Table 6.4. Depth penetration results (shoals-1000T) (Optech 2005)

Laser measurement depth (m)	$\boldsymbol{K_d(m^{-1})}$	$\boldsymbol{K_d}$d
-39.40	0.08	3.15
-44.45	0.10	4.45
-39.79	0.10	3.98

Based on the experienced gained using the SHOALS system, the USACE adopted part of the Interagency Working Group's National Coastal Mapping Strategy as a new set of survey standards, known as quality levels (QL) (Table 5.5; Figure 5.3.13). The vertical accuracy and planned spot spacing density determine the QL. The goal of the new survey standards is to match the U.S, Geological Survey (USGS) 3D Elevation Program (3DEP) topographic survey standards on land (Dewberry 2012; Snyder 2012) and the IHO S-44 standards at water depths greater than 20 m (IHO 2008). It is also important to note that the vertical USACE quality level scale is for vertical uncertainty evaluation and not object detection in order to match IHO specifications (IHO order 1b). The USGS Quality Levels were defined using RMSE terms to match the IHO definitions (95% confidence level). The IHO TVU definitions were converted to RMSE based on the assumption that the distributions are Gaussian.

Table 6.5. Vertical USACE Quality level definitions for ALB Surveys, where *D* is the water depth in meters.

Bathy Lidar Quality Level	Point Density (pt/m^2)	Nominal Pulse Spacing (m)	Vertical RMSE (m)
QL1B	1.00	1.0	0.095 + 0.00275D
QL2B	0.25	2.0	0.095 + 0.00275D
QL3B	0.25	2.0	0.185 + 0.00275D
QL4B	0.04	5.0	0.185 + 0.00275D
QL5B	0.04	5.0	0.463 + 0.00275D

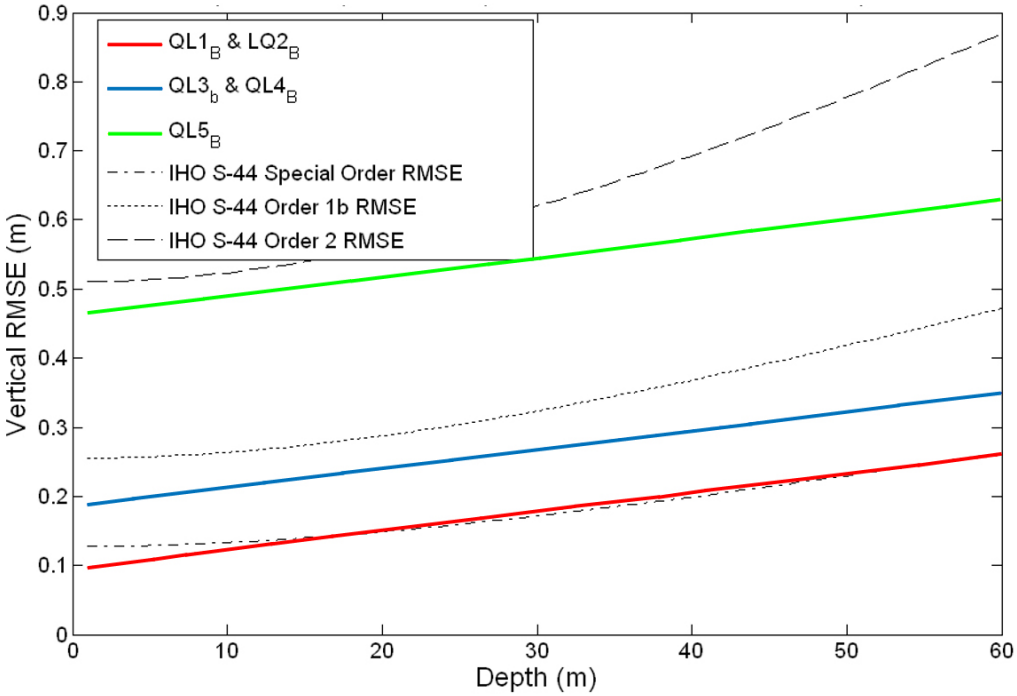

Figure 6.4.2. Vertical RMSE plots describing USACE lidar vertical quality level definitions with respect to the IHO survey standards.

The performance evaluation tests for the CZMIL system were conducted by the USACE and the Navy. The systems were mounted on a Beechcraft King Air 200. Geometric calibration of the CZMIL was conducted during June, 2013. A coarse boresight angle evaluation was conducted over the water surface (offshore Bay St. Louis, MS). After a rough approximation of the boresight angles from the offshore survey, a second ALB survey was conducted over Stennis airport, Kiln, MS (Figure 5.3.14). The flat airport runway makes it possible to calculate errors/uncertainties manually and/or automatically using numeric analysis. All the geometric parameters were then evaluated over structures with pitched roofs. The ALB datasets were compared to ground truth reference datasets. The airport runway was measured using an Optech Lynx Mobile Mapper (range precision of 5 mm at 1σ) survey from October of 2011 with a laser point density of 571 pts/m^2. Several pitched roofs were measured using a Trimble VX Spatial Station. Both ground truth surveys were referenced using Trimble R8 RTK data on an NGS published control monument (BH2999). In addition to a geometric calibration, an average point density on land of 2.17 pts/m^2 was calculated for a section in the middle of the swath over a flat area. This high point density value for the CZMIL is attributed to the 7 laser measurements for each transmitted pulse and the circular scanning that provides forward and backward-looking scans over the same area. The comparison results between the ground truth data and the CZMIL survey were in good agreement (Figure 5.3.14 right image).

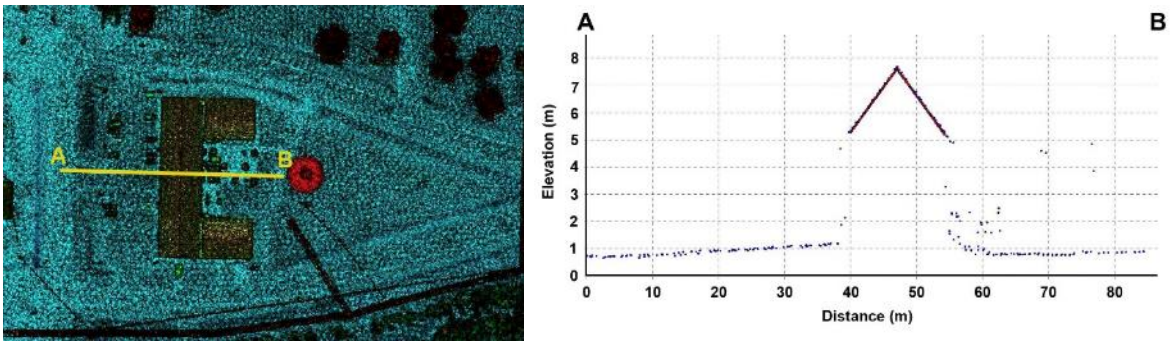

Figure 6.4.3. Geometric calibration of the CZMIL data: (Left) elevation map of Stennis, MS and (right) side profile over the JALBTCX facility. The black lines were calculated based on measurements conducted by Trimble VX Spatial Station.

The relative accuracy tests for CZMIL were conducted by the USACE in two locations: offshore Bay St. Louis, MS, USA (June, 2013) and over the SFTF, Fort Lauderdale, FL, USA (August, 2013). In both flights, the CZMIL system was mounted in a Beechcraft King Air 200. Although MBES surveys were conducted as reference for the acceptance test, a hydrographic level bathymetry has not yet been produced (the survey was undergoing revision during the publication time of this section). Instead, bathymetry generated from the CHARTS acceptance test dataset over Fort Lauderdale, FL, USA was used as a reference (June-July, 2005). The CZMIL surveys were conducted at 200% coverage with a spot spacing of $2\ m \times 2\ m$. A maximum depth was calculated to be around 30 m based on the density of the laser measurement criterion from the lidar survey. Due to potential changes in shallow water bathymetry during the 8 years between the surveys, the bathymetry datasets were compared at depths greater than 5 m. The preliminary results, using more than 4.5 million laser measurements, showed a 2σ standard deviation of 0.20 to 0.29 m with a 0.11 m RMSE for the Shallow channel measurements and a 2σ standard deviation of 0.33 to 0.34 m with a 0.17 m RMSE for the Deep channel measurements (Table 5.6; Figure 5.3.15). The point density of the central shallow channel (i.e., one laser measurement per laser pulse) at a 200% coverage was 0.26 pts/m^2. Further work is expected this year (2014) before recommendation for operation can be made.

Table 6.6. Preliminary results for CZMIL (Ft. Lauderdale, FL).

	Shallow channel		Deep	
	2σ	RMSE	2σ	RMSE
130507_1742	0.20 m	0.11 m	0.34 m	0.17 m
130509_2023	0.21 m	0.11 m	0.33 m	0.17 m
130509_2334	0.29 m	0.11 m	0.33 m	0.17 m

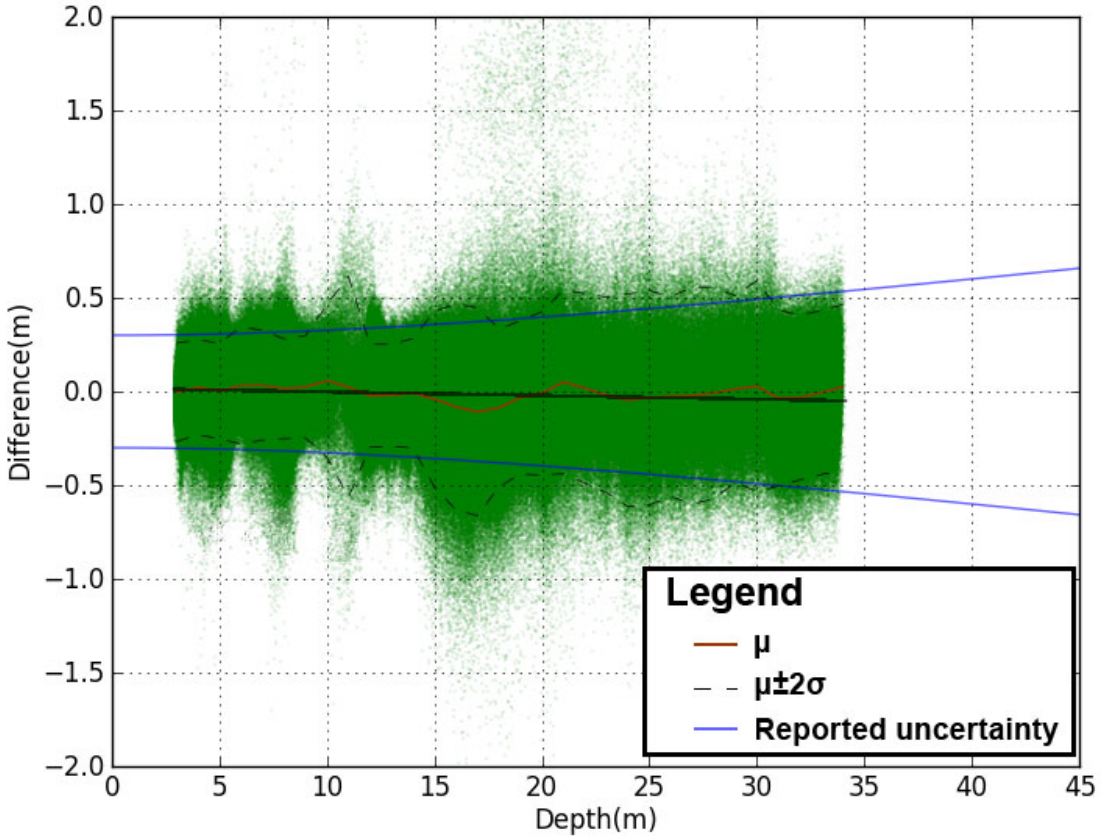

Figure 6.4.4. Scatter plot from a relative accuracy test for the deep channel measurements of CZMIL system.

6.4.2 NOAA performance evaluation tests

NOAA also evaluated the SHOALS-1000T system. A performance evaluation test was conducted by NOAA and Fugro Pelagos (Lockhart, Dushan, and Millar 2005; Fugro Pelagos 2008). Similar to the USACE, the goals of the NOAA test were also to evaluate depth penetration capability (maximum depth), vertical accuracy underwater, and horizontal accuracy underwater. However, the survey standards of the USACE and NOAA tests were different. The USACE and U.S. Navy tests compared the results to meet IHO Order 1 standards (IHO 2008) and a penetration depth of $K_d * d > 3$ (K_d is the diffuse attenuation coefficient and d is depth), whereas the NOAA and Fugro tests evaluated how well the ALB accuracy test met different levels of IHO standard (i.e., Special order, Order 1 or Order 2) and if an ALB survey at 200% coverage could be used with a Combined Uncertainty and Bathymetric Estimator (CUBE) algorithm. NOAA did not require an evaluation for topographic applications from the SHOALS-1000T system.

The NOAA and Fugro performance evaluation tests were conducted over the Shilshole Bay near Seattle, WA, USA using a Beechcraft King Air 90 aircraft (Figure 5.3.16). The tests were conducted during August, 2007 and were compared to a reference bathymetry collected in 2005 using a Reson 8101 multibeam system. These tests included survey lines over the same area collected at different altitudes

(300 m and 400 m) and spot spacings (3 m X 3 m, 4 m X 4 m, and 5 m X 5 m). The ALB survey data were tide coordinated and converted from WGS-84 to mean low lower water (MLLW) using a NOAA tide gauge that was located near the study site (Port of Seattle, WA).

A geometric calibration was conducted prior to the relative accuracy tests. Two ground GPS base stations were used in the geometric calibration. The two stations provided both quality control and redundancy in the event that one of the two systems was disturbed or the equipment experienced a failure. The aircraft remained within 30 km of an operational base station at all times during survey. The internal positioning solution was determined using Applanix POSPac. After the geometric calibration, survey data collected for the accuracy tests were compared to bathymetry derived from the MBES survey. The accuracy results showed that the mean difference ranged between -0.14 m to 0.07 m with a standard deviation of about 0.12 m to 0.13 m. Results from a statistical analysis of the survey datasets indicated that the survey data from SHOALS-1000T can meet IHO order 1 standards (S-44 version 4; (IHO 2008). However, SHOALS-1000T survey data at 200% overlap provides only a single weak solution (primary solution) in CUBE for the detection of small shallow features. This is likely because of data sparseness and the size of the ALB footprints. As a result, the seafloor surface may not be accurately represented for all shallow areas captured within the point cloud dataset and further work is required.

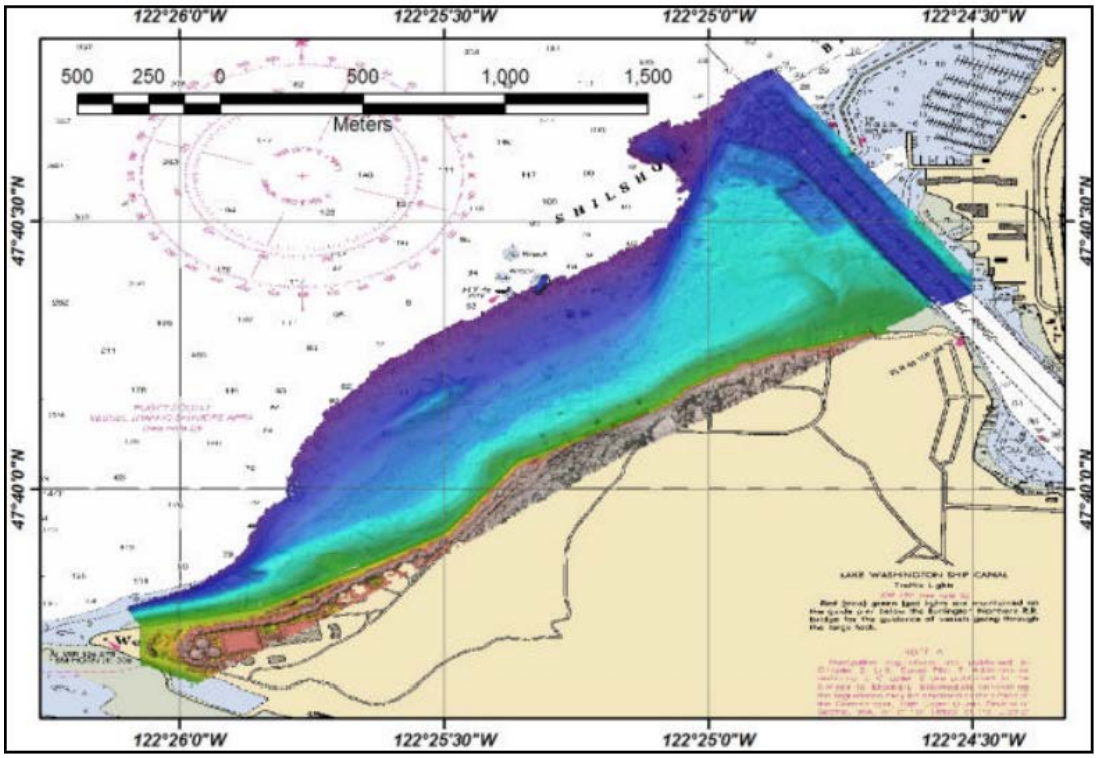

Figure 6.4.5. Shilshole Bay study site: Gridded bathymetry from the SHOALS-1000T survey overlaid on a NOAA Chart (Lockhart, Dushan, and Millar 2005).

In 2013, the Remote Sensing Division (RSD) in NOAA's National Geodetic Survey (NGS) procured a Riegl VQ-820-G to compliment the division's topo-bathy operations (namely, shoreline mapping). The goals for the performance evaluation were to evaluate depth penetration capability, vertical accuracy underwater and horizontal accuracy underwater. Similar to the USACE, NGS also adopted QL survey

standards of the Interagency Working Group's National Coastal Mapping Strategy (Table 5.5; Figure 5.3.13). The ALB system was mounted on a DeHavilland Twin Otter (DHC-6) for both the geometric calibration and accuracy tests.

Geometric calibration flights were conducted after each installation of the sensor suite. An example of NOAA's geometric calibration conducted during June, 2013 over land (Sun City, FL) is described. The calibration site was selected in a suburban environment with many houses that have pitched roofs and open flat surfaces, such as cul-de-sac roads. The GPS baseline between the base station and aircraft are kept to a minimum, so that the uncertainties associated with the trajectory file are minimized (Figure 5.3.17). The raw data were initially processed to a point cloud referenced to an appropriate coordinate system. The average density of the laser measurements was around 40 measurements per square meter (#/m^2), and certain areas of the calibration site with high overlap had up to $180\ \#/m^2$ (Figure 5.3.18). The initial boresight angles were calculated and verified in a three-step procedure. First, an initial examination of the relative offset between adjacent scan lines is performed. The offset observed is utilized to assist in finding tie objects between different scans. A tie object is a planar surface, point, or sphere found in a scan. An observation consists of the matching of two similar objects in overlapping scans. Between 30,000 to 70,000 observations are typically identified for a geometric calibration flight. Second, the distances of the observations and a standard deviation are calculated for estimation of the current fit. Third, an adjustment is calculated for optimal boresight angles to achieve a best fit between all scans in the data set. The data is then reprocessed with the newly calculated boresight angles. The third step was repeated until the standard deviation of distances between objects converged to a value between 1 to 3 cm with further adjustment iterations providing negligible differences. Various techniques are utilized to analyze the results from qualitative examination of intensity data and hillshade images to look for unusual scan or geometrical artifacts to quantitative differences between flat surfaces in overlapping scans. The results from the Boresight Calibration procedure were verified using control points measured in cul-de-sac areas using rapid static GNSS field-surveys. The average difference from the comparison between the ALB survey to the control points was -0.012 cm vertical difference with a standard deviation of 0.039 m.

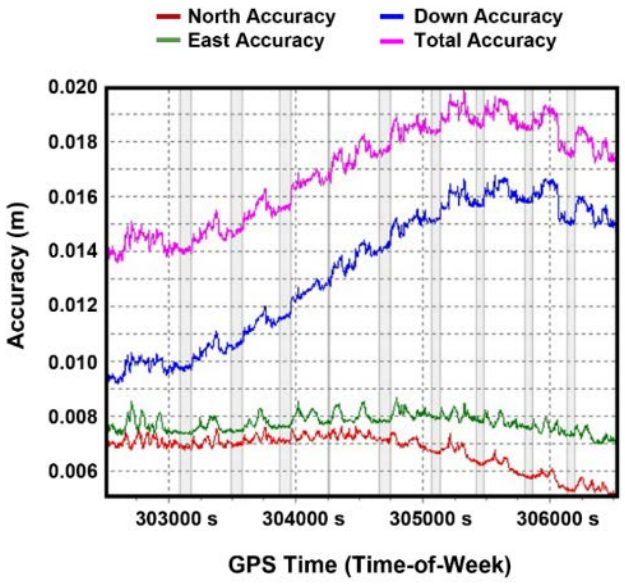

Figure 6.4.6. Initial accuracy of the aircraft during the Boresight Calibration procedure reported by Applanix POSPac. The vertical grey areas mark the periods during ALB acquisition and the spikes in accuracy indicate turning of the aircraft from one survey line to another.

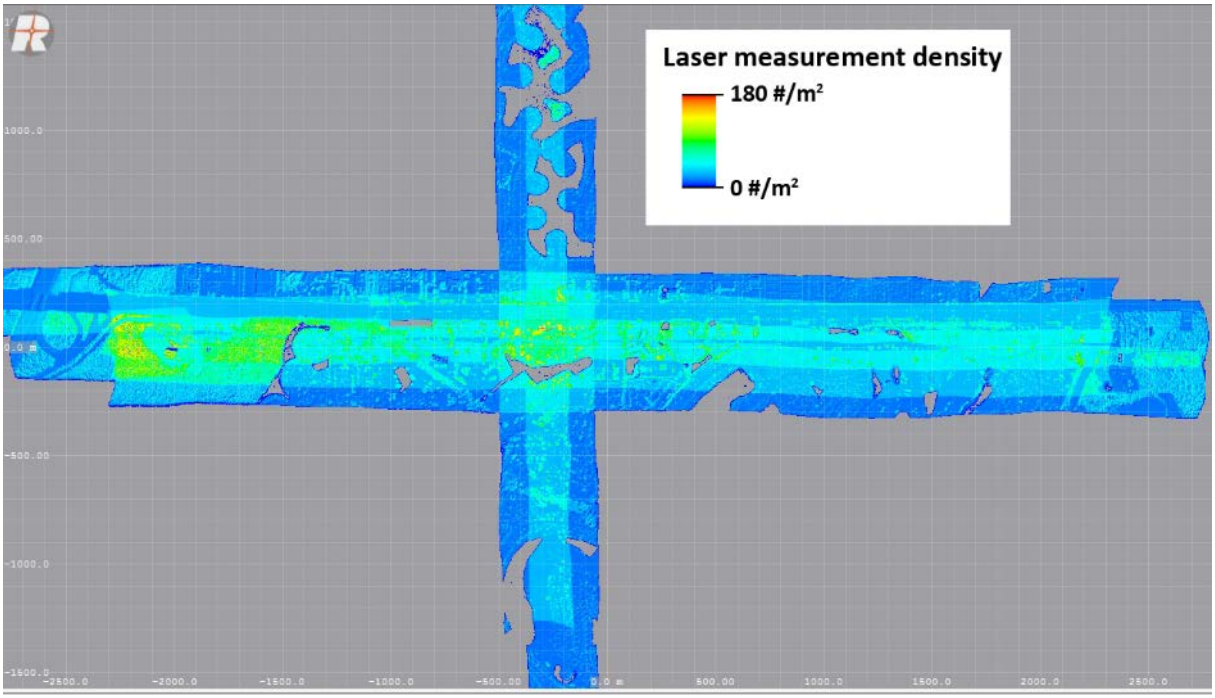

Figure 6.4.7. Density map of the Boresight Calibration site used for calculating the boresight angles for the Riegl VQ-820-G.

Next, a set of relative accuracy tests were conducted over coastal areas (from dry land into shallow bathymetry) and over offshore sites. The evaluation over coastal areas was conducted at Ft. DeSoto, FL

and Island Beach State Park, NJ. The ALB surveys were compared against Post Processing Kinematics (PPK) GPS and rapid static GNSS field-surveys. Shoreline transects were collected perpendicular to the shoreline using PPK GPS and rapid static GNSS field-surveys. The shallow-water survey transects were obtained by a field survey crew wading into approximately waist-deep waters with range-pole or wheel-mounted GNSS antenna. Based on 13,526 samples a mean offset of 4 cm was calculated with a standard deviation of 5.5 cm. The evaluation test over offshore sites compared the Riegl VQ-820-G ALB survey data that was collected in March, 2012 to a SHOALS 1000T survey collected by the USACE USACE/JALBTCX in January, 2012 over Ft. Lauderdale, FL. Figure 5.3.19 shows the difference values between SHOALS 1000T to VQ-820-G dataset Stable areas such as the upper beach face and roads agreed well between the two datasets and the difference between the two datasets was within the tolerance defined for accuracy test (typically, RMSE < 10 cm). However, the two ALB surveys were collected at different seasons resulting in a non-uniform difference, where the beach profile (i.e., the nearshore morphology) changed between the two surveys.

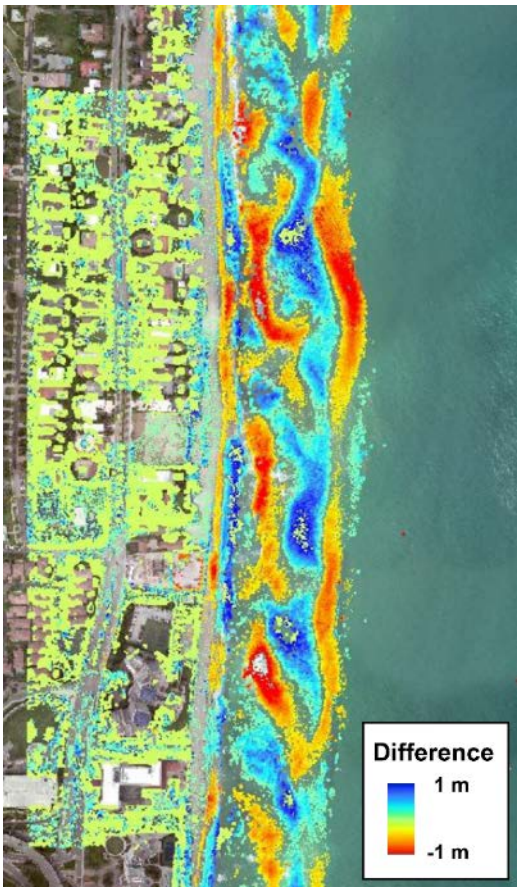

Figure 6.4.8. Difference map comparing a SHOALS-1000T survey to a Riegl VQ-820-G survey over Ft. Lauderdale, FL.

6.5 References

ASPRS. 2008a. “Common Lidar Data Exchange Format - LAS Industry Initiative 1.2.” http://www.asprs.org/a/society/committees/standards/asprs_las_format_v12.pdf.

———. 2008b. “LAS Specification, Version 1.4-R13.” Bethesda, MD: American Society of Photogrammetry and Remote Sensing. http://www.asprs.org/a/society/committees/standards/asprs_las_format_v12.pdf.

———. 2010. “LAS Specification: Version 1.3.-R11.” http://www.asprs.org/a/society/committees/standards/LAS_1_3_r11.pdf.

Beaudoin, Jonathan, Paul Johnson, and Ashton F Flinder. 2013. “R/V Falkor Multibeam Echosounder System Review.” Vol. Technical. Durham, NH: University of New Hampshire (UNH) Center for Coastal and Ocean Mapping (CCOM)/Joint Hydrographic Center (JHC). http://ccom.unh.edu/publications.

Chen, Yang, and Gérard Medioni. 1992. “Object Modelling by Registration of Multiple Range Images.” *Image and Vision Computing* 10 (3): 145–55. doi:10.1016/0262-8856(92)90066-C.

Dewberry. 2012. “National Enhanced Elevation Assessment.” http://www.dewberry.com/services/geospatial/national-enhanced-elevation-assessment.

El-Sheimy, Naser, Caterina Valeo, and Ayman Habib. 2005. *Digital Terrain Modeling: Acquisition, Manipulation, and Applications*. *Artech House Remote Sensing Library*. Norwood, MA: Artech House. http://library.books24x7.com/assetviewer.aspx?bookid=14812&chunkid=1&rowid=2.

Filin, Sagi. 2003. “Recovery of Systematic Biases in Laser Altimeters Using Natural Surfaces.” *Photogrammetric Engineering and Remote Sensing* 69 (11): 1235–42. http://eserv.asprs.org/PERS/2003journal/nov/2003_nov_1235-1242.pdf.

Fugro Pelagos. 2008. “Determination of SHOALS-100T Hydrographic Lidar TPU Model and Target Detection Test: Shilsole Bay, Puget Sound, WA.” Vol. Survey Rep. Sand Diego, CA: Fugro.

Gonsalves, Michael Oliver. 2010a. “A Comprehensive Uncertainty Analysis and Method of Geometric Calibration for a Circular Scanning Airborne Lidar.” Edited by Stephan Howden. *ProQuest Dissertations and Theses*. Hattiesburg, MS: The University of Southern Mississippi. http://search.proquest.com/docview/835075165/fulltextPDF/BB0E363A81F246C3PQ/1?accountid=10267.

———. 2010b. “Flat-Bottomed World You Make Thoselidar Swirls around: Contrasting a Ship-Based Acoustic Patch Test with an Automated Calibration Routine for a Circular-Scanning Airborne Lidar System.” In *Canadian Hydrographic Conference 2010*. Quebec, QC, Canada.

Habib, Ayman. 2009. “Accuracy, Quality Assurance, and Quality Control of LiDAR Data.” In *Topographic Laser Ranging and Scanning: Principles and Processing*, edited by Jie Shan and Charles K Toth, 269–94. Boca Raton, FL: CRC Press.

Habib, Ayman, A P Kersting, Ki In Bang, and Dong-Cheon Lee. 2010. “Alternative Methodologies for the Internal Quality Control of Parallel LiDAR Strips.” *Geoscience and Remote Sensing, IEEE Transactions On* 48 (1): 221–36. doi:10.1109/TGRS.2009.2026424.

IHO. 2008. “IHO Standards for Hydrographic Surveys.” Vol. S-44. Monaco: International Hydrographic Organization. http://www.thsoa.org/pdf/s44_4.pdf.

Imahori, Gretchen, Jeff Ferguson, Toshi Wozumi, David Dave Scharff, Shachak Pe’eri, Christopher E Parrish, Stephen A White, Inseong Jeong, Jon Sellars, M Aslaksen, et al. 2013. “A Procedure for Developing an Acceptance Test for Airborne Bathymetric Lidar Data Application to NOAA Charts in Shallow Waters.” *NOAA Technical Memorandum CS 32*. Vol. NOS CS-32. Silver Spring, MD: National Oceanographic and Atmospheric Administration. http://www.nauticalcharts.noaa.gov/csdl/publications/TM_NOS-CS32_FY13_Lidar.pdf.

Imahori, Gretchen, Jeff Ferguson, Toshi Wozumi, David Scharff, Shachak Pe’eri, Christopher E. Parrish, Stephen A. White, Inseong Jeong, Jon Sellars, and M. Aslaksen. 2013. “A Procedure for

Developing an Acceptance Test for Airborne Bathymetric Lidar Data Application to NOAA Charts in Shallow Waters." *NOAA Technical Memorandum CS 32*. Vol. NOS CS-32. Silver Spring, MD: National Oceanographic and Atmospheric Administration. http://www.nauticalcharts.noaa.gov/csdl/publications/TM_NOS-CS32_FY13_Lidar.pdf.

LaRocque, Paul E, John R Banic, and A G Cunningham. 2004. "Design Description and Field Testing of the SHOALS-1000 Airborne Bathymeter." In *Laser Radar Technology and Applications IX*, SPIE 5412:162–84. SPIE. doi:10.1117/12.564924.

Lockhart, Carol, Arumugam Dushan, and David Millar. 2005. "Meeting Hydrographic Charting Specifications with SHOALS-1000T Airborne Lidar Bathymeter." In *U.S. Hydro 2005*. San Diego, CA. http://www.thsoa.org/us05papers.htm.

Ocean Surveys, Inc. 2009. "Shallow Water Multibeam Hydrographic and Side Scan Sonar Survey." Vol. Field No: Old Saybrook, CT: NOAA/NOS/OCS Descriptive Report. http://surveys.ngdc.noaa.gov/mgg/NOS/coast/H10001-H12000/H11896/DR/H11896.pdf.

OCS. 2014. "FIeld Procedures Manual." National Oceanic and Atmospheric Administration: Office of Coast Survey. http://www.nauticalcharts.noaa.gov/hsd/fpm/2014_FPM_Final.pdf.

Optech. 2005. "Technical Report for JALBTCX." Vol. DACW42-01-. Toronto, Ontario, CA: Optech Incorporated.

Pe'eri, Shachak, Lynnette V Morgan, William D Philpot, and Andrew A Armstrong. 2011. "Land-Water Interface Resolved from Airborne LIDAR Bathymetry (ALB) Waveforms." *Journal of Coastal Research* SI 62. Coastal Education and Research Foundation: 75–85. doi:10.2112/SI_62_8.

Schenk, Toni. 2001. "Modeling and Recovering Systematic Errors in Airborne Laser Scanners." *Technical Notes in Photogrammetry*. Vol. 19. Columbus, Ohio: The Ohio State University.

Snyder, G. I. 2012. "National Enhanced Elevation Assessment at a Glance." Vol. U.S. Geolo. U.S.G.S. http://pubs.usgs.gov/fs/2012/3088/.

Toth, Charles K. 2009. "Strip Adjustment and Registration." In *Topographic Laser Ranging and Scanning: Principles and Processing*, edited by Jie Shan and Charles K Toth, 235–68. Boca Raton, FL: CRC Press, Taylor and Francis Group. http://www.crcnetbase.com/isbn/9781420051438.

USACE. 2012. "Scope of Work: National Coastal Mapping Program - Lake Michigan." Vol. EN Project. Kiln, MS: U.S. Corps of Engineers.

Vaughn, C R, J L Button, W B Krabill, and D Rabine. 1996. "Georeferencing of Airborne Laser Altimeter Measurements." *International Journal of Remote Sensing* 17 (11). Taylor & Francis: 2185–2200. doi:10.1080/01431169608948765.

Wehr, Aloysius. 2009. "LiDAR Systems and Calibration." In *Topographic Laser Ranging and Scanning: Principles and Processing*, edited by Jie Shan and Charles K Toth, 129–72. Boca Raton, Florida: CRC Press, Taylor and Francis Group. ftp://ftp.ecn.purdue.edu/jshan/Zproject/proofs/04/51423_C004_corr.pdf.

White, Stephen. 2007. "Utilization of Lidar and NOAA's Vertical Datum Transformation Tool (VDatum) for Shoreline Delineation." In *Marine Technology Society/IEEE Oceans Conference*. Vancouver, BC: IEEE. doi:10.1109/OCEANS.2007.4449147.

Wozencraft, Jennifer M. 2010. "Requirements for the Coastal Zone Mapping and Imaging Lidar (CZMIL)." In *Algorithms and Technologies for Multispectral, Hyperspectral, and Ultraspectral Imagery XVI, April 5, 2010 - April 8*, SPIE 7695:The Society of Photo-Optical Instrumentation Engin. Orlando, FL: SPIE. doi:10.1117/12.851891.

———. 2014. "USACE Information Products."

eCommons (2019) https://doi.org10.7298/jxm9-g971

7 APPLICATIONS, ANCILLARY SYSTEMS, AND FUSION

Lead Author: Jennifer Wozencraft[a]

Contributing Authors: Lauren Dunkin[b], Eve Eisemann[b] , and Molly Reif[c]

a) Director, Joint Airborne Lidar Bathymetry Technical Center of Expertise (JALBTCX) USACE Engineer, Research and Development Center, Coastal and Hydraulics Laboratory
b) Joint Airborne Lidar Bathymetry Technical Center of Expertise (JALBTCX) USACE Engineer, Research and Development Center, Coastal and Hydraulics Laboratory
c) Joint Airborne Lidar Bathymetry Technical Center of Expertise (JALBTCX) USACE Engineer, Research and Development Center, Environmental Laboratory

The number of applications for ALB data has grown exponentially since the first systems became operational in the late 1980's and early 1990's. In those early days, the primary application was nautical charting. Since then, as more systems were developed and fielded, and users gained access to the unique datasets provided by these systems, uses have expanded into a wide variety of coastal engineering and coastal zone management applications. Many of these applications take advantage of the regional-scale, reoccurring elevation and depth data provided by ALB systems. Others utilize semi-automated and automated techniques to extract features from the lidar elevation data, or from lidar waveforms.

Many of the applications that you see in this chapter require data from ancillary systems. One of the primary ancillary data types required for many coastal applications is concurrent topography. It is rare to see a survey requirement that does not include "seamless topography and bathymetry." Some ALB systems collect topographic elevation data concurrently with the bathymetric lidar, either using the green laser or collinear infrared for topography, or by integrating an infrared laser and receive optics into the ALB system. Other systems do not have a built-in topographic capability but are frequently flown with stand-alone topographic lidar sensors. Most ALB sensors are flown with down-looking imagery capability. When ALB systems were first fielded, these cameras were important in the QA/QC phase of data processing for situational awareness. They were video cameras or later, low resolution digital cameras. As the value of imagery grew beyond just assistance in data processing, the quality of cameras integrated with ALB sensors improved. Concurrent high-resolution mosaics are now a common deliverable for airborne coastal surveys.

JALBTCX and others have integrated hyperspectral imagers into their sensor suites, primarily to enable generation of new environmental products. Sensor fusion combines lidar and lidar-derived products with imagery data. One type of sensor fusion that you will see in this chapter is elevation (or depth)-informed thematic mapping. A more complex form of sensor fusion combines lidar depths, reflectivity, and water column attenuation with hyperspectral imagery for production of hyperspectral sea-floor reflectance and water column properties.

This chapter will briefly highlight a number of applications for ALB data that have evolved over the past 25 year of ALB operations: nautical charting, navigation project monitoring, regional sediment management, post-storm response, geomorphological feature extraction, and environmental mapping. It

is not exhaustive, but gives an overview of the breadth of operational applications for ALB. The chapter closes with a look into future applications.

7.1 Nautical charting

Nautical charting was one of the early drivers for the development of ALB and remains one of the major uses of the technology today. Canada and Australia have a long-standing history of using ALB for nautical charting (since 1985 and 1993, respectively) that continues today. In the US, NAVOCEANO, NOAA, and the National Geospatial-Intelligence Agency (NGA) all use ALB for the production of nautical charts. NAVOCEANO has collected data all over the world since 1996 to support its tactical nautical charting mission in the Bahamas (West and Lillycrop 1999), Mexico (Pope et al. 1997), Honduras, Nicaragua, Belize, Haiti, Martinique, Philippines, Japan, Marshall Islands, Micronesia, Palau, Northern Marianas, Guam, Samoa, New Zealand (Graham et al. 1999), Bahrain, Oman, Portugal (Lillycrop, Pope, and West 2000), Israel, Morocco, and Kenya. NOAA has used ALB for the production of nautical charts for the continental U.S. and in Alaska, Puerto Rico, and the U.S. Virgin Islands. USACE, NAVOCEANO, NOAA and USGS jointly funded a multi-purpose survey mission for the six major Hawaiian Islands in 1999 and 2000 (West 2001) for the creation of nautical charts, coral reef mapping, and flood hazard mapping. The most recent and extensive NOAA ALB surveys are the result of large efforts to update nautical charts in the aftermath of powerful storms like Hurricanes Sandy, Harvey, Irma, and Maria. NOAA frequently uses ALB datasets of opportunity, such as those from the USACE national Coastal Mapping Program in the production of nautical charts.

ALB is used in the production of nautical charts in a number of ways. It may be the sole source of depth data for a chart, or may be used in combination with acoustic, boat-based sensors. In many cases, ALB is operated in advance of boat surveys to help define areas of safe navigation for the survey boats, as well as to provide data for the charts. Some ALB sensors have topographic capability or are paired with a topographic lidar to provide seamless coverage across the land/water interface. The seamless coverage allows for the extraction of shorelines for inclusion on nautical charts. Ancillary camera data enables thematic attribution of shoreline segments. In certain optimal survey conditions, ALB is used to detect objects that are included on nautical charts. Recently, the French Hydrographic and Oceanographic Office (SHOM) started a national program of coastal mapping that supports nautical charting and a number of other uses (Pastol 2011), and South Korean Hydrographic Office (KHOA) has made investments in both ALB surveys and systems. A number of countries issue tenders for contract surveys that include ALB.

7.2 Navigation project monitoring

USACE developed the SHOALS system to augment the existing USACE hydrographic survey capability by providing fast, accurate hydrographic surveys along 40,000 km of federally maintained navigation channels (Lillycrop and Banic 1992). Shoaling, or deposition of sediment in navigation channels, reduces navigability and requires dredging. ALB data is valuable for comparing multiple navigation channel surveys to identify hotspots or morphological trends (Irish and White 1998; Wozencraft and Irish 2000; McClung 1998) that can be leveraged to better maintain these areas through various techniques (channel re-alignment, advanced maintenance dredging, etc.). Figure 7.2.1 shows a topographic and bathymetric DEM of the area near Baker's Haulover Inlet in southeast Florida. The heavy, black, dashed lines represent the federally authorized channel for this inlet. Lidar datasets collected for this navigation

channel in June and November 2004, January 2006, and October 2009 were analyzed to estimate a yearly shoaling rate. The high point density of coastal lidar data allow for highly accurate sediment volume calculations. This becomes particularly useful when dealing with tidal inlets and their associated features. The shoaling rate is visualized in the Figure 7.2.1 call-out box (3-D projection), where red indicates areas of higher shoaling and blue indicates areas of little change or even scour. The table shows the average, maximum, and minimum volume of sand in the navigation channel for the four surveys. An alternative analysis is to present channel navigability as a percentage of the congressionally authorized channel depth (L. M. Dunkin and McCormick 2011).

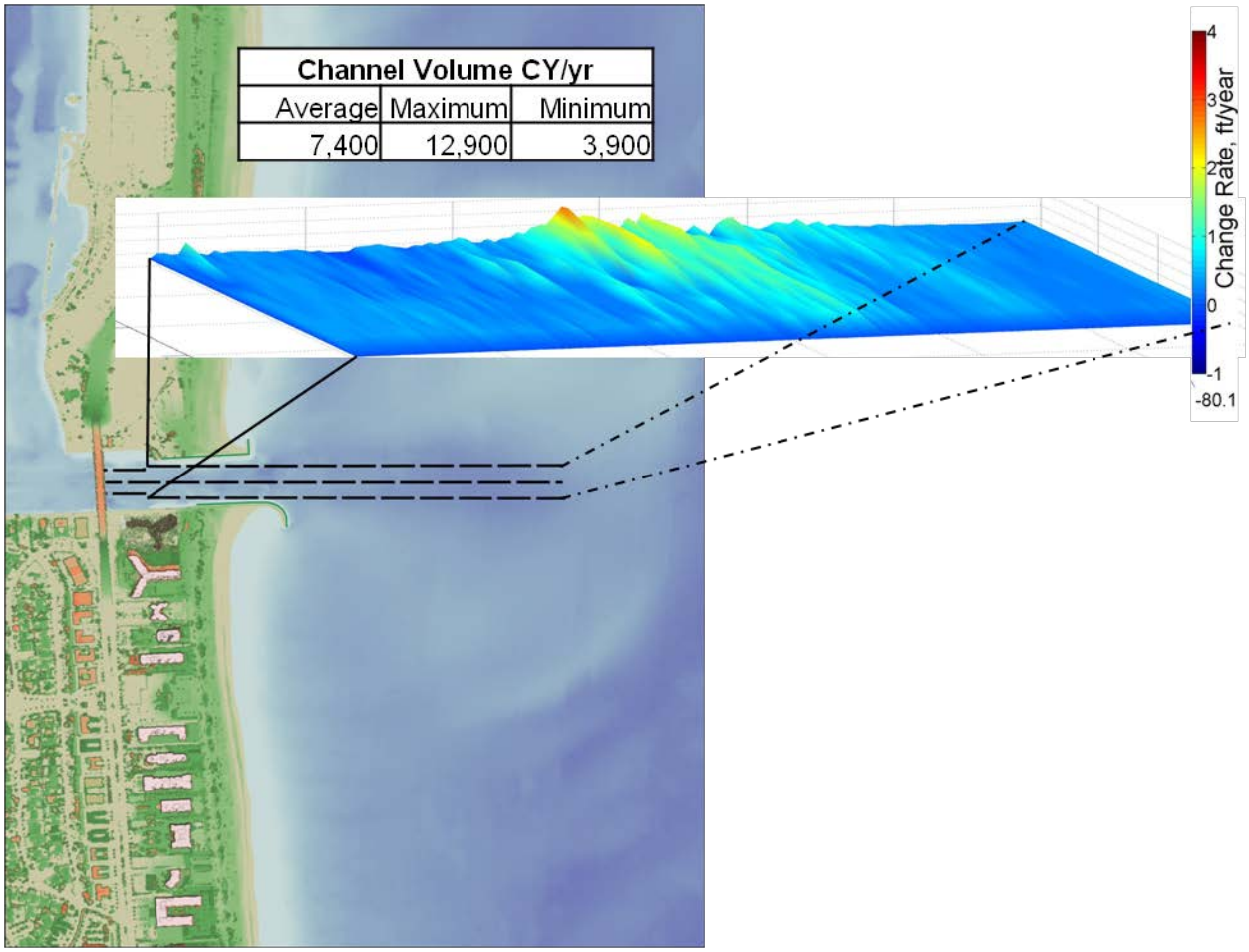

Figure 7.2.1. Channel shoaling rate at Baker's Haulover Inlet, FL. The background image is a topographic and bathymetric DEM of the area. The heavy, black, dashed lines represent the federally authorized channel for this inlet. Lidar datasets collected for this navigation channel in June and November 2004, January 2006, and October 2009 were analyzed to estimate a yearly shoaling rate. The shoaling rate is visualized in the call-out box. Red indicates areas of higher shoaling and blue indicates areas of scour. The table shows the average, maximum, and minimum volume of sand within the authorized channel footprint for the 4 surveys.

Airborne coastal lidar has been used to survey a variety of coastal structures, including navigation structures, like jetties and breakwaters, as well as shoreline protection structures, like detached breakwaters and groins (Irish and White 1998). These structures serve crucial purposes for navigation functionality and coastal protection, but monitoring them can be resource-intensive, requiring manual

inspection that often only provides a qualitative assessment. Airborne coastal lidar surveys can provide a fast, high-resolution snapshot of a coastal structure. DEMs produced from the lidar data can provide a snapshot of the above and below water condition of a coastal structure and surrounding coastal features. Structure elevation, length, volume, and other measurements can be extracted from DEMs (Reif et al. 2012; Irish and White 1998) to assist with coastal planning and assessments.

Structure functionality often depends on the condition of the structure. A time series of lidar DEMs is useful for structure condition assessments, providing quantification of change over a period of time. Structure volume change, rubble-mound structure side slope steepening, and erosion/deposition adjacent to the structure can be quantified (Irish and White 1998). Metrics extracted from lidar data can be used to monitor structure condition through time. Figure 7.2.2 is a set of cross-sections extracted from 3 years of data for a navigation structure at Hampton Harbor, New Hampshire. In addition, design profiles for navigation channels and structures can be compared to lidar surfaces, and the results may be used in metrics describing how well the channel or structure has maintained its design profile. The charts in Figure 7.2.3 quantify the volume difference between the design profile and cross sections extracted from lidar data collected in 2010, 2011, and 2014. A positive volume is called "cut," where the lidar surface has a higher elevation than the water line. A negative volume is called "fill," where the lidar surface has a lower elevation than the water line. Structure material can be tracked as it is eroded from its original intended use location, and the impacts of coastal structures on coastal processes can be quantified by evaluating changes elevation changes in consecutive lidar datasets (Irish and White 1998; Mohr, Pope, and McClung 1999).

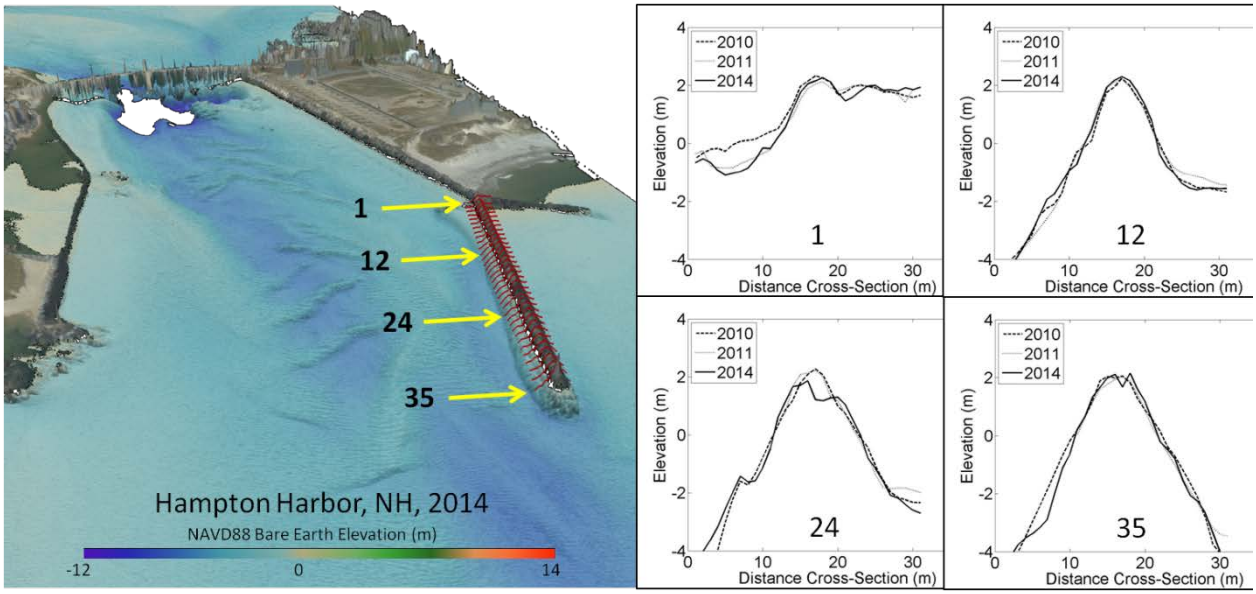

Figure 7.2.2. Cross-sections extracted from 3 years of data at a navigation structure in Hampton Harbor, NH. The cross-sections are numbered 1-35 from landward to seaward, and show how much the structure has changed from 2010-2014.

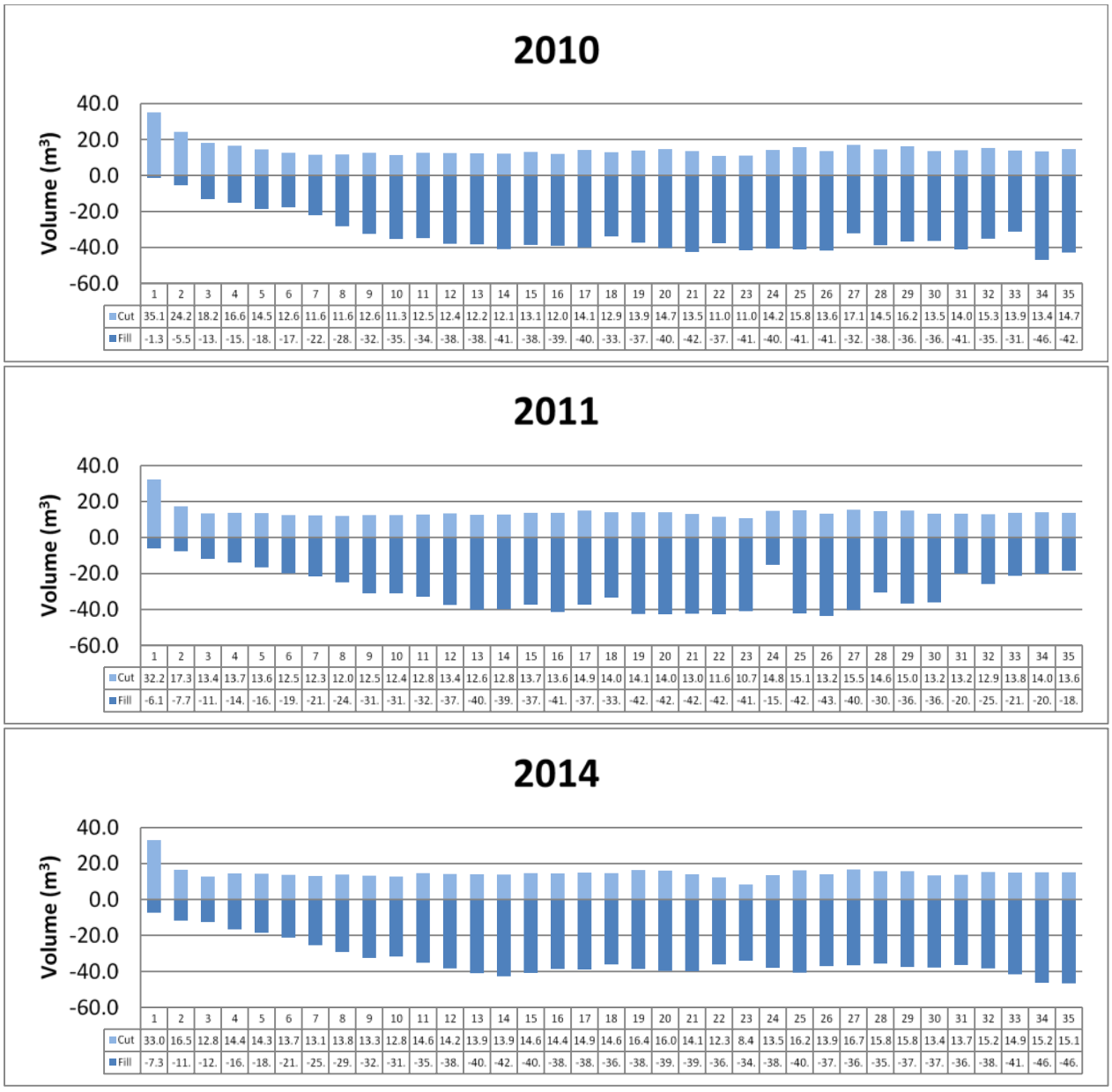

Figure 7.2.3. Structure volume above and below the water line computed from lidar data collected in 2010, 2011, and 2014. Each bar in the graph represents one of the cross-sections shown in Figure 7.2.2, numbered 1 to 35 landward to seaward, and left to right in the graph. A positive volume is called "cut," where the lidar surface has a higher elevation than the water line. A negative volume is called "fill," where the lidar surface has a lower elevation than the water line.

Quantifying nearshore coastal change around navigation channels and structures can improve navigation project management by providing an understanding of erosion and deposition patterns in the immediate vicinity. Ebb shoals are important morphological features that need to be quantified to determine the amount of sediment that may be available for nourishment of downdrift beaches through natural sediment bypassing and/or used as a borrow source for projects. In addition, the ebb shoal volume, compared to a theoretical no-inlet system, is important to quantify the inlet sink effect for sediment budgets.

Automated procedures for identifying watersheds in a hydrological context are used to identify the boundary of the shoal features. The ebb shoal boundary for Big Sarasota Pass, Florida, is shown by the black hashed polygonal areas in Figure 7.2.4. This footprint is used for volume and volume change calculations based on ALB surveys from June and November of 2004, January 2006, and June 2010, shown in the table. At this inlet, sediment transport is from north to south as evidenced by offset ebb shoal and drumstick barrier island to the south. Notice the channel (shown in heavy black lines) bisects the ebb shoal in an area that is shallower than the more southerly portion as the tidal flow naturally scours out the portion of the channel and moves in a southerly direction.

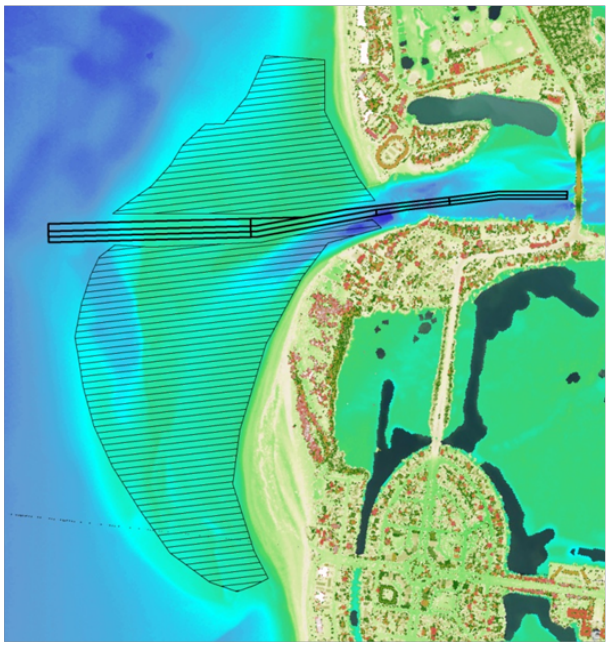

Volume Change (CY)

Survey	Total
6/2010--6/2004	6,932
6/2010--1/2006	-89,785
6/2010--11/2004	-65,302
1/2006--6/2004	147,968
1/2006--11/2004	292,443
11/2004--6/2004	-163,402

Figure 7.2.4. Ebb shoal volume calculations for Big Sarasota Pass, FL. The black hashed polygonal areas are the boundary of the ebb shoal as determined by automated routines that operate on lidar DEMs. The heavy black lines demarcate the authorized alignment of the Federal navigation channel at this inlet. The table is a series of volume changes calculated between lidar datasets within the ebb shoal boundary.

7.3 Regional sediment management

USACE manages navigation, coastal storm damage risk reduction, and environmental restoration projects in the coastal zone. Until the late 1990's these projects were funded and managed as individual units, and in some cases, individual navigation structures were managed separately from the navigation channels they were designed to stabilize. Regional Sediment Management (RSM) is a management construct in which all the projects in a region, where region is defined by coastal processes, are managed as a holistic system (Lillycrop, et al. 2011). The main goals of RSM are to realize operational efficiencies among projects, and to manage in concert with natural processes to minimize the effect of management actions like dredging and the placement of dredged materials. In many cases, environmental benefits are realized through RSM.

Managing projects on a regional basis requires regional datasets. Sediment movement, deposition, and erosion along a coastline is a regional process by nature, therefore, efforts to manage and understand sediment dynamics in the coastal zone must be conducted on such a scale. The regional nature of airborne coastal lidar makes it an ideal tool for conducting surveys for RSM on a large scale (Wozencraft and Irish 2000). The USACE National Coastal Mapping Program (NCMP) was initiated in 2004 to produce the recurring, regional, high-resolution, high-accuracy, data necessary to implement regional sediment management practices at USACE coastal projects (Wozencraft and Millar 2005).

Sediment budgets are a fundamental part of the RSM strategy, allowing for quantification of sediment movement and potential impacts of projects across a coastal region. Sediment volume change calculated within delineated sediment budget 'cells' are combined with knowledge of transport directions and dredging or placement activity to develop a detailed picture of sediment sources, sinks, and fluxes for the area of interest (Rosati 2005). Volume changes can be derived for sections of a study area to quantify sediment inputs and outputs on a fine scale (Irish and Lillycrop 1997; Irish, Lillycrop, and Parson 1997; Wozencraft 2001; Wozencraft and Irish 2000). These volumes can then be incorporated into regional or project-scale sediment budgets (West and Wiggins 2000). Multiple coastal lidar datasets collected in an area of interest can quantify coastline response to known variations in sediment supply, such as a sediment deficit (Xhardé, Long, and Forbes 2011) to further inform sediment budget development. Comparison of bare-earth topo-bathy DEMs quantifies elevation and sediment volume changes on the beach and nearshore and can help identify sand transport pathways through the coastal zone (Irish and Lillycrop 1997; Mohr, Pope, and McClung 1999; Wozencraft 2001; Wozencraft and Lillycrop 2006). Sediment transport within the coastal zone can also be calculated using bathymetry derived from airborne coastal lidar surveys. Along with wave data, both the cross-shore and along-shore transport rates can be inferred from lidar bathymetry data (Irish and White 1998).

Initial studies applying airborne coastal lidar to assess sediment movement on a regional scale were conducted by the RSM Demonstration Program in the USACE Mobile District. As a part of this program, repeat, regional lidar topobathy datasets collected along 360 km of Gulf of Mexico shoreline, from Dauphin Island, Alabama, in the west to Apalachicola Bay, Florida, in the east were included in a single RSM region (Wozencraft and Irish 2000). Four airborne lidar datasets (Oct. and Nov. 1995, Dec. 1996, Nov, 1997) collected by the SHOALS-200 were utilized to conduct a detailed, quantitative sediment management assessment of East Pass inlet, Florida. Qualitatively, the location of the ebb shoal, sediment dredging, placement, as well as the development of scour holes associated with navigation structures and channel currents were observed. Elevation difference plots were created between datasets each dataset to quantify elevation changes over time across the inlet. A volumetric analysis conducted within each of six areas including the channel, adjacent beaches, and ebb shoal produced the volume of sediment lost or added to each area within each time slice (Figure 7.3.1, Table 7.1). Trends observed from this data coupled with qualitative observations from the digital elevation models and elevation difference plots provide a full picture of sediment movement through the system. This analysis illustrates the how airborne coastal lidar datasets can provide useful qualitative and quantitative sediment volume and morphological data.

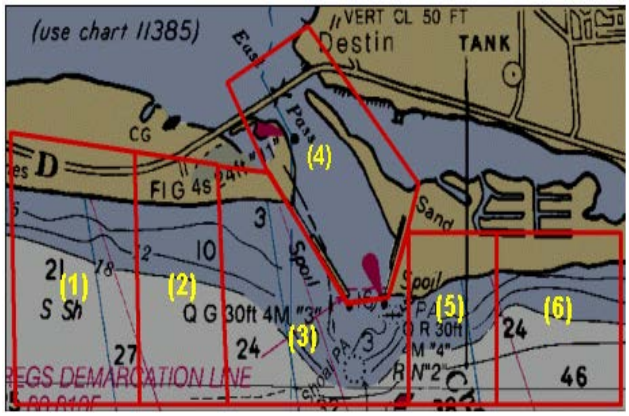

Figure 7.3.1. East Pass, Florida. Red lines delineate sediment budget cells for sand volume calculations (Wozencraft and Irish 2000).

Table 7.1. *Sand volume computations for East Pass, Florida. Volumes are thousands of m3.* (Wozencraft and Irish 2000)

	1	2	3	4	5	6
1995	X	X	1.6	5.3	X	X
1995-1996	X	X	-8.3	-10.8	X	X
1996-1997	-13.4	-5.2	-11.8	-1.2	-1.7	-8.0

To support engineers using lidar-derived volume changes in their sediment budgets, NCMP began developing a standard method for analyziang beach change in 2010. The method utilizes NCMP datasetsand produces volume and shoreline change in shore-perpendicular bins, for entire regions of coastline. The methodology was refined through several years of operations and in 2016 was incorporated into an ARCGIS extension called the JALBTCX Toolbox. This methodology can be used across many coastal regions, and produce consistent data products for coastal assessments and sediment volume change analysis (Robertson et al. 2018). The JALBTCX Toolbox was used to compute volume and shoreline change between the NCMP data collected in 2004/5 with NCMP data collected in 2009/2010 for the eastern Gulf of Mexico and Atlantic coast shorelines.

7.4 Post-storm response

The volume and shoreline change tools in the JALBTCX Toolbox have been used most extensively in recent years to quantify changes due to coastal storms, specifically Hurricanes Matthew (2016), Irma (2017) Maria (2017), Florence (2018), and Michael (2018). Airborne coastal lidar surveys have been flown after major storm events since the mid-1990's. These early surveys evaluated storm impacts at the project scale for the Federal navigation project at East Pass, FL (Irish et al. 1996), beach nourishment project at Longboat Key, FL (Irish and Lillycrop 1999), and a 40 km stretch of FL Atlantic coast (Zhang et al. 2005). Response to the 2004 and 2005 hurricane season, which saw the landfall of Hurricanes Charley, Frances, Ivan, Jeanne, Dennis, Katrina, and Wilma, marked a change to larger scale impact assessments using airborne coastal lidar. The USGS flew the NASA EAARL system before and after some of these storms to quantify the impacts of the storms for their Hurricane and Extreme Storm Impact Studies (Sallenger, Wright, and Lillycrop 2005; Sallenger et al. 2006). USACE used the EAARL data and collected data with CHARTS for many of these storms as well. The data were used in developing Project Impact Reports that USACE uses to request funds from Congress for rebuilding projects to their pre-storm or design condition (Wozencraft and Millar 2005) and to quantify land cover changes (Reif, Macon, and Wozencraft 2011).

The airborne coastal lidar mapping response to Hurricane Sandy was the first lidar response that was more tactical in nature. USGS and USACE put together a large, multi-state, post-storm response effort where the goal was to not only collect the data as quickly as possible after the storm, but to also deliver the data in a matter of days after collection for use by emergency responders. EAARL and CZMIL deployed in New Jersey and New York to support this effort (Wozencraft 2013). The post-storm data were compared with data collected before the storm along the entire stretch of coastline. The coastline was divided into analysis sections and a paper map product was developed for each (Figure 7.4.1). The volume and shoreline change analysis were performed using an early version of the JALBTCX Toolbox, and the paper maps were generated using a combination of ARCGIS and Excel.

CZMIL and the JALBTCX Toolbox were more recently deployed after Hurricanes Matthew, Irma, Maria, and Michael. After Hurricane Matthew, JALBTCX deployed two CZMIL systems to collect data for the coastlines of Florida, Georgia, South Carolina, North Carolina, and Virginia, in the period of one month. These data supported USACE in development of Project Impact Reports for Federal beach projects in the area, and to assess the broader impact of the storm. Data for federal beach projects were delivered within days of collection, and data for the entire survey area were delivered within a month of the end of survey. The JALBTCX Toolbox produced shoreline and volume change for the entire region that were published in an interactive web tool (https://www.arcgis.com/home/item.html?id=d1ee0da4887046edbc9ff05c66d40708). FEMA requested JALBTCX surveys for the east coast of Florida, the Florida Keys, and Collier County of the west coast of Florida in the aftermath of Hurricane Irma. The intent of these surveys was to determine eligibility of coastal communities for public assistance grants to install emergency protective measures. Eligibility is based on elevation above the 5% flood exceedance level, and the amount of assistance was based on the quantity of sand needed to restore the beach to this elevation, both of which were determined from the lidar data. For the post-Irma surveys JALBTCX delivered final data products within five days of collection for the entire area, and volume change analysis was complete a month from the end of survey. FEMA funded JALBTCX surveys and computation of beach sand volume loss along the coastline of Puerto Rico in the aftermath of Hurricane Maria. The data and computed volumes support the Natural and Cultural Resources Sector in their beach erosion assessment for the Puerto Rico Recovery Plan. After Hurricane Michael, FEMA and the State of Florida jointly funded JALBTCX surveys along the impacted area of the Florida Panhandle. The data and change analysis supported local communities in assessing damage from the storm, and in preparing for future storm events.

7.5 Geomorphological feature extraction

Various techniques have been developed through the years for the extraction of features from coastal lidar datasets, for a variety of applications. Some of the features that will be discussed in this section are shown in the graphic in *Figure 7.5.1*: shoreline, dune crest, dune toe, and dune volume. Others are beach width, which is the distance between the dune toe and the shoreline; bluff or cliff edges, which are an analog of the dune crest, but on uplifted rocky and cohesive sediment coastlines; and shoreline change, which is a comparison of position of the shoreline between two surveys.

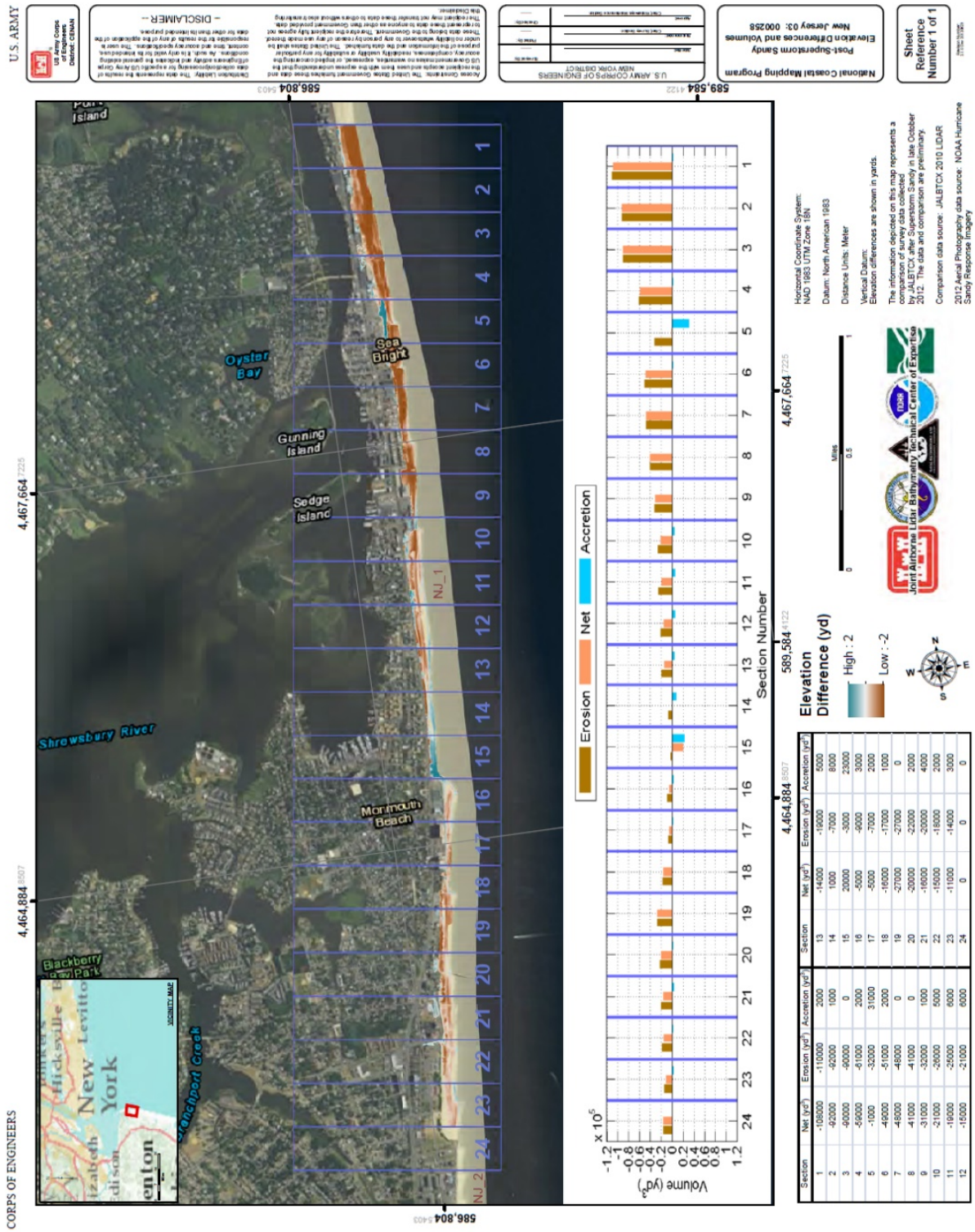

Section	Net (yd³)	Erosion (yd³)	Accretion (yd³)
1	-106000	-110000	2000
2	-92000	-92000	1000
3	-90000	-90000	0
4	-58000	-61000	2000
5	-1000	-32000	31000
6	49000	-51000	2000
7	-48000	-48000	0
8	-41000	-41000	0
9	-31000	-32000	1000
10	-21000	-26000	5000
11	-19000	-25000	6000
12	-15000	-21000	6000
13	-14400	-19000	5000
14	1000	-7000	8000
15	20000	-3000	23000
16	-5000	-8000	3000
17	-5000	-7000	2000
18	-16000	-17000	1000
19	-27000	-27000	0
20	-20000	-22000	2000
21	-16000	-20000	4000
22	-15000	-18000	2000
23	-11000	-14000	3000
24	0	0	0

Figure 7.4.1. JALBTCX preliminary change detection product near Sea Bright, New Jersey. The brown and blue overlay near the shoreline indicates where erosion (brown) and accretion (blue) have occurred. The graph and table give quantities of sand volume change (Wozencraft 2013).

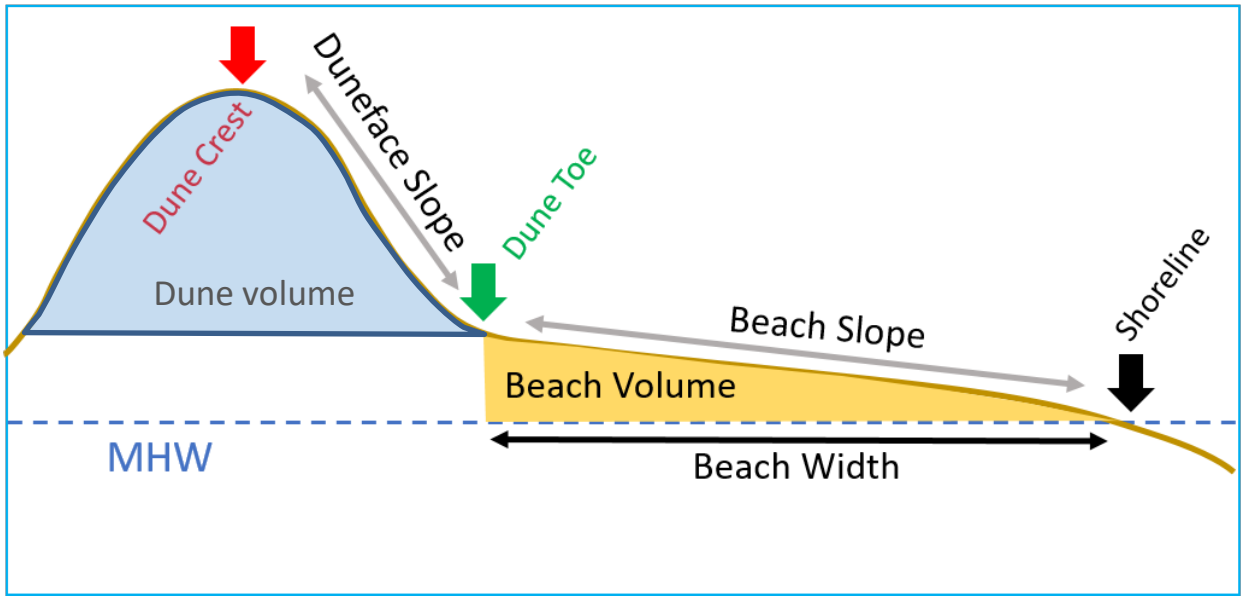

Figure 7.5.2. Schematic of a cross-shore profile. Inflection points help identify the location of the dune crest and dune toe. The shoreline location is the zero elevation on the profile relative to a specified vertical datum. Dune volume is bounded by the dune toe and seaward-most line of infrastructure.

7.5.1 Shorelines and shoreline change

The term shoreline nominally refers to the geographic location of the land-water interface. Because this location changes with the tides, winds, and waves, it is common practice to develop a shoreline that is aligned with a particular tidal or orthometric datum, depending on end use of the derived shoreline vector. Uses of shoreline and shoreline change data include:

- Definition of legal boundaries, as in the National Shoreline produced by NOAA's National Geodetic Survey, and included on nautical charts (Aslaksen et al. 2012)
- ascertain the temporal and spatial variability alongshore erosion hotspots (List, Farris, and Sullivan 2006) and their causes (McNinch 2004; Schupp, McNinch, and List 2006)
- monitoring shorelines in the vicinity of Federal navigation projects (Irish and White 1998; Stauble 2003)
- monitoring performance of coastal storm damage reduction projects (Bocamazo, Grosskopf, and Buonuiato 2011).
- identifying long-term coastal change hazards (Stockdon et al. 2002).

There are two main approaches for extracting shoreline from lidar data, on is DEM-based and the other is profile-based. The DEM approach uses spatial analysis tools in a GIS to extract a contour at the desired elevation. If the DEM is vertically referenced to the desired datum, the zero contour is extracted (White 2007; White et al. 2011) Otherwise, an elevation contour coincident with the difference between the vertical reference of the DEM and the desired datum elevation is selected, such as mean high water

(Robertson, William et al. 2004). Profile-based approaches (Stockdon et al. 2002; Weber, List, and Morgan 2005) locate the intersection of a local MHW datum elevation along a series of lidar-derived beach profiles. The shoreline is generated by connecting these locations in the alongshore direction.

7.5.2 Dune and depositional coastal features

Topography derived from airborne lidar surveys along the coast can be used to assess dune features, including their volumes and locations (Gares, Wang, and White 2006; Wozencraft et al. 2018). Storm surge channels, formed by erosion during storms, as well as relict beach ridges, indicating past shoreline progradation, can be observed using lidar topography, as was done along Galveston Island, Texas to assess coastal erosion (Wallace, Anderson, and Rodriguez 2009). Beach slope and its alongshore variability was derived from lidar data for a section of coastline in Paspébiac, Quebec, providing information about wave action on the shoreline (Xhardé, Long, and Forbes 2011). Tracking the growth and development of spits and other depositional features is possible with this data as well (Xhardé, Long, and Forbes 2011). Four topobathy lidar datasets capturing the Ship Island barrier island, located along the Mississippi Gulf Coast, USA, were used to track changes in dune, beach, and subaqueous features over several years (Eisemann et al. 2018). Automated processes have been developed to extract the location of the dune peak, the mean and max dune peak heights, and the beach width for a certain stretch of coast (L. M. Dunkin and McCormick 2011).

The USGS has been extracting dune parameters from coastal lidar data for a number of years to examine the vulnerability of beaches to inundation during hurricanes (Stockdon, Doran, and Sallenger 2009). The general approach is to calculate inflection points on cross-shore profiles extracted from lidar data at certain intervals along the coast. Dunes act as the first natural line of defense against waves and runup during storm events. Locating the dune fields and monitoring change or recovery after a storm is important for understanding the level of protection that is available and can be used to plan for improvements that may be needed to increase upland protection. USGS delivers operational forecasts of the probability of wave collision, overwash, coastal inundation, and total water levels, based on dune metrics extracted from lidar datasets.

The location of the dune crest, dune toe, and shoreline may be presented in a variety of ways, such as dots or lines on a map (Figure 7.5.2). While shoreline has a constant zero elevation, the elevation of the dune crest and dune toe vary alongshore, and can be presented in a graph along with other parameters, such as beach width (Figure 7.5.3). Beach width can be calculated as the distance from the shoreline to the dune toe (Figure 7.5.1). Plotting extracted dune crest heights within a geographical context can demonstrate the alongshore variability in dune crest height, and how individual dune crest heights relate to the mean for a region. With repeat DEM datasets, dune elevation and location changes can be mapped to better understand the dynamics of the dune system in a region.

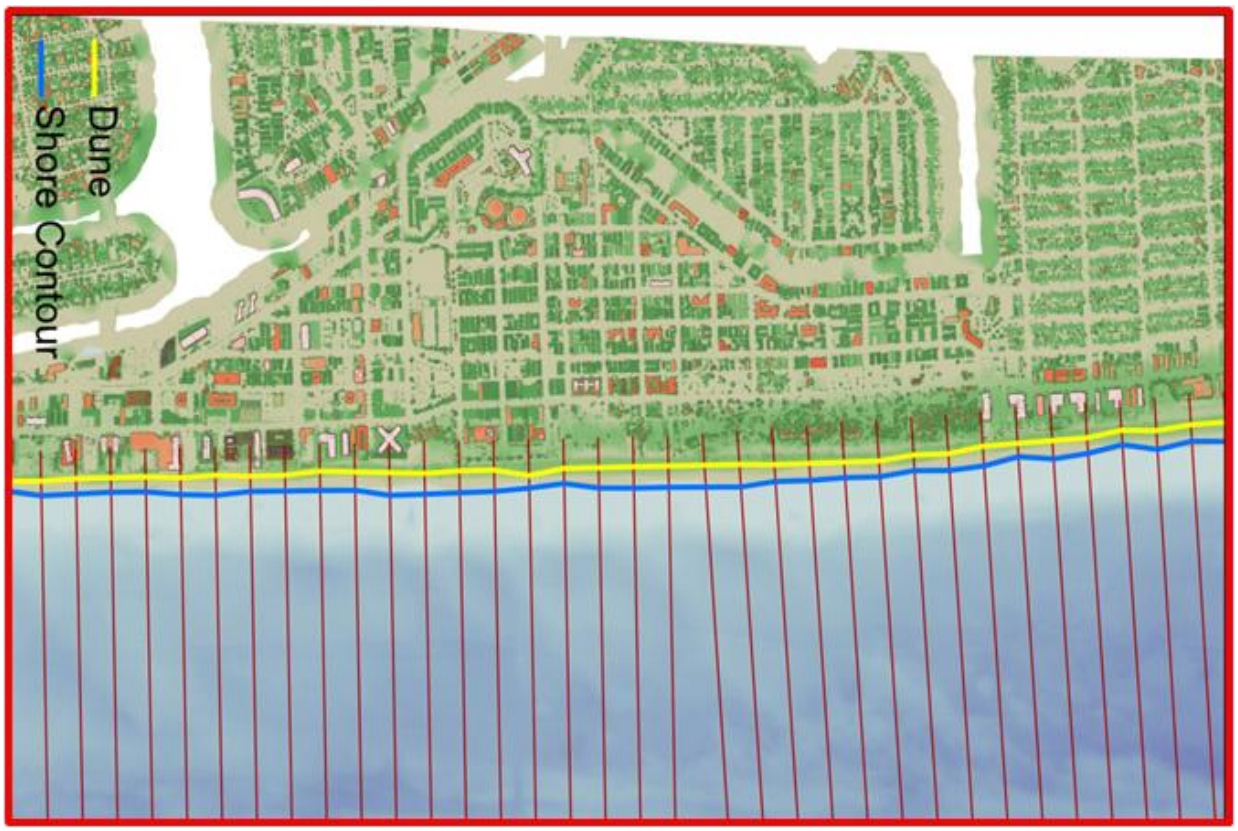

Figure 7.5.3. Dune crest (yellow) and shoreline location (blue) for a small section (3 km) of the Florida Panhandle east of East Pass (Destin). The red vertical lines indicate the location of cross-shore profiles from which the dune crest and shoreline locations were extracted.

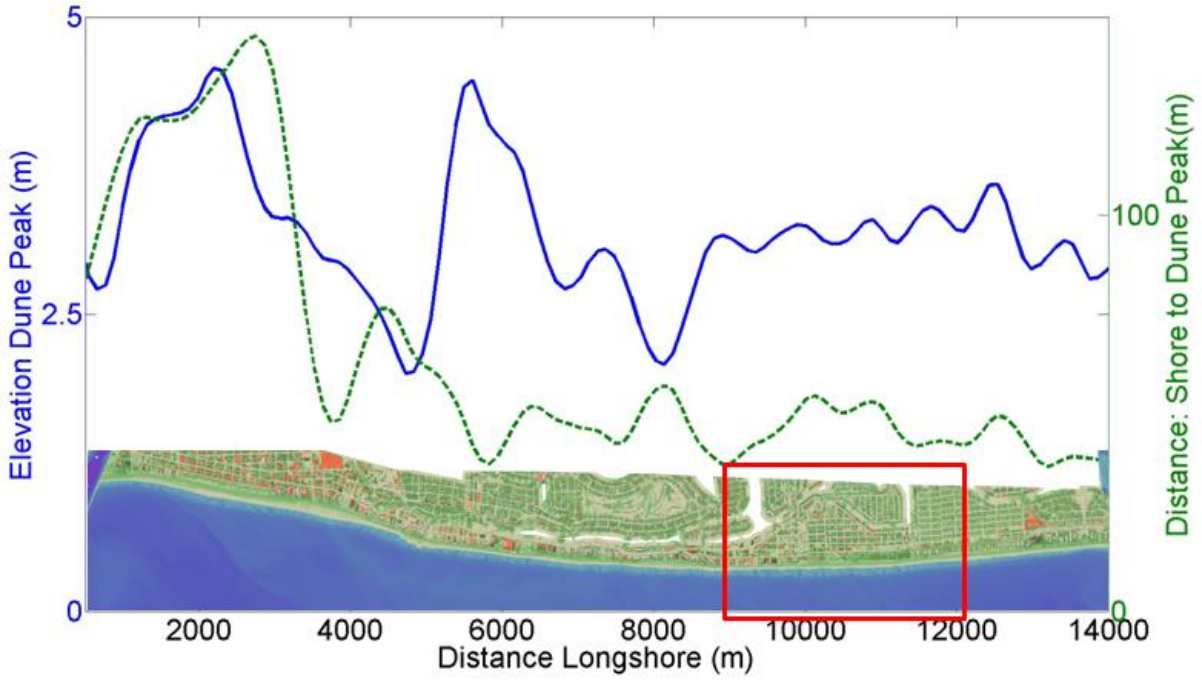

Figure 7.5.4. Alongshore variability in dune crest height (blue) and beach width (green) for a larger section (14 km) of the Florida Panhandle east of East Pass (Destin). The red box is the area shown in Figure 7.5.2.

7.5.3 Bluff and cliff edge detection

Bluff erosion is the primary source of sediment in the nearshore zone along coastlines in the Great Lakes region of the United States and Canada, (Baird 2002). Cliff erosion also provides an important source of sediment to the littoral zone, typically coupled with riverine and gully inputs (Young and Ashford 2006). Bluff and cliff edge retreat rates can be converted to volume contributions to the local sediment budgets using simple assumptions (Baird 2002; Young and Ashford 2006). Bluff and cliff edges both mark the line of landward retreat before land and property is lost due to erosion, so the ability to assess these geomorphic features and compare the results across multiple surveys is invaluable for understanding the condition and vulnerability of these regions (Reif et al. 2013). Airborne coastal lidar data has been used to determine bluff edges using both manual interpretation of DEMs and automated procedures similar to those described above for dune crests. In the manual procedure, the bluff edge is hand digitized from hillshade renderings of coastal lidar DEMs (Hapke and Reid 2007; Hapke, Malone, and Kratzmann 2009). Automated methods can identify the bluff edge as the location where the variation in slope along a lidar elevation transect is at a maximum (Liu et al. 2009).

JALBTCX has improved these automated processes by extracting the bluff edge from bare earth DEMs, which greatly reduces lidar pre-processing, and excludes buildings and vegetation from the analysis to find the bluff edge. Transects are extracted from the bare earth DEMs with spot elevations spaced 1 meter along the profile and 10 meter alongshore spacing between profiles. Transects are analyzed profile-wise with a custom set of algorithms to find the location of the maximum change in slope in addition to meeting specific threshold values that are implemented to prevent deviations in the bluff line from being extracted. The bluff edge location for each transect is joined with the neighboring points to create a continuous line for the region. The automated process is demonstrated for a portion of Lake Erie, NY using bare earth DEMs generated from lidar data collected during the 2007 NCMP survey (Figure 7.5.4). Bluff edge change rates were calculated using the GIS extension, Digital Shoreline Analysis System (DSAS), developed by the USGS (Thieler et al. 2009) to compare the lidar derived bluff line to an 1874 digitized bluff line. The spatial variability of the bluff edge change rates makes having the lidar elevation data, particularly the bare earth DEMs, invaluable for monitoring efforts. Bluff edge change rates can be used to assist coastal planners and engineers for sediment budget analyses, coastal mapping, land use planning, and permitting.

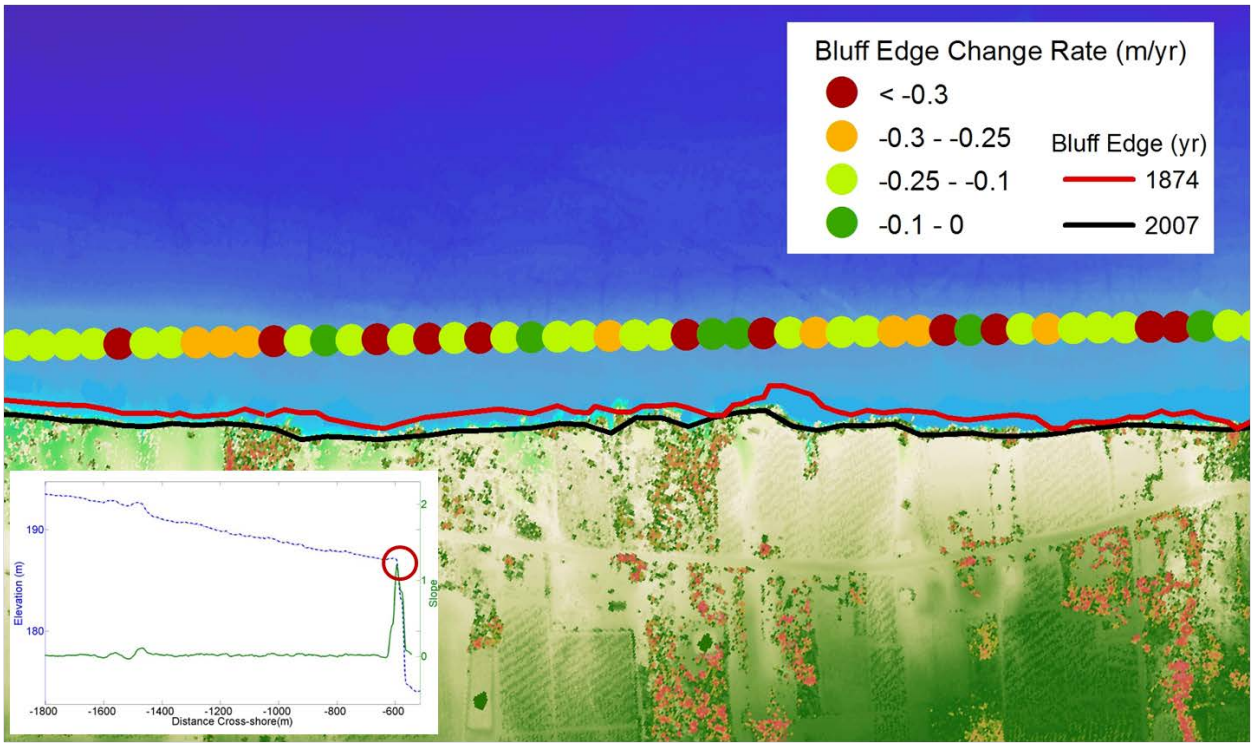

Figure 7.5.5 . Long-term bluff edge change rate for a portion of Lake Erie (New York) and an example profile plot of the elevation (blue dashed line) and slope (green line) where the location of the maximum slope (bluff edge) is identified (red circle). (From Reif et al. 2013).

Similar automated detection methodologies used on seacliffs incorporate further advancements to accommodate the more complex geometries of cliffs, with terraces and varying slope gradients (Palaseanu-Lovejoy et al. 2016).

7.6 Environmental mapping

Environmental mapping with airborne coastal lidar falls into the two broad categories of land cover classification and seafloor classification. Some environmental mapping is performed using ALB elevation and depth data alone. Studies of seafloor complexity calculate rugosity (topographic roughness) from ALB depth data (Walker, Riegl, and Dodge 2008), at varying spatial scales (Zawada and Brock 2009; Pittman, Costa, and Battista 2009). Lidar waveform shape parameters used in concert with ALB depths have informed seafloor classifications of seagrass (C.-K. Wang and Philpot 2007) bottom sediment and algal cover (Cottin, Forbes, and Long 2009), and a number of estuarine supralittoral, intertidal, and subtidal habitats (Chust et al. 2010). Lidar intensity data, a measure the light energy returning from the seafloor, identified areas of shell fragment off the coast of New Jersey (C.-C. Wang and Tang 2012), and sand laden with tailings from copper mining (Reif et al. 2013). ALB-derived measurements of seafloor complexity have demonstrated skill in predicting diversity and abundance of fish and corals (Pittman, Costa, and Battista 2009) and species diversity of benthic communities (Collin, Long, and Archambault 2011). A series of metrics extracted from EAARL lidar waveforms collected over land describe

vegetation communities (Nayegandhi et al. 2006; Palaseanu-Lovejoy et al. 2009). These projects utilize a variety of supervised, unsupervised, and machine learning techniques.

The integration of hyperspectral imagers with ALB sensors enables elevation-informed thematic mapping for environmental applications over land. Combining the height information in lidar data with spectral information available in imagery improves the capability of both data sets to characterize environmental conditions in the coastal zone. A supervised classification combining lidar elevation with hyperspectral image band ratios identified invasive Phragmites australis on a dredge material placement site (Reif et al. 2013). Future surveys and classifications may be used to determine effectiveness of herbicide treatments. A series of lidar and hyperspectral image surveys were collected over the south shore of Lake Pontchartrain in New Orleans, immediately after Hurricane Katrina and in the following years. These datasets were used to develop a highly-automated decision tree classifier that uses height-above-ground calculated from lidar DEMs and hyperspectral bands and band ratios to produce a basic landcover classification. Analysis of the Lake Pontchartrain landcover classifications documents changes in vegetation communities and housing in this hurricane impacted area (Reif, Macon, and Wozencraft 2011). New techniques have been developed to quantify dune vegetation density, wherein dune features extracted from lidar DEMs constrain image analysis to identify pixels that contain vegetation, then computes dune density with neighborhood statistics (Wozencraft et al. 2018).

Sensor fusion of ALB and hyperspectral imagery enables a number of new products. Spectral optimization algorithms use lidar-derived depth, attenuation, and bottom reflectance as constraints in the spectral decomposition of the water column and seafloor (Kim, Park, and Tuell 2010). Using this method, the atmosphere, water column, and seafloor signals are decomposed into their component constituents, and incorporated into the radiative transfer equation inversion process through a series of analytical and empirical relationships, all well-established in the ocean optics community (Wozencraft and Park 2013). The results of this approach are spectral water-leaving reflectance, water column attenuation, *Chlorophyll a* and colored dissolved organic matter absorption, spectral seafloor reflectance, and abundance images depicting the proportionate contributions of seafloor constituents in each pixel based on input bottom spectra (Aitken et al. 2010). Spectral seafloor reflectance images generated using spectral optimization were analyzed to discriminate between submerged vegetation species of eelgrass and macroalgae in support of nearby dredging operations (Reif et al. 2012). The eelgrass maps produced using this product exhibited more detail and granularity than maps produced through heads-up digitizing of aerial photography. Spectral seafloor reflectance images and ALB depths informed a benthic mapping study in support of RSM off the west coast of Maui Figure 7.6.1. The goal of the study was to locate sand to support RSM initiatives, and sensitive habitats that might be impacted by dredging and placement operations.

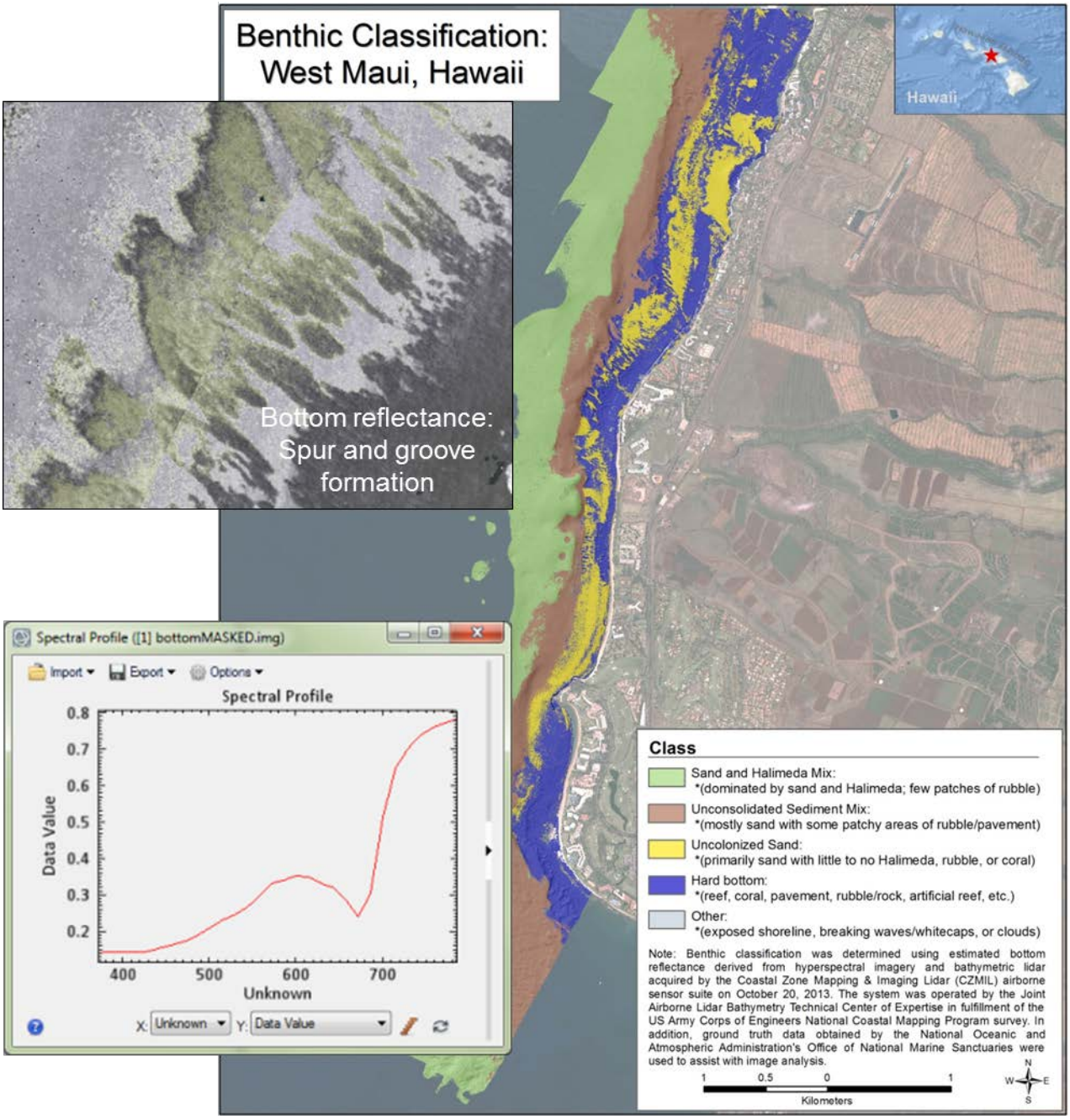

Figure 7.6.1. Benthic classification map generated for regional sediment management study off the coast of west Maui, identifying areas of sand and Halameda mix, unconsolidated sediment mix, uncolonized sand, and hard bottom.

7.7 Summary and future work

This chapter has identified a number of applications for airborne coastal lidar, used alone, or in concert with ancillary passive imagers in a sensor fusion paradigm: nautical charting, navigation project monitoring, regional sediment management, post-storm response, geomorphological feature extraction,

and environmental mapping. The relative speed with which these technologies can collect very large areas make them ideal tools for change detection and coastal characterization at both local and regional scales. Recent work combines the products and applications presented in this chapter to support applications such as landscape evolution modeling (Reif and Swannack 2014) and habitat suitability models for sea turtle nesting (L. Dunkin et al. 2016; Yamamoto et al. 2012).

Synoptic views of coastal condition can be compiled from a number of the products demonstrated in this chapter. One example is a coastal dashboard that visualizes indices comprising features extracted from airborne coastal lidar and ancillary datasets (Wozencraft et al. 2018). This is useful for coastal practitioners as they plan for projects or monitor a stretch of coast. The example in Figure 7.7.1 shows a geomorphological index that includes beach width, dune height, and shoreline change. The environmental index indicates presence of critical habitats including seagrass, wetlands, and dune vegetation. The human use index looks at coastal development in terms of impervious surfaces. The pie charts show indices for navigation projects including stability of offshore shoals features, how well structures match their design profiles, and how much of the navigation channel is at or below the authorized channel depth.

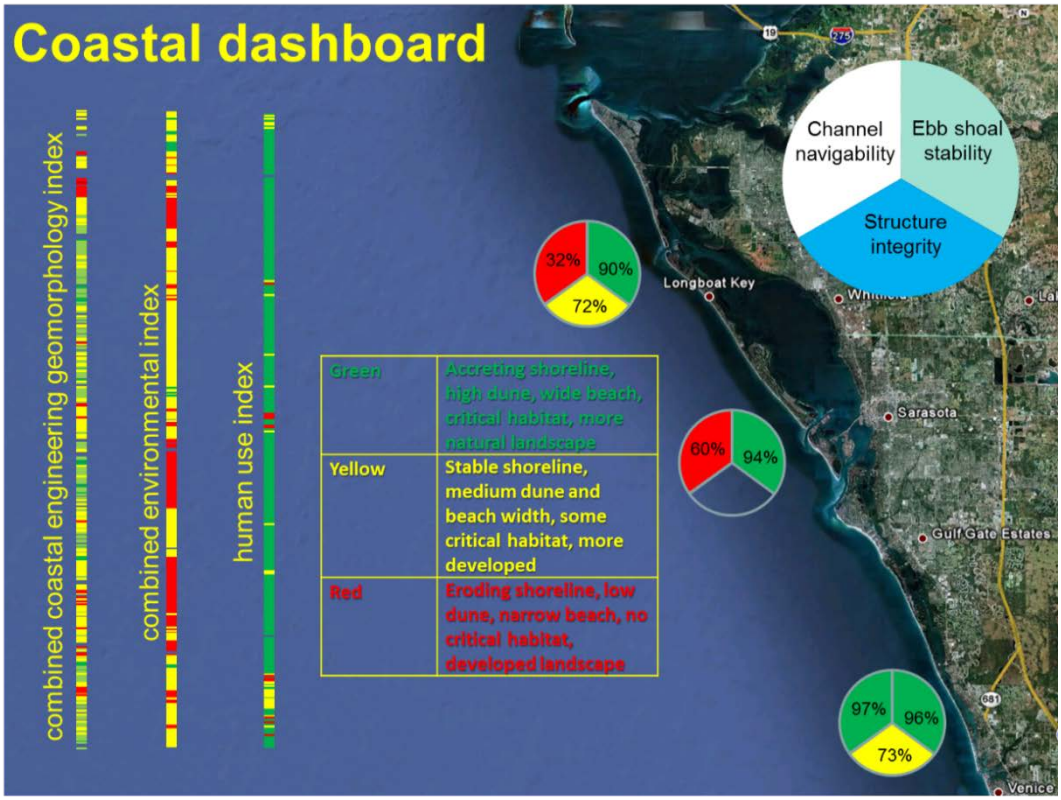

Figure 7.7.1. Coastal dashboard of demonstration area from Tampa Bay south to Venice Inlet, Florida. The set of stoplight indicators generated from extracted geomorpological, environmental, and infrastructure metrics and parameters, give an immediate illustration of coastal conditions. Figure adapted from Wozencraft et al., 2018.

Airborne coastal mapping data are also uniquely available to support studies of coastal resilince, which require data and information about many different aspects of the coastal zone. Features extracted from

airborne coastal mapping data can be used to define an index of coastal resilience. *Figure 7.7.2* shows a conceptual model where features extracted from airborne coastal mapping data are used in a multi-criteria index that notionally defines coastal resilience. The resilience index will soon be validated against results from the last hurricane season. The time series of coastal mapping data available before and after storms from 2004 to present has yet to be analyzed in terms of what we can learn about impacts and recovery from coastal storms, and how that can inform planning for future events and engineering coastal resilience.

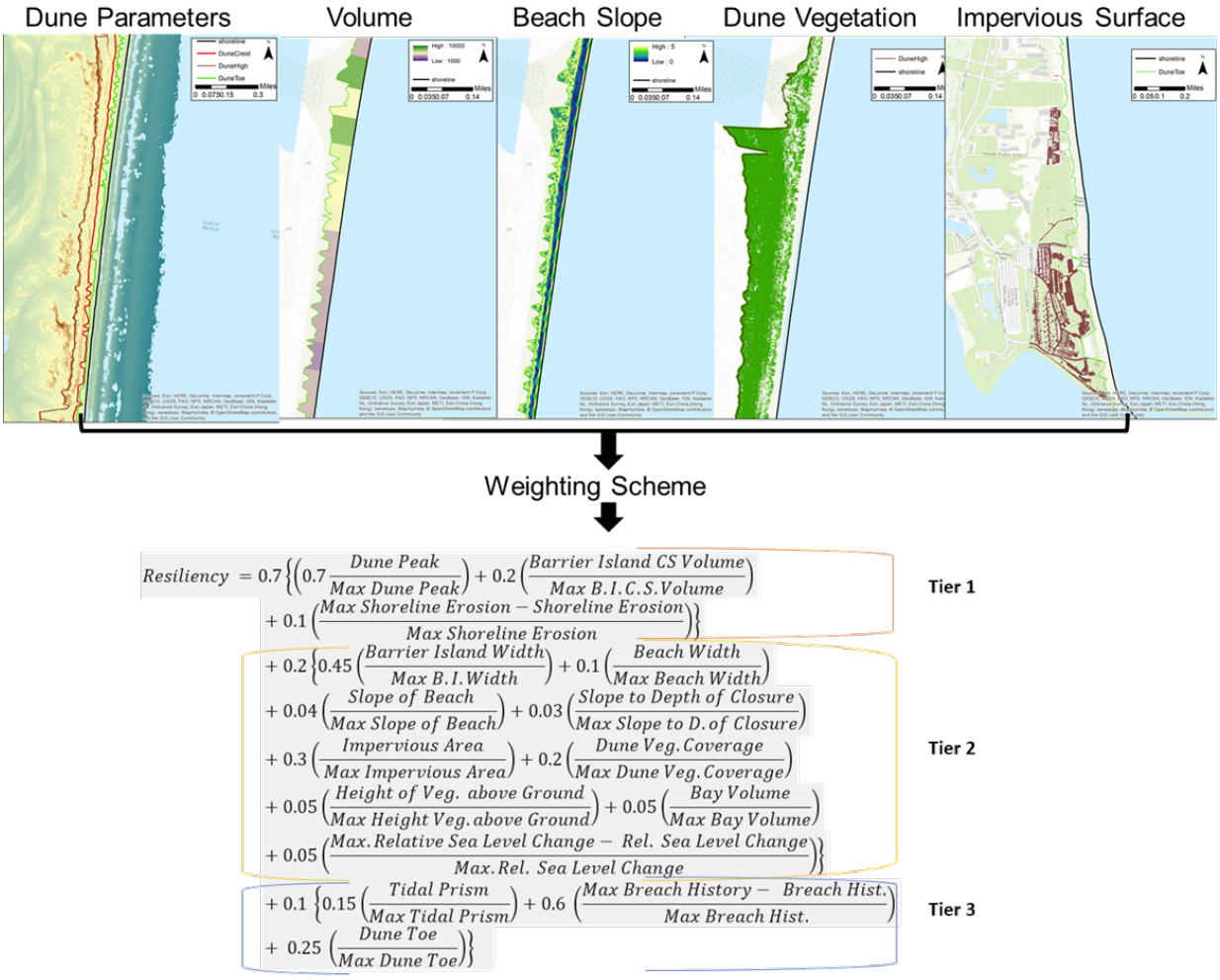

Figure 7.7.2. Features extracted from airborne coastal mapping data and proposed weighting scheme for multi-criteria resiliency index

We have only begun to scratch the surface of what can be learned from these valuable datasets. New systems with expanded capabilities and deployment from new platforms will enable even more exciting work in the realm of airborne coastal mapping applications.

7.8 References

Aitken, Jennifer, Vinod Ramnath, Viktor I. Feygels, Abhinav Mathur, Minsu Kim, Joong Yong Park, and Grady H. Tuell. 2010. "Prelude to CZMIL: Seafloor Imaging and Classification Results Achieved with CHARTS and the Rapid Environmental Assessment (REA) Processor." In *Algorithms and Technologies for Multispectral, Hyperspectral, and Ultraspectral Imagery XVI, April 5, 2010 - April 8*, 7695:The Society of Photo-Optical Instrumentation Engin. Optech International, 7225 Stennis Airport Road, Kiln, MS 39556, United States: SPIE. https://doi.org/10.1117/12.851915.

Aslaksen, M.L., K. Waters, Jennifer M. Wozencraft, Christopher L. Macon, John Brock, C. Wayne Right, and Christopher E. Parrish. 2012. "Coastal Applications." In *Manual of Airborne Topographic Lidar*, edited by M.S. Renslow.

Baird, W.F. & Assoc. 2002. "Regional Sediment Management (RSM), Sediment Budget for St. Joseph, MI to Michigan City." In *USACE Report Prepared for Detroit District USACE*.

Bocamazo, L.M., W.G. Grosskopf, and F.S. Buonuiato. 2011. "Beach Nourishment, Shoreline Change, and Dune Growth at Westhampton Beach, New York, 1996-2009." In *Symposium to Honor Dr. Nicholas C. Kraus*, edited by T.M. Roberts, J.D. Rosati, and P. Wang, Proceeding:181–91.

Chust, Guillem, Maitane Grande, Ibon Galparsoro, Adolfo Uriarte, and Angel Borja. 2010. "Capabilities of the Bathymetric Hawk Eye LiDAR for Coastal Habitat Mapping: A Case Study within a Basque Estuary." *Estuarine Coastal and Shelf Science* 89 (3): 200–213. https://doi.org/10.1016/j.ecss.2010.07.002.

Collin, Antoine, Bernard F. Long, and Phillippe Archambault. 2011. "Benthic Classifications Using Bathymetric LIDAR Waveforms and Integration of Local Spatial Statistics and Textural Features." *Journal of Coastal Research* 27 (February): 86–98. https://doi.org/10.2112/SI_62_9.

Cottin, Antoine G., Donald L. Forbes, and Bernard F. Long. 2009. "Shallow Seabed Mapping and Classification Using Waveform Analysis and Bathymetry from SHOALS Lidar Data." *Canadian Journal of Remote Sensing* 35 (5): 422–34.

Dunkin, Lauren M., and John McCormick. 2011. "Monitoring Shore Protection Projects along the Florida Panhandle Using Three-Dimensional Spatial Data." In . Proceedings. San Diego, CA: ASCE. https://doi.org/10.1061/41190(422)62.

Dunkin, Lauren, Molly Reif, Safra Altman, and Todd Swannack. 2016. "A Spatially Explicit, Multi-Criteria Decision Support Model for Loggerhead Sea Turtle Nesting Habitat Suitability: A Remote Sensing-Based Approach." *Remote Sensing* 8 (7): 573. https://doi.org/10.3390/rs8070573.

Eisemann, Eve R, Davin J Wallace, Maarten C Buijsman, and Troy Pierce. 2018. "Response of a Vulnerable Barrier Island to Multi-Year Storm Impacts: LiDAR-Data-Inferred Morphodynamic Changes on Ship Island, Mississippi, USA." *Geomorphology* 313: 58–71. https://doi.org/https://doi.org/10.1016/j.geomorph.2018.04.001.

Gares, Paul A, Yong Wang, and Stephen A White. 2006. "Using LIDAR to Monitor a Beach Nourishment Project at Wrightsville Beach, North Carolina, USA." *Journal of Coastal Research* 22 (5): 1206–19. http://www.jstor.org.proxy.library.cornell.edu/stable/4300387.

Graham, T., K. Smith, J. Spittal, and G. R. West. 1999. "Improving the Efficiency, Safety and Economy of the New Zealand National Nautical Charting Program through the Integrated Use of the SHOALS System in a Multi-Sensor Survey." In *Proc. U.S. Hydrographic Conference*, 11 pp. Mobile, AL.

Hapke, C.J., S. Malone, and M. Kratzmann. 2009. "National Assessment of Historical Shoreline Change: A Pilot Study of Historical Coastal Bluff Retreat in the Great Lakes, Erie, Pennsylvania." In *USGS Open-File Report 2009-1042*.

Hapke, C.J., and D. Reid. 2007. "National Assessment of Shoreline Change Part 4: Historical Coastal Cliff Retreat along the California Coast." In *USGS Open File Report 20047-1133*.

Irish, Jennifer L., and W. Jeff Lillycrop. 1997. "Monitoring New Pass, Florida, with High Density Lidar Bathymetry." *Journal of Coastal Research* 13 (4): 1130–40. https://doi.org/10.2307/4298721.

———. 1999. “Scanning Laser Mapping of the Coastal Zone: The SHOALS System.” *ISPRS Journal of Photogrammetry and Remote Sensing* 54 (2–3): 123–29. https://doi.org/10.1016/S0924-2716(99)00003-9.

Irish, Jennifer L., W. Jeff Lillycrop, and Larry E. Parson. 1997. “Accuracy of Sand Volumes as a Function of Survey Density.” In *Part 1 (of 4), September 2, 1996 - September 6*, 3:3736–49. Proceedings of the 1996 25th International Conference on Coastal Engineering. US Army Engineer Waterways, Experiment Station, Vicksburg, United States: ASCE.

Irish, Jennifer L., J. E. Thomas, Larry E. Parson, and W. Jeff Lillycrop. 1996. “Monitoring Storm Response with High Density Lidar Bathymetry: The Effects of Hurricane Opal on Florida’s Panhandle.” In *Proc. 2nd Int. Airborne Remote Sensing Conf.*, III:723–32. San Francisco, CA.

Irish, Jennifer L., and T. E. White. 1998. “Coastal Engineering Applications of High-Resolution Lidar Bathymetry.” *Coastal Engineering* 35 (1–2): 47–71. https://doi.org/10.1016/S0378-3839(98)00022-2.

Kim, Minsu, Joong Yong Park, and Grady H. Tuell. 2010. “A Constrained Optimization Technique for Estimating Environmental Parameters from CZMIL Hyperspectral and Lidar Data.” In *SPIE 7695: Algorithms and Technologies for Multispectral, Hyperspectral, and Ultraspectral Imagery XVI, April 5-8, 2010*. Vol. 7695. SPIE. https://doi.org/10.1117/12.851989.

Lillycrop, W. Jeff, and John R. Banic. 1992. “Advancements in the US Army Corps of Engineers Hydrographic Survey Capabilities: The SHOALS System.” *Marine Geodesy*, Mar. Geod. (USA), 15 (2–3): 177–85. https://doi.org/10.1080/01490419209388053.

Lillycrop, W. Jeff, Robert W. Pope, and Geraint R. West. 2000. “Rapid Environmental Assessment with Lidar.” *GPS World: News and Applications of the Global Positioning System*, November 2000.

List, Jeffrey H., Amy S. Farris, and Charlene Sullivan. 2006. “Reversing Storm Hotspots on Sandy Beaches: Spatial and Temporal Characteristics.” *Marine Geology* 226 (3–4): 261–79. https://doi.org/10.1016/j.margeo.2005.10.003.

Liu, Jung-Kung, Rongxing Li, Sagar Deshpande, Xutong Niu, and Tian-Yuan Shih. 2009. “Estimation of Blufflines Using Topographic Lidar Data and Orthoimages.” *Photogrammetric Engineering & Remote Sensing* 75 (1): 69–79. https://www.asprs.org/wp-content/uploads/pers/2009journal/january/2009_jan_57-68.pdf.

McClung, J. K. 1998. “High Density Lidar Data: A Monitoring Tool for East Pass Florida.” In *Proc. 5th Int’l Conf. on Remote Sensing for Marine and Coastal Environmnents*, I:75–82. San Diego, CA.

McNinch, Jesse E. 2004. “Geologic Control in the Nearshore: Shore-Oblique Sandbars and Shoreline Erosional Hotspots, Mid-Atlantic Bight, USA.” *Marine Geology* 211 (1–2): 121–41. https://doi.org/10.1016/j.margeo.2004.07.006.

Mohr, M. C., J. Pope, and J. K. McClung. 1999. “Coastal Response to a Detached Breakwater System; Presque Isle, Pennsylvania, USA.” In *Proc. 4th International Symposium on Coastal Engineering and Science of Coastal Sediment Processes*, 3:2010–25. Long Island, NY: American Society of Civil Engineers.

Nayegandhi, Amar, John C. Brock, C. Wayne Wright, and Michael J. O’Connell. 2006. “Evaluating A Small Footprint, Waveform-Resolving Lidar Over Coastal Vegetation Communities.” *Photogrammetric Engineering and Remote Sensing* 72 (12): 1407–17. https://doi.org/0099-1112.

Palaseanu-Lovejoy, Monica, Jeffrey J. Danielson, Cindy Thatcher, Amy C. Foxgrover, Patrick L. Barnard, John C. Brock, and Adam Young. 2016. “Automatic Delineation of Seacliff Limits Using Lidar-Derived High-Resolution DEMs in Southern California.” *Journal of Coastal Research* SI (76): 162–73. https://doi.org/10.2112/SI76-014.

Palaseanu-Lovejoy, Monica, Amar Nayegandhi, John Brock, Robert Woodman, and C Wayne Wright. 2009. “Evaluation of Airborne Lidar Data to Predict Vegetation Presence/Absence.” *Journal of Coastal Research* 25 (6): 83–97. http://www.jstor.org.proxy.library.cornell.edu/stable/25737455.

Pastol, Yves. 2011. “Use of Airborne LIDAR Bathymetry for Coastal Hydrographic Surveying: The French Experience.” *Journal of Coastal Research* 62 (March): 6–18. https://doi.org/10.2112/SI_62_2.

Pittman, Simon J., Bryan M. Costa, and Timothy A. Battista. 2009. “Using Lidar Bathymetry and Boosted Regression Trees to Predict the Diversity and Abundance of Fish and Corals.” *Journal of Coastal Research* 25 (6): 27–38. https://doi.org/10.2112/SI53-004.1.

Pope, Robert W., B. A. Reed, Geraint R. West, and W. Jeff Lillycrop. 1997. “Use of an Airborne Laser Depth Sounding System in a Complex Shallow-Water Environment.” In *Proc. 15th Int’l Hydro Conference*, 10 pgs. Monaco.

Reif, Molly K., Christopher L. Macon, and Jennifer M. Wozencraft. 2011. “Post-Katrina Land-Cover, Elevation, and Volume Change Assessment along the South Shore of Lake Pontchartrain, Louisiana, USA.” *Journal of Coastal Research*, 30–39. https://doi.org/10.2112/SI_62_4.

Reif, Molly K., C. Piercy, J. Jarvis, B. Sabol, Christopher L. Macon, R. Lloyd, H. Colarusso, Heidi M. Dierssen, and Jennifer Aitken. 2012. *A Case Study of Ground Truth Sampling to Support Sensing Research and Development: Submersed Aquatic Vegetation Species Discrimination Using an Airborne Hyperspectral/Lidar System*. DOER Technical Notes Collection. Vicksburg, MS: U.S. Army Engineer Research and Development Center.

Reif, Molly K., and T. M. Swannack. 2014. “Development of Landscape Metrics to Support Process-Driven Ecological Modeling.” ERDC/EL TR-14-6. Vicksburg, MS.

Reif, Molly K, Jennifer M Wozencraft, Lauren M Dunkin, Charlene S Sylvester, and Christopher L Macon. 2013. “A Review of U.S. Army Corps of Engineers Airborne Coastal Mapping in the Great Lakes.” *Journal of Great Lakes Research* 39: 194–204. https://doi.org/https://doi.org/10.1016/j.jglr.2012.11.002.

Robertson, William, V, Dean Whitman, Keqi Zhang, and Stephen P Leatherman. 2004. “Mapping Shoreline Position Using Airborne Laser Altimetry.” *Journal of Coastal Research* 20 (3): 884–92. http://www.jstor.org.proxy.library.cornell.edu/stable/4299347.

Robertson, Quin, Lauren M. Dunkin, Zhifei Dong, Jennifer M. Wozencraft, and Keqi Zhang. 2018. “Florida and US East Coast Beach Change Metrics Derived from LiDAR Data Utilizing ArcGIS Python Based Tools.” In *Beach Management Tools - Concepts, Methodologies and Case Studies*, 239–58. Coastal Research Library. Springer, Cham.

Rosati, Julie Dean. 2005. “Concepts in Sediment Budgets.” *Journal of Coastal Research* 212 (March): 307–22. https://doi.org/10.2112/02-475A.1.

Sallenger, Asbury H., Hilary F. Stockdon, Laura A. Fauver, Mark Hansen, David Thompson, C. Wayne Wright, and W. Jeff Lillycrop. 2006. “Hurricanes 2004: An Overview of Their Characteristics and Coastal Change.” *Estuaries and Coasts; Port Republic* 29 (6): 880–88. https://doi.org/http://dx.doi.org.proxy.library.cornell.edu/10.1007/BF02798647.

Sallenger, Asbury H., C. Wayne Wright, and W. Jeff Lillycrop. 2005. “Coastal Impacts of the 2004 Hurricanes Measured with Airborne Lidar; Initial Results.” *Shore and Beach* 73 (2&3): 10–14.

Schupp, Courtney A., Jesse E. McNinch, and Jeffrey H. List. 2006. “Nearshore Shore-Oblique Bars, Gravel Outcrops, and Their Correlation to Shoreline Change.” *Marine Geology* 233 (1–4): 63–79. https://doi.org/10.1016/J.MARGEO.2006.08.007.

Stauble, Donald K. 2003. “The Use of Shoreline Change Mapping in Coastal Engineering Project Assessment.” *Journal of Coastal Research*, 178–206. http://www.jstor.org/stable/25736606.

Stockdon, Hilary F., Jr. Sallenger, Asbury H., Jeffrey H. List, and Rob A. Holman. 2002. “Estimation of Shoreline Position and Change Using Airborne Topographic Lidar Data.” *Journal of Coastal Research* 18 (3): 502–13. http://www.jstor.org.proxy.library.cornell.edu/stable/4299097.

Stockdon, Hilary F, Kara S Doran, and Asbury H Sallenger. 2009. “Extraction of Lidar-Based Dune-Crest Elevations for Use in Examining the Vulnerability of Beaches to Inundation During Hurricanes.” *Journal of Coastal Research* 25 (6 Supplement. Special Issue No 53): 59–65. http://www.jstor.org.proxy.library.cornell.edu/stable/25737452.

Thieler, E.R., E.A. Himmelstoss, J.L. Zichichi, and A. Ergul. 2009. “The Digital Shoreline Analysis System (DSAS) Version 4.0, an ArcGIS Extension for Calculating Shoreline Change URL: .” In *U.S. Geological Survey Open-File Report 2008-1278*. http://pubs.usgs.gov/of/2008/1278/.

Walker, Brian K., Bernhard Riegl, and Richard E. Dodge. 2008. “Mapping Coral Reef Habitats in Southeast Florida Using a Combined Technique Approach.” *Journal of Coastal Research* 24 (5): 1138–50. https://doi.org/10.2112/06-0809.1.

Wallace, Davin J., John B. Anderson, and Antonio B. Rodriguez. 2009. “Natural versus Anthropogenic Mechanisms of Erosion along the Upper Texas Coast.” In *America’s Most Vulnerable Coastal Communities*. Geological Society of America. https://doi.org/10.1130/2009.2460(10).

Wang, Chau-Chang, and Dajun Tang. 2012. “Application of Underwater Laser Scanning for Seafloor Shell Fragments Characterization.” *Journal of Marine Science and Technology-Taiwan* 20 (1): 95–102.

Wang, Chi-Kuei, and William D. Philpot. 2007. “Using Airborne Bathymetric Lidar to Detect Bottom Type Variation in Shallow Waters.” *Remote Sensing of Environment* 106 (1): 123–35. https://doi.org/10.1016/j.rse.2006.08.003.

Weber, Kathryn M., Jeffrey H. List, and Karen L.M. Morgan. 2005. “An Operational Mean High Water Datum for Determination of Shoreline Position from Topographic Lidar Data.” *Open-File Report*. https://doi.org/10.3133/OFR20051027.

West, Geraint R. 2001. “In Deeper Waters.” *POB*, March 2001.

West, Geraint R., and W. Jeff Lillycrop. 1999. “Feature Detection and Classification with Airborne Lidar - Practical Experience.” In *Proc. Shallow Survey 99*. Sydney, Australia.

West, Geraint R., and C. E. Wiggins. 2000. “Airborne Mapping Sheds Light on Hawaiian Coasts and Harbors.” *Earth Observation Magazine (EOM)*, 2000.

White, Stephen A. 2007. “Utilization of Lidar and NOAA’s Vertical Datum Transformation Tool (VDatum) for Shoreline Delineation.” In *Marine Technology Society/IEEE Oceans Conference*, 1–6. Vancouver, BC: IEEE. https://doi.org/10.1109/OCEANS.2007.4449147.

White, Stephen A., Christopher E. Parrish, Brian R. Calder, Shachak Pe’eri, and Yuri Rzhanov. 2011. “LIDAR-Derived National Shoreline: Empirical and Stochastic Uncertainty Analyses.” *Journal of Coastal Research*, no. 62 (Special Issue): 62–74. https://doi.org/10.2112/SI_62_7.

Wozencraft, Jennifer M. 2001. “Sand Volumes and Transport Pathways for Gulf of Mexico Regional Sediment Management.” In *Coastal Dynamics ’01*, 693–702. Proceedings. Bergen, Norway: ASCE. https://doi.org/10.1061/40566(260)71.

———. 2013. “Using LiDAR to Assess Storm Damage Caused by Hurricane Sandy.” *LiDAR Magazine*, March 2013.

Wozencraft, Jennifer M., Lauren M. Dunkin, Molly K. Reif, and E. Eisemann. 2018. “A Spatial Index Approach to Coastal Monitoring: A Florida Case Study.” Edited by R Almar, L P Almeida, Viet N Trung, and Sall. *Journal of Coastal Research*, no. 81 (Special Issue): Tropical, Coastal, and Estutarine Dynamics: 67–75. https://www-jstor-org.proxy.library.cornell.edu/stable/26552353.

Wozencraft, Jennifer M., and Jennifer L. Irish. 2000. “Airborne Lidar Surveys and Regional Sediment Management.” In *Proc. 20th EARSeL Symposium*, 11 pgs. Dresden, Germany: European Association of Remote Sensing Laboratories EARSeL.

Wozencraft, Jennifer M., and W. Jeff Lillycrop. 2006. “JALBTCX Coastal Mapping for the USACE.” *The International Hydrographic Review* 7 (2): 28–37. https://journals.lib.unb.ca/index.php/ihr/article/view/20763.

Wozencraft, Jennifer M., and David Millar. 2005. “Airborne Lidar and Integrated Technologies for Coastal Mapping and Nautical Charting.” *Marine Technology Society Journal* 39 (3): 27–35. https://doi.org/10.4031/002533205787442440.

Wozencraft, Jennifer M., and Joong Yong Park. 2013. “Integrated LiDAR and Hyperspectral.” In *Coral Reef Remote Sensing*, 1st ed., 175–91. Dordrecht: Springer Netherlands. https://doi.org/10.1007/978-90-481-9292-2_7.

Xhardé, Régis, Bernard F. Long, and Donald L. Forbes. 2011. “Short-Term Beach and Shoreface Evolution on a Cuspate Foreland Observed with Airborne Topographic and Bathymetric LIDAR.” *Journal of Coastal Research*, no. Special Issue No 62: Applied Lidar Techniques (March): 50–61. https://doi.org/10.2112/SI_62_6.

Yamamoto, Kristina H., Rebecca L. Powell, Sharolyn Anderson, and Paul C. Sutton. 2012. “Using LiDAR to Quantify Topographic and Bathymetric Details for Sea Turtle Nesting Beaches in Florida.” *Remote Sensing of Environment* 125 (October): 125–33. https://doi.org/10.1016/j.rse.2012.07.016.

Young, Adam P, and Scott A Ashford. 2006. “Application of Airborne LIDAR for Seacliff Volumetric Change and Beach-Sediment Budget Contributions.” *Journal of Coastal Research* 22 (2): 307–18. http://www.jstor.org.proxy.library.cornell.edu/stable/4300288.

Zawada, David G., and John C. Brock. 2009. “A Multiscale Analysis of Coral Reef Topographic Complexity Using Lidar-Derived Bathymetry.” *Journal of Coastal Research* 25 (6): 6–15. https://doi.org/10.2112/SI53-002.1.

Zhang, Keqi, Dean Whitman, Stephen Leatherman, and William V. Robertson. 2005. “Quantification of Beach Changes Caused by Hurricane Floyd Along Florida’s Atlantic Coast Using Airborne Laser Surveys.” *Journal of Coastal Research* 211 (1): 123–34. https://doi.org/10.2112/02057.1.

FULL REFERENCE LIST

Abady, Lydia, Jean-Stéphane Bailly, Nicolas Baghdadi, Yves Pastol, and Hani Abdallah. 2014. "Assessment of Quadrilateral Fitting of the Water Column Contribution in Lidar Waveforms on Bathymetry Estimates." *Geoscience and Remote Sensing Letters, IEEE* 11 (4): 813–17. https://doi.org/10.1109/LGRS.2013.2279271.

Abbot, Ralph H., and Michael F. Penny. 1975. "Air Trials of an Experimental Laser Bathymeter." Vol. Tech Note. Salisbury, South Australia: Weapons Research Establishment, Department of Defence.

Abdullah, Q A. 2004. "Photogrammetric Platforms." In *Manual of Photogrammetry. Fifth Edition*, edited by J Chris McGlone, Edward M Mikhail, and James S Bethel, 705–17. Bethesda, MD: ASPRS. https://doi.org/978-1570830716.

Abramowitz, M., and I. A. Stegun. 1972. *Handbook of Mathematical Functions with Formulas, Graphs, and Mathematical Tables (Partially Mathcad-Enabled)*. U.S. Department of Commerce, NIST. http://app.knovel.com/hotlink/toc/id:kpHMFFGMT1/handbook-mathematical/handbook-mathematical.

Abrosimov, D. L., and Alexander G. Luchinin. 1999. "Signal Statistics of Lidar Sounding of the Upper Ocean through Its Rough Surface." *Izvestiya, Atmospheric and Oceanic Physics (in Russian)* 35: 266–72.

Allocca, David M, Mark A London, Thomas P Curran, Brian M Concannon, V Michael Contarino, Jennifer Prentice, Linda J Mullen, and Timothy J Kane. 2002. "Ocean Water Clarity Measurement Using Shipboard Lidar Systems." In *Ocean Optics: Remote Sensing and Underwater Imaging*, 4488:106–14. San Diego, CA: SPIE 4488. https://doi.org/10.1117/12.452807 [doi].

Aly, Kamal M., and E. Esmail. 1993. "Refractive Index of Salt Water: Effect of Temperature." *Optical Materials* 2 (3): 195–99. https://doi.org/10.1016/0925-3467(93)90013-Q.

Anderson, N., P. Bellemare, M. J. Casey, K. Malone, R. MacDougal, D. Monahan, Robert A. O'Neil, and S. Till. 1983. "Beginning the Second Hundred Years - the Laser Sounder." In *Proceedings of Centennial Canadian Hydrographic Service Conference*. Ottawa, Ontario, CA: Fisheries and Aquatic Services, Special Publ. 67.

ANSI. 2005. "Safe Use of Lasers Outdoors." Vol. ANSI Z136. Laser institute of America. https://doi.org/978-0-912035-66-6.

———. 2014. "American National Standard for Safe Use of Lasers." *ANSI Z136.1-2014*. http://webstore.ansi.org/RecordDetail.aspx?sku=ANSI+Z136.1-2014.

Apresian, L A, and Yu A Kravstov. 1983. *The Theory of Radiative Transfer*. Nauka (in Russian).

ASPRS. 2008a. "Common Lidar Data Exchange Format - LAS Industry Initiative 1.2." 2008. http://www.asprs.org/a/society/committees/standards/asprs_las_format_v12.pdf.

———. 2008b. "LAS Specification, Version 1.4-R13." Bethesda, MD: American Society of Photogrammetry and Remote Sensing. http://www.asprs.org/a/society/committees/standards/asprs_las_format_v12.pdf.

———. 2010. "LAS Specification: Version 1.3.-R11." http://www.asprs.org/a/society/committees/standards/LAS_1_3_r11.pdf.

Austin, Roswell W. 1974. "The Remote Sensing of Spectral Radiance from below the Ocean Surface." In *Optical Aspects of Oceanography*, edited by N G Jerlov and E Steemann Nielsen, 317–44. New York: Academic Press.

Austin, Roswell W., and George Halikas. 1976. “The Index of Refraction of Seawater.” *Final Report*. Vol. SIO Ref. 7. La Jolla, California: Scripps Institute of Oceanography. http://misclab.umeoce.maine.edu/education/VisibilityLab/reports/SIO_76-1.pdf.

Austin, Roswell W., and T. J. Petzold. 1984. “Spectral Dependence Of The Diffuse Attenuation Coefficient Of Light In Ocean Waters.” https://doi.org/10.1117/12.943302.

Avco Everett Research Laboratory Inc. 1975. “Airborne Oceanographic Lidar System, NASA Contractor Report CR-141407, Final Report.” Everett MA.

Axelsson, Rune, and Mats Alfredsson. 1999. “Capacity and Capability for Hydrographic Missions.” In *Proc. 1999 U.S. Hydrographic Conference*. Mobile, AL. http://www.jalbtcx.org/downloads/Publications/30Axelsson_Alfredsson_99.pdf.

Baird, W.F. & Assoc. 2002. “Regional Sediment Management (RSM), Sediment Budget for St. Joseph, MI to Michigan City.” In *USACE Report Prepared for Detroit District USACE*.

Baltsavias, E P. 1999. “Airborne Laser Scanning: Basic Relations and Formulas.” *ISPRS Journal of Photogrammetry and Remote Sensing* 54 (2–3): 199–214. https://doi.org/10.1016/S0924-2716(99)00015-5.

Banic, John R., Sebastian Sizgoric, and W. Jeff Lillycrop. 1990. “Second-Generation Airborne Lidar System for Hydrographic Applications.” In *Proc. Oceanology International*. Brighton, England.

Banic, John R., Sebastian Sizgoric, and Robert O’Neil. 1986. “Scanning Lidar Bathymeter For Water Depth Measurement.” In *Laser Radar Technology and Applications.*, edited by James M. Cruickshank and Robert C. Harney, 663:187. Optech Inc, Downsview, Ont, Can, Optech Inc, Downsview, Ont, Can: SPIE. https://doi.org/10.1117/12.938673.

Beaudoin, Jonathan, Paul Johnson, and Ashton F Flinder. 2013. “R/V Falkor Multibeam Echosounder System Review.” Vol. Technical. Durham, NH: University of New Hampshire (UNH) Center for Coastal and Ocean Mapping (CCOM)/Joint Hydrographic Center (JHC). http://ccom.unh.edu/publications.

Bierwirth, P. N., T. J. Lee, and R. V. Burne. 1993. “Shallow Sea-Floor Reflectance and Water Depth Derived by Unmixing Multispectral Imagery.” *Photogrammetric Engineering and Remote Sensing* 59 (3): 331–38. http://eserv.asprs.org/PERS/1993journal/mar/1993_mar_331-338.pdf.

Billard, Brian, Ralph H Abbot, and Michael F Penny. 1986a. “Airborne Estimation of Sea Turbidity Parameters from the Wrelads Laser Airborne Depth Sounder.” *Applied Optics* 25 (13): 2080–88. https://doi.org/10.1364/AO.25.002080.

———. 1986b. “Modeling Depth Bias in an Airborne Laser Hydrographic System.” *Applied Optics* 25 (13): 2089–98.

Bocamazo, L.M., W.G. Grosskopf, and F.S. Buonuiato. 2011. “Beach Nourishment, Shoreline Change, and Dune Growth at Westhampton Beach, New York, 1996-2009.” In *Symposium to Honor Dr. Nicholas C. Kraus*, edited by T.M. Roberts, J.D. Rosati, and P. Wang, Proceeding:181–91.

Bortkovskii, R. S., B. N. Egorov, V. M. Kattsov, and T. V. Pavlova. 2007. “Model Estimates for the Mean Gas Exchange between the Ocean and the Atmosphere under the Conditions of the Present-Day Climate and Its Changes Expected in the 21st Century.” *Izvestiya, Atmospheric and Oceanic Physics* 43 (3): 378–83. https://doi.org/10.1134/S0001433807030127.

Bravo-Zhivotovski, Dmitri, D M Dolin, Alexander G Luchinin, and V A Savel’ev. 1969. “On the Structure of a Narrow Light Beam in Sea Water.” *Izv. Akad. Nauk SSSR, Fiz. Atmos. Okeana* 5 (2): 160.

Bremmer, H. 1964. “Random Volume Scattering.” *Radio Science* 68D (9): 967–81. https://doi.org/http://dx.doi.org/10.6028/jres.068D.096.

Brock, John C., C. Wayne Wright, Tonya D. Clayton, and Amar Nayegandhi. 2004. “LIDAR Optical Rugosity of Coral Reefs in Biscayne National Park, Florida.” *Coral Reefs* 23 (1): 48–59. https://doi.org/10.1007/s00338-003-0365-7.

Brooks, M. W., E. Culpepper, Gary C. Guenther, and Paul E. LaRocque. 1998. “Advancements and Applications of the SHOALS Laser Bathymetry System.” In *Proc. ION GPS 98*, 8. Institute of Navigation, Nashville, TN. https://www.ion.org/publications/abstract.cfm?articleID=3057.

Bunkin, Alexei F., Vladimir K. Klinkov, Vladislav A. Lukyanchenko, and Sergey M. Pershin. 2011. “Ship Wake Detection by Raman Lidar.” *Applied Optics* 50 (4): A86–89. https://doi.org/10.1364/AO.50.000A86.

Bunkin, Alexei F., and Konstantin I. Voliak. 2001. *Laser Remote Sensing of the Ocean: Methods and Applications*. Vol. 56. John Wily & Sons.

Calder, M. 1980. “WRELADS - The Australian Laser Depth Sounding System.” *The International Hydrographic Review* 57 (1). https://journals.lib.unb.ca/index.php/ihr/article/view/23621.

Cariou, J., and J. Lotrian. 1982. “Transmission Characteristics of a Pulsed Laser Beam in Natural Sea-Water: Determination of the Attenuation Coefficients in the 415-660 Nm Spectral Range.” *Journal of Physics D: Applied Physics* 15 (10): 1873–80. https://doi.org/10.1088/0022-3727/15/10/007.

Carswell, Allan I., and Sebastian Sizgoric. 1974. “Underwater Probing with Laser Radar.” In *Proceedings of the Uses of Lasers for Hydrographic Studies*, 89–104. Wallops Island, VA: NASA SP-375. https://ntrs.nasa.gov/archive/nasa/casi.ntrs.nasa.gov/19750022452.pdf.

Casey, M. J., Robert A. O’Neil, and P. Conrad. 1985. “The Advent of LARSEN.” In *Proc. Canadian Hydro. Conf.* Halifax, Nova Scotia, CA.

Chen, Yang, and Gérard Medioni. 1992. “Object Modelling by Registration of Multiple Range Images.” *Image and Vision Computing* 10 (3): 145–55. https://doi.org/10.1016/0262-8856(92)90066-C.

Churnside, James H. 2010. “Lidar Signature from Bubbles in the Sea.” *Optics Express* 18 (8): 8294–99. https://doi.org/10.1364/OE.18.008294.

Chust, Guillem, Maitane Grande, Ibon Galparsoro, Adolfo Uriarte, and Angel Borja. 2010. “Capabilities of the Bathymetric Hawk Eye LiDAR for Coastal Habitat Mapping: A Case Study within a Basque Estuary.” *Estuarine Coastal and Shelf Science* 89 (3): 200–213. https://doi.org/10.1016/j.ecss.2010.07.002.

Collin, Antoine, Phillippe Archambault, and Bernard Long. 2008. “Mapping the Shallow Water Seabed Habitat with the SHOALS.” *IEEE Transactions on Geoscience and Remote Sensing* 46 (10): 2947–55. https://doi.org/10.1109/TGRS.2008.920020.

Collin, Antoine, Antoine G. Cottin, Bernard F. Long, Pim Kuus, John Hughes Clarke, Phillippe Archambault, Gunho Sohn, and John Miller. 2007. “Statistical Classification Methodology of SHOALS 3000 Backscatter to Mapping Coastal Benthic Habitats.” In *2007 IEEE International Geoscience and Remote Sensing Symposium, IGARSS 2007, June 23, 2007 - June 28*, 3178–81. Department of Geology, INRS-ETE, University of Quebec, QC, Canada: Institute of Electrical and Electronics Engineers Inc. https://doi.org/10.1109/IGARSS.2007.4423520.

Collin, Antoine, Bernard Long, and Phillippe Archambault. 2011a. “Benthic Classifications Using Bathymetric LIDAR Waveforms and Integration of Local Spatial Statistics and Textural Features.” *Journal of Coastal Research* 27 (February): 86–98. https://doi.org/10.2112/SI_62_9.

Collin, Antoine, Bernard F. Long, and Phillippe Archambault. 2011b. "Benthic Classifications Using Bathymetric LIDAR Waveforms and Integration of Local Spatial Statistics and Textural Features." *Journal of Coastal Research* 27 (February): 86–98. https://doi.org/10.2112/SI_62_9.

Collis, R. T. H., and P. B. Russell. 1976. "Lidar Measurement of Particles and Gases by Elastic Backscattering and Differential Absorption." In *Laser Monitoring of the Atmosphere*, edited by E. Hinkley, 71–151. Springer Berlin Heidelberg. https://doi.org/10.1007/3-540-07743-X_18.

Cottin, Antoine G., Donald L. Forbes, and Bernard F. Long. 2009. "Shallow Seabed Mapping and Classification Using Waveform Analysis and Bathymetry from SHOALS Lidar Data." *Canadian Journal of Remote Sensing* 35 (5): 422–34.

Cox, Charles, and Walter Munk. 1954a. "Measurement of the Roughness of the Sea Surface from Photographs of the Sun's Glitter." *Journal of the Optical Society of America* 44 (11): 838–50. https://doi.org/10.1364/JOSA.44.000838.

———. 1954b. "Statistics of the Sea Surface Derived from Sun Glitter." *Journal of Marine Research* 13: 198–227.

Cunningham, Linda L. 1972a. "Test Report on Pulsed Light Airborne Depth Sounder PLADS." Vol. 6620-102–7. Washington, D.C.: Naval Oceanographic Office.

Cunningham, Linda L. 1972b. "Test Report on Pulsed Light Airborne Depth Sounder PLADS." Vol. 6620-102–7. Washington, D.C.: Naval Oceanographic Office.

Degnan, John J., Roman Machan, Edward Leventhal, Gabriel Jodor, Christopher B. Field, and J. Marcos Sirota. 2011. "Cryosphere and Biomass Measurements Using a Photon-Counting 3D Imaging Lidar." In *CLEO 2011: Laser Applications to Photonic Applications*, ATuA3. Washington, D.C.: OSA. https://doi.org/10.1364/CLEO_AT.2011.ATuA3.

Dekker, Arnold, Vittorio Brando, Janet M Anstee, Suzanne Fyfe, Timothy Malthus, and Evanthia Karpouzli. 2006. "Remote Sensing of Seagrass Ecosystems: Use of Spaceborne and Airborne Sensors." In *Seagrasses: Biology, Ecology and Conservation*, 347–59. Springer Netherlands. https://doi.org/10.1007/978-1-4020-2983-7_15.

Dekker, Arnold G, V E Brando, Janet M Anstee, N Pinnel, T Kutser, J Hoogenboom, S W M Peters, et al. 2002. "Imaging Spectroscopy of Water." In *Imaging Spectroscopy: Basic Principle and Prospective Applications*, edited by Freek D van der Meer, 307–60. Netherlands: Springer. https://doi.org/10.1007/978-0-306-47578-8.

Dewberry. 2012. "National Enhanced Elevation Assessment." 2012. http://www.dewberry.com/services/geospatial/national-enhanced-elevation-assessment.

Dierssen, Heidi M., Richard C. Zimmerman, Robert A. Leathers, T. Valerie Downes, and Curtiss O. Davis. 2003. "Ocean Color Remote Sensing of Seagrass and Bathymetry in the Bahamas Banks by High-Resolution Airborne Imagery." *Limnology and Oceanography* 48 (1, Part 2; Light in Shallow Waters): 444–55. http://www.jstor.org/stable/3597765.

Dolin, Lev S., and Iosif M. Levin. 1991. *Reference Book on the Underwater Vision Theory*. Leningrad: Gidrometeoizdat Press (in Russian).

Dolin, Lev S., Iosif M. Levin, O. V. Kopelevich, and Victor I. Feigels. 1988. "Few-Parameter Models of Light Field at Sea, and Integral Parameters of the Phase Function of Water." *Izvvestiya, Atmospheric and Oceanic Physics* 24 (11): 1217–22.

Dolin, Lev S., and V. A. Savel'ev. 1971a. "Characteristics of the Backscattering Signal and Pulse Radiation of Turbid Media by a Narrow Directional Light Beam." *Atmospheric and Oceanic Physics* 7 (5): 505–10.

Dolin, Lev S. 1964. “Light Beam Scattering in a Turbid Medium Layer.” *IIzv. Vyssh. Uchebn. Zaved. Radiofiz.* 7: 471–78.

Dolin, Lev S, and V A Savel’ev. 1971b. “Determining the Parameters of a Back-Scattered Signal of Pulsed Radiation in a Turbid Medium with a Narrow Directed Laser Beam.” *Izv. Akad. Nauk SSSR, Fiz. Atmos. Okeana* 7: 505.

Dolin, LevS, and V A Savel’ev. 1979. “On the Theory of Narrow Light Beam Propagation in a Stratified Scattering Medium.” *IIzv. Vyssh. Uchebn. Zaved. Radiofiz.* 12: 1310–17.

Dolina, I S, Lev S Dolin, Iosif M Levin, A A Rodionov, and V A Savel’ev. 2007. “Inverse Problems of Lidar Sensing of the Ocean.” In *Proceedings of the III International Conference Current Problems of Natural Waters*, 6615:66150C-1-66150C – 10. St. Petersburg, Russia: SPIE 6615. https://doi.org/10.1117/12.740451.

Donelan, M., M. S. Longuet-Higgens, and J. S. Turner. 1972. “Periodicity in Whitecaps.” *Nature* 239 (5373): 449–51. https://doi.org/10.1038/239449a0.

Dorogin, A. N., O. V. Kopelevich, Iosif M. Levin, and Viktor I. Feigels. 1988. “Correlation among Some Hydrooptical Properties.” In *Optics of the Sea and the Atmosphere (in Russian)*, 136–37. Academy of Science of the USSR.

Duarte, Carlos M. 1991. “Seagrass Depth Limits.” *Aquatic Botany* 40 (4): 363–77. https://doi.org/10.1016/0304-3770(91)90081-F.

Dunkin, Lauren M., and John McCormick. 2011. “Monitoring Shore Protection Projects along the Florida Panhandle Using Three-Dimensional Spatial Data.” In . Proceedings. San Diego, CA: ASCE. https://doi.org/10.1061/41190(422)62.

Dunkin, Lauren, Molly Reif, Safra Altman, and Todd Swannack. 2016. “A Spatially Explicit, Multi-Criteria Decision Support Model for Loggerhead Sea Turtle Nesting Habitat Suitability: A Remote Sensing-Based Approach.” *Remote Sensing* 8 (7): 573. https://doi.org/10.3390/rs8070573.

Duntley, Seibert Q. 1954. “Measurements of the Distribution of Water Wave Slopes.” *Journal of the Optical Society of America* 44 (7): 574_1. https://doi.org/10.1364/JOSA.44.0574_1.

———. 1971. “Underwater Lighting by Submerged Lasers and Incandescent Sources.” Vol. SIO Ref. 7. La Jolla, CA: Scripps Institution of Oceanography Visibility Laboratory. http://oai.dtic.mil/oai/oai?verb=getRecord&metadataPrefix=html&identifier=AD0730721.

Egan, James P. 1975. *Signal Detection Theory and ROC Analysis*. Academic Press.

Eisemann, Eve R, Davin J Wallace, Maarten C Buijsman, and Troy Pierce. 2018. “Response of a Vulnerable Barrier Island to Multi-Year Storm Impacts: LiDAR-Data-Inferred Morphodynamic Changes on Ship Island, Mississippi, USA.” *Geomorphology* 313: 58–71. https://doi.org/https://doi.org/10.1016/j.geomorph.2018.04.001.

El-Sheimy, Naser, Caterina Valeo, and Ayman Habib. 2005. *Digital Terrain Modeling: Acquisition, Manipulation, and Applications*. *Artech House Remote Sensing Library*. Norwood, MA: Artech House. http://library.books24x7.com/assetviewer.aspx?bookid=14812&chunkid=1&rowid=2.

Elfouhaily, T., Bertrand Chapron, K. Katsaros, and Douglas Vandemark. 1997. “A Unified Directional Spectrum for Long and Short Wind-Driven Waves.” *Journal of Geophysical Research* 102 (97): 15781–96. https://doi.org/10.1029/97JC00467.

FDA. 2013. “Performance Standards for Light-Emitting Products.” Code of Federal Regulations, Title 21, Volume 8. http://www.accessdata.fda.gov/scripts/cdrh/cfdocs/cfcfr/cfrsearch.cfm?fr=1040.10.

Feigels, Victor I. 1992. “Lidars for Oceanographical Research: Criteria for Comparison, Main Limitations, Perspectives.” In *Ocean Optics XI*, 1750:473–85. San Diego, CA: SPIE 1750. https://doi.org/10.1117/12.140676.

Feigels, Victor I., Blair Evans, Lev Feygels, Gary C. Guenther, and Yuri I. Kopilevich. 2002. “Prediction of Bathymetric Lidar Performance with Ocean Scientific 2001 Simulation Code.” In *SPIE 4488, Ocean Optics: Remote Sensing and Underwater Imaging*, edited by Robert J. Frouin and Gary D. Gilbert, SPIE 4488:61–70. San Diego, CA, United States: SPIE. https://doi.org/10.1117/12.452826.

Feigels, Victor I., and Yuri I. Kopilevich. 1993a. “Ocean-Scientific for Windows: User’s Guide.” EG&G Washington Analytical Service, Inc.

———. 1993b. “Remote Sensing of Subsurface Layers of Turbid Sea Water with the Help of Optical Lidar System.” In *SPIE 2048: Underwater Light Measurements*, 34–42. https://doi.org/10.1117/12.165508.

———. 1994a. “Applicability of Lidar Remote Sensing Methods for Vertical Structure Investigation of Ocean Optical Properties Distribution.” In *SPIE 2258: Ocean Optics XII*, edited by Jules S Jaffe, 2258:449–57. https://doi.org/10.1117/12.190087.

———. 1994b. “Lasers for Lidar Bathymetry and Oceanographic Research: Choice Criteria.” In *Proceedings of IGARSS ’94 - 1994 IEEE International Geoscience and Remote Sensing Symposium*, 1:475–77. Proceedings of the 1994 International Geoscience and Remote Sensing Symposium. St. Petersburg Inst of Fine, Mechanics Optics, St. Petersburg, Russia: IEEE. https://doi.org/10.1109/IGARSS.1994.399157.

———. 1996. “Optimization of Laser Wavelength in Oceanographic Lidars.” In *CIS Selected Papers: Laser Remote Sensing of Natural Waters: From Theory to Practice, November 1, 1996 - November 1*, 2964:128–37. St. Petersburg Institute of Fine Mechanics and Optics (PIFMO), Department of Laser Technology and Ecological Engineering, 14 Sablinskaya st., St. Petersburg, 197101, Russia: SPIE. https://doi.org/10.1117/12.258343.

Feigels, Viktor I, and Yuri I Kopilevich. 1993. “Ocean-Scientific for Windows, Basic Concepts, Description of the Theory.” EG&G Washington Analytical Service, Inc.

Ferguson, Gerald D. 1975. “Blue-Green Lasers for Underwater Applications.” In *SPIE Conference on Ocean Optics, Aug. 19-20*, 64:150–56. San Diego, CA: International Society for Optics and Photonics. https://doi.org/10.1117/12.954503.

Fernandez-Diaz, Juan Carlos, Craig L. Glennie, William E. Carter, R. L. Shresha, Michael P. Sartori, and Abhinav Singhania. 2014. “Multicolor Terrain Mapping Documents Critical Environments.” *Eos*. https://doi.org/10.1029/2016eo053489.

Fernandez-Diaz, Juan Carlos, Craig L. Glennie, William E. Carter, Ramesh L. Shrestha, Michael P. Sartori, Abhinav Singhania, Carl J. Legleiter, and Brandon T. Overstreet. 2014. “Early Results of Simultaneous Terrain and Shallow Water Bathymetry Mapping Using a Single-Wavelength Airborne LiDAR Sensor.” *IEEE Journal of Selected Topics in Applied Earth Observations and Remote Sensing* 7 (2): 623–35. https://doi.org/10.1109/JSTARS.2013.2265255.

Feygels, Viktor I., Minsu Kim, Joong Yong Park, and Yuri I. Kopilevich. 2014. “A Universal Parameter for the Comparison of Lidar Bathymeters.” In *15th Annual JALBTCX Airborne Coastal Mapping and Charting Worshop*. Mobile, AL. http://shoals.sam.usace.army.mil/Workshop_Files/2014/Day3_pdf/1100_Feygels.pdf.

Feygels, Viktor I., Yuri I. Kopilevich, Joong Yong Park, Minsu Kim, and Jennifer Aitken. 2014. “Particularities of Hydro Lidar Missions in the Asia-Pacific Region.” In *SPIE 9262: Lidar Remote*

Sensing for Environmental Monitoring XIV, edited by Upendra N. Singh and Kazuhiro Asai, 92620X. https://doi.org/10.1117/12.2069871.

Feygels, Viktor I., Joong Yong Park, Jennifer M. Wozencraft, Jennifer Aitken, Christopher Macon, Abhinav Mathur, Andy Payment, et al. 2013. "CZMIL (Coastal Zone Mapping and Imaging Lidar): From First Flights to First Mission through System Validation." In *Proceedings of SPIE*, edited by W W Arnone Hou RA, 8724:87240A-1-87240A – 15. Baltimore, MD: SPIE. https://doi.org/10.1117/12.2017935.

Feygels, Viktor I., C. Wayne Wright, Yuri I. Kopilevich, and Alexey I. Surkov. 2003a. "Narrow-Field-of-View Bathymetrical Lidar: Theory and Field Test." In *Ocean Remote Sensing and Imaging II*, SPIE 5155:1–11. San Diego, CA: SPIE. https://doi.org/10.1117/12.506951.

Feygels, Viktor I, Yuri I Kopilevich, Alexey Surkov, James K Yungel, and Michael J Behrenfeld. 2003. "Airborne Lidar System with Variable Field-of-View Receiver for Water Optical Properties Measurement." In *Ocean Remote Sensing and Imaging II, August 5, 2003 - August 6*, 5155:12–21. EG and G Technical Service Inc., Wallops Flight Facility, Wallops Island, VA 23337: SPIE. https://doi.org/10.1117/12.506976.

Feygels, Viktor I, Joong Yong Park, Jennifer Aitken, Minsu Kim, Andy Payment, and Vinod Ramnath. 2012. "Coastal Zone Mapping and Imaging Lidar (CZMIL): First Flights and System Validation." In *Remote Sensing of the Ocean, Sea Ice, Coastal Waters, and Large Water Regions 2012*, SPIE 8532. Edinburgh, U.K. https://doi.org/10.1117/12.2014617.

Feygels, Viktor I, Charles Wayne Wright, Yuri I Kopilevich, and Alexey I Surkov. 2003b. "Narrow-Field-of-View Bathymetrical Lidar: Theory and Field Test." In *Ocean Remote Sensing and Imaging II*. Vol. SPIE 5155. San Diego, CA: SPIE. https://doi.org/10.1117/12.506951.

Filin, Sagi. 2003. "Recovery of Systematic Biases in Laser Altimeters Using Natural Surfaces." *Photogrammetric Engineering and Remote Sensing* 69 (11): 1235–42. http://eserv.asprs.org/PERS/2003journal/nov/2003_nov_1235-1242.pdf.

Fuchs, Eran, and Abhinav Mathur. 2010. "Utilizing Circular Scanning in the CZMIL System." In *5-18 Apr 2010*, SPIE 7695. Optech International, 7225 Stennis Airport Rd, Kiln, MS 39556: SPIE. https://doi.org/10.1117/12.851936.

Fuchs, Eran, and Grady H. Tuell. 2010. "Conceptual Design of the CZMIL Data Acquisition System (DAS): Integrating a New Bathymetric Lidar with a Commercial Spectrometer and Metric Camera for Coastal Mapping Applications." In *SPIE 7695, Algorithms and Technologies for Multispectral, Hyperspectral, and Ultraspectral Imagery XVI, April 5-8, 2010*, edited by Sylvia S. Shen and Paul E. Lewis, SPIE 7695:769501. Orlando, FL: SPIE. https://doi.org/10.1117/12.851919.

Fugro Pelagos. 2008. "Determination of SHOALS-100T Hydrographic Lidar TPU Model and Target Detection Test: Shilsole Bay, Puget Sound, WA." Vol. Survey Rep. Sand Diego, CA: Fugro.

Gares, Paul A, Yong Wang, and Stephen A White. 2006. "Using LIDAR to Monitor a Beach Nourishment Project at Wrightsville Beach, North Carolina, USA." *Journal of Coastal Research* 22 (5): 1206–19. http://www.jstor.org.proxy.library.cornell.edu/stable/4300387.

Gluch, T., J. Piwowar, S. J. Till, and Robert A. O'Neil. 1983. "The Bathymetric Estimator Serach Technique for Processing Airborne Lidar Data." In *Proceedings of the 8th Candian Symposium on Remote Sensing*. Montreal, Quebec, CA.

Goetz, A. F.H., Gregg Vane, Jerry E Solomon, and Barrett N Rock. 1985. "Imaging Spectrometry for Earth Remote Sensing." *Science* 228 (4704): 1147–53. https://doi.org/10.1126/science.228.4704.1147.

Gonsalves, Michael Oliver. 2010a. “A Comprehensive Uncertainty Analysis and Method of Geometric Calibration for a Circular Scanning Airborne Lidar.” Edited by Stephan Howden. *ProQuest Dissertations and Theses*. Hattiesburg, MS: The University of Southern Mississippi. http://search.proquest.com/docview/835075165/fulltextPDF/BB0E363A81F246C3PQ/1?accountid=10267.

———. 2010b. “Flat-Bottomed World You Make Thoselidar Swirls around: Contrasting a Ship-Based Acoustic Patch Test with an Automated Calibration Routine for a Circular-Scanning Airborne Lidar System.” In *Canadian Hydrographic Conference 2010*. Quebec, QC, Canada.

Goodman, L.R. 1975. “Laser Hydrography User Requirements Workshop, Minutes.” NASA Wallops Flight Center, Wallops Island, VA: National Oceanic and Atmospheric Administration, Rockville, MD.

———. 1976. “Laser Hydrography Technical Review Workshop, Minutes.” Rockville, MD.

Gorchakova, G. I., and A. A. Isakov. 1976. “Some Results on Light Scattering in the Location Angles Domain (in Russian).” In *1st All-Union Conference on Atmospheric Optics*, 218–21. Tomsk, IOA SO AN SSSR.

Gordon, Howard R. 1982. “Interpretation of Airborne Oceanic Lidar: Effects of Multiple Scattering.” *Applied Optics* 21 (16): 2996–3001. https://doi.org/10.1364/AO.21.002996.

Gordon, Howard R., Otis B. Brown, and M. M. Jacobs. 1975. “Computed Relationships between the Inherent and Apparent Optical Oroperties of a Flat Homogeneous Ocean.” *Applied Optics* 14 (2): 417–27. https://doi.org/10.1364/AO.14.000417.

Gordon, Howard R., R. C. Smith, and J. Ronald. V. Zaneveld. 1979. “Introduction to Ocean Optics.” In *Proceedings of SPIE Ocean Optics VI, Vol. 208*. La Jolla, California.

Gordon, Howard R., and Menghua Wang. 1994. “Retrieval of Water-Leaving Radiance and Aerosol Optical-Thickness over the Oceans with SeaWIFS - A Preliminary Algorithm.” *Applied Optics* 33: 443–52.

Graham, T., K. Smith, J. Spittal, and G. R. West. 1999. “Improving the Efficiency, Safety and Economy of the New Zealand National Nautical Charting Program through the Integrated Use of the SHOALS System in a Multi-Sensor Survey.” In *Proc. U.S. Hydrographic Conference*, 11 pp. Mobile, AL.

Guenther, Gary C. 1977. “AOL Flight Test and Data Analysis Plan (Unpublished Manuscript).” Riverdale, MD.

———. 1985a. *Airborne Laser Hydrography: System Design and Performance Factors*. Rockville, MD: NOAA Professional Paper Series, National Ocean Service 1. http://shoals.sam.usace.army.mil/downloads/Publications/AirborneLidarHydrography.pdf.

———. 2001. “Airborne Lidar Bathymetry.” In *Digital Elevation Model Technologies and Applications: The DEM User’s Manual*, edited by D. Maune, 1st ed., 253–320. Bethesda, Maryland: ASPRS. http://www.asprs.org/a/publications/2009PubsCatalog.pdf.

———. 2007. “Airborne Lidar Bathymetry.” In *Digital Elevation Model Technologies and Applications: The DEM Users Manual, 2nd Edition*, edited by D F Maune, 2nd ed., 253–320. Bethessda, Maryland: ASPRS. http://www.asprs.org/a/publications/2009PubsCatalog.pdf.

Guenther, Gary C., M. W. Brooks, and Paul E. LaRocque. 1998. “New Capabilities of the SHOALS Airborne Lidar Bathymeter.” In *5th Int’l Conf. on Remote Sensing for Marine and Coastal Environments*, 1:47–55. ERIM International.

Guenther, Gary C., and Robert W. Thomas. 1984. “Effects Of Propagation-Induced Pulse Stretching In Airborne Laser Hydrography.” In *SPIE 0489: Ocean Optics VII*, edited by Marvin A. Blizard, 287–

96. Monterey, CA: International Society for Optics and Photonics. https://doi.org/10.1117/12.943315.

Guenther, Gary C., Robert W. L. Thomas, and Paul E. LaRocque. 1996. “Design Considerations for Achieving High Accuracy with the SHOALS Bathymetric Lidar System.” In *SPIE 2964, CIS Selected Papers: Laser Remote Sensing of Natural Waters: From Theory to Practice, November 1, 1996*, edited by Victor I Feigels and Y Kopelivich, 2964:54–71. St. Petersburg, Russia: Society of Photo-optical Instrumentation Engineers (SPIE). https://doi.org/10.1117/12.258353.

Guenther, Gary C. 1985b. *Airborne Laser Hydrography: System Design and Performance Factors*. Rockville, MD: NOAA Professional Paper Series, National Ocean Service 1. http://shoals.sam.usace.army.mil/downloads/Publications/AirborneLidarHydrography.pdf.

Guenther, Gary C, Thomas J Eisler, Jack L Riley, and Steven W Perez. 1996. “Obstruction Detection and Data Decimation for Airborne Laser Hydrography.” In *1996 Canadian Hydrographic Conference*. Halifax, Nova Scotia, Canada. http://handle.dtic.mil/100.2/ADA487820.

Habib, Ayman. 2009. “Accuracy, Quality Assurance, and Quality Control of LiDAR Data.” In *Topographic Laser Ranging and Scanning: Principles and Processing*, edited by Jie Shan and Charles K Toth, 269–94. Boca Raton, FL: CRC Press.

Habib, Ayman, A P Kersting, Ki In Bang, and Dong-Cheon Lee. 2010. “Alternative Methodologies for the Internal Quality Control of Parallel LiDAR Strips.” *Geoscience and Remote Sensing, IEEE Transactions On* 48 (1): 221–36. https://doi.org/10.1109/TGRS.2009.2026424.

Hamamatsu. 2007. *Photomultiplier Tubes: Basics and Applications*. Vol. 3rd. Hamamatsu Photonics, K.K. http://www.hamamatsu.com/resources/pdf/etd/PMT_handbook_v3aE-Chapter1.pdf.

Haner, D A, B T McGuckin, R T Menzies, C J Bruegge, and V Duval. 1998. “Directional-Hemispherical Reflectance for Spectralon by Integration of Its Bidirectional Reflectance.” *Applied Optics* 37: 3996–99. https://doi.org/10.1364/AO.37.003996.

Hapke, C.J., S. Malone, and M. Kratzmann. 2009. “National Assessment of Historical Shoreline Change: A Pilot Study of Historical Coastal Bluff Retreat in the Great Lakes, Erie, Pennsylvania.” In *USGS Open-File Report 2009-1042*.

Hapke, C.J., and D. Reid. 2007. “National Assessment of Shoreline Change Part 4: Historical Coastal Cliff Retreat along the California Coast.” In *USGS Open File Report 20047-1133*.

Helstrom, C. W. 1968. *Statistical Theory of Signal Detection*. Pergamon Press, Oxford.

Hickman, G. D., C. S. Gault, A. H. Ghovanlou, E. J. Friedman, and J. E. Hogg. 1974. “Airborne Laser Shallow Water Bathymetric System.” Technical Report ONR/NOAA/USGS Contract No. N000-14-71C-0202 Final Rep. Alexandria, VA: Sparcom, Inc.

Hickman, G. D., and A. H. Ghovanlou. 1973. *Preliminary Design Criteria*. Technical Report ONR/NOAA/USGS Contract No. N000-14-71C-0202. Alexandria, VA: Sparcom, Inc.

Hickman, G. D., J. E. Hogg, and A. H. Ghovanlou. 1972. *Pulsed Neon Laser Bathymetric Studies Using Simulated Delaware Bay Waters*. Technical Report ONR/NOAA/USGS Contract No. N000-14-71C-0202. Alexandria, VA: Sparcom, Inc.

Hickman, G D, and J E Hogg. 1969. “Application of an Airborne Pulsed Laser for near Shore Bathymetric Measurements.” *Remote Sensing of Environment* 1 (1): 47–58. https://doi.org/10.1016/S0034-4257(69)90088-1.

Holmes, Robert W. 1970. “The Secchi Disk in Turbid Coastal Waters.” *Limnology and Oceanography* 15 (5): 688–94. https://doi.org/10.4319/lo.1970.15.5.0688.

Holthuijsen, Leo H. 2007. *Waves in Oceanic and Coastal Waters*. Cambridge University Press.

IEC. 2014. *Safety of Laser Products. IEC 60825-1:2014*. International Electrotechnical Commission (IEC). https://webstore.iec.ch/publication/3587.

IHO. 2008. "IHO Standards for Hydrographic Surveys." Vol. S-44. Monaco: International Hydrographic Organization. http://www.thsoa.org/pdf/s44_4.pdf.

Imahori, Gretchen, Jeff Ferguson, Toshi Wozumi, David Dave Scharff, Shachak Pe'eri, Christopher E Parrish, Stephen A White, et al. 2013. "A Procedure for Developing an Acceptance Test for Airborne Bathymetric Lidar Data Application to NOAA Charts in Shallow Waters." *NOAA Technical Memorandum CS 32*. Vol. NOS CS-32. Silver Spring, MD: National Oceanographic and Atmospheric Administration. http://www.nauticalcharts.noaa.gov/csdl/publications/TM_NOS-CS32_FY13_Lidar.pdf.

Irish, Jennifer L., and W. Jeff Lillycrop. 1997. "Monitoring New Pass, Florida, with High Density Lidar Bathymetry." *Journal of Coastal Research* 13 (4): 1130–40. https://doi.org/10.2307/4298721.

———. 1999. "Scanning Laser Mapping of the Coastal Zone: The SHOALS System." *ISPRS Journal of Photogrammetry and Remote Sensing* 54 (2–3): 123–29. https://doi.org/10.1016/S0924-2716(99)00003-9.

Irish, Jennifer L., W. Jeff Lillycrop, and Larry E. Parson. 1997. "Accuracy of Sand Volumes as a Function of Survey Density." In *Part 1 (of 4), September 2, 1996 - September 6*, 3:3736–49. Proceedings of the 1996 25th International Conference on Coastal Engineering. US Army Engineer Waterways, Experiment Station, Vicksburg, United States: ASCE.

Irish, Jennifer L., J. K. McClung, and W. Jeff Lillycrop. 2000. "Airborne Lidar Bathymetry: The SHOALS System." *The International Navigation Association, PIANC Bulletin* 103: 43–45.

Irish, Jennifer L., J. E. Thomas, Larry E. Parson, and W. Jeff Lillycrop. 1996. "Monitoring Storm Response with High Density Lidar Bathymetry: The Effects of Hurricane Opal on Florida's Panhandle." In *Proc. 2nd Int. Airborne Remote Sensing Conf.*, III:723–32. San Francisco, CA.

Irish, Jennifer L., and T. E. White. 1998. "Coastal Engineering Applications of High-Resolution Lidar Bathymetry." *Coastal Engineering* 35 (1–2): 47–71. https://doi.org/10.1016/S0378-3839(98)00022-2.

Ishimaru, Akira. 1978. *Wave Propagation and Scattering in Random Media: Multiple Scattering, Turbulence, Rough Surfaces, and Remote Sensing*. *IEEE/OUP Series on Electromagnetic Wave Theory*. Vol. 2. Academic Press.

Jerlov, Nils Gunnar. 1976. *Marine Optics*. Amsterdam: Elsevier. http://www.sciencedirect.com/science/bookseries/04229894/14.

Johnson, Bruce D., and Robert C. Cooke. 1981. "Generation of Stabilized Microbubbles in Seawater." *Science* 213 (4504): 209–11. http://www.jstor.org/stable/1687157.

Karlsson, Torbjorn. 2011. "Uncertainties Introduced by the Ocean Surface When Conducting Airborne Lidar Bathymetry Surveys." Lund, Sweden: Lund Institute of Technology.

Keeler, R. N., and Bobby Lee Ulich. 1994. "Some Aspects of Wide-Beam Imaging Lidar Performance." In *SPIE 2258, Ocean Optics XII*, edited by Jules S Jaffe, 2258:480–500. SPIE. https://doi.org/10.1117/12.190091.

Kerker, Milton. 1969. *The Scattering of Light and Other Electromagnetic Radiation*. Vol. 16. New York: Elsevier. https://doi.org/10.1016/B978-0-12-404550-7.50001-4.

Kim, Hongsuk H., P. Cervenka, and C. Lankford. 1975. “Development of an Airborne Laser Bathymeter.” Vol. NASA TN D-. Washington, D.C.: NASA. https://ntrs.nasa.gov/archive/nasa/casi.ntrs.nasa.gov/19750025550.pdf.

Kim, Hongsuk H., and Philip T. Ryan. 1973. “The Use of Lasers for Hydrographic Studies.” In *NASA SP-375*, edited by Hongsuk H. Kim and Philip T. Ryan, 202. Conference Proceedings. Wallops Island, VA, VA: National Aeronautics and Space Administration. http://ntrs.nasa.gov/search.jsp?R=19750022452.

Kim, Minsu, Yuri I. Kopilevich, Viktor I. Feygels, Joong Yong Park, and Jennifer M. Wozencraft. 2016. “Modeling of Airborne Bathymetric Lidar Waveforms.” *Journal of Coastal Research* Spec.Issue (76): 18–30. https://doi.org/10.2112/SI76-003.

Kim, Minsu, Joong Yong Park, and Grady H. Tuell. 2010. “A Constrained Optimization Technique for Estimating Environmental Parameters from CZMIL Hyperspectral and Lidar Data.” In *SPIE 7695: Algorithms and Technologies for Multispectral, Hyperspectral, and Ultraspectral Imagery XVI, April 5-8, 2010*. Vol. 7695. SPIE. https://doi.org/10.1117/12.851989.

Kirk, J T O. 1994. “Light and Photosynthesis in Aquatic Ecosystems. 2nd Edition, Xvi, 509p. Cambridge University Press, 1994. Price £50.00.” *Journal of the Marine Biological Association of the United Kingdom*. Cambridge Journals Online. https://doi.org/10.1017/S0025315400044180.

Kopilevich, Yuri I. 2002. “Prediction of Bathymetric Lidar Performance with Ocean Scientific 2001 (052001) Simulation Code” 4488 (052001): 61–70.

Kopilevich, Yuri I., and Victor I. Feigels. 1993. “Characteristics of Light Backscattering by Sea Water and Lidar Sounding of Water Column.” In *SPIE 2048: Underwater Light Measurements*, 85–95. https://doi.org/10.1117/12.165494.

———. 2002. “On Multispectral Lidar Sounding of Ocean Waters.” In *SPIE 4488, Ocean Optics: Remote Sensing and Underwater Imaging*, edited by Robert J. Frouin and Gary D. Gilbert, 4488:51–60. San Diego, CA: International Society for Optics and Photonics. https://doi.org/Unsp 4488-12\r10.1117/12.452804.

Kopilevich, Yuri I., Viktor I. Feygels, and Alexey I. Surkov. 2003. “Mathematical Modeling of Input Signals for Oceanographic Lidar Systems.” In *SPIE 5155: Ocean Remote Sensing and Imaging II*, 5155:30–39. St. Petersburg Inst. Fine Mech./Opt., 14 Sablinskaya St., St. Petersburg, 197101, Russia: SPIE. https://doi.org/10.1117/12.506980.

Kopilevich, Yuri I., Viktor I. Feygels, Grady H. Tuell, and Alexey I. Surkov. 2005a. “Measurement of Ocean Water Optical Properties and Seafloor Reflectance with Scanning Hydrographic Operational Airborne Lidar Survey (SHOALS): I. Theoretical Background.” In *SPIE 5885, Remote Sensing of the Coastal Oceanic Environment, July 31, 2005 - August 1*, 5885:1–9. Optech International, Inc., 7225 Stennis Airport Drive, Kiln, MI 39556, United States: SPIE. https://doi.org/10.1117/12.618923.

Kopilevich, Yuri I, Viktor I Feygels, Grady H Tuell, and Alexey Surkov. 2005b. “Measurement of Ocean Water Optical Properties and Seafloor Reflectance with Scanning Hydrographic Operational Airborne Lidar Survey (SHOALS): I. Theoretical Background.” In *SPIE 5885, Remote Sensing of the Coastal Oceanic Environment, July 31, 2005 - August 1*, 5885:1–9. Optech International, Inc., 7225 Stennis Airport Drive, Kiln, MI 39556, United States: SPIE. https://doi.org/10.1117/12.618923.

Kopilevich, Yuri I, M E Kononenko, and E I Zadorozhnaya. 2010. “The Effect of the Forward-Scattering Index on the Characteristics of a Light Beam in Sea Water.” *Journal of Optical Technology* 77 (10): 598–601. https://doi.org/10.1364/JOT.77.000598.

———. 2011. “Prediction of Bathymetric Lidar Performance with the Account for the VSF Shape.” In *ONW 2011: Current Problems in Optics of Natural Waters*, 183–86. St. Petersburg, Russia.

Kopilevich, Yuri I, and A G Surkov. 2008. “Mathematical Modeling of the Input Signals of Oceanological Lidars.” *Journal of Optical Technology* 75 (5): 321–26. https://doi.org/10.1364/JOT.75.000321.

Koschmieder, H. 1924. “Theorie Der Horizontalen Sichtweite.” *Beiträge Zur Physik Der Freien Atmosphäre* 12: 171–81.

Kovalev, Vladimir A. 2004. “Elastic Lidar : Theory, Practice, and Analysis Methods.” Hoboken, N.J.: John Wiley. http://proxy.library.cornell.edu/login?url=http://onlinelibrary.wiley.com/book/10.1002/0471643173.

Krekova, Margarita M., G. M. Krekov, and Vitalii S. Shamanaev. 2004. “Influence of Air Bubbles in Seawater on the Formation of Lidar Returns.” *Journal of Atmospheric and Oceanic Technology* 21 (5): 819–24. https://doi.org/10.1175/1520-0426(2004)021<0819:IOABIS>2.0.CO;2.

Kuriksha, A. A. 1973. “Quantum Optics and Quantum Location (Statistical Theory).” *Soviet Radio*.

LaRocque, Paul E. 2012. “Aquarius System: Compact Shoreline Mapper.” In *13th Annual JALBTCX Coastal Mapping & Charting Workshop*. Chicago, Illinois: JALBTCX.

LaRocque, Paul E., and Ahmed Shaker Abdel-Rahman. 2014. “New Multi-Wavelength Lidar System for 3D Land Classification & Coastal Bathymetry.” In *European Lidar Mapping Forum*. Amsterdam.

LaRocque, Paul E., John R. Banic, and A. Grant Cunningham. 2004a. “Design Description and Field Testing of the SHOALS-10001 Airborne Bathymeter.” In *Laser Radar Technology and Applications IX, April 13, 2004 - April 15*, 5412:162–84. Optech Incorporated, 100 Wildcat Road, Toronto, Ont. M3J 2Z9, Canada: SPIE. https://doi.org/10.1117/12.564924.

LaRocque, Paul E., Murtaza Safri, Wai Yeung Yan, and Ahmed Shaker. 2016. “New Hardware and Software for the Multispectral Optech Titan.” In *17th Annual JALBTCX Airborne Coastal Mapping and Charting Technical Workshop*. Silver Spring, MD.

LaRocque, Paul E, John R Banic, and A G Cunningham. 2004b. “Design Description and Field Testing of the SHOALS-1000 Airborne Bathymeter.” In *Laser Radar Technology and Applications IX*, SPIE 5412:162–84. SPIE. https://doi.org/10.1117/12.564924.

Lebed’ko, E. G., L. F. Porfir’ev, and F. I. Hajtun. 1984. *Theory and Design of Optical-Electronic Systems*. Leningrad: Mashinostoenie (in Russian).

Lee, Mark. 2003. “Benthic Mapping of Coastal Waters Using Data Fusion of Hyperspectral Imagery and Airborne Laser Bathymetry.” University of FLorida. http://etd.fcla.edu/UF/UFE0000730/lee_m.pdf.

Lee, Mark, and Grady H. Tuell. 2003. “A Technique for Generating Bottom Reflectance Images from SHOALS Data.” In *U.S. HYDRO 2003*. New Orleans, LA.

Levin, BR. 1960. *Theory of Random Processes and the Applications in Radiotechnique (In Russion)*. Soviet Radio, Moscow.

Levin, Iosif M., and O. V. Kopelevich. 2003. “Relationships between Seawater Optical Properties at 550 Nm.” In *Current Probles in Optics of Natural Waters (ONW 2003)*, edited by Iosif M Levin and Gary D Gilbert. St. Petersburg, Russia.

Levis, C. A., W. G. Swarner, C. E. Prettyman, and G. W. Reinhardt. 1973. “An Optical Radar for Airborne Use over Natural Waters.” In *Proc. Oceans ’73*, 76–83. IEEE. https://doi.org/10.1109/OCEANS.1973.1161234.

Li, Wei, Kecheng Yang, Min Xia, Jionghui Rao, and Wei Zhang. 2009. “Influence of Characteristics of Micro-Bubble Clouds on Backscatter Lidar Signal.” *Opt.Express* 17 (20): 17772–83. https://doi.org/10.1364/OE.17.017772.

Lillycrop, W. Jeff, and John R. Banic. 1992. “Advancements in the US Army Corps of Engineers Hydrographic Survey Capabilities: The SHOALS System.” *Marine Geodesy*, Mar. Geod. (USA), 15 (2–3): 177–85. https://doi.org/10.1080/01490419209388053.

Lillycrop, W. Jeff, and L. L. Estep. 1995. “Generational Advancements in Coastal Surveying and Mapping.” *Sea Technology* 36 (6): 10–16.

Lillycrop, W. Jeff, Jennifer L. Irish, and Larry E. Parson. 1997. “SHOALS System.” *Sea Technology* 38 (6): 17–25.

Lillycrop, W. Jeff, Larry E. Parson, and Jennifer L. Irish. 1996. “Development and Operation of the SHOALS Airborne Lidar Hydrographic Survey System.” In *CIS Selected Papers: Laser Remote Sensing of Natural Waters: From Theory to Practice, November 1, 1996 - November 1*, 2964:26–37. US Army Engineer Waterways Experiment Station, Coastal Engineering Research Center, 3909 Halls Ferry Road, Vicksburg, MS 39180-6199, United States: SPIE. https://doi.org/10.1117/12.258351.

Lillycrop, W. Jeff, Robert W. Pope, and Geraint R. West. 2000. “Rapid Environmental Assessment with Lidar.” *GPS World: News and Applications of the Global Positioning System*, November 2000.

Liu, Jung-Kung, Rongxing Li, Sagar Deshpande, Xutong Niu, and Tian-Yuan Shih. 2009. “Estimation of Blufflines Using Topographic Lidar Data and Orthoimages.” *Photogrammetric Engineering & Remote Sensing* 75 (1): 69–79. https://www.asprs.org/wp-content/uploads/pers/2009journal/january/2009_jan_57-68.pdf.

Lockhart, Carol, Arumugam Dushan, and David Millar. 2005. “Meeting Hydrographic Charting Specifications with SHOALS-1000T Airborne Lidar Bathymeter.” In *U.S. Hydro 2005*. San Diego, CA. http://www.thsoa.org/us05papers.htm.

Loisel, Hubert, Xavier Meriaux, Jean-François Berthon, and Antoine Poteau. 2007. “Investigation of the Optical Backscattering to Scattering Ratio of Marine Particles in Relation to Their Biogeochemical Composition in the Eastern English Channel and Southern North Sea.” *Limnology and Oceanography* 52 (2): 739–52.

Luchinin, Alexander G. 1987. “Some Properties of a Backscattered Signal in Laser Sounding of the Upper Ocean through a Rough Surface.” *Izvestiya, Atmospheric and Ocean Physics (in Russian)* 23: 725–29.

Lutomirski, R., S. Halmbach, Thomas P. Curran, and J. Gibbons. 1994. “Performance Modelling and Analysis of the Ocean Water Lidar (OWL) Hydrographic System.” In *U.S. Hydrographic Conference*, 200–205.

Lyzenga, David R. 1978. “Passive Remote Sensing Techniques for Mapping Water Depth and Bottom Features.” *Applied Optics* 17 (3): 379–83. http://ao.osa.org/abstract.cfm?URI=ao-17-3-379.

Maffione, Robert A., and David R. Dana. 1996. “In-Situ Characterization of Optical Backscattering and Attenuation for Lidar Applications.” In *Laser Remote Sensing of Natural Waters: From Theory to Practice*, 2964:152–61. St. Petersburg, Russia: SPIE 2964. https://doi.org/10.1117/12.258345.

Malone, A. K., M. J. Casey, and D. Monahan. 1983. “Scanning Lidar Bathymeter: (1) Deployment Strategies and (2) Data Processing.” *Lighthouse: Journal of the Candian Hydrographers Assn.* 27: 2–12. http://fohcan.org/lighthouse/ed27high.pdf.

Mandlburger, Gottfried, Martin Pfennigbauer, M. Wieser, U. Riegl, and N. Pfeifer. 2016. “Evaluation of a Novel UAV-Borne Topo-Bathymetric Laser Profiler.” In *ISPRS - International Archives of the Photogrammetry, Remote Sensing and Spatial Information Sciences*, XLI-B1:933–39. Copernicus GmbH. https://doi.org/https://doi.org/10.5194/isprs-archives-XLI-B1-933-2016.

McClung, J. K. 1998. “High Density Lidar Data: A Monitoring Tool for East Pass Florida.” In *Proc. 5th Int’l Conf. on Remote Sensing for Marine and Coastal Environmnents*, I:75–82. San Diego, CA.

McKean, Jim, Dave Nagel, Daniele Tonina, Philip Bailey, Charles Wayne Wright, Carolyn Bohn, and Amar Nayegandhi. 2009. “Remote Sensing of Channels and Riparian Zones with a Narrow-Beam Aquatic-Terrestrial LIDAR.” *Remote Sensing* 1 (4): 1065–96. https://doi.org/10.3390/rs1041065.

McLean, John W., and Jonathan D. Freeman. 1996. “Effects of Ocean Waves on Airborne Lidar Imaging.” *Applied Optics* 35 (18): 3261–69. https://doi.org/10.1364/AO.35.003261.

McLean, John W., and J. T. Murray. 1998. “Streak Tube Lidar Allows 3-D Surveillance.” *Laser Focus World*, 171–76.

Measures, Raymond M. 1984. *Laser Remote Sensing: Fundamentals and Applications*. 1st ed. New York: John Wiley & Sons.

———. 1992. *Laser Remote Sensing: Fundamentals and Applications*. 2nd ed. Vol. 2nd. New York: John Wiley & Sons. https://doi.org/0471081930, 9780471081937.

Medwin, Herman. 1970. “In Situ Acoustic Measurements of Bubble Populations in Coastal Ocean Waters.” *Journal of Geophysical Research* 75 (3): 599–611. https://doi.org/10.1029/JC075i003p00599.

Miles, M. K., W. Jeff Lillycrop, M. F. Kidby, and Larry E. Parson. 1994. “Transfer of the SHOALS System Technology to the U.S. Army Corps of Engineers.” In *U.S. Army Corps of Engineers 1994 Training Symposium, Survey and Mapping, Remote Sensing/GIS, SM:2D 1*.

Mobley, Curtis D. 1994. *Light and Water: Radiative Transfer in Natural Waters*. San Diego: Academic Press. http://www.curtismobley.com/LightandWater.zip.

Mobley, Curtis D., Emmanuel Boss, and Collin Roesler. 2013. “Ocean Optics Web Book.” 2013.

Mobley, Curtis D., and Rudolph W. Preisendorfer. 1988. “A Numerical Model for the Computation of Radiance Distributions in Natural Waters with Wind-Roughened Surface.” Vol. NOAA Tech. Seattle, WA: NOAA. http://www.pmel.noaa.gov/publications/search_abstract.php?fmContributionNum=813.

Mohr, M. C., J. Pope, and J. K. McClung. 1999. “Coastal Response to a Detached Breakwater System; Presque Isle, Pennsylvania, USA.” In *Proc. 4th International Symposium on Coastal Engineering and Science of Coastal Sediment Processes*, 3:2010–25. Long Island, NY: American Society of Civil Engineers.

Monahan, Edward C., and Mingzhi Lu. 1990. “Acoustically Relevant Bubble Assemblages and Their Dependence on Meteorological Parameters.” *IEEE Journal of Oceanic Engineering* 15 (4): 340–49. https://doi.org/10.1109/48.103530.

Monahan, Edward C., and IognáidÓ Muircheartaigh. 1980. “Optimal Power-Law Description of Oceanic Whitecap Coverage Dependence on Wind Speed.” *Journal of Physical Oceanography* 10 (12): 2094–99. https://doi.org/10.1175/1520-0485(1980)010<2094:OPLDOO>2.0.CO;2.

Monahan, Edward C., and G. Mac Niocaill. 1986. “Oceanic Whitecaps and Their Role in the Air-Aea Exchange Process.” In , edited by Edward C. Monahan and Gearóid Mac Niocaill. Vol. 2. Oceanographic Sciences Library. Dordrecht: Springer Netherlands. https://doi.org/10.1007/978-94-009-4668-2.

Monin, A S. 1983. “Physical Optics of the Ocean.” In *Ocean Optics*, edited by A S Monin. Vol. 1. Nauka, Moscow (in Russian).

Moniteq, Ltd. 1983a. “Determination of Parameters of Significance for Accuracy Optimization of a Scanning Lidar Bathymeter.” Concord, Ontario, Canada: Canadian Hydrographic Service.

———. 1983b. “Development of Correction Algorithms for Accurate Interpretation of Lidar Bathymetry Data.” Concord, Ontario, Canada: Canadian Hydrographic Service Contract No. 31SS.FP802-1-2168.

Moran, Steven E., Bobby Lee Ulich, William P. Elkins, Richard J. Strittmatter, and Michael J. DeWeert. 1997. “Intensified CCD (ICCD) Dynamic Range and Noise Performance.” In *SPIE 3173: Ultrhigh- and High-Speed Photography and Image-Based Motion Measurement*, 28 pages. SPIE. https://doi.org/10.1117/12.294535.

Morel, André, and Hubert Loisel. 1998. “Apparent Optical Properties of Oceanic Water: Dependence on the Molecular Scattering Contribution.” *Applied Optics* 37 (21): 4765–76. https://doi.org/10.1364/AO.37.004765.

Nayegandhi, Amar, J. C. Brock, and C. Wayne Wright. 2005. “Classifying Vegetation Using NASA’s Experimental Advanced Airborne Research Lidar (EAARL) at Assateague Island National Seashore.” In *Proc. ASPRS Annual Conference, Baltimore, MD, [CD-ROM].*, Session 25, paper ID 500001, 15 pp. Baltimore, MD.

Nayegandhi, Amar, John C. Brock, and C. Wayne Wright. 2009. “Small-Footprint, Waveform-Resolving Lidar Estimation of Submerged and Sub-Canopy Topography in Coastal Environments.” *International Journal of Remote Sensing* 30 (4): 861–878. https://doi.org/10.1080/01431160802395227.

Nayegandhi, Amar, John C. Brock, C. Wayne Wright, and Michael J. O’Connell. 2006. “Evaluating A Small Footprint, Waveform-Resolving Lidar Over Coastal Vegetation Communities.” *Photogrammetric Engineering and Remote Sensing* 72 (12): 1407–17. https://doi.org/0099-1112.

NODC. 2013. “World Ocean Atlas 2013.” US Department of Commerce, NOAA National Centers for Environmental Information. 2013. http://www.nodc.noaa.gov/OC5/woa13f/index.html.

Nordstrom, G. 2000. “The Swedish Hydrogaphic Service on the Eve of a New Millenium.” *Integrated Coastal Zone Management* Spring: 37–40.

Ocean Surveys, Inc. 2009. “Shallow Water Multibeam Hydrographic and Side Scan Sonar Survey.” Vol. Field No: Old Saybrook, CT: NOAA/NOS/OCS Descriptive Report. http://surveys.ngdc.noaa.gov/mgg/NOS/coast/H10001-H12000/H11896/DR/H11896.pdf.

OCS. 2014. “FIeld Procedures Manual.” National Oceanic and Atmospheric Administration: Office of Coast Survey. http://www.nauticalcharts.noaa.gov/hsd/fpm/2014_FPM_Final.pdf.

Olesen, B, and K Sand-Jensen. 1993. “Seasonal Acclimatization of Eelgrass Zostera Marina Growth to Light.” *Marine Ecology Program Series* 94 (1): 91–99. https://doi.org/10.3354/meps094091.

Open_University. 2005. *Waves, Tides, and Shallow-Water Processes*. Edited by Gerry Bearman. *Open University Oceanography Series*. Vol. 4. Boston, MA: Butterworth-Heinmann.

Optech. 2005. “Technical Report for JALBTCX.” Vol. DACW42-01-. Toronto, Ontario, CA: Optech Incorporated. ftp://140.116.80.210/array1/for_test/toCHS/%B2Ĥ@%A6%B8%B4%C1%A4%A4%B3%F8%A7i%AE%D1/%AA%FE%A5%F3%A4T.%B3z%A4%F4%A5%FA%B9F%B0ѦH%E5%C4m%B9q%A4l%C0%C9/Optech_2004_CHARTS_Field_Test_Report.pdf.

Ott, L. M. 1965. “Underwater Ranging Measurements Using Blue-Green Laser.” Warminster, PA (Confidential): Naval Air Develpment Center, Report No. NADC-AE-6519.

Ott, L. M., H. Krumboltz, and A. K. Witt. 1971a. “Detection of Submerged Submarine by an Optical Ranging and Detection System and Detection of Pulses by a Submarine.” In *8th U.S. Navy Symposium of Military Oceanography, Vol. II*. Naval Postgraduate School, Monterey, CA (CONFIDENTIAL).

Ott, L M, H Krumboltz, and A K Witt. 1971b. “Detection of Submerged Submarine by an Optical Ranging and Detection System and Detection of Pulses by a Submarine.” In *8th U.S. Navy Symposium of Military Oceanography, Vol. II*. Naval Postgraduate School, Monterey, CA.

Palaseanu-Lovejoy, Monica, Jeffrey J. Danielson, Cindy Thatcher, Amy C. Foxgrover, Patrick L. Barnard, John C. Brock, and Adam Young. 2016. “Automatic Delineation of Seacliff Limits Using Lidar-Derived High-Resolution DEMs in Southern California.” *Journal of Coastal Research* SI (76): 162–73. https://doi.org/10.2112/SI76-014.

Park, Joong Yong, Vinod Ramnath, Viktor I. Feygels, Minsu Kim, Abhinav Mathur, Jennifer Aitken, and Grady H. Tuell. 2010a. “Active-Passive Data Fusion Algorithms for Seafloor Imaging and Classification from CZMIL Data,” 769515. http://dx.doi.org/10.1117/12.851991.

Park, Joong Yong, Vinod Ramnath, Viktor I Feygels, Minsu Kim, Abhinav Mathur, Jennifer Aitken, and Grady H Tuell. 2010b. “Active-Passive Data Fusion Algorithms for Seafloor Imaging and Classification from CZMIL Data,” 769515. http://dx.doi.org/10.1117/12.851991.

Parson, Kevin J., and Michael P. Harvan. 1990. “Power Oscillator as a LIDAR Transmitter.” In *SPIE 1302: Ocean Optics X*, edited by Richard W. Spinrad, 583–90. Orlando, FL: International Society for Optics and Photonics. https://doi.org/10.1117/12.21472.

Pastol, Yves. 2011. “Use of Airborne LIDAR Bathymetry for Coastal Hydrographic Surveying: The French Experience.” *Journal of Coastal Research* 62 (March): 6–18. https://doi.org/10.2112/SI_62_2.

Pe’eri, Shachak, James V Gardner, Larry G Ward, and John Ru Morrison. 2011. “The Seafloor: A Key Factor in Lidar Bottom Detection.” *IEEE Transactions on Geoscience and Remote Sensing* 49 (3): 1150–57. https://doi.org/10.1109/TGRS.2010.2070875.

Pe’eri, Shachak, Lynnette V Morgan, William D Philpot, and Andrew A Armstrong. 2011. “Land-Water Interface Resolved from Airborne LIDAR Bathymetry (ALB) Waveforms.” *Journal of Coastal Research* SI 62: 75–85. https://doi.org/10.2112/SI_62_8.

Pe’eri, Shachak, and William D. Philpot. 2007. “Increasing the Existence of Very Shallow-Water LIDAR Measurements Using the Red-Channel Waveforms.” *IEEE Transactions on Geoscience and Remote Sensing* 45 (5): 1217–23. https://doi.org/10.1109/TGRS.2007.894584.

Penny, Michael F. 1982. “Laser Hydrography in Australia.” In *Proceedings of the International Conference on Lasers ’81*.

Penny, Michael F., Ralph H. Abbot, D. M. Phillips, Brian Billard, D. Rees, D. W. Faulkner, D. G. Cartwright, et al. 1986. “Airborne Laser Hydrography in Australia.” *Applied Optics* 25 (13): 2046–58. https://doi.org/10.1364/AO.25.002046.

Petrie, Gordon, and Charles K Toth. 2009. “Terrestrial Laser Systems.” In *Topographic Laser Ranging and Scanning: Principles and Processing*, edited by Jie Shan and Charles K Toth, 87–128. Boca Raton, FL: CRC Press,Taylor and Francis Group.

Pfennigbauer, Martin, and Frank Steinbacher. 2012. “Riverbed Surveying - High Resolution Shallow Water Mapping from an Airborne Platform.” *Hydro International* 16.

Pfennigbauer, Martin, Clifford Wolf, Josef Weindopf, and Andreas Ullrich. 2014. “Online Waveform Processing for Demanding Target Situatons.” In *Proc. SPIE 9080: Laser Radar Technology and Applications XIX and Atmospheric Propagation XI*. Baltimore, MD: SPIE. https://doi.org/10.1117/12.2052994.

Philpot, William D. 1989. “Bathymetric Mapping with Passive Multispectral Imagery.” *Applied Optics* 28 (8): 1569–78. https://doi.org/10.1364/AO.28.001569.

Pike, E. R. 1974. *Photon Correlation and Light Beating Spectroscopy: Introductory Lecture*. Edited by H. Z. Cummins and E. R. Pike. Boston, MA: Springer US. https://doi.org/10.1007/978-1-4615-8906-8.

Pilgrim, D. A. 1984. “The Secchi Disk in Principle and in Use.” *The Hydrographic Journal* 33 (July): 25–30.

Pittman, Simon J., Bryan M. Costa, and Timothy A. Battista. 2009. “Using Lidar Bathymetry and Boosted Regression Trees to Predict the Diversity and Abundance of Fish and Corals.” *Journal of Coastal Research* 25 (6): 27–38. https://doi.org/10.2112/SI53-004.1.

Pope, J., and W. Jeff Lillycrop. 1988. “Development of a Helicopter Lidar Bathymeter System.” In *Proc. U.S. Army Corps of Engineers Surveying Conf.*, 213–16. Ft. Belvoir, VA.

Pope, Robert W., B. A. Reed, Geraint R. West, and W. Jeff Lillycrop. 1997. “Use of an Airborne Laser Depth Sounding System in a Complex Shallow-Water Environment.” In *Proc. 15th Int’l Hydro Conference*, 10 pgs. Monaco.

Preisendorfer, Rudolph W. 1976. *Hydrologic Optics*. Vol. 1: Basic P. Honolulu, Hawaii: National Oceanic and Atmospheric Administration Environmental Research Laboratories. http://archive.org/details/hydrologicopt00prei.

Preisendorfer, Rudolph W., and Curtis D. Mobley. 1985. “Unpolarized Irradiance Reflectances and Glitter Patterns of Random Capillary Waves on Lakes and Seas, by Monte Carlo Simulation.” *NOAA Tech. Memo*. Vol. ERL PMEL-6. http://www.pmel.noaa.gov/publications/search_abstract.php?fmContributionNum=784.

Prettyman, C. E., and M. D. Cermak. 1969. “Time Variation of the Rough Ocean Surface and Its Effect on an Incident Laser Beam.” *Geoscience Electronics, IEEE Transactions on Geoscience Electronics* 7 (4): 235–43. https://doi.org/10.1109/TGE.1969.271357.

Quan, Xiaohong, and Edward S. Fry. 1995. “Empirical Equation for the Index of Refraction of Seawater.” *Applied Optics* 34 (18): 3477–80. https://doi.org/10.1364/AO.34.003477.

Raiffa, Howard. 1968. *Applied Statistical Decision Theory*. Cambridge, Mass.: M.I.T. Press. http://newcatalog.library.cornell.edu/catalog/31356.

Ramnath, Vinod, Viktor I. Feygels, Yuri I. Kopilevich, Joong Yong Park, and Grady H. Tuell. 2010. “Predicted Bathymetric Lidar Performance of Coastal Zone Mapping and Imaging Lidar (CZMIL).” In *Algorithms and Technologies for Multispectral, Hyperspectral, and Ultraspectral Imagery XVI, April 5, 2010 - April 8*, 7695:The Society of Photo-Optical Instrumentation Engin. Optech International Inc., 7225 Stennis Airport Drive, Kiln, MS 39556, United States: SPIE. https://doi.org/10.1117/12.851978.

Rees, Simon M., Jacqueline Staromlynska, Michael P. Gillyon, and Julianne R. Davy. 1996. “High-Performance Optical Filter for the Australian Laser Airborne Depth Sounder.” In *SPIE 2964: Laser Remote Sensing of Natural Waters: From Theory to Practice*, edited by Victor I. Feigels and Yurij I. Kopilevich, 138–44. St. Petersburg, Russia: International Society for Optics and Photonics. https://doi.org/10.1117/12.258344.

Reif, Molly K., Christopher L. Macon, and Jennifer M. Wozencraft. 2011. “Post-Katrina Land-Cover, Elevation, and Volume Change Assessment along the South Shore of Lake Pontchartrain, Louisiana, USA.” *Journal of Coastal Research*, 30–39. https://doi.org/10.2112/SI_62_4.

Reif, Molly K., C. Piercy, J. Jarvis, B. Sabol, Christopher L. Macon, R. Lloyd, H. Colarusso, Heidi M. Dierssen, and Jennifer Aitken. 2012. *A Case Study of Ground Truth Sampling to Support Sensing Research and Development: Submersed Aquatic Vegetation Species Discrimination Using an Airborne Hyperspectral/Lidar System*. DOER Technical Notes Collection. Vicksburg, MS: U.S. Army Engineer Research and Development Center.

Reif, Molly K, Jennifer M Wozencraft, Lauren M Dunkin, Charlene S Sylvester, and Christopher L Macon. 2013. “A Review of U.S. Army Corps of Engineers Airborne Coastal Mapping in the Great Lakes.” *Journal of Great Lakes Research* 39: 194–204. https://doi.org/https://doi.org/10.1016/j.jglr.2012.11.002.

Renslow, Michael. 2012. *Manual of Airborne Topographic Lidar*. Vol. First. Bethesda, Maryland: American Society of Photogrammetry and Remote Sensing.

Robertson, William, V, Dean Whitman, Keqi Zhang, and Stephen P Leatherman. 2004. “Mapping Shoreline Position Using Airborne Laser Altimetry.” *Journal of Coastal Research* 20 (3): 884–92. http://www.jstor.org.proxy.library.cornell.edu/stable/4299347.

Robertson, Quin, Lauren M. Dunkin, Zhifei Dong, Jennifer M. Wozencraft, and Keqi Zhang. 2018. “Florida and US East Coast Beach Change Metrics Derived from LiDAR Data Utilizing ArcGIS Python Based Tools.” In *Beach Management Tools - Concepts, Methodologies and Case Studies*, 239–58. Coastal Research Library. Springer, Cham.

Rosati, Julie Dean. 2005. “Concepts in Sediment Budgets.” *Journal of Coastal Research* 212 (March): 307–22. https://doi.org/10.2112/02-475A.1.

Ross, Monte. 1966. *Laser Receivers: Devices, Techniques, Systems*. New York, NY: Wiley.

Ryan, J. S., and Robert A. O’Neil. 1980. “Field Trials of an Airborne Lidar Bathymeter.” In *Proceedings of the 19th Annual Canadian Hydrographic Conference*. Halifax, Nova Scotia, CA: Canadian Hydrographers Assn.

Sakitt, B. 1973. “Indices of Discriminability.” *Nature* 241 (5385): 133–34. https://doi.org/10.1038/241133a0.

Saleh, Bahaa E. A., and Malvin Carl Teich. 1991a. *Fundamentals of Photonics*. 1st ed. New York: Wiley-Interscience. http://web.ebscohost.com/ehost/ebookviewer/ebook/nlebk_26193_AN?sid=305fb078-c2e9-47a7-a406-694f63a9402c@sessionmgr198&vid=1&format=EB.

Saleh, Bahaa E A, and Malvin C Teich. 1991b. *Fundamentals of Photonics*. New York: Wiley-Interscience. http://web.ebscohost.com/ehost/ebookviewer/ebook/nlebk_26193_AN?sid=305fb078-c2e9-47a7-a406-694f63a9402c@sessionmgr198&vid=1&format=EB.

Saleh, Bahaa E A, and Malvin Carl Teich. 2007. *Fundamentals of Photonics*. 2nd ed. New York: Wiley-Interscience. http://web.ebscohost.com/ehost/ebookviewer/ebook/nlebk_26193_AN?sid=305fb078-c2e9-47a7-a406-694f63a9402c@sessionmgr198&vid=1&format=EB.

Sallenger, Asbury H., Hilary F. Stockdon, Laura A. Fauver, Mark Hansen, David Thompson, C. Wayne Wright, and W. Jeff Lillycrop. 2006. “Hurricanes 2004: An Overview of Their Characteristics and Coastal Change.” *Estuaries and Coasts; Port Republic* 29 (6): 880–88. https://doi.org/http://dx.doi.org.proxy.library.cornell.edu/10.1007/BF02798647.

Sallenger, Asbury H., C. Wayne Wright, and W. Jeff Lillycrop. 2005. “Coastal Impacts of the 2004 Hurricanes Measured with Airborne Lidar; Initial Results.” *Shore and Beach* 73 (2&3): 10–14.

Schenk, Toni. 2001. “Modeling and Recovering Systematic Errors in Airborne Laser Scanners.” *Technical Notes in Photogrammetry*. Vol. 19. Columbus, Ohio: The Ohio State University.

Segelstein, David J. 1981. “The Complex Refreactive Index of Water.” *Ph.D. Dissertation, Department of Physics, University of Missouri-Kansas City*. Department of Physics, University of Missouri-Kansas City, MO.

Setter, C., and R. J. Willis. 1994. “LADS—From Development to Hydrographic Operations.” In *US Hydro. Conference*, 134–39.

Shaker, Ahmed, Wai-Yeung Yan, Paul E. LaRocque, Salem Morsy, and Nagwa El-Ashmawy. 2015. “Multi-Wavelength Lidar Data: Potentials of the New Technology in Land Cover Classification.” In *ASPRS Annual Conference*. Tampa, FL: ASPRS.

Shannon, John G. 1975. “Correlation of Beam and Diffuse Attenuation Coefficients Measured in Selected Ocean Waters.” In *Ocean Optic IV*, 64:3–11. San Diego, CA: International Society for Optics and Photonics. https://doi.org/10.1117/12.954489.

Short, Frederick T, and Sandy Wyllie-Echeverria. 1996. “Natural and Human-Induced Disturbance of Seagrasses.” *Environmental Conservation* 23 (01): 17. https://doi.org/10.1017/S0376892900038212.

Sinclair, Mark J. 1997. “LADS Mk II Aircraft Launched.” *Hydro International*, December 1997.

———. 1998. “Australians Get on Board with New Laser Airborne Depth Sounder.” *Sea Technology*, 1998.

Sinclair, Mark J., D. J. Stephenson, and T. Spurling. 1999. “High Resolution Surveys in Shallow Water - LADS.” In *Proc. Shallow Survey 99*, 9 pp. Sydney, Australia: Australian Defence Science and Technology Organization.

Sizgoric, Sebastian, John R. Banic, and Gary C. Guenther. 1992. “1970-1990: Airborne Lidar Hydrography Status.” In *EARSeL Advances in Remote Sensing, Vol. 1, No.2 - II*. Firenza, Italy: EARSeL. http://www.earsel.org/Advances/1-2-1992/1-2_15_Sizgoric.pdf.

Skogvik, J., and Axelsson Rune. 2001. “Experience and Results from Swedish Laser Surveys and Post-Processing of Laser Bathymetry Data.” In *Proc. Hydro 2001, Special Pub. 42*, Paper 20. Norwich, England.

Smart, Jeffrey H., and Kang Hyon K. Kwon. 1996. “Comparisons between In-Situ and Remote Sensing Estimates of Diffuse Attenuation Profiles.” In *SPIE 2964: Laser Remote Sensing of Natural Waters: From Theory to Practice*, edited by Victor I. Feigels and Yurij I. Kopilevich, 2964:100–109. International Society for Optics and Photonics. https://doi.org/10.1117/12.258356.

Snyder, G. I. 2012. “National Enhanced Elevation Assessment at a Glance.” Vol. U.S. Geolo. U.S.G.S. http://pubs.usgs.gov/fs/2012/3088/.

Solomon, Evan A., Miriam Kastner, Ian R. MacDonald, and Ira Leifer. 2009. “Considerable Methane Fluxes to the Atmosphere from Hydrocarbon Seeps in the Gulf of Mexico.” *Nature Geosci* 2 (8): 561–65. https://doi.org/10.1038/ngeo574.

Sorenson, G. P., Richard C. Honey, and J. R. Payne. 1966. “Analysis of the Use of Airborne Laser Radar for Submarine Detection and Ranging.” Vol. Final. SRI Report No. 5583, Stanford Research Institute, Alexandria, VA: GKY & Associates, Inc.

Sorooshian, Armin, Luz T. Padro, Athanasios Nenes, Graham Feingold, Allison McComiskey, Scott P. Hersey, Harmony Gates, Haflidi H. Jonsson, Steven D. Miller, and Graeme L. Stephens. 2009. “On the Link Between Ocean Biota Emissions, Aerosol, and Maritime Clouds: Airborne, Ground, and Satellite Measurements Off the Coast of California.” *Global Biogeochemical Cycles* 23 (4): n/a-n/a. https://doi.org/10.1029/2009GB003464.

Spurling, T., and G. Perry. 1997. “A New Generation Laser Airborne Depth Sounder.” In *XVth International Hydrographic Conerence*, Session IV:1.1-1.16. Monaco: International Hydrographic Organization.

Steinbacher, Frank, Martin Pfennigbauer, Markus Aufleger, and A Ullrich. 2012. “High Resolution Airborne Shallow Water Mapping.” In *ISPRS 2012*. Melbourme, Australia.

Steinvall, Ove K., Hakan Klevebrant, Jorgen Lexander, and Anders Widen. 1981. “Laser Depth Sounding in the Baltic Sea.” *Applied Optics* 20 (19): 3284. https://doi.org/10.1364/AO.20.003284.

Steinvall, Ove K., K. Koppari, U. Lejdebrink, J. Winell, M. Nilsson, R. Ellsen, and E. Gjellan. 1997. “Theories and Experience of the Swedish Airborne Laser System.” In *Proc. XVth International Hydrographic Conference*, IV.3.1. Monaco.

Steinvall, Ove K., and Kurt R. Koppari. 1996. “Depth Sounding Lidar: An Overview of Swedish Activities and Future Prospects.” In *CIS Selected Papers: Laser Remote Sensing of Natural Waters: From Theory to Practice*, edited by Victor I. Feigels and Yurij I. Kopilevich, SPIE 2964:2–25. St. Petersburg, Russia: SPIE. https://doi.org/10.1117/12.258342.

Steinvall, Ove K., Kurt R. Koppari, and Ulf C. M. Karlsson. 1993. “Experimental Evaluation of an Airborne Depth-Sounding Lidar.” *Optical Engineering* 32 (6): 1307–21. https://doi.org/10.1117/12.135859.

———. 1994. “Airborne Laser Depth Sounding: System Aspects and Performance.” In *Proc. SPIE 2258: Ocean Optics XII*, edited by Jules Jaffe, 392–412. Bergen, Norway: SPIE. https://doi.org/10.1117/12.190082.

Stigebrandt, A. 1991. “Computations of Oxygen Fluxes through the Sea Surface and the Net Production of Organic Matter with Application to the Baltic and Adjacent Seas.” *Limnol.Oceanogr* 36 (3): 444–54. https://doi.org/10.4319/lo.1991.36.3.0444.

Stockdon, Hilary F., Jr. Sallenger, Asbury H., Jeffrey H. List, and Rob A. Holman. 2002. “Estimation of Shoreline Position and Change Using Airborne Topographic Lidar Data.” *Journal of Coastal Research* 18 (3): 502–13. http://www.jstor.org.proxy.library.cornell.edu/stable/4299097.

Stockdon, Hilary F, Kara S Doran, and Asbury H Sallenger. 2009. “Extraction of Lidar-Based Dune-Crest Elevations for Use in Examining the Vulnerability of Beaches to Inundation During Hurricanes.” *Journal of Coastal Research* 25 (6 Supplement. Special Issue No 53): 59–65. http://www.jstor.org.proxy.library.cornell.edu/stable/25737452.

Sugimoto, N, Z Liu, P Voelger, A Shimizu, Y Sasano, K Asai, M Ishizu, T Itabe, and T Imai. 2001. “Science Applications of the Multi-FOV Lidar for ATMOS-B1/ERM.” *SPIE* 4153. https://doi.org/10.1117/12.417074.

Svetlykh, Alexander A., and Victor I. Feigels. 1993. “Gain in Lidar Performance Provided by Increase of Pulse-Repetition Rate and Narrowing of Optical Filter Band.” In *SPIE 2111: Symposium on Russian Airborne Geophysics and Remote Sensing*, edited by Norman Harthill, 75–94. Golden, CO: International Society for Optics and Photonics. https://doi.org/10.1117/12.162884.

Terrill, Eric J., W Kendall Melville, and Dariusz Stramski. 2001. “Bubble Entrainment by Breaking Waves and Their Influence on Optical Scattering in the Upper Ocean.” *Journal of Geophysical Research: Oceans* 106 (C8): 16815. https://doi.org/10.1029/2000JC000496.

Thieler, E.R., E.A. Himmelstoss, J.L. Zichichi, and A. Ergul. 2009. “The Digital Shoreline Analysis System (DSAS) Version 4.0, an ArcGIS Extension for Calculating Shoreline Change URL: .” In *U.S. Geological Survey Open-File Report 2008-1278*. http://pubs.usgs.gov/of/2008/1278/.

Thorpe, S. A. 1982. “On the Clouds of Bubbles Formed by Breaking Wind-Waves in Deep Water, and Their Role in Air -- Sea Gas Transfer.” *Philosophical Transactions of the Royal Society of London.Series A, Mathematical and Physical Sciences* 304 (1483): 155–210. http://www.jstor.org/stable/36969.

———. 1985. “Small-Scale Processes in the Upper Ocean Boundary Layer.” *Nature* 318 (6046): 519–22. https://doi.org/10.1038/318519a0.

Toth, Charles K. 2009. “Strip Adjustment and Registration.” In *Topographic Laser Ranging and Scanning: Principles and Processing*, edited by Jie Shan and Charles K Toth, 235–68. Boca Raton, FL: CRC Press, Taylor and Francis Group. http://www.crcnetbase.com/isbn/9781420051438.

Tuell, Grady H., Ken Barbor, and Jennifer M. Wozencraft. 2010. “Overview of the Coastal Zone Mapping and Imaging Lidar (CZMIL): A New Multi-Sensor Airborne Mapping System for the U.S. Army Corps of Engineers.” In *SPIE 7695: Algorithms and Technologies for Multispectral, Hyperspectral, and Ultraspectral Imagery XVI, April 5-8, 2010*, SPIE 7695:The Society of Photo-Optical Instrumentation Engin. Optech International, 7225 Stennis Airport Dr., Kiln, MS 39556, United States: SPIE. https://doi.org/10.1117/12.851905.

Tuell, Grady H., Viktor I. Feygels, Yuri I. Kopilevich, Alan D. Weidemann, A. Grant Cunningham, Reza Mani, Vladimir Podoba, Vinod Ramnath, Joong Yong Park, and Jennifer Aitken. 2005. “Measurement of Ocean Water Optical Properties and Seafloor Reflectace with Scanning Hydrographic Operational Airborne Lidar Survey (SHOALS): II. Practical Results and Comparison with Independent Data.” In *SPIE 5885: Remote Sensing of the Coastal Oceanic Environment, July 31- August 1, 2005*, edited by Robert J. Frouin, Marcel Babin, and Shubha Sathyendranath, 5885:58850E-58850E – 13. San Diego, CA: SPIE. https://doi.org/10.1117/12.619215.

Tuell, Grady H., and Joong Yong Park. 2004. “Use of SHOALS Bottom Reflectance Images to Constrain the Inversion of a Hyperspectral Radiative Transfer Model,” 185–93. http://dx.doi.org/10.1117/12.564929.

Tuell, Grady H., Joong Yong Park, Jennifer Aitken, Vinod Ramnath, Viktor I. Feygels, and Yuri I. Kopilevich. 2005. “Fusion of SHOALS Bathymetric Lidar and Passive Spectral Data for Shallow Water Rapid Environmental Assessment.” In *Oceans 2005 - Europe, June 20, 2005 - June 23*, 2:1046–51. Optech International, 7225 Stennis Airport Drive, Kiln, MS 39520, United States: Institute of Electrical and Electronics Engineers Computer Society. https://doi.org/10.1109/OCEANSE.2005.1513202.

Tulldahl, H. Michael, and Ove K. Steinvall. 2004. “Simulation of Sea Surface Wave Influence on Small Target Detection with Airborne Laser Depth Sounding.” *Applied Optics* 43 (12): 2462–83. https://doi.org/10.1364/AO.43.002462.

Tulldahl, H. Michael, and Sofia A. Wikström. 2012. “Classification of Aquatic Macrovegetation and Substrates with Airborne Lidar.” *Remote Sensing of Environment* 121: 347–57. https://doi.org/10.1016/j.rse.2012.02.004.

Tulldahl, H Michael, Marie Andersson, and Ove Steinvall. 2000. “Airborne Laser Depth Sounding: Improvements in Position Adn Depth Estimates by Local Corrections for Sea Surface Slope.” In *Oceans 2000 MTS/IEEE*, 2:1421–29. Providence, RI: IEEE. https://doi.org/10.1109/OCEANS.2000.881803.

Tyler, John E. 1968. “The Secchi Disc.” *Limnology and Oceanography* 13 (1): 1–6. https://doi.org/10.4319/lo.1968.13.1.0001.

Ulich, Bobby Lee, Philip Lacovara, Steven E. Moran, and Michael J. DeWeert. 1997. “Recent Results in Imaging Lidar.” In *SPIE 3059, Advances in Laser Remote Sensing for Terrestrial and Oceanographic Applications*, 3059:95–108. https://doi.org/10.1117/12.277603.

USACE. 2012. “Scope of Work: National Coastal Mapping Program - Lake Michigan.” Vol. EN Project. Kiln, MS: U.S. Corps of Engineers.

Vasilkov, Alexander P., Yuri A. Goldin, and Boris A. Gureev. 1993. “Airborne Lidar Remote Sensing of Vertical Distribution of Sea Water Scattering Coefficient.” In , 1936:233–44. SPIE. https://doi.org/10.1117/12.157108.

Vaughn, C R, J L Button, W B Krabill, and D Rabine. 1996. “Georeferencing of Airborne Laser Altimeter Measurements.” *International Journal of Remote Sensing* 17 (11): 2185–2200. https://doi.org/10.1080/01431169608948765.

Walker, Brian K., Bernhard Riegl, and Richard E. Dodge. 2008. “Mapping Coral Reef Habitats in Southeast Florida Using a Combined Technique Approach.” *Journal of Coastal Research* 24 (5): 1138–50. https://doi.org/10.2112/06-0809.1.

Walker, Ronald E, and John W McLean. 1999. “Lidar Equations for Turbid Media with Pulse Stretching.” *Applied Optics* 38 (12): 2384–97.

Wallace, Davin J., John B. Anderson, and Antonio B. Rodriguez. 2009. “Natural versus Anthropogenic Mechanisms of Erosion along the Upper Texas Coast.” In *America’s Most Vulnerable Coastal Communities*. Geological Society of America. https://doi.org/10.1130/2009.2460(10).

Wandinger, Ulla. 2005. “Introduction to Lidar.” In *Lidar : Range-Resolved Optical Remote Sensing of the Atmosphere*, 1–18. New York: Springer Science+Business Media. https://doi.org/10.1007/0-387-25101-4_1.

Wang, Chau-Chang, and Dajun Tang. 2012. “Application of Underwater Laser Scanning for Seafloor Shell Fragments Characterization.” *Journal of Marine Science and Technology-Taiwan* 20 (1): 95–102.

Wang, Chi-Kuei, and William D. Philpot. 2002. “Using SHOALS LIDAR System to Detect Bottom Material Change.” In *IGARSS ’02*, 5:2690–92. https://doi.org/10.1109/IGARSS.2002.1026743.

———. 2007. “Using Airborne Bathymetric Lidar to Detect Bottom Type Variation in Shallow Waters.” *Remote Sensing of Environment* 106 (1): 123–35. https://doi.org/10.1016/j.rse.2006.08.003.

Wang, Chi-Kuei, William Philpot, Minsu Kim, and Hou-Meng Lei. 2011. “A Monte Carlo Study of the Seagrass-Induced Depth Bias in Bathymetric Lidar.” *Optics Express* 19 (8): 7230. https://doi.org/10.1364/OE.19.007230.

Weber, Kathryn M., Jeffrey H. List, and Karen L.M. Morgan. 2005. “An Operational Mean High Water Datum for Determination of Shoreline Position from Topographic Lidar Data.” *Open-File Report*. https://doi.org/10.3133/OFR20051027.

Weber, Thomas C., Anthony P. Lyons, and David L. Bradley. 2005. “An Estimate of the Gas Transfer Rate from Oceanic Bubbles Derived from Multibeam Sonar Observations of a Ship Wake.” *Journal of Geophysical Research: Oceans* 110 (C4): C04005. https://doi.org/10.1029/2004JC002666.

Wehr, Aloysius. 2009. “LiDAR Systems and Calibration.” In *Topographic Laser Ranging and Scanning: Principles and Processing*, edited by Jie Shan and Charles K Toth, 129–72. Boca Raton, Florida: CRC Press, Taylor and Francis Group. ftp://ftp.ecn.purdue.edu/jshan/Zproject/proofs/04/51423_C004_corr.pdf.

Wellington, M. 2001. “The Laser Airborne Depth Sounder (LADS) - a Broad Range of Applications.” In *Hydro 2001*, Special Pu:11 pp. Norwich, England: The Hydrographic Society.

West, Geraint R. 2001. “In Deeper Waters.” *POB*, March 2001.

West, Geraint R., and W. Jeff Lillycrop. 1999. “Feature Detection and Classification with Airborne Lidar - Practical Experience.” In *Proc. Shallow Survey 99*. Sydney, Australia.

West, Geraint R., and C. E. Wiggins. 2000. “Airborne Mapping Sheds Light on Hawaiian Coasts and Harbors.” *Earth Observation Magazine (EOM)*, 2000.

Westbrook, Graham K., Kate E. Thatcher, Eelco J. Rohling, Alexander M. Piotrowski, Heiko Pälike, Anne H. Osborne, Euan G. Nisbet, et al. 2009. “Escape of Methane Gas from the Seabed along the West Spitsbergen Continental Margin.” *Geophysical Research Letters* 36 (15): n/a. https://doi.org/10.1029/2009GL039191.

White, Stephen. 2007. “Utilization of Lidar and NOAA’s Vertical Datum Transformation Tool (VDatum) for Shoreline Delineation.” In *Marine Technology Society/IEEE Oceans Conference*. Vancouver, BC: IEEE. https://doi.org/10.1109/OCEANS.2007.4449147.

White, Stephen A., Christopher E. Parrish, Brian R. Calder, Shachak Pe’eri, and Yuri Rzhanov. 2011a. “LIDAR-Derived National Shoreline: Empirical and Stochastic Uncertainty Analyses.” *Journal of Coastal Research*, 62–74. https://doi.org/10.2112/SI_62_7.

White, Stephen A, Christopher E Parrish, Brian R Calder, Shachak Pe’eri, and Yuri Rzhanov. 2011b. “LIDAR-Derived National Shoreline: Empirical and Stochastic Uncertainty Analyses.” *Journal of Coastal Research*, 62–74. https://doi.org/10.2112/SI_62_7.

Wilson, John, and John Hawkes. 1998. *Optoelectronics: An Introduction (3rd Edition)*. Prentice-Hall. https://doi.org/978-0131039612.

Witt, A. K., John G. Shannon, M. B. Rankin, and L. A. Fuchs. 1976. “Air/Underwater Laser Radar Test Results, Analysis, and Performance Predictions.” Warminster, PA (Confidential).

Wong, H., and A. Antoniou. 1991. “Characterization and Decomposition of Waveforms for Larsen 500 Airborne System.” *Geoscience and Remote Sensing, IEEE Transactions On* 29 (6): 912–21. https://doi.org/10.1109/36.101370.

———. 1994. “One-Dimensional Signal-Processing Techniques for Airborne Laser Bathymetry.” *IEEE Transactions on Geoscience and Remote Sensing* 32 (1): 35–46. https://doi.org/10.1109/36.285187.

Woolf, David K. 1993. “Bubbles and the Air-sea Transfer Velocity of Gases.” *Atmosphere-Ocean* 31 (4): 517–40. https://doi.org/10.1080/07055900.1993.9649484.

Wozencraft, Jennifer M. 2001. “Sand Volumes and Transport Pathways for Gulf of Mexico Regional Sediment Management.” In *Coastal Dynamics ’01*, 693–702. Proceedings. Bergen, Norway: ASCE. https://doi.org/10.1061/40566(260)71.

———. 2002. “Complete Coastal Mapping with Airborne Lidar.” In *Ocean’s 2002 Conference and Exhibition, October 29, 2002 - October 31*, 2:1194–98. Jt. Airborne Lidar Bathymetry T.C.E., US Army Corps of Eng., Mobile Dist., 109 St. Joseph Street, Mobile, AL 36602, United States: Institute of Electrical and Electronics Engineers Inc. https://doi.org/10.1109/OCEANS.2002.1192136.

———. 2010a. “Requirements for the Coastal Zone Mapping and Imaging Lidar (CZMIL).” In *Algorithms and Technologies for Multispectral, Hyperspectral, and Ultraspectral Imagery XVI, April 5, 2010 - April 8*, SPIE 7695:The Society of Photo-Optical Instrumentation Engin. Orlando, FL: SPIE. https://doi.org/10.1117/12.851891.

———. 2013. “Using LiDAR to Assess Storm Damage Caused by Hurricane Sandy.” *LiDAR Magazine*, March 2013.

Wozencraft, Jennifer M., Lauren M. Dunkin, Molly K. Reif, and E. Eisemann. 2018. “A Spatial Index Approach to Coastal Monitoring: A Florida Case Study.” Edited by R Almar, L P Almeida, Viet N Trung, and Sall. *Journal of Coastal Research*, no. Special IsSpecial Issue 81: Tropical, Coastal, and Estutarine Dynamics: 67–75.

Wozencraft, Jennifer M., and Jennifer L. Irish. 2000. “Airborne Lidar Surveys and Regional Sediment Management.” In *Proc. 20th EARSeL Symposium*, 11 pgs. Dresden, Germany: European Association of Remote Sensing Laboratories EARSeL.

Wozencraft, Jennifer M., and W. Jeff Lillycrop. 2003. “SHOALS Airborne Coastal Mapping: Past, Present, and Future.” *Journal of Coastal Research* SI (81): 207–15. https://www-jstor-org.proxy.library.cornell.edu/stable/25736607.

———. 2006. “JALBTCX Coastal Mapping for the USACE.” *The International Hydrographic Review* 7 (2): 28–37. https://journals.lib.unb.ca/index.php/ihr/article/view/20763.

Wozencraft, Jennifer M., and David Millar. 2005. “Airborne Lidar and Integrated Technologies for Coastal Mapping and Nautical Charting.” *Marine Technology Society Journal* 39 (3): 27–35. https://doi.org/10.4031/002533205787442440.

Wozencraft, Jennifer M., and Joong Yong Park. 2013. “Integrated LiDAR and Hyperspectral.” In *Coral Reef Remote Sensing*, 1st ed., 175–91. Dordrecht: Springer Netherlands. https://doi.org/10.1007/978-90-481-9292-2_7.

Wozencraft, Jennifer M. 2010b. “Requirements for the Coastal Zone Mapping and Imaging Lidar (CZMIL).” In *Algorithms and Technologies for Multispectral, Hyperspectral, and Ultraspectral Imagery XVI, April 5, 2010 - April 8*, SPIE 7695:The Society of Photo-Optical Instrumentation Engin. Orlando, FL: SPIE. https://doi.org/10.1117/12.851891.

———. 2014. “USACE Information Products.”

Wright, C. Wayne, and John C. Brock. 2002. “EAARL: A Lidar for Mapping Shallow Coral Reefs and Other Coastal Environments.” In *Proceedings of the Seventh International Conference on Remote Sensing for Marine and Coastal Environments*, 8. Miami, Florida. https://www.tib.eu/en/search/id/TIBKAT%3A35324662X/Proceedings-Seventh-International-Conference-on/.

Wright, C. Wayne, Christine Kranenburg, Timothy A. Battista, and Christopher E. Parrish. 2016. “Depth Calibration and Validation of the Experimental Advanced Airborne Research Lidar, EAARL-B.” *Journal of Coastal Research* SI (76): 4–17. https://doi.org/10.2112/SI76-002.

Wu, Lei, Xiaopeng Wang, Hongru Yang, Bing Yu, Chao Chen, Bin Yang, Liang Yuan, et al. 2012. “Signal-to-Noise Performance Analysis of Streak Tube Imaging Lidar Systems. II. Theoretical Analysis and Discussion.” *Applied Optics* 51 (36): 8836–47. https://doi.org/10.1364/AO.51.008836.

Xhardé, Régis, Bernard F. Long, and Donald L. Forbes. 2011. “Short-Term Beach and Shoreface Evolution on a Cuspate Foreland Observed with Airborne Topographic and Bathymetric LIDAR.” *Journal of Coastal Research*, no. Special Issue No 62: Applied Lidar Techniques (March): 50–61. https://doi.org/10.2112/SI_62_6.

Yamamoto, Kristina H., Rebecca L. Powell, Sharolyn Anderson, and Paul C. Sutton. 2012. “Using LiDAR to Quantify Topographic and Bathymetric Details for Sea Turtle Nesting Beaches in Florida.” *Remote Sensing of Environment* 125 (October): 125–33. https://doi.org/10.1016/j.rse.2012.07.016.

Yang, Eric, and Paul E. LaRocque. 2010. “SHOALS Object Detection.” *The International Hydrographic Review*, no. 3 (March): 24–36. https://journals.lib.unb.ca/index.php/ihr/article/view/20849.

Yang, Eric, Michael Sitar, Paul E LaRocque, Wenbo Pan, Karen Francis, and David Reid. 2009. “Small Object Detection Using SHOALS Bathymetric Lidar.” In *U.S. HYDRO 2009*. Norfolk, VA. http://www.thsoa.org/hy09/0514A_03.pdf.

Yang, Hongru, Lei Wu, Xiaopeng Wang, Chao Chen, Bing Yu, Bin Yang, Liang Yuan, et al. 2012. “Signal-to-Noise Performance Analysis of Streak Tube Imaging Lidar Systems. I. Cascaded Model.” *Applied Optics* 51 (36): 8825–35. https://doi.org/10.1364/AO.51.008825.

Young, Adam P, and Scott A Ashford. 2006. “Application of Airborne LIDAR for Seacliff Volumetric Change and Beach-Sediment Budget Contributions.” *Journal of Coastal Research* 22 (2): 307–18. http://www.jstor.org.proxy.library.cornell.edu/stable/4300288.

Zawada, David G., and John C. Brock. 2009. “A Multiscale Analysis of Coral Reef Topographic Complexity Using Lidar-Derived Bathymetry.” *Journal of Coastal Research* 25 (6): 6–15. https://doi.org/10.2112/SI53-002.1.

Zhang, Keqi, Dean Whitman, Stephen Leatherman, and William V. Robertson. 2005. “Quantification of Beach Changes Caused by Hurricane Floyd Along Florida’s Atlantic Coast Using Airborne Laser Surveys.” *Journal of Coastal Research* 211 (1): 123–34. https://doi.org/10.2112/02057.1.

Zhang, Xiaodong, Marlon R. Lewis, and Bruce D. Johnson. 1998. “Influence of Bubbles on Scattering of Light in the Ocean.” *Applied Optics* 37 (27): 6525. https://doi.org/10.1364/AO.37.006525.

Zimmerman, Richard C. 2003. “A Biooptical Model of Irradiance Distribution and Photosynthesis in Seagrass Canopies.” *Limnology and Oceanography* 48 (1, Part 2; Light in Shallow Waters): 568–85. https://doi.org/10.4319/lo.2003.48.1_part_2.0568.

———. 2006. “Light and Photosynthesis in Seagrass Meadows.” In *SEAGRASSES: BIOLOGY, ECOLOGYAND CONSERVATION*, 303–21. Springer Netherlands. https://doi.org/10.1007/978-1-4020-2983-7_13.

APPENDIX A. STANDARD WORDS, PHRASES, ACRONYMS

Acronym	Meaning	Section
3DEP	3D Elevation Program	5.4;
AEL	Accessible Emission Limits	3.5;
ALARMS	Airborne Laser Radar Mine Sensor	2.2;
ALB	Airborne Lidar Bathymeter	2.0, 2.2; 2.3; 2.4; 3.0; 3.1; 3.2; 3.3; 3.4; 3.5; 4.4; 5.0; 5.1; 5.2; 5.3; 5.4;
ANSI	American National Standards Institute	3.1; 3.5;
AOL	Airborne Oceanographic Lidar	2.3; 3.1;
AOP	Apparent Optical Property	2.0; 2.3; 4.3;
APD	Avalanche Photodiode	3.1; 3.3; 3.4;
ASCII	American Standard Code for Information Interchange	5.3;
ASPRS	American Society of Photogrammetry and Remote Sensing	5.3;
BIST	Built-In Self Test	5.2; 5.3; 5.4;
BRDF	Bidirectional Reflectance Distribution Function	2.4;
CASI	Compact Airborne Spectrographic Imager	2.2
CCRS	Canadian Centre for Remote Sensing	2.2;
CHARTS	Compact Hydrographic Airborne Rapid Total Survey	5.3; 5.4;
CHS	Canadian Hydrographic Service	2.2;
CIR	Color InfraRed	2.3;
COTS	Commercial-off-the-shelf	5.3;
CUBE	Combined Uncertainty and Bathymetric Estimator	5.4;
CW	Continuous wave	3.4
CZMIL	Coastal Zone Mapping and Imaging Lidar	3.1; 3.2; 3.3; 3.5; 4.3; 4.4; 5.4;
DEM	Digital Elevation Model	4.1;
DGPS	Differential Geographic Positioning System	3.1;
DSTO	Defence, Science and Technology Organization	2.1;
EAARL	Experimental Advanced Airborne Research Lidar	3.1;
ECEF	Earth Centered, Earth Fixed	4.1;
ECKV	Elfouhaily, Chapron, Katsaros, and Vandemark (wave spectrum)	2.2
eNOHD	Extended Nominal Ocular Hazard Distance	3.5
EnvRF	Environmental Response Function	3.2;
ERDC	Engineer Research and Development Center (USACE)	
EVLR	Extended Variable Length Records	5.3;
FDA	Food and Drug Administration	3.5;
FEMA	Federal Emergency Management Agency	2.3;
FOA	Försvarets forskningsanstalt (Swedish National Defense Institute)	2.2;
FOB	Fiber Optics Bundle	3.3;
FOV	Field of View	3.1; 3.2; 3.3;
FWHM	Full Width Half Maximum	3.2; 3.3;
GAPD	Geiger Mode APD	3.1;
GNSS	Global Navigation Satellite System	4.1; 5.4;
GPS	Geographic Positioning System	3.1; 5.2; 5.4;
IBF	IMU Body Frame	4.1;
IEC	International Electrotechnical Commission	3.5;
ICP	Iterative Closest Point	5.3
IHO	International Hydrographic Organization	3.1; 5.1; 5.2; 5.3; 5.4;
IMU	Inertial Measurement Unit	3.1; 3.5; 4.1; 5.2; 5.3;
ImpRF	Impulse Response Function	3.2; 4.3;
INS	Inertial Navigation System	5.2; 5.3;

Acronym	Meaning	Section
IOP	Inherent Optical Property	2.0; 2.3; 3.0; 3.3; 3.4; 4.2; 4.3;
JALBTCX	Joint Airborne Lidar Bathymetry Technical Center of Expertise	5.3; 5.4;
LADS	Laser Airborne Depth Sounder	3.1; 5.3;
LAS	Laser File Format (ASPRS)	5.3;
LGF	Local Geodetic Frame	4.1;
lidar	not LiDAR or LIDAR	
LMSL	Local Mean Sea Level	5.3;
MAPPS	A national association of photogrammetry, mapping and geospatial firms (originally Management Association of Private Photogrammetric Surveyors)	2.2;
MBES	Multibeam Echo Sounder	3.1; 5.3; 5.4;
MLLW	Mean Low Low Water	2.4; 5.3; 5.4;
MPE	Maximum Permissible Exposure	3.1; 3.5;
MOB	Main Operating Base	2.1;
NAD	North American Datum	3.1; 5.3
NADC	Naval Air Development Center	2.3;
NAVD	North American Vertical Datum	5.3;
NAVOCEANO	Naval Oceanographic Office	2.3;
NALL	Navigable Area Limit Line	5.1;
NCALM	National Center for Airborne Laser Mapping	2.2;
NCMP	National Coastal Mapping Program	2.3; 5.1; 5.3;
Nd:YAG	Neodymium-doped Yttrium-Arsenide-Garnet (crystal or laser)	2.3; 3.1; 3.5;
NED	North-East-Down coordinate system	4.1
NGS	National Geodetic Survey	5.4;
NOAA	National Oceanographic and Atmospheric Administration	2.3; 5.1; 5.3; 5.4;
NOHD	Nominal Ocular Hazard Distance	3.5;
MLLW	Mean Low Low Water	5.3; 5.4;
MPE	Maximum Permissible Exposure	3.1; 3.5
OCS	Ocean Coastal Survey	5.3;
ONR	Office of Naval Research	2.3;
PRF	Pulse Repetition Frequency	3.1; 3.5;
PFMABE	Pure File Magic (PFM) Area Based Editor	
PMT	Photomultiplier Tube	3.1; 3.3; 3.4
POS	Position and Orientation System	
PPK GPS	Post Processing Kinematic GPS	5.4;
PRF	Pulse Repetition Frequency	3.1; 3.5
QL	Quality Levels	5.4;
RAN	Royal Australian Navy	2.1;
REA	Rapid Environmental Assessment	4.4
RMSE	Root Mean Square Error	5.3; 5.4;
RTE	Radiative Transfer Equation	3.3;
SAV	Submerged Aquatic Vegetation	2.4;
SBF	Sensor Body Frame	4.1;
SFTF	South Florida Testing Facility	5.4;
SHOALS	Scanning Hydrographic Operational Lidar Survey	2.2; 2.3; 2.4; 3.1; 3.5; 4.4; 5.3; 5.4;
SW	Swath width	3.1; 3.3; 3.5
SNR	Signal-to-Noise Ratio	5.2
TSS	Topography of the Sea Surface	5.3;
THU	Total Horizontal Accuracy	5.3;
TIN	Triangle Irregular Network	5.3;

Acronym	Meaning	Section
TVU	**Total Vertical Accuracy**	**5.3; 5.4;**
USACE	**U.S. Army Corps of Engineers**	**2.2; 5.1; 5.3; 5.4;**
USGS	**United States Geological Survey**	**2.3; 5.4;**
USM	**University of Southern Mississippi**	**2.3**
UTM	**Universal Transverse Mercator**	**5.3;**
VLR	**Variable Length Records**	**5.3;**
VSF	**Volume Scattering Function**	**2.3; 3.3, 4.2; 4.3;**
WRE	**Weapons Research Establishment**	**2.1;**
WGS	**World Geodetic System**	**3.1;**

APPENDIX B. LIST OF SYMBOLS

	Α Δ Φ Θ Ρ Ω	*A B C D E F G H I J K L M N O P Q R S T U V W X Y Z*			
Letter	***Symbol***	***Quantity; description***	***SI Units***	***1st Eq. or Fig.***	***1st Sec.***
	Greek				
Α α					
	$\alpha(\lambda)$, $\alpha(z,\lambda)$	Atmospheric attenuation coefficient	m^{-1}	(3.1.1)	**3.1.1**
	$\alpha(z_{sf}(\mathbf{r}),\mathbf{r})$	Angle between the local normal to the surface at a boundary and the lidar beam axis, Oz		(4.3.29)	**4.3.2.4**
Β β					
	$\beta, \beta(\theta), \beta(\boldsymbol{r},\theta), \beta(\boldsymbol{n})$	Volume scattering function (VSF) – may depend on coordinate **r** or directional vector **n**	$m^{-1}sr^{-1}$	(3.3.5)	**3.3.2.2**
	$\beta(z,\boldsymbol{r},\boldsymbol{n}_1\wedge\boldsymbol{n}_2)$	The volume scattering function for the angle $\boldsymbol{n_1}\wedge\boldsymbol{n_2}$, where $\boldsymbol{n_1}$ is the direction of beam propagation and $\boldsymbol{n_2}$ is the direction of the scattered light; the function is taken to be zero if the point $\{z(t),\mathbf{r}\}$ is not within the water body. When the water is vertically and horizontally homogeneous, then $\beta(z,\boldsymbol{r},\boldsymbol{n}_1\wedge\boldsymbol{n}_2)\equiv\beta(\boldsymbol{n}_1\wedge\boldsymbol{n}_2)$	$m^{-1}sr^{-1}$	(4.3.16)	**4.3.2.2**
	β_π	Lidar backscattering coefficient	$m^{-1}sr^{-1}$	After (3.3.12)	**3.3.2.2**
	$\beta_{atm}(z,\lambda)$	Atmospheric backscattering coefficient	$m^{-1}sr^{-1}$	(3.1.5)	**3.1.2**
	$\beta_{lg}(\theta)$	Large particle volume scattering function	$m^{-1}sr^{-1}$	(5.2.10)	**5.2**
	β_{sg}	Average bending angle of the seagrass leaf orientation with respect to the zenith	deg	(3.4.6)	**3.4.3**
	$\beta_{sm}(\theta)$	Small particle volume scattering function	$m^{-1}sr^{-1}$	(5.2.10)	**5.2**
	$\beta_w(\theta)$	Volume scattering function for pure sea water	$m^{-1}sr^{-1}$	(5.2.10)	**5.2**

	$A\,\Delta\,\Phi\,\Theta\,P\,\Omega$	*A B C D E F G H I J K L M N O P Q R S T U V W X Y Z*			
Letter	***Symbol***	***Quantity; description***	***SI Units***	***1st Eq. or Fig.***	***1st Sec.***
$\Gamma\,\gamma$					
	$\gamma(z(t),\mathbf{r})$	Function characterizing the reflection/scattering behavior of irradiance on the leading-edge plane at boundary surfaces (air-water interface, bottom, solid body in the water).	---	(4.3.28)	**4.3.2.4**
$\Delta\,\delta$					
	δ	delta function	---	(3.3.16)	**4.3.2.2**
	δ_2	A 2D delta function	---	(4.3.62)	**4.3.2.7**
$H\,\eta$					
	η	Total optical system loss factor	---	(3.1.5)	**3.1.2**
	η_R	Transmittance of the receiver optical system	---	after (4.4.1)	**4.4.1**
$\Theta\,\theta$					
	θ	Scattering angle	rad, deg	after (3.3.5)	**3.3.2.2**
		Scanning angle		(5.1.1)	**5.1.1**
	θ_1	Incidence angle	rad, deg	(3.2.1)	**3.2.1**
	θ_2	Transmission angle (angle of refraction)	rad, deg	(3.2.1)	**3.2.1**
	θ_a	The angle between the emitted lidar beam axis and the local perpendicular to the water surface	rad, deg	(3.2.2); Figure 3.2.1	**3.2.1**
	θ_c	Zenith angle of a collimated beam incident to the seagrass bed plane	rad, deg	(3.4.6)	**3.4.3**
	θ_{max}	Maximum scan angle	rad, deg	(4.1.2)	**4.1.2**
	θ_{sun}	Solar zenith angle in air	rad, deg	(3.4.4)	**3.4.2**
	θ_a^{sun}			Table 5.1	**4.3**
	θ_{sg}	average bending angle of the seagrass leaf orientation with respect to the zenith	rad, deg	(3.4.6); Figure 3.4.3	**3.4.3**
	θ_w	Refraction angle in the water;	rad, deg	(3.2.2); Figure 3.2.1	**3.2.1**

	$A\,\Delta\,\Phi\,\Theta\,P\,\Omega$	*A B C D E F G H I J K L M N O P Q R S T U V W X Y Z*			
Letter	***Symbol***	***Quantity; description***	***SI Units***	***1st Eq. or Fig.***	***1st Sec.***
	θ_w^{sun}	Solar incidence angle in water	rad, deg	(5.3.1)	**5.3**
	Θ_E	The sounding pulse divergence - the full plane angle of conical distribution of emitted power at 1/e level	rad, deg	(4.1.1); Figure 4.2.1	**4.1.1**
	Θ'_E	The sounding pulse divergence (equivalent geometry)	rad, deg	Figure 4.2.4	**4.2.1**
	Θ_R	The angular width of lidar receiver sensitivity distribution (supposed conical) at 1/e level (FOV)	rad, deg	after (3.2.1)	**4.2.1**
	Θ'_R	The angular width of lidar receiver sensitivity distribution (equivalent geometry)	rad, deg	Figure 4.3.3	**4.3.2.2**
K κ					
	κ	yaw (boresight angle); The position vector in the IBF	rad, deg	(5.1.4)	**5.1.3**
Λ λ					
	λ	wavelength	nm	(3.3.1)	**3.3.1.2**
	λ	longitude	deg	(5.1.1)	**5.1.5**
M μ					
	μ	mean	–––	–––	**general**
P ρ					
	ρ	reflectance coefficient	---	–––	**general**
	ρ	the target point	m	(6.3.1)	**6.3.2**
	ρ_{sf}	reflection coefficient of the water surface	---	after Figure 3.3.7	**4.2.2**
	ρ_w	(Effective) reflection coefficient of the water surface; not R_f or ρ_f		(3.4.1)	**3.4**
	ρ_{bot}	bottom reflectance	---	after (4.3.29)	**4.3.2**
	ρ_b	bottom reflectance	---	(3.4.1)	**3.4**
	ρ_{sb}	reflectance of a submerged, solid body	---	after (4.3.29)	**4.3.2**

	$A\,\Delta\,\Phi\,\Theta\,P\,\Omega$	*A B C D E F G H I J K L M N O P Q R S T U V W X Y Z*			
Letter	***Symbol***	***Quantity; description***	***SI Units***	***1st Eq. or Fig.***	***1st Sec.***
	ρ_{sg}	reflectance of sea grass	---	(3.4.6)	**3.4.3**
$\Sigma\,\sigma$					
	σ	Standard deviation	–––	–––	**general**
	σ_u , σ_c	Standard deviation of the slope distribution in the upwind (u) and crosswind (c) directions	$m^2 s^{-2}$	–––	**3.2.2**
	Σ	Area of the receiver telescope pupil	m^2	(4.3.13)	**4.3.2.1**
$T\,\tau$					
	τ	transmission coefficient	---		**general**
	τ_a	Optical thickness of the atmospheric path length	---	(3.4.1)	**3.4**
	τ_p	Emitted/transmitted laser pulse duration	s	(3.1.5), (4.3.10)	**3.1.2** **4.3.1**
	τ_F	Fresnel transmission at the air-water interface		(4.3.13)	**4.3.2.1**
	τ_R	Duration of the effective sounding pulse, of total response time. For Gaussian responses of all the components, we have $\tau_R^2 = \tau_p^2 + \tau_{PMT}^2 + \tau_{amp}^2 + \tau_{digit}^2$	s	after (4.2.8)	**4.2.2**
	$\tau_{amp}, \tau_{PMT}, \tau_{dig}$	Response time of amplifier, detector, digitizer,…	s	(4.3.10)	**4.3.1**
$\Phi\,\phi$					
	φ	latitude	rad, deg	(5.1.11)	**5.1.5**
	φ	pitch (boresight angle)	rad, deg	(5.1.4)	**5.1.2**
	Φ_{sg}	Seagrass shoot density	m^{-1}	(3.4.6)	**3.4.3**
$X\,\chi$					
	$\chi(\theta)$	Volume scattering phase function (VSPF); $x(\vartheta) \equiv \frac{1}{b}\beta(\vartheta)$	sr^{-1}	(3.3.9)	**3.3.2.2**
	$\chi_s(\theta)$	Small-angle (forward-scattering) component of the phase function	sr^{-1}	(4.3.32)	**4.3.2.5**

	A Δ Φ Θ P Ω	***A B C D E F G H I J K L M N O P Q R S T U V W X Y Z***			
Letter	***Symbol***	***Quantity; description***	***SI Units***	***1st Eq. or Fig.***	***1st Sec.***
	$\tilde{\chi}_s(\mathbf{p})$	Fourier transformation of the phase scattering function $\chi_s(\mathbf{n}_t)$		(4.3.44)	**4.3.2.5**
	$\chi[\cdot]$	The channel Watt-count characteristic - a count-valued monotonically increasing function of argument in Watts. Describes the conversion of a continuous function to discrete (quantized) values.	counts	(4.3.2)	**4.3.1**
Ω ω					
	ω	roll (boresight angle)	rad, deg	(5.1.4)	**5.1.2**
	ω_0	Single scattering albedo, $\omega_0 = b/c$	---	(3.3.16)	**3.3.2.2**
	ω_0^*	Value of for which $Q(c^*, \omega_0)$ is minimized: $Q(c^*, \omega_0^*) = \min_{\omega_0} Q(c^*, \omega_0)$	---	(5.2.13)	**5.2**
	$\omega(t)$	Instrument response function	s^{-1}	(4.2.7)	**4.2.2**
	$\omega_{PMT}(t)$	PMT response function	s^{-1}	(4.3.9)	**4.3.1**
	$\omega_{amp}(t)$	Amplifier response function	s^{-1}	(4.3.9)	**4.3.1**
	$\omega_{dig}(t)$	Digitizer response function	s^{-1}	(4.3.9)	**4.3.1**
	Ω	The (effective) solid angle. $\Omega = \pi \Theta R^2/4$ for both Gaussian & stepmodel cases	sr	(3.3.5); Figure 3.3.6	**3.3.2.2**

	Α Δ Φ Θ P Ω	*A B C D E F G H I J K L M N O P Q R S T U V W X Y Z*			
Letter	***Symbol***	***Quantity; description***	***SI Units***	***1st Eq. or Fig.***	***1st Sec.***
	Western				
A, a					
	a, $a(\lambda)$	Absorption coefficient	m^{-1}	(3.3.3)	**3.3.2.1**
	a	semi-major axis of the ellipsoid	m	(5.1.12)	**5.1.5**
		IHO order coefficient	---	(6.3.1)), Table 6.1	**6.3.3**
	$a_{bs}(k(\mathrm{z}))$	the contribution from small-angle scattering to the attenuation of spatial harmonics of the spatial frequency k in the initial distribution of radiance within a light beam when propagated over the distance z in a turbid medium	m^{-1}	(4.3.54)	**4.3.2.5**
	a_e	Effective attenuation coefficient that accounts for both absorption and scattering: $a < a_e < a + b$	m^{-1}	before Figure 4.2.6	**4.2.2**
	a_s	Effective absorption coefficient for small-angle (collimated) beam, $a_s = a + 2b_b$	m^{-1}	(4.3.34)	**4.3.2.5**
	a_{sg}	Seagrass leaf absorption coefficient	m^{-1}	(3.4.7)	**3.4.3**
	A	Area	m^2	(4.1.1)	**3.3.2.2**
	A_r	ALB receiver's aperture area	m^2	(3.1.5)	**3.1.2**
	A_{noise}	Amplitude of the signal	---	(6.2.1)	**6.2.2**
	A_{signal}	Amplitude of the noise	---	(6.2.1)	**6.2.2**
B, b					
	b	IHO order coefficient	---	(6.3.1)); Table 6.1	**6.3.3**
	b, $b(\lambda)$	(Total) scattering coefficient: $b = b_f + b_b$	m^{-1}	(3.3.7)	**3.3.2.2**
	b_b	Backward scattering coefficient	m^{-1}	(3.3.11a,b); (5.2.11)	**3.3.2.2**
	b_f	Forward scattering coefficient	m^{-1}	(3.3.11a,b); (5.2.11)	**3.3.2.2**

	Α Δ Φ Θ P Ω	*A B C D E F G H I J K L M N O P Q R S T U V W X Y Z*			
Letter	***Symbol***	***Quantity; description***	***SI Units***	***1st Eq. or Fig.***	***1st Sec.***
	b_{lg}	Small-angle scattering coefficient for small particles	m^{-1}	(5.2.9)	**5.2**
	b_{sm}	Small-angle scattering coefficient for small particles	m^{-1}	(5.2.9)	**5.2**
	b_s	Small-angle scattering coefficient, $b_s = b - 2b_b$	m^{-1}	(4.3.24)	**4.3.2.5**
	b_w	Small-angle scattering coefficient for hydrosol free (pure) water	m^{-1}	(5.2.9)	**5.2**
	B_{sg}	Relative biomass height distribution for a given area	m	(4.4.6)	**3.4.3**
C, c					
	c	Speed of light in the air	$m\ s^{-1}$	(3.1.5)	**3.1.2**
	c, $c(\lambda)$	Beam attenuation coefficient: $c = a + b$	m^{-1}	(3.3.13)	**3.3.2.2**
	c^*	Value of the beam attenuation coefficient that minimizes the functional Q , $Q(c^*) = \min_c Q(c)$	m^{-1}	(5.2.4)	**5.2**
	$C(Q)$	Scaling function for input energy: $C(Q) \equiv \chi[Q \cdot \max R(t)]$	---	(4.4.7)	**4.4.2**
D, d					
	d	Water depth	m	(6.3.1))	**6.3.3**
	d^{bot}	cross-section of the sounding beam near the bottom	m	(4.2.5)	**4.2.1**
	d^{sf}	diameter of the lidar beam near the water surface	m	(4.1.3)	**4.1.2**
	$\mathbf{d}_{O_w}^{SBF}$	normalized direction vector directed toward the surface point P in the SBF	---	(5.1.1)	**5.1.1**
	$\mathbf{d}_a$	a unit in-air direction vector; $\mathbf{d}_a = \boldsymbol{X}_{O_w}^{LGF}/R$	---	Figure 5.1.2, (5.1.7)	**5.1.4**
	$\mathbf{d}_w$	a unit in-water direction vector	---	Figure 5.1.2; (5.1.10)	**5.1.4**
	$\boldsymbol{d}_{\boldsymbol{O_w}}^{\boldsymbol{LGF}}$	In-air unit vector directed toward the surface point, P, in the local geodetic frame (LGF)	---	(5.1.6)	**5.1.3**
	$\mathbf{d}_{P_b}^{LGF}$	In-water unit vector directed toward the bottom point P_b in the local geodetic frame (LGF)	---	(5.1.9)	**5.1.4**

	A Δ Φ Θ P Ω	***A B C D E F G H I J K L M N O P Q R S T U V W X Y Z***			
Letter	***Symbol***	***Quantity; description***	***SI Units***	***1st Eq. or Fig.***	***1st Sec.***
	Δd	Depth error	m	(4.5.1)	**5.5.2**
	Δd_{sg}	Seagrass leaf thickness	m	(3.4.7)	**3.4.3**
	$D(t)$	Digitized output electric signal; the temporal distribution of the digitizer counts. D(t) is the final waveform and includes not only p(t) but all R(t) effects.	$counts$	(4.3.2)	**4.3.1**
	D_{const}	Digitized constant optical signal	$counts$	(4.3.4)	**4.3.1**
	$D^{exp}(t)$	experimentally-derived waveform	$counts$	(4.3.12)	**4.3.1**
	$D_Q^{calibr}(t)$	Output calibrated electrical signal	$counts$	(4.4.5)	**4.4.2**
E, e					
	e	Eccentricity of the ellipsoid	---	(5.1.12)	**5.1.5**
	E, $E(\lambda)$,$E(z,\lambda)$	Irradiance	$W{\cdot}m^{-2}$	before (3.3.1)	**3.3.1.2**
	E_0	Incident Irradiance	Wm^2	(3.3.6)	**3.3.2.2**
	E_d, $E_d(\lambda)$, $E_d(z,\lambda)$	Downwelling irradiance	Wm^2	(3.3.1)	**3.3.1.2**
	E_E, $E_E(z(t),\boldsymbol{r})$	Emitted irradiance	Wm^2	(4.3.26)	**4.3.2.4**
	E_R, $E_R(z(t),\boldsymbol{r})$,	Received irradiance	Wm^2	(4.3.26)	**4.3.2.4**
	$E_{E,R}$	Shorthand notation for *either* emitted or received irradiance	Wm^2	(4.3.31)	**4.3.2.5**
	$E_{sun}(\lambda)$	Solar irradiance at the Earth's surface	Wm^2	(3.4.4)	**3.4.2**
F, f					
	f	scan rate	s^{-1}	(4.1.4)	**4.1.2**
	f_d	detector sampling rate	s^{-1}	(4.1.9)	**4.1.2**
	$F_D(h_s)$	Function to account for the effect of forward scattering on the decay of the lidar signal with water depth	---	(5.3.3)	**5.3**

	A Δ Φ Θ P Ω	***A B C D E F G H I J K L M N O P Q R S T U V W X Y Z***			
Letter	***Symbol***	***Quantity; description***	***SI Units***	***1st Eq. or Fig.***	***1st Sec.***
G, g					
	G	Green's function; $G(z_1, \boldsymbol{r}_1, \boldsymbol{n}_1; z_2, \boldsymbol{r}_2, \boldsymbol{n}_2)$	---	(3.3.19)	**4.3.2.3**
	G_{st}	Heaviside step function	---	(4.3.89)	**4.3.3.1.3**
	G_F	the "lidar geometric factor", $0 \leq \mathrm{G_F(z)} \leq 1.0$; $\mathrm{G_F(z)} = 1$ for monostatic lidars	---	(3.1.5)	**3.1.2**
H, h					
	h	ellipsoid height	m	(5.1.12)	**5.1.5**
	h_c	peak canopy height	m	(3.4.6)	**3.4.3**
	h_s	slant path in the water (in-water propagation distance along the beam center)	m	(3.4.1); Figure 4.3.6; (4.3.73)	**3.4**
	$h_s^{max}(b_s, \Theta_R)$	The maximum value of h_s for given values of b_s *and* Θ_R	m	after (5.3.4)	**5.3**
	h^{bot}	bottom depth	m	Figure 4.2.4	**4.2.1**
	Δh_s^{bot}	geometric stretch of the **bottom**-reflected lidar signal	m	Figure 4.2.4	**4.2.1**
	H	Thickness of an atmospheric layer	m	(3.1.1)	**3.1.1**
		height of the lidar above the sea surface	m	(4.1.1)	**4.1.1**
		heading orientation of the IBF with respect to the LGF	rad, deg	(5.1.5)	**5.1.3**
	H'	height of the lidar above the sea surface (equivalent geom.)	m	Figure 4.2.4	**4.2.1**
	H_s	slant distance between the lidar and the sea surface (along the lidar axis)	m	Before (3.1.5); Figure 4.2.1	**3.1.2; 4.2.1**
	H_s'	slant distance between the lidar and the sea surface (equivalent geometry)	m	(4.2.5); Figure 4.2.4	**4.2.1**
	ΔH_s	departure of a spherical surface from a plane surface	m	(4.2.2); Figure 4.2.2	**4.2.1**
	ΔH^{sf}	geometric stretch of the **surface**-reflected lidar signal	m	Figure 4.2.3	**4.2.1**

	A Δ Φ Θ P Ω	***A B C D E F G H I J K L M N O P Q R S T U V W X Y Z***			
Letter	***Symbol***	***Quantity; description***	***SI Units***	***1st Eq. or Fig.***	***1st Sec.***
I, i					
	$\boldsymbol{i}$	Square root of -1	---	(3.3.2)	**3.3.2.1**
	$I, I(\lambda)$	Radiance **(not L)**	Wm^2sr^{-1}	(3.4.4)	**3.4.2**
	$I(t,\boldsymbol{r},\boldsymbol{n},\lambda)$	$I(t,\boldsymbol{r},\boldsymbol{n}) = I(x(t),\boldsymbol{r}_\perp,\boldsymbol{n}_\perp)$. The radiance of a monochromatic light beam at wavelength λ **r** is 3D Cartesian coordinate vector, and **n** is the 3D directional (unit) vector; $x(t)$ is the Cartesian coordinate axis along the beam axis in the water, $\mathbf{r}_\perp$ is the 2D coordinate vector in the plane perpendicular to Oz (the beam front), and $\mathbf{n}_\perp$ is the projection of **n** on the plane	Wm^2sr^{-1}		
	$I_{aE}(x,\boldsymbol{r_a},\boldsymbol{n_a})$,	Specifies $I_E(x,\boldsymbol{r},\boldsymbol{n})$ for the actual problem	Wm^2sr^{-1}	(4.3.60)	**4.3.2**
	$I'_{aE}(z,\boldsymbol{r},\boldsymbol{n})$,	The radiance of the actual emitted (E) sounding pulse in the equivalent geometry	Wm^2sr^{-1}	(4.3.60)	**4.3.2.7**
	$I'_{aR}(z,\boldsymbol{r},\boldsymbol{n})$	The radiance of the actual received (R) sounding pulse in the equivalent geometry			
	$I_{bot}(\lambda)$	Radiance reflected back from the sea floor	Wm^2sr^{-1}	(3.4.4)	**3.4.2**
	$I_E(t,\boldsymbol{r},\boldsymbol{n})$, $I_R(t,\boldsymbol{r},\boldsymbol{n})$	$I_E(t,\boldsymbol{r},\boldsymbol{n}) = I_E(x(t),\boldsymbol{r}_\perp,\boldsymbol{n}_\perp)$, $I_R(t,\boldsymbol{r},\boldsymbol{n}) = I_R(x(t),\boldsymbol{r}_\perp,\boldsymbol{n}_\perp)$ The radiance of the actual emitted (*E*) or received (R) pulse sounding pulse.	Wm^2sr^{-1}	(4.3.17)	**4.3.2.2**
	$I'_E(z,\boldsymbol{r},\boldsymbol{n})$, $I'_R(z,\boldsymbol{r},\boldsymbol{n})$	The radiance of the actual emitted (*E*) or received (R) sounding pulse in the equivalent geometry	Wm^2sr^{-1}	(4.3.16)	**4.3.2.2**
	$I'_{E,R}(z,\boldsymbol{r},\boldsymbol{n})$	Shorthand notation for *either* emitted (E) or received (R) radiance of the sounding pulse in the equivalent geometry	Wm^2sr^{-1}	(4.3.16)	**4.3**
	$I'_{E,R+}(0,\boldsymbol{r},\boldsymbol{n})$	Shorthand notation for *either* $\mathrm{I}'_\mathrm{E}(0,\mathbf{r},\mathbf{n})$ or $I'_{R+}(z(t),\boldsymbol{r},\boldsymbol{n}')$	Wm^2sr^{-1}		**4.3**
	$I'_E(z,\boldsymbol{r},\boldsymbol{n_t})$	$I'_E(z,\boldsymbol{r},\boldsymbol{n_t}) = I'_E(z,\boldsymbol{r},\boldsymbol{n})$ when $n_z \approx 1$, $\lvert\mathbf{n}_t\rvert \ll 1$	Wm^2sr^{-1}	After (4.3.25)	**4.3.2.4**
	$I'_E(0,\boldsymbol{r},\boldsymbol{n})$ $I'_R(0,\boldsymbol{r},\boldsymbol{n})$	Normalized characteristic function of the lidar for the emitted (E) and received (R) radiance	Wm^2sr^{-1}	(4.3.16) (4.3.20)	**4.3.2.2**

	A Δ Φ Θ P Ω	***A B C D E F G H I J K L M N O P Q R S T U V W X Y Z***			
Letter	***Symbol***	***Quantity; description***	***SI Units***	***1st Eq. or Fig.***	***1st Sec.***
	$I'_{R+}(z(t), \boldsymbol{r}, \boldsymbol{n}')$	A "fictitious" radiance field describing the receiver sensitivity distribution propagating through the medium $\mathrm{I}'_{R+}(0, \mathbf{r}, \mathbf{n}) \equiv \mathrm{I}'_R(0, \mathbf{r}, -\mathbf{n})\,, n_z \geq 0$	Wm^2sr^{-1}	(4.3.23)	**4.3.2.4**
	$I'_{R+}(z, \boldsymbol{r}, \boldsymbol{n_t})$	$I'_{R+}(z, \boldsymbol{r}, \boldsymbol{n_t}) = I'_{R+}(z, \boldsymbol{r}, \boldsymbol{n})$ when $n_z \approx 1\,, \quad \lvert\mathbf{n}_t\rvert \ll 1$	Wm^2sr^{-1}	After (4.3.25)	**4.3.2.5**
	$I^{up}(t, z = 0, \boldsymbol{r}, \boldsymbol{n})$	$I^{up}(t, z = 0, \boldsymbol{r}, \boldsymbol{n})$, Upwelling (backscattered) arriving at the plane (at $z = 0$) of lidar receiver pupil	Wm^2sr^{-1}	(4.3.15)	**4.3.2.2**
	$I^{up}_{\delta}(t, z = 0, \boldsymbol{r}, \boldsymbol{n})$	I^{up} for the case of an infinitesimal (delta function) pulse	Wm^2sr^{-1}	(4.3.19)	**4.3.2.3**
	$I_R^{norm}(0, \boldsymbol{r}, \boldsymbol{n})$	The normalized characteristic function of the lidar receiver	Wm^2sr^{-1}	(4.3.14)	**4.3.2.2**
	$\hat{I}(z, \mathbf{k}, \mathbf{n}_t)$	frequency domain expression for radiance at z		(4.3.36)	**4.3.2.5**
	$\tilde{I}(z, \mathbf{k}, \mathbf{p})$	source function: $\tilde{I}(z, \mathbf{k}, \mathbf{p}) = \frac{1}{2\pi}\int \exp(i\mathbf{n}_t\mathbf{p})\, \hat{I}(z, \mathbf{k}, \mathbf{n}_t)\, d^2\mathbf{n}_t$		(4.3.47); (4.3.79)	**4.3.2.7**
	$\hat{I}'(z, \mathbf{k}, \mathbf{n}_t)$	$\hat{I}'(\mathrm{z}, \mathbf{k}, \mathbf{n}_t) = \hat{I}(\mathrm{z}, \mathbf{k}, \mathbf{n}_t)\exp\left\{-\int_{z_0}^{z}[i\boldsymbol{n}_t\boldsymbol{k} - c]dz'\right\}$		(4.3.38)	**4.3.2.5**
	$\widetilde{I'}(z, \mathbf{k}, \mathbf{p})$	$\widetilde{I'}(z, \mathbf{k}, \mathbf{p}) = \dfrac{1}{2\pi}\int \exp(i\mathbf{n}_t\mathbf{p})\, \hat{I}'(\mathrm{z}, \mathbf{k}, \mathbf{n}_t) d^2\mathbf{n}_t \quad ,$		(4.3.42)	**4.3.2.5**
	$\widetilde{I'}_{E,R+}(z_0, \mathbf{k}, \mathbf{k}(z))$	$\dfrac{1}{(2\pi)^2}\iint I'_{E,R+}(z_0, \mathbf{r}, \mathbf{n})\ exp\{i\mathbf{r}\mathbf{k} + i\mathbf{n}_t\mathbf{k}(z - z_0)\}\, d^2\mathbf{r}\, d^2\mathbf{n}_t$		(4.3.57)	**4.3.2.5**
J, j					
	$J_0()$	0th order Bessel function of the first kind	---	(4.3.92)	4.3.3.1.3
K, *k*					
	k	Water attenuation coefficient based on the ALB receiver's IFOV	m^{-1}	(3.4.1)	**3.4**
	$\boldsymbol{k}$	Spatial frequency resulting from the Fourier Transform of the two-2D spatial vector, $\boldsymbol{r}$	m^{-1}	(4.3.35)	**4.3.2.5**
	K_d	Diffuse attenuation coefficient (downwelling irradiance)	m^{-1}	(3.3.1)	**3.3.1.2**
	K_{sys}	System attenuation function: $K_{sys} = a + b_b$	m^{-1}	(4.3.13)	**4.3.2.1**

	A Δ Φ Θ P Ω	*A B C D E F G H I J K L M N O P Q R S T U V W X Y Z*			
Letter	***Symbol***	***Quantity; description***	***SI Units***	***1st Eq. or Fig.***	***1st Sec.***
	$K'_{sys}(h_s)$	$K'_{sys}(h_s) = -\ln F_D(h_s)$	m^{-1}	(5.3.4)	**5.3**
M, m					
	MPE	Maximum permissible exposure	Wm^2	(4.1.1)	**4.1.1**
	m	Complex index of refraction	---	(3.3.2)	**3.3.2.1**
		VSF shape parameter from Dolin's model $m = [0.142 - 0.132 \cdot \overline{\cos\theta}]^{-1/2}$	---	(4.3.77)	**4.3.3.1.2**
N, n					
	n	The refractive index (real part)	---	(3.3.2)	**3.3.2.1**
	$\mathbf{n}$	3D unit vector, $\mathbf{n} = \{n_z, n_x, n_y\}$; in Sec. 4.1.4, $\mathbf{n}$ is an upward normal vector at the water surface	---	Figure 3.3.4 (3.3.6)	**3.3.2.1**
	$\boldsymbol{n}'$	3D unit vector for the equivalent geometry	---	(4.3.16)	**4.3.2.2**
	n_1	Index of refraction in medium 1 (real part)	---	(3.2.1)	**3.2.1**
	n_2	Index of refraction in medium 2 (real part)	---	(3.2.1)	**3.2.1**
	$\mathbf{n_0}$	unit vector specifying the incident direction	---	Figure 3.3.4	**3.2.1**
	$\mathbf{n_1}$	Unit vector in the direction of beam propagation	---	(4.3.18)	**4.3.2.2**
	$\mathbf{n_2}$	Unit vector in the direction of scattered radiation	---	(4.3.18)	**4.3.2.2**
	n_a	Index of refraction of air	---	Figure 3.2.1	**3.2.1**
	$\mathbf{n_a}$	specifies the unit vector $\boldsymbol{n}$ in the actual problem	---	before (4.3.60)	**4.3.2.7**
	$\mathbf{n_{a\,t}}$	Specifies $\boldsymbol{n}_t$ for the actual problem; $\mathbf{n}_{at} \equiv (n_{a=}, n_{a\perp})$	---	(4.3.60); Figure 4.3.5	**4.3.2.7**
	$n_{a=}$ and $n_{a\perp}$	Transverse components of the 3D directional vector $\mathbf{n}_a$	---	(4.3.64)	**4.3.2.7**
	n_i	The refractive index (imaginary part); $n_i = a\lambda/4\pi$	---	(3.3.2)	**4.3.2.1**
	$\mathbf{n_t}$	$\boldsymbol{n_t} = \{n_x, n_y\}$; then $\mathbf{n} = \{n_z, n_x, n_y\} = \{n_z, \mathbf{n}_t\}$	---	(4.3.30); Figure 4.3.5	**4.3.2.4**

	A Δ Φ Θ P Ω	*A B C D E F G H I J K L M N O P Q R S T U V W X Y Z*			
Letter	***Symbol***	***Quantity; description***	***SI Units***	***1st Eq. or Fig.***	***1st Sec.***
	n_w	Index of refraction of water	---	Figure 3.2.1	**3.2.1**
	n_z	Component of the unit vector, **n,** oriented along the receiver axis.	---	Figure 4.3.3	**4.3.2.2**
O, o					
	O_IBF	The origin of the IMU body frame (IBF) coordinate system, located at the IMU center	---	(5.1.3)	**5.1.2**
	O_LGF	The origin of the LGF coordinate system	---	Figure 5.1.2	**5.1.3**
	O_SBF	The origin of the sensor-body-frame (SBF) coordinate system	---	Before (5.1.2)	**5.1.2**
	O	Location of the beam axis at the lidar	---	Figure 4.2.4	**4.2.1**
	O_b	Location of the beam axis at the bottom	---	Figure 4.2.4	**4.2.1**
	O_w	Location of the beam axis at the water surface	---	Figure 4.2.4	**4.2.1**
	O'	Location of the lidar receiver in the equivalent geometry	---	Figure 4.2.4	**4.2.1**
P, p					
	$p(t)$	Transmitted pulse shape (time-dependent); Normalized s.t. $\int_0^\infty p(t)\,dt = 1$	s^{-1}	(4.3.6)	**4.2.2**
	$\mathbf{p}$	the frequency domain version of $\mathbf{n}_t$		(4.3.42)	**4.3.2.5**
	P	pitch orientation of the IBF with respect to the LGF	rad, deg	(5.1.5)	**5.1.3**
	$P(r)$	Total measured power at r	W	(3.3.14)	**3.3.2.2**
	P_a	Power absorbed	W	(3.3.4)	**3.3.2.2**
	P_{atm}	Power backscattered by the atmosphere	W	(3.1.5)	**3.1.2**
	P_{bot}	Laser power returning from seafloor	W	(3.4.1)	**3.4**
	$\vec{P}_G$	Vector offset between the laser unit and the IMU body frame with respect to the laser unit coordinate system	m	(6.3.1)	**6.3.2**
	P_i	Incident radiant power	W	(3.3.4); Figure 3.3.8	**3.3.2.2**

	Α Δ Φ Θ P Ω	***A B C D E F G H I J K L M N O P Q R S T U V W X Y Z***			
Letter	***Symbol***	***Quantity; description***	***SI Units***	***1st Eq. or Fig.***	***1st Sec.***
	P_{noise}	Background noise in the lidar return	W	(6.2.1)	**6.2.2**
	P_0	Laser output power; The actual transmitted laser pulse power is $W \cdot p(t)$ with W being the pulse energy (Sec. 2.3.2.2)	W	(3.1.5)	**3.1.2**
	P_s, $P_s(\boldsymbol{n})$	Power scattered (in direction **n)**	W	(3.3.5)	**3.3.2.2**
	P_{signal}	Signal in the lidar return	W	(6.2.1)	**6.2.2**
	PRF	Pulse repetition frequency	s^{-1}	(4.1.1)	**4.1.1**
Q, q					
	Q	Transmitted pulse energy	J	(4.1.1)	**4.1.1**
	Q'	Transmitted pulse energy in the equivalent geometry, $Q^{eq} = Q \cdot \tau_F^2$	J	(4.3.16)	**4.3.2.2**
R, r					
	r	distance	m	(3.3.4); Figure 3.3.6	**3.3.2.2**
		range (distance from the lidar)	m	(4.1.8)	**4.1.3**
	r_a	range (distance from the lidar)	m	(5.1.2)	**5.1.2**
	r_N	the position in the ECEF coordinates, $r_N = \frac{a}{\sqrt{1-e^2 \sin^2 \varphi}}$	m	(5.1.12)	**5.1.5**
	Δr	range resolution	m	(4.1.9)	**4.1.3**
	r_E	Initial sounding beam radius	m	(4.3.60)	**4.3.2.7**
	$r_=$	the separation distance from the principal line of a point on the leading-edge plane	m	(4.3.58); Figure 4.3.4	**4.3.2.6**
	$r_\perp$	The component of **r** perpendicular to the plane of incidence	m	(4.3.64); Figure 4.3.5	**4.3.2.7**
	$\mathbf{r}$	A 2D vector, $\mathbf{r} = (r_x, r_y)$, describing the location on the $\mathbf{n_t}$ plane	m	Figure 4.3.3; (3.3.14)	**4.3.2.2**
	$\mathbf{r_a}$	the 2D coordinate vector perpendicular to the beam axis	m	(4.3.60)	**4.3.2.4**
		Reflectance coefficient (unpolarized light)	---	(3.2.2)	**3.2.1**

	$\Delta \Phi \Theta P \Omega$	A B C D E F G H I J K L M N O P Q R S T U V W X Y Z			
Letter	**Symbol**	**Quantity; description**	**SI Units**	**1st Eq. or Fig.**	**1st Sec.**
	R	roll orientation of the IBF with respect to the LGF	rad, deg	(5.1.5)	**5.1.3**
	$R(t)$	The channel response to lidar pulse (including laser pulse and electronic response), or **effective sounding pulse shape.** $R(t) \equiv p(t) * \omega(t)$.	s^{-1}	(4.2.7); (4.2.8)	**4.2.2; 4.3.1**
	$R_{\parallel}$	Reflection coefficient parallel polarized radiation	---	(3.2.2)	**3.2.1**
	$R_{\perp}$	Reflection coefficient perpendicular polarized radiation	---	(3.2.2)	**3.2.1**
	R_{∞}	Remote sensing reflectance over optically deep waters	---	(3.4.5)	**3.4.3**
	R_b	Remote sensing bottom reflectance	sr^{-1}	(3.4.5)	**3.4.3**
	R_{RS}	Remote sensing reflectance	sr^{-1}	(3.4.5)	**3.4.3**
	$R_{yaw,pitch,roll}$	the rotation matrix between the Inertial Navigation System (INS) body and the mapping frame	---	(6.3.1)	**6.3.1**
	$R_{\alpha,\beta}$	the scan angle rotation in the laser sensor frame	---	(6.3.1)	**6.3.1**
	$R_{\Delta\omega,\Delta\varphi,\Delta x}$	the boresight rotation matrix between the laser frame and the INS body frame	---	(6.3.1)	**6.3.1**
	R_{∞}	Remote sensing reflectance over optically deep waters	sr^{-1}	(3.4.5)	**3.4.3**
	$\boldsymbol{R}_{LGF}^{ECEF}$	rotation matrix that transforms an arbitrary position vector in LGF to the position vector in ECEF	-	(5.1.11)	**5.1.5**
	$\boldsymbol{R}_{O\_LGF}^{ECEF}$	rotation matrix to transform the geodetic position of O_LGF into the position in ECEF coordinates	-	(5.1.12)	**5.1.5**
	$\boldsymbol{R}_{SBF}^{IBF}$	rotation matrix to transform $\boldsymbol{X}_P^{SBF}$ to $\boldsymbol{X}_P^{IBF}$	-	(5.1.3)(5.1.4)	**5.1.2**
	$\boldsymbol{R}_{IBF}^{LGF}$	rotation matrix to transform $\boldsymbol{X}_P^{IBF}$ to $\boldsymbol{X}_P^{LGF}$	-	(5.1.5)	**5.1.3**
	$R_{yaw,pitch,roll}$	boresight matrix between the laser frame and the INS body frame	---	(6.3.1)	**6.3.2**
	$R_{\alpha,\beta}$	scan angle rotation in the laser sensor frame	---	(6.3.1)	**6.3.2**

	Α Δ Φ Θ P Ω	*A B C D E F G H I J K L M N O P Q R S T U V W X Y Z*			
Letter	***Symbol***	***Quantity; description***	***SI Units***	***1st Eq. or Fig.***	***1st Sec.***
	$R_{\Delta\omega,\Delta\phi,\Delta\kappa}$	boresight matrix between the laser frame and the INS body frame	---	(6.3.1)	**6.3.2**
	$R_{\Omega,\Phi,\mathrm{K}}$	Rotation matrix for the co-alignment between test strips	---	(6.3.2)	**6.3.2**
S, s					
	s	the 2D Cartesian coordinate vector in the plane parallel to the water surface	m	Before (4.3.64); Figure 4.3.5	**4.3.2.4**
	$s_{=}$	The component of **s** parallel to the plane of incidence	m	(4.3.64)	**4.3.2.4**
	$s_{\perp}$	The component of **s** perpendicular to the plane of incidence	m	(4.3.64)	**4.3.2.4**
	S	Scale factor for geo-location	---	(6.3.2)	**6.3.2**
	$S^{back}(t)$	Power of the elastic backscattering signal from the water column.	W	(4.3.12)	**4.3.2.1**
	$S_{\delta}(t)$	The "impulse response function" (ImpRF). The input optical signal - temporal distribution of signal light power at the detector input FOR DELTA_SHAPED transmitted pulse	W	(4.2.6)	**4.2.2**
	$S_{\delta}^{back}(t)$	Power of the elastic backscattering signal from the water column for the infinitesimal pulse.	W	(4.3.20)	**4.3.2.3**
	$S_p(t)$	The "environmental response function" (EnvRF). The actual input optical signal - temporal distribution of signal light power at the detector input FOR ACTUAL transmitted pulse of the shape $p(t)$	W	(4.2.6)	**4.2.2**
	S_{const}	A constant optical signal	W	(4.3.4)	**4.3.1**
	$S_R(t)$	The “real waveform” retrievable from the output lidar signal	W	(4.2.8)	**4.2.2**
	$S_R^{exp}(t)$	Experimental optical signal, the “real” waveform	W	(4.3.12)	**4.3.1**
	$S_R^{sim}(t)$	Simulated signal	W	(5.2.2)	**5.2**
	$S_Q^{calib}(t)$	Calibration input optical signal	W	(4.4.4)	**4.4.2**
	SW	Swath width	m	(4.1.2)	**4.1.2**

	A Δ Φ Θ P Ω	*A B C D E F G H I J K L M N O P Q R S T U V W X Y Z*			
Letter	***Symbol***	***Quantity; description***	***SI Units***	***1st Eq. or Fig.***	***1st Sec.***
T, t					
	t	time	s	(4.1.8)	**general**
	Δt	Time interval between consecutive observations	s	(4.1.9)	**4.1.3**
		Time difference (Δt) between two peak positions or half-peak positions	s	(4.5.1)	**5.5.2**
	t_-	Time corresponding to a near-surface horizon deep enough to obviate the need to account for surface effects.	s	(5.2.3)	**5.2**
	t_+	Time corresponding to a near-bottom horizon for which bottom reflection is still undetected.	s	(5.2.3)	**5.2**
	t_a	time of travel from O_LGF to the first peak of the waveform	s	Figure 5.1.2	**5.1.4**
	t_i	time of travel of experimental waveforms within the interval, $t_- \leq t_i \leq t_+$	s	Below (5.2.3)	**5.2**
	Δt_{HP}^{bot}	Bias of the estimated location of the bottom relative to the true location using the half peak (HP) algorithm	m	Figure 5.5.4	**5.5.2**
	Δt_{P}^{bot}	Bias of the estimated location of the bottom relative to the true location using the peak (P) algorithm	m	Figure 5.5.4	**5.5.2**
	Δt_{HP}^{surf}	Bias of the estimated location of the water surface relative to the true location using the half peak (HP) algorithm	m	Figure 5.5.4	**5.5.2**
	Δt_{P}^{surf}	Bias of the estimated location of the surface relative to the true location using the peak (P) algorithm	m	Figure 5.5.4	**5.5.2**
	t_w	time of travel from the first peak of the waveform to the bottom point, O_b	s	Figure 5.1.2	**5.1.4**
	t^{bot}	time the central part of the pulse arrives at the bottom	s	Figure 4.2.4	**4.2.1**
	Δt^{bot}	bottom-reflected pulse duration	s	Figure 4.2.4	**4.2.1**
	t^{sc}	$t^{sc}(b_s, \Theta_R) \equiv 2h_s^{max}(b_s, \Theta_R)/nc$, the upper limit of the backscattered signal argument that corresponds to a negligible impact of forward scattering	s	(5.3.5)	**5.3**
	t^{sf}	time that light from the central part of the pulse front, after reflection from the water surface, arrives at the receiver	s	Before (4.2.4); Figure 4.2.3	**4.2.1**
	Δt^{sf}	surface-reflected pulse duration (geometrical stretch of the surface-reflected pulse)	s	(4.2.4); Figure 4.2.3	**4.2.1**

	A Δ Φ Θ P Ω	*A B C D E F G H I J K L M N O P Q R S T U V W X Y Z*			
Letter	***Symbol***	***Quantity; description***	***SI Units***	***1st Eq. or Fig.***	***1st Sec.***
	$T(H,\lambda)$	Two-way atmospheric transmission term	---	(3.1.1)	**3.1.1**
U, u					
V, v					
	v	velocity	kts, ms^{-1}	(4.1.8)	**4.1.4**
	V_r	Visual range: the distance at which an object can be seen with the unaided eye. The visual range is determined only by the contrast of an object with its background,	m	(3.1.3)	**3.1.1**
	V	volume	m^3	(3.3.6); Figure 3.3.7	**2.3.2.2**
	V_{lg}	volume concentrations for large suspended particles	m^{-1}	(5.2.7)	**5.2**
	V_{sm}	volume concentrations for small suspended particles	m^{-1}	(5.2.8)	**5.2**
	v_{plat}	airborne platform velocity	kts	(4.1.4)	**4.1.2**
W, w					
	W	cluster constant: $W = \exp(-2\tau_a)/(H_s n_w + h_s)^2$	m^{-2}	(3.4.2)	**3.4**
X, x					
	Δx	along track sample spacing	m	(4.1.4)	**4.1.2**
	$(x_{q_i}, y_{q_i}, z_{q_i})$	Vector position of a point cloud	m	(6.3.2)	**6.3.2**
	$(X_T, Y_T, Z_T)^T$	translation vector between test strips	m	(6.3.2)	**6.3.2**
	$\boldsymbol{X}_{O_w}^{ECEF}$	Position vector in ECEF coordinates	m	(5.1.13)	**5.1.5**
	$\boldsymbol{X}_{O\_LGF}^{ECEF}$		m	(5.1.13)	**5.1.5**
	$\boldsymbol{X}_{O_{SBF}}^{IBF}$	lever-arm vector to the SBF origin in the IMU Body Frame (IBF)	m	(5.1.13)	**5.1.2**

	$A\,\Delta\,\Phi\,\Theta\,P\,\Omega$	*A B C D E F G H I J K L M N O P Q R S T U V W X Y Z*			
Letter	***Symbol***	***Quantity; description***	***SI Units***	***1st Eq. or Fig.***	***1st Sec.***
	$\boldsymbol{X}_{O_w}^{IBF}$	position vector to a surface lidar return point, O_w, in a local geodetic frame (LGF)	m	(5.1.6)	**5.1.3**
	$\boldsymbol{X}_{O_w}^{LGF}$	position vector to a surface lidar return point, O_w, in a local geodetic frame (LGF)	m	(5.1.6)	**5.1.3**
	$\boldsymbol{X}_{P_b}^{LGF}$	position vector to a bottom lidar return point, O_b, in a local geodetic frame (LGF)	m	(5.1.10)	**5.1.4**
	$\boldsymbol{X}_{O_w}^{SBF}$	Position vector of the lidar point, O_w, in the Sensor Body Frame (SBF)	m	(5.1.3)	**5.1.2**
	$\vec{X}_G$	Vector ground position	m	(6.3.1)	**6.3.2**
	$\vec{X}_0$	Vector from the origin of the ground coordinate	m	(6.3.1)	**6.3.2**
Y, y					
	Δy	cross-track sample spacing	m	(4.1.5)	**4.1.2**
Z, z					
	z	Distance from the lidar	m	(3.1.1)	**3.1.1**
	z	water depth variable	m	(3.3.1)	**3.3.2**
	z	distance along the slant path	m	Figure 4.3.3	**4.3.2.2**
	z_0	the lidar altitude above the interface in the equivalent problem, $z_0 = H'$	m	Before (4.3.4);	**4.3.2.5**
	$z(t)$	Total distance of the source from the leading edge, $z(t) \equiv ct/2n$	m	(4.3.58)	**4.3.2.6**
	z_a	Distance along the beam axis from the pupil plane	m	Figure 4.3.4; (4.3.60)	**4.3.2.6**
	z_t	the in-water path of a ray traveling along the lidar axis	m	(4.3.57)	**4.3**
	$z_w(t, r_=)$	distance covered by a ray traveling from the water surface to the leading-edge plane along a path that is parallel to the lidar axis	m	(4.3.58)	**4.3.2.6**
	$z_{sf}(\boldsymbol{r})$	notates when the variable $\{z(r)\}$ lies exactly on the water surface.	m	(3.1.1)	**4.3.2.4**